Bulletin of the Mineral Research and Exploration

http://bulletin.mta.gov.tr

Holocene activity of the Orhaneli Fault based on palaoseismological data, Bursa, NW Anatolia

Volkan ÖZAKSOY[a*], Hasan ELMACI[b], Selim ÖZALP[c], Meryem KARA[d] and Tamer Y. DUMAN[e]

[a]*Akdeniz University, Faculty of Engineering, Department of Geological Engineering 07058 Konyaaaltı Antalya Turkey. orcid.org/0000-0002-8126-8134.*
[b]*General Directorate of Mineral Research and Exploration, Directorate of Geological Studies, 06800 Çankaya/Ankara. orcid.org/0000-0002-5076-1153.*
[c]*General Directorate of Mineral Research and Exploration, Directorate of Geological Studies, 06800 Çankaya/Ankara. orcid.org/0000-0002-6755-4206.*
[d]*General Directorate of Mineral Research and Exploration, Eastern Mediterranean Regional Directorate 01360 Çukurova/Adana. orcid.org/0000-0002-9143-815X.*
[e]*Fugro Sial Earth Sciences Consultancy and Engineering Ltd. 06690 Çankaya/Ankara. orcid.org/0000-0003-3556-2217.*

Research Article

Keywords:
Orhaneli fault, palaeoseismology, Holocene, Biga Peninsula, NW Anatolia.

ABSTRACT

Orhaneli Fault is 30 km long, right-lateral strike-slip fault with dominant reverse component located in the Biga Peninsula. This fault controls the southern margin of the Quaternary Orhaneli Basin. Additionally, it cuts the metamorphic rocks of the Tavşanlı Zone, Cretaceous ophiolitic units and Neogene/Quaternary sediments, and can be easily recognized on aerial photographs and in the field due to linearity and fault scarps. Elongated ridges, offset valleys and fault saddles observed along the fault are important geomorphological features indicating fault activity. This study presents the results of the first palaeoseismological study on the Orhaneli Fault. Two trenches were excavated along the fault. These trenches, named Serçeler and Kusumlar, exhibited that metamorphic rocks of the Tavşanlı Zone were thrust onto Quaternary sediments by the fault. The study encountered evidences of four large earthquakes accompanied by surface rupture in Quaternary. The results of Serçeler trench indicated the older earthquake occurred between 22,000±3,200 BC and 6,600±800 BC, and the most recent earthquake occurred before 770-415 BC. The Kusumlar trench data showed that the older earthquake occurred between 6,660 BC and 3,085 BC, and the most recent event in the period after 650 AD. Any interpretation could not be made about the recurrence period between palaeoearthquakes. In this study, Holocene activity on the Orhaneli Fault was proven. If this fault, with 30 km total length comprising two segments, ruptured as a single piece, it has the potential to produce an earthquake with Mw=6.9.

Received Date: 28.05.2017
Accepted Date: 29.09.2017

1. Introduction

Turkey is one of the world's most seismically active country, located within the Alpine-Himalayan Orogenic Belt. The Anatolian platelet is moving westward along the North Anatolian and East Anatolian Faults and rotating in anticlockwise direction due to the northward movement of the Arabian plate (Figure 1A; McKenzie, 1972; Dewey and Şengör, 1979; Şengör et al., 1985). After this orogenesis, neotectonic period began nearly 12 million years ago in the Middle Miocene (Barka and Hancock, 1984; Şengör et al., 1985) and Anatolia became one of the most seismically active regions in the Eurasian continent. The tectonic escape of the Anatolian platelet linked to the closure between the Arabian and Eurasian plates caused the formation of four neotectonic provinces (Figure 1A) (Şengör et al., 1985). These are (1) the Eastern Anatolian contractional province, (2) the Northern Anatolian strike-slip province, (3) the Central Anatolian "Ova" province and (4) the Western Anatolian extensional province (Şengör et al., 1985).

* *Corresponding author: Volkan ÖZAKSOY, volkano@akdeniz.edu.*
http://dx.doi.org/10.19111/bulletinofmre.413248

The Southern Marmara region, containing the Biga Peninsula, represents a transition zone between the North Anatolian Fault System and the West Anatolian extensional province (Barka, 1992; Barka and Kadinsky-Cade, 1988; Dewey and Şengör, 1979; Emre et al., 2012; Emre et al., 2013; Şaroğlu et al., 1992; Şengör et al., 2005) (Figure 1A, B). The tectonic structures within the South Marmara region are generally represented by right-lateral strike-slip faults, forming a wide arc geometry expanding toward the south (Emre et al., 2011*a*, *b*, 2012, 2013) (Figure 1B). The Orhaneli Fault forms the eastern wing of this arc structure together with the Mustafakemalpaşa and Manyas Faults (Emre et al., 2011*a*, *b*) (Figure 1B). Orhaneli Fault is first shown as an active, right-lateral strike-slip fault on the Turkish Active Fault Map by Emre et al. (20111*a*, *b*, 2013). This study was aimed to prove its Holocene activity as part of the Turkish Palaeoseismology Research Project (TURKPAP). In this palaeoseismological study, structural geology, sedimentology, geomorphology and radiocarbon/OSL dating methods were applied. It is expected that this study and other previous studies will help to understand the seismicity of the region (Kop et al., 2016; Kürçer et al., 2017; Özalp et al., 2013, 2016*a*, *b*) and the seismic hazard assessment.

2. Regional Geology

The study area is located nearly 60 km south of Bursa (Figure 1B). In the region between Bursa and Orhaneli, there is a large variety of geological units. The most important reason for this variety is that the area contains two tectonic units separated from each other by the Izmir-Ankara Suture Zone (IASZ) (Okay and Tüysüz, 1999). These tectonic units are represented by rocks of Sakarya and Tavşanlı zones. The lithological units observed commonly between Orhaneli and Bursa may be separated into four groups.

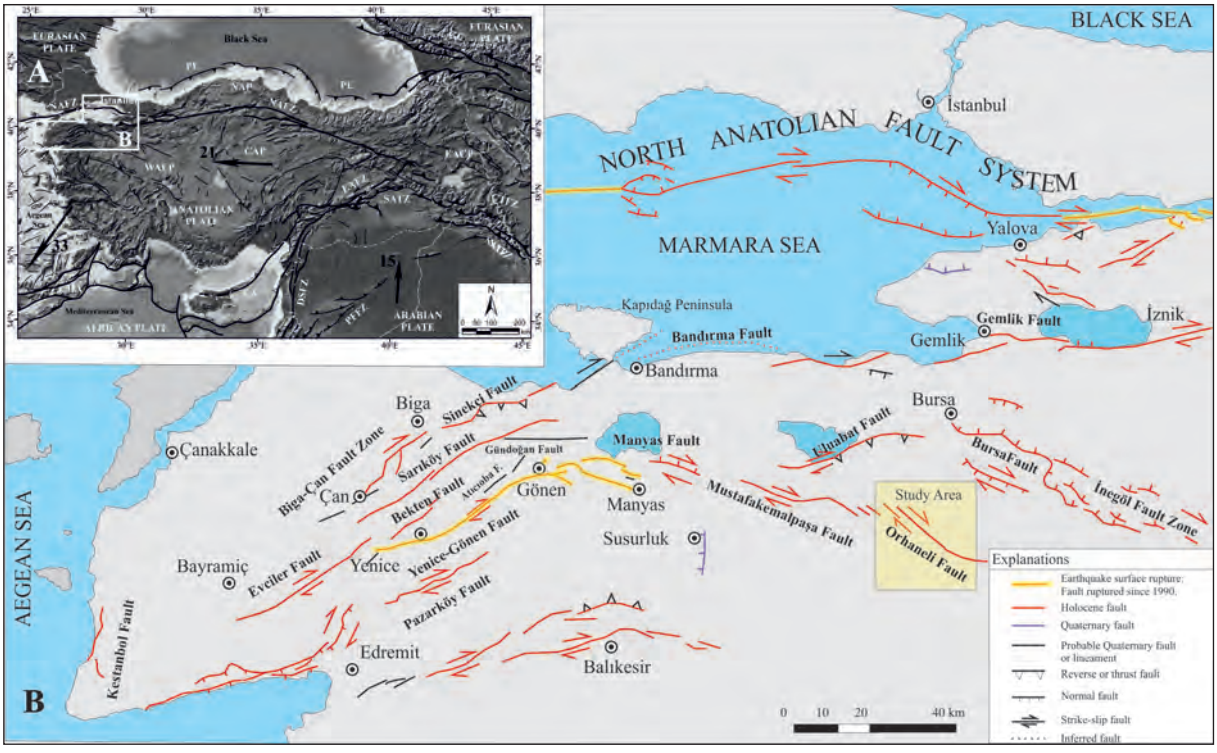

Figure 1- A) Simplified active tectonic map of Turkey and surroundings. Active faults in Turkey taken from Emre et al. (2013), active faults from surrounding area taken from Duman et al. (2016) and references in both. Neotectonic regions taken from Şengör et al. (1985). Subduction zones shown by thick lines and open triangles, with triangles representing the direction of subduction. Thick lines with black filled triangles are thrust faults, black lines with open triangles show reverse faults. Large black arrows indicate the motion rates (mm/yr) for plates compared to the Eurasian Plate (calculated from GPS) (Reilinger et al., 2006). AA: Aegean Arc, CY: Cypriot Arc, DSFZ: Dead Sea Fault Zone, EAFZ: East Anatolian Fault Zone, NAFZ: North Anatolian Fault Zone, SEATZ: South East Anatolian Thrust Zone, WAER: West Anatolian Extensional Region, CAR: Central Anatolian Region, EACR: East Anatolian Compression Region, NAR: North Anatolian Region, PFCZ: Palmira Fault Curve Zone. GeoMap Application data used for digital elevation model. B) Active fault map for the Marmara Region and the study area (adapted from Emre et al., 2013).

a) North of the IASZ, rocks from the Sakarya Zone with ages ranging from Palaeozoic to Cretaceous.

b) Ophiolitic rocks from the northern branch of the Neotethys Ocean

c) Metamorphic and granitic rocks of Tavşanlı Zone south of the İASZ belonging to the Anatolide-Tauride Block

d) Sedimentary and volcanic rocks overlying or cutting these units of Miocene and younger ages.

The rocks outcropping and forming the basement in the area of the Orhaneli Fault belong to the Tavşanlı Zone. These were formed by burial to more than 60 km long and blueschist facies metamorphism on the northern edge of the Anatolide-Tauride Block linked to ophiolite obduction in the Late Cretaceous (Okay et al., 1998). The blueschist rocks commonly observed in the Orhaneli region are mainly represented by mica schist, phyllite and metabasites and are called the Orhaneli Group (Okay, 1985) (Figure 2). The Triassic metamorphic series at the base of the Orhaneli Group is represented by mica schists called the Kocasu formation (Okay, 2004). Kocasu formation is overlain by a marble series with kilometres of thickness. This marble was first called the İnönü Marble by Servais (1982) and is represented by white-grey coloured, occasionally banded carbonates. The age of this formation varies from Late Triassic to Cretaceous (Kaya et al., 2001).

Ophiolitic rocks (Burhan Ophiolite) are commonly observed north and south of Orhaneli and mainly represented by peridotite, gabbro, pyroxenite and diabase (Okay et al., 1998). The Burhan Ophiolite represents mantle and lower crust of Tethys oceanic lithosphere and is reported to have been emplaced on the Anatolide-Tauride platform in the Late Cretaceous (Okay et al., 1998; Okay, 2011). These rocks are tectonically located above the units of Tavşanlı Zone. These units are also cut by the Early Eocene Orhaneli Granodiorite (Harris et al., 1994) (Figure 2).

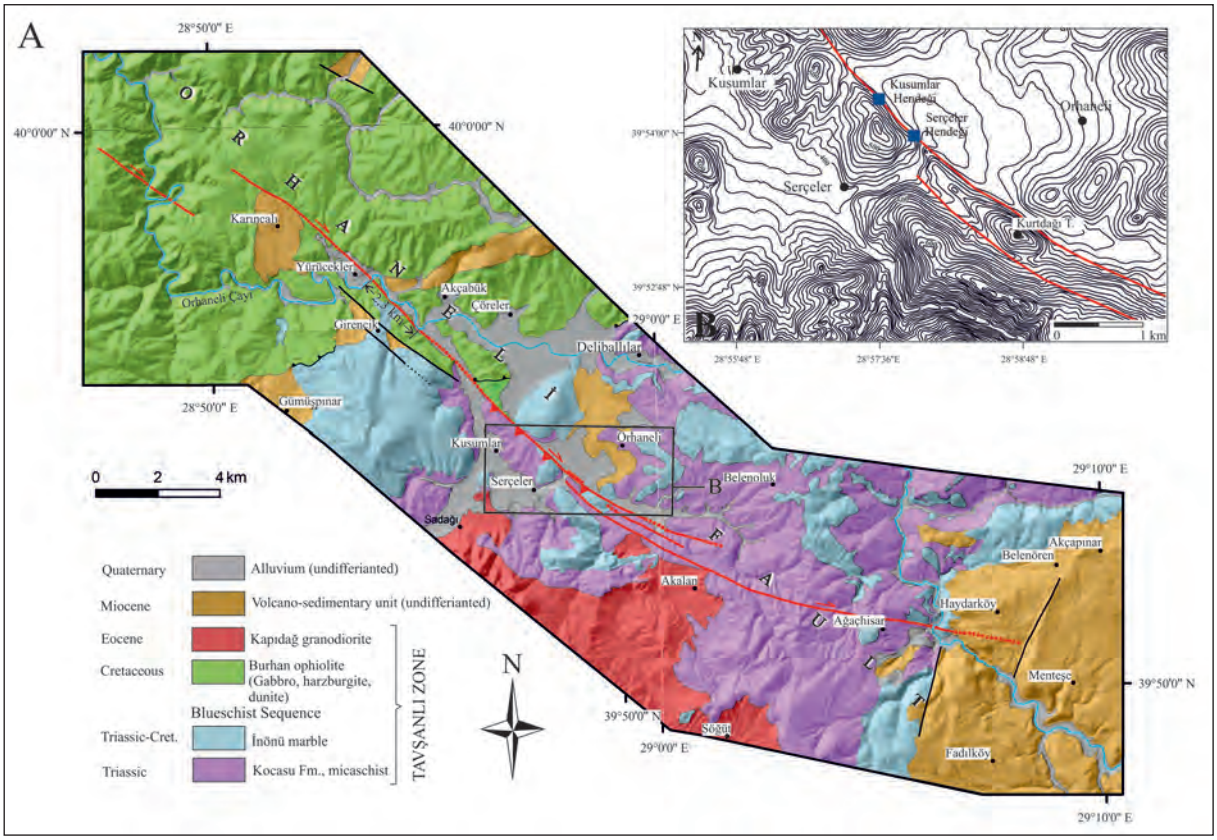

Figure 2- A) Geologic map of Orhaneli Fault and close surroundings (Map: adapted from Konak (2002), Türkecan and Yurtsever (2002) and MTA digital database; Stratigraphy: taken from Okay et al. (1998). B) Fault morphology and trench locations.

Neogene-Quaternary sediments unconformably overlie both the ophiolitic rocks and the rocks belonging to the Tavşanlı Zone (Figure 2). Neogene units are generally represented by sedimentary rocks deposited in lacustrine and fluvial facies, containing occasional lignite beds with economic importance. Quaternary units outcrop in a broad area south of Orhaneli. The Quaternary sediments generally comprise fluvial, floodplain and slope debris.

3. General Characteristics of Orhaneli Fault

Orhaneli Fault located in the South Marmara Region forms the eastern limb of the Manyas Bend together with the Mustafakemalpaşa Fault (Emre et al., 2011*a, b*) (Figure 1B). The geological fault was first shown on a geological map after work by Okay et al. (1998) though its character was undetermined. This fault as active fault was first named by Emre et al. (2011, 2013) and is shown on the Turkish Active Fault Map (Figure 1B).

The Orhaneli Fault has NW-SE orientation and 30 km length on the revised Turkish Active Fault Map (Emre et al., 2013). The southeast section of the fault between Menteşe and Akalan villages has N80°W orientation, making a slight bend to the northwest with N50°W orientation and ends near Karıncalı village in the NW (Figure 2A).

The fault comprises two geometrically separated segments (Figure 2A). These are the 19 km-long NW segment south of Orhaneli which links with a right extensional stepover to the 13 km-long second segment in the SE. In this section, both segments overlap eachother by nearly 1.5 km (Figure 2A). In the NW, the fault links to Mustafakemalpaşa Fault with a series of right-lateral faults varying in length from 4 to 5 km within a zone of 11 km wide (Emre et al., 2011*a, b*) (Figure 1B and 2A).

The most significant data related to Quaternary activity of the Orhaneli Fault is a 2.3 km of right-lateral offset observed in Orhaneli stream (Figure 2A, B). Further northwest, the same stream is similarly identified to have 2.5 km of right lateral offset due to the Mustafakemalpaşa Fault (Emre et al., 2011*b*).

In terms of morphology, the fault is clearly observed on aerial photographs and in the field due to continuous lineament and fault scarps, especially in the section north of Yürücekler and Serçeler villages. Nearly 2 km east of Serçeler village, the long axis of Kurtdağı Hill has an elongated ridge appearance parallel to the strike of the fault (Figure 2B).

4. Seismicity in the Historical and Instrumental Periods

The devastated earthquakes occurring in South Marmara region in the historical period (<1900) appear to be distributed along and around active faults north of the study area (Table 1 and Figure 3). There is no historical earthquake record related to the Orhaneli Fault in the historical period. Additionally historical earthquakes occurred in Mustafakemalpaşa in 1850 and 1851 appear to be the closest historical earthquakes to the Orhaneli Fault (Table 1).

When earthquake records of the instrumental period (1900-2012) (Kadirioğlu et al., 2016) are considered, small and moderate magnitude earthquake activity is observed in the surrounding area (Figure 3). There is not any earthquake activity on the Orhaneli Fault. However, in the vicinity with left step-over structure between Mustafakemalpaşa Fault in the west, there is earthquake activity with magnitude less than 5. In the east, in the section between Orhaneli and Oylat Faults, especially around Domaniç, the density of earthquakes with moderate magnitude varying between 5 and 6 is noteworthy. According to instrumental period records, the largest earthquake occurred in the region is the 6 October 1964 Manyas Earthquake (Ms: 6.9).

Table 1- Historical period earthquake record from the South Marmara Region (modified from Tan et al., 2008). References in the table: *a)* Ergin et al., 1967; *b)* Ergin et al., 1971; *c)* Soysal et al., 1981; *d)* Ambraseys and Finkel, 1991; *e)* Ambraseys and Jackson, 1998; *f)* Kondorskaya and Ulomov, 1999; *g)* Ambraseys and Jackson, 2000; *h)* Ambraseys, 2002.

No	Date	Coordinates		Magnitude (M)	Intensity (Io)	Location	References*
		Latitude (N)	Longitude (E)				
1	***24.11.29***	40.50	28.90	6.3	***IX***	İznik, İzmit	*a*
2	***? .?.30***	40.50	29.50	6.6	***?***	İznik-Yalova	*f*
3	***10.11.117***	40.40	27.80	7.0	***VII***	Erdek, Kapıdağ Yarımadası	*c, d, h*
4	***03.05.170***	40.10	28.00	6.6	***IX***	Bandırma, Erdek	*a, c*
5	***02.12.362***	40.42	29.72	6.9	***IX***	İznik	*a*
6	***11.10.368***	40.42	29.72	6.9	***VII***	İznik	*c, d, e, h*
7	***?.11.368***	40.10	27.80	6.8	***VIII***	M. Kemalpaşa	*c, d, h*
8	***07.04.460***	40.39	27.80	6.9	***?***	Cyzicus (Erdek)	*a, d, e, h*
9	***?.?.464***	40.40	27.85	7.4	***VIII***	Cyzicus (Erdek), Bandırma	*a, c*
10	***06.09.543***	40.39	27.80	6.9	***IX-X***	Cyzicus (Erdek)-Bandırma?	*a, c, d*
11	***23.09.1064***	40.40	28.90	6.9	***IX***	İznik, Bandırma, Cyzicus (Erdek)	*a, c, h*
12	***26.11.1143***	40.18	29.06	6.0	***?***	Bursa	*B*
13	***15.03.1419***	40.50 40.40	30.50 29.30 (h)	7.0<Ms<7.8 7.2 (*h*)	***?***	Geyve ? Bursa (h)	*e, h*
14	***10.05.1556***	40.30	27.80	7.2	***VIII***	Erdek, Edincik	*a, d, g, h*
15	***?.?.1674***	40.18	29.10	6.0	***?***	Bursa	*a, c*
16	***25.05.1719***	40.70	29.80	7.4	***?***	İzmit	*g*
17	***19.04.1850***	40.10	28.30	6.1	***?***	Mustafakemalpaşa	*g*
18	***?.?.1851***	40.03	28.40	6,0	***?***	Mustafakemalpaşa	*f*
19	***28.02.1855***	40.00	28.50	7.4	***?***	Ulubat	*e*
20	***11.04.1855***	40.20	29.10 (*c*)	6.6 (*e*)	***X (c)***	Bursa	*c, d, e*

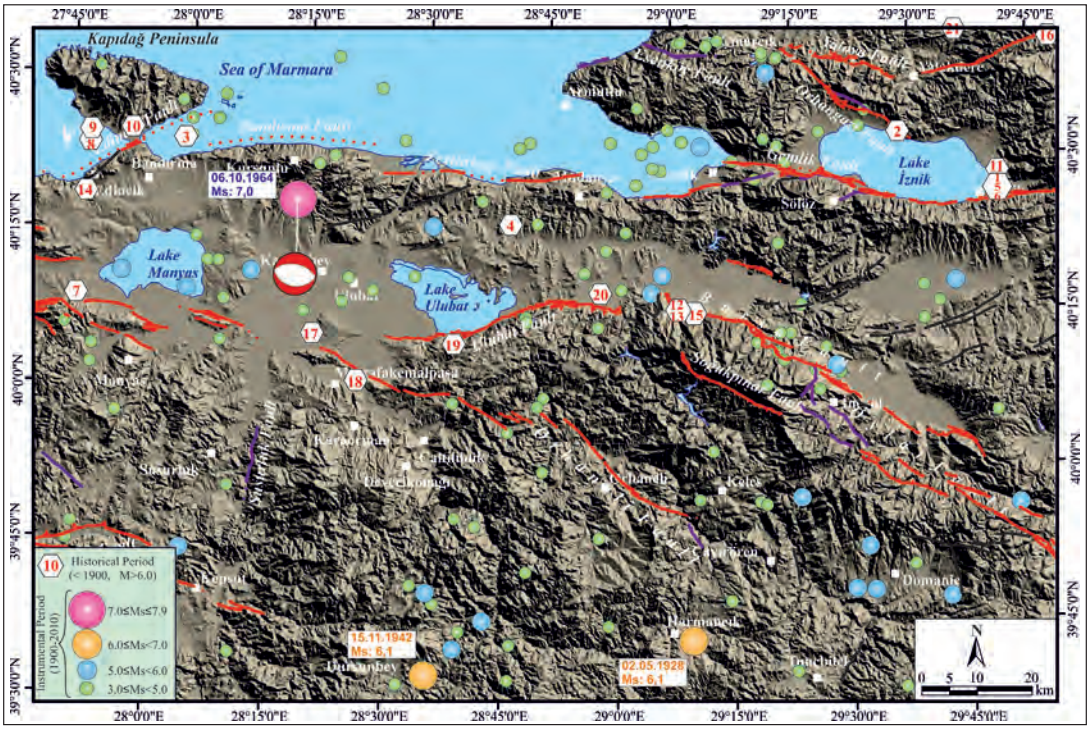

Figure 3- Earthquakes from the historical (see Table 1) and instrumental periods (Kadirioğlu et al., 2016) on the Active Fault Map (Emre et al., 2013). Solution of the 1964 Manyas Earthquake taken from Taymaz et al. (1991).

5. Palaeoseismological Studies

Before palaeoseismological trench studies, aerial photograph analysis of 1: 35.000 scale photographs and later field studies of appropriate areas for excavation determined on aerial photographs were carried out. In the field, there was no data found about surface rupture morphology. As a result, in areas determined by aerial photograph and field studies, geomorphological structures related to Holocene activity were assessed. In the 1 to 2 km section of the Orhaneli Fault between Kusumlar and Serçeler villages, fault morphology is clearly observed (Figures 2 and 4). Therefore, the boundary between Quaternary basin and metamorphic bedrocks belonging to the Tavşanlı Zone outcropping in the southwest Orhaneli was chosen as the target site for excavation (Figure 2 and 4).

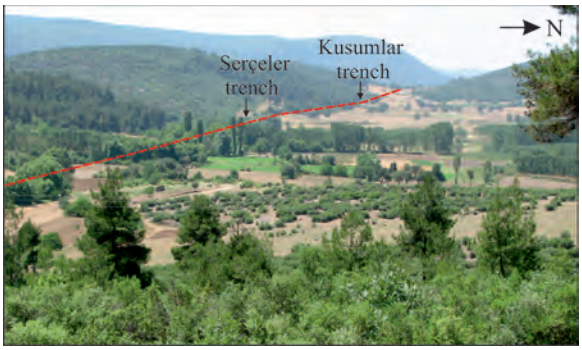

Figure 4- Trench locations, fault scarps and topographic saddle structure of the Orhaneli Fault (looking SW).

In two different areas along the Orhaneli Fault, trenches were opened perpendicular to the fault with depth from 3 to 3.5 metres. The trench walls were gridded at one metre intervals in horizontal and vertical directions, and detailed cross-section drawings made to determine the stratigraphy of the trench walls. Using tectono-stratigraphic relations, the earthquake horizons were defined. To clearly understand the stratigraphy of the trenches and the earthquake horizons, samples of charcoal and organic materials were taken from stratigraphic units in the trench walls. These samples were dated with the AMS - ^{14}C (radiocarbon) method at BETA Analytic Laboratory in Miami (Florida, USA) (Table 2). Additionally, from some units where AMS - ^{14}C samples could not be found, OSL (optically stimulated luminescence) samples were taken and age dating was performed at the Nuclear Sciences Institute of Ankara University (Table 3).

Table 2- Radiocarbon ages (^{14}C) obtained from Serçeler and Kusumlar trenches.

Sample No	Laboratory No (BETA)	Stratigraphic Unit	Sample Material	Measured Radiocarbon Age (BP)	$\delta^{13}C$ (‰)	Corrected radiocarbon Age (BP)	Corrected Age (2σ)
SERÇELER TRENCH							
OSCNW-01	390691	Unit 7	Organic Sediment	2530±30	-28,5	2470±30	BC 770 - 415
KUSUMLAR TRENCH							
OK2-C-E01	390692	Unit 6	Coal Sediment	1220±30	-23,9	1240±30	AD 680 - 880
OK2-C-W02	390693	Unit 6	Organic Sediment	NA	NA	1670±30	AD 265 - 275 330 - 420
OK2-C-W06	390694	Unit 6	Organic Material	1340±30	-22,9	1370±30	AD 640 - 675
OK2-C-W08	390695	Unit 6	Coal Sediment	1290±30	-24,3	1300±30	AD 660 - 770
OK2-C-W09	390696	Unit 5	Coal Sediment	4380±30	-26,3	4360±30	BC 3085- 3065

Table 3- OSL (Optically Stimulated Luminescence) ages obtained from Serçeler and Kusumlar trenches.

Sample No.	Stratigraphic Unit	Depth (m)	Conjugate dose (Gy)	OSL age (1000 yrs)
OSRLONW-02	Unit 3	0,70	76,3 ± 8,9	24,0 ± 3,2
OSRLONW-03	Unit 4	0,43	28,3 ± 2,2	8,7 ± 0,8
OSRLONW-05	Unit 2	1,95	133,4 ± 12,2	79,7 ± 9,2
OKSLONW-06	Unit 3a	0,72	33,5 ± 4,9	11,6 ± 1,8
OK2-O-W02	Unit 3b	2,55	27,4 ± 1,8	8,6 ± 1,2

5.1. Serçeler Trench

The trench area was located nearly 1.2 km north of Serçeler village (Figures 2 and 4). The 12 m long, 4 m wide and 3 m deep trench was excavated perpendicular to the fault strike. The trench was opened on the topographic slope break considered to be equivalent to the fault scarp at the boundary between metamorphic rocks of the Tavşanlı Zone and Quaternary sediments (Figures 4 and 5A). Microtopographic mapping was completed using a total station at 20 cm contour intervals over nearly 15.000 m^2 area near the excavation site and surroundings (Figure 5B). The fault follows maximum topographic slope break.

The most prominent event in the Serçeler trench is that metamorphic rocks of the bedrock thrusted over Quaternary units within the nearly 5 m wide fault zone (Figures 6 and 7). The rake angle of fault striations were generally 70° and higher. As a result,

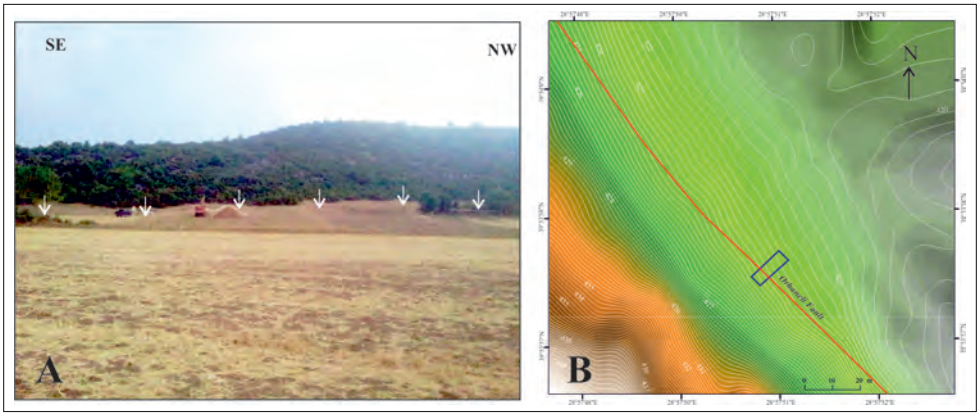

Figure 5- A) Excavation area and fault scarp for Serçeler Trench. White arrows indicate the extension of the fault in the field. B) Microtopographic map of the Serçeler trench area. Contour interval is 20 cm.

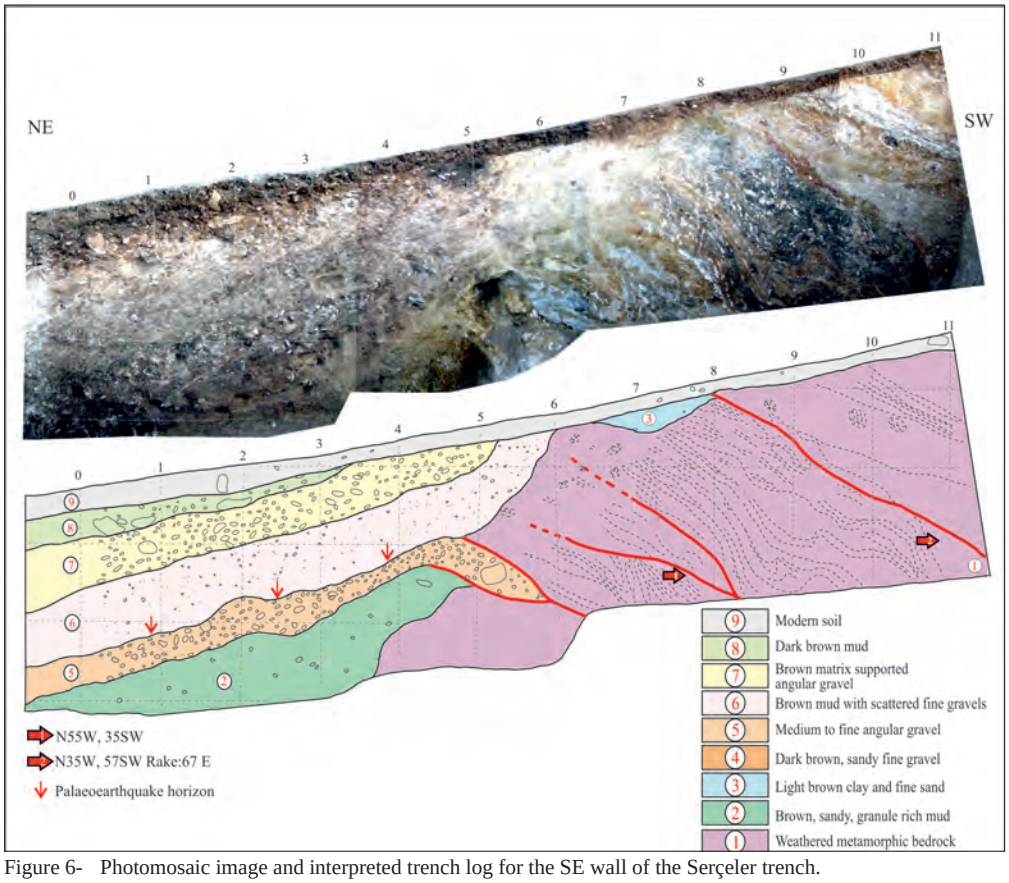

Figure 6- Photomosaic image and interpreted trench log for the SE wall of the Serçeler trench.

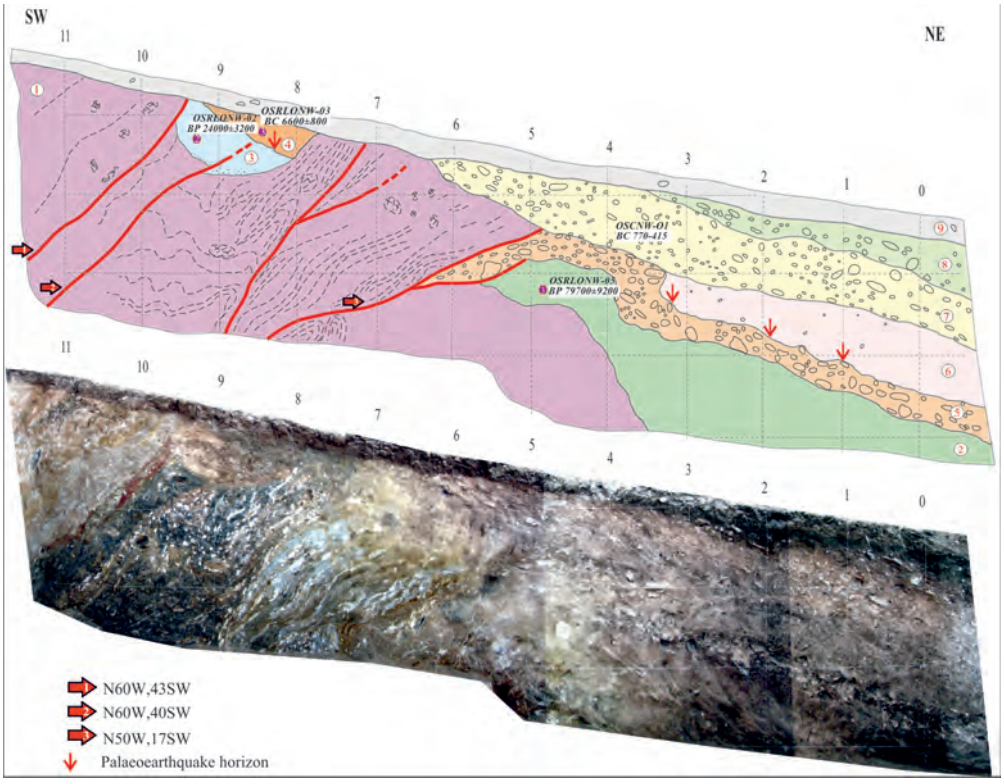

Figure 7- Photomosaic image and interpreted trench log for the NW wall of the Serçeler trench.

in this segment of the Orhaneli Fault where kinematic data may be obtained, the fault has reverse fault character with a right-lateral component (Figure 11). The general strikes of the faults measured in the trench were N50°W, which is in accordance with the strike shown on the Turkish Active Fault Map.

The oldest unit observed in the Serçeler trench is metamorphic bedrock of Tavşanlı Zone, shown on logs as unit 1 (Figures 6 and 7). Primary schistosity can be clearly seen within 4 to 4.5 m wide shear zone despite the intense weathering.

The second stratigraphic unit in the trench is Quaternary sediments. While a part of the sediments overlies unconformably the bedrocks, other part lies below the bedrock units by a series of reverse faults.

Unit 2 is represented by brown, sandy granular mud. It was dated to 79.700±9.200 BP (Before Present) by OSL method (Figure 7 and Table 3). The units 3 and 4 are characterized by gully fill deposits on the bedrock. The 60 cm thick unit is represented by fine pebbles and mud with granules (Figures 6 and 7). The base of this gully (unit 3) is cut and offset by the fault. Within the same gully fill, unit 4 is not affected by the fault. The OSL samples taken from unit 3 and unit 4 provided ages of 24.000±3.200 BP and 8.700±800 BP, respectively (Figure 7 and Table 3). Unit 5 is represented by angular-semiangular, medium-coarse pebbles. Unit 5 is cut by the fault and overlain by the bedrock. This level, affected by the oldest earthquake was covered by unit 6 after a erosinal process.

Unit 7 comprises angular gravels in brownish muddy matrix (Figures 6 and 7). Samples taken from this unit provided a C^{14} age of 2530±30 BP (Table 2). This unit is overlain by the dark-brown, blocky, muddy unit 8. All units in the trench are overlain by modern soil level unit 9. This dark brown soil level has mean thickness of 20 cm, with angular pebbles and sandy-muddy composition (Figures 6 and 7).

5.1.1. Palaeoseismological Interpretation

In Serçeler trench, the oldest event in Holocene (or Pleistocene) occurred due to fault observed between 7 and 10th m in the northwest wall. This fault, cutting bedrock units, cuts unit 3 toward the surface and is overlain by unit 4 (Figure 7). The most important

data supporting this event is the presence of colluvial wedge deposits and nearly 15 cm of reverse offset of the gully floor. OSL age of unit 3 containing gully fill sediments cut by the fault is 24.000±3.000 BP. The OSL age of unit 4, interpreted as the earthquake horizon is 6.600±800 BC. As a result, this earthquake must have occurred in the Early Holocene or before, between 24.000±3.200 BP and 6.600±800 BC.

The next earthquake found in Serçeler trench occurred when unit 5 was deformed by the reverse fault-3. Later this unit was covered by unit 7 in the northwest wall (Figures 6 and 7). In the SE wall, this relationship is more clearly observed (Figure 6). Here unit 5 and the fault affected it appear to be overlain by unit no. 6 interpreted as *"earthquake horizon"*. Because age data could not be obtained from unit 6, the closest age data for this earthquake must be before the formation of unit 7, or before 770-415 BC.

5.2. Kusumlar Trench

Kusumlar Trench was excavated nearly 600 m NW of Serçeler trench (Figures 2B and 4). The trench excavated perpendicular to the fault strike is 4 m wide, 3 m deep and 15 m long. As with the Serçeler trench, this trench was opened on the topographic slope break thought to be equivalent of the fault scarp (Figure 8). Kusumlar trench site lies on the boundary between metamorphic basement and Quaternary sediments.

As in Serçeler trench, the basement rocks in this trench were thrust over Quaternary units (Figures 9 and 10). The fault has N53°W, 23°SW strike and dip, with rake angles of fault striations reaching 85-90°. Therefore, the fault is almost a *"pure thrust fault"* in this excavation (Figure 11).

In Kusumlar trench, same as in Serçeler trench, the oldest unit shown as 1 on the log is metamorphic rocks belonging to the Tavşanlı Zone (Figures 9 and 10). Although this unit is highly weathered, primary textures are still visible. The sediments from the Quaternary period observed in the trench were divided into seven stratigraphic units.

Stratigraphically the oldest unit 2 is 1 to 1.5 m thick, coffee-brown, clay sediment rich in pebbles and caliche. Above this, the unit called 3a is represented by light brown, pebbly mud. Unit 3a is 30 cm thick, pinching-out toward the fault zone. The unit marked 3b is whitish-green coloured, weakly layered mud. Above this unit, unit 4 is 20 to 25 cm thick with light brown mud and angular pebble level. The unit 5 is 20-25 cm thick, black mud with angular clasts. The clasts are generally derived from metamorphic basement unit.

After the deposition of these units, the bedrock and sediment fill were experienced an erosional process. The erosional level was covered by unit 6. The apparent thickness of the unit is between 75 and 80 cm, and represented by brown, fine-medium angular pebble-rich mud. This unit displays thickening toward a topographic saddle in NE. The clasts are irregular and disorganised indicating the topographic saddle filled by gravelly mud flow. The sequence in the trench ends with the modern dark-brown soil level of 20 to 25 cm thickness.

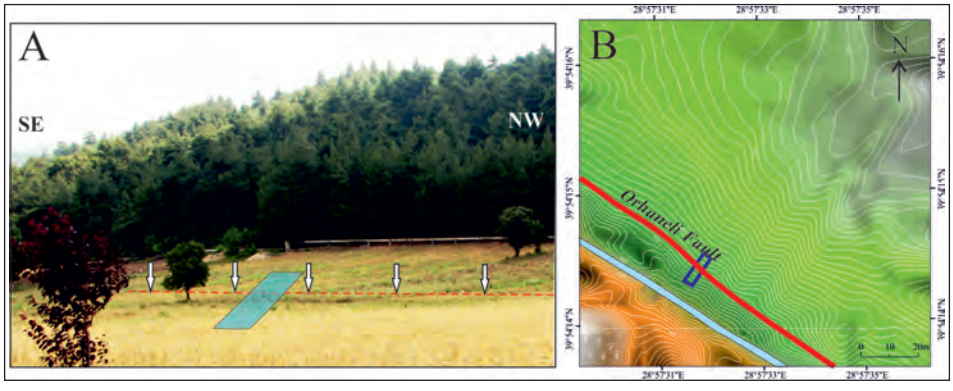

Figure 8- A) General appearance of the area of the Kusumlar trench, white arrows show location of the fault, blue rectangle shows the excavation area. B) Microtopography map of the trench area and close surroundings. Contour interval is 20 cm.

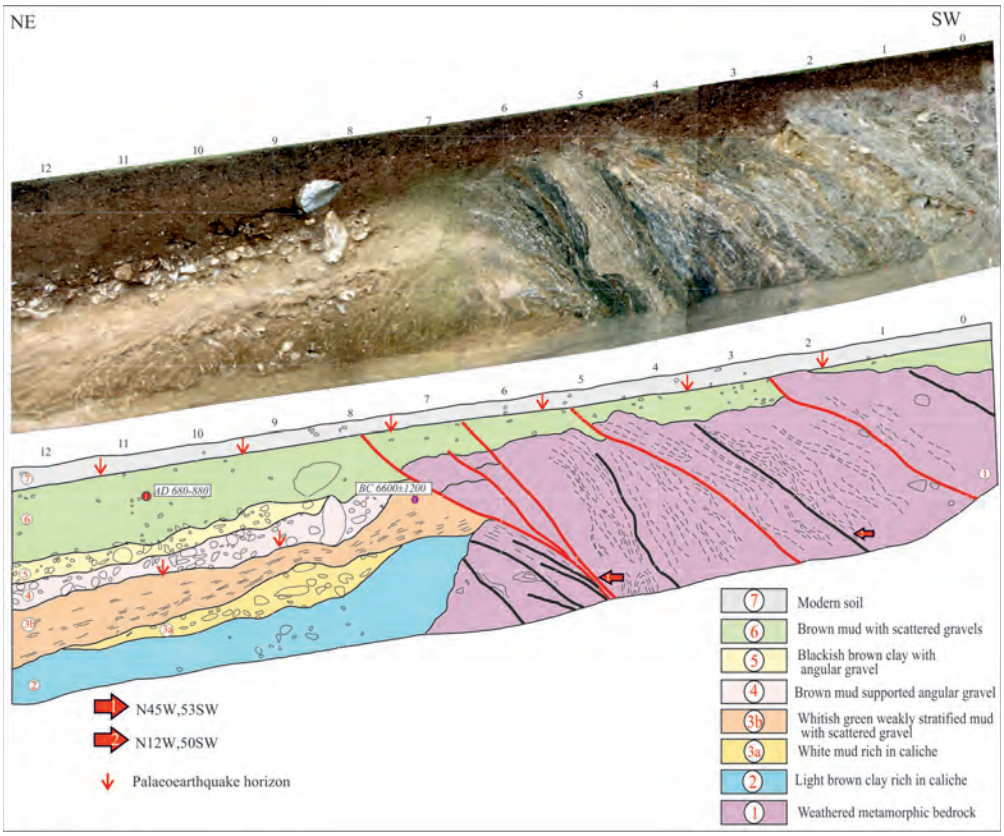

Figure 9- Photomosaic image and interpreted trench log for the SE wall of the Kusumlar trench.

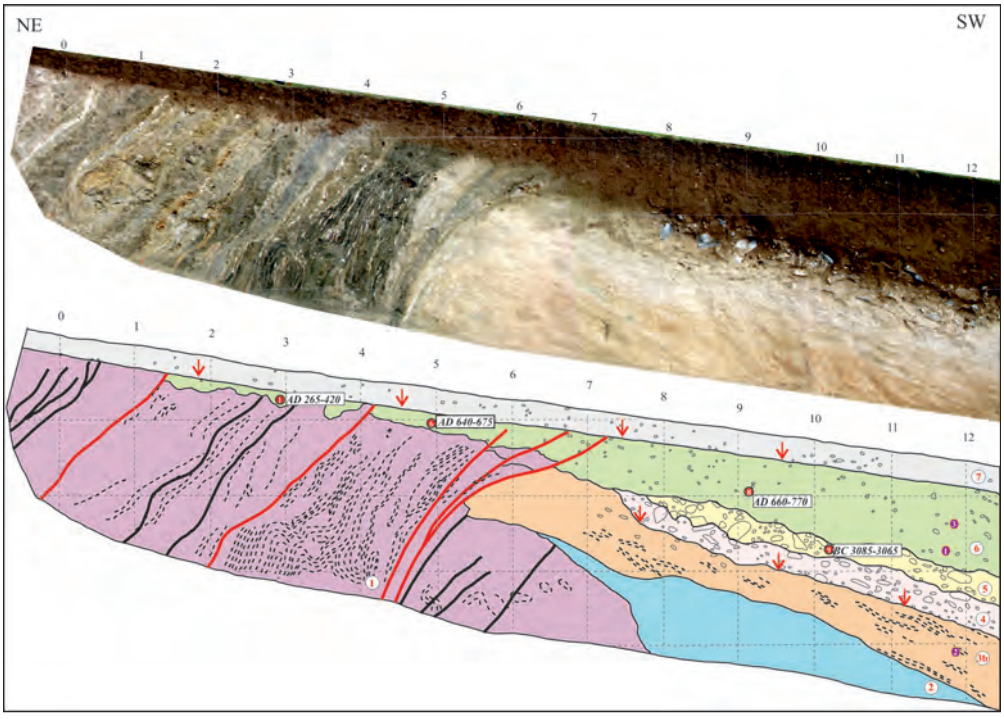

Figure 10- Photomosaic image and interpreted trench log for the NW wall of the Kusumlar trench.

5.2.1. Palaeoseismological Interpretation

The penultimate event in Kusumlar trench occurred by thrusting of the bedrock above unit 3b (Figures 9 and 10). According to an OSL dating of unit 3b, the date is reported as 6.600±1200 BC (Table 3). Among the units overlying it, only unit 5 dated to 3.085-3065 BC based on ^{14}C age. Accordingly, this event (Event-1) must have occurred between 6.600±1200 and 3.065-3085 BC.

Event-2 (last) is characterised by a fault cutting unit 6 and reaching to the base of unit 7 (modern soil level) (Figures 9 and 10). Samples taken from unit 6 reported a mean ^{14}C age of 660-770 AD (Table 2). As a result, Event-2 must have occurred after 660-770 AD.

5.3. Structural Data

Slip data from fault planes observed in the trench walls were measured for defining the kinematic properties of Orhaneli Fault. Generally kinematic markers such as slickenlines or groove marks were preserved in soft sediments like clay and silt on the fault planes. These structures were clearly observed in Kusumlar and Serçeler trenches, and the slip data were measured (Figure 11 A and B). These data showed that the fault remained under the effect of continuous similar tectonic deformation for a long time. The method recommended by Marrett and Allmendinger (1990) involving FaultKinWin 7.0.0 [computer program developed by R.A. Almendinger et al. (2012) for analysis of fault plane data] was used for fault plane analyses and the results are presented as focal mechanism solutions (Figure 11C).

A total of 5 slip data were measured in the trenches were assessed within the FaultKinWin program. The Orhaneli Fault was found out to have been affected by NE-SE oriented compression and the fault has reverse/thrust fault character with very small right-lateral component (Figure 11C).

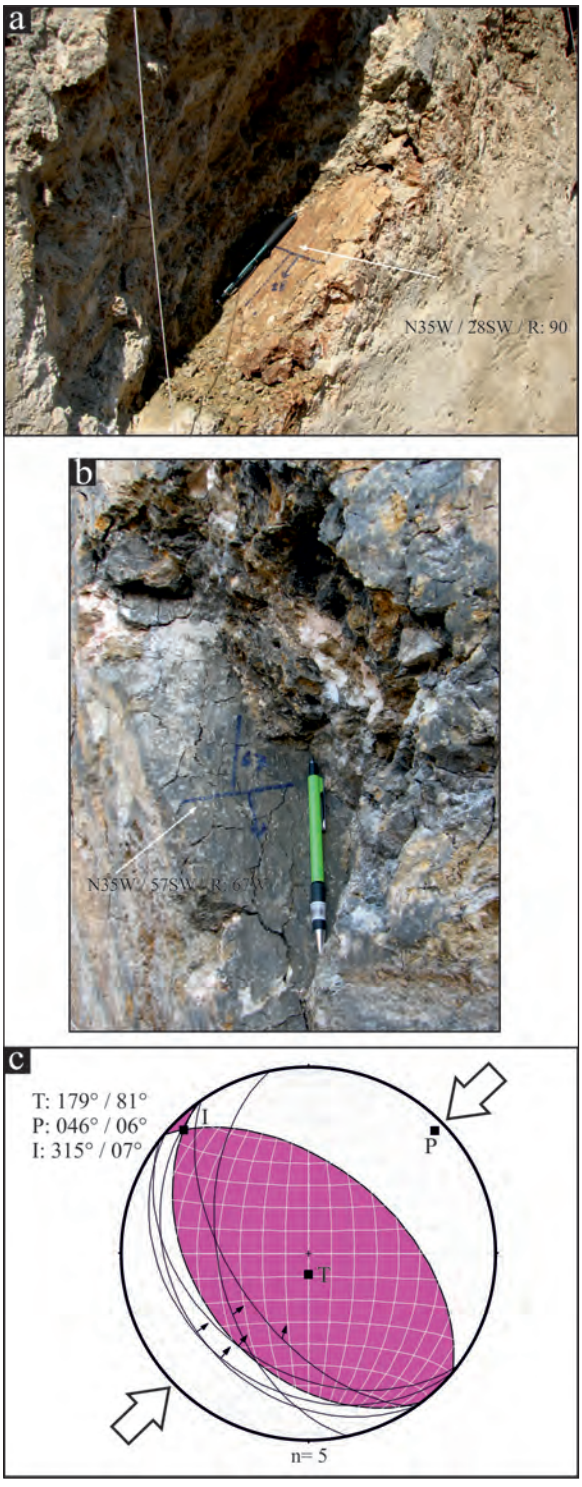

Figure 11- Photographs related to fault planes in A) Kusumlar Trench and B) Serçeler Trench. C) Data obtained from fault planes in the trenches displayed on an equal-area lower hemisphere (P: compression axis, T: extensional axis, I: intermediate axis). Fault plane solutions used the FaultKinWin V. 1.2.2. software (Marret and Allmendinger, 1990; Allmendinger et al., 2012).

6. Discussion and Conclusions

There are many active faults in the Biga Peninsula representing a transitional belt between the West Anatolian extensional tectonic regime and the North Anatolian Fault Zone (Barka, 1992; Barka and Kadinsky-Cade, 1988; Dewey and Şengör, 1979; Emre et al. 2012; 2013; Şaroglu et al., 1992; Şengör et al., 2005). These faults located in the region are generally right-lateral strike-slip faults, displaying an arc geometry widening toward the south (Figure 1B) (Emre et al., 2011*a*, *b*, 2013). The Orhaneli Fault forming the eastern wing of this arc was reported to be a right-lateral strike-slip fault by Emre et al. (2011*a*, 2012, 2013). Additionally, measurements on the fault planes during this study showed that the fault striations generally have rake angles between 70 to 80°; thus the NW segment of this fault basically has *"reverse fault"* character with very small amount of *"right lateral strike-slip"* component (Figure 11).

The fault planes observed in the trenches have general strike of N50°W, in accordance with the strike of the Orhaneli Fault on the Turkish Active Fault Map. During a palaeoseismology study of the Mustafakemalpaşa Fault, Kop et al. (2016) determined this fault had reverse slip component with right-lateral strike-slip character. This situation shows that the reverse component reduces and the right-lateral strike-slip component increases from Orhaneli Fault to Mustafakemalpaşa Fault in the northwest. Additionally, in the far northwest, the Manyas Fault representing the apex of the Manyas Bend nearly has *"pure normal fault"* character (Taymaz et al., 1991; Kürçer et al., 2017).

The stratigraphic and structural elements in Serçeler and Kusumlar trenches showed that four earthquakes were determined to have resulted in surface ruptures in Quaternary. At least, two of them occurred in Holocene. Especially Kusumlar trench showed that the first Holocene earthquake occurred between. 6,600±1, 200 and 3,085-3,065 BC (Figure 12; blue bar, earthquake no. 3), and the other earthquake occurred after 660-770 AD (Figure 12; blue bar, earthquake no. 1). In Serçeler trench the ante penultimate earthquake occurred between 22,000 ± 3,200 BC and 6,600 ± 800 BC (Figure 12; blue bar, earthquake no. 4) with the final earthquake observed to have occurred before 770 to 415 BC (Figure 12; blue bar, earthquake no. 2). According to palaeoseismologic results from Mustafakemalpaşa Fault located to the northwest, the oldest earthquake was before 2,190 BC (Figure 12; orange bar, earthquake no. 3) with the next earthquake between 815 BC and 1310 AD (Figure 12; orange bar, earthquake no. 2) and the final earthquake known to have occurred after 1425 AD (Figure 12; orange bar, earthquake no. 1) (Kop et al., 2016). The authors correlated the last event to the historical 1850 and 1851 earthquakes (Figure 12; orange bar, earthquake no. 1) and the penultimate event to the 368 AD earthquake (Figure 12; orange bar, earthquake no. 2). The last earthquake determined in this study may be related to the historical 1850 or 1851 earthquakes (Figure 12; blue bar, earthquake no. 1). If this possibility is correct, these earthquakes may have occurred due to the Orhaneli and Mustafakemalpaşa Faults together with each other. Kürçer et al. (2017) in addition to the last earthquake on the Manyas Fault in 1964 (Figure 12; yellow bar, earthquake no. 1) correlated the previous event to the 1323 AD earthquake (Figure 12; yellow bar, earthquake no. 2). When all these data are displayed on a timescale, it appears that there is a migration of earthquakes from the Orhaneli Fault toward the northwest, to the Mustafakemalpaşa and Manyas Faults, respectively (Figure 12). Here, no matter how broad the time interval is for the formation ages of some earthquakes, it is understood that there

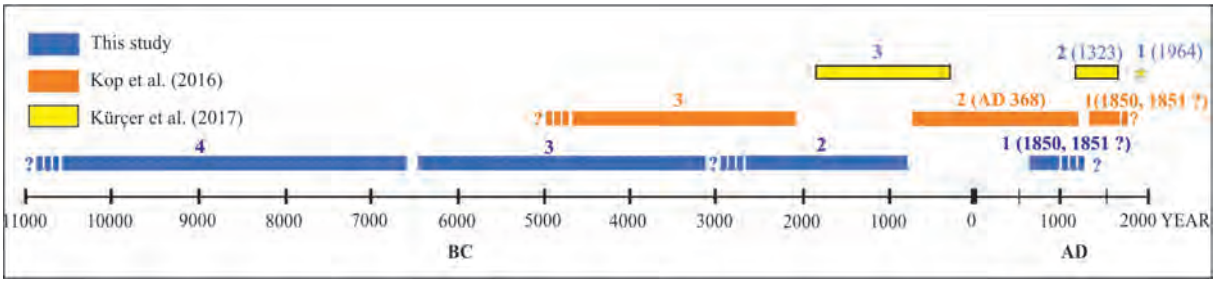

Figure 12- Palaeoseismological results for Orhaneli (this study), Mustafakemalpaşa (Kop et al., 2016) and Manyas (Kürçer et al., 2017) faults. Numbers are formation intervals for earthquakes, brackets refer to historical period earthquakes while yellow stars show instrumental period earthquakes.

is a large possibility that these earthquakes migrated from the SE (Orhaneli Fault) toward the NW (Manyas Fault).

There is similarity between the nearly 2.3 km right-lateral offset on the Orhaneli Stream (Figure 2) due to the fault, with the 2.5 km right-lateral offset of the same stream by the Mustafakemalpaşa Fault to the northwest (Emre et al., 2011*b*; Kop et al., 2016). According to this offset data from Orhaneli Stream, with drainage foundation known to be the Late Pliocene, the geologic slip rate of the Mustafakemalpaşa Fault was reported by Emre et al. (2011*b*) as 1 mm/yr, while Kop et al. (2016) suggested 0.7 mm/yr. In spite of the limited data availability, based on the offset caused by the Orhaneli Fault on the same streambed, the geologic slip rate may be proposed as 0.9-1 mm/yr. However, according to studies completed in the south Marmara Region in recent years, the incision ages of large valleys in the region are reported to be younger than 300.000 years (Kazancı et al., 2014). When this data is considered, the geologic slip rate may be recommended as 0.76 mm/yr.

Using data from this study and previous studies, it is not possible to make any interpretation of the recurrence interval for palaeo-earthquakes occurring in the region. However, according to calculations using the formula from Wells and Coppersmith (1994), if the Orhaneli Fault with total length of 30 km comprising two geometric segments fractured in a "*single piece*" it appears that it could produce an earthquake with magnitude Mw: 6.87. Similarly, Kop et al. (2016) stated that the Mustafakemalpaşa Fault could produce an earthquake with magnitude between Mw: 6.47 and 7.04.

In conclusion, for the first time activity twice in Holocene was determined for the Orhaneli Fault in this study. Rapidly increasing industrialisation and agricultural activities in the South Marmara Region have caused a rapid increase in population and the opening of new settlement areas. As a result, studies related to the active fault properties in the region gain great importance in terms of society. The data produced in this study will provide a significant contribution to earthquake risk analyses which are necessary for planning of all types of engineering structures and new settlement areas to be developed in the region currently and in the future.

Acknowledgements

This study was completed within the auspices of the "Turkish Palaeoseismology Research Project" led by the Directorate of Geological Studies of the General Directorate of Mineral Research and Exploration (Project Special Code No: 2013-30-14-07). We thank the reviewers Prof.Dr. Volkan Karabacak, Prof.Dr. Hasan Sözbilir, Prof.Dr. Levent Gülen and Dr. Hisao Kondo for their constructive criticism and contributions to the development of the manuscript.

References

Allmendinger, R. W., Cardozo, N., Fisher, D. 2012. Structural geology algorithms: Vectors and tensors in structural geology (302 p.). Cambridge: Cambridge University Press.

Ambraseys, N.N. 2002. The seismic activity of the Marmara Sea region over the last 2000 years. Bulletin of the Seismological Society of America, 92 (1), 1-18.

Ambraseys, N.N., Finkel, C.F. 1991. Long term seismicity of İstanbul and of the Marmara region. Terra Nova 3, 527-539.

Ambraseys, N.N., Jackson, J.A. 1998. Faulting associated with historical and recent earthquakes in the Eastern Mediterranean region. Geophysical Journal International 133, 390-406.

Ambraseys, N.N., Jackson, J.A. 2000. Seismicity of the sea of Marmara (Turkey) since 1500. Geophysical Journal International 141, F1-F6.

Barka, A.A. 1992. The North Anatolian Fault. Annales Tectonicae, 6, 164–195.

Barka, A. A., Hancock, P. L. 1984. Neotectonic deformation patterns in the convex -northwards arc of the North Anatolian fault zone. In" The Geological Evolution of the Eastern Mediterranean region", edited by J.E.Dixon and A.H.F.Robertson. Spec. Publ. Geol.Soc.London. 763-773.

Barka, A.A., Kadinsky-Cade, K. 1988. Strike-slip fault geometry in Turkey and its influence on earthquake activity. Tectonics, 7, 663–684.

Dewey, J.F., Şengör, A.M.C. 1979. Aegean and surrounding regions: Complex multiplate and continuum tectonics in a convergent zone. Geological Society of America Bulletin, 90, 84–92.

Duman, T.Y., Çan, T., Emre, Ö., Kadirioğlu, F.T., Baştürk, N.B., Kılıç, T., Arslan, S., Özalp, S., Kartal, R.F., Kalafat, D., Karakaya, F., Azak, T.E., Özel, N.M., Ergintav, S., Akkar, S., Altınok, Y., Tekin, S., Cingöz, A., Kurt, A.İ. 2016. Seismotectonics

database of Turkey. Bulletin of Eartquake Engineering, DOI 10.1007/s10518-016-9965-9

Emre. Ö., Doğan, A., Özalp, S., Yıldırım, C. 2011*a*. 1:250.000 Scale Active Fault Map of Turkey Bandırma (NK 35-11b) Quadrangle. Maden Tetkik ve Arama 1:250.000 Scale Active Fault Map Series of Turkey, Serial No: 3, 55p., Ankara, Turkey (in Turkish) ISBN: 978-605-4075-86-4.

Emre. Ö., Doğan, A., Özalp, S. 2011*b*. 1:250.000 Scale Active Fault Map of Turkey Balıkesir (NJ 35-3) Quadrangle. MTA 1:250.000 Scale Active Fault Map Series of Turkey, Serial No: 4, 35p., Ankara, Turkey (in Turkish).

Emre, Ö., Doğan, A., Yıldırım, C. 2012. Biga Yarımadasının diri fayları ve deprem potansiyeli. In: Yüzer, E. and Tunay, G (Eds.), Biga Yarımadası'nın Genel ve Ekonomik Jeolojisi, General Directorate of Mineral Research and Exploration, Special Publication Series-28, 163-198, Ankara-Turkey (in Turkish).

Emre, Ö., Duman, T.Y., Özalp, S., Elmacı, H., Olgun, Ş., Şaroğlu, F. 2013. Açıklamalı Türkiye Diri Fay Haritası. Ölçek 1:1.250.000, VI+89s.+bir pafta, Maden Tetkik ve Arama Genel Müdürlüğü, Özel Yayın Serisi-30, Ankara-Türkiye.

Ergin, K., Güçlü, U., Uz, Z. 1967. A Catalog of Earthquakes for Turkey and Surrounding Area (11 A.D. to 1964 A.D.). Technical Report, İstanbul Technical University, Faculty of Mines, Institute of Physics of the Earth, No. 24, 169 p.

Ergin, K., Güçlü, U., Aksay, G. 1971. A Catalog of Earthquakes of Turkey and Surrounding Area (1965–1970). Technical Report, İstanbul Technical University, Faculty of Mines, Institute of Physics of the Earth, no. 28.

Harris, N.B.W., Kelley, S.P., Okay, A.I. 1994. Postcollision magmatism and tectonics in northwest Turkey. Contributions to Mineralogy and Petrology, 117, 241-252.

Kadirioğlu, F.T., Kartal , R.F, Kılıç, T., Kalafat, D., Duman, T.Y., Eroğlu Azak, T., Özalp, S., Emre, Ö. 2016. An Improved Earthquake Catalogue (M ≥ 4.0) for Turkey and Its Near Vicinity (1900-2012). Bulletin of Earthquake Engineering, (in press) doi: 10.1007/s10518-016-0064-8

Kaya, O., Kozur, H., Sadeddin, W., Helvacı, H. 2001. Late Norian conodont age for a metacarbonate unit in NW Anatolia, Turkey. Geobios, 34, 527-532.

Kazancı, N., Emre, Ö., Erturaç, K., Leroy, S., Öncel, S., İleri, Ö., Toprak, Ö. 2014. Güney Marmara Bölgesindeki Büyük Vadilerin Olası Deşilme Zamanı. Maden Tetkik ve Arama Dergisi, Sayı: 148, s: 1-17, Ankara, Türkiye.

Konak, A. 2002. 1:500.000 Ölçekli Türkiye Jeoloji Haritası İzmir Paftası. Maden Tetkik ve Arama Genel Müdürlüğü, Ankara, Türkiye.

Kondorskaya, N.V., Ulomov, V.I. 1999. Special catalogue of earthquakes of the Northern Eurasia (SECNE). URL: http://socrates.wdcb.ru/scetac/ and http://www.seismo.ethz.ch/gshap/neurasia/nordasiacat.txt

Kop, A., Özalp, S., Elmacı, H., Kara, M., Duman, T.Y. 2016. Active Tectonic and Paleoseismological Features of the Western Section of Mustafakemalpaşa Fault; Bursa, NW Anatolia. Geodinamica Acta, 28, 4, 363-378.

Kürçer, A., Özaksoy, V., Özalp, S., Uygun-Güldoğan, Ç., Özdemir, E., Duman, T.Y. 2017. The Manyas Fault Zone (Southern Marmara Region, NW Turkey): Active Tectonics and Paleoseismology. Geodinamica Acta, 29, 1, 42-61.

Marrett, R. A., Allmendinger, R. W. 1990. Kinematic analysis of fault-slip data. Journal of Structural Geology, 12, 973–986.

McKenzie, D. 1972. Active tectonics of the Mediterranean region. Geophysical Journal of the Royal Astronomical Society, 30, 109-195.

Okay, I.A. 1985. Kuzeybatı Anadolu'da yer alan metamorfik kuşaklar. Ketin Simpozyumu Kitabında, Türkiye Jeoloji Kurumu Yayını, 83-92.

Okay, I.A. 2004. Tectonics and High Pressure Metamorphism in northwest Turkey. Field trip guide book - P01, 32nd International Geological Congress, APAT, Italy, 56 pp.

Okay, I.A. 2011. Tavşanlı Zonu: Anatolid-Torid Bloku'nun Dalma-Batmaya Uğramış Kuzey Ucu. Maden Tetkik ve Arama Dergisi, Sayı: 142, Ankara.

Okay, A.I., Tüysüz. O. 1999. Tethyan sutures of northern Turkey. In "The Mediterranean Basins: Tertiary extension within the Alpine orogen" (eds. B. Durand, L. Jolivet, F.Horváth ve M.Séranne), Geological Society of London, Special Publication 156.

Okay, A.I., Harris, N.B.W., Kelley, S.P. 1998. Exhumation of blueschists along a Tethyan suture in northwest Turkey. Tectonophysics, 285, 275-299.

Özalp, S., Emre, Ö., Doğan, A. 2013. Kuzey Anadolu Fayı Güney Kolu'nun segment yapısı ve Gemlik

Fayı'nın paleosismik davranışı, KB Anadolu. Maden Tetkik ve Arama Dergisi, 147, 1-17, Ankara.

Özalp, S., Kürçer, A., Özdemir, E., Duman, T.Y. 2016. The Bekten Fault: The paleoseismic behaviour and kinematic characteristics of an intervening segment of the North Anatolian Fault Zone, Southern Marmara Region, Turkey. Geodinamica Acta, 28, 4, 347-362.

Reilinger, R., McClusky, S., Vernant, P., Lawrence, S., Ergintav, S., Cakmak, R., Ozener, H., Kadirov, F., Guliev, I., Stepanyan, R., Nadariya, M., Hahubia, G., Mahmoud, S., Sakr, K., ArRajehi, A., Paradissis, D., Al-Aydrus, A., Prilepin, M., Guseva, T., Evren, E., Dmitrotsa, A., Filikov, S.V., Gomez, F., Al-Ghazzi, R., Karam, G. 2006. GPS constraints on continental deformation in the Africa-Arabia-Eurasia continental collision zone and implications for the dynamics of plate interactions. Journal of Geophysical Research, 111, B05411.

Servais, M. 1982. Collision et suture téthysienne en Anatolie Centrale, étude structurale et métamorphique (HP-BT) de la zone nord Kütahya. Ph.D. Thesis, Universite de Paris-Sud, Centre d'Orsay, 374 s.

Soysal, H., Sipahioğlu, S., Kolçak, D., Altınok, Y. 1981. Historical Earthquake Catalogue of Turkey and Surrounding Area (2100 B.C.–1900 A.D.). Technical Report, TÜBİTAK, Project No. TBAG-341, 87 p., İstanbul.

Sözbilir, H., Özkaymak, Ç., Uzel, B., Sümer, Ö., Eski, S., Tepe, Ç. 2016*a*. Palaeoseismology of the Havran-Balıkesir Fault Zone: evidence for past earthquakes in the strike-slip-dominated contractional deformation along the southern branches of the NorthAnatolian fault in northwest Turkey. Geodinamica Acta, 28, 4, 254–272.

Sözbilir, H., Sümer, Ö., Özkaymak, Ç., Uzel, B., Güler, T., Eski, S. 2016*b*. Kinematic analysis and palaeoseismology of the Edremit Fault Zone: evidence for past earthquakes in the southern branch of the North Anatolian Fault Zone, Biga Peninsula, NW Turkey. Geodinamica Acta, 28, 4, 273–294.

Şaroğlu, F., Emre, Ö., Kuşçu, İ. 1992. Active Fault Map of Turkey. 1:1,000,000 Scale, General Directorate of Mineral Research and Exploration, Ankara-Turkey.

Şengör, A.M.C., Görür, N., Şaroglu, F. 1985. Strike-slip faulting and related basin formation in zones of tectonic escape: Turkey as a case study. In: Biddle, K.T. and Christie-Blick, N. (Eds.), Strike-Slip Deformation, Basin Formation, and Sedimentation, Spec. Publ. Soc. Econ. Paleontol. Mineral., 37, 227–264.

Şengör, A.M.C., Tüysüz, O., İmren, C., Sakınç, M., Eyidoğan, H., Görür, N., Le Pichon, X., Rangin, C. 2005. The North Anatolian Fault: A new look. Annu. Rev. Earth Planet. Sci., 33, 37-112.

Tan, O., Tapırdamaz, M.C., Yörük, A. 2008. The earthquake catalogues for Turkey. Turk. J. Earth Sci., 17, 405-418.

Taymaz, T., Jackson, J.A., McKenzie, D. 1991. Active tectonics of the North and Central Aegean Sea. Geophysical Journal International, 106, 433-490.

Türkecan, A., Yurtsever, A. 2002. 1:500.000 Ölçekli Türkiye Jeoloji Haritası İstanbul Paftası. Maden Tetkik ve Arama Genel Müdürlüğü, Ankara, Türkiye.

Wells, D., Coppersmith, K. 1994. New empirical relationships among magnitude, rupture length, rupture width, rupture area and surface displacement. Bull. Seism. Soc. Am., 84, 974-1002.

Bull. Min. Res. Exp. (2018) 156: 17-40

Bulletin of the Mineral Research and Exploration

http://bulletin.mta.gov.tr

The neotectonics of NE Gaziantep: The Bozova and Halfeti strike-slip faults and their relationships with blind thrusts, Turkey

Nuray ŞAHBAZ[a*] and Gürol SEYİTOĞLU[b]

[a]*TPAO, Department of Exploration, Söğütözü District, 2180th street, No 86, 06100 Çankaya / Ankara, Turkey.*
orcid.org/0000-0001-8334-7437
[b]*Ankara University, Dept. of Geological Engineering, Tectonics Research Group, 06830 Gölbaşı / Ankara, Turkey.*
orcid.org/0000-0001-7993-898X

Research Article

Keywords:
Neotectonics, SE Turkey, Gaziantep, Bozova Fault, earthquake, structural evaluation.

Received Date: 02.03.2017
Accepted Date: 02.10.2017

ABSTRACT

In the northeast of Gaziantep, east-west trending thrusts, northeast-southwest trending left lateral strike-slip faults and northwest-southeast right lateral strike-slip faults are located. They are typical features of the neotectonics of southeast Anatolia, Turkey. Detailed mapping of these structures and structural data obtained from field studies indicate that east-west trending thrust faults and related fault propagation folds is post-Pliocene. The strike-slip faults that cut these structures should be younger than the thrust fault. On the other hand, the recent seismic activity in the southeast Anatolia (2011.10.23 – M=7.3 Van; 2012.06.14 – ML=5.5 Şırnak-Silopi earthquakes) shows that north-south compression is taken by both thrusting and strike-slip faulting.

1. Introduction

In southeast Turkey, at the south of Bitlis suture zone, there are very few articles regarding the detailed investigation of structures in the area defined as the Arabian foreland (Biddle et al., 1987; Perinçek et al., 1987; Çemen et al., 1990; Seyitoğlu et al., 2017) (Figures 1a and b). However, there are many unpublished reports belonging to these structures in the archive of TPAO (Yoldemir, 1985, 1987; Çemen, 1986; Lisenbee 1986, 1987; Yoldemir et al., 1992; Yoldemir and Sefunç, 1999; Sefunç, 2003). In articles, which explain regional and wide areas, the structures in the Arabian foreland have a tendency to be shown simply by fold axes (Şengör et al., 1985; 2008; Yılmaz, 1993; Okay, 2008). However, in Iran the structures in the Zagros foreland were detailedly studied in terms of blind thrusts, strike-slip faults and seismicity (Berberian, 1995; Hatzfeld et al., 2010; Agard et al., 2011; Farzipour-Saein et al., 2009; Joudaki et al., 2016).

Field observations carried out in the northeast of Gaziantep in order to contribute to the deficiency in the literature regarding the detail examination of the structures in the Arabian foreland in southeast Anatolia are presented in this article.

The geological map, which had been taken by a permission of the Turkish Petroleum, Systems Interpretation Unit, was revised by the Arc-Map software and used in simplified form as a result of field observations. The simplification was made to divide the lithostratigraphy in the region into four groups as; the Allochthonous, Cretaceous, Tertiary and Quaternary units (Figures 1c and 2).

2. Regional Geology

The study area is located in south of the Besni town of Adıyaman and north of the Halfeti town of Şanlıurfa. The field is restricted by the East Anatolian Fault Zone (EAFZ) in the west and the Bozova Fault in the east (Figure 1c). The left lateral strike -slip Halfeti fault, which is located at the center of the area and extends in NE-SW direction, is one of the youngest fault of the region. It also cuts the asymmetrical anticlines, which

* *Corresponding author: Nuray ŞAHBAZ, nsahbaz@tp.gov.tr*
http://dx.doi.org/ 10.19111/bulletinofmre.401216

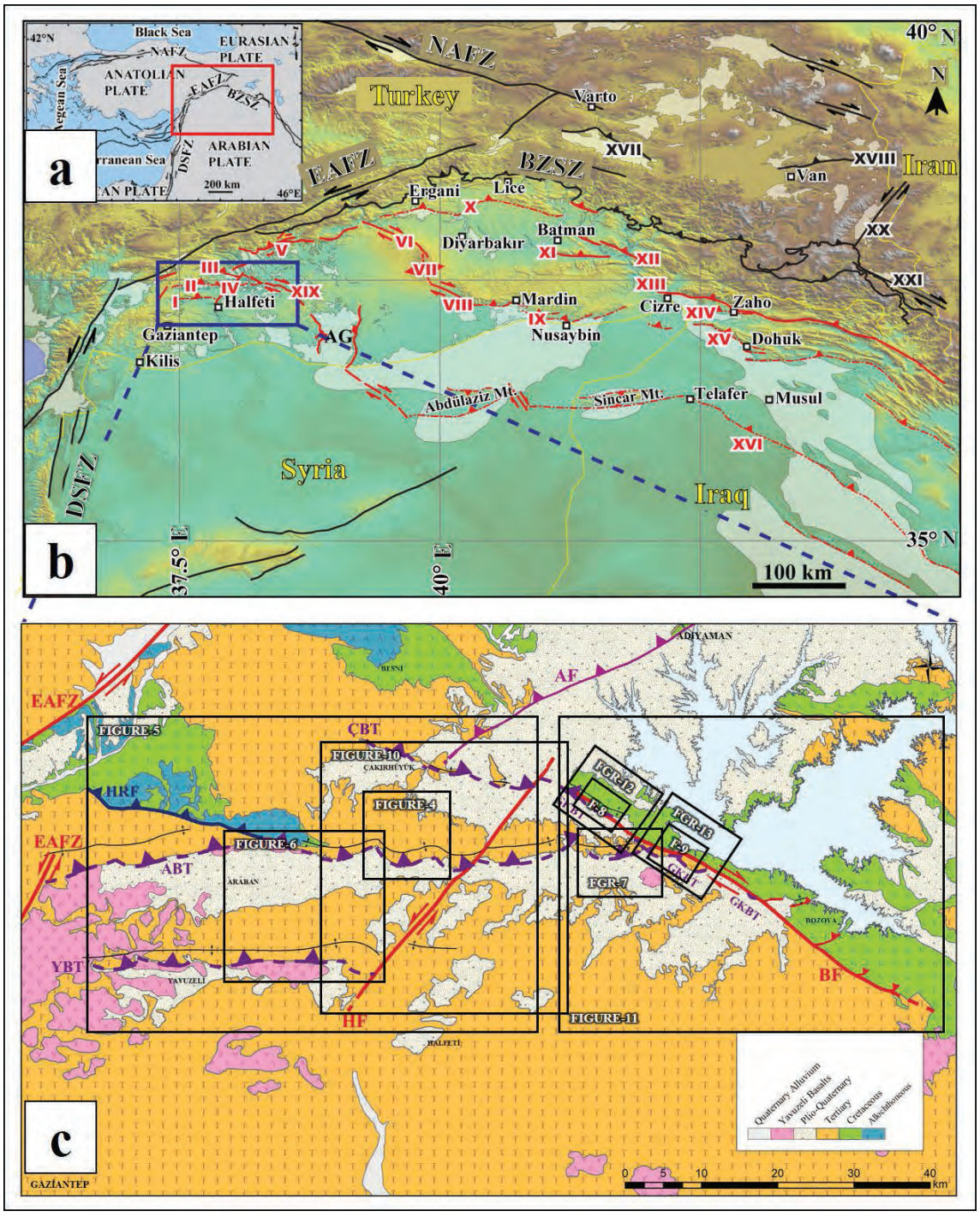

Figure 1- **(a)** The neotectonic elements of Turkey and its close vicinity, **(b)** the map showing the neotectonics of the Southeastern Anatolia, Northern Syria and Iraq (Seyitoğlu et al., 2017**). DSFZ:** Dead Sea Fault Zone (Hall et al., 2005; Krasheninnikov et al., 2005)**, EAFZ:** East Anatolian Fault Zone, **NAFZ:** North Anatolian Fault Zone (Şaroğlu et al., 1992). **BZSZ:** Bitlis-Zagros Suture Zone (Emre et al., 2013**). I-** Yavuzeli Blind Thrust; **II-** Araban Blind Thrust; **III-** Çakırhüyük Blind Thrust; **IV-** Halfeti Fault; **V-** Adıyaman Thrust Zone; **VI-** Northern Karacadağ Fault; **VII-** Karacadağ Extension Fracture; **VIII-** Southern Karacadağ Fault; **IX-** Mardin Blind Thrust Zone; **X-** Ergani-Silvan Blind Thrust; **XI-** Raman Thrust Fault; **XII-** Garzan Thrust Fault; **XIII-** Cizre Thrust Fault; **XIV-** Silopi Blind Thrust; **XV-** Bikhayr Blind Thrust Zone; **XVI-** Sincar-Kerkük Blind Thrust Zone; **XVII-** Muş Thrust Fault; **XVIII-** Van Thrust Fault; **XIX-** Bozova Fault; **XX-** Başkale Fault; **XXI-** Şemdinli-Yüksekova Fault; **AG-** Akçakale-Harran Graben, **(c)** the geological map of the N Gaziantep. (Simplified from the map TPAO, 2014). **EAFZ**: East Anatolian Fault Zone, **AF**: Adıyaman Fault, **HF**: Halfeti Fault, **BF**: Bozova Fault, **HRF:** Harmancık Fault, ÇBT: Çakırhüyük Blind Thrust, **ABT**: Araban Blind Thrust, **YBT**: Yavuzeli Blind Thrust, **GKBT**: Gemrik-Karababa Blind Thrust.

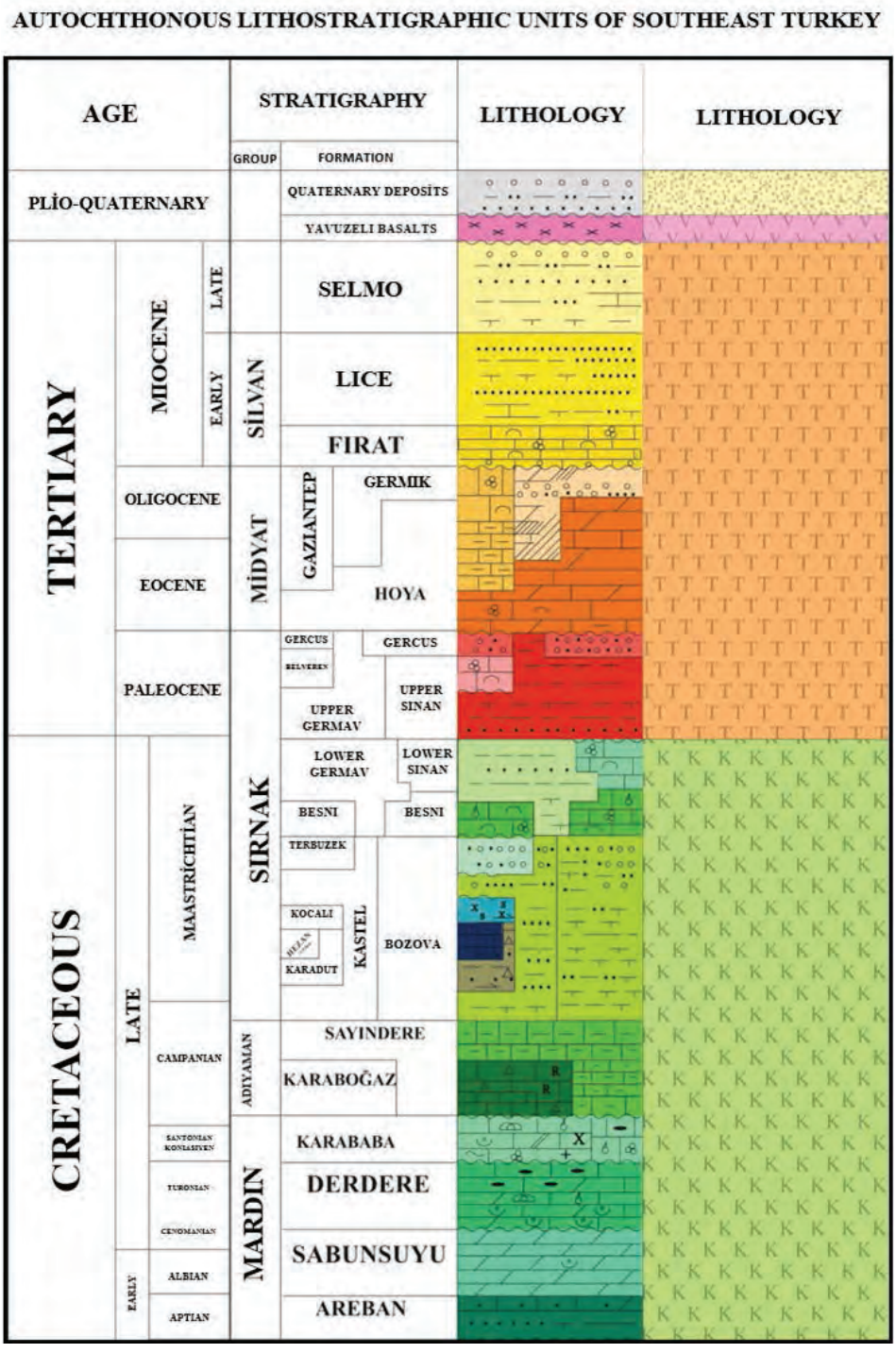

Figure 2- The generalized stratigraphic section of the Southeastern Anatolia (simplified from Güven vd., 1991). The outcropping units in the study area were used in the map by being simplified and presented in the second lithology column.

are formed by Çakırhüyük, Araban and Yavuzeli blind thrusts from north to south, respectively (Çemen, 1990; Seyitoğlu et al., 2017) (Figure 1c). While the Tertiary units (Midyat and Silvan Group) outcrop on highlands, which are formed by the asymmetrical anticlines in the study area, the depression areas in front of these anticlines are covered by the Quaternary alluvium and the Yavuzeli basalts. The Yavuzeli basalts are widely observed in the region towards west (Figure 1c).

2.1. Stratigraphy

2.1.1. Allochthonous Units

The Allochthonous units were investigated under two groups as the Koçali and Karadut Complexes. The Koçali Complex was first defined by Sungurlu (1972) and are composed of ultrabasic rocks, volcanics, serpentinites and cherty limestones with radiolarites, and exhibits an irregular internal structure (Yoldemir, 1987). The data obtained from radiolarites within the complex show that the age of formation is Late Jurassic – Early Cretaceous (Tuna, 1973). The Karadut Complex is composed of silicified limestone, cherty, siliceous shales, cherty limestones, conglomeratic much fossilliferous limestones and clayey limestones (Yoldemir, 1987). The data obtained from the various lithologies of the Karadut Complex show that the unit has formed between Cenomanian-Early Turonian times (Sungurlu, 1972; Perinçek, 1978) (Figures 1c and 2).

2.1.2. Cretaceous Units

The Cretaceous units were studied under three groups as: the Mardin, Adıyaman and Şırnak Groups.

The Mardin Group is composed of limestone, dolomite, marl, sandstone and shale and has been deposited between Aptian-Early Santonian-Early Campanian in depressions of coastline-shallow sea-inner shelf environments (Schmidt, 1935*a*, Tuna, 1973, Sungurlu, 1972, Erenler 1989, Çoruh, 1991). The Group, from bottom to top, is formed by the Araban, Sabunsuyu, Derdere and Karababa formations and outcrops in the Karababa Mountain (Figures 1c and 2).

The Adıyaman Group was deposited on the *Mardin* Group in deep marine environment in the Campanian (Gossage, 1956; Çoruh, 1991; Güven et al., 1991; Perinçek and Çemen, 1991). The units belonging to this group, from bottom to top, is formed by the Karaboğaz and Sayındere formations in the region (Figure 2).

The Şırnak Group has been deposited between the Late Campanian-Late Maastrichtian above the *Adıyaman* Group in an environment which shows a transition from deep marine to terrestrial (Tromp, 1940; Çoruh, 1991; Güven et al., 1991). It is formed by the Bozova, Terbüzek, Besni, Germav and Sinan formations (Figure 2).

2.1.3. Tertiary Units

Tertiary units are gathered under Midyat and Silvan Groups.

The Midyat Group has been deposited between the Late Paleocene-Early Oligocene times and is composed of marl, shale, sandstone, conglomerate and limestone (Maxson, 1936; Açıkbaş, et al., 1979). It is formed by the terrestrial Gercüş, shallow marine Hoya and deep marine Gaziantep formations (Figure 2).

The Silvan Group is unconformably located on the Midyat Group and is formed by the Fırat and Lice formations (Tolun, 1960; Açıkbaş, et al., 1981; Duran, et al., 1988; 1989; Batı, 1991). It was deposited in the Early Miocene on the shelf margin, bank reefs and in deep marine environments, and it is composed of limestone, dolomite, sandstone and shale (Figure 2).

The Şelmo formation is of Upper Miocene-Lower Pliocene and was deposited in beach, continental and tidal flat environments. It is composed of conglomerate, sandstone, siltstone and shale (Bolgi, 1961; Çemen, et al., 1990) (Figure 2).

The Yavuzeli Basalt is generally composed of reddish-dark brown-dark gray and blackish, unlayered but is sometimes very thick layered lava flow with pores filled with calcite. The age of these basalts are Upper Miocene according to the stratigraphic setting on the map (Ulu, 2002) (Figure 2).

2.1.4. Quaternary Units

They are generally formed by loose compacted pebble, sand and mudstone on river beds and plains, and in the form of pebble, sand and mud stocks on river valleys and plains (Ulu, 2002).

2.2. Tectono-sedimentary Evolution

The geology of the southeastern Anatolia is made up of three tectonic belts which extends in the E-W directions. They are divided from south to north as; the Arabian Platform, Fold Belt and the Nappe Zone or the Orogenic Belt (Yılmaz, 1990; Yılmaz and Yiğitbaş, 1990). The units of the Arabian Platform are divided into three groups as the pre-allochthonous, allochthonous and post-allochthonous units based on the emplacement of the Cretaceous allochthonous (Yılmaz, 1993). Pre-allochthonous units are made up of sedimentary deposits ranging from Precambrian to Upper Cretaceous. Of these, the units up to the

Devonian present thick, shallow marine, clastic deposits. However, these deposits have then turned into neritic carbonates between Devonian and Cretaceous (Yılmaz, 1993). The region has taken its recent shape under the effect of three large tectonic activity in Cretaceous, Eocene and in Miocene times (Yılmaz, 1993; Yiğitbaş and Yılmaz, 1996; Robertson et al., 2016).

With the closure of the southern branch of the Neotethys in the Upper Cretaceous (end of Campanian, beginning of Maastrichtian), the allochthonous units settled on the platform was formed by two sections as the ophiolitic assemblage (the Kızıldağ ophiolite) and the mélange underneath (Yılmaz, 1993). The section under the ophiolite is composed of two assemblages which separates from each other by thrust sheets with different and a complex internal structure. Among them, the Koçali Complex has a mélange characteristic (Rigo de Righi and Cortesini, 1964), however the Karadut Complex has a flyschoidal character (Sungurlu, 1974; Perinçek, 1979). This period is also the depositional age of the syn-tectonic Kestel basin which developed in front of the allochthones moving southward (Sungurlu, 1974; Görür et al., 1987; Güven et al., 1991; Robertson et al., 2016).

The northern margin of the Arabian Platform in this period has been affected by the compressional regime and thrusts have formed, whereas; the intra-continental fragmentation have formed in the southern regions and the normal faults constituting the half-grabens in the region have developed (Şemşir et al., 1992).

At the end of the Lower Maastrichtian, the north of the basin became shallow and uplifted because of the global sea level decrease in all over the world (Haq et al., 1988). Thus; the terrestrial Terbüzek formation was deposited in basal sandstone and conglomerate facies over allochthones. However, in foreland areas, where the allochthones cannot reach the neritic carbonates such as the Sinan and Besni and their deep equivalents in lateral direction, the shaley units of the Germav formation continued its deposition (Yılmaz, 1993).

The Middle-Upper Maastrichtian stage ends with a sea withdrawal period which is highly felt in the northern parts of the southeast Anatolian region. The shallow limestones of the Belveren formation were deposited in topographically suitable areas of the region by the sea level that reaches its maximum in Mid-Paleocene starting from the Lower Paleocene, and in deeper parts the Germav formation continued to deposit (Güven et al., 1991).

In last stages of the northward subduction in the Eocene, the first collision of the Arabian-Eurasian continents occurred (Robertson et al., 2016). While the continental Gercüş formation was deposited in northern parts, these units were then overlain by the limestones of the Midyat Group due to the sea level rise. These limestones were then overlain by the limestones of the Oligocene-Early Miocene Fırat formation (Tuna, 1973; Yılmaz, 1984).

In the Miocene time, the northern parts became increasingly deeper in vertical direction due to the movement of the Miocene nappes, and the deposits of the Lice formation including the Early Miocene turbiditic basin facies were developed in this environment (Duran et al., 1988). The Şelmo formation, which developed due to the closure of the basin, was deposited in the terrestrial environment. Even the youngest members of the Şelmo Formation were affected from the continuous compression in the region (Öğrenmiş, 2006). All these units were then overlain by the Yavuzeli basalts, which have been effective up to historical times starting from the Upper Miocene (Ercan and Fujitani, 1990; Ulu, 2002). Finally; the Yavuzeli basalt were covered by Quaternary alluvium in the area.

3. Young Structures in the Study Area

The most distinctive structural elements in the area are Suvarlı, Karadağ and Faldağı anticlines associated with Çakırhüyük, Araban and Yavuzeli blind thrusts (Seyitoğlu et al., 2017). These anticlines are fragmented by the NE-SW trending East Anatolian Fault (EAF) in the west and NW-SE trending Bozova-Halfeti (Kemerli) Faults in the east (Figure 1c).

Çemen (1986, 1990) stated that the Suvarlı anticline was formed by the Late Miocene Harmancık reverse fault. It is also mentioned in the report that, the Harmancık Fault ends in the Kemerli Fault, but the the Suvarlı anticline has been shifted 500 meters by the Kemerli Fault. The investigations carried out in this area were performed by using the studies of Çemen (1986, 1990). Sefunç (2003) approved the relationship of the Suvarlı anticline with the Harmancık Fault in the Turkish Petroleum report in which the seismic data had been used. He also acclaimed that the Harmancık Fault did not end within the Kemerli Fault, but connected with the Bozova Fault in the east.

The neotectonic structures in the Southeast Anatolia under the N-S contraction have generally developed as E-W thrusts, N-S opening structures, NE-SW left lateral strike-slip faults and NW-SE right lateral strike-slip faults (Şengör et al., 1985; Dewey et al., 1986; Seyitoğlu et al., 2017). First, the E-W trending blind thrust systems then the strike-slip fault systems will be considered in the study area.

3.1. Çakırhüyük, Araban and Yavuzeli Blind Thrusts

The most remarkable morphology in the area, which remains between the south of the Besni town of Adıyaman and the NE Gaziantep, is the E-W extending Quaternary alluvial plains where Çakırhüyük, Araban and Yavuzeli settlements are located from north to south (Figure 1c). These plains are restricted by the NE-SW trending EAFZ in the west and cut by the Halfeti Fault in the east (Figure 1c). The common features of these plains in which Çakırhüyük, Araban and Yavuzeli settlements are located is that their northern margins are restricted by the E-W and WNW-SSE oriented asymmetrical anticlines. As it is clearly seen in the remote sensing analyses and the geological map (TP Systems Interpretation Unit) carried out in the anticlines, which was formed by Eocene Midyat Limestones, the southern limbs of anticlines are steeper than the northern limbs. The drainage system, which developed according to this positioning, is shorter in the south of the fold axis, but is longer in the north (Seyitoğlu et al., 2017) (Figures 3a, b, c). The locations of the asymmetrical anticlines

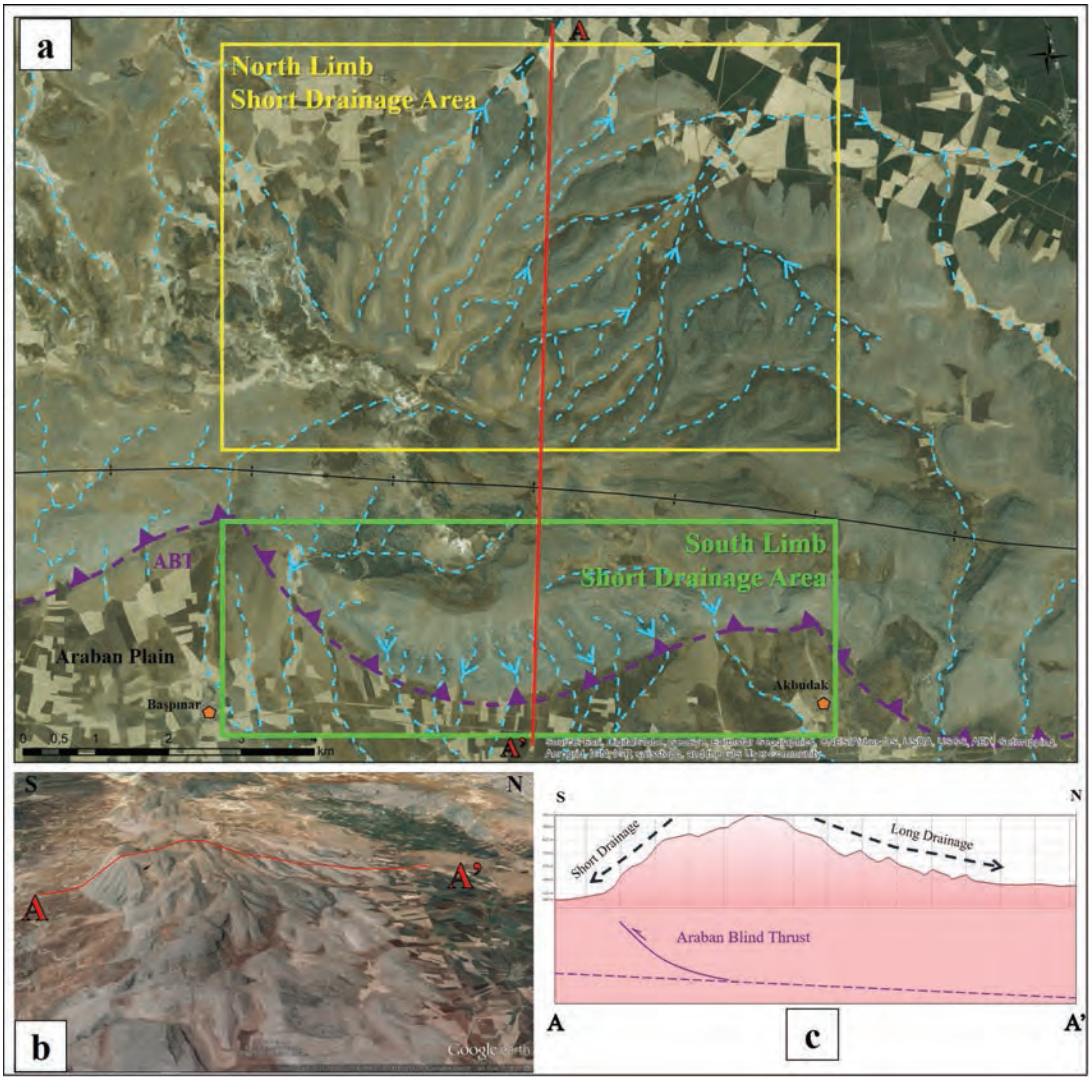

Figure 3- **(a)** Drainage network that developed on the northern and southern limbs of the Gemrik asymmetrical anticline. **ABT**: Araban Blind Thrust, **(b)** Google Earth image showing different dips on the southern and northern limbs of the Gemrik asymmetrical anticline, **(c)** topographical section taken both from the northern and southern limbs of the Gemrik asymmetrical anticline and short/long drainage relationship.

remind the fault propagation folds that developed in the hanging wall blocks of the blind thrusts dipping in N-NE directions. The blind thrusts, which form these asymmetrical anticlines, should have restricted the northern margins of the Çakırhüyük, Araban and Yavuzeli plains (Seyitoğlu et al., 2017) (Figures 4a, b, c). In the Araban Plain for different purposes drilled wells by Turkey Petroleum , MTA and DSI to be seen in the (Figure 5a, b, c), the thickness of the Quaternary units deposited on the Yavuzeli basalt reaches 380 meters in the north just in front of the blind thrusts, but gradually decreases towards south. It shows that

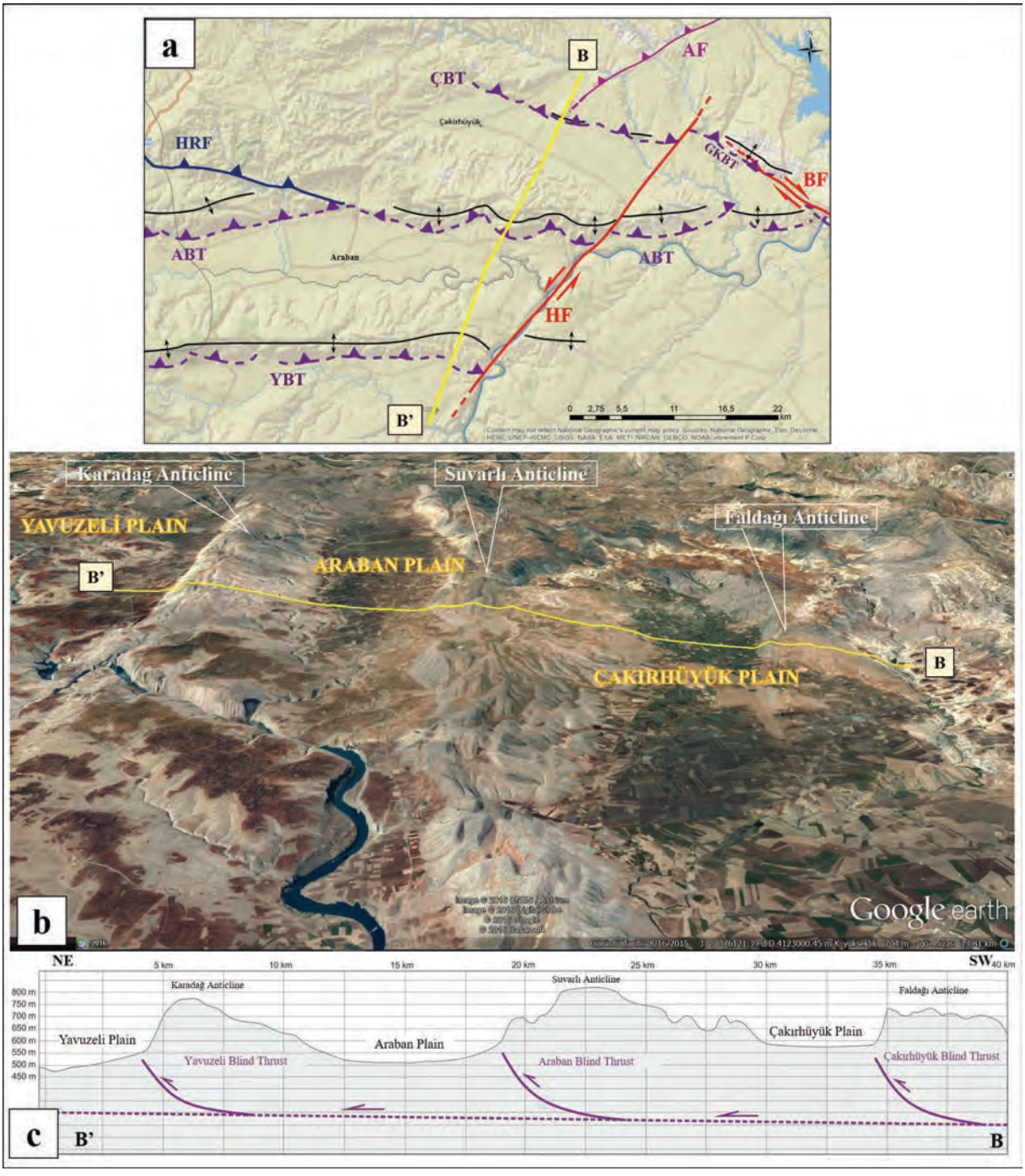

Figure 4- **(a)** Yavuzeli, Araban, Çakırhüyük plains and the map showing the structural elements. **AF**: Adıyaman Fault, **HF**: Halfeti Fault, **BF**: Bozova Fault, **HRF**: Harmancık Fault, ÇBT: Çakırhüyük Blind Thrust, **ABT**: Araban Blind Thrust, **YBT**: Yavuzeli Blind Thrust, **GKBT**: Gemrik-Karababa Blind Thrust, **(b)** Google Earth image of the Yavuzeli, Araban, Çakırhüyük Plains, **(c)** Yavuzeli, Araban, Çakırhüyük Blind Thrusts and the NE-SW directed topographical section showing the locations of the plains.

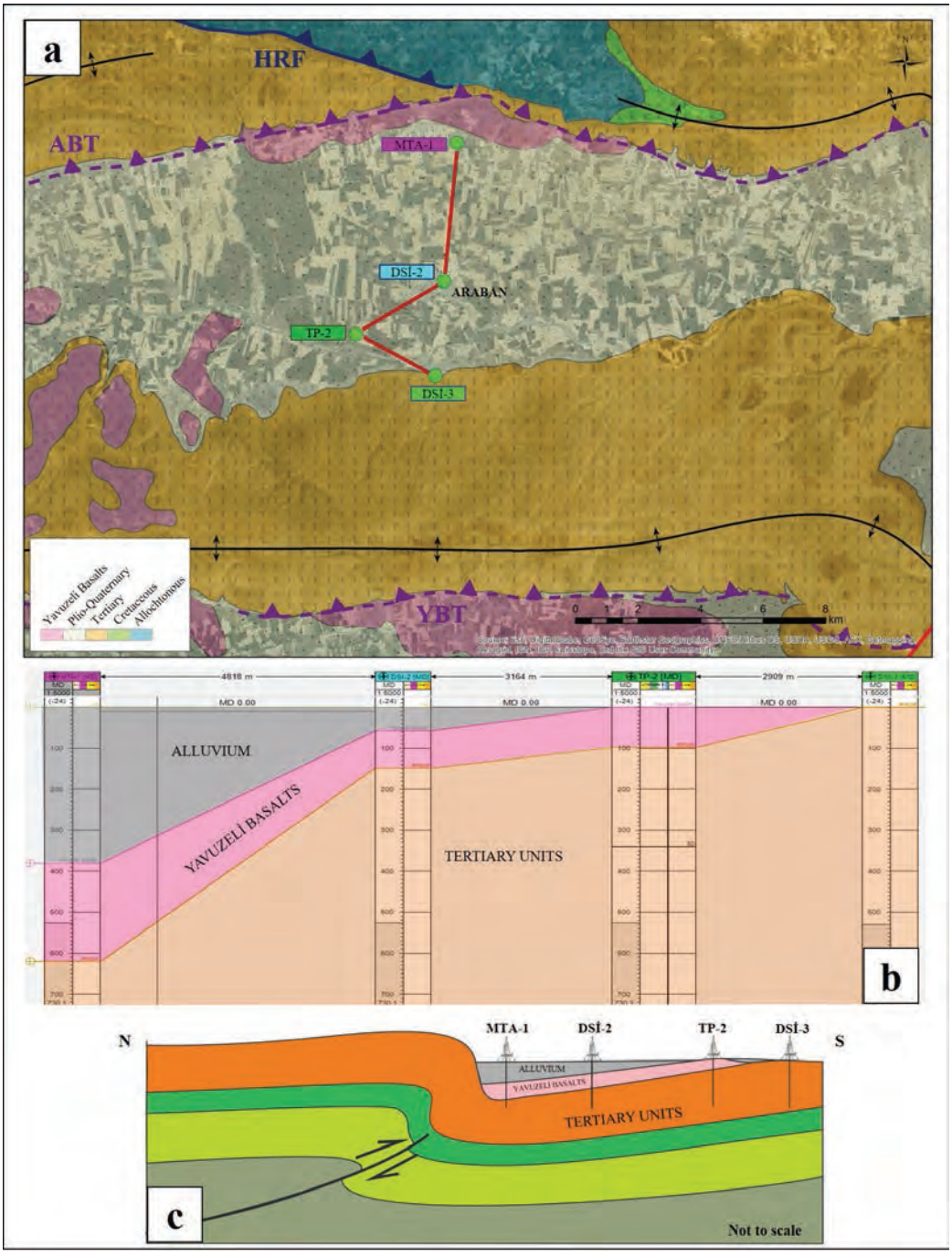

Figure 5- **(a)** Geologic map showing the drilling locations excavated in the Araban Plain by TPAO, MTA and DSI (State Water Works) for different purposes. **HRF:** Harmancık Fault, **ABT:** Araban Blind Thrust, **YBT:** Yavuzeli Blind Thrust, **(b)** N-S directing correlations of the wells MTA-1, DSI-2, TP-2 and DSI-3 excavated in the Araban Plain, **(c)** N-S directing schematic cross section passing through the Araban Plain.

the blind thrusts, which restrict plains from north control the deposition of the Quaternary alluvium and these thrusts, could be active structures. On the road cut between the Kuyulu and Karapınar, the shear zone cleavages, which developed on the segment reaching the surface, the section above the hanging block in the eastern continuation of the Araban blind thrust, show that this movement belongs to reverse faulting (Figures 6a, b, c). The structural data above the fault plane observed in the stone quarry in north of the Akdere village also verify this fact (Figures 6a, d, e).

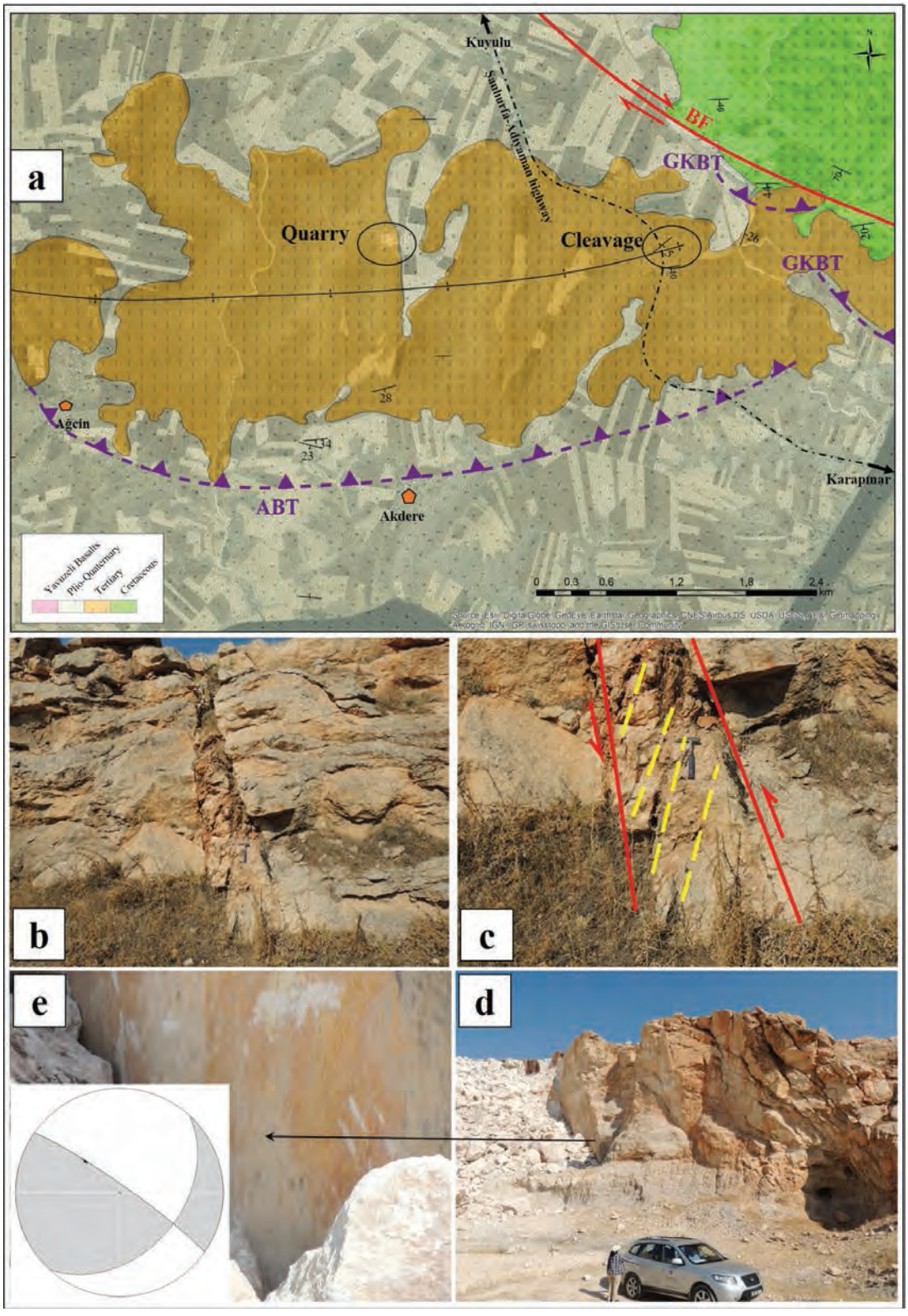

Figure 6- **(a)** Geological map of north of the Akdere village. **BF:** Bozova Fault, **ABT:** Araban Blind Thrust, **GKBT**: Gemrik-Karababa Blind Thrust, **(b)** shearing cleavages within the fault zone cutting the limestones of the Eocene Midyat Group, **(c)** the hanging wall should have moved upward -reverse fault- according to the position of the shear cleavage developed parallel to the S1 axis of the strain ellipse, **(d)** the plane of a different reverse fault in the stone quarry located in north of the Akdere village, **(e)** close up view of the fault surface and the equal area lower hemisphere stereographical projection formed by the striations measured on the fault plane.

3.2. Gemrik-Karababa Blind Thrust

Çemen et al. (1990), also by benefiting from the previous studies, defined Gemrik, Karababa and Dutluca anticlines, and stated that the fold axes were in NW-SE directions and their axial planes dipped towards NE by taking measurements from the fold limbs.

The field studies and remote sensing analyses carried out also showed that these anticlines were asymmetrical and the layers in the southern limbs were at high angle. Furthermore; there were also detected overturned layers inside the main valley in the NW of the Durak village (Figures 7a, b, e). As it can be anticipated from the deformed layers of the Şelmo Formation, the Gemrik-Karababa-Dutluca anticlines should have formed in post-Pliocene time.

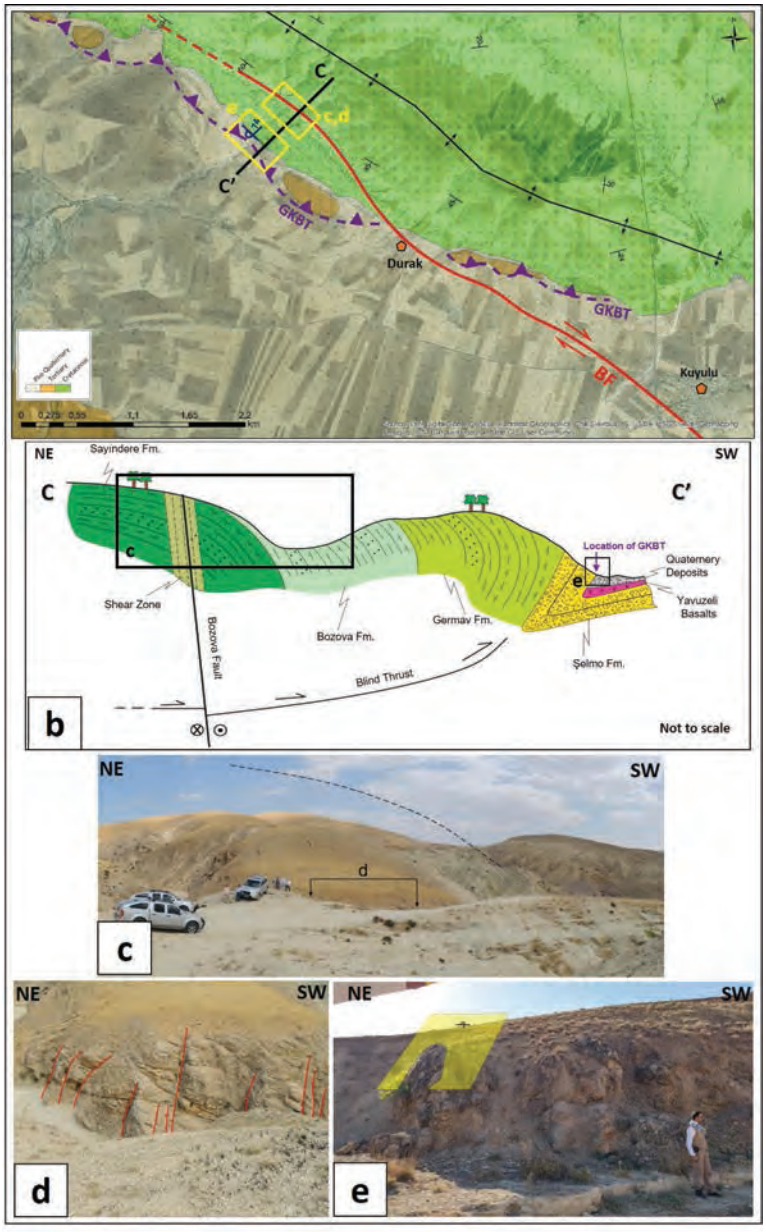

Figure 7- **(a)** Geological map of the Gemrik Anticline surround. **BF**: Bozova Fault, **GKBT:** Gemrik-Karababa Blind Thrust, **(b)** geological cross section prepared along the C-C' profile, **(c)** field view of the Gemrik Anticline, **(d)** shear zone of the Bozova Fault which cuts the Gemrik Anticline, **(e)** overturned layers which formed in the Pliocene Şelmo formation with the effect of the Gemrik-Karababa Blind Thrust.

All these data allow the Gemrik-Karababa-Dutluca anticlines to be interpreted as the fault propagation folds, which developed on the hanging wall of the blind thrusts, and the Gemrik-Karababa Blind Thrust to be drawn at the end of steeply dipping S-SW limbs of the asymmetrical anticlines (Figures 8a, b). The Gemrik-Karababa Blind Thrust and the Araban Blind Thrust approach each other in the north of the Karapınar village (Figure 8a).

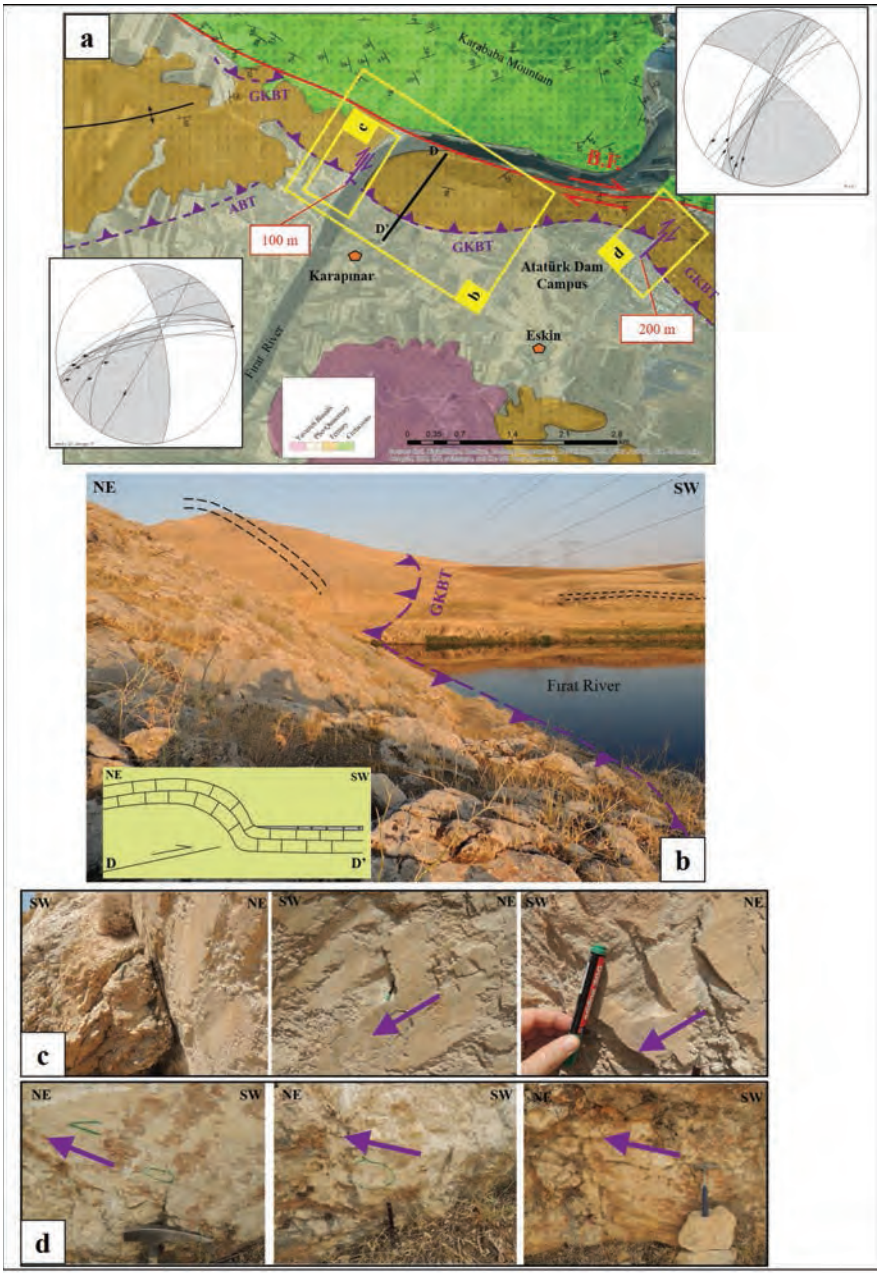

Figure 8- **(a)** Geological map belonging to the Atatürk Dam vicinity and the equal area lower hemisphere stereographical projection formed by the data measured on the fault plane of tear faults offsetting the blind thrust line which was drawn to the front of the steeply dipping beds of the asymmetrical Gemrik-Karababa anticline. **BF:** Bozova Fault, **GKBT**: Gemrik-Karababa Blind Thrust, **(b)** view from the northern limb of the Karababa asymmetrical anticline and its schematic relationship with the probable blind thrust, **(c)** views of the structures (striations, carrot structures and slickensides) belonging to the tear faults located near the Fırat River, the south of the Atatürk Dam discharge area, **(d)** striations of the tear fault at the tunnel exit located in the northwest of the Atatürk Dam settlement (Purple arrows show the movement direction of the missing block).

On section, where the Fırat (Euphrates) River erodes the Karababa anticline and at the tunnel exit around the Atatürk Dam settlement, the Gemrik-Karababa Blind Thrust has been shifted nearly 100-200 meters by the NE-SW trending right lateral strike-slip tear faults. The structural data regarding them is presented in figures 8a, c and d.

3.3. Halfeti Fault

The Halfeti Fault, is a NE-SW trending strike-slip fault which extends between Yarımtepe in the north and the Sarılar village in the south. It was first mapped by Peksü (1976) and defined by Çemen (1986) as the Kemerli Fault. It was emphasized by Çemen (1990) that the fault shifted the Suvarlı anticline 500 meters leftward and was conjugate of the Bozova Fault.

The northeastern extension of the Halfeti Fault passes through the western side of the Yarım Tepe (hill) from the traceable southeast end of the Gemrik-Karababa and Çakırhüyük Blind Thrusts (north of Beşyol) (Figure 9a). It is well observed in the north of Halfeti, in NE-SW directions between the east of the Sarılar village and the northwest of the Fıstıklıdağ village. It directly limits the Yavuzeli and Araban plains and shifts the Suvarlı anticline laterally 2.5 km to the left. The E-W directed flow of the Fırat River between the Atatürk Dam and the Halfeti Fault returns to NE-SW direction with the effect of the fault in the southwest of the Fıstıklıdağ village and flows along the fault zone (Figure 9a).

The structural data obtained from the northeast and southwest parts of the Halfeti Fault show that

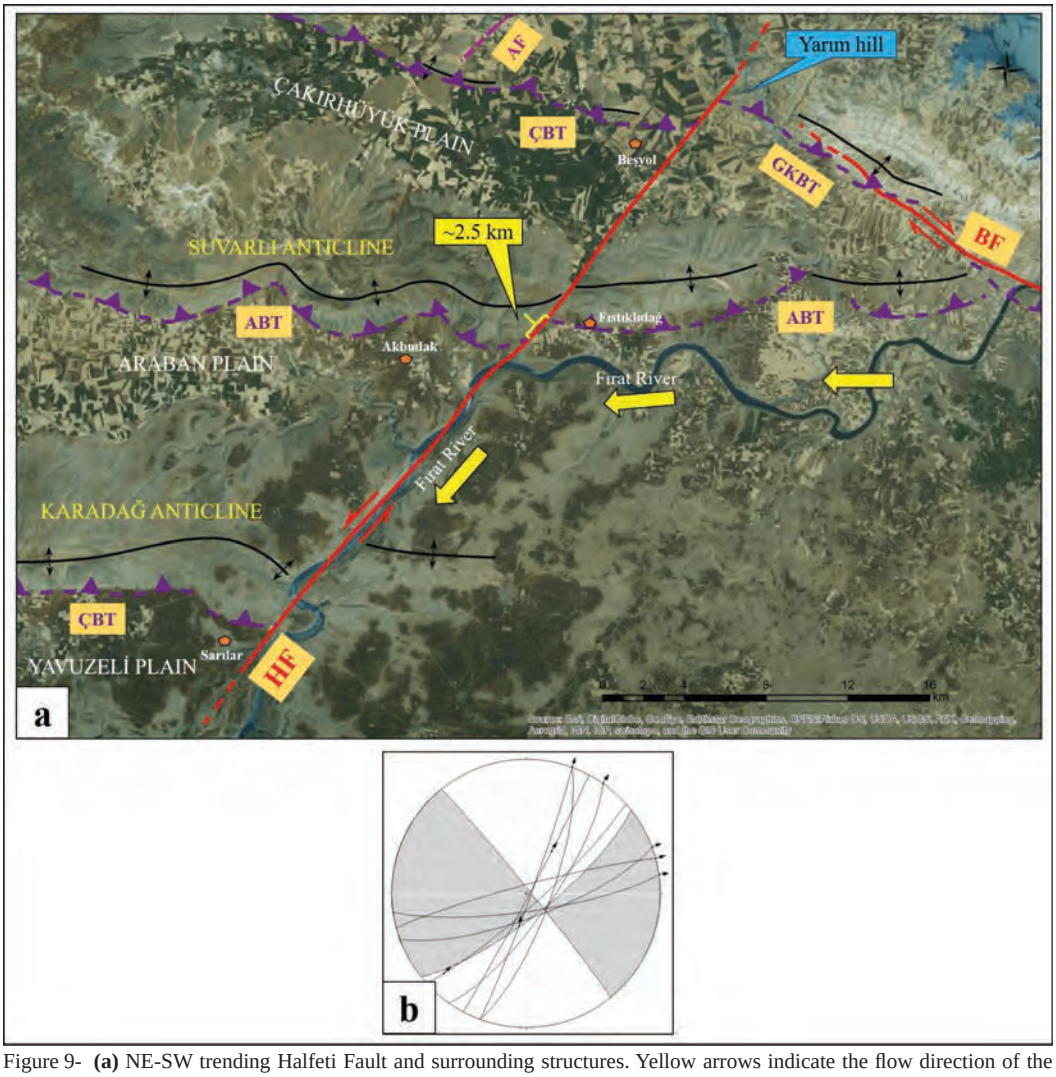

Figure 9- **(a)** NE-SW trending Halfeti Fault and surrounding structures. Yellow arrows indicate the flow direction of the Fırat River controlled by the Halfeti Fault. **HF**: Halfeti Fault, **BF**: Bozova Fault, **ABT**: Araban Blind Thrust, ÇBT: Çakırhüyük Blind Thrust, **GKBT**: Gemrik-Karababa Blind Thrust, **(b)** the equal area lower hemisphere stereographical projection formed according to the striations measured on the planes of the Halfeti Fault.

this structure is the left lateral strike-slip in character (Figure 9b). The Halfeti Fault should be one of the youngest faults that was formed in Quaternary in the region as it cuts the anticlines associated with the Gemrik-Karababa and Araban blind thrusts which developed in the post Pliocene.

3.4. Bozova Fault

First studies regarding the Bozova Fault began in 1960's. It was made by the American Overseas Petroleum Limited and the Bozova Fault was described as the high angle reverse fault. Sungurlu (1972) defined the Bozova Fault, which had uplifted the region starting from Permian to Cretaceous. He also stated that the fault had controlled the deposition in the region in Coniacian-Santonian times, then reworked as normal fault in the Miocene time.

Çemen et al. (1990) defined the Bozova Fault, which had been previously described as a strike-slip fault with reverse component in the maps made by Perinçek et al. (1987), as the right lateral strike-slip fault. They also emphasized that the first reverse movement on the Bozova Fault had occurred in the Oligocene, then moved as a strike-slip fault in the Late Miocene or Early Pliocene times. In the same study, the folds around Bozova Fault were examined and stated that the fold axes of Gemrik, Karababa and Dutluca anticlines in the northeastern block of fault are nearly parallel to the Bozova Fault showing no genetic relationship between folds and Bozova Faults. However, the open folds having axes of northeast-southwest in the southwestern block of the fault were attributed to the Bozova Fault (Çemen et al., 1990).

The NW-SE extending Bozova Fault, which is also shown in the active faults of the General Directorate of Mineral Research and Exploration (MTA) (Duman et al., 2012), is distinctively followed starting from the Durak village in the northwest until the Küçük Tülmen village in the southeast (Figure 10a). The NE-SW trending thrust faults, which developed as segments separating from the Bozova Fault, are observed in Arıkök, NW of Bozova and around the Küçük Tülmen village.

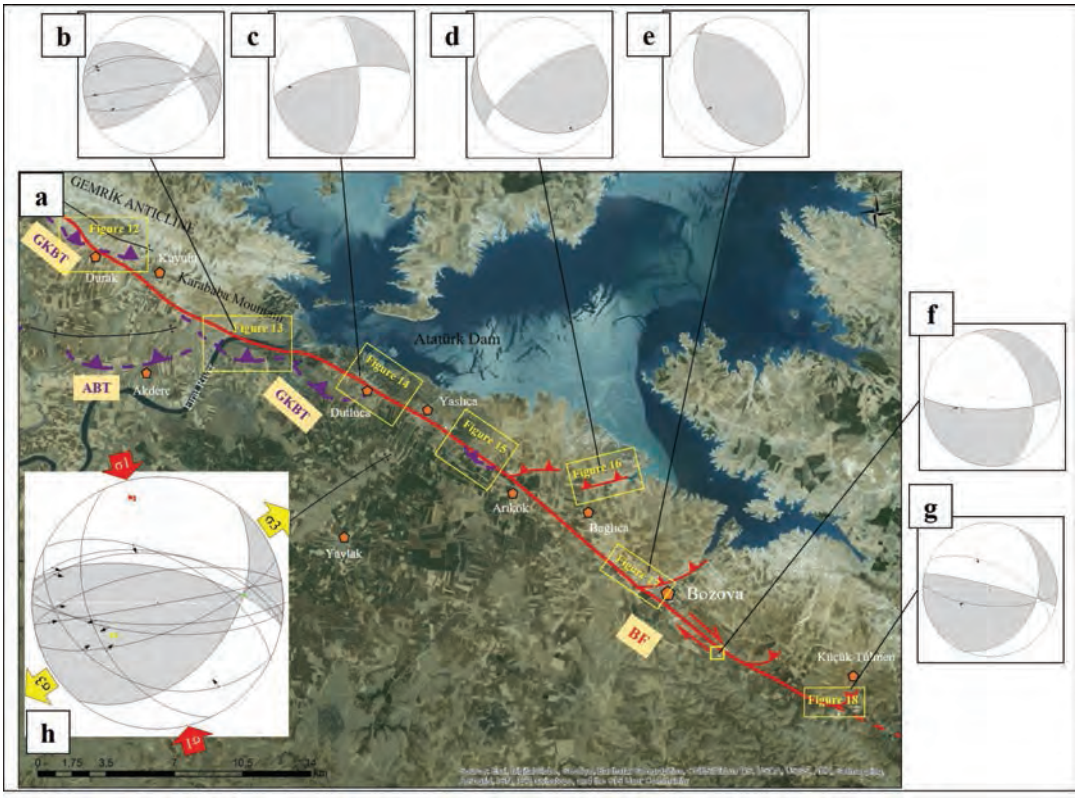

Figure 10- **(a)** General view of the Bozova Fault, **BF:** Bozova Fault, **GKBT:** Gemrik-Karababa Blind Thrust, **ABT**: Araban Blind Thrust. The equal area lower hemisphere stereographical projection formed by the structural data measured on the fault planes located in; **(b)** the east of the Atatürk Dam, **(c)** the north of the Dutluca village, **(d)** the northeast of the Bağlıca village, **(e)** the northwest of the Bozova town, **(f)** the southeast of the Bozova town, **(g)** the vicinity of the Küçük Tülmen village, **(h)** the equal area lower hemisphere stereographical projection and stress directions formed by the total assessment of the structural data measured on the Bozova Fault.

The data belonging to the northwest end of the Bozova Fault is seen in shear zones cutting the Karababa anticline (Figures 7 and 10). One of the most significant geomorphological data are the warps in the northwest of the Durak village, along the river flowing towards the southeast observed both on field studies and on Google Earth images (Figure 11).

The fault passes through the Durak village, cuts the Gemrik-Karababa Blind Thrust and reaches the Kuyulu village. This fault, which cuts again the Karababa Blind Thrust in the southwest of the Kuyulu village, is seen in such a way to cut the Karababa Mountain anticline as being parallel to its axis. The Fırat River should be chasing this line just in front

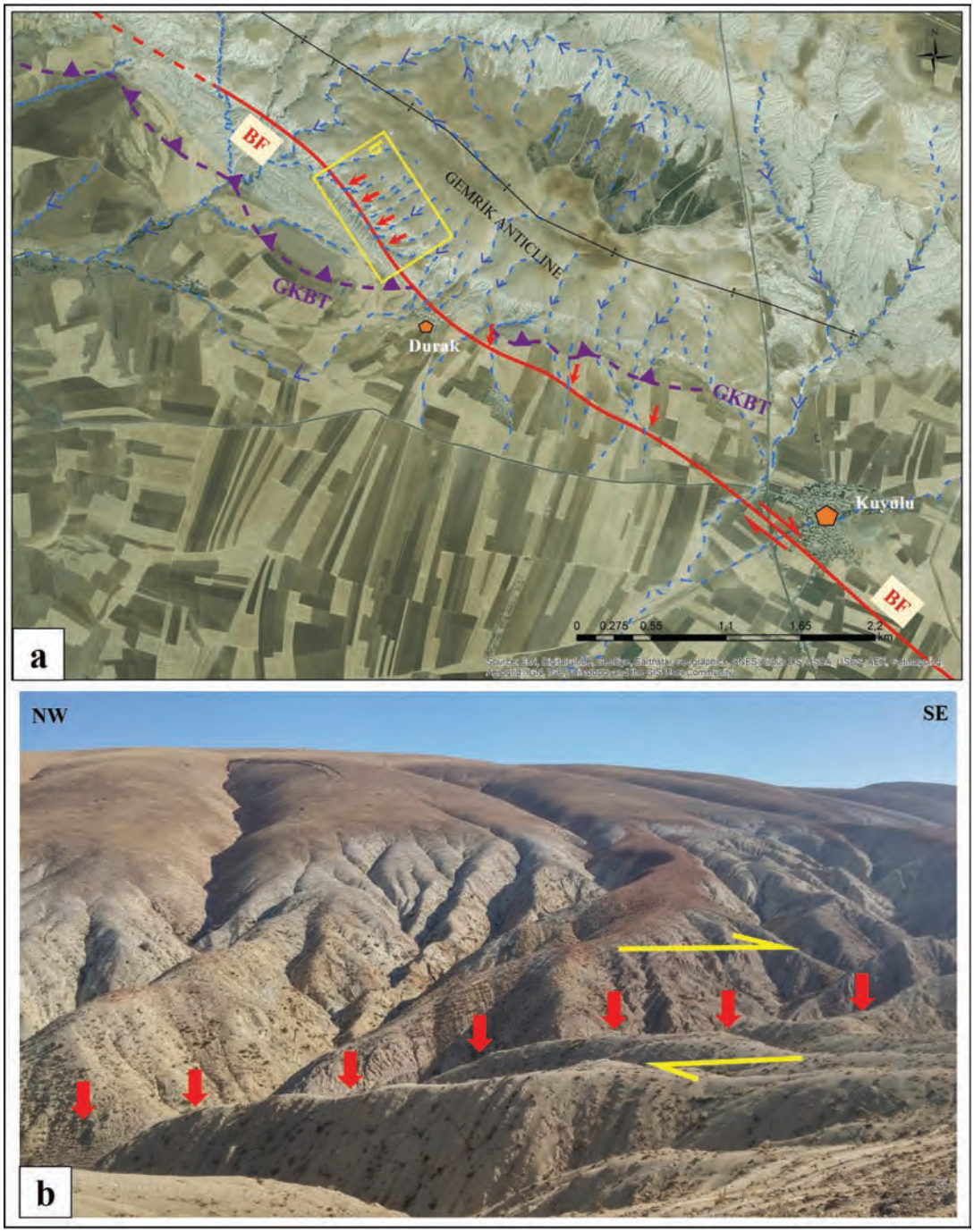

Figure 11- **(a)** The map showing the distortions that formed in stream channels by the effect of the Bozova Fault, the north of the Durak village, **(b)** the field view (red arrows indicate where the Bozova Fault passes through). **BF:** Bozova Fault, **GKBT:** Gemrik-Karababa Blind Thrust.

of the Atatürk Dam (Figure 12). The fault cuts the Gemrik-Karababa Blind Thrust and the Dutluca anticline as being parallel to the its axis just in north of Dutluca passing through the southern part of the Atatürk Dam, then it reaches the Arıkök village via Yaslıca. In the area, which remains between the Atatürk Dam and the Dutluca village, there are observed slip surfaces and shearing developed under the effect of fault in the Sayındere formation (Figure 13). The Gemrik-Karababa Blind Thrust is cut again in the northwest of Arıkök. The limb of the anticline located on the hanging wall of this thrust is clearly cut, and this situation is distinctively observed both on the field and in Google Earth images (Figure 14).

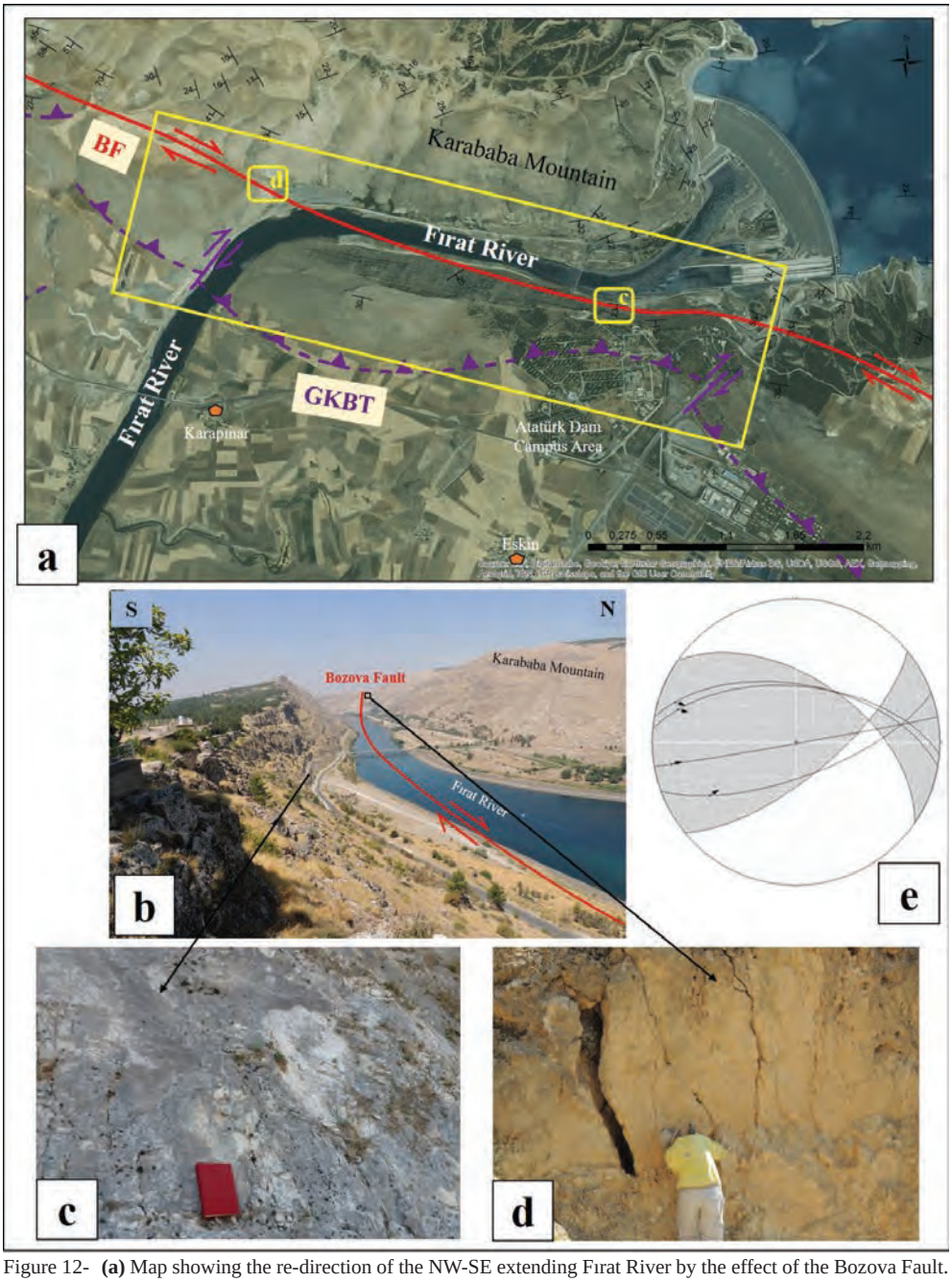

Figure 12- **(a)** Map showing the re-direction of the NW-SE extending Fırat River by the effect of the Bozova Fault. Yellow squares indicate the locations of photos in c and d. **BF:** Bozova Fault, **GKBT:** Gemrik-Karababa Blind Thrust, **(b)** photo showing the extension of the Bozova Fault along the Fırat River, **(c)** the fault plane located on the southern block of the Bozova Fault, **(d)** the fault plane located on the northern block of the Bozova Fault, **(e)** the equal area lower hemisphere stereographical projection formed by the structural data measured on fault planes.

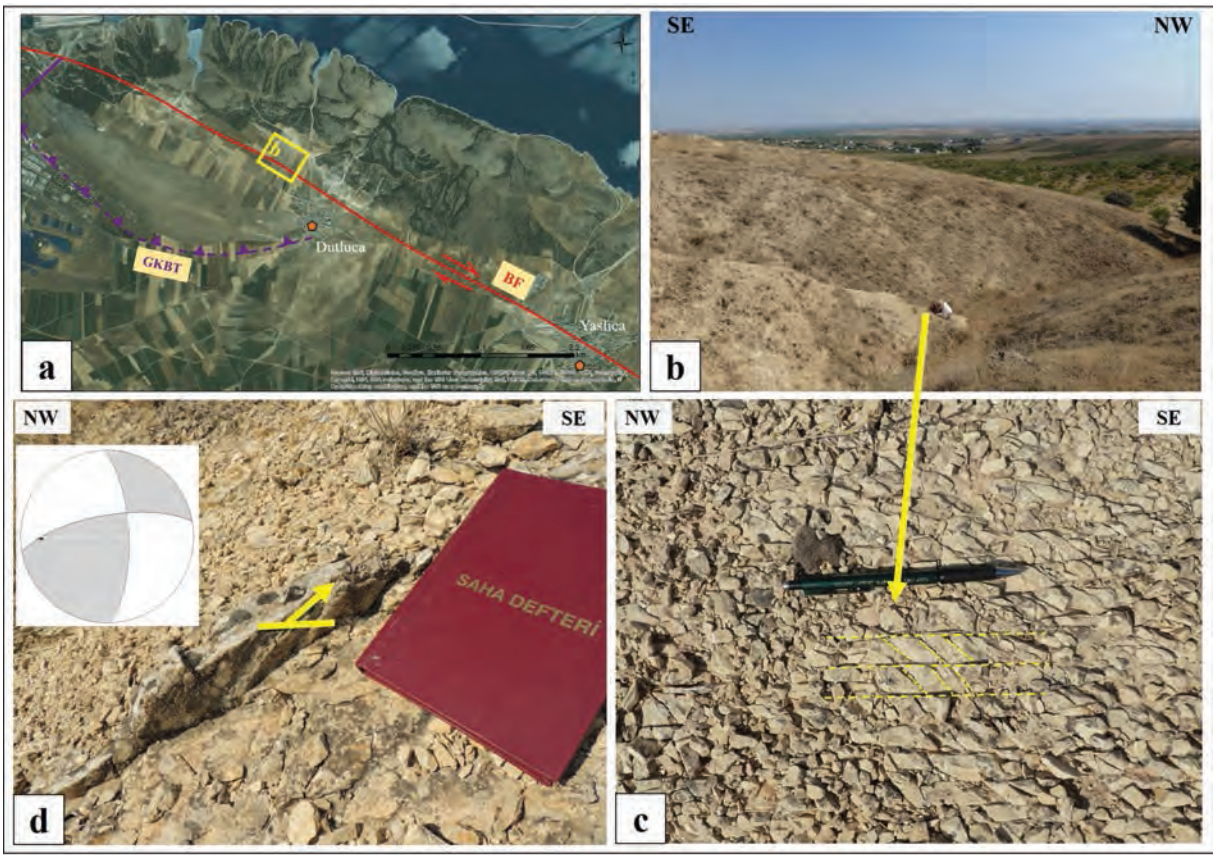

Figure 13- **(a)** Map showing the extension of the Bozova Fault in north of the Dutluca village, **GKBT:** Gemrik-Karababa Blind Thrust, **(b)** the shear zone formed in the Sayındere formation by the effect of the Bozova Fault, **(c)** joint systems developed in the Sayındere formation due to the Bozova Fault, **(d)** the striations of the Bozova Fault in the Sayındere formation and the equal area lower hemisphere stereographical projection made with this measurement.

As it is mentioned above, the Bozova Fault cuts the formerly developed Gemrik-Karababa Blind Thrust in many places and the tear faults mentioned in Figure 8, which are associated with this thrust, are kinematically unconformable.

The topography is undulated in the north of the Bağlıca village and the layers belonging to the Sayındere formation in this area form an asymmetrical anticline of which its one limb reaches 90°. This situation verifies the presence of thrusts of the Bozova Fault drawn by Duman et al. (2012) (Figure 15).

The Bozova Fault runs parallel to the Şanlıurfa-Adıyaman road between Arıkök and Bozova (Figure 10a). There are observed a color change and fragility due to the hydrothermal activity in the limestones of the Sayındere formation just in the northwest of the Bozova town (Figures 16a, b, c). The layers of the Sayındere formation just in the north of the Bozova town to gain a dip of 40° in S-SW direction could be the indicator of a thrust development as well as in the east of Arıkök (figure 16a).

In the southeast of the Bozova settlement, the structural data showing the right lateral movement of the Bozova Fault, which runs parallel to the Adıyaman-Şanlıurfa road, can be seen in stones quarries excavated along the road sides. It becomes difficult to follow the Bozova Fault after it makes a curvature towards the Küçük Tülmen village, and there is not any morphological evidence showing that it continues towards the southeast (Figure 17).

The total assessment (Figure 10h) of the structural data collected from the Bozova Fault (Figures 12-17), shows that the fault in the northwest end and in the middle part is right lateral strike-slip with thrust component and dips towards the northeast. The focal mechanism solutions of the earthquakes occurring in the southeastern end of the Bozova Fault, where it is connected to the Akçakale-Harran Graben in the region

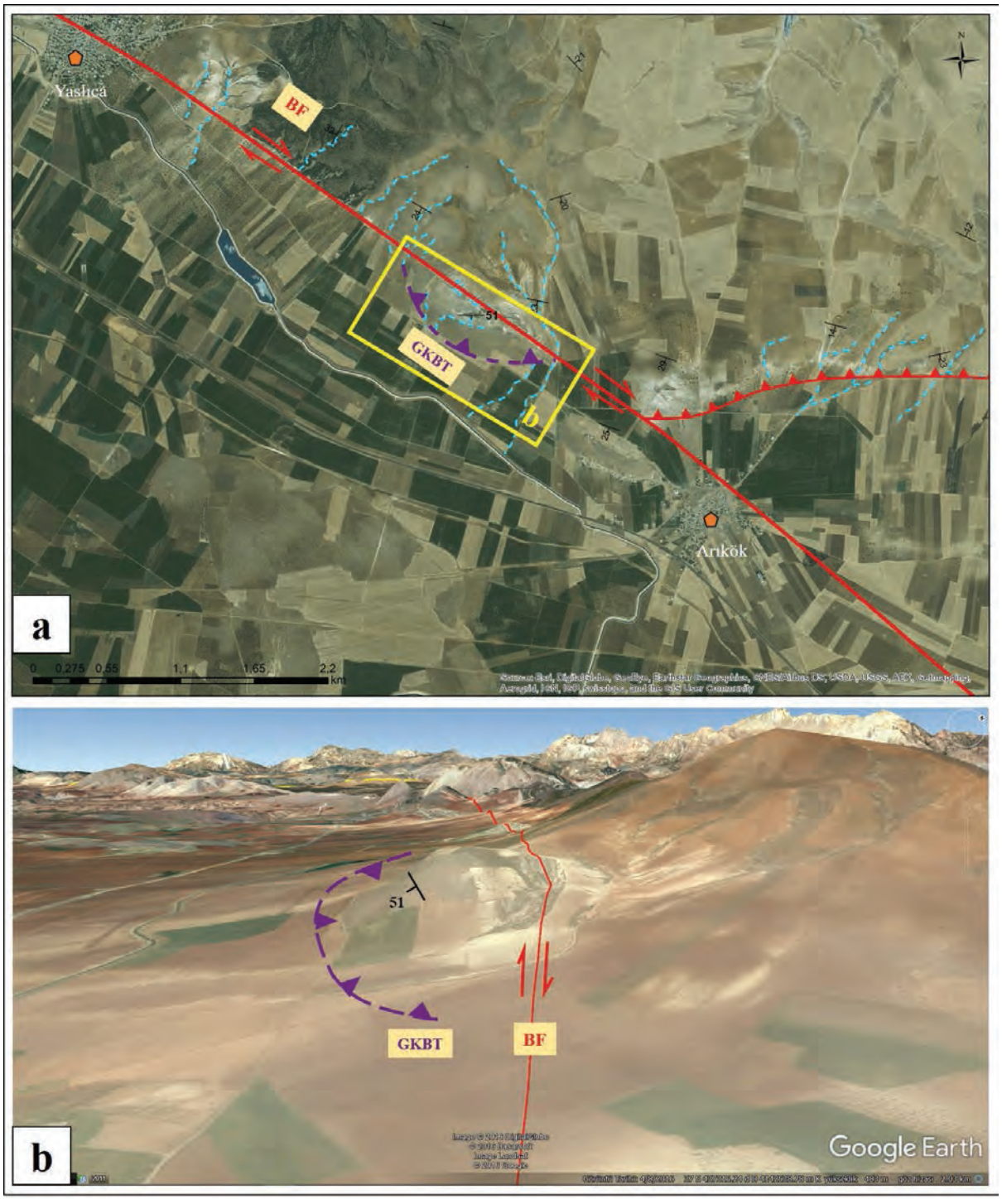

Figure 14- **(a)** Map showing the cross cutting of the Gemrik-Karababa Blind Thrust by the Bozova Fault in northwest of the Arıkök village, **GKBT**: Gemrik-Karababa Blind Thrust, **(b)** the anticline limb cut by the Bozova Fault on the hanging wall of the Gemrik-Karababa Blind Thrust (looking north).

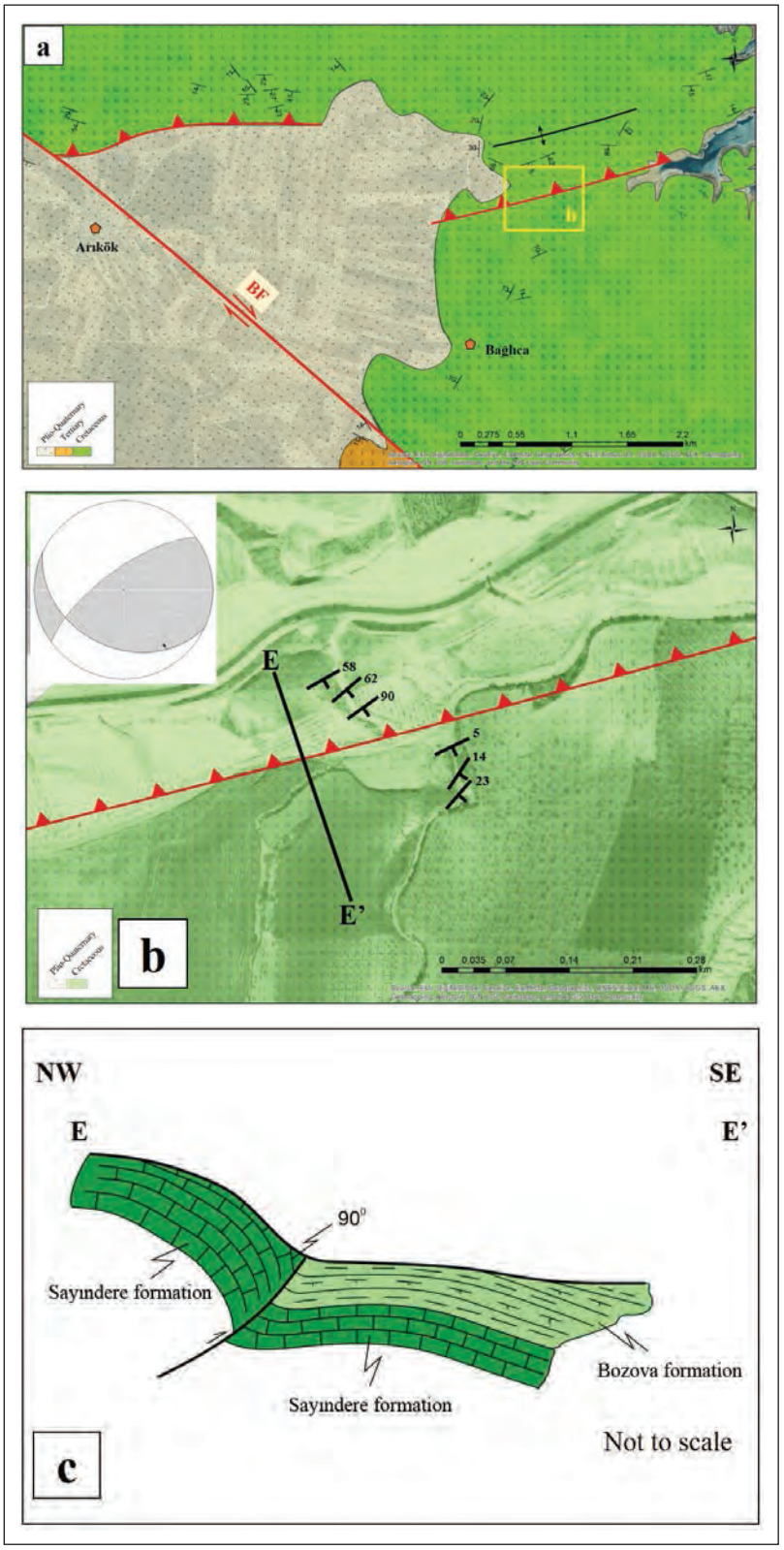

Figure 15- **(a)** Geological map showing the thrust segments of the Bozova Fault around the Bağlıca village. **BF:** Bozova Fault, **(b)** geological map showing the dip change developed in layers of the Sayındere Formation by the effect of the thrust fault located in northeast of the Bağlıca village and the equal area lower hemisphere stereographical projection formed by the structural data measured on this fault, **(c)** geological cross section of the profile E-E'.

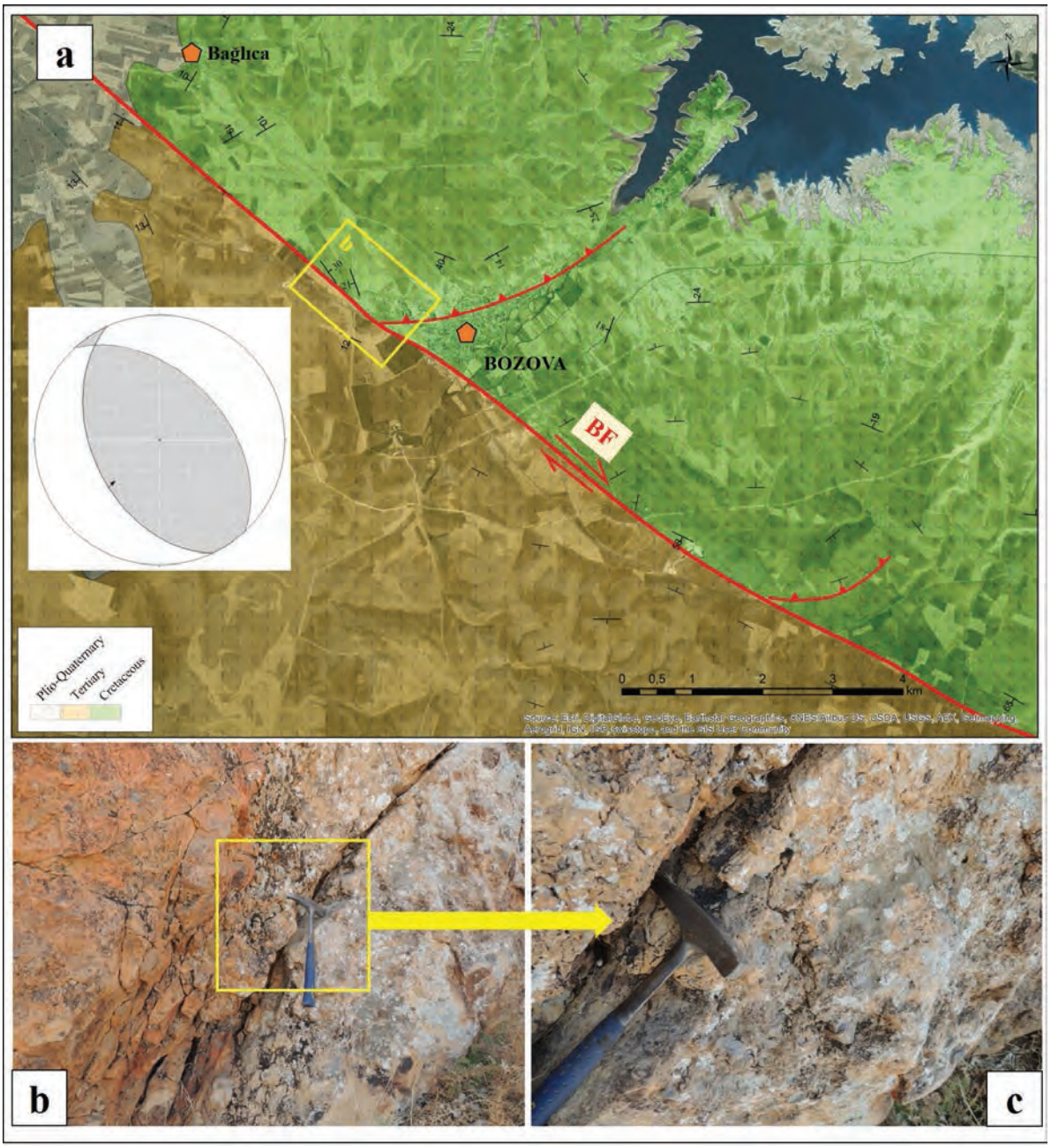

Figure 16- **(a)** Geological map showing the location of the Bozova Fault in north of the Bozova town and the equal area lower hemisphere stereographic projection formed by the structural data measured on the thrust segment separating from the fault, **BF:** Bozova Fault, **(b)** and **(c)** photos showing the color change and cataclastic zone that formed by the hydrothermal activity in the Sayındere formation.

(Kartal et al., 2011; Seyitoğlu et al., 2017), states that the Bozova Fault evolved into a right lateral fault with normal component, dipping southwest and has an helicoidal geometry (Figure 18). The seismic activity, which has recently occurred in the region (2017.03.02 Samsat earthquake, M=5.5), revealed the presence of a segment that runs sub parallel to the Bozova Fault, trending in NW-SE direction, with the southeast end approaching to the Bozova Fault (Figure 18). The depth distribution of the seismic activity, which occurs on this segment and the northeastward dipping plane shown in the focal mechanism solution of the USGS, are seen in compatible with each other (Figure 19). It is theoretically anticipated that the strike-slip fault segments are connected to one shearing zone at depth (Naylor et al., 1986).

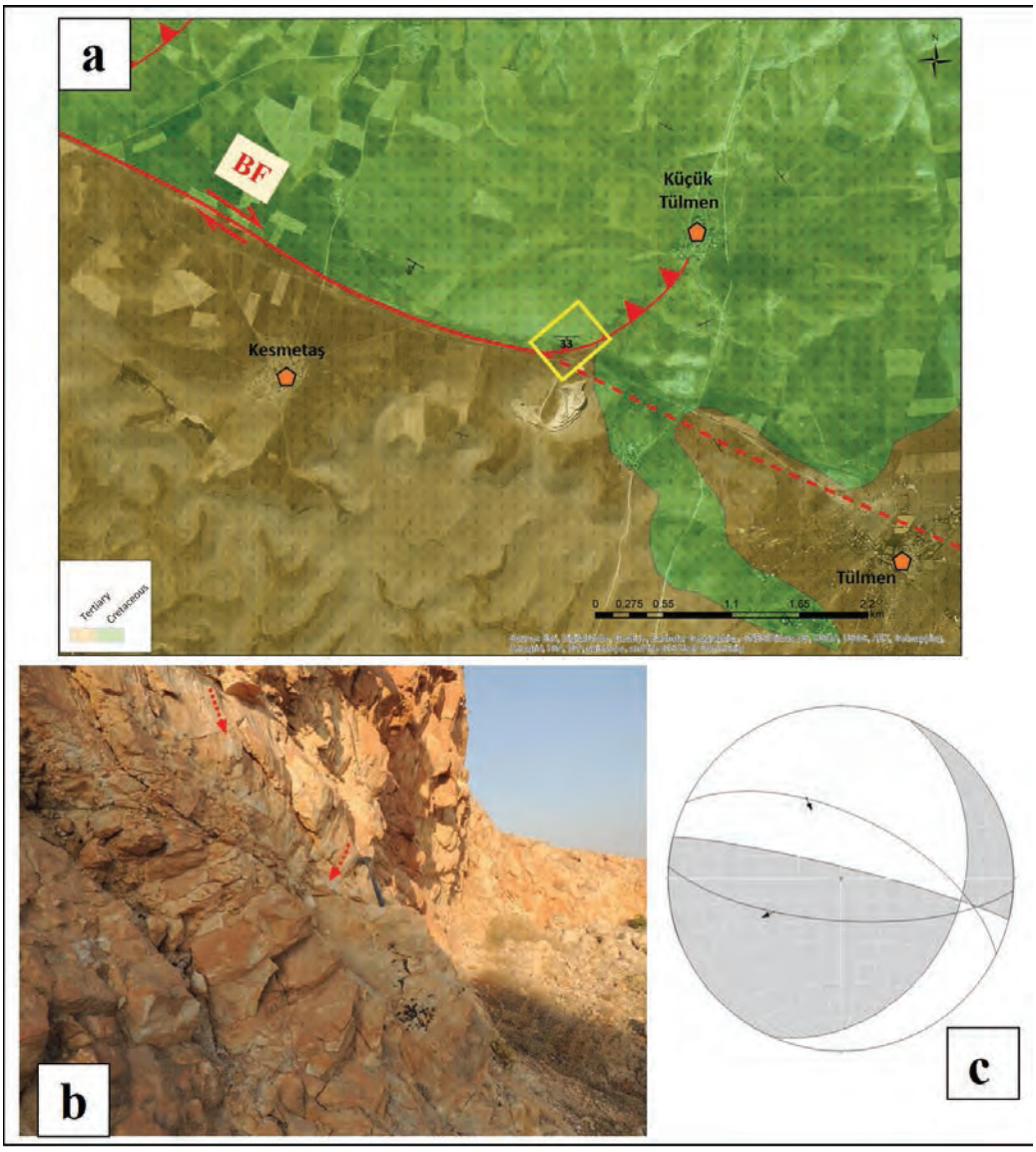

Figure 17- **(a)** Geological map of the Küçük Tülmen village surround where the Bozova Fault is last observed morphologically, **BF:** Bozova Fault, **(b)** view from the striations of the fault surface, **(c)** the equal area lower hemisphere stereographical projection formed by the data measured of the fault plane.

4. Discussion and Results

The E-W trending thrust faults, the NW-SE right lateral strike-slip faults and the NE-SW left lateral strike-slip faults which are the typical neotectonic structures of the Southeastern Anatolia, are all located in the NE Gaziantep. The thrust faults in the area were defined as blind thrusts by means of the fault propagation folds developed on hanging walls of the faults (e.g. Çakırhüyük, Araban, Yavuzeli Blind Thrusts and Gemrik-Karababa Blind Thrusts). The presence of the Şelmo Formation, which folded in the Gemrek-Karababa anticline, shows that the blind thrusts in the study area developed in the post Pliocene. The Araban Blind Thrust and the Gemrik-Karababa Blind Thrust are distinctively cut by the left lateral Halfeti Fault and by the right lateral Bozova Fault, and they are the youngest structures. However, these relationships do not show that the E-W trending blind thrusts are not active, because the blind thrust associated recent earthquakes [2011.10.23 Van earthquake - M=7.3: Doğan and Karakaş (2013); Elliot et al., (2013); 2012.06.14 - ML=5.5 Şırnak-Silopi earthquake: Seyitoğlu et al., 2017)] developed in the Eastern and Southeastern Anatolia show that the blind thrusts too have a potential to generate earthquakes and actively compensate the regional N-S contraction like the strike-slip faults.

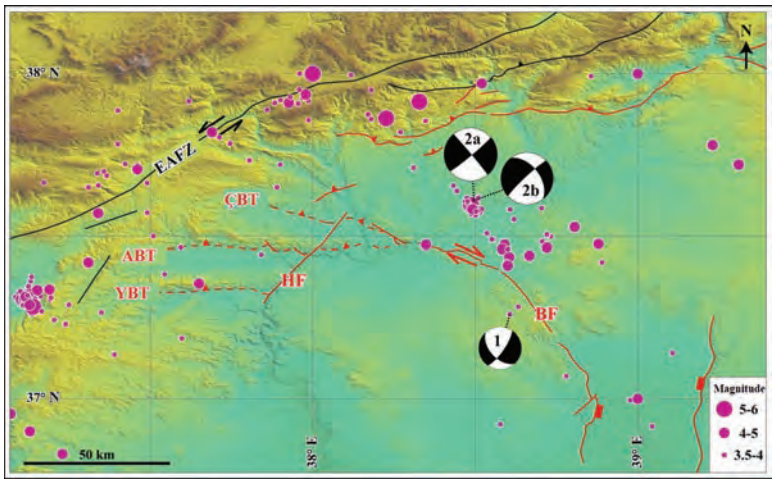

Figure 18- The seismic activity around the Bozova Fault (data belong to AFAD and include earthquakes from 1990-recent with M≥3.5). The focal mechanism solution of the 2015.11.10 (M=3.6) earthquake (1) (Seyitoğlu et al., 2017); 2017.03.02 (M=5.5) the focal mechanism solution of Samsat earthquake (2a AFAD, 2b USGS). **ÇBT**: Çakırhüyük Blind Thrust, **ABT**: Araban Blind Thrust, **YBT**: Yavuzeli Blind Thrust, **HF**: Halfeti Fault, **BF**: Bozova Fault.

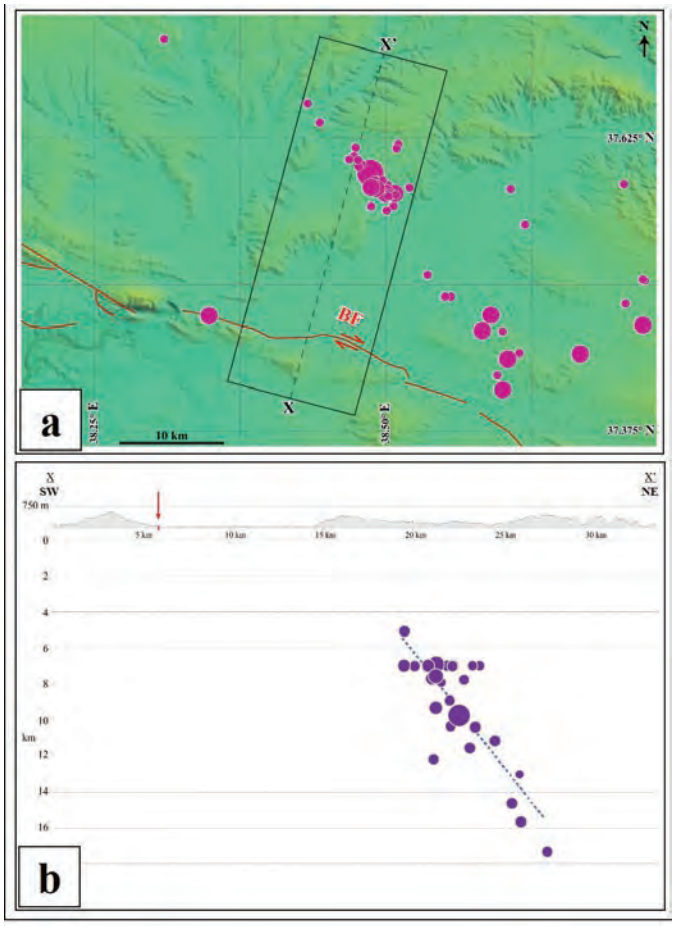

Figure 19- **(a)** The epicenter and depth distribution of the seismic activity around the Bozova Fault. The rectangle area shows the data used in the depth distribution, **(b)** topographical section is 5 times exaggerated and red arrow shows the trace of the Bozova Fault on the surface. The dashed blue line represents the fault dip in the USGS focal mechanism solution.

Acknowledgements

This article is produced from the MSc thesis, which is about to be completed by the first author in Ankara University. Due to the facilities provided in the field studies authors would like to thank Turkish Petroleum Co. We are thankful to Dr. Korhan Esat for his supports for the earthquake data, and to invaluable referees, to Prof. Erdinç Yiğitbaş, Assoc. Prof. Ali Farzipour-Saein, Assist. Prof. Hakan Güneyli and to Dr. Selim Özalp for their critiques and suggestions in developing this article.

References

Açıkbaş, D., Sungurlu, O., Akgül, A., Erdoğan, T.,1979. Geology and petroleum possibilities of Southeast Turkey. TPAO report no: 1410

Açıkbaş, D., Akgül, A., Erdoğan, L. T. 1981. Güneydoğu Anadolu'nun hidrokarbon olanakları ve Baykan-Şirvan-Pervari yöresinin jeolojisi. TPAO report no: 1543.

American Overseas Petroleum Limited. 1960. Geological report on the SAF-Bozova trend- License no:8. TPAO report no: 765

Agard, P., Omrani, J., Jolivet, L., Whitechurch, H., Vrielynck, B., Spakman, W., Monie, P., Meyer, B., Wortel, R. 2011. Zagros orogeny: a subduction-dominated process. Geol Mag 148, 692-725.

Batı, Z. 1991. X. Bölge kuzeyinin Miyosen palinostratigrafisi. TPAO report no: 1683.

Berberian, M. 1995. Master "blind" thrust faults hidden under the Zagros folds: active basement tectonics and surface morphotectonics. Tectonophysics 241, 193-224

Biddle, K.T., Bultman, T.R., Fairchild, L.H., Yılmaz, P.O. 1987. An approach to structural interpretation of the southeast Turkey fold and thrust belt. Proceedings of 7th Biannual Petroleum Congress of Turkey. UCTEA Chamber of Petroleum Engineers, 78-88.

Bolgi, T. 1961. V. Petrol Bölgesi seksiyon ölçmeleri AR/TPO/261 nolu saha ile Reşan-Dodan arası batısındaki sahanın striktüel etüdleri. TPAO report no: 162.

Çemen, İ. 1986. Structural geology of the western part of the Araban tectonic block implications concerning petroleum potential of the region. TPAO report no: 2239.

Çemen, İ. 1990. Araban Tektonik Bloğu Doğu Kısmının Yapısal Jeolojisi ve Petrol Potansiyeli. TPAO report no: 2727.

Çemen, İ., Perinçek, D., Ediger, Ş. V., Akça, L. 1990. Güneydoğu Anadolu'daki Bozova doğrultu atımlı Fault: üzerindeki ilk hareket ters faylanma olan faylara bir örnek. Türkiye 8. Petrol Kongresi, 169-179.

Çoruh, T. 1991. Adıyaman civarında (XI. Bölge kuzeybatısı ve XII. Bölge) yüzeyleyen Kampaniyen-Tanesiyen istifinin biyostratigrafisi ve paleocoğrafik evrimi. TPAO report no: 1656.

Dewey, J.F. Hempton, M.R., Kidd, W.S.F., Şaroğlu. F., Şengör. A.M.C. 1986. Shortening of continental lithosphere: the neotectonics of Eastern Anatolia a young collision zone. In: Coward M P, Ries A C, editors. Collision Tectonics. Geol Soc Lond Spec Publ: 19, 3-36 (Robert M. Shackleton volume).

Doğan, B., Karakaş, A. 2013. Geometry of co-seismic surface ruptures and tectonic meaning of the 23 October 2011 Mw 7.1 Van earthquake (East Anatolian Region, Turkey). J Struc Geol: 46, 99-114.

Duman, T.Y. Emre, Ö., Olgun, Ş., Özalp, S., 2012. 1:250.000 Scale Active Fault Map Series of Turkey, Cizre (NJ38-9) Quadrangle. Serial number: 53, General Directorate of Mineral Research and Exploration, Ankara-Turkey.

Duran, O., Şemşir, D., Sezgin, İ. Perinçek D. 1988. Güneydoğu Anadolu'da Midyat ve Silvan Gruplarının Stratigrafisi, Sedimantolojisi ve Petrol Potansiyeli. TPJD Bulletin. 2, 99 -126.

Duran, O., Şemşir, D., Sezgin, İ. Perinçek D. 1989. Güneydoğu Anadolu'da Midyat ve Silvan Gruplarının stratigrafisi, sedimantolojisi ve paleocoğrafyası, paleontolojisi, jeoloji tarihi, rezervuar ve diyajenez özellikleri ve olası petrol potansiyeli. TPAO report no: 2563.

Elliot, J. R. Copley, A. C., Holley, R., Scharer, K., Parsons, B., 2013. The 2011 Mw 7.1 Van (Eastern Turkey) earthquake. Journal of Geophysical Research, Solid Earth, 118, 1-19.

Emre, Ö., Duman, T.Y., Özalp, S., Elmacı, H., Olgun, Ş., Şaroğlu, F., 2013. Active fault map of Turkey with an explanatory text 1:1,250,000 scale. Special Publication Series 30, General Directorate of Mineral Research and Exploration, Ankara, Turkey. ISBN: 978- 605-5310-56-1.

Ercan, T. Fujitani, T., 1990. Doğu ve Güneydoğu Anadolu Neojen-Kuvaterner Volkanitlerine İlişkin Yeni

Jeokimyasal, Radyometrik ve İzotopik Verilerin Yorumu. Bulletin of Mineral Research and Exploration 110, 143-164.

Erenler, M., 1989. XI-XII. Bölge güney alanlarındaki kuyularda Mesozoyik çökel istifinin mikro paleontolojik incelenmesi. TPAO report no: 1364.

Farzipour-Saein, A., Yassaghi, A., Sherkati, S., Koyi, H. 2009. Mechanical stratigraphy and folding style of the Lurestan region in the Zagros Fold - Thrust belt, Iran. Journal of the Geological Society, London 166, 1101-1115.

Gossage, D. W. 1956. Compiled progress report on the geology of part of Petroleum District VI, Southeast Turkey: N. V. Turkse Shell. Report no. GRT. 2, 22 p.

Görür, N., Çelikdemir, E., Dülger, S. 1987. Güneydoğu Anadolu X, XI. ve XII. Petrol Bölgelerinde Mardin Grubu Karbonatlarının Sedimantolojisi: Yayılım, fasiyes, çökelme ortamı ve paleocoğrafya. TPAO report no: 2321

Güven, A., Dinçer, A., Tuna, M. E., Çoruh, T. 1991, Güneydoğu Anadolu Kampaniyen-Paleosen otokton istifinin stratigrafisi, TPAO report no: 2828.

Hall, J.K., Krasheninnikov, VA., Hirsch, F., Benjamini, C., Flexer, A. 2005. Geological Framework of the Levant. Volume II: The Levantine basin and Israel. Historical Productions-Hall, Jerusalem, Israel. ISBN: 965-7297-03-6.

Haq, B.U. Hardenbol, J., Vaıl, R.P. 1988. Mesozoic and Cenozoic chronostratigraphy and cycles of sea level change. Society of Economic Paleontologists and Mineralogists Special Publication 42, 71-108

Hatzfeld, D., Authemayou, C., Van Der Beek, P., Bellier, O., Lave, J., Oveisi, B., Tatar, M., Tavakoli, F., Walpersdorf, A., Yamini-Fard, F. 2010. The kinematics of the Zagros Mountains (Iran). In: Leturmy P, Robin C, editors. Tectonic and Stratigraphic Evolution of Zagros and Makran during the Mesozoic–Cenozoic. Geol Soc Lond Spec Publ 330: 19–42. DOI: 10.1144/SP330.3.

Joudaki, M., Farzipour-Saein, A., Nilfouroushan, F. 2016. Kinematics and surface pattern of the Anaran basement fault zone in NW of the Zagros fold-thrust belt. International Journal of Earth Sciences 105, 869-883.

Kartal, R. F., Zünbül, S., Kadirioğlu, F. T. 2011. Atatürk Barajı Havzasının Depremselliği. 15. ATAG Workshop

Krasheninnikov, V.A., Hall, J.K., Hirsch, F., Benjamini, C., Flexer, A., 2005. Geological Framework of the Levant. Volume I: Cyprus and Syria. Historical Productions-Hall, Jerusalem, Israel. ISBN: 965-7297-02-8.

Lisenbee, A.L. 1986. Structural Studies of Selected Areas in Southeast Anatolia. TPAO report no: 2229

Lisenbee, A.L. 1987. Report of investgiation tectonic analysis of the Adıyaman to Harzo region-southeast Anatolia-(with notes on the Harran graben Bozova trend). TPAO report no: 2236

Maxson, J. H., 1936. Geology and petroleum possibilities of the Hermis dome. Directorate of Mineral Research and Exploration Compilation no: 255. 25 s.

Naylor, M.A., Mandl, G., Sijpesteijn, C.H.K. 1986. Fault geometries in basement-induced wrench faulting under different initial stress states. Journal of Structural Geology 8, 737–752.

Okay, A.I. 2008. Geology of Turkey: a synopsis. Anschnitt 21, 19-42.

Öğrenmiş, İ.Y. 2006. Şelmo Formasyonu'nun Kahta (Adıyaman) kuzeyindeki yüzeylemelerinde sedimantolojik incelemeler, Yüksek Lisans Tezi. Fırat Üniversitesi. 55 s. (unpublished)

Peksü, M. 1976. M40c, M40d, N39a, N39b, N40a, N40b, 1/50000 ölçekli jeoloji haritaları. TPAO arşivi (Compilation).

Perinçek, D. 1978. V-VI-IX. Bölge (Güneydoğu Anadolu otokton-allokton birimler) jeoloji sembolleri. TPAO report no: 6657.

Perinçek, D. 1979. Hazro, Korudağ-Çüngüş, Maden, Hazar, Elazığ, Malatya dolayının jeolojisi. TPAO report no: 1395

Perinçek, D. Günay, Y., Kozlu, H., 1987. New observations on strike-slip faults in east and southeast Anatolia. Proceedings of 7th Biannual Petroleum Congress of Turkey. UCTEA Chamber of Petroleum Engineers, 89-103.

Perinçek, D. Ve Çemen, İ. 1991. Late Cretaseous-Paleogene structural evoluation of the structural highs of Southern Anatolia. Ozan Sungurlu Symposium Notifications. 386-403

Rigo De Righi, M., and Cortesini, A. 1964. Gravity tectonics in foothills structure belt of Southeast Turkey. Am. Assoc. Pet. Geol. Bull. 48, 1911-1937.

Robertson, A., Boulton S.J., Taslı, K., Yıldırım, N., İnan, N., Yıldız, A., Parlak, O. 2016. Late Cretaceous - Miocene sedimentary development of the Arabian continental margin in SE Turkey (Adıyaman region): Implications for regional palaeogeography and the closure history of Southern Neotethys. J Asian Earth Sci 115, 571-616

Schmidt, K. 1935a. First report over geological and paleontological: Directorate of Mineral Research and Exploration Compilation no: 1532

Sefunç, A. 2003. Adıyaman, Bozova, Kızılin, Harmancık ve Kemerli faylarının sismik verilerle tanımı. TPAO report no: 4430

Seyitoğlu, G., Esat, K., Kaypak, B. 2017. The neotectonics of southeast Turkey, northern Syria, and Iraq: the internal structure of the Southeast Anatolian Wedge and its relationship with recent earthquakes. Turkish Journal of Earth Sciences 26, 105-126.

Sungurlu, O. 1972. VI. Bölge Gölbaşı-Gerger arasındaki sahanın jeolojisi, TPAO report no: 802

Sungurlu, O. 1974. VI. Bölge kuzey sahalarının jeolojisi, Türkiye 2. Petrol Kongresi, 85-108.

Şaroğlu, F., Emre, Ö., Kuşçu, İ. 1992. Active Fault Map of Turkey. Directorate of Mineral Research and Exploration Publication.

Şemşir, D., Duran, O., Alaygut, D., Kaya, M.A., Kumsal, K., Güngör, H., ve Aydemir, V. 1992. XI–XII. bölgelerde Beşikli, Doğu Beşikli, Tokaris, Bakacak sahalarıyla İkizce-Taşlık kuyuları civarının stratigrafisi, tektoniği, yeraltı jeolojisi ile Karaboğaz Fm ve Mardin Grubunun sedimantolojoisi, diyajenezi elektrofasiyes analizi ve rezervuar değerlendirmesi, TPAO report no: 3051

Şengör, A.M.C., Görür, N., Şaroğlu, F. 1985. Strike-slip deformation basin formation and sedimentation: Strike-slip faulting and related basin formation in zones of tectonic escape: Turkey as a case study. In: Biddle KT, Christie-Blick N, editors. Strike-slip faulting and basin formation. Soc Econ Paleontol Min Spec Publ 37, 227-264.

Şengör, A.M.C., Özeren, M.S., Keskin, M., Sakınç, M., Özbakır, A.D., Kayan, İ. 2008. Eastern Turkish high plateau as a small Turkic-type orogen: Implications for post-collisional crust-forming processes in Turkic-type orogens. Earth-Sci Rev 90, 1-48.

Tolun, N., 1960. Stratigraphy and tectonics of Southeastern Anatolia. Révue de la Faculté des Sciences de l'Université D'İstanbul, Tome XXV, Fasc. 3-4, série B, 204-264 p.

TPAO, 2014. Map Archive (Anonymous). Ankara, Türkiye.

Tromp, S. W. 1940. Preliminary report on the oil possibilities of S.E. Turkey, based on a re-interpretation of microfaunal and sub-surface data (Cenubu Şarki Türkiye'nin stratigrafisi, strüktür vecleri ve petrol imkanları ile bunların mücavir mıntıkalarla mukayesesi). Directorate of Mineral Research and Exploration Compilation no: 1216. 74 s.

Tuna, D. 1973. VI. Bölge litostratigrafi birimleri adlamasının açıklayıcı raporu. TPAO report no: 813.

Ulu, Ü. 2002. 1:500.000 Ölçekli Türkiye Jeoloji Haritası Hatay Paftası. Türkiye 1/500.000 Ölçekli Jeoloji Haritaları, No: 16, M. Şenel (Ed.), Maden Tetkik ve Arama Genel Müdürlüğü, Ankara.

Yılmaz, Y. 1984. Amanos dağlarının jeolojisi. TPAO report no: 1920 .

Yılmaz, Y. 1990. Allochthonous terranes in the Tethyan Middle East Anatolia and the surrounding regions. Phil. Trans. Royal Society of London, A331, 611-624.

Yılmaz, Y. 1993. New evidence and model on the evolution of the southeast Anatolian orogen. Geol Soc Am Bull 105, 251-271.

Yılmaz, Y., Yiğitbaş, E. 1990. SE Anadolu'nun farklı ofiyolitik –metamorfik birlikleri ve bunların jeolojik evrimdeki rolü. Türkiye 8. Petrol kongresi, Jeoloji Bildirileri, s. 128-140.

Yiğitbaş, E., Yılmaz, Y. 1996. New evidence and solution to the Maden complex controversy of the Southeast Anatolian orogenic belt (Turkey). Geol Rundsc 85, 250–263.

Yoldemir, O. 1985. Suvarlı (Adıyaman) yakın dolayının jeolojisi: TPAO report no: 2113.

Yoldemir, O. 1987. Suvarlı-Haydarlı-Narlı Gaziantep arasında kalan alanın jeolojisi, yapısal durumu ve petrol olanakları: TPAO report no: 2257.

Yoldemir, O., Akça, L., Şengündüz, N., Gürgey, A., Turan, M., Güngör, H., Aydemir, V. 1992. Araban-Suvarlı sahalarının stratigrafik, tektonik ve rezervuar değerlendirmesi: TPAO report no: 3114.

Yoldemir, O., Sefunç. A. 1999. Kemerli, Burç ve Batı Bozova alanının jeoloji, jeofizik ve hidrokarbon potansiyelini değerlendirme ve belirlenen prospekt alanlar. TPAO report no: 2113.

Bull. Min. Res. Exp. (2018) 156: 41-66

Bulletin of the Mineral Research and Exploration

http://bulletin.mta.gov.tr

Neotectonic and morphotectonic characteristics of the Elmali basin and near vicinities

Şule GÜRBOĞA[a*] and Özgür AKTÜRK[b]

[a]*General Directorate of Mineral Research and Exploration, Marine Research Department, Çankaya/Ankara. orcid.org/0000-0002-5225-5895*
[b]*Akdeniz University, Department of Geological Engineering, Antalya. orcid.org/0000-0001-7703-5779*

Research Article

Keywords:
Elmalı basin, active fault, morphometric analysis, SW Turkey.

ABSTRACT

Elmalı Basin, which consists of the Elmalı county and some villages, approximately 120 km far from Antalya city, is one of the recent depositional areas in the extensional neotectonic region of southwestern Turkey. The basin provides significant data for the understanding of the geological evolution to record from the basement to recent depositional units. For this reason, these kinds of structures are used to determine the deformations phases for the evolutionary history of basin formation. In the content of the study, following applications have been investigated: (a) mapping of the area and structures in 1/25.000 scale, (b) information about deformation and tectonic activity along the basin margin faults, (c) the distribution of peak ground acceleration (PGA) in case of an earthquake with 6.5 magnitude and (d) morphometric analyzes of the basin to understand the tectonic uplift by using the digital elevation model. The new results combined with existing data imply that the Elmalı Basin has a number of deformation structures and active faults on both western and eastern sites of the basin. Depending on the morphometric indices, western side of the basin created higher uplift ratio compared with the eastern side of the basin.

Received Date: 09.12.2016
Accepted Date: 28.09.2017

1. Introduction

The study area Elmalı basin and its near vicinities is the recent depositional area inside the border of Antalya city (Figure 1). In the regional aspect, the area is located on a controversial area where the evolution of Taurus and Isparta Angle have different geological history, the initiation of recent tectonic regime and type of tectonic regime. As it is known from the principals, recent depositional areas are the main target to investigate the tectonic records. In order to understand the recent tectonic and deformational structures, previous discussions are also summarized briefly.

Although the Elmalı basin is located on the II. Degree earthquake zone (AFAD, 1996), there is no active fault according to Map of Active Faults in Turkey (Emre et al., 2013) (Figure 1). Although the lack of active fault in the area, there are historical and instrumental earthquakes around here that is why the study area is in the II. Degree earthquake zone. The most critical point here is that there is no detailed investigation in the study area up to now and probably many geological data are expected to be available because of the existence of recent deposits. Eventually, both the recent sedimentation features and the existence of deformation structures indicate some clues the necessity of detailed investigation in the area during the first field excursion.

In this research, three main objectives are considered. First one is the stratigraphic and tectonic characteristics of the basin fill. 1/25.000 scaled geological map of the study area containing the unit boundaries, boundary relations and deformation structures are examined and mapped. The second objective is to calculate the expected peak ground acceleration (PGA) values derived from a possible earthquake. The values area calculated to provide foreground data for future hazard and risk maps. The last one is the morphometric analyzes to obtain

* *Corresponding author: Şule GÜRBOĞA, sule.gurboga@gmail.com*
http://dx.doi.org/10.19111/bulletinofmre.399090

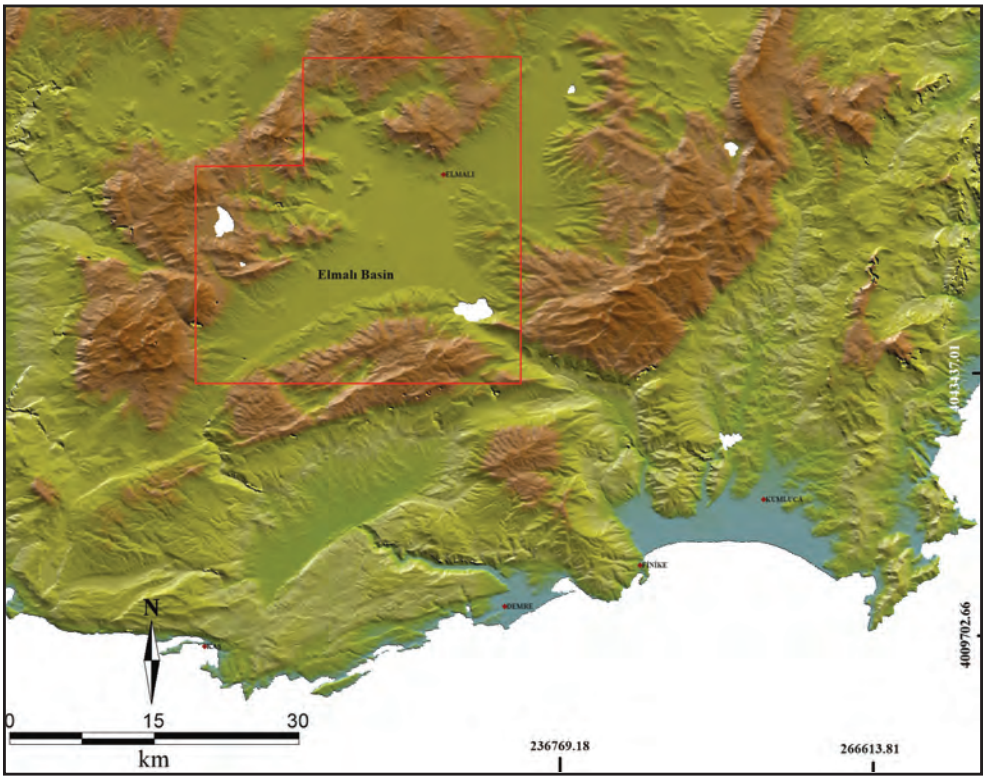

Figure 1- Location map of the study area (red border indicates the target area).

information about the uplift ratio resulted from the tectonic activity of the basin margins by using the digital elevation model.

The Elmalı Basin is a recent depositional area located in the western wings of Isparta Angle, within the western Anatolian extensional neotectonic region. Due to its location and current position, it has great importance to understand the geological evolution of the region (Figure 1).

Studies involving the structural data of the neotectonic period around Elmalı and its vicinities are very limited in the literature. In addition, there are different studies in relation to the paleotectonic evolution of Isparta Angle, especially in the northern part of the basin. Isparta Angle, which is "Λ" shaped morphology, was first described by Blumental (1951, 1963) and two different ideas about the formation of this structure have been put forward. The first one is that it is a structure separating the Taurus into two parts (eastern and western) (Dumont, 1979; Kelling et al., 2005) and another idea claimed that the Taurus mountain formation originates from the twisting of the northward direction to the clockwise and counterclockwise rotation during the Early Paleocene-Early Pliocene (Poisson, 1977; Akay and Uysal, 1985; Kissel and Poisson, 1987; Robertson, 1993; Piper et al., 2002; Poisson et al., 2003).

Moreover, Isparta Angle is issued for controversy about the initiation age of the neotectonic period and the type of recent tectonic regime. A group of scientists think that this structure is still active and deformed by compression regime (Akay and Uysal, 1988; Boray et al., 1985; Barka et al., 1995; Yılmaz et al., 2000; Poisson et al., 2003; Kelling et al., 2005; Alçiçek et al., 2006), on the other hand others argue that it is under the control of the extensional tectonic regime characterized by normal faults (Koçyiğit, 1996; Glover and Robertson, 1998*a*, *b*; Koçyiğit et al., 2000; Koçyiğit and Özacar, 2003; Poisson et al., 2003; Koçyiğit, 2005; Koçyiğit and Deveci, 2007). Previous studies carried out in many basins located inside and outside of Isparta Angle include marine and terrestrial sediments that have deposited in the last phase of the compressional regime. These are Çameli, Acıpayam, Karamanlı, Burdur, Isparta, Senirkent, Dinar, Dombayova–Sandıklı, Karadirek, Sinanpaşa, Haydarlı–Karaadilli, Gelendost, Beyşehir–Yarıkkaya, Şuhut and Akşehir–Afyon (Ercan et al., 1978; Koçyiğit, 1984*a* and 1984*b*; Boray et al., 1985; Karaman, 1986;

Şenel et al., 1989; Price and Scott, 1991; Yağmurlu, 1991; Akgün and Akyol, 1992; Koçyiğit et al., 2000; 2001; Koçyiğit and Özacar, 2003; Alçiçek et al., 2005; Koşun et al., 2009). Without these basins located to the north of Isparta Angle are composed of only terrestrial sediments. The age range of the basin infill varies between Early Miocene and Middle Pliocene (Koçyiğit, 1981; Koçyiğit et al., 2000; Alçiçek vd., 2005; Kelling et al., 2005; Koçyiğit, 2005; Keller and Villari, 1972; Becker-Platen et al., 1977; Besang et al., 1977; Koçyiğit, 1981, 1983, 1984*a*; Ercan et al., 1985: Çevikbaş et al., 1988; Yağmurlu et al., 1997; Erkül et al., 2005; Aldanmaz, 2006). To summarize, there is no complete consensus on the formation mechanism of Isparta Angle and the age of its formation, the types of tectonic regime and its age affecting the region. The circumstance is especially important for the current basins that must be examined and evaluated with the point of view. No detailed mapping of the Elmalı basin, analysis of faults and slip data have been conducted in any of the studies so far. In addition to this, detailed field data about the stratigraphic features of the allochton units, Beydağları autochthonous and nappes in the region (Poisson and Poignant, 1974; Özgül, 1976) and the relationship between Miocene-Recent sediments of some basins in Teke peninsula are given in detail (Brunn et al., 1973; Şenel et al., 1996; Koşun et al., 2009).

Consequently, there are two different ideas about the age of formation for Isparta Angle and the type of recent tectonic regime: (a) The age of Isparta Angle is Late Miocene and the tectonic regime continues without any interruption (Boray et al., 1985; Yağmurlu et al., 1997, Alçiçek et al., 2006; Karaman, 2010); (b) The recent tectonic regime of Isparta Angle are controlled by the extensional forces and the onset age of neotectonic period is Early Quaternary (Koçyiğit, 1996; Glover and Robertson, 1998*b*; Koçyiğit et al., 2000; Koçyiğit and Özacar, 2003; Poisson et al., 2003; Koçyiğit, 2005; Koçyiğit and Deveci, 2007). The types and onset age of the tectonic regime and the deformation phases of the units, which are still controversial in the literature, have been examined based on the deposits around Elmalı basin and significant results have been obtained.

2. Methodology

The primary and fundamental method is to prepare the detailed geological mapping based on observations in the field and to analyze the fault slip data measured from the fault planes with the TENSOR program (Angelier, 1994). Before doing the field study, the literature survey was completed. Then, 1/25.000 scale geological map of the basin was prepared, the fault and deformation structures were measured and analyzed. In addition, morphometric analyzes are carried out to determine the tectonic effect at the watershed boundaries. In order to perform these analyzes, digital elevation model derived from 1/25.000 scale topographic map was produced by using MapInfo 11.5 and Global Mapper 16.0 programs. To determine of geomorphologic evolution and active tectonic structures of the study area, the relationships between rock resistance and topography has been issued to calculate the morphometric indices “Mountain Front Sinuosity (Smf)”, “Valley floor width-to-height ratios (Vf)” and “Stream length-gradient index (SL)”.

Lastly, the PGA values that would occur in the event of an earthquake with magnitude 6.5 are considered using the attenuation relationship formula proposed by Ulusay et al. (2004). This data also carries the quality of base data for future hazard and risk maps.

3. Geology of the Study Area

3.1. Stratigraphy

There are different types of units representing the age range between from Mesozoic to recent within the study area. As mentioned in previous studies, autochthonous and allochthonous units are the subject of different studies especially outside of the study area (Figure 2). The previous studies are generally related to the nappe tectonics and the formation mechanism of Isparta Angle that have prevailed in the region. In this study, contact relations between the current sediments and older depositions in the basin have been revealed.

The Beydağları carbonate platform is overlaid by two different nappe slices. These are named as Lycian nappes in the northwest and Antalya nappes in the east (Brunn et al., 1971; Poisson, 1977; Gutnic et al., 1979; Robertson, 2000). It has been suggested that the Antalya nappes is emplaced from the southeast part of the Beydağları during the Late Cretaceous and Paleocene (Poisson, 1977; Gutnic et al., 1979; Robertson, 2000) and its origin is related to the closure of the southern branch of Neotethys (Robertson et al., 2003;). It is also suggested that the emplacement of Lycian nappes is during the Late Cretaceous and it is in the same location from Langian to present. Thus, the Lycian nappes are related to the closure of the northern limb of the Neotethys (Poisson, 1977).

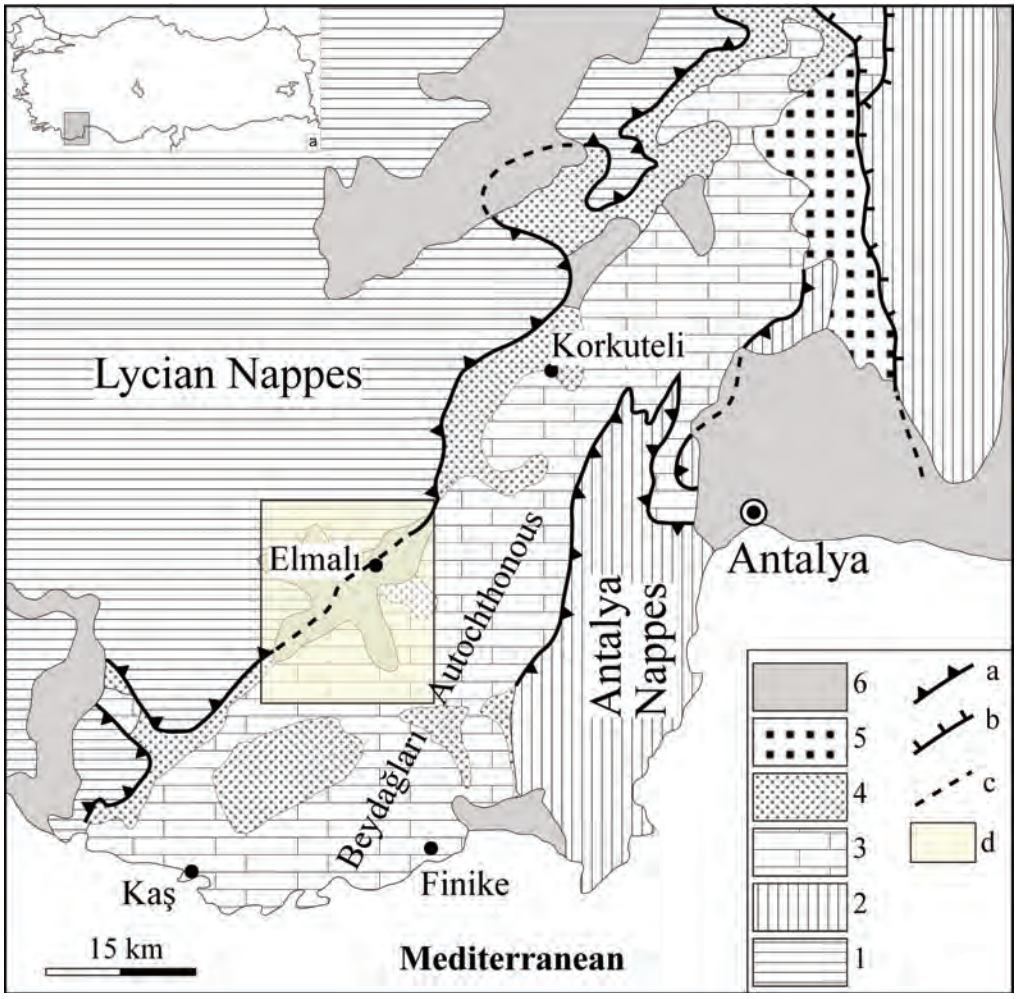

Figure 2- A generalized geological map showing the tectonic units in the study area and surroundings (Hayward, 1982; Meşhur and Akpınar, 1984; Şenel et al., 1992; Aksoy and Aksarı, 2008). 1. Lycian nappes, 2. Antalya nappes, 3. Beydağları autochthonous (Upper Triassic-Oligocene), 4. Beydağları autochthonous (Lower-Middle Miocene), 5. Aksu basin sediments (Lower-Middle Miocene), 6. Plio-Quaternary; a) paleotectonic thrusts, b) Normal faults, c) Possible faults, d) The interested area is shown in figure 3.

Geological features of the Lycian Nappes located in the NW of the Elmalı Basin and also within the boundaries of the study area is subjected to different researches (Hayward, 1982; Aksoy and Aksarı, 2008). According to these studies, Lycian nappes are generally composed of four tectonic slices: Yeşilbarak, Lower, Ophiolite and Upper Nappes. The tectonic slices are separated from each other with low angle thrust faults. The emplacement of Lycian nappes on the Beydağları autochthonous was probably happened in Early Langian, and the reason for emplacement is the shortening in the crust due to compression (Şengör et al., 1984). Studies carried out in the following years emphasize that this last movement of Lycian nappes in the Middle Miocene will not represent crustal compression/contraction and a rootless emplacement has been mentioned (Seyitoğlu et al., 1992; Collins and Robertson, 1998). After the formation of large-scale tectonic events, the development and stratigraphic features of some recent basins have been researched from Miocene to present, but not much information has been obtained in the Elmalı Basin.

The Elmalı Basin located between autochthonous and allochthonous tectonic slices are one of the medium-sized basins on the Teke peninsula, where the recent tectonic regime is controversial. As a result of detailed field excursion, it is seen that a number of units with different ages are located along the margins and within the basin (Figure 3). The uppermost part of the Lycian nappes and the Quaternary sediments were investigated within the scope of the study and their deformations were examined.

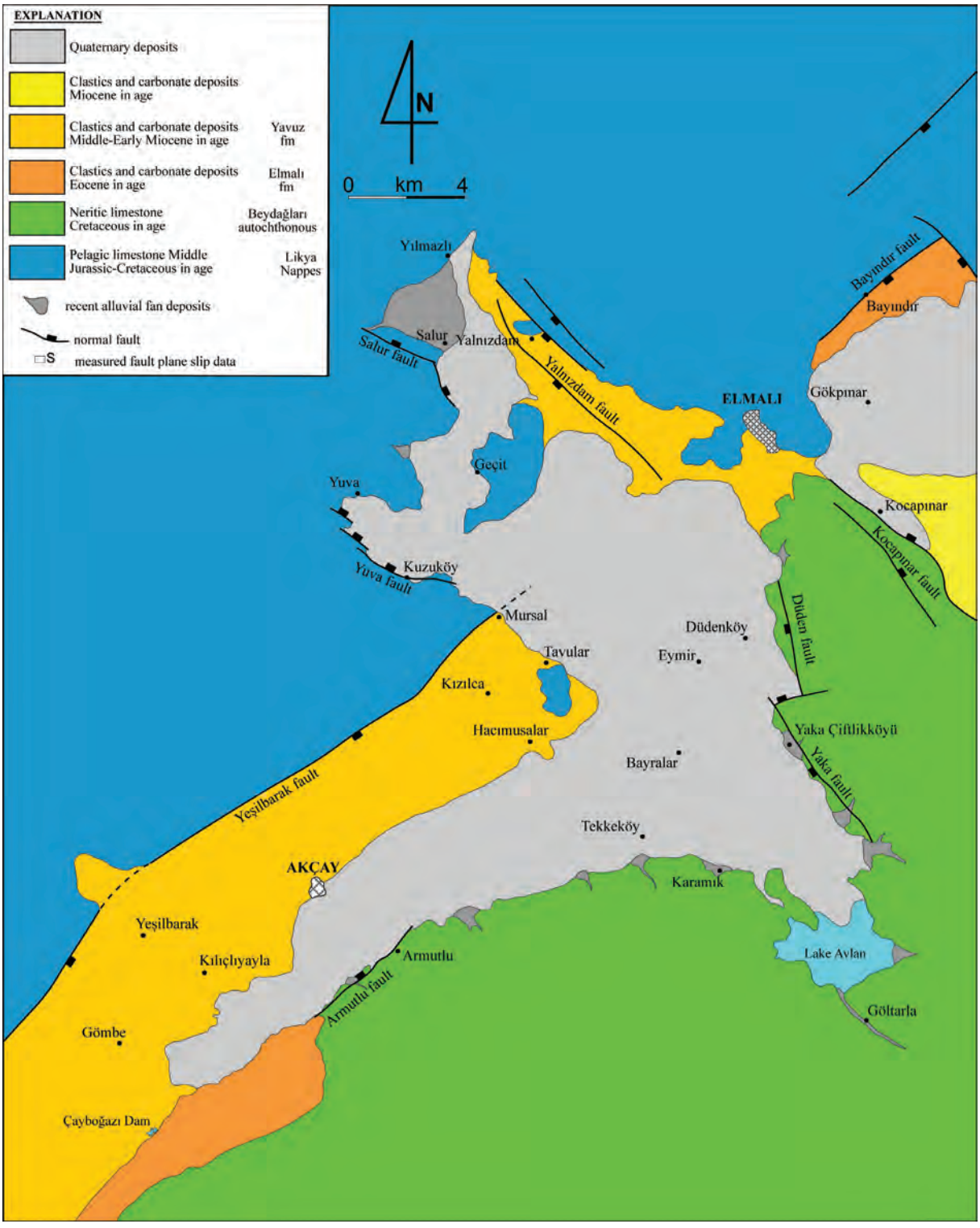

Figure 3- 1/25.000 scale geology map of Elmalı Basin.

The oldest formation of upper nappe is Elmalı formation (Eocene) and named by Önalan (1979). The formation is generally composed of sandstone, claystone and siltstone alternations (Figure 4), and wedge-shaped conglomerate layers at the upper part of the formation.

Yavuz formation is widespread in the area, which is found in the NE and SW parts of the study area (Şenel et al., 1989). The formation consists of clastic limestone in the lower level and claystone, sandstone alternation to the upper level (Figure 5).

Figure 4- Close-up view of the Elmalı formation (looking to NNE).

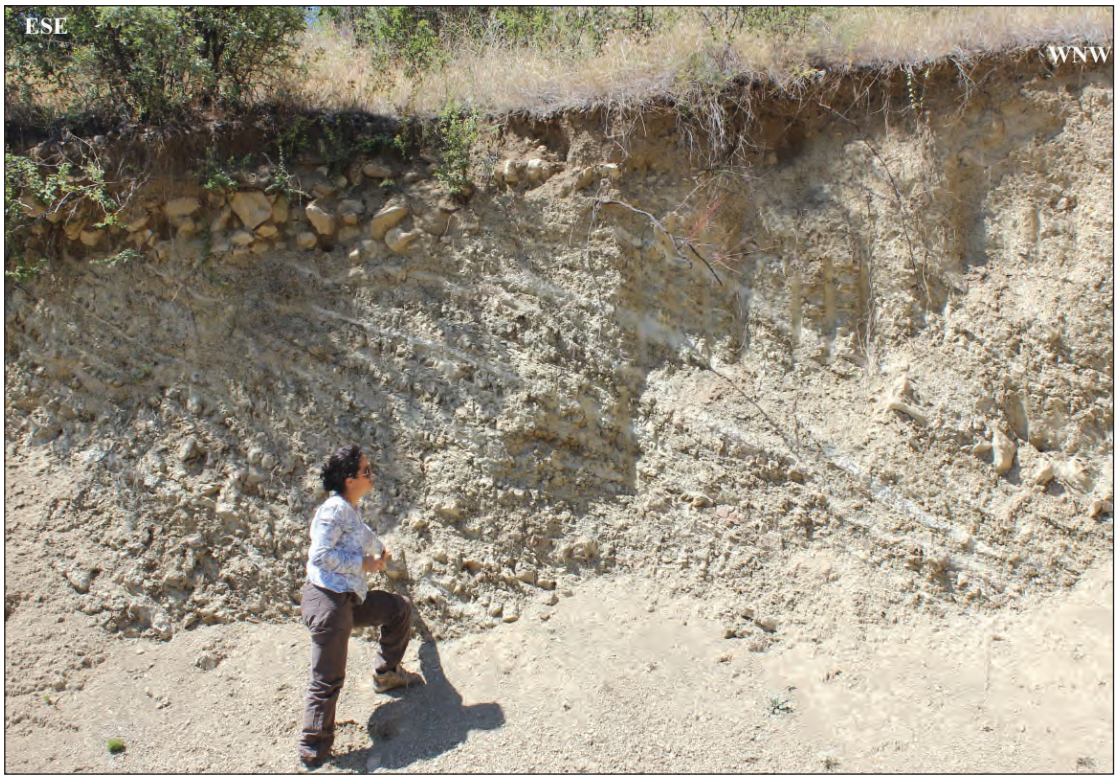

Figure 5- Close up view of Yavuz formation (looking to SSW).

The Elmalı and Yavuz formations belonging to the Yeşilbarak nappe are located along the margins and are also important to identify the recent tectonic regime. Deformation structures related to active basin margin faults and their analysis are presented in the tectonic section. Another formation the Taşkesiği that belongs to the upper nappe is observed along the margins (Figure 6).

The formation consisting of thick massive limestone layers is seen in the north-northwest part of the Elmalı county and shown on the map without being separated by Lycian nappes. Miocene units overlie the gray limestone-clastics alternations of Lycian nappes with unconformably (Figure 7), and the youngest Elmalı basin sediments overlie unconformably on all these units and their deposition is still lasting. Lake Avlan in the southernmost part of the Elmalı Basin shows the water level of the basin and serves the discharge of the water to the south (Figure 8). The relationship of the recent sediments of the Elmalı basin and active faults is presented in the following sections.

Figure 6- Close up view of the Taşkesi formation (looking to S).

Figure 7- Close up view of the Miocene sediments (looking to ENE).

Figure 8- General view of Lake Avlan (looking to E).

3.2. Tectonic Properties

The area is affected under the compressional tectonic regime during the Alpine orogenic process (Colin, 1962; Brunn et al., 1971; Poisson, 1977; Önalan, 1979; Erakman et al., 1982; Akay and Uysal, 1985; Şenel et al., 1987, 1989; Robertson, 1993; Şenel, 1997*a, b, c*), later on it became more complicated after emplacement process of the Antalya nappes on the Beydağları autochthonous during Danian age. In the following phases, the Lycian nappes became active in the Eocene period, and Antalya nappes emplaced in the northwest of the Beydağları autochthonous that finished the nappes activities. The last phase of the Lycian nappes emplacement corresponds to the end of the Middle Miocene (Şenel et al., 1989; Hayward, 1982; Şengör et al., 1984; 1992; Aksoy and Aksarı, 2008). All of the thrusting stages have changed the characters as extensional motions after Upper Miocene and thus the formation of the recent basins started (Şenel, 1997*a, b, c*). One of these basins, Elmalı, is still an active depositional area and the margin faults cut and displace recent deposits accumulated in the basin. The main stress axes have been determined from the paleostress analyses of slip plane data obtained from fault surface. The faults are explained in further part of the text. As it can be seen from the geological map given in figure 3, the active faults in the study area are Düden, Yaka, Yeşilbarak, Yuva, Salur and Yalnızdam faults. These are firstly named and described in this study.

3.2.1. Düden fault

The Düden fault is N-S trending, dipping to W, approximately 4 km length normal fault and eastern boundary of the basin. It defines the contact between the basement and Plio-Quaternary deposits and it is the reason for the brecciation of the basement rocks (Figure 9a). The weathering process results the formation of fault clay (Figure 9b) and the slip data in the fault plane are clearly observed due to the well-protected fault slip lines (Figure 9c). The results of the fault slip data analyses; the Düden fault is a normal fault with ~ 85º rake and locally indicates an extensional in NNE-SSW direction. The extensional direction is compatible with Western Anatolia at the regional scale.

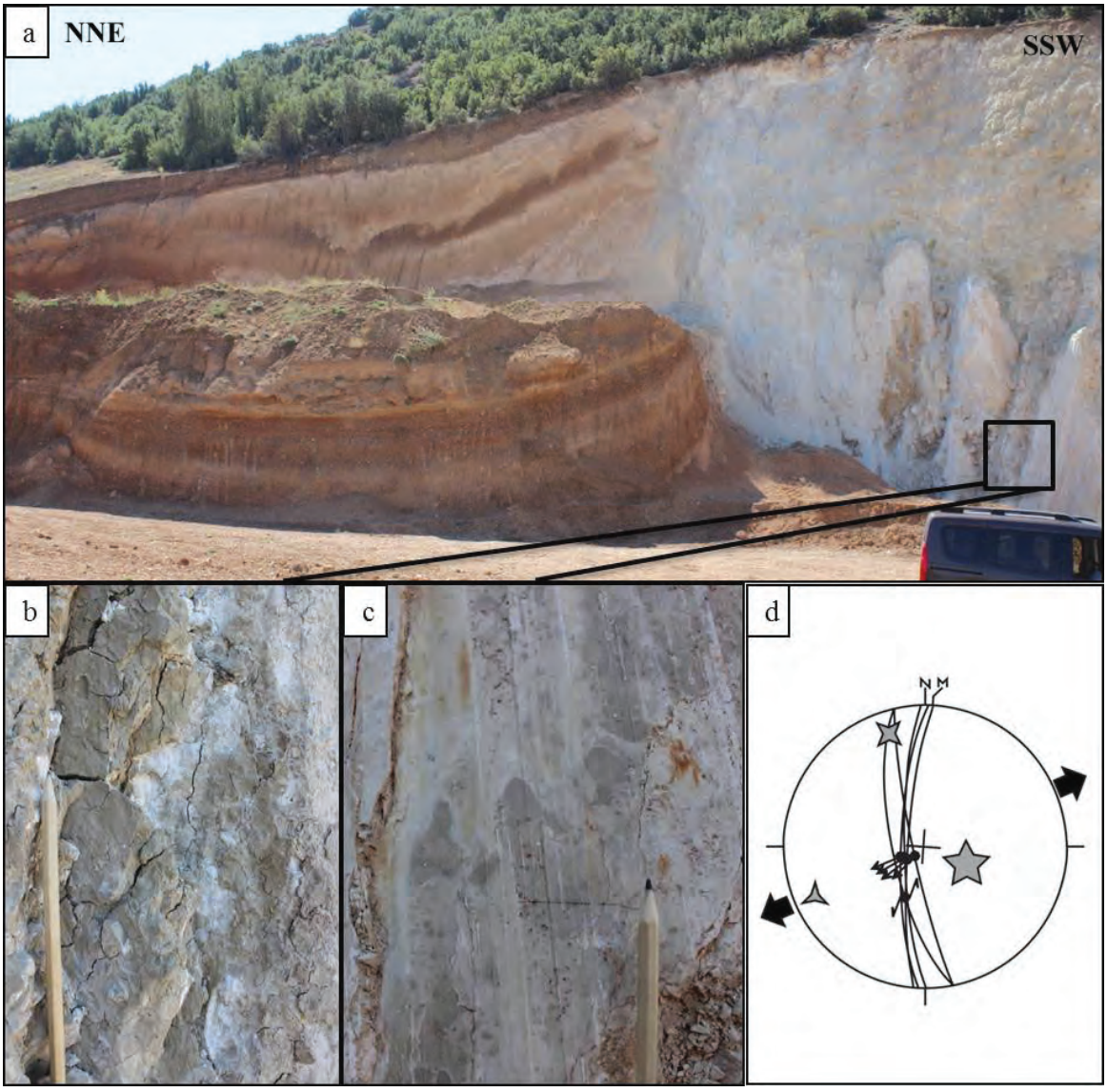

Figure 9- a) The field photograph from the Düden fault is the boundary between the basement and Plio-Quaternary units; b) Close up view of fault clays and slip plane data in the fault zone; c) Close up view of slip lines; d) Paleostress analysis of fault slip data.

3.2.2. Yaka Fault

It is another eastern boundary of the basin. Yaka fault is NNW-SSE trending, 6 km length and located on the east of Yakaçiftlik village. It cuts and displaces the Quaternary units along the eastern margin of the basin and has an important role among the recent structures. Although the Yaka Fault does not have the potential to produce destructive earthquakes, it gives the evidence for the recent activity of the eastern margin of the basin during the Quaternary time. Due to the lack of fine-grained material to record the slip data in the fault zone, a single plane solution is used to stress analyses and a local extension is found in NE-SW direction (Figure 10). The result indicates that the fault is active because it cuts off the recent terrace units and shows a step fault morphology towards the basin.

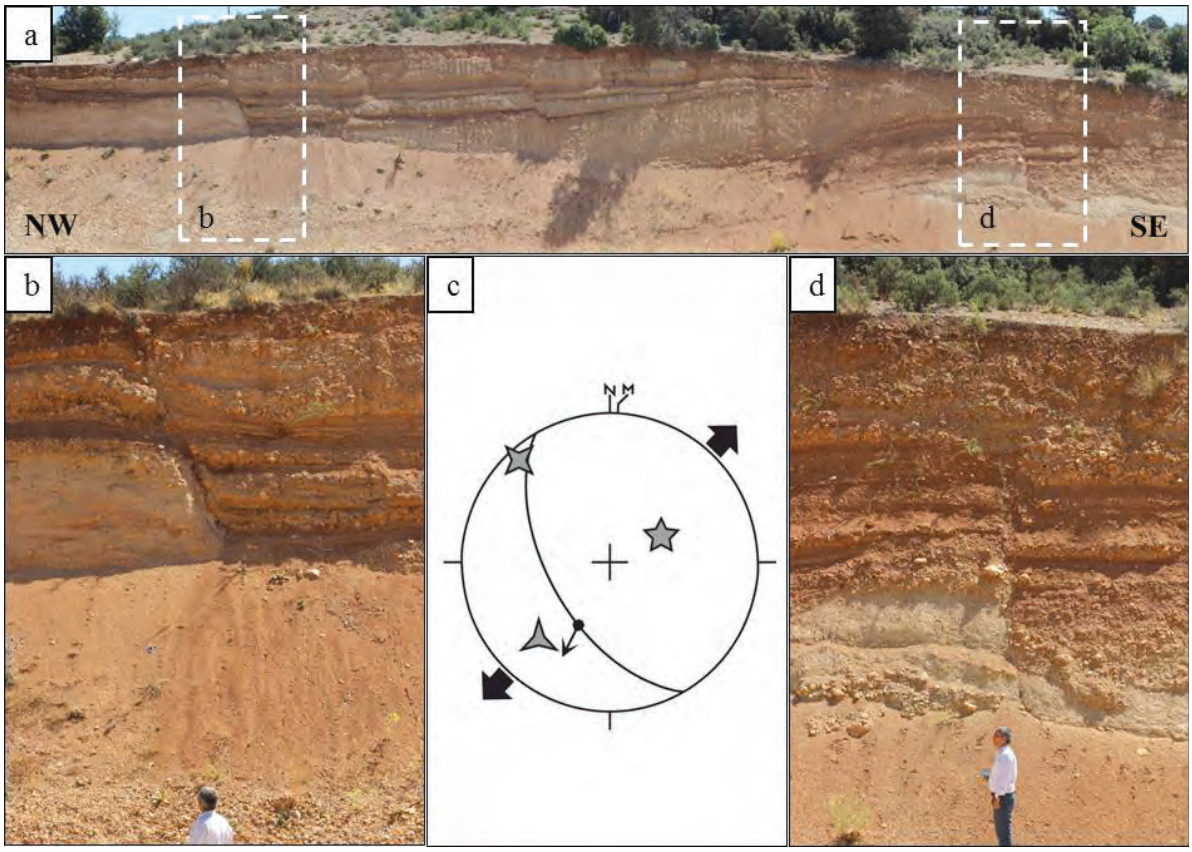

Figure 10- a) General view of the Yaka Fault; b) Close up view of the main branch of the Yaka Fault; c) The paleostress analysis result obtained by using the single plane solution of the Yaka Fault; d) Close up view of second order step like faults of Yaka Fault.

3.2.3. Yeşilbarak Fault

Yeşilbarak Fault is a NE-SW trending, 16 km length normal fault, and NW boundary of the basin (Figure 11a). Although, the Yeşilbarak fault was an important structure between the Lycian nappes and the Beydağları autochthonous during the paleotectonic period (Figure 2), the measured slip data during the neotectonic period and field observations indicate that it is a normal fault displacing the Plio-Quaternary units in the vertical direction. The observation is discussed separately in the discussion part after the morphometric analyzes. Stereographic projection analysis of the slip data (Figure 11b) reveals that the dominant extensional direction is NW-SE.

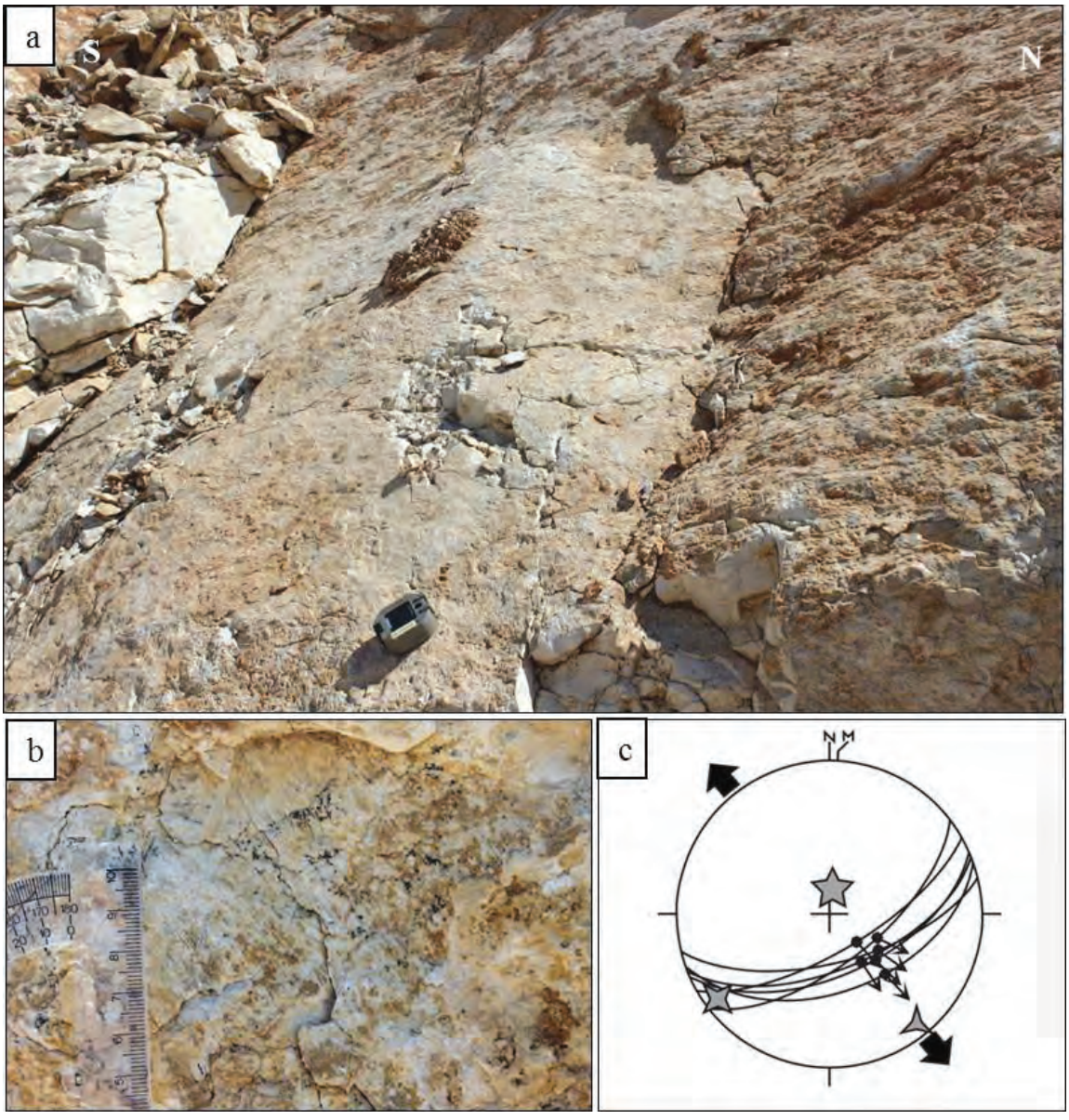

Figure 11- a) General view of Yeşilbarak Fault; b) Close up view of fault slip data; c) Stereographic projection analysis of the Yeşilbarak Fault.

3.2.4. Yuva Fault

Yuva fault that is the northwestern boundary of Elmalı Basin and approximately perpendicular to the Yeşilbarak fault is NW-SE trending, 4 km length and it defines the boundary between basement rocks (pelagic limestone, Likya nappes) and Quaternary units (Figure 12a). Striations on the fault plane is clear after the sloping scree had been removed (Figure 12b). As a result of the slip data analyses, N-S extensional direction is obtained.

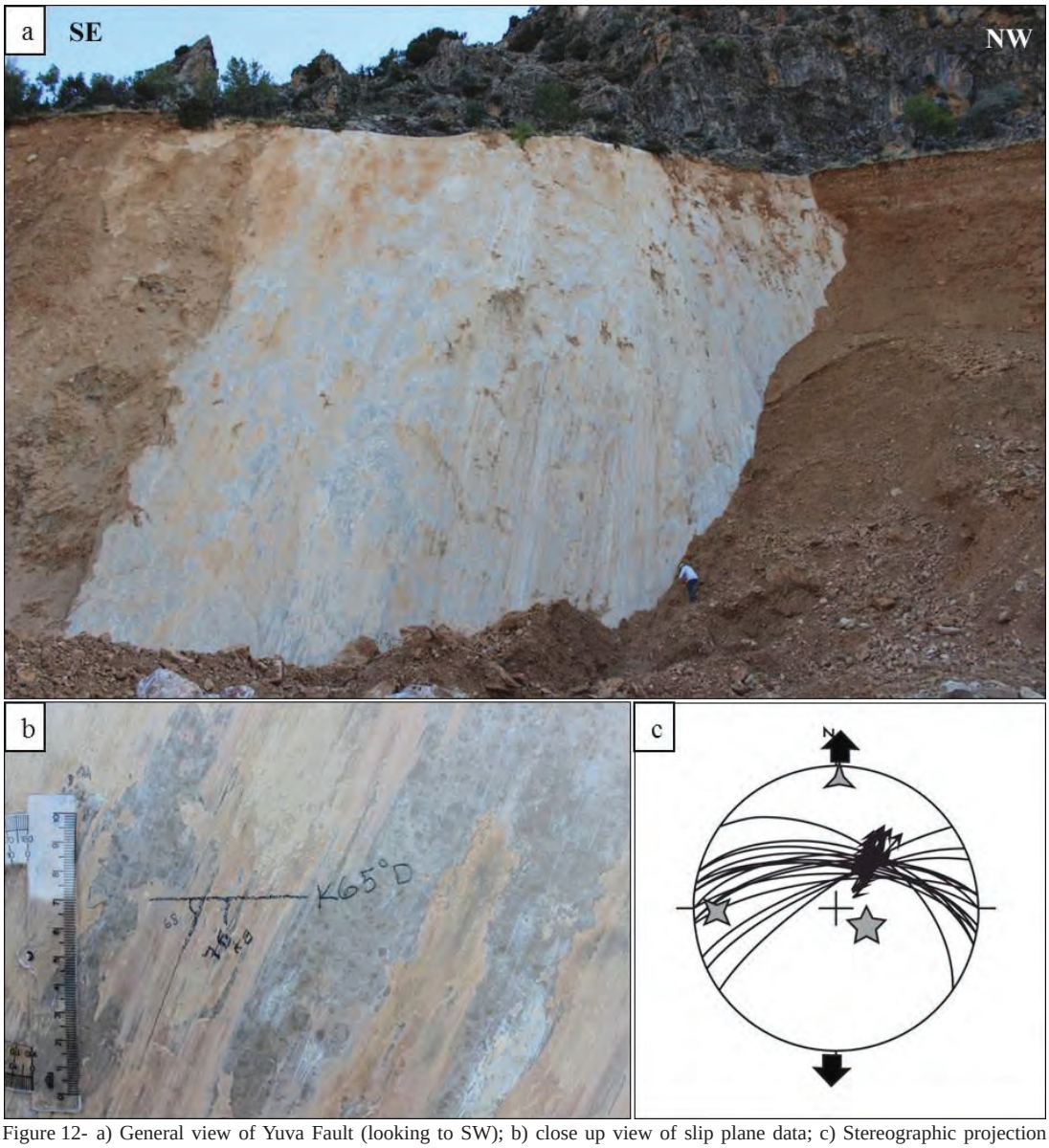

Figure 12- a) General view of Yuva Fault (looking to SW); b) close up view of slip plane data; c) Stereographic projection analysis of the Yeşilbarak Fault.

3.2.5. Salur Fault

Salur fault is NNW-SSE trending, 4 km length, NW boundary of the basin and affects in the initial stage of the basin. The fault is the boundary between Quaternary and basement units (Figure 13). Although the fault plane is observed morphologically, the slip data on the surface cannot be obtained. There is a wide alluvial fan on the hangingwall block and on top of it there is an area of greenhouses due to the sufficient underground water.

Figure 13- General view of Salur fault (looking to NW).

3.2.6. Yalnızdam Fault

Yalnizdam fault is NW-SE trending, dipping towards SW, 6 km length normal fault. Step like morphology is identical between the Quaternary and basement units (Figure 14). Even though the trace of fault is observed on the ground surface, slip plane data cannot be found.

Elmalı Basin has been controlled by the active faults having different strike and length. The magnitude of earthquakes and their impact on the settlements that will be caused by some of these faults have been examined in detail below.

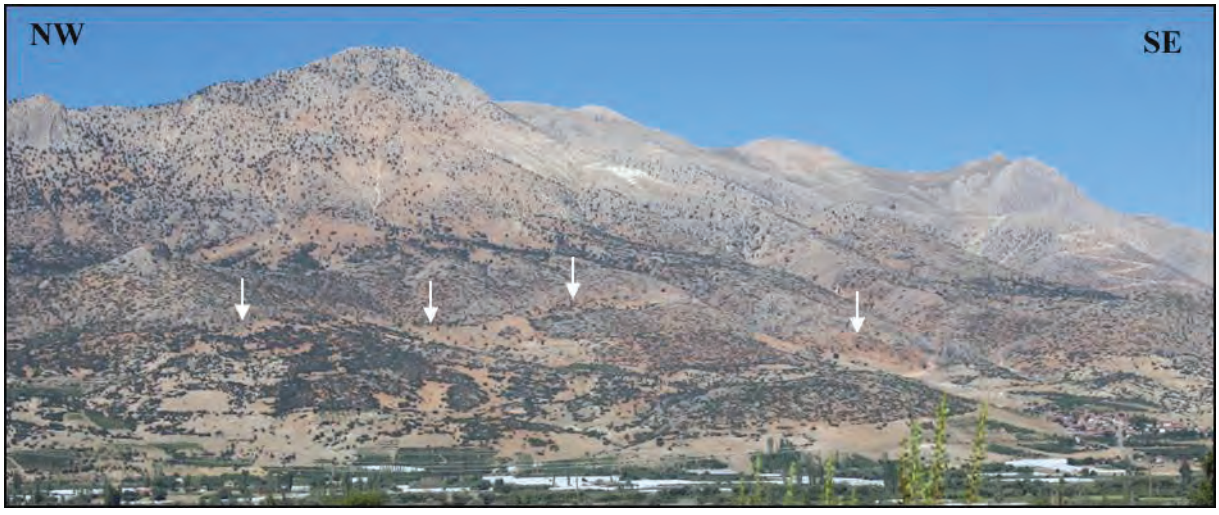

Figure 14- General view of Yalnızdam fault (looking to NE).

3.3. Determination of Peak Ground Acceleration

The earthquakes in the Elmalı Basin and its vicinity are examined from 1900 to the present (Figure 15). It is observed that the earthquakes in size 3-4 are common in the region and these earthquakes are distributed in NE-SW direction that is compatible in the general direction of the basin. Coordinate and depth information of them are presented in table 1. The depths of earthquakes are usually shallow and there are no events associated with the crust. The focal mechanism solution of the 4.5 magnitudes in 2010 on the northwestern side of Havran lake indicate that the fault is normal with the lateral component. All of the faults which did not produce an earthquake of destructive magnitude in the instrumental period has the capacity to produce a moderate earthquake. For the reason, it is necessary to consider the probability of an earthquake in hazard maps of the region.

Although any destructive earthquake did not happen recently, the probable earthquake magnitude sourced from the margin boundary faults are calculated Ms=6.3 for the Yeşilbarak fault, Ms=5 for the 4 km Yuva fault, Ms=6.3 for the Yuva and Düden faults and Ms=5.4 for the 7 km Yalnızdam fault (Aydan et al., 2002).

The presence of settlements in and around the Elmalı Basin increases the probable damage and loss of life in case of a medium-sized earthquake. For this reason, the peak ground acceleration values that would occur randomly in different units in the Elmalı basin and the values were calculated for Ms=6.5. The

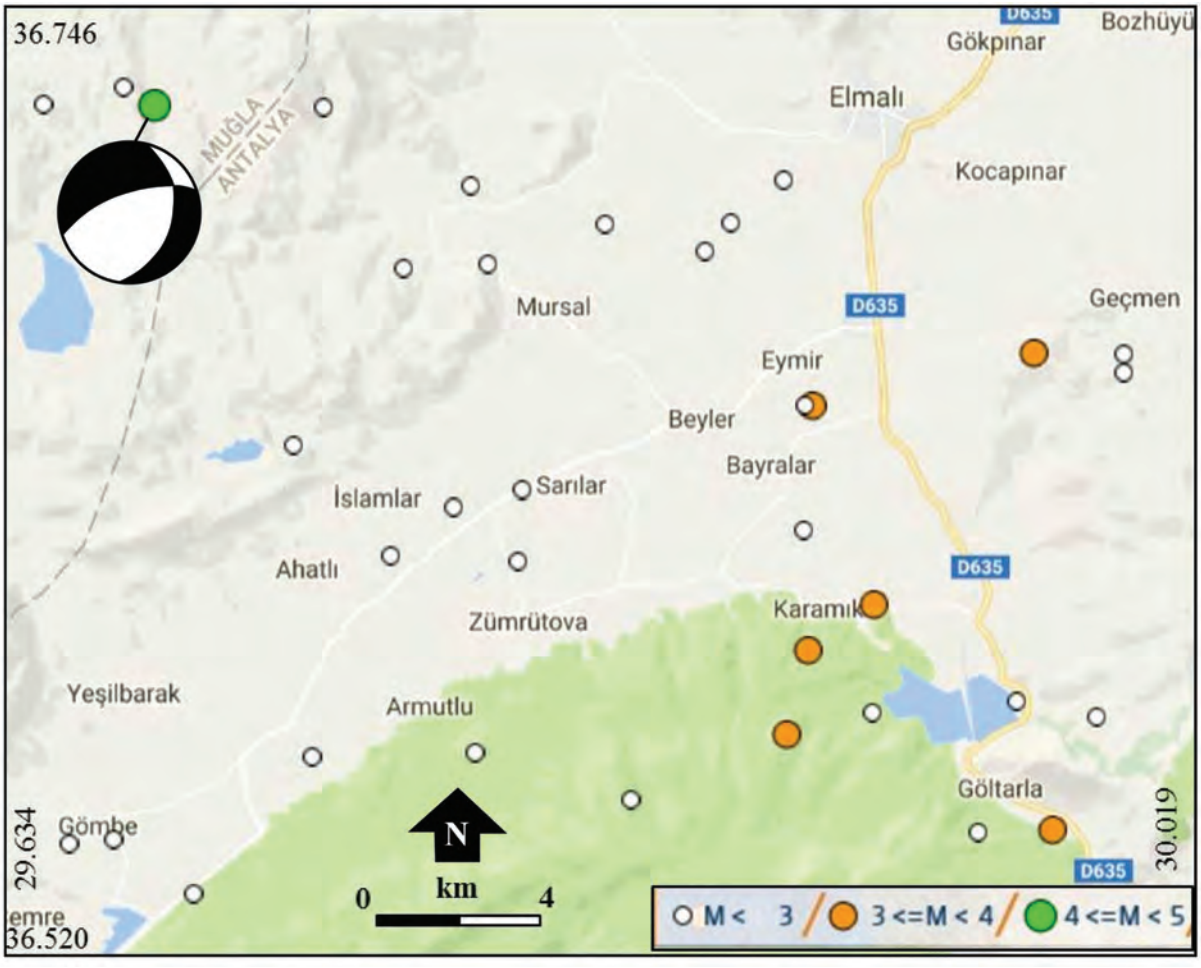

Figure 15- Distribution of recent earthquakes in Elmalı Basin and surrounding areas from 1900 to present (earthquakes from KOERI (2017) and AFAD (2017) catalogs).

Table 1- List of earthquakes between 01/01/1900 - 13/02/2017, 36.520 - 36.746 N and 29.634 - 30.019 E coordinate range, with a magnitude between 0 <= M <10. The earthquake in orange color is shown in figure 15 with focal mechanism solutions.

Date (UTC)	Latitude	Longitude	Depth	Magnitude type	Magnitude	Location
30/12/2016 06:37:39	36.6343	29.8063	7	ML	1.6	ANTALYA-ELMALI
30/03/2016 20:27:57	36.733	29.7428	7	ML	1	ANTALYA-ELMALI
18/09/2015 04:39:56	36.6695	29.999	7.01	ML	1.9	ANTALYA-ELMALI
13/06/2015 03:45:03	36.6958	29.865	7	ML	1.1	ANTALYA-ELMALI
03/05/2015 21:32:27	36.5445	29.6755	7.03	ML	1.5	ANTALYA-KAŞ
04/04/2015 04:37:54	36.624	29.8965	7.09	ML	1.6	ANTALYA-ELMALI
16/08/2014 18:45:44	36.5433	29.661	6.92	ML	1.4	ANTALYA-KAŞ
01/07/2014 11:21:49	36.668	29.97	49.8	Mw	3.5	ANTALYA-ELMALI
23/04/2014 16:12:35	36.5656	29.7388	7.52	ML	1.4	ANTALYA-ELMALI
16/04/2014 00:43:31	36.5761	29.9901	62.27	ML	2.3	ANTALYA-ELMALI
06/04/2014 02:01:26	36.6563	29.8971	7	ML	1.8	ANTALYA-ELMALI
18/11/2013 20:52:19	36.6457	29.733	6.99	Ml	2.1	ANTALYA-ELMALI
04/09/2013 11:29:16	36.577	29.9183	6.97	Ml	2.2	ANTALYA-ELMALI
06/08/2013 20:16:39	36.5463	29.9523	6.88	Ml	2.2	ANTALYA-ELMALI
13/03/2013 01:06:54	36.5303	29.701	7.22	Ml	1.9	ANTALYA-KAŞ
09/03/2013 23:07:57	36.5802	29.9647	7	Ml	2	ANTALYA-ELMALI
11/01/2013 07:26:34	36.7028	29.8327	6.99	Ml	2.6	ANTALYA-ELMALI
10/01/2013 03:34:27	36.5668	29.7912	6.9	Ml	2.9	ANTALYA-ELMALI
27/02/2011 05:22:15	36.6177	29.7642	7	Md	2.4	ANTALYA-ELMALI
14/07/2010 08:12:14	36.7143	29.8898	7	Md	2.5	ANTALYA-ELMALI
31/05/2010 17:55:21	36.5547	29.841	7.14	Md	2.7	ANTALYA-ELMALI
27/05/2010 00:16:00	36.738	29.6785	7	Md	2.7	MUGLA-FETHİYE
26/05/2010 18:57:14	36.6912	29.7683	7	Md	2.5	ANTALYA-ELMALI
26/05/2010 18:35:59	36.6302	29.7845	7	Md	2.6	ANTALYA-ELMALI
26/05/2010 17:53:17	36.6925	29.7952	7	Md	2.6	ANTALYA-ELMALI
26/05/2010 15:29:26	36.6162	29.8048	7	Md	2.6	ANTALYA-ELMALI
26/05/2010 15:14:13	36.703	29.8733	7	Md	2.6	ANTALYA-ELMALI
26/05/2010 14:37:11	36.5915	29.8978	30	Md	3.1	ANTALYA-ELMALI
26/05/2010 14:22:21	36.7312	29.6883	20.66	Ml	4.5	ANTALYA-ELMALI
02/07/2009 07:05:40	36.6035	29.9187	6.68	Md	3	ANTALYA-ELMALI
09/11/2008 12:55:57	36.6645	29.999	6.43	Md	2.8	ANTALYA-ELMALI
07/03/2008 10:44:13	36.6545	29.8992	6.84	Md	3.3	ANTALYA-ELMALI
07/02/2007 06:25:13	36.5455	29.9759	28.93	Md	3.4	ANTALYA-ELMALI
05/10/2005 10:56:49	36.5701	29.891	30.1	Md	3.6	ANTALYA-ELMALI
28/07/2005 23:48:30	36.7126	29.7899	2.44	Md	2.8	ANTALYA-ELMALI
28/12/2004 00:01:20	36.7334	29.6528	9.29	Md	2.8	MUĞLA-FETHİYE

magnitude value has been converted from Ms to Mw based on the formula given below (Aydan et al., 2002) (Figure 16).

$$M_w = 0.6798M_s+2.0402$$

M_w = 6.5 is calculated.

Then, peak ground acceleration (PGA) values that will occur as a result of such earthquake will be calculated by using the following formula.

$$PGA=2.18\ e^{0.0218(33.3M_W - Re + 7.8427S_A + 18.9282S_B}$$

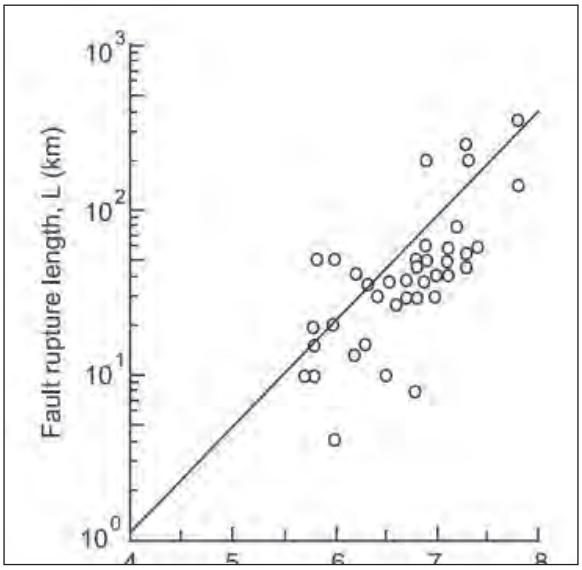

Figure 16- The relationship between Ms and surface rupture (Aydan et al., 2002).

S_A and S_B the values defining the rock or soil types (Ulusay et al., 2004). Where;

$S_A = S_B = 0$ basement rocks (hard rock),

$S_A = 1$ and $S_B = 0$ soil (Miocene units)

$S_A = 0$ and $S_B = 1$ loose units (Plio-Quaternary and alluvial deposits)

Re = the distance between fault and control points

According to the distribution of PGA values, PGA=0.35 g for recent basin fill, PGA=0.27 g for Miocene units and PGA=0.23 g for basement rocks. The closets settlements are chosen as control points. Briefly, PGA values indicate that if a moderate earthquake happens around the Elmalı basin, the result can be harmful for the people.

4. Morphometric Analyses of Elmalı Basin

Morphometry is defined as the quantitative measurement of the landscape. Morphometric analyzes are especially carried out in order to reveal the geomorphological features along the river basins. The geomorphological features of the basin are calculated by using digital elevation model and the obtained results are transformed into morphometric indices to be meaningful for tectonics. Each parameter sets a different characteristic of the basin and determines its impact on basin development (Schumm, 1986; Keller and Pinter, 1996). In this study, the valley floor width to valley height ratio (Vf), mountain front sinuosity (Smf) and the stream length-gradient index (SL) are calculated to determine whether the formation of the Elmalı Basin is tectonically controlled or not. The indices are determined for 4 different valleys (A, B, C, D) and for Smf value (1, 2, 3) for 3 different mountain front areas (Figure 17).

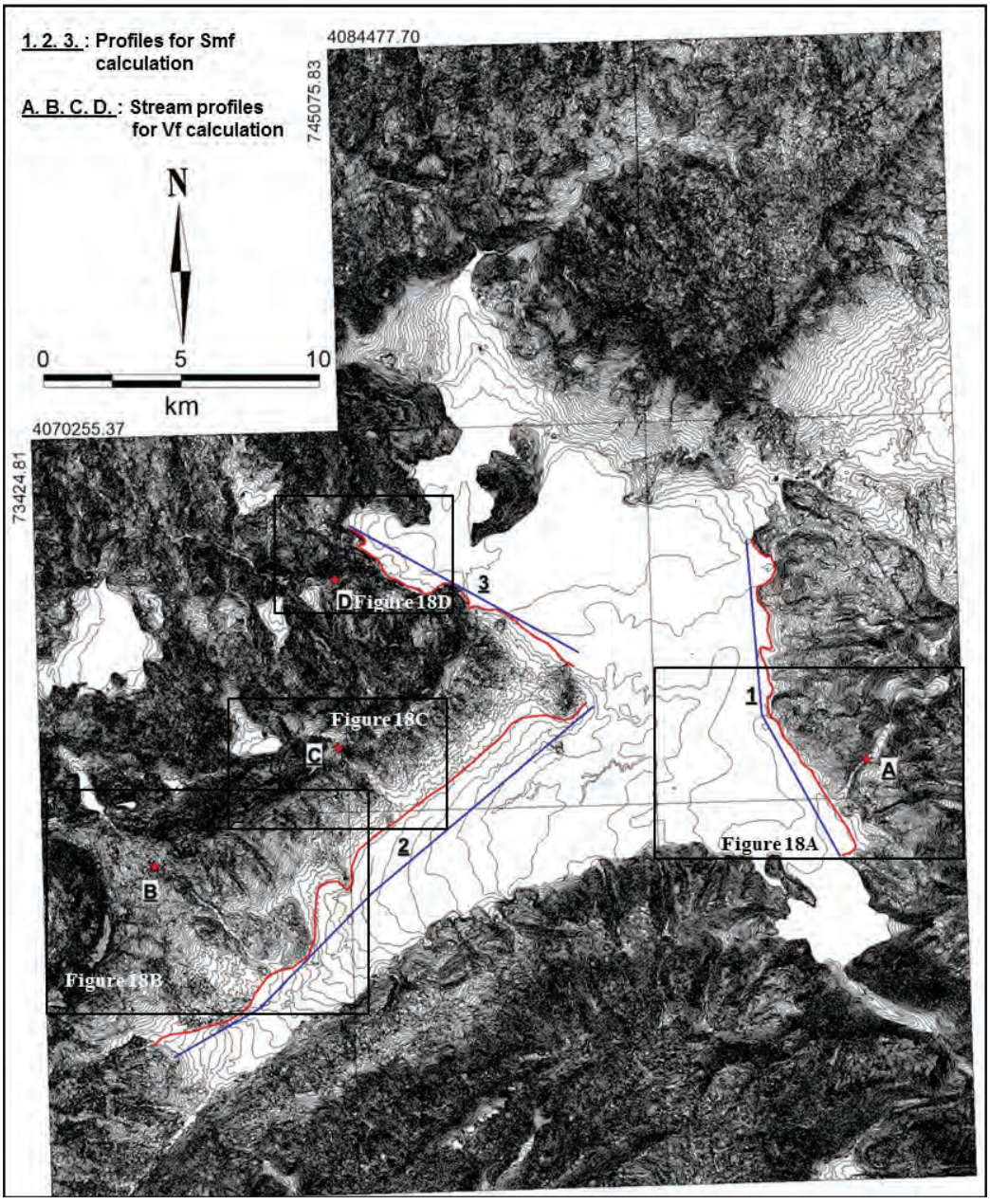

Figure 17- Map showing the contours of the study area and the locations of morphometric indices. Vf for A, B, C and D; Smf indices for 1, 2 and 3 are calculated.

4.1. The Valley Floor Width to Valley Height Ratio (Vf)

The index provides a distinction between the relatively high Vf value for wide valley floor and the low Vf value for V-shaped valleys. Low Vf values generally indicate that there is a significant relationship between deep valley and the tectonic effect, which is associated with elevated and actively digging valleys, while high Vf values indicate relatively low tectonic effect due to the relationship with low upward rate (Bull and McFadden, 1977; Rockwell et al., 1984; Keller and Pinter, 1996). The determined Vf value ranges and their results are given in table 2.

Table 2- Vf values ranges and their meanings.

Range of values	Identifications
$Vf \leq 0.5$	High tectonic activity
$1 < Vf < 0.5$	Moderate tectonic activity
$Vf \geq 1$	Low tectonic activity

The Vf value is calculated using the following formula;

$$Vf = 2Vfw/[(Eld - Esc) + (Erd - Esc)]$$

where;

Vf: **T**he **V**alley **F**loor width to **V**alley **H**eight ratio

Vfw: the width of the valley floor

Eld: elevations of the left-hand valley

Erd: elevations of the right-hand valley

Esc: the elevation of the stream channel or valley floor

For the Elmalı Basin, Vf calculations were made in the Akarca (A), Çayır (B), Gavurçay (C) and Değirmen (D) sub-basins respectively.

The calculated values along the profiles taken perpendicular to the A, B, C and D stream valleys with a range from 0.09 to 0.75 (Figure 18, Table 3). The Akarca stream flowing towards the SW in the footwall block of Yaka fault, which controls the eastern part of the basin; the Çayır and Gavurçay streams flowing towards the east in the footwall block of Yeşilbarak Fault, which controls the western part of the basin; and Değirmenderesi stream in the footwall block of Yuva fault indicate that the Vf values are dominantly lower than 0.5. Vf values are plotted along the streams, it increases as move away from the basin, revealing that the tectonic effect increases in the basin (Table 3).

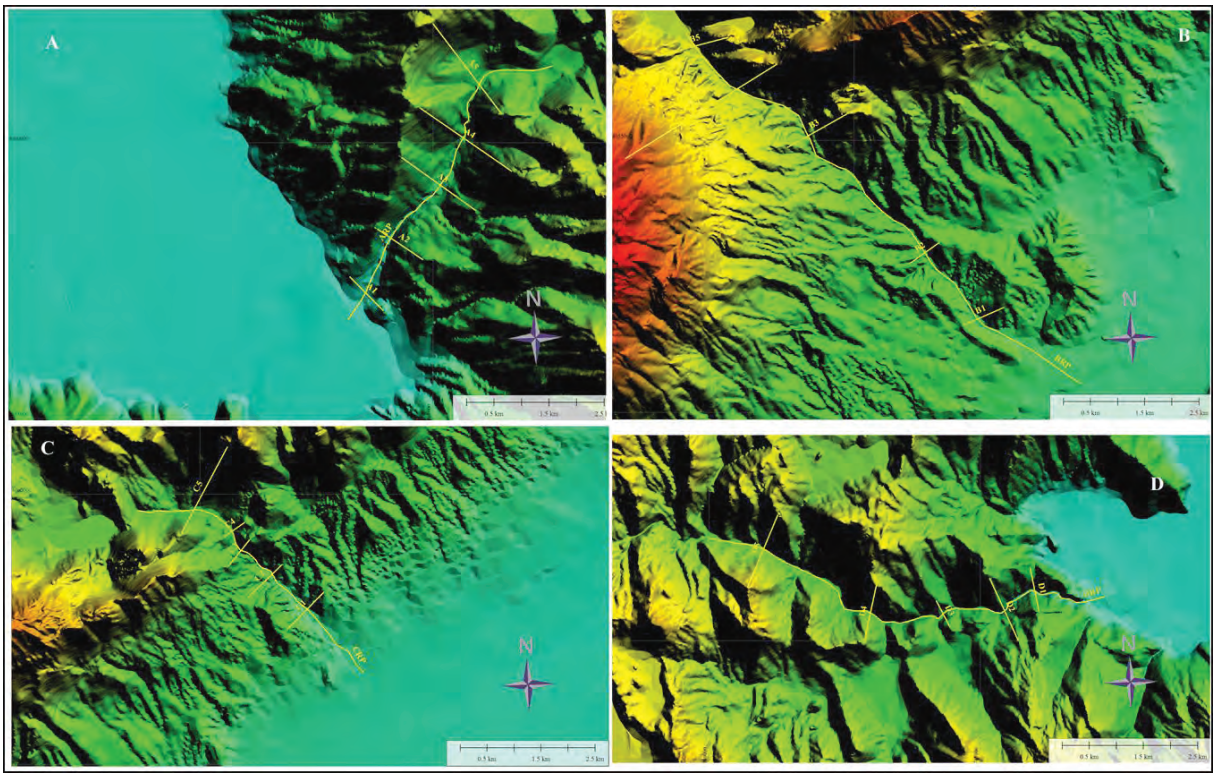

Figure 18- Digital elevation models (A1-A5 and B1-B5) showing stream profiles (RP) and a cross-section taken is perpendicular to the valleys with morphometric analysis.

Table 3- Calculated Vf values and the graphs to indicate the changes in the basin.

Profile name		Vf	Towards the basin center
A			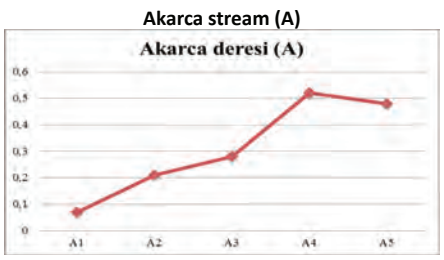
	A1	0,07	
	A2	0,21	
	A3	0,28	
	A4	0,52	
	A5	0,48	
B			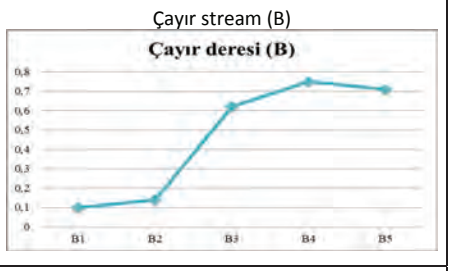
	B1	0,10	
	B2	0,14	
	B3	0,62	
	B4	0,75	
	B5	0,71	
C			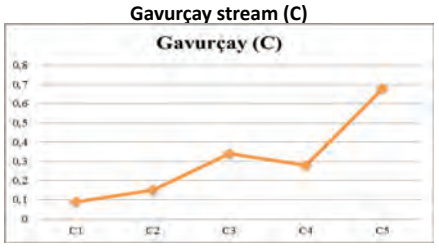
	C1	0,09	
	C2	0,15	
	C3	0,34	
	C4	0,28	
	C5	0,68	
D			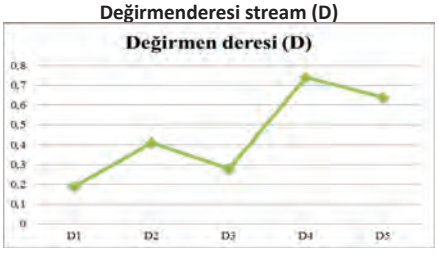
	D1	0,19	
	D2	0,41	
	D3	0,28	
	D4	0,74	
	D5	0,64	

4.2. Mountain Front Sinuosity (Smf)

The Mountain front sinuosity (Smf) is used to define the effect of tectonics in the basin development processes and compared with the Vf value (Rockwell et al., 1984; Silva et al., 2003). The low values of the Smf indices, one of the effective methods used for the determination of tectonic activity, indicate high tectonic effect while the high values indicate the low tectonic effect and increased erosion effect. The meaning of the Smf results are shown in table 4. Smf value is calculated by the following formula;

Table 4- Smf values and their meanings.

Range of values	Identifications
Smf = 1	High tectonic activity
Smf > 1	Low tectonic activity

$$Smf = Lmf / Ls$$

where,

Lmf = the total length of the mountain front (red lines in figure 17)

Ls = the straight line length of the mountain front along the Lmf (blue lines in figure 17).

The Smf value for the **1**, **2** and **3** mountain fronts are calculated (Figure 17, Table 5). As is evident from the Smf values, the degree of tectonic activity is clearly obtained at the basin margins, suggesting that the tectonic activity at the different edges of the basin has a similar rate.

Table 5- Calculated mountain front sinuosity (Smf) (for location look at figure 17).

Profile name	Smf
1	1.18
2	1.12
3	1.17

4.3. The Stream Length-Gradient Index (SL)

The Stream Length-Gradient Index (SL) is calculated to assess the relationship between possible tectonic activity, rock resistance and topography along a valley (Hack, 1973; Keller and Pinter, 2002). The range of values and their representations in the literature for the SL value are listed in table 6. The index is calculated by the following formula;

$$SL=(\Delta H/\Delta L)L$$

where;

ΔH: the change in elevation of the reach,

ΔL: the length of the reach,

L: the total length from midpoint of the reach of interest upstream to the highest point on the channel

Table 6- SL value ranges and media properties they represent.

Range of values	Identifications
$SL \geq 500$	The existence of high resistant rocks and/or high tectonic activity
$300 \leq SL < 500$	The existence of moderate resistant rocks and/or moderate tectonic activity
$SL < 300$	The existence of low resistant rocks and/or low tectonic activity

SL values were calculated for A, B, C and D drainages where Vf values were calculated (Figure 17, Table 7). The results of the analysis show that the tectonic activity in the study area is moderate.

Table 7- Calculated SL values.

Stream profiles for SL	SL
A	329
B	401
C	335
D	341

The results of the morphometric analysis based on digital elevation model in the study area reveal the effectiveness of tectonic activity along the valley profiles. The most important point to be emphasized here is that, considering the age of the units, the rate of rising is not high, but the effect of tectonic activity appears in the region.

5. Discussion and Conclusion

The Elmalı Basin which is located about 120 km far from Antalya is a recent depositional basin, forming under the control of NE-SW trending normal faults and it is between the neritic limestones of the allochthonous Lycian and the autochthonous Beydağları nappes. Some previous scientific studies related to the paleotectonic evolution of nappes tectonism is not the main topic of this study but they are summarized inhere. Besides, the main aims of the study;

- detailed geological mapping and stratigraphic properties of Quaternary tectonic activity of the basin,
- analysis of the slip plane data was performed and the effective stress distributions were determined,
- peak ground acceleration values on the different soil types due to a moderate earthquake were calculated and
- morphometric indices were calculated in order to determine the relationship between tectonics and morphology.

According to the Turkey Active Fault Map (Emre et al., 2013), which was renovated in 2013, no active faults bounding the Elmalı Basin are observed. However, the active faults have been determined and mapped as a result of the detailed field study, which cut and displaced the recent deposits. These are Düden,

Yaka, Yeşilbarak, Yuva, Salur and Yalnızdam faults and the results of measurement and analysis of fault slip data, the dominant characters of them are normal faulting. Slip plane data belonging to the NW-SE trending Salur fault between the basement and recent units and NW-SE trending Yalnızdam fault between Miocene and recent deposits could not be observed during the field study. On the other hand, fault planes and slip plane data ENE-WSW extensional direction in N-S trending Düden fault, NE-SW extensional direction in NW-SE trending Yaka fault, NW-SE extensional direction in NE-SW trending Yeşilbarak fault and N-S extensional direction in E-W trending Yuva fault were measured and analyzed. These data prove Quaternary activity of the faults. Paleostress analyses from the active fault in the study area is compatible with the regional extensional direction in Western Anatolia which is the approximately N-S direction. Some incompatibilities for the regional extension direction are the results of uneven fault traces and some local anomalies. In addition, there is no moderate or destructive earthquake during the instrumental period so no focal mechanism solution in the study area. Despite that the extensional tectonic regime has many evidences for the normal faulting in the study area.

The lack of devastating earthquake in and near the basin does not mean that a destructive earthquake will not affect the settlement in the area. For the reason, peak ground acceleration (PGA) values are calculated based on 20 km distance and Mw=6.5 magnitude earthquake. The PGA values emerge; 0.35 g for recent basin fill, 0.27 g for Miocene units and 0.23 g for the basement. It is obvious that the damage will be increased in the settlements villages around the basin. As general conclusion based on the earthquake potential of the area is that the slip rate of the study area is slow.

Geomorphological analyzes are carried out in order to determine the effect of tectonism in the formation of the Elmalı Basin and its structures within the scope of this study. The most important effect on the formation of surface morphology is stream pattern, which shows significant features depending on tectonic movements. In this study, three different parameters are used. These are the Vf, the Smf and the SL. Both Vf and Smf values indicate that the western margin of Elmalı basin is more active than the eastern margin. According to Vf, Smf and SL analyze made in 4 different sub-basins, the basins are asymmetric and younger basins.

Acknowledgement

This study was supported by the FBA-2015-680 Scientific Research Projects of Akdeniz University. We would like to thanks to all referees for their valuable comments to organize the first manuscript and to get the final version of the manuscript.

References

AFAD, 1996. Türkiye Deprem Bölgeleri Haritası, Afet ve Acil Durum Yönetimi Başkanlığı.

AFAD, 2017. Afet ve Acil Durumu Yönetimi Başkanlığı, Deprem Kayıt Kataloğu.

Akay, E., Uysal, Ş. 1985. Stratigraphy, Sedimentology and Structural Geology of the Neogene Deposits in the West of Central Taurides (Antalya), Mineral Research and Exploration Directorate of Turkey (MTA) Report no.7799 [in Turkish, unpublished].

Akay, E., Uysal. Ş. 1988. Orta Torosların post-Eosen tektoniği, Maden Tetkik ve Arama Dergisi, 108, 57-68.

Akgün, F., Akyol, E. 1992. Yukarıkaflıkara ve Yarıkkaya (Isparta) kömürlerinin karşılaştırmalı palinostratigrafisi ve paleoekolojisi [Correlative palinostratigraphy and palaeoecology of the Yukarıkaflıkara and Yarıkkaya (Isparta) coals], Turkish Association of Petroleum Geologists Bulletin 4, 129–139 [in Turkish with English abstract].

Aksoy, R., Aksarı, S. 2008. Elmalı (Antalya, Batı Toroslar) Kuzeyinde Likya Naplarının Jeolojisi, S.Ü. Müh.-Mim. Fak. Derg., 23, 2.

Alçiçek, M.C., Kazancı, N., Özkul, M. 2005. Multiple rifting pulses and sedimentation in the Çameli Basin, southwestern Anatolia, Turkish Sedimentary Geology 173, 409–431.

Alçiçek, M.C., Ten Veen, J.H., Özkul, M. 2006. Neotectonic development of the Çameli Basin, southwestern Anatolia, Turkey. In: AHF Robertson ve D Mountrakis (eds.), Tectonic Development of the Eastern Mediterranean Region, Geological Society of London, Special Publication, 260, 591–611.

Aldanmaz, E. 2006. Mineral–Chemical Constraints on the Miocene Calc–Alkaline and Shoshonitic Volcanic Rocks of western Turkey: disequilibrium phenochryst assemblages as indicators of magma storage and mixing conditions, Turkish Journal Earth Sciences, 15, 47–73.

Angelier, J. 1994. Fault slip analysis and paleostress reconstruction, in P.L. Hancock, ed., Continental Deformation: Pergamon Press, Oxford, p. 53−100.

Aydan, Ö., Kumsar, H., Ulusay, R. 2002. How to infer the possible mechanism and characteristics of earthquakes from the striations and ground surface traces of existing faults, JSCE, Earthquake Structural Engineering Div. 19 (2), 199–208.

Barka A.A., Reilinger, R.E., Şaroğlu, F., Şengör, A.M.C. 1995. Isparta Angle: Its importance in the noetectonics of the Eastern Mediterranean Region. In: Pişkin, D., Ergün, M., Savaşçın, M.Y. ve Tarcan, G. (eds.), International Earth Science Colloquium on the Aegean Region, 3–18.

Becker–Platen, J., Benda, L., Steffens, P. 1977. Litho und biostratigraphiche Deutung radiometrischer Altersbestimungen aus dem Jungtertiar der Turkei, Geologischen Jahrbuch Reihe B, 25, 139–167.

Besang, C., Eckhardt, F.C., Harre, W., Kreuzer, H., Muller, P. 1977. Radiometriche Altersbestimungen an Neogenen Eruptivgesteinen der Turkei, Geologischen Jahrbuch Reihe B 25, 3–36.

Blumenthal, M.M. 1951. Batı Toroslar'da Alanya ard ülkesinde jeolojik incelemeler [Geological investigations in Alanya hinterland, western Taurides], Bulletin of Mineral Research and Exploration (MTA) of Turkey, 5, 194.

Blumenthal, M.M. 1963. Le Systeme structural de Taurus sud Anatolien: Livre a la mem. Prof. P. Fallot, Memihsser, Buletin de la Société Gélogique de France, 11, 611–662.

Boray, A., Şaroğlu, F., Emre, Ö. 1985. Isparta büklümünün kuzey kesiminde Doğu–Batı daralma için bazı veriler, Geological Engineering, 23, 9–20 [in Turkish with English abstract].

Brunn , J.H., Dumont, J.F., Granciansky, P. De., Gutnic, M., Juteau, Th., Monod, O., Poisson, A. 1971. Outline of the geology of the Western Taurids. In Geology and History of Turkey, A.S. Campbell Ed. Petrol Expl. Soc. of Libya, Tripoli.

Brunn, J.H. Argyriadis, L., Marcoux, J., Poisson, A., Ricou, L.E. 1973. Antalya Ofiyolit naplarının orijini lehine ve aleyhine kanıtlar, Cumhuriyetin 50. Yılı Yerbilimleri Kong. Tebliğleri, 58-69, Ankara.

Bull, W.B., McFadden, L.D. 1977. Tectonic geomorphology north and south of the Garlock fault, California. Geomorphology in Arid Regions, 115-138.

Colin, H.J. 1962. Geologische Untersuchungen im Raume Fethiye-Antalya-Kaş-Finike (SW Anatolien), Bulletin of Mineral Research and Exploration (MTA) of Turkey, 59, Ankara.

Collins, A.S., Robertson, A.H.F. 1998. Processes of Late Cretaceous to late Miocene episodic thrustsheet translation in the Lycian Taurides, SW Turkey, Journal of Geological Society 155, 759–772.

Çevikbaş, A., Ercan, T., Metin, Ş. 1988. Geology and regional distribution of Neogene volcanics between Afyon and Şuhut, Journal of Pure and Applied Sciences 21, 479–499.

Dumont, J. F. 1979. Isparta kıvrımı ve Antalya naplarının orijini; Torosların Üst Kretase tektojenezi ile oluşmuş yapısal düzeninin büyük bir dekroşman, transtorik arızayla ikiye ayrılması varsayımı [Origin of the Isparta Angle and Antalya Nappes; Hypothesis of that the Upper Cretaceous tectogenesis–induced stratigraphy of Turides has been broken–up into two parts by a big decollement (trans–taurique scar)], Bulletin of Mineral Research and Exploration (MTA) of Turkey, 86, 56–67.

Emre, Ö., Duman, T.Y., Özalp, S., Elmacı, H., Olgun, Ş., Şaroğlu, F. 2013. Açıklamalı Türkiye Diri Fay Haritası. Ölçek 1:1.250.000, Maden Tetkik ve Arama Genel Müdürlüğü, Özel Yayın Serisi-30, Ankara.

Erakman, B., Meşhur, M., Gül, M.A., Alkan, H., Öztaş, Y., Akpınar, M. 1982. Fethiye – Köyceğiz Tefenni-Elmalı-Kalkan arasında kalan alanine jeolojisi, Türkiye 6. Petrol Kongresi, Jeoloji Bildirileri, 23-31, Ankara.

Ercan, T., Dinçel, A., Metin, S., Türkecan, A., Günay, E. 1978. Uflak yoresindeki Neojen havzaların jeolojisi [Geology of Nogene basins in Uflak area], Geological Society of Turkey Bulletin, 21, 97–106 [in Turkish with English abstract].

Ercan, T., Satır, M., Kreuzer, H., Türkecan, A., Günay, E., Çevikbaş, A., Ateş, M., Can, B. 1985. Batı Anadolu Senozoyik volkanitlerine ait yeni kimyasal, izotopik ve radyometrik verilerin yorumu [Interpretation of new chemical, isotopic and radiometric age data for western Anatolian Cenozoic volcanics], Geological Society of Turkey Bulletin, 28, 121–136 [In Turkish with English abstract].

Erkül, F., Helvacı, C., Sözbilir, H. 2005. Stratigraphy and geochronology of the Early Miocene volcanic units in the Bigadic borate basin, western Turkey, Turkish Journal of Earth Sciences, 14, 227–253.

Glover, C.P., Robertson, A.H.F. 1998*a*. Neotectonic intersection of the Aegean and Cyprus Tectonic

arcs: extensional and strike–slip faulting in the Isparta Angle, SW Turkey, Tectonophysics, 298, 103–132.

Glover, C.P., Robertson, A.H.F. 1998*b*. Role of regional extension and uplift in the Plio–Pleistocene evolution of the Aksu basin, SW Turkey, Journal of the Geological Society London, 155, 365–387.

Glover, C.P., Robertson, A.H.F. 2003. Origin of tufa (cool-water carbonate) and related terraces in the Antalya area, SW Turkey, Geological Journal, 38, 329–358.

Gutnic, M., Monod, O., Poisson, A., Dumont, J. F. 1979. Géologie des Taurides Occidentales (Turquie), Memoires Société géoloque de France 137, 112, Paris.

Hack, J.T. 1973. Stream-profile analysis and stream-gradient index: U.S. Geological Survey, Journal Research, 1, 4, 421-429.

Hayward, A.B. 1982. Türkiye'nin güneybatısındaki Beydağları ve Susuzdağ masiflerinde Miyosen yaşlı kırıntılı tortulların stratigrafisi, TJK Bull., 25(2), 81-89.

Karaman, E. 1986. Burdur dolayının genel stratigrafisi [General stratigraphy of Burdur area], Bulletin of Isparta Engineering Faculty, 2, 23–36 [in Turkish with English abstract].

Karaman, M.E. 2010. The Isparta Angle and its reletationship with Aegean–Cyprus Tectonic Arcs, SW Turkey, XIX Congress of the Carpathian Balkan Geological Association Thessaloniki, Greece, 23–26 September.

Keller, J., Villari, R. 1972. Rhyolotic ignimbrite in the region of Afyon (Central–Anatolia), Bulletin Volcanologique, 36, 342–358.

Keller, E.A., Pinter, N. 1996. Active Tectonics, Prentice Hall, New Jersey.

Kelling, G., Robertson, A.H.F., Buchem, F.V. 2005. Cenozoic sedimentary basins of southern Turkey: an introduction, Sedimentary Geology, 173, 1–13.

Kissel, C., Poisson, A. 1987. Etude Paléomagnétique des formation Cénozoiques des Beydağları (Tauride occidentals), Comptes Rendue de I'Academie des Seciences de Paris, 304, 343–348.

Kissel, C., Averbuch, O., Frizon De Lamotte, D., Monod, O., Allerton, S. 1993. First paleomagnetic evidence for a post–Eocene clock–wise rotation of the Western Taurides thrust belt east of Isparta reentrant (southwestern Turkey), Earth and Planetary Sciences Letters, 117, 1–14.

Koçyiğit, A. 1981. Isparta Büklümünde (Batı Toroslar) Toros karbonat platformunun evrimi [Evolution of the Tauride carbonate platform in the Isparta Angle (Western Turides)], Bulletin of the Geological Society of Turkey, 24, 15–23 [in Turkish with English abstract].

Koçyiğit, A. 1983. Hoyran gölü (Isparta Büklümü) dolayının tektoniği [Tectonics of Lake Hoyran (Isparta Angle) area]. Bulletin of the Geological Society of Turkey, 26, 1–10 [in Turkish with English abstract].

Koçyiğit, A. 1984*a*. Güneybatı Türkiye ve yakın dolayında levha içi yeni tektonik gelişim [A new intracontinental tectonic regime in southwest Turkey and its close vicinity], Bulletin of the Geological Society of Türkey 27, 1–16 [in Turkish with English abstract].

Koçyiğit, A., 1984*b*. Tectonostratigraphic characteristics of Hoyran Lake region (Isparta Bend). In: Tekeli, O ve Göncüoğlu, C. (eds), Geology of the Tauirus belt, International Symposium, 26–29 September 1983, Proceeding, 53–67, Ankara–Turkey.

Koçyiğit, A. 1996. Lakes region graben–horst system, SW Turkey: Differential stretching and commencement age of the extensional tectonic regime. In: TÜBİTAK–Universities–Maden Tetkik ve Arama, Görür, N. (coordinator), National Marine Geological and Geophysical Programme–Workshop, Proceedings, 99–103, İstanbul.

Koçyiğit, A. 2005. Denzili Graben–Horst System and the eastern limit of the West Anatolian continental extension: basin fill, structure, deformational mode, throw amount and episodic evolutionary history, SW Turkey, Geodinamica Acta, 18, 167–208.

Koçyiğit A., Ünay, E., Saraç, G. 2000. Episodic graben formation and extensional neotectonic regime in west Central Anatolia and the Isparta Angle: a key study in the Akşehir–Afyon graben, Turkey, Geological Society of London, Special Publication, 173, 405–421.

Koçyiğit, A., Rojay, B., Cihan, M., Özacar, A. 2001. The June 6, 2000, Orta (Çankırı, Turkey) Earthquake: Sourced from a New Antithetic Sinistral Strike–slip Structure of the North Anatolian Fault System, the Dodurga Fault Zone, Turkish Journal of Earth Sciences, 10, 69–82.

Koçyiğit, A., Özacar, A. 2003. Extensional Neotectonic Regime through the NE Edge of the Outer Isparta Angle, SW Turkey: New field and seismic Data, Turkish Journal of Earth Sciences, 12, 67–90.

Koçyiğit, A., Deveci, Ş. 2007. A N–S–trending active extensional structure, the Şuhut (Afyon) Graben: commencement age of the extensional neotectonic period in the Isparta Angle, SW Turkey, Turkish Journal of Earth Science, 16, 391–416.

KOERI, 2017. Kandilli Rasathanesi Deprem Kayıt Kataloğu.

Koşun, E., Poisson, A., Çiner, A., Wernli, R., Monod, O. 2009. Syn-tectonic sedimentary evolution of the Miocene Çatallar Basin, southwestern Turkey, Journal of Asian Earth Sciences 34, 3, 466-479.

Meşhur, M., Akpınar, M. 1984. Yatağan-Milas-Bodrum ve Karacasu-Kale-Acıpayam-Tavas civarlarının jeolojisi ve petrol olanakları, TPAO, Arama Grubu Rep., 1963.

Önalan, M. 1979. Geology of Elmalı-Ka district. Istanbul Üniversitesi, Fen Fakültesi, Doktora Tezi (PhD Thesis), 1—139 (in Turkish).

Özgül, N. 1976. Toroslar'da bazı temel jeoloji özellikleri, Türkiye Jeol. Kurumu Bülteni, 19, 65-78.

Piper, J.D.A., Gürsoy, H., Tatar, O., İşseven, T., Koçyiğit, A. 2002. Paleomagnetic evidence for the Gondwanic origin of the Taurides and rotation of the Isparta Angle, southern Turkey, Geological Journal, 37, 317–336.

Poisson, A. 1977. Recherches geologiques dans les Taurides Occidentales (Turquie): these d'etat; Univ. de Paris–Sud, Orsay, 795.

Poisson, A., Poignant, A. F. 1974. Korkuteli Bölgesindeki Miyosen Transgresyonunun Tabanı Olan Karabayır Formasyonu (Antalya İli).

Poisson, A., Wernli, R., Sagular, E.K., Temiz, H. 2003. New data concerning the age of the Aksu Thrust in the south of the Aksu valley, Isparta Angle (SW Turkey): consequences for the Antalya Basin and the Eastern Mediterranean, Geological Journal, 38, 311–327.

Price, S. P., Scott, B. 1991. Pliocene Burdur basin, SW Turkey: tectonics, seismicity and sedimentation, Journal of the Geological Society London, 148, 345–354.

Robertson, A.H.F. 1993. Mesozoic-Tertiary sedimentary and tectonic evolution of Neotethyan carbonate platforms, margins and small ocean basins in the Antalya Complex, Southwest Turkey. In Frostick, L.E., and Steel, R. (Eds.), Tectonic Controls and Signatures in Sedimentary Successions, Spec. Publ. Int. Assoc. Sedimentol., 20, 415−465.

Robertson, A.H.F. 2000. Tectonic evolution of the Cyprus in its Easternmost Mediterranean setting. In: Panayides, I., Xenophontos, C. & Malpas, J. (eds) Proceedings of the 3rdInternational Conference on the Geology of the Eastern Mediterranean. Geological Survey Department, Nicosia, 11-44.

Robertson, A. H. F., Poisson, A., Akıncı, Ö. 2003. Developments in research concerning Mesozoic-Tertiary Tethys and neotectonics in the Isparta Angle, SW Turkey, Geological Journal, 38, 195-234.

Rockwell, T.K., Keller, E.A., Johnson, D.L. 1984. Tectonic geomorphology of alluvial fans and mountain fronts 478 near Andntura, California, Tectonic Geomorphology, 183-207.

Schumm, S. A. 1986. Alluvial River Response to Active Tectonics, Studies in Geophysics, Panel on Active Tectonics, 80–94, National Academy Press.

Seyitoğlu, G., Scott, B. 1992. Late Cenozoic crustal extension, basin formation and volcanism in west Turkey. International workshop: Work in progress on the Geology of Türkiye, Abstracts, p. 61–62. Keele University, England, UK.

Silva, P.G., Goy, J.L., Zazo, C., Bardají, T. 2003. Faulth-generated mountain fronts in southeast Spain: 480 Geomorphologic assessment of tectonic and seismic activity, Geomorphology 50, 203-225.

Şenel, M. 1997*a*. 1:100 000 ölçekli Türkiye Jeoloji Haritaları, Fethiye-L7 paftası. No: 1, Maden Tetkik ve Arama, Ankara.

Şenel, M.. 1997*b*. 1/100.000 ölçekli Türkiye Jeoloji Haritaları, Fethiye-L8 paftası. No :2, Maden Tetkik ve Arama, Ankara.

Şenel, M., 1997*c*. 1/100.000 ölçekli Türkiye Jeoloji Haritaları, Fethiye-L9 paftası. No:3, Maden Tetkik ve Arama, Ankara.

Şenel, M., Selçuk, H., Bilgin, Z.R., Şen, M.A., Karaman, T., Erkan, M., Kaymakçı, H., Örçen. S., Bilgin, C. 1987. Likya naplarının ön cephe özellikleri, Türkiye Jeoloji Kurultayı, Bildiri özleri, 8 Ankara.

Şenel, M., Selçuk, H., Bilgin, Z. R., Şen, M. A., Karaman, T. Dinçer, M.A., Durukan, E., Arbas, A., H., Örçen, S., Bilgin, C. 1989. Çamei (Denizli)- Yeşilova (Burdur)-Elmalı (Antalya) ve dolayının jeolojisi, MTA Genel Müdürlüğü Rapor no: 9429, Ankara, (unpublished).

Şenel, M., Dalkılıç, H., Gedik, L., Serdaroğlu, M., Bölükbaşı, A.S., Metin, S., Esentürk, K., Bilgin, A.Z., Uguz, F.J., Korucu, M., Özgül, N. 1992. Eğridir-Yeni-şarbademli-Gebiz ve Geriş-Köprülü (Isparta-

Antalya) arasında kalan alanların jeolojisi, Maden Tetkik ve Arama Raporu 9390, TPAO Rap. No: 3132, 559 s., Ankara, (unpublished).

Şenel, M., Akdeniz, N., Öztürk, E.M., Özdemir, T. Kadınkız, G., Metin, Y., Öcal, H., Serdaroğlu, M., Örçen, S. 1994. Fethiye (Muğla)-Kalkan (Antalya) ve kuzeyinin jeolojisi, MTA Genel Müdürlüğü Rapor no: 9761, Ankara, (unpublished).

Şenel, M., İgedik, İ., Dalkılıç, H., Serdaroğlu, M., Bilgin, A. Z., Uğuz, M. F., Bölükbaşı, A. S., Korucu, M., Özgül, N. 1996. Isparta Büklümü Doğusunda, otokton ve allokton birimlerin stratigrafisi (Batı Toroslar), Maden Tetkik ve Arama Dergisi, 118, 111-160.

Şengör, A.M.C, Satır, M., Akkök, R. 1984. Timing of tectonic events in the Menderes Massif, western Turkey: implications for tectonic evolution and evidence for Pan-African basement in Turkey, Tectonics, 4, 693-707.

Ulusay, R., Tuncay, E., Sönmez, H., Gökçeoğlu, C. 2004. An attenuation relationship based on Turkish strong motion data and iso-acceleration map of Turkey, Engineering Geology, 74(3-4), 265-291.

Yağmurlu, F. 1991. Yalvaç–Yarıkkaya Neojen havzasının stratigrafisi ve depolanma ortamı [Stratigraphy and depositional setting of the Yalvaç–Yarıkkaya Neogene basin], Bulletin of the Geological Society of Turkey 34, 9–19 [in Turkish with English abstract].

Yağmurlu, F., Savaşçın, Y., Ergun, M. 1997. Relation of alkaline volcanism and active tectonism within the evolution of the Isparta Angle, SW Turkey, Journal of Geology, 105 (6), 717–728.

Yılmaz, Y., Genç, Ş. C., Gürer, F., Bozcu, M., Yılmaz, K., Karacık, Z., Altunkaynak, Ş., Elmas, A. 2000. When did the western Anatolian grabens begin to develop?, Geological Society, London, Special Publication, 173, 353–384.

Bull. Min. Res. Exp. (2018) 156: 67-86

Bulletin of the Mineral Research and Exploration

http://bulletin.mta.gov.tr

Syn-sedimentary deformation structures in the Early Miocene lacustrine deposits, the basal limestone unit, Bigadiç basin (Balıkesir, Turkey)

Calibe KOÇ-TAŞGIN[a*], İbrahim TÜRKMEN[b] and Cansu DİNİZ-AKARCA[c]

[a]*Fırat University, Fac. of Eng., Dept. of Geol. Eng., 23119,Elazığ, Turkey. orcid.org/0000-0002-5439-7379*
[b]*Balıkesir University, Fac. of Eng., Dept. of Geol. Eng., 10145, Balıkesir, Turkey. orcid.org/0000-0003-4420-7268*
[c]*Balıkesir University, Fac. of Eng., Dept. of Geol. Eng., 10145,Balıkesir, Turkey. orcid.org/0000-0003-3421-1765*

Research Article

Keywords:
Soft sediment deformation structures, lacustrine, slumps, rock falls, Bigadiç.

ABSTRACT

In the Western Anatolian region, NE-SW, E-W directional basins were developed which were limited to the extension-related faults beginning in the late Oligocene to early Miocene. The fillings of these basins consist of fluvial – lacustrine deposits containing volcanic and volcaniclastic intercalations. These deposits include intensive local unconformities and soft sediment deformation structures. The filling of the Bigadiç Neogene Basin which is one of these basins, constitute base limestone unit, lower tuff unit, lower borate unit, upper tuff unit and upper borate unit. The base limestone unit composed of claystone, marl, limestone, dolomitic limestone facies was deposited in the deep lacustrine environment. The soft sediment deformation structures were defined in the base limestone unit, which outcroped in the south of Bigadiç. These are: slumps, rock falls, chaotic structures, clastic dykes, synsedimentary faults and breccia limestone. Deformation mechanisms are related essentially to the increase of slopes of layers, liquidization and fluidization. In the study area; regional tectonics, sedimentological data, and deformation structures are evaluated together, it is concluded that these structures are formed by tectonic and seismic (earthquakes related to tectonic origin and syndepositional magmatic activities).

Received Date: 26.12.2016
Accepted Date: 14.09.2017

1. Introduction

The extension that began in late Oligocene-early Miocene, the latter periods of the continuing collision following the closure of the northern branch of the Neotethys in the Western Anatolia region, has continued until today (Altunkaynak and Yılmaz, 1998; Westaway, 2006). This extensional tectonism has caused the development of metamorphic core complexes, the fault controlled NE-SW and E-W directional sedimentary basins (Figure 1) and the settlements of magmatic rocks (Savaşçın and Güleç, 1990; Seyitoğlu and Scott, 1994; Seyitoğlu, 1997; Altınkaynak and Yılmaz, 1998; Yılmaz et al., 2001). The extension, which was formed in Neogene in the Western Anatolia region, mainly affected the Menderes massive (Harris et al., 1994; Okay and Satır, 2000; Jolivet et al., 2013). These basins, which contain volcano sedimentary deposits, were developed by detachment faults defined in the Menderes massive. In the period during which the extensional tectonism is affective the NE directional Soma, Bigadiç, Demirci, Gördes and Selendi basins developed (Koçyiğit et al., 1999; Yılmaz et al., 2000; Bozkurt, 2000, 2003; Işık et al., 2003; Bozkurt and Sözbilir, 2004). The fillings of these basins, which unconformably overlie the pre Miocene basement, are represented by the fluvial-lacustrine deposits containing volcanic and volcanoclastic intercalations (Erkül and Tatar Erkül, 2010). These are generally the multi-staged basins (Sözbilir, 2007). The first stage, which represents the Oligocene- early Miocene period, constitutes the opening (formation) period of basins. However; the second stage (20-7 my) is the

* *Corresponding author: Calibe KOÇ-TAŞGIN, calibekoc@firat.edu.tr*
http://dx.doi.org/10.19111/bulletinofmre.378545

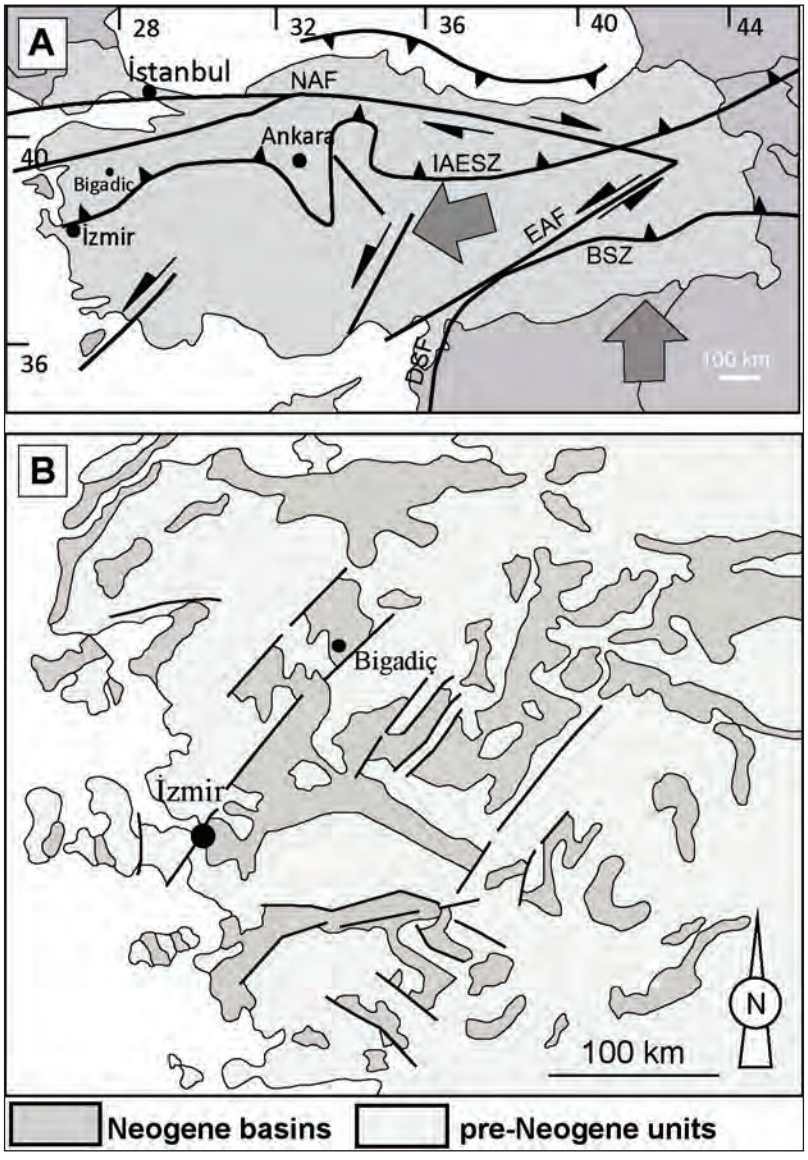

Figure 1- **a)** Main structural characteristics in Turkey; **NAF:** North Anatolian Fault; **IAESZ:** İzmir-Ankara-Erzincan Suture Zone; **BSZ**: Bitlis Suture Zone; **EAF**: East Anatolian Fault; **DSF**: Dead Sea Fault, **b)** Neogene basins in the Western Anatolia (modified from Garcia-Veigas and Helvacı, 2013).

period in which fillings of basins have developed. During the infilling of basins, the normal and slip faults in different angles have also accompanied to the sedimentation. In the last stage; E-W directional, normal and strike-slip faults have developed (Sözbilir, 2007). The Bigadiç Neogene basin, which was opened at the beginning of Late Oligocene-early Miocene, has been filled until the end of Early Miocene. During the sedimentation that controls this basin the tectonic events stated above have been effective and their traces have been observed in it. Besides; the locations and geometries of NE-SW directional slip faults (Figure 2), which cut basin infillings after the sedimentation, show that these are the continuation of faults that control the basin. The deposits here contain local stratigraphic unconformities associated with the tectonism controlling the basin (intra-formational unconformities). The dips of the upper tuff beds and overlying upper borate unit reach up to 80 degrees in some places. The radiometric age data obtained from volcanic rocks varying from basalt to rhyolite show that these basins have been under the effect of volcanism during early-middle Miocene (Erkül and Tatar Erkül, 2010). The unconformity and deformation

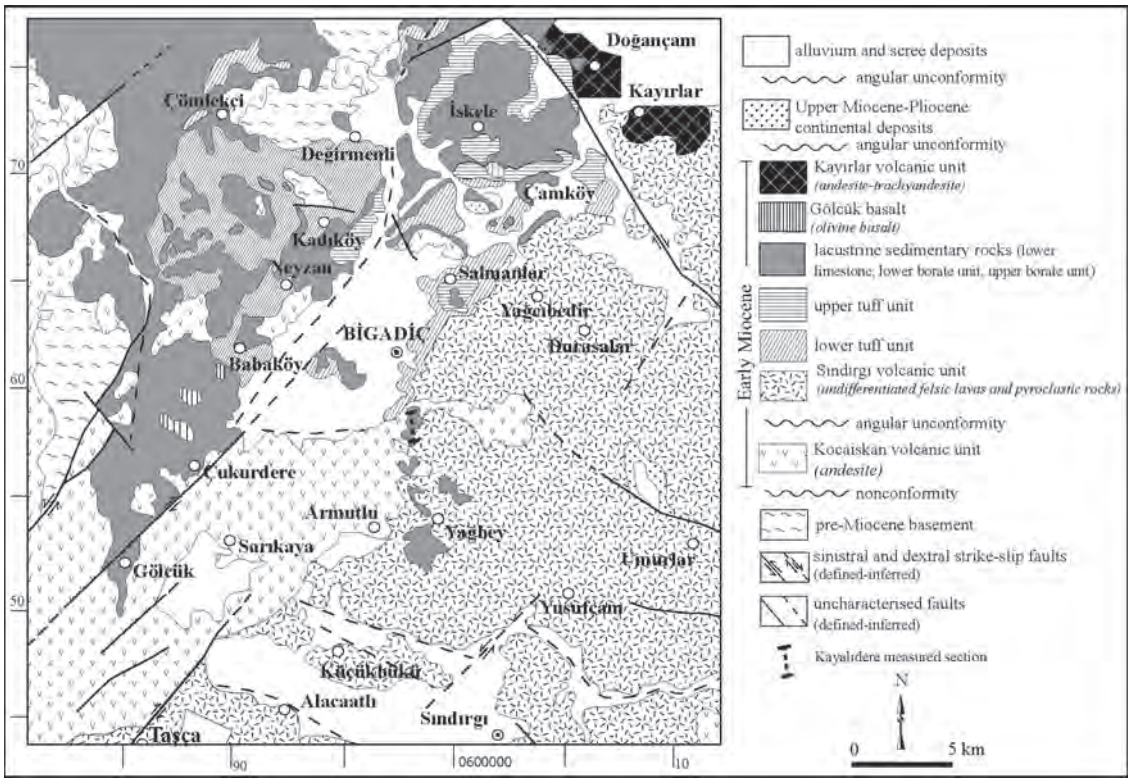

Figure 2- The geological map of the study area and its vicinity (modified from Erkül, 2006).

structures in these deposits can be associated with detachment faults controlling the development of basins. The deformation structures formed by the earthquake induced vibrations that are caused by these faults are defined as seismites (Seilacher, 1969). The seismites have been observed in many environments too (in fluvial, delta, lacustrine, etc.) (Owen, 1995; Gibert et al., 2005; Moretti and Sabato, 2007; Koç-Taşgın and Türkmen, 2009; Mastrogiacomo et al., 2012). The soft sediment deformation structures have been developed in the lacustrine environment in this study. The lacustrine environments are depositional environments, which most clearly reflect the results of seismic and tectonic activity during sedimentation as the deformation structure.

The purpose of this study is to define the soft sediment deformation structures, which were observed within the basal limestone unit located in the Bigadiç volcano sedimentary deposit in the Bigadiç basin, and interpret the formation mechanism.

2. Stratigraphy

The outcropping rock in the vicinity of the study area is the deformed Late Cretaceous- Paleocene flysch zone which is formed by big olistolith and ophiolitic blocks within chaotic sediments (Okay et al., 1996, 2001; Erkül et al., 2005*a*) (Figures 2 and 3). This unit is unconformably overlain by the early Miocene Kocaiskan volcanics, the Bigadiç volcano sedimentary deposit, the late Miocene-Pliocene terrigenous deposits and Quaternary sediments (Erkül et al., 2005*a* and *b*).The Kocaiskan volcanics cover an area of more than 800 km^2 and are the earliest products of the early Miocene volcanic activity in the Bigadiç region. In previous studies, it has been defined as the basal volcanic (Gündoğdu et al., 1989; Helvacı, 1995). The unit is formed by andesitic intrusions, pyroclastic rocks and volcanic origin sedimentary rocks (Erkül et al., 2005*a*).

Sındırgı volcanics, Gölcük basalts, Kayırlar volcanics and Şahinkaya volcanics constitute the volcanic units of the Bigadiç volcano-sedimentary deposit. However; the lacustrine units of this unit is composed by basal limestone, lower tuff, lower borate, upper tuff and upper borate units (Figure 2). Sındırgı volcanics are composed of dacitic and rhyolitic intrusions, massive and autobrecciated lava flows and pyroclastic deposits. Dacitic and rhyolitic rocks cover large areas in the eastern and southern parts of Bigadiç. Gölcük basalts spread out between

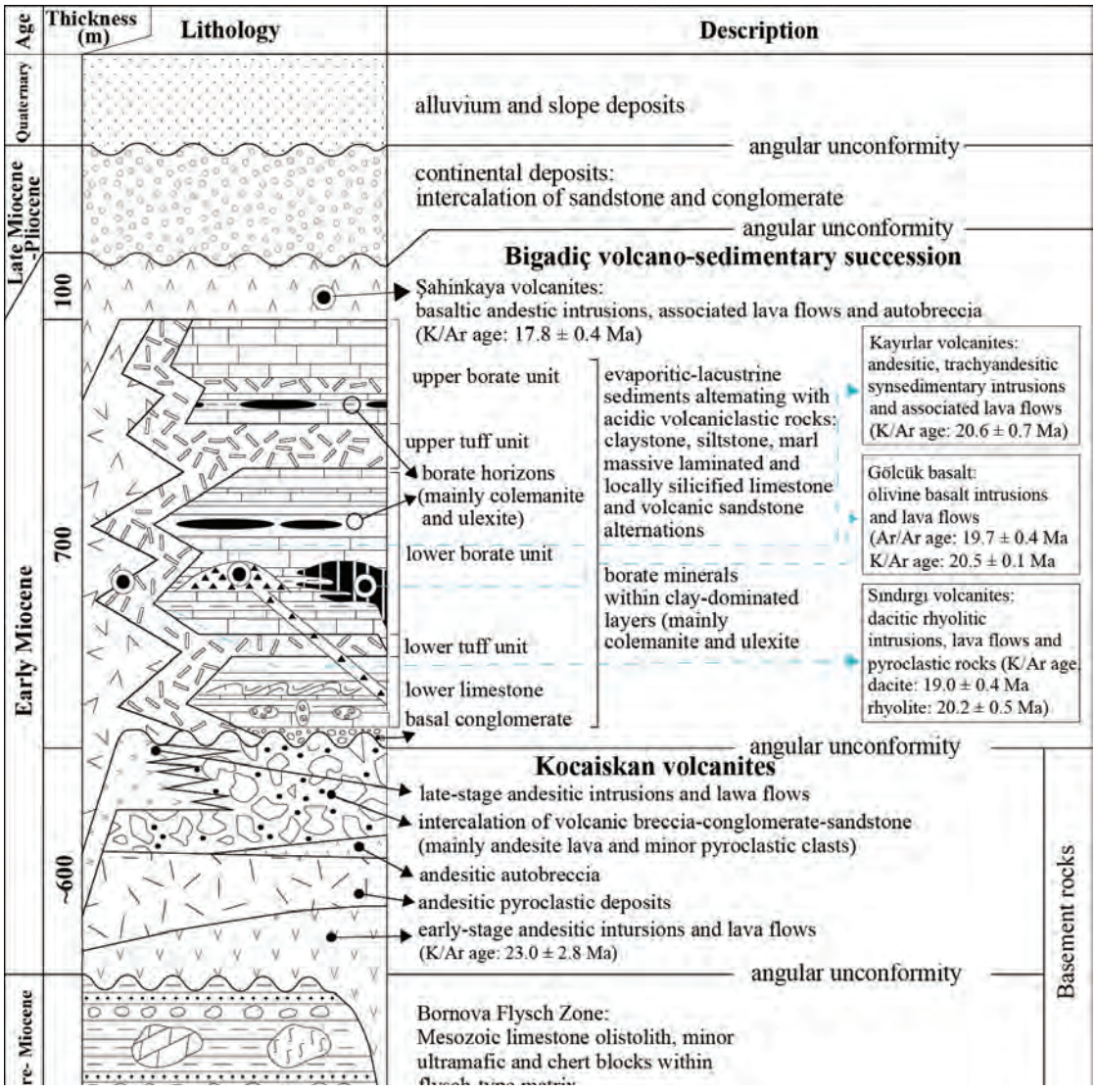

Figure 3- Generalized stratigraphic section of the study area (modified from Erkül, 2005*b*).

Gölcük and Babaköy, and are composed of olivine basalt dykes and volcanic domes in NE direction. It also spreads around Çamköy. Kayırlar volcanics are made up of trachyandesitic dykes, massive and auto brecciated lava flows in Doğançam and Kayırlar regions. Şahinkaya volcanics are basaltic and andesitic dykes, and are composed of lavas intercalating with dykes and auto brecciated pyroclastic rocks (Erkül et al., 2005*a*).

Lacustrine units were divided into 5 units and studied by Helvacı (1995). The same classification was followed in this study too. These units from bottom to top are; the units of basal limestone, lower tuff, lower borate, upper tuff and upper borate. The unit, which is represented by the intercalation of limestone, dolomitic limestone, claystone, marl and tuff, was named as the "Basal Limestone" and constitutes the main topic of this study. The unit unconformably overlies the Kocaiskan volcanics and is also conformably overlain by the lower tuff unit. The lower tuff unit a wide spread unit between Bigadiç and Cagis, is represented by coarse grained, thick layered (25 cm) or thickly bedded gray-white tuffs,which is up to 150 m thick. Economically important lower borate unit in the study area is composed of limestone, cherty limestone, tuffite, claystone and marls. The upper tuff unit is represented by "zeolitic" tuffs in the lower layers and as fine grained tuffs in the upper layers. The upper borate unit is represented by boron-claystone-limestone-tuff intercalation in the lower layers; claystone-limestone-tuff intercalation with

organic material in the middle layers and by medium to fine grained laminated sandstone in the uppermost layers. In the same layers of the unit, the slumps and associated syn-sedimentary faults were developed.

The terrestrial deposits unconformably overlie the Miocene volcano-sedimentary deposits. The Upper Miocene-Pliocene red and beige sandstone and conglomerate layers of fluvial origin outcrops around Kocaiskan. These are unconformably overlain by unconsolidated clastic sediments of Quaternary age.

3. Sedimentological Characteristics of the Basal Limestone Unit

The basal limestone unit is represented by the intercalation of limestone, dolomitic limestone, claystone, marl and tuff. The measured thickness of the unit in this study is nearly 200 m (Figure 4). Mention the attitude of beds at proper positions in this paragraph. The deposit begins with dolomitic limestones that have much fractured and jointed structures and passes into banded tuff- cleavaged limestone-marl intercalation in the upper layers, and into claystone-limestone-tuff intercalation in the uppermost layers. The limestones are generally bedded and occasionally massive in character. The bedding thickness of cream to beige colored limestones is approximately 10 cm. They also have 2-3 cm thickness in some places and intercalate with tuffs. The marls are gray to green in color and observed as intercalating with tuff and limestone layers. They occasionally have the characteristics of conchoidal cleavage and consist of volcanic clastics in sand and pebble (1 cm) sizes. The medium to coarse silt size tuffs commonly exhibits lamination while at places they exhibit bedded nature also fractures and cracks in tuffs are filled with calcite.

The organic, laminated facies with carbonate clastics are composed of micritic carbonates, silt size clastic material and the intercalation of organic rich layers. It is considered that these were formed at the bottom sections of a less energetic, cold lake, which is not much saline, and presents seasonal bedding (Donovan, 1980). Similar facies (marl/limestone and mudstone/marl laminites) were interpreted as the perennial lacustrine deposits (Tanner, 2002). In these facies there were not encountered any evidence indicating shore (palustrine) or shallow regions (caliche for palustrine environments, desiccation cracks, wave origin structures for shallow environments, fossil diversity).

Sedimentological data obtained in this study indicate that the unit has sometimes been affected from the volcanism and deposited in deep lake environment. According to its relationship with volcanic units, the age of the unit was given as the Lower Miocene (Erkül et al., 2005*a*). Helvacı and Alaca (1991) detected the age of unit as the Lower Miocene according to its stratigraphic relationship with units at the bottom and top. Even though the washed samples of Basal Limestone unit yielded limited number of shells it was not possible to date and hence Lower Miocene age asigned by previous workers is followed in this study.

4. Soft Sediment Deformation Structures

Soft sediment deformation is a term used for the variation of fabric and layers of recently deposited sediments (Nichols, 2009). It is generally formed in granular sediments of which soft-sediment deformation structures are saturated with water. This strength loss is related with the liquefaction and/or fluidity of the water which develops as a result of the pore water pressure (Allen, 1982; Owen, 1987). In addition; the soft sediment deformation structures were also observed in carbonate rock deposits (Demicco and Hardie, 1994) and defined as seismite by some researchers (Weaver and Jeffcoat, 1978; Pratt, 1998, 2002; Kahle, 2002; Jewell and Ettenshon, 2004; André et al., 2004; McLaughlin and Brett, 2004).

Such structures were encountered in lakes (Sims, 1973; Hempton and Dewey, 1983; Scott and Price, 1988; Karling and Abella, 1992; Alfaro et al., 1997; Jones and Omoto, 2000; Rodriguez-Pascua et al., 2000; Moretti and Sabato, 2007; Koç-Taşgın and Türkmen, 2009), in deltaic environments (Gibert et al., 2005; Owen and Moretti, 2008), in shallow marine and tidal environments (Johnson, 1977; Bhattacharya and Bandyopadhyay, 1998; Molina et al., 1998; Rossetti, 1999; Rossetti et al., 2000; Rossetti and Goes, 2000; Moretti et al., 2001; Spalluto et al., 2007; Mastrogiacomo et al., 2012; Chen and Suk Lee, 2013) and in fan delta deposits (Postma, 1983). Besides; there are experimental studies related with the formation of these structures (Kuenen, 1958; Nichols et al., 1994; Owen, 1996; Moretti et al., 1999).

Within basal limestone unit the soft sediment deformation structures in different types were defined in many layers of the Kayalıdere section (Figure 4). These structures are explained below in detail.

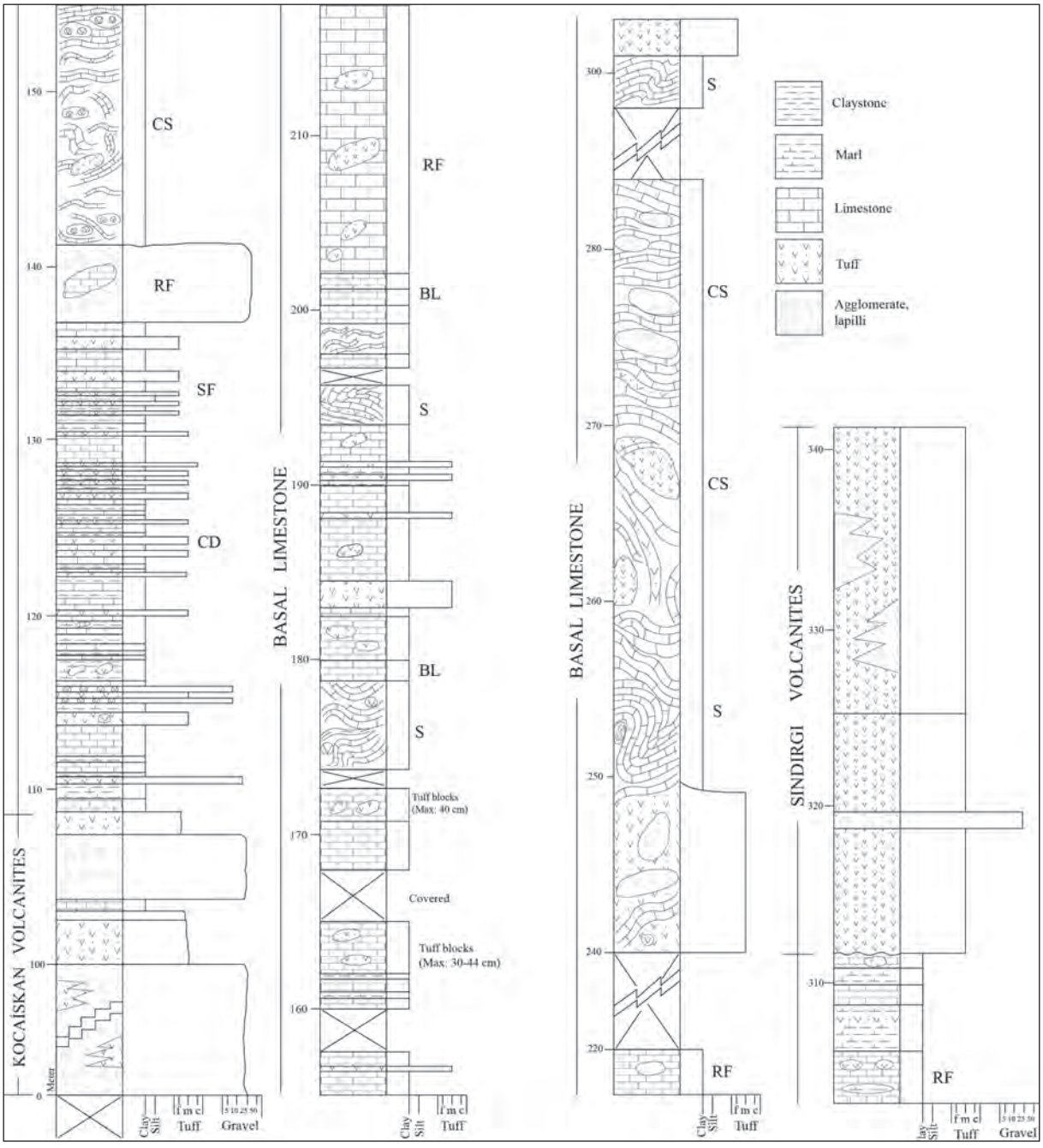

Figure 4- Kayalıdere measured section. Deformation structures are marked on the section. **S:** Slump Features, **CS:** Chaotic Structures, **RF:** Rock Fall, **CDS**: Clastic Dyke and Sills, **SF**: Syn-sedimentary Faults, **BL**: Brecciated Limestone.

4.1. Slump Structures

Slump structures were observed and defined along the road cuts around the Kayalıdere village where Basal Limestone units are well exposed (Figures 4-6). The structures,which are encountered at different levels of the unit, especially have affected bedded limestones. It has sometimes affected the thin bedded limestones and dolomitic limestone layers and sometimes tuff and marl layers, and formed slump structures of different dimensions. The size of small scale slump structures varies in between 20-100 cm. Also, the syn-sedimentary faults were formed towards the end portions of folds related with slump structures (Figure 5D). The slip amounts of these faults, which have the characteristics of inverse fault, are approximately 10 cm. These structures were observed in depth intervals

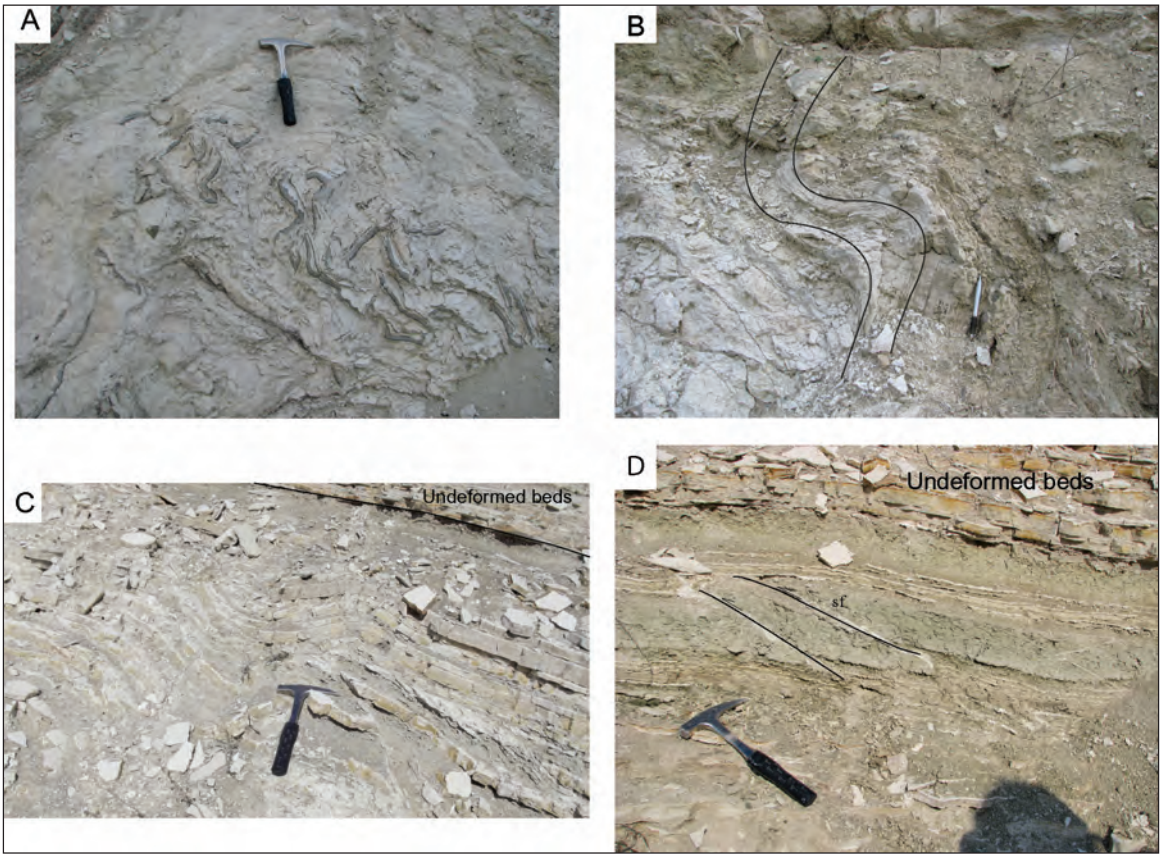

Figure 5- Small scale slump structures. These structures were developed in; **a)** dolomitic limestones **b)** bedded limestones and **c)** marl-limestone intercalation. **d)** syn-sedimentary inverse faults associated with slump structures.

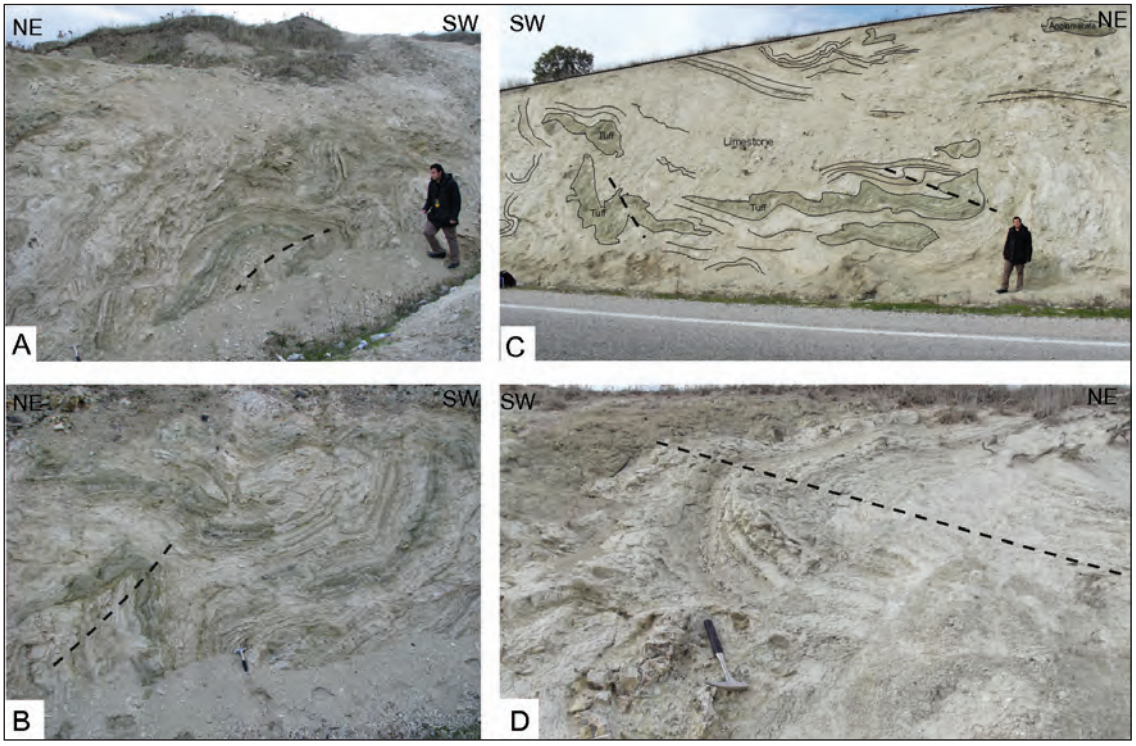

Figure 6- Large scale slump structures; **a)** and **b)** claystone, marl, limestone and tuff layers, **c)** tuff layers associated with limestones, **d)** slump structures observed in bedded limestones.

of 142-155 m, 174-179 m, 193-198.5 m and 240-301 m in the Kayalıdere measured section (Figure 4). The slump structures detected in limestones between of 142-147 meter are associated with chaotic sediments (tuff blocks and volcanic rock clastics). The layers are observed as bended and folded in different directions. The sediments here moved generally in the direction of SW (220°).

Interpretation: Slump structures develop due to the downward slip of the mass of sediment from the slope. These structures are characterized by inverse faults, isolated or continuous folds in the ends and by extensional structures over the head (Martinsen, 1994; Spalluto et al., 2007; Owen et al., 2011; Alsop and Marco, 2011, 2013). Slump structures are formed by steepening of slopes due to excess loading (due to rapid sedimentation), deposition (accumulation) and by earthquakes (Allen, 1982; Mills, 1983; Keefer, 1984; Owen, 1987; Van Loon and Brodzikowski, 1987; Moretti, 1996; Shanmugam, 2017). They may also occur due to the sloping of layers related with tectonic activities (faulting etc.) (Maltman, 1994*a*, 1994*b*; Siegenthaler et al., 1987; Mastrogiacomo et al., 2012; Perucca et al., 2014).

4.2. Chaotic Structures

Chaotic structures, which are observed in a couple of layers within the Basal Limestone unit (especially in the upper layers), are seen in the mixed form of slump structures and rock falls (Figures 4-7). The slump structures observed here have mostly moved in the direction of SW (210°-220°) and occasionally in the direction of NE (40°-45°). The planes of fold axes are horizontal, sub-horizontal and vertical. Slump structures influenced bedded limestones and tuff layers intercalating with them, and formed chaotic folds. The limestones consist of agglomerate and tuff blocks with sizes even reaching 3 m. The long axes of these blocks are both horizontal and vertical. These chaotic structures are either bounded by calcarous cement or tuffaceous material. It is also seen that these structures are occasionally associated with normal faults.

Interpretation: The complex or chaotic soft sediment deformation structures may occur in layers which have been affected by a couple of deformation phase. These deformation phases should have been repeated in short intervals. The deformation phase or phases, which follow the complexities formed by the main deformation phase (e.g. such as the aftershocks following an earthquake), could make the succession more complex (Mazumder et al., 2016). In the formation of chaotic sediments here, the faults controlling the basin and syn-tectonic activities such as volcanic and seismic activites associated with these faults should have been effective (Basilone et al., 2014).

4.3. Rock Falls

These generally occurs in pebble, fragment (mention size) and large blocks (mention dimension) of varying lithologies that recurs at different levels within the Basal limestone unit (Figures 4, 8 and 9). It is seen that these rock fragments are sometimes related with slumps and sometimes with chaotic sediments. There are also observed floating rock blocks within limestone. Within marl and limestone,

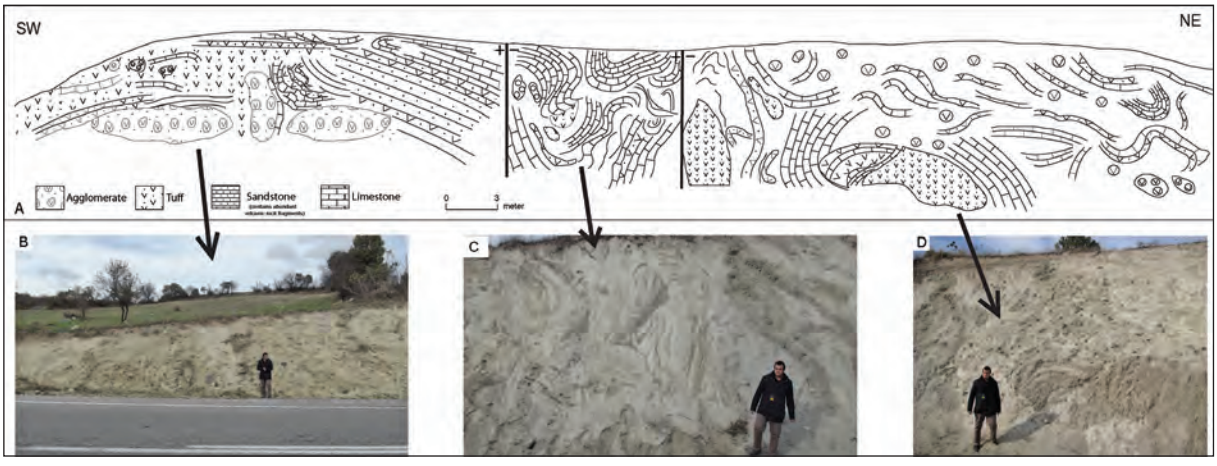

Figure 7- Chaotic structures, **a)** geological cross section showing chaotic structures, **b)** agglomerate blocks and slump structures, **c)** slump structures affecting the bedded limestones and tuff clastics, **d)** tuff block and slump structures.

the fragments and blocks of tuff and volcanic rock fragments (10-15 cm) take place. The size of tuff fragments vary between 20 and 100 cm. The size of agglomerate blocks observed in tuff reaches 6 m (Figure 7). Commonly the limestone beds below such agglomeratic blocks are observed to be deformed / buckled and sunken down/downwarped, similar to blocks (Figure 8a, b).

Interpretation: Rock falls are the most frequently seen mass movements associated with earthquakes. These movements occur on slopes at angles more than 40° (Keefer, 1984). They accumulate as colluvial or in tens of meters ahead the bottom section of steep slopes (Keefer, 1999). According to Montenant et al. (2007), the rock falls are gravity associated events originating from earthquakes. These rock fall deposits that reaches couple of meters in thickness could have been developed because of seismic event related with block faulting and extension effective in basin (Bozkurt and Sözbilir, 2004; Sözbilir, 2007; Erkül and Tatar Erkül, 2010).

Figure 8- **a)** and **b)** agglomerate blocks observed within limestones. Limestone layers under the block are deformed.

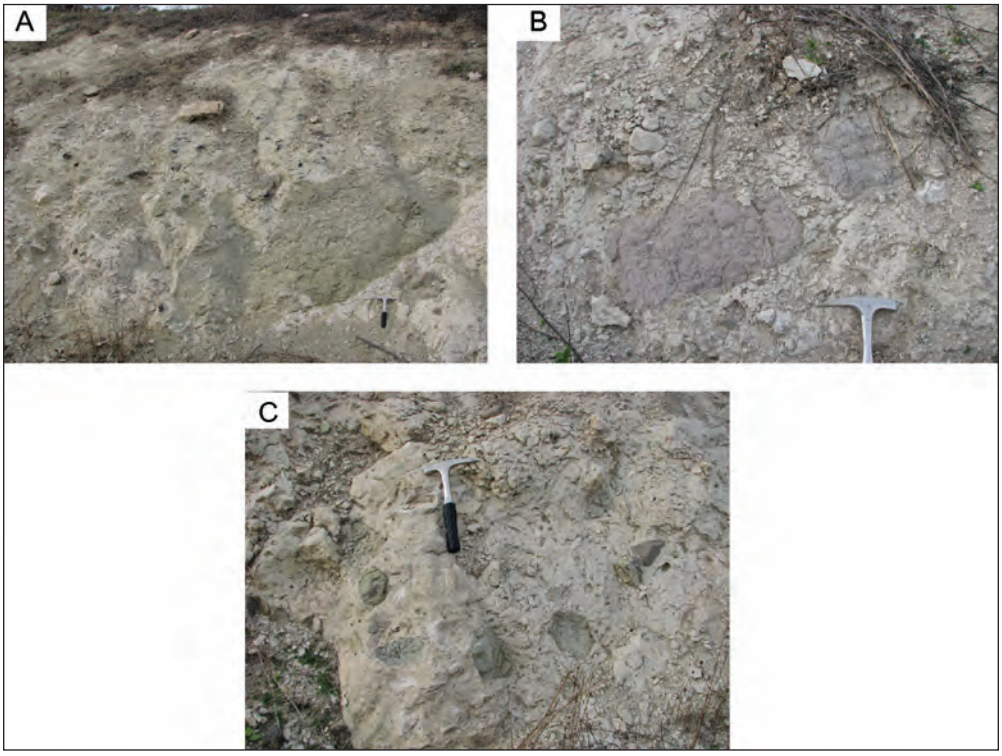

Figure 9- Rock falls in small scale, **a)** and **b)** tuff clastics, **c)** volcanic rock fragments.

4.4. Clastic Dykes and Sills

The clastic dykes observed in the study area occur between clayey limestone and fine to medium grained tuff. The deformation in question continues tens of meters laterally (Figure 10). The fine grained tuffs located in lower layers deformed limestones by intruding into them. The vertical length of dykes reaches 30 cm occasionally and that at places dike intrude through both limestone and medium grained tuff and intrudes in to the coarse grained tuff. Dyke formation began in the lower layer in the form of a very thin fracture and reached 7 cm thickness in maximum in the upper layers. The sills, which are the product of tuffs, show lateral continuity within limestones as connected with dykes.

Interpretation: The best indicator of liquefaction and fluidization as the soft sediment deformation structure is the water escape structures. For example; the dish and column structures, sand volcanoes, clastic dyke and sills (Mills, 1983). Dykes are generally formed by the upward transportation of sediments with pore water (Lowe, 1975, Owen et al., 2011; Mazumder et al., 2016; Onorato et al., 2016). The water escape structures are formed by the liquefaction and fluidization of the water in sands restricted by low permeable layers (Owen, 1987; Moretti and Sabato, 2007). Such clastic dykes could also be formed as a result of the upward movement of liquefied sediment under the pressure of upper layers (Daley, 1971; Rossetti, 1999; Montenant et al., 2007). Dykes and sills observed in the study area should have developed as being associated with the upward and lateral movement of tuffs as a result of liquefaction and fluidization (Rodriguez-Pascua et al., 2000).

4.5. Syn-sedimentary Faults

The syn-sedimentary fault, which is observed in the Basal Limestone unit especially affected tuff-limestone-marl facies, (Figure 11) and are generally in the characteristics of steeply inclined normal fault. Normal faults, which affect the deep lacustrine deposits, have formed horst and grabens in occasions. Over the layers of horst portions the breakdowns and detachments were developed. The net slip amount of the faults vary between 30 cm to 1 m.

Interpretation: The brittle deformation is associated with cohesive behavior of the sediment. When the pore water pressure in sediments increases and it is not strong enough to liquefy the sediment pressure then the brittle deformation occurs (Owen, 1987; Vanneste

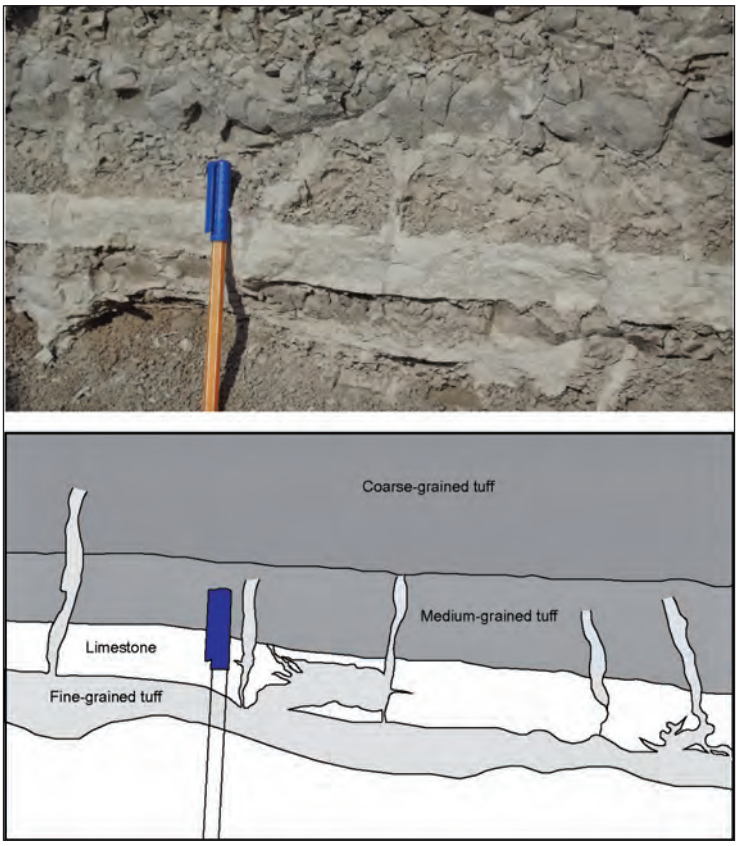

Figure 10- Clastic dyke and sills. Dyke and sills formed by the fine grained tuffs affected clayey limestones and medium to coarse grained tuffs.

Figure 11- Syn-sedimentary normal faults affecting the claystone, marl, limestone and tuff layers.

et al. 1999). Rosetti and Goes (2000) emphasize that these structures are associated with unconsolidated or poorly consolidated sediments. The structures investigated in the study area have developed after the partial consolidation of sediment.

4.6. Brecciated Limestones

The brecciation is observed in bedded limestones and partly in massive limestones (Figure 12). It has also affected limestone blocks which are observed in the form of rock fall. In brecciated layers, occasionally the angular limestone pebbles with sizes reaching 15 cm are observed. There were also observed brecciated limestone fragments within tuffs. These are generally grain supported.

Interpretation: The liquefactions, which are formed by the increasing pressure of entrapped water in pores of the early calcite cemented carbonate sediments cause brecciation (Clukey et al., 1985). Breccias defined in this study area associated with the liquefaction and some of the breccias observed in limestone blocks within tuffs should have developed during the transportation.

5. Triggering Mechanism

In order to detect the triggering mechanism, it is necessary to discuss all triggering mechanisms in the light of paleo-environmental analyses.

The presence of steeply inclined slopes is important for the formation of slump structures. The facies analyses carried out in the succession during the study indicate that the depositional environment is flat or sub-flat. Though it is considered that steep slopes are the main factors for the formation of slump structures, these may also occur at low angle slopes (even at degree of 1°) (Shepard, 1955; Field et al., 1982; Mills, 1983). It is stated that these structures, which occur on flat areas, are generally associated with paleoseismic activities (Bhattacharya and Bandyopadhyay, 1998; Rossetti and Santos, 2003; Spalluto et al., 2007; Garcia-Tortosa et al., 2011). Slump structures may occur due to excess load (related to the rapid sedimentation) (Allen, 1982). The entrapped waters among grains cause the increase in pore water pressure in next periods and the grains to become weak during rapid sedimentation. There was not observed any sudden coarse grained facies entrance in the study area. In poorly consolidated sediments, the most probable reason for the formation of slump structures is the increase in slope angles (steepening). Slump structures are formed when the bedded layers are inclined enough to exceed the stability limit. The slope increase in layers develops due to the deposition and tectonic movements. At the same time; the erosions, which are formed by water flows or turbiditic currents, may cause the increase in the slope angle (Mills, 1983). The facies characteristics and environmental data of the study area indicate that the deposition and current activities are not effective in the development of structures here. Slump structures here should have been formed as a result of increase in slope angle with the effect of seismic activities. The tremors, which occurred as a result of seismic shocks and/or volcanic activities, might have caused the decrease in the cohesion of sediments in inclined layers and sliding.

The formation of deformation structures such as chaotic sediments and rock falls are associated

Figure 12- Brecciated limestones.

with seismic and tectonic activities (Keefer, 1999; Montenant et al., 2007). The normal faults, which affected the basin during sedimentation, caused topographic reliefs in the basin. These rises caused rock falls in block and fragment sizes belonging to basal volcanics.

The liquefaction of buried layers begins with seismic activity (Clague et al., 1992) and the groundwater movements can cause these layers to be fluent (Guhman and Pederson, 1992). However; the hydraulic tension, which develops depending on the instant periods of the groundwater, widely causes the formation of local structures in young sediments. The dykes defined in this study show continuity in tens of meters. The rapid sedimentation may cause the formation of sand dykes (Parize and Fries, 2003). Facies overlying the dykes in this study show that these are not related with the rapid sedimentation. The sand dykes may also be formed by big storm waves (Martel and Gibling, 1993). However; the probability of big storm movements to be effective is weak in relatively deep lacustrine environments. The periodical tensions that are formed by seismic waves cause the pore water pressure to increase and the liquefaction (Owen and Moretti, 2011). The mechanism, which initiates the formation of sand dykes here, may be associated with seismic shocks (Mills, 1983; Audemard and De Santis, 1991; Obermeier et al., 1993; Obermeier, 1996; Rodríguez- Pascua et al., 2000) and/or tremors caused by the volcanic activities. The tremors, which are related to volcanic activities and frequently control the basin, should have initiated the liquefaction and fluidization event (Samaila et al., 2006; Tian et al., 2014; Zhou et al., 2017).

The sedimentological characteristics of deposits, their abundances and relationships with other deformation structures, which were formed by small scale normal faults show that these are developed based on the seismic activities (Vanneste et al., 1999). The normal faults known in the study area indicate that the region is controlled by an extensional tectonic movement. Syn-sedimentary faults with normal character are compatible with the regional tectonism. In other words; the syn sedimentary faults in the study area should have developed as associated with seismic movements due to the extensional tectonic activity in the region.

The breccias observed in limestones deposited in marine environments were developed by big storm movements (Seguret et al., 2001; Chen and Lee, 2013). The limestones deposited in the lacustrine environment have weak probability to get influenced from big storm movements. The observation of brecciation in footwall blocks in places indicates that these are associated with both transportation and seismic activity.

The liquefaction can be initiated depending on several factors. These factors affect the deposition environment both externally (allogenically) and internally (autogenically). The allogenic factors are tectonic movements and earthquakes. The factor affecting the depositional environment internally are autogenic in character, and these are; the wave motions, strikes due to the breaking of waves, stormy pressure vibrations in strong water flows, shear tension due to tsunami and tidal movements, rapid sediment rise, glacial melting in badly drained sediments or the groundwater movements (Owen and Moretti, 2011). There was not detected any evidence supporting autogenic factors that could initiate the formation of soft sediment deformation structures in the Basal Limestone unit. In other words; it seems quite difficult to associate these deformation structures, which developed in the lacustrine environment, with the triggering mechanism such as the shear tension related to wave motions, tsunami. So; in this case, the allogenic factors (tectonic movements, volcanism and earthquakes) should have been effective in the formation of deformation structures observed in the study area.

It is known that the faults associated with extension, which began in late Oligocene-early Miocene in the Western Anatolia region, are very effective during the formation of NE-SW and E-W directional basins and the deposition of volcano-sedimentary deposit. The sedimentation in the Bigadiç Neogene basin was controlled by tectonism and volcanism (Helvacı and Alaca, 1984, 1991). There are many and significantly large faults in the region. The step faulting system constitutes one part of these faults (Gündoğdu, 1982, 1984; Yılmaz et al., 1982; Baysal et al., 1985, 1986). During the sedimentation in the Bigadiç Neogene Basin, the NE-SW directional oblique slip, normal faults, strike slip faults and anticlines/synclines have developed (Erkül et al., 2005*a*). When the locations of faults and the characteristics of the basin fill are studied, it is seen that these faults are the basic structures controlling the development of the basin and one part of these continue their functions as syn sedimentary faults (Figure 13) (Baysal et al., 1986; Erkül et al., 2005*a*).It is seen that the sedimentation

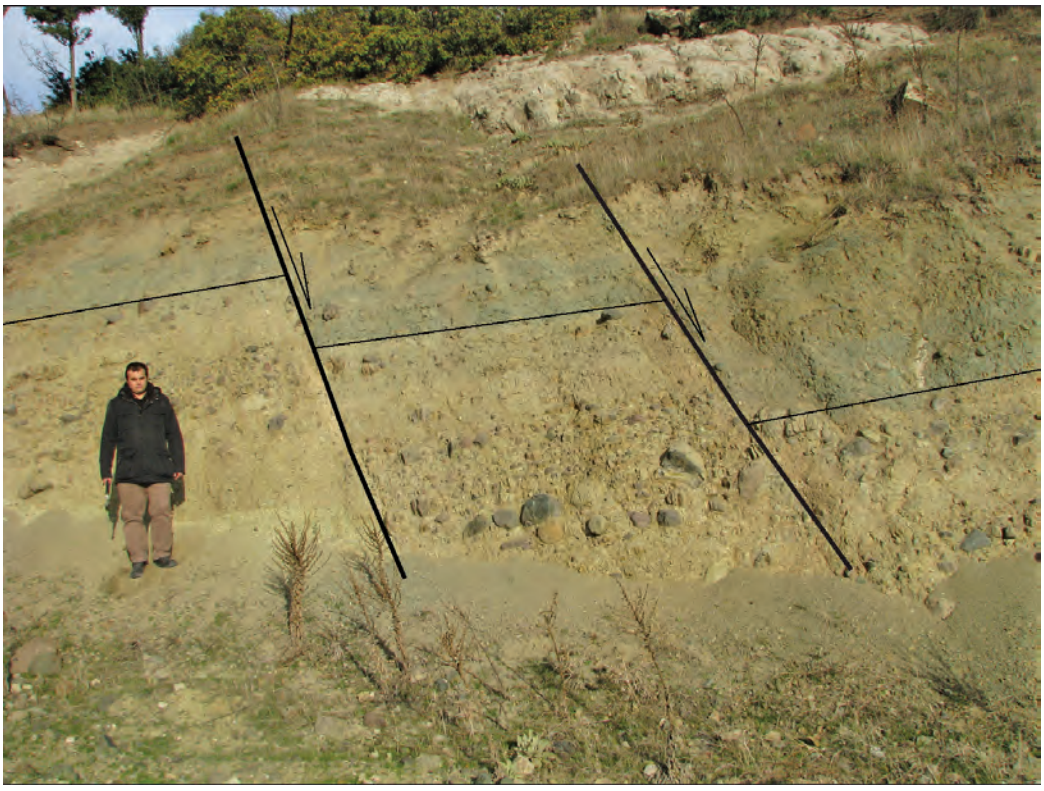

Figure 13- Sinsedimanter normal faults observed in Kocaiskan volcanics.

in the basin, which developed in trans-tensional zone, is intensively accompanied by volcanism in addition to the faulting. During the sedimentation, the volcanism and dykes 100 m in width 2 km in length developed in the region together with intrusions (Erkül et al., 2005*a*). Accordingly; the earthquakes, which were formed as a result of magmatic activities synchronously with tectonics and deposition, should have been effective in addition to the tectonism, which is the main mechanism triggering the development of deformation structures here.

Seismic shocks may cause liquefaction and/or fluidization in unconsolidated sediments (Seilacher, 1969; Lowe, 1975; Sims, 1975). The tendency of seismic activities to form in the basin, which is restricted by fault, is higher (Mastalerz and Wojewoda, 1993; Bhattacharya and Bandyopadhyay, 1998; Koç-Taşgın and Türkmen, 2009; Koç-Taşgın, 2011; Koç-Taşgın et al., 2011). For the formation of liquefaction, the magnitude of the smallest earthquake should be greater than 5 (Audemard and De Santis, 1991). So; the earthquakes with magnitudes greater than 5 should have been effective during deposition in the region.

6. Results

In this study, the morphological characteristics of soft sediment deformation structures observed in the Early Miocene basal limestone unit around Bigadiç were established and formation mechanism was interpreted. In the lake, where the basal limestone was deposited, it was seen that both the tectonism and volcanism accompanied the sedimentation. Generally; tuffs and agglomerate levels in fewer amounts developed as being associated with the volcanism. Tectonic activities effective in the basin and earthquakes associated with tectonic and magmatic activities caused the formation of deformation structures.

The deformation structures restricted with undeformed layers from lower and upper layers and show lateral continuity in tens of meters (clastic dykes) indicate that these were developed in response to seismic activities. The structures defined in the study area show resemblance to seismic and tectonic origin deformation structures, which were defined by Seilacher, (1969); Moretti et al. (1999); Rodríguez-Pascua et al. (2000); Rossetti and Góes, (2000); Moretti and Sabato, (2007); Mastrogiacomo et al.

(2012) and experimentally approved by Kuenen, (1958) and Owen, (1996) in previous studies. It was determined that other factors (the shear tension due to wave motions, tsunami and tidal movements, rapid sedimentation, and groundwater movements), which could form deformation, were not effective in the study area.

In and around the study area, the soft sediment deformation structures were intensely observed in the Early Miocene lower and upper borate unit (Günen and Varol, 2004; Koç-Taşgın and Türkmen, 2014). This situation indicates that tectonic, seismic and associated magmatic activities in the region (Erkül et al., 2005*a* and *b*) have continued during periods when these sediments had been deposited.

Acknowledgements

This study has been supported by the TUBITAK Project Number as; 112Y237. We would like to thank to Assist. Prof. Serkan Üner (Yüzüncü Yıl University) and other investigator who made constructive suggestions and contributions. We are thankful to all staffs who contributed to this article in the editorial board of MTA and to Research Assistant Onur Alkaç (Fırat University) for his helps during computer drawings.

References

Alfaro, P., Moretti, M., Soria, J.M. 1997. Soft-sediment deformation structures induced by earthquakes (seismites) in Pliocene lacustrine deposits (Guadix-Baza Basin, Central Betic Cordillera), Eclogae Geologicae Helvetiae 90, 531-540.

Allen, J.R.L. 1982. Sedimentary structures: their character and physical basis. Developments in Sedimentology. Elsevier, Amsterdam (663 p.).

Alsop, G.I., Marco, S. 2011. Soft-sediment deformation within seismogenic slumps of the Dead Sea basin. Journal of Structural Geology 33, 433–457.

Alsop, G.I., Marco, S. 2013. Seismogenic slump folds formed by gravity-driven tectonics down a negligible subaqueous slope. Tectonophysics 605, 48–69.

Altunkaynak, Ş., Yılmaz, Y. 1998. The Mount Kozak magmatic complex, Western Anatolia. Journal of Volcanology and Geothermal Research 85, 1-4, 211-231.

André, J.P., Saint Martin, J.P., Moissette, P., Garcia, F., Corné, J.J., Ferrandini, M. 2004. An unusual Messinian succession in the Sinis Peninsula, western Sardinia, Italy. Sedimentary Geology. 167, 41–55.

Audemard, F.A., De Santis, F. 1991. Survey of liquefaction structures induced by recent moderate earthquakes. International Association for Engineering Geology and the Environment 44, 5-16.

Basilone, L., Lena, G., Gasparo-Morticelli, M. 2014. Synsedimentary - tectonic, soft - sediment deformation and volcanism inthe rifted Tethyan margin from the Upper Triassic – Middle Jurassicdeep-water carbonates in Central Sicily. Sedimentary Geology, 308, 63-79.

Baysal, O., Salancı, B., Batman, B., Yılmaz, O., Kasapoğlu, B., Şahbaz, A., Görmüş, S., Kocaefe, S., Gündoğdu, N., Kazanoğlu, H., Şentürk, A., Öner, M., Bayhan, H., Cerit, O., Karayiğit, A.İ., Yalçın, H., Tolluoğlu, Ü., Demirel, İ.H., Genç, Y., Dilaver, T., Temel, A., Çetin, H., Bağcı, G. 1985. Bigadiç Borat Havzası Jeolojisi ve ekonomik maden potansiyelinin tespit edilmesi projesi. H.Ü. Yerbilimleri Uygulama ve Araştırma Merkezi Proje Kodu : YUVAM/84-3; 256 p.

Baysal, O., Batman, B., Yılmaz, O., Görmüş, S., Şahbaz, A., Cerit, O., Yalçın, H., Karayiğit A.İ., Salancı, B., Bayhan, H. 1986. Bigadiç Borat havzası ve yakın çevresinin jeolojik incelenmesi. H.Ü. Yerbilimleri Uygulama ve Araştırma Merkezi, Beytepe – Ankara, Proje no: YUVAM/85-1, 90 p. (unpublished).

Bhattacharya, H.N., Bandyopady, S. 1998. Seismites in a Proterozoic tidal succession, Singhbhum, Bihar, India. Sedimentary Geology 119, pp. 239—252.

Bozkurt, E. 2000. Timing of extension on the Büyük Menderes Graben, western Turkey, and its tectonic implications. Geological Society, London, Special Publications 173, 1, 385-403.

Bozkurt, E. 2003. Origin of NE-trending basins in western Turkey. Geodinamica Acta, 16, 61-81.

Bozkurt, E., Sözbilir, H. 2004. Tectonic evolution of the Gediz Graben: field evidence for an episodic, two-stage extension in Western Turkey. Geological Magazine, 141, 1, 63-79.

Chen, J., Lee,. H.S. 2013. Soft-Sediment deformation structures in Cambrian Siliciclastic and carbonate storm deposits (Shandong Province, China): Differential liquefaction and fluidization triggered by storm-wave loading. Sedimentary Geology 288, 81-94.

Clague, J.J., Naesgaard, E., Sy, A. 1992. Liquefaction features on the Fraser delta: evidence for prehistoric earthquakes? Canadian Journal of Earth Sciences, 29, 8, 1734-1745.

Clukey, E.C., Kulhawy, F.H., Liu, P.L.-F., Tate, G.B., 1985. The impact of wave loads and pore-water pressure generation on initiation of sediment transport. Geo-Marine Letters 5, 177–183.

Daley, B. 1971. Diapiric and other deformational structures in an Oligocene argillaceous limestone. Sedimentary Geology 6, 29-51.

Demicco, R.V., Hardie, L.A. 1994. Sedimentary structures and early diagenetic features of shallow marine carbonate deposits. S.E.P.M. Atlas Series 1, 265 p.

Donovan, R.N. 1980. Lacustrine cycles, fish ecology and stratigraphic zonation in the Middle Devonian of Cathness. Scottish Journal of Geology 16, 35-50.

Erkül, F., Helvacı, C., Sözbilir, H. 2005*a*. Evidence for two episodes of volcanism in the Bigadic borate basin and tectonic implications for western Turkey. Journal of Geology 40, 545-570.

Erkül, F., Helvacı, C., Sözbilir, H. 2005*b*. Stratigraphy and geochronology of the Early Miocene volcanic units in the Bigadic¸ borate basin, Western Turkey. Turkish Journal of Earth Science 14, 227-253.

Erkül, F., Helvacı, C., Sözbilir, H. 2006. Olivine basalt and trachyan desite peperites formed at the subsurface/surface interface of a semi-arid lake: An example from the Early Miocene Bigadic¸ basin, western Turkey. Journal of Volcanology and Geothermal Research 149, 240–262.

Erkül, F., Tatar Erkül, S. 2010. Erken Miyosen Alaçamdağ (Dursunbey-Balıkesir) Magmatik Kompleksinin Jeolojisi ve Batı Anadolu Genleşme Tektoniğindeki Konumu. Maden Tetkik ve Arama Dergisi 141, 1-27.

Field, M.E., Gardner, V., Jennings, A.E., Edwards, B.D. 1982. Earthquake-induced sediment failures on a 0.25° slope, Klamath River delta, California. Geology 10, 542–546.

García-Tortosa, F.J., Pedro Alfaro, P., Gibert, L., Scott, G. 2011. Seismically induced slump on an extremely gentle slope (b1°) of the Pleistocene Tecopa paleolake (California). Geology 39, 1055–1058.

Garcia-Veigas, J., Helvacı, 2013. Mineralogy and sedimentology of the Miocene Göcenoluk borate deposits, Kırka district, Western Anatolia, Turkey. Sedimentary Geology 290, 85-96.

Gibert, L., Sanz de Galdeano, C., Alfaro, P., Scott, G., López Garrido, A.C. 2005. Seismic induced slump in Early Pleistocene deltaic deposits of the Baza Basin (SE Spain). Sedimentary Geology 179, 279–294.

Guhman, A.I., Pederson, D.T. 1992. Boiling sand springs, Dismal River, Nebraska: agents for formation of vertical cylindrical structures and geomorphic change. Geology 20, 8–10.

Gündoğdu, M.N. 1982. Neojen yaşlı Bigadiç sedimanter baseninin jeolojik, mineralojik ve jeokimyasal incelenmesi: Dok. Tezi, 386s, 3 ek, Hacettepe Üniversitesi, Ankara. (unpublished).

Gündoğdu, M.N. 1984. Bigadiç gölsel Neojen baseninin jeolojisi. Hacettepe Üniversitesi Yerbilimleri Dergisi 11, 91-104.

Gündoğdu, M.N., Bonnot-Courtois, C., Clauer, N. 1989. Isotopic and chemical signatures of sedimentary smectite and diagenetic clinoptilolite of a lacustrine Neogene basin near Bigadiç, western Turkey. Applied Geochemistry. 4, 635– 644.

Günen, E., Varol, B. 2004. Bigadiç Neojen havzasında sedimantasyonla yaşıt tektonik yapılar. Evaporitler Tuzlar Semineri, 19-23 Ocak 2004. 317-328.

Harris, N.B.W., Kelley, S., Okay, A.I. 1994. Post collision magmatism and tectonics in Northwest Anatolia. Contributions to Mineralogy and Petrology 117 (3), 241–252.

Helvacı, C. 1995. Stratigraphy, mineralogy and genesis of the Bigadic¸ borate deposits, western Turkey. Econ. Geol. 90, 1237– 1260.

Helvacı, C., Alaca, O. 1984. “Geology and Mineralogy of the Bigadiç Borate Deposits,” Book of Abstracts, 38th Scientific and Technical Congress of the Geological Society of Turkey, 110-111.

Helvacı, C., Alaca, O. 1991. Bigadiç Borat yatakları ve çevresinin jeolojisi ve mineralojisi. Maden Tetkik ve Arama Dergisi 113, 61-92.

Hempton, M.R., Dewey, J.S. 1983. Earthquake-induced deformational structures in young lacustrine sediments, East Anatolian Fault, southeast Turkey. Tectonophysics 98, T14–T17.

Işık, V., Seyitoğlu, G., Çemen, İ. 2003. Ductile-brittle transition along the Alasehir detachment fault and its structural relationship with the Simav detachment fault, Menderes massif, western Turkey. Tectonophysics 374 1-2, 1-18.

Jewell, H.E., Ettenshon, R. 2004. An ancient seismite response to Taconian far-field forces: the Cane Run Bed, Upper Ordovician (Trenton) Lexington Limestone, central Kentucky (USA). Journal of Geodynamics 37, 487–511.

Johnson, H.D. 1977. Sedimentation and water escape structures in some late Precambrian shallow marine sandstones from Finnmark, North Norway. Sedimentology 24, 389-411.

Jolivet, L., Faccenna, C., Huet, B., Labrousse, L., Le Pourhiet, L., Lacombe, O., Lecomte, E., Burov, E., Yoann Denèle, Brun, J.P., Philippon, M., Paul, A., Salaün, G., Karabulut, H., Piromallo, C., Monié, P., Gueydan, F., Okay, A., Oberhänsli, R., Pourteau, A., Augier, R., Gadenne, L., Driussi, O. 2013, Aegean tectonics: Strain localisation, slab tearing and trench retreat, Tectonophysics, 597–598, 1-33.

Jones, A.P., Omoto, K. 2000. Towards establishing criteria for identifying trigger mechanisms for soft-sediment deformation: a case study of Late Pleistocene lacustrine sands and clays, Onikobe and Nakayamadaira basins, northeastern Japan. Sedimentology 47, 1211–1226.

Kahle, C.F. 2002. Seismogenic deformation structures in microbialities and mudstones, Silurian Lockport Dolomite, Northwestern Ohio, USA. J. Sedimentary Research 72, 201–216.

Karling, R.E., Abella, S.E.B. 1992. Paleoearthquakes in the Pugeot Sound Region recorded in sediments from lake Washington, USA. Science 258, 1617–1619.

Keefer, D.F. 1984. Landslides caused by earthquakes, Geological Society of America Bulletin 95, 406-421.

Keefer, D.F. 1999. Earthquake-induced landslides and their effects on alluvial fans. Journal of Sedimentary Research, 69, 84-104.

Koç-Taşgın, C. 2011. Seismically-generated hydroplastic deformation structures in the Late Miocene lacustrine deposits of the Malatya Basin, eastern Turkey. Sedimentary Geology, 235, 264-276.

Koç-Taşgın, C., Türkmen, I. 2009. Analysis of soft-sediment deformation structures in Neogene fluvio-lacustrine deposits of Çaybağı Formation. Eastern Turkey. Sedimentary. Geology. 218, 16–30.

Koç-Taşgın, C., Orhan, H., Türkmen, İ., Aksoy, E. 2011. Soft-sediment deformation structures in the late Miocene Şelmo Formation around Adıyaman area, Southeastern Turkey. Sedimentary Geology, 235, 3-4, 277-291.

Koç-Taşgın, C., Türkmen, İ. 2014.Bigadiç (Balıkesir) Yöresi Neojen Çökellerinin Sedimantolojik Özellikleri. TÜBİTAK 112Y237 Nolu proje. 94s.

Koçyiğit, A., Yusufoğlu, H., Bozkurt, E. 1999. Evidence from the Gediz graben for episodic two-stage extension in western Turkey. Journal of the Geological Society 156, 605-616.

Kuenen, P.H. 1958. Experiments in geology. Transactions. Geological Society of Glasgow 23, 1–28.

Lowe, D.R. 1975. Water escape structures in coarse grained sediments. Sedimentology, 22, 157-204.

Maltman, A. 1994*a*. The geological deformation of sediments. Chapman & Hall, London (362 pp.).

Maltman, A. 1994*b*. Introduction and overview. In: Maltman, A. (Ed.), The Geological Deformation of Sediments. Chapman & Hall, London, 1–35.

Martel, A.T., Gibling, M.R. 1993. Clastic dykes of the Devono-Carboniferous Horton Bluff Formation, Nova Scotia: storm-related structures in shallow lakes. Sedimentary Geology 87, 103–119.

Martinsen, O.J. 1994. Mass movements. In: Maltman, A., (Ed.,), The geological Deformation of Sediments. Chapman and Hall, London, pp. 127-165.

Mastalerz, K., Wojewoda, J. 1993. Alluvial fan sedimentation along an active strike-slip fault: Plio-Pleistocene Pre-Kaczawa fan, SW Poland. Int. Assoc. Sedimentary Geology 196, 5-30.

Mastrogiacomo, G., Moretti, M., Owen G., Spalluto. 2012. Tectonic triggering of slump sheets in the Upper Cretaceous carbonate succession of the Porto Selvaggio area (Salento Peninsula, southern Italy): Synsedimentary tectonics in the APULİAN Carbonate Platform. Sedimentary Geology, 269-270, 15-27.

Mazumder, R., Tom van Loon, A.J., Malviya, V., Arima, M., Ogawa, Y. 2016. Soft-sediment deformation structures in the Mio-Pliocene Misaki Formation within alternating deep-sea clays and volcanic ashes (Miura Peninsula, Japan). Sedimentary Geology 344, 323-335.

McLaughlin, P.I., Brett, C.E. 2004. Eustatic and tectonic control on the distribution of marine seismites: examples from the Upper Ordovician of Kentucky, USA. Sedimentary Geology 168, 165–192.

Mills, P.C. 1983. Genesis and diagnostic value of soft-sediment deformation structures — a review. Sedimentary Geology 35, 83–104.

Molina, J.M., Alfaro, P., Moretti, M., Soria, J.M. 1998. Soft-sediment deformation structures induced by cyclic stress of storm waves in tempestites (Miocene, Guadalquivir Basin, Spain). Terra Nova 10, 145–150.

Montenant, C., Barrier, P., d'Estevou, P.O., Hibsch, C. 2007. Seismites: an attempt at critical analysis and classification. Sedimentary Geology 196, 5-30.

Moretti, M. 1996. Le strutture sedimentarie deformative. Studio dellemodalita di deformazone e dell'origine attreverso esempifossili e modellizazione in laboratorio. PhD Universita degli Studi di Bari, Itally. 232 p.

Moretti, M., Sabato, L. 2007. Recognition of trigger mechanisms for soft-sediment deformation in the Pleistocene lacustrine deposits of the Sant 'Arcangelo Basin (Southern Italy): seismic shock vs. overloading. Sedimentary Geology 196, 31–45.

Moretti, M., Alfaro, P., Caselles, O., Canas, J.A. 1999. Modeling seismites with a digital shaking table. Tectonophysics 304, 369–383.

Moretti, M., Soria, J.M., Alfaro, P., Walsh, N. 2001. Asymmetrical soft-sediment deformation structures triggered by rapid sedimentation in turbiditic deposits (Late Miocene, Guadix basin, Southern Spain). Facies 44, pp.283–294.

Nichols, G. 2009. Sedimentology and Stratigraphy, Wilet-Blackwell, 419p.

Nichols, R.J., Sparks, R.S.J., Wilson, C.J.N. 1994. Experimental studies of the fluidization of layered sediments and the formation of fluid escape structures. Sedimentology 41, 233–253.

Obermeier, S.F. 1996. Use of liquefaction-induced features for paleoseismic analysis— an overview of how liquefaction features can be distinguished from other features and how their distribution and properties of source sediment can be used to infer the location and strength of Holocene paleo-earthquakes. Engineering Geology 44, 1–76.

Obermeier, S.F., Martin, J.R., Frankel, A.D., Youd, T.L., Munson, P.J., Munson, C.A., Pond, E.C. 1993. Liquefaction evidence for one or more strong Holocene earthquakes in the Wabash Valley of southern Indiana and Illinois, with a preliminary estimate of magnitude. U.S. Geol. Surv. Prof. Pap. 1536, 27p.

Okay, A.I., Satır, M. 2000. Coeval plutonism and magmatism in a latest Oligocene metamorphic core complex in Northwest Turkey. Geological Magazine 137 (5), 495–516.

Okay, A.Ü., Satır, M., Sıyako, M., Monie, P., Metzger, R., Akyüz, S. 1996. Paleo- and Neo-Tethyan events in northwestern Turkey: geologic and geochronologic constraints. In: Yin, A. and Harrison, T.M. (eds), The Tectonic Evolution of Asia, pp.420-441.

Okay, A.Ü., Tansel, Ü., Tüysüz, O. 2001. Obduction, subduction and collision as reflected in the Upper Cretaceous-Lower Eocene sedimentary record of western Turkey. Geological Magazine 138, 117-142.

Onorato, M.R., Perucca, L., Coronato, A., Rabassa, J., López, R. 2016. Seismically-induced soft-sediment deformation structures associated with the Magallanes-Fagnano Fault System (Isla Grande de Tierra del Fuego, Argentina). Sedimentary Geology, 344, 135-144.

Owen, G. 1987. Deformation processes in unconsolidated sands. In: Jones, M.E., Preston, R.M.F. (Eds.), Deformation of Sediments and Sedimentary Rocks, Geol. Soc. (London) Spec. Pub No. 29, 11–24.

Owen, G. 1995. Soft-sediments deformation in Upper Proterozoic Torridonian Sandstones (Applecross Formation) at Torridon. Northwest Scotland. J. Sedimentary Research A65, 495-504.

Owen, G. 1996. Experimental soft-sediment deformation structures formed by the liquefaction of unconsolidated sands and some ancient examples, Sedimentology 43, 279-293.

Owen, G., Moretti, M. 2008. Determining the origin of soft-sediment deformation structures: a case study from Upper Carboniferous delta deposits in south-west Wales, UK. Terra Nova 20, 237–245.

Owen, G., Moretti, M. 2011. Identifying triggers for liquefaction-induced soft-sediment deformation in sands. Sedimentary Geology 235, 141-147.

Owen, G., Moretti, M., Alfaro, P. 2011. Recognizing triggers for soft-sediment deformation: current understanding and future direction. Sedimentary Geology 235, 133-140.

Perucca, L.P., Godoy, E., Pantano, A. 2014. Late Pleistocene-Holocene earthquake-induced slumps and soft-sediment deformation structures in the Acequion River valley, Central Precordillera, Argentina, Geologos 20, 2.

Parize, O., Fries, G. 2003. The Vocontian clastic dykes and sills: a geometric model. In: Van Rensebergen, P., Hillis, R.R., Maltman, A.J., Morley, C.K. (Eds.), Subsurface Sediment Mobilization, Geol. Soc. Spec. Publ., vol. 216. Geological Society of London, London, 51–71.

Postma, G. 1983. Water escape structures in the context of a mass-flow dominated conglomeratic fan-delta (Abrioja Formation, Pliocene, Almeria Basin, SE Spain), Sedimentology 30, 91–103.

Pratt, B.R. 1998. Molar-tooth structure in Proterozoic carbonate rocks: origin from synsedimentary earthquakes, and implications for the nature and evolution of basins and marine sediment. Geological Society America Bulletin 110, 1028–1045.

Pratt, B.R. 2002. Tepees in peritidal carbonates: origin via earthquake induced deformation, with example from the Middle Cambrian of western Canada. Sedimentary Geology 153, 57–64.

Rodríguez-Pascua, M.A., Calvo, J.P., De Vicente, G., Gómez-Gras, D. 2000. Soft-sediment Deformation Structures Interpreted as Seismites in Lacustrine Sediments of the Prebetic Zone, SE Spain, and Their Potential use as Indicators of Earthquake Magnitudes During the Late Miocene, Sedimentary Geology 135, 117-135.

Rossetti, D.F. 1999. Soft-sediment deformation structures in late Albian to Cenomanian deposits, Sao Luis Basin, northern Brazil: evidence for palaeoseimicity. Sedimentology 46, 1065-1081.

Rossetti, D.F., Goes, A.M. 2000. Deciphering the sedimentological imprint of paleoseismic events: an example from the Aptian Codó Formation, northern Brazil. Sedimentary Geology 135, 137-156.

Rossetti, D.F., Santos Jr., A.E. 2003. Events of sediment deformation and mass failure in Upper Cretaceous estuarine deposits (Cametá Basin, northern Brazil) as evidence for seismic activity. Sedimentary Geology 161,107–130.

Rossetti, D.F., Goes, A.M., Truckenbrodt, W., Anaisse, J. 2000. Tsunami-induced large-scale scour-and-fill structures in Late Albian to Cenomanian deposits of the Grajau Basin, Northen Brazil. Sedimentology 47, 309-323.

Samaila, N.K., Abubakar, M.B., Dike, E.F.C., Obaje, N.G. 2006. Description of soft-sediment deformation structures in the Cretaceous Bima Sandstone from the Yola Arm, Upper Benue Trough, Northeastern Nigeria. African Earth Sciences 44, 66-74.

Savaşçın, M. Y., Güleç, N. 1990. Relationship between magmatic and tectonic activities in western Turkey. M.Y. Savaşçın ve A.H. Eronat (Eds), International Earth Science Colloquum on the Aegean Region (IESCA) Proceedings, pp.300-313.

Scott, B., Price, S. 1988. Earthquake-induced structures in young sediments. Tectonophysics 147, 165–170.

Seguret, M., Moussine-Pouchkine, A., Gabaglia, G.R., Bouchette, F. 2001. Storm deposits and storm-generated coarse carbonate breccias on a pelagic outer shelf (South-East Basin, France). Sedimentology 48, 231-254.

Seilacher, A. 1969. Fault-graded beds interpreted as seismites. Sedimentology 13, 155–159.

Seyitoğlu, G. 1997. Late Cenozoic tectono-sedimentary development of the Selendi and Usak- Gure basins: a contribution to the discussion on the development of east-west and North trending basins in western Turkey. Geological Magazine 134, 163-175.

Seyitoğlu, G., Scott, B. 1994. Late Cenozoic basin development in west Turkey: Gordes basin tectonics and sedimentation. Geological Magazine 131, 631-637.

Shepard, P.H. 1955. Delta-front valleys bordering the Mississippi distributaries. Geological Society America Bulletin 66, 1489-1498.

Shanmugam, G. 2017. Global case studies of soft-sediment deformation structures (SSDS): Definitions, classifications, advances, origins, and problems. Journal of Palaeogeorapghy 6(4), 251-320.

Siegenthaler, C., Finger, W., Kelts, K., Wang, S. 1987. Earthquake and seiche deposits in Lake Lucerne, Switzerland. Eclogae Geologicae Helvetiae 80, 241–260.

Sims, J.D. 1973. Earthquake-induced structures in sediments in Van Norman Lake, San Fernando, California. Science 182, 161–163.

Sims, J.D. 1975. Determining earthquake recurrence intervals from deformational structures in young lacustrine sediments, Tectonophysics 29, 141-152.

Sözbilir, H. 2007. Menderes Masifi'nin yüzeylemesini belgeleyen Tersiyer yaşlı sedimenter havzaların oluşum mekanizması, yaşı ve çökel istifleri. Menderes Masifi Kollokyumu, Ankara.

Spalluto, L., Moretti, M., Festa, V., Tropeano, M. 2007. Seismically-induced slumps in Lower-Maastrichtian peritidal carbonates of the Apulian Platform (southern Italy). Sedimentary Geology 196, 81-98.

Tanner L.H. 2002. Borate formation in a perennial lacustrine setting: Miocene-Pliocene Furnace Creek Formation, Death Valley, California, USA, Sedimentary Geology 148, 1-2, 259-274.

Tian, H.S., Zhang, B.H., Zhang, S.H., Lü, M.Y. 2014. Neogene seismites and seismic volcanic rocks in the Linqu area, Shandong Province, E China. Geologos 20(2), 125-137.

Van Loon, A.J., Brodzikowski, K. 1987. Problems and progress in the research on soft-sediment deformations, Sedimentary Geology 50, 167-193.

Vanneste, K., Meghraoui, M., Camelbeek, T. 1999. Late Quaternary earthquake-related soft-sediment deformation along the Belgian portion of the Feldbiss Fault, Lower Rhine Graben system, Tectonophysics 309, 57-79.

Weaver, J.D., Jeffcoat, R.E. 1978. Carbonate ball and pillow structures. Geological Magazine 115, .245–253.

Westaway, R. 2006. Cenozoic cooling histories in the Menderes Massif western Turkey, may be caused by erosion and flat subduction, not low-angle normal faulting. Tectonophysics 412, 1-2, 1-25.

Yılmaz, O., Gündoğdu, M., Gümüş, S. 1982. Neojen Yaşlı Bigadiç Volkanosedimanter Havzasının Jeolojisi, Etibank Proj. 82p. (unpublished).

Yılmaz, Y., Genç, S.C., Gürer, F., Bozcu, M., Yılmaz, K., Karacık, Z., Altunkaynak, Ş., Elmas, A. 2000. When did the western Anatolian grabens begin to develop? E. Bozkurt, J.A. Winchester and J.D.A. Piper (Ed.), Tectonics and Magmatism in Turkey and the Surrounding Area. Geological Society, London, Special Publications, 353-384.

Yılmaz, Y., Genç, S.C., Karacık, Z., Altunkaynak, I. 2001. Two contrasting magmatic associations of NW Anatolia and their tectonic significance. Journal of Geodynamics 31, 243-271.

Zhou,Y.Q., Peng, T. M.,Zhou, T.F., Zhang, Z.K., Tian, H., Liang, W.D., Yu, T., Sun, L.F. 2017. Soft-sediment deformation structures related to volcanic earthquakes of the Lower Cretaceous Qingshan Group in Lingshan Island, Shandong Province, East China. Journal of Palaeogeography (in print).

Bulletin of the Mineral Research and Exploration

http://bulletin.mta.gov.tr

The effect of submarine thermal springs of Doğanbey Cape (Seferihisar - İzmir) on foraminifer, ostracod and mollusc assemblages

Engin MERİÇ[a], İpek F. BARUT[b], Atike NAZİK[c], Niyazi AVŞAR[d], M. Baki YOKEŞ[e], Mustafa ERYILMAZ[f], Fulya YÜCESOY-ERYILMAZ[g], Erol KAM[h], Bora SONUVAR[i] and Feyza DİNÇER[j]

[a]*Moda Hüseyin Bey Sokak No: 15/4, 34710, Kadıköy, İstanbul. orcid.org/0000-0002-5975-3678*
[b]*İstanbul University, Institute of Marine Sciences and Management, 34134, Vefa, İstanbul. orcid 0000-0002-4255-0268*
[c]*Çukurova University, Fac. of Eng. and Arch., Dept. of Geol. Eng., 01330, Balcalı, Adana. orcid.org/0000-0001-7996-7430*
[d]*Çukurova University, Fac. of Eng. and Arch., Dept. of Geol. Eng., 01330, Balcalı, Adana*
[e]*Hanımefenedi Sokak No: 160/9, 34384, Şişli, İstanbul. orcid.org/0000-0002-9440-4561*
[f]*Mersin University, Fac. of Eng., Dept. of Geol. Eng., 33343, Çiftlikköy, Mersin. orcid 0000-0002-3342-768x*
[g]*Mersin University, Fac. of Eng., Dept. of Geol. Eng., 33343, Çiftlikköy, Mersin. orcid 0000-0003-3714-6903*
[h]*Yıldız Technical University, Fac. of Sci. and Letters, Dept. of Physics, 34220 Esenler, İstanbul. orcid.org/0000-0001-5850-5464*
[i]*Tramola International Applied Marine Research, 35250, Konak, İzmir. orcid.org/0000-0001-9894-3709*
[j]*Nevşehir University, Fac. of Eng. and Arch., Dept. of Geol. Eng. 50300, Nevşehir. orcid.org/0000-0001-6105-4369*

Research Article

Keywords:
Doğanbey Cape (İzmir), submarine hot water springs, benthic foraminifers, molluscs, ostracods.

ABSTRACT

The aim of this study was to figure out the effects of the submarine hot water springs located on the coast of Doğanbey Cape (north of Kuşadası Bay) on various micro- and macrofaunal assemblages living around these springs. Young sediment samples were collected from different depths at 15 stations. The benthic foraminifer, ostracod and mollusc faunas were investigated. 35 genera and 61 species of benthic foraminifers, 16 genera and 20 species of ostracods and 14 genera and 15 species of molluscs were identified. Typical Aeegan foraminifer fauna was found to be dominant. Besides, individuals with colored tests or abnormal morphology, as well as alien species, which are frequently observed on the Aegean coasts were also observed in the study area. The foraminifer, ostracod and mollusc species also constituted typical Aegean fauna. It is known that the ecological conditions experienced of the Amphistegina lobifera Larsen individuals in typical Aegean benthic foraminifer assemblage have an effect on the abundance distribution. Ideal conditions for Amphistegina lobifera Larsen was found to be 18.00-32.00 m depth range and 19-20°C temperatures. CTD conductivity values gradually increased near to the hot water spring but a decrease in the number of individuals were observed. Chemical analyzes in sediment samples were performed with X-Ray Fluorescence Analysis Spectrometer (WDXRF). Heavy metal ingredients (Cr, Mn, Co, Ni, Cu, Zn and Pb) of the sediments were evaluated, concentrations were recorded as Cr>Ni>Mn in samples DB1-DB6 and also in DB15; Mn>Cr>Ni in DB8-DB11 and DB13-DB14; Cr>Mn>Ni in DB7 and in DB12. The radioactive elements U and Th were found to be high in DB9, DB10 and DB11. The chemical and radioactive properties of the sediments were observed to affect the tests of benthic foraminifers, where as no such effect was found on ostracod and mollusc tests.

Received Date: 30.03.2017
Accepted Date: 28.09.2017

1. Introduction

This study was carried out to investigate the effects of submarine hot springs, which are located on the southern coasts of the Doğanbey Cape (the northern end of Kuşadası Bay), on the benthic foraminifer, ostracod and mollusc fauna living around them (Figures 1, 2 and 3). Both quantitative and qualitative variations of the bottom sediments were evaluated under physical, chemical and radioactive conditions where micro and macro fauna assemblages are present in this area.

* *Corresponding author: İpek F. BARUT, barutif@istanbul.edu.tr*
http://dx.doi.org/10.19111/bulletinofmre.363329

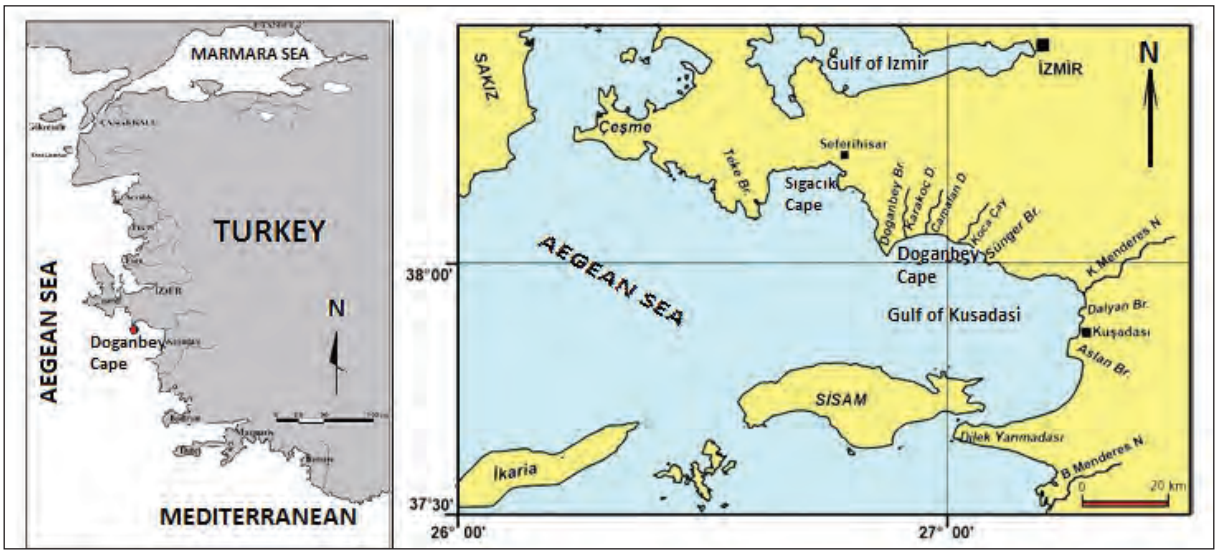

Figure 1- Location map of the investigation area.

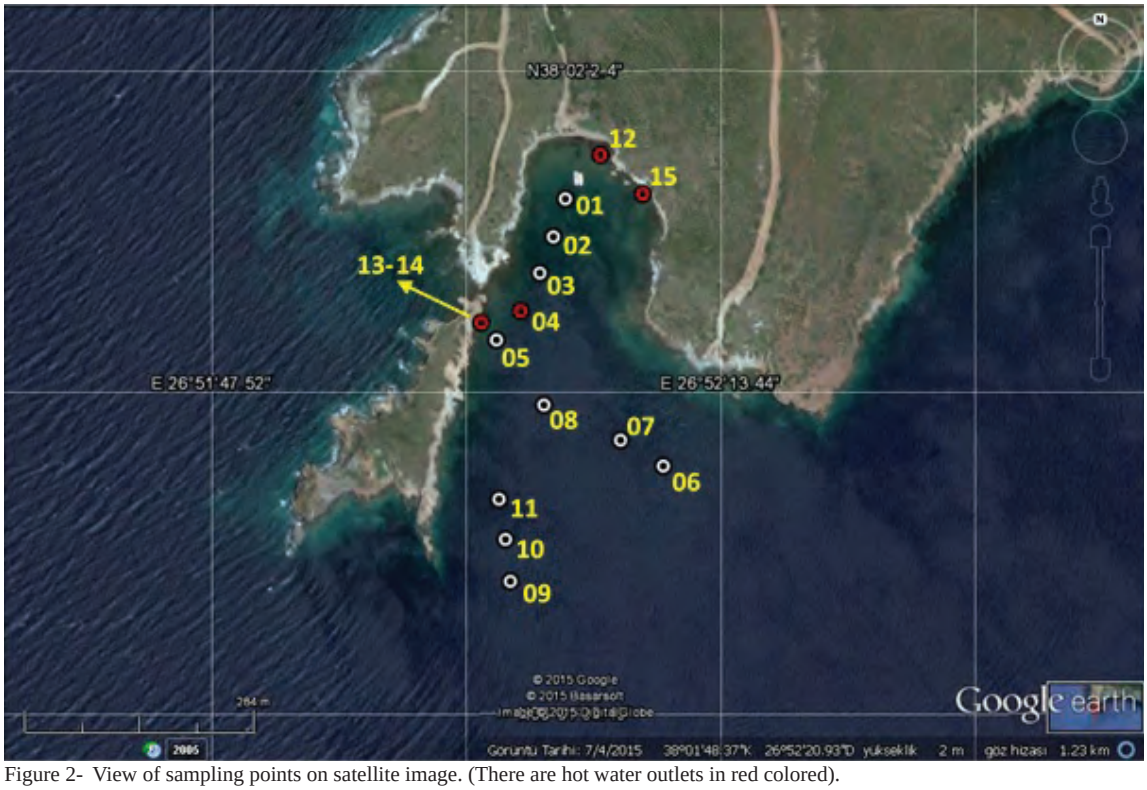

Figure 2- View of sampling points on satellite image. (There are hot water outlets in red colored).

The water depth at which samples were collected, varies between 0.20-31.80 meters, bottom water temperatures vary between 19.95-23.32°C and the bottom salinity values vary between 38.99-39.24‰ (Table 1). The micro and macro fauna biodiversity, which is the topic of research, has the faunal characteristics of the Eastern Aegean Sea. Although the life in the region is quite poor in shallow areas, it is rich in medium to deep regions. The micro and macro faunas observed are similar with the ones observed at the other studies carried out on the Aegean coasts (Avşar and Meriç, 2001; Meriç and Avşar, 2001; Meriç et al., 2002*a, b*, 2003*a, b*, 2004, 2009*a, b, c*, 2010, 2011, 2012*a, b*, 2014; Avşar et al., 2009; Öztürk et al., 2014).

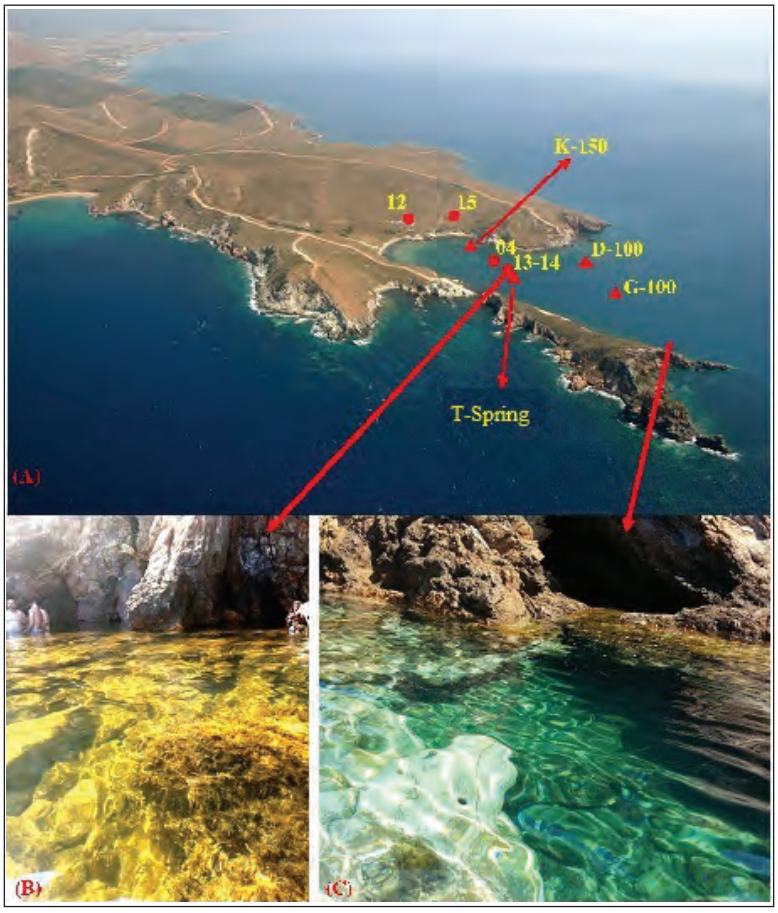

Figure 3- A- Hot water points (circle) and water sample reception stations (triangle) on the aerial photo of Doğanbey Burnu; B- Coastal area with hot water outlet; C- Coastal area without hot water outlet. (Aerial photograph: http://erkmensenan.blogspot.com.tr/2010/07/lebedos-urkmez.html).

Table 1- Coordinates, depth, temperature, salinity and conductivity values of bottom water at sampling points. (* Temperature, salinity and conductivity measurements were made with RBR XR-620 CTD)

Sample ID	Coordinates (WGS 84)		Depth (m)	Temperature* (°C)	Salinity* (‰)	EC* (mS/cm)
	North	East				
01	38° 1'57.29"	26°52'5.58"	3.70	22.949	39.224	56.359
02	38° 1'55.76"	26°52'4.97"	5.50	22.877	39.233	56.290
03	38° 1'54.30"	26°52'4.28"	7.00	22.647	39.231	56.026
04	38° 1'52.77"	26°52'3.30"	5.50	22.673	39.205	56.022
05	38° 1'51.60"	26°52'2.07"	7.50	22.834	39.199	56.199
06	38° 1'46.52"	26°52'10.57	15.85	19.950	39.235	52.987
07	38° 1'47.56"	26°52'8.39"	18.00	20.260	39.226	53.326
08	38° 1'48.98"	26°52'4.49"	19.00	19.887	39.205	52.881
09	38° 1'41.87"	26°52'2.78"	31.80	18.984	39.208	51.884
10	38° 1'43.56"	26°52'2.53"	27.70	19.830	39.177	52.789
11	38° 1'45.18"	26°52'2.20"	21.20	20.187	39.243	53.265
12	38° 1'59.06"	26°52'7.36"	1.00	---	---	---
13	38° 1'52.30"	26°52'1.30"	0.30	---	---	---
14	38° 1'52.30"	26°52'1.30"	0.30	23.323	38.990	56.486
15	38° 1'57.49"	26°52'9.52"	0.20	---	---	---

2. The Oceanography and Recent Sediment Distribution of the Northern Marine Area of the Kuşadası Bay

In previous studies, which bays the marine area located between the Küçük Menderes River and Sığacık Bay, the depth and recent sediment distribution maps have been prepared (Eryılmaz et al., 1998, Eryılmaz and Aydın, 2001; Eryılmaz and Yücesoy-Eryılmaz, 2001, 2014; Eryılmaz et al., 2014) (Figure 1). According to these studies the maximum depth in Doğanbey Bay is approximately 75 m (Figures 4 and 5). The most significant rivers of the Doğanbey Bay are Karakoç, Çamalan and Koca streams (Figure 1). Küçük Menderes River, which flows into the Kuşadası Bay at a distance of 30 km, is the most important river in the region. Only the Küçük Menderes River continues to flow due to less precipitation during summer.

According to the studies mentioned above, the region is under the effect of the Mediterranean climate. The average annual precipitation amount is 659.5 mm. The prevailing wind directions at the region are north and northwest, and the annual average wind velocity is in 5 knots (9.3 km/h). The study area is a light windy region (Meteoroloji Bülteni, 1984; Eryılmaz et al., 1998; Eryılmaz and Aydın, 2001; Eryılmaz and Yücesoy-Eryılmaz, 2001, 2014; Eryılmaz et al., 2014). According to Erol (1991, 1997), Eryılmaz (1996), Eryılmaz et al. (1998), big and small faults striking perpendicular to the coast were observed along the rocky shoreline with cliffs in the Sığacık Bay between the Teke Cape and Seferihisar. Beaches are well developed in the Doğanbey Bay and a 3 km wide delta is found on the mouth of Koca stream. These marine areas have been filled by terrigenous sediments, which were transported by rivers, and formed recent lowlands.

According to previous studies, the sea bottom topography located between the Sığacık Bay and Doğanbey Cape deepens with a slope of 2-6% towards the open sea. At 600-800 m away from the coast, the sea reaches a depth of 20 m. The bathymetrical depth contours run parallel to the coast as; -10, -20, -50 and -100 m. These contours get much closer to each other in Doğanbey and Sünger Capes and depths suddenly increase in these areas. The average slope in this region is 4% and the sea bottom has a quite flat like appearance (Figures 4 and 5) (Eryılmaz, 1996, 2003; Eryılmaz et al., 1998; Eryılmaz and Yücesoy-Eryılmaz, 2001, 2014).

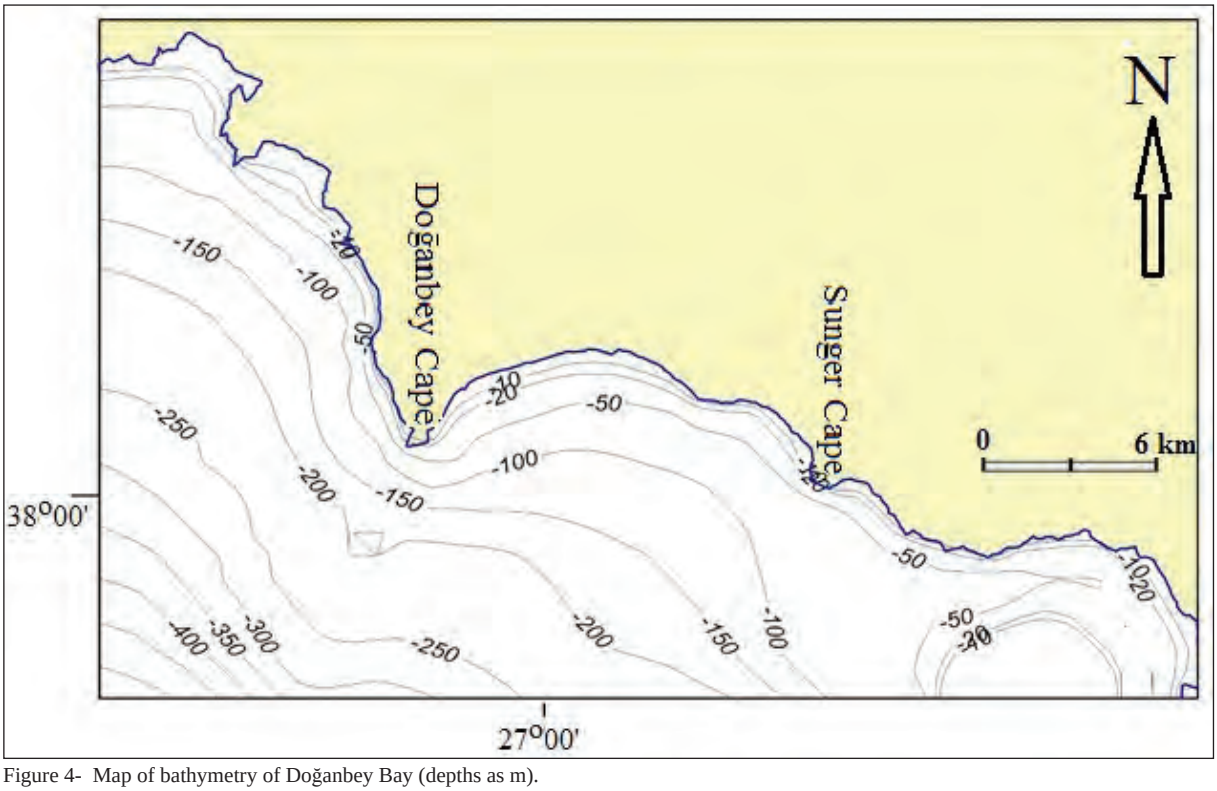

Figure 4- Map of bathymetry of Doğanbey Bay (depths as m).

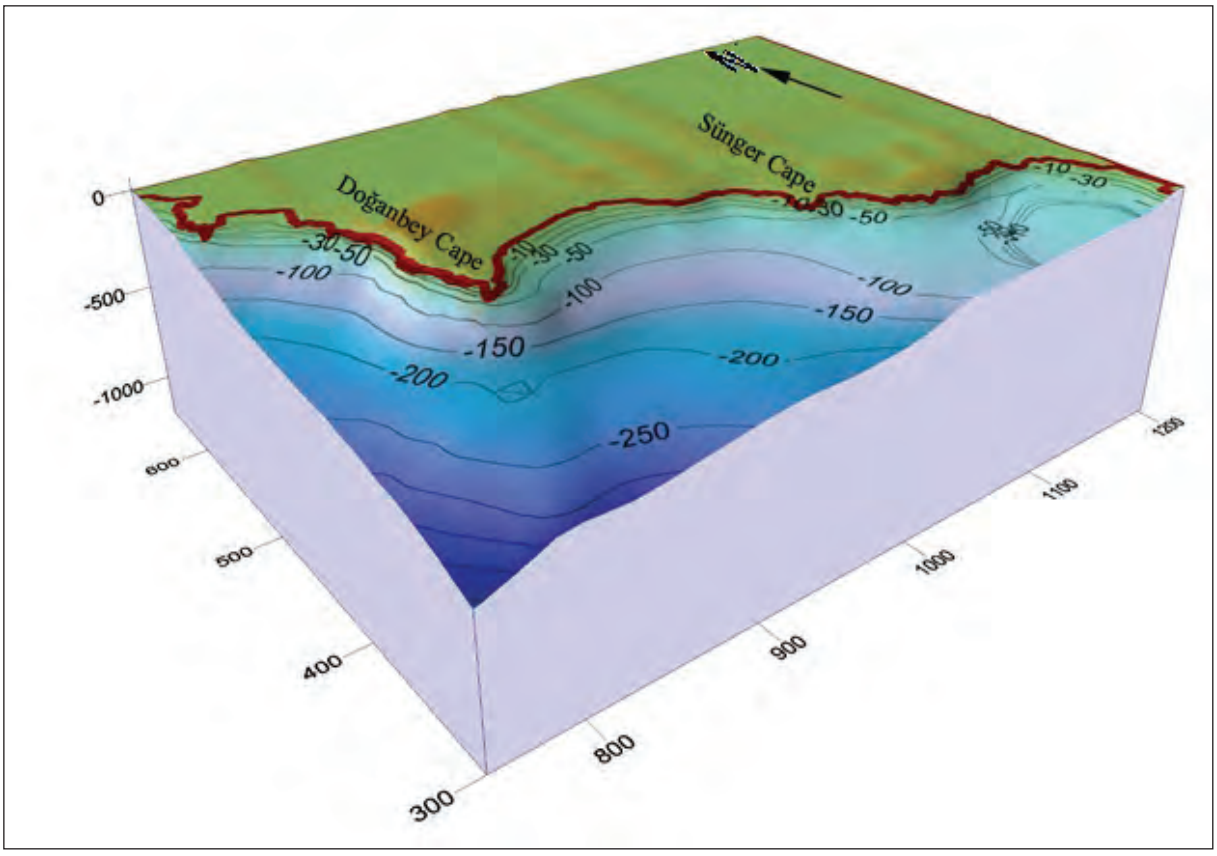

Figure 5- The 3D bathymetry and morphological appearance of Doğanbey Bay (depths as m).

In the study of Eryılmaz and Aydın (2001), the total of 48 recent sediment samples were collected from the sea bottom of the Doğanbey Bay in order to determine the characteristics of bottom sediments. In the study area, the temperature and salinity values were measured seasonally in standard stations using the CTD instrument in the water column ranging from surface to the sea bottom and then these areas were mapped. Besides; the short term seasonal flow measurements were taken at the surface, at 20 m depth and at the sea bottom in one station. Sieve and wet analysis methods were applied to recent sediment samples, which were taken from the surface of the sea bottom, and the results were classified in ternary diagrams (Folk, 1974). Sediments were classified according to the grain size and the results were assessed using bathymetry map. Thus, the sediment distribution map of the region in scale of 1:30.000 was prepared.

According to the studies of Eryılmaz and Eryılmaz-Yücesoy (2001, 2014), the variations of seasonal minimum, average and maximum temperatures with respect to depth in the Doğanbey Bay are as follows; 16.99-17.00°C at the surface, 15.70-16.27°C at -50 m in the spring; 17.80-25.55°C at the surface, 16.77-17.26°C at -50 m in the summer; 21.26-22.27°C at the surface, 17.52-19.88°C at -50 m in the fall, and 14.90-15.20°C at the surface, 14.93-15.20°C at -50 m in the winter (Figure 6a).

The variation of the seasonal minimum, average and maximum salinity values with respect to depth in the region were measured as ‰38.98 at the surface; ‰39.03 at the depth of 150 m in the spring, ‰39.26 at the surface, ‰39.16 at the depth of 150 m in the summer, ‰38.66 at the surface; ‰38.30 at the depth of 150 m in the fall and ‰38.42 at the surface; ‰38.43 at the depth of 150 m in the winter (Figure 6b) (Eryılmaz and Yücesoy-Eryılmaz, 2001, 2014; Meriç et al., 2009*b*, 2010; Yokeş et al., 2014).

Within the scope of studies of Eryılmaz and Eryılmaz-Yücesoy (2001, 2014), the short term seasonal flow measurements were taken in two stations of DK-01 (-21 m) and DK02 (-36 m) (Figures 7 and 8). It not possible to mention about a general flow system in the region with the flow data obtained.

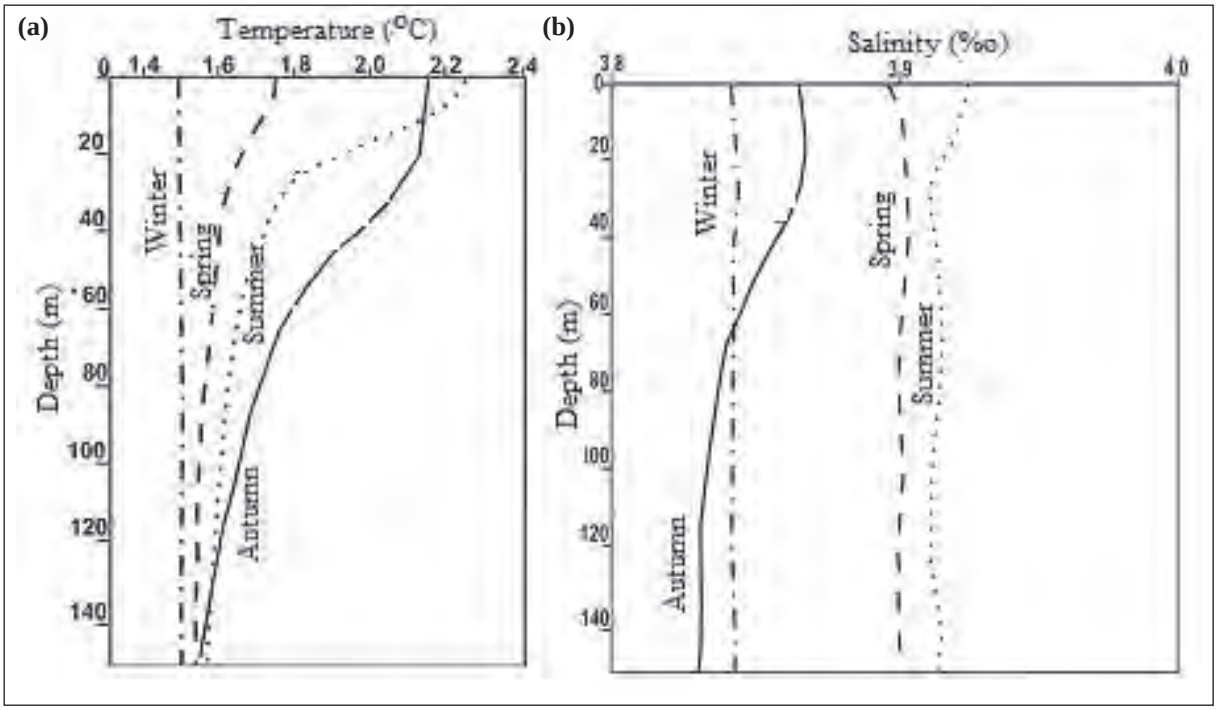

Figure 6- The seasonal average temperature (a) and seasonal average salinity values (b) at Doğanbey Bay.

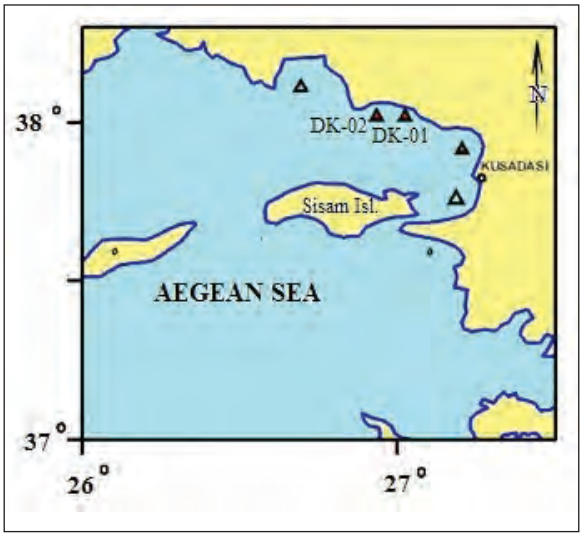

Figure 7- Map of the stations measuring the seasonal discharge at Doğanbey Bay.

In the winter the general flow system returns from west to east and moves very slowly. This mass movement changes direction in northern coasts of the Kuşadası Bay and turns into coastal flows. These flow types are also observed in the Sığacık and Doğanbey bays. Sometimes by the effect of southern winds which blow continuously and strongly, the surface and counter clockwise flows develop. The increase of salinity at the surface layer in the summer and density differences that occur due to the temperature differences between the sea surface and bottom cause local flows in marine areas closer to the coast. Besides; the Etesian winds that blow in the region from west to east in the afternoon cause local flows along the coasts (Figure 8).

Within the scope of studies of Eryılmaz and Aydın (2001) and Eryılmaz and Yücesoy-Eryılmaz (2014), the coastal and bottom sediments were formed from coarse to fine grained sediments which had been carried by the local flows and waves along rivers into the sea. The materials, which were detached by waves from the coast and transported from the land, become smaller by being subjected to re-erosion under the effect of waves and flows in the sea. It is also observed that the sediment grain size becomes smaller from coast to offshore in the region (Figure 9). The sediment distribution in the Doğanbey Bay is mostly lithogenic originally and generally the low cohesive silty material is dominant. While the coarse grained and clastic cohesionless material takes place in the high energy coasts, the cohesive material accumulates in deep regions away from the coast.

According to the studies of Eryılmaz and Aydın (2001), Eryılmaz and Yücesoy-Eryılmaz (2014), the sediments located in the study area are formed from 6

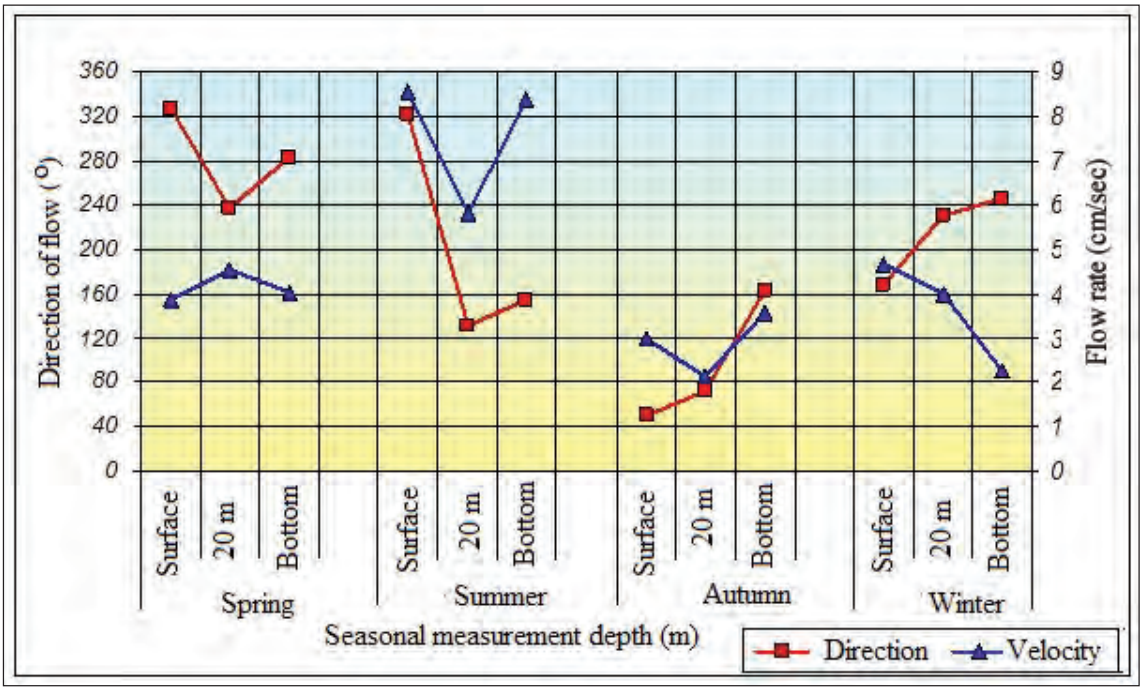

Figure 8- The seasonal flow velocity and direction at Doğanbey Bay.

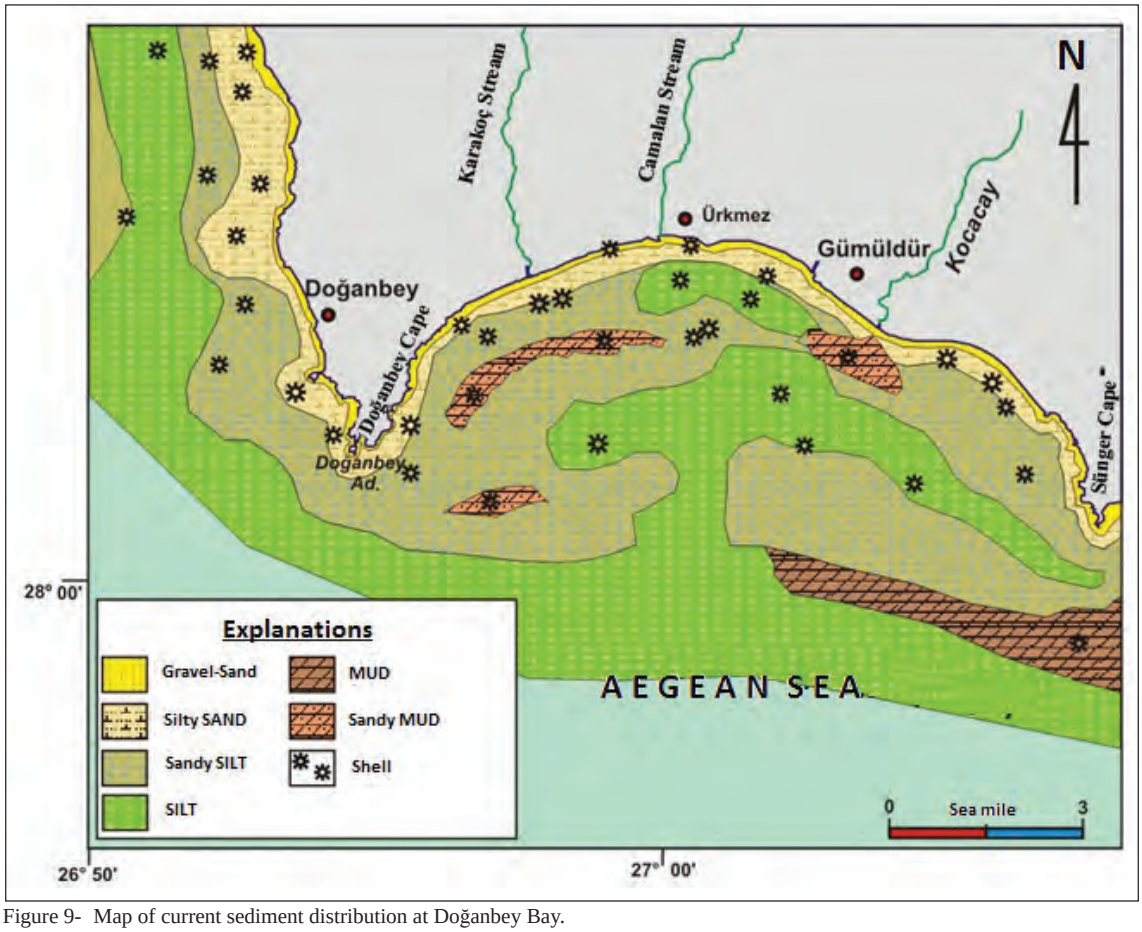

Figure 9- Map of current sediment distribution at Doğanbey Bay.

types of material as rock, pebble, sand, silt and mud. Sandy materials are made up of pebbly sand, sand and silty sand. The sand unit continues to the depth of 7 m. Silty sand is observed until the depth of 20 m respectively. Between the depths of 20-50 meters, the lensoidal sandy mud is located between sandy silt and silt. Sandy silt continues to the depth of 100 meters. However; the silty material reaches down to 200 meters. Moreover; the muddy sediments are observed at a narrow region between the depths of 100-150 meters. All these sediments in the region are observed in the form of parallel bands compatible with the shape of the coastline. The grain size distribution generally changes from coarse to fine from coast to the sea bottom in this region and form bands which make transitions to each other as being parallel to the thin coastal line (Figure 9). A delta was formed in the mouth of Kocaçay River which flows into the Doğanbey Bay and thin sand has been deposited on the shore of delta. The Küçük Menderes River, which flows along the gently inclined riverbed for long distances, only transports silt and clay sized terrigenous material into the sea. It has been determined that these materials had been transported down to the bottom of the open sea in times of river floods.

3. Material and Method

The recent sediment samples were collected by 11 liter ground sampler digger from 15 points at different depths in southeast of the Doğanbey Cape, in 16th of August, 2015 and examined in order to evaluate in terms of foraminiferal, ostracod and mollusc assemblages. Besides; the physical properties of the sea water (temperature and salinity) were synchronously measured by RBR XR-620 CTD instrument at each ground sample station. The foraminifer and ostracod analyses in sediment samples were performed according to Babin (1980) and Bignot (1985). 10% H_2O_2 was added on to the dry samples weighed 10 gr and left for 24 hours. Thereafter; samples were washed on 0.063 mm sized sieve by pressurized water, dried on 50°C oven then sieved on 2, 1, 0.5, 0.25, 0.125 mm sized sieves. These samples were then examined under binocular microscope and foraminifer, ostracod and molluscs were separated from the content.

The measurements of chemical elements (in ppm and ppb) in sediment samples were performed at the Çekmece Nuclear Research and Training Center (ÇNAEM) using a Wavelength Dispersive X-Ray Fluorescence (WDXRF) Spectrometer. The quantitative and qualitative analyses of the elements between Boron (B) and Uranium (U) were carried out by using the X0 ray tube, crystals in different types (LiF220, PX10, GeIII-C, PE 202-C), two sensors, collimators in variable sizes and specifications and relevant software. TDS is the total dissolved solid amount in one liter (mg/L).

During the preparation of sediment samples for counting, the material was first crushed in 200 mesh size and dried. The samples, which are kept in the desiccator, were weighed 12 gr, mixed with 3 gr of wax, placed into 40 mm diameter mold and then compressed into pellet form using 35 tons of pressure. Total Alfa SM 7110 C and Total Beta analyses were carried out by the ASTM D 1890-05 method using Berthold Lb 770 Low Level 10 Channel Proportional Counter instrument. By taking 500 ml water from the sample, the Alfa precipitation (250 ml) and EPA 900.0 (250 ml) methods were studied (MDAα: 0.007 Bq/L, MDAβ: 0.008 Bq/L).

Photographing the abnormal advanced foraminifera and the microprobe analyses of colored foraminifer tests were carried out using Philips XL 305 FEG instrument in Material Science and Engineering Department of the Gebze Technical University. The electron microprobe quantitative analyses were concluded by using the computer controlled Jeol-733 electron microprobe device and online ZAFM quantitative analysis program.

4. Findings

4.1. Micro and Macro Fauna

4.1.1. Distribution of Genera and Species of Benthic Foraminifers

The benthic foraminifer assemblage mirror the typical Aegean Sea fauna (Avşar and Meriç, 2001; Meriç and Avşar, 2001; Meriç et al., 2002*a*, *b*; 2003*a*, *b*; 2004; 2009*a*, *b*, *c*; 2010, 2011, 2012*a*, *b*; 2014). In 13 of 15 samples the foraminifer assemblages is different. This property was also encountered in some genera and species observed in the Mediterranean (Table 2).

The situation which is attractive for the study area is having the characteristics of being the 3rd region in which *Amphistegina lobifera* Larsen individuals are abundantly observed around hot springs that are known or considered to exist in the Kuşadası Bay or

Table 2- The distribution of samples benthic foraminifera genus and species.

Foraminifera	1	2	3	4	5	6	7	8	9	10	11	13	14
Lagenammina fusiformis							+	+					
İridia diaphana								+	+				
Spiroplectinella sagittula								+	+				
Eggerelloides advenus											+		
Eggerelloides scabrus				+			+			+			
Textularia bocki							+	+	+	+	+		
Vertebralina striata							+	+	+	+	+		
Nubecularia lucifuga								+	+	+	+		
Adelosina cliarensis								+	+	+			
Adelosina duthiersi								+					
Adelosina mediterranensis								+	+				
Adelosina partschi								+					
Adelosina pulchella								+	+				
Spiroloculina excavata							+		+				
Spiroloculina ornata								+	+	+	+		
Siphonaperta aspera								+		+	+		
Cycloforina contorta								+					
Cycloforina villafranca						+							
Lachlanella undulata								+					
Lachlanella variolata								+					
Massilina secans								+					
Quinqueloculina bidentata							+						
Quinqueloculina disparilis							+	+	+				
Quinqueloculina jugosa									+				
Quinqueloculina laevigata								+					
Quinqueloculina lamarckiana	+					+	+						
Quinqueloculina seminula	+												
Miliolinella labiosa											+		
Pseudotriloculina laevigata								+					
Pseudotriloculina oblonga								+					
Pseudotriloculina rotunda								+	+	+	+		
Pseudotriloculina sidebottomi							+						
Triloculina marioni							+	+	+	+	+		
Sigmoilinita costata		+						+		+	+		
Sigmoilinita edwardsi			+										
Peneroplis pertusus	+						+	+	+				
Peneroplis planatus							+	+	+		+		+
Cyclorbiculina compressa											+		
Sorites orbiculus								+			+		
Eponides concameratus								+	+	+			
Neoeponides bradyi								+	+		+		
Neoconorbina terquemi								+					
Rosalina bradyi						+		+	+	+			
Rosalina floridensis	+							+	+				
Rosalina globularis	+												
Discorbinella bertheloti												+	+
Cibicides advenum	+												
Lobatula lobatula							+	+	+	+	+		
Cyclocibicides vermiculatus								+			+		

Table 2- continued.

Foraminifera	1	2	3	4	5	6	7	8	9	10	11	13	14
Planorbulina mediterranensis							+	+	+	+	+	+	
Cibicidella variabilis								+	+	+	+		
Asterigerinata mamilla						+							
Amphistegina lessonii								+					
Amphistegina lobifera					+	+	+	+	+	+	+		+
Nonion depressulum	+					+							
Ammonia compacta							+	+		+			
Ammonia parkinsoniana	+						+	+	+	+	+		
Ammonia tepida									+				+
Elphidium advenum								+	+	+	+		
Elphidium complanatum							+	+	+				
Elphidium crispum	+						+	+	+	+	+		

in the NW of the Karaburun Peninsula of the Aegean Sea. The excess abundance of foraminifers (more than 25 individuals) in samples 7, 8, 9, 10 and 11 is a remarkable case for the region (Plates 1 and 2) .

4.1.2. Distribution of Genera and Species of Ostracods

The sediment samples are not rich in ostracod genera, species and individuals. Ostracods were described only in 10 examined samples. They are fewer in samples 1, 4, 6, 13, 14, but quite a few in samples 7, 8, 9, 10, 11 as it was observed in the foraminifer assemblage (Table 3).

Total of 16 genera and 20 species were identified in samples of the Doğanbey bottom sediments. For the description of genus and species, Van Morkhoven (1963), Hartmann and Puri (1974), Bonaduce et al. (1975), Breman (1975), Yassini (1979), Guillaume et al. (1985), Athersuch et al. (1989), Zangger and Malz (1989), Mostafawi and Matzke-Karasz (2006), Joachim and Langer (2008) and "MarBEF Data System" (http://www.marbef.org/data/) were heavily used.

4.1.3. Distribution of Genera and Species of Molluscs

Typically the mollusc fauna of the Aegean Sea is dominant in this area as bivalve and gastropod (Öztürk et al., 2014). In 7 of 15 examined samples (4, 6, 7, 8, 9, 10, 11) gastropods and bivalves were observed. Total of 14 genera and 18 species were found in gastropods.

Some differences were observed among samples based on the number of genus and species content.

Table 3- The distribution of samples ostracoda genus and species.

Ostracoda	1	4	6	7	8	9	10	11	13	14
Cytherella alvearium		+				+		+	+	
Neonesidea corpulenta					+	+	+	+		
Neonesidea formosa				+	+	+	+	+		
Triebelina raripila						+				
Aurila convexa						+	+			
Cytheridea neapolitana			+							
Jugosocythereis prava				+	+	+		+		
Urocythereis oblonga					+					
Acantocythereis hystrix				+	+		+	+		
Cytheretta adriatica	+									
Bosquetina carinella					+					
Semicytherura incongruens						+				
Loxoconcha bairdi					+	+	+		+	
Loxoconcha gibberosa				+	+	+	+	+		+
Cytherois sp.				+	+	+	+	+		
Xestoleberis aurantia		+		+	+	+	+			+
Xestoleberis communis				+	+	+	+	+	+	+
Xestoleberis depressa				+	+	+				
Ekpontocypris pirifera							+	+		
Macropyxis adriatica						+	+	+		

In samples 4 and 6; one genus and species, in sample 11; 9 species, in sample 10; 11 species, in sample 9; 13 species, in sample 7; 15 species and as the richest sample point in sample 8; 20 species were identified for bivalves and gastropods (Table 4).

Table 4- The distribution of samples gastropoda with bivalv genus and species.

Gastropoda	**4**	**6**	**7**	**8**	**9**	**10**	**11**
Jujubinus exasperatus				+	+	+	+
Jujubinus striatus				+			
Tricolia pullus			+	+			
Cerithium vulgatum				+			
Bittium latreillii				+	+	+	+
Bittium reticulatum			+	+	+	+	+
Bittium scabrum		+	+	+	+	+	+
Cerithidium submamillatum				+			
Turritella turbona				+	+		
Pusillina inconspicua			+				
Pusillina lineolata				+			+
Pusillina marginata							+
Alvania cimex				+		+	+
Alvania mamillata				+			
Trophonopsis muricatus			+				
Chauvetia mamillata			+				
Raphitoma linearis						+	
Chrysallida sp.				+			
Retusa truncatula				+			
Haminoea sp.			+	+			
Bivalvia							
Nucula hanleyi					+		
Nuculana pella					+		
Striarca lactea				+		+	
Flexopecten glaber glaber					+		
Flexopecten hyalinus			+	+			
Limaria tuberculata			+			+	
Dosinia exoleta				+	+	+	
Myrtea spinifera					+		
Glans trapezia				+	+		
Venericardia antiquata			+				
Parvicardium exiguum			+				
Parvicardium scriptum			+				
Papillocardium papillosum	+		+		+	+	+
Gari sp.							
Gouldia minima			+	+	+	+	+
Hiatella rugosa			+				

4.2. The Evaluation of Geochemical Properties of Sediment Samples

The geochemical properties of the environmental conditions (as like heavy metal, trace element and radioactive element etc.) are effective on the population and numerical values of different species, morphological anomaly or coloring features of meiofauna assemblages observed in the study. Within this scope, it was observed from Cr, Mn, Co, Ni, Cu, Zn and Pb heavy metal distribution of sediment samples that in sediments between D1-D6 and in D15 Cr>Ni>Mn; between D8-D11, in D13 and D14 Mn>Cr>Ni; in D7 and D12 Cr>Mn>Ni (Figure 10) (Table 5). In the distribution of sediments with respect to each other, it was observed that the values of Co, Cu, Zn and Pb are low, whereas the values of Cr, Ni and Mn are high. When the shale values of Krauskopf (1982) were compared with sediment samples, it was observed that Fe was the highest; Cr, Co and Ni were high; and Zn and Cu were observed as the lowest. Also; correlating shale values of Krauskopf (1982), it was detected that Mn value in DB13 and Pb value in DB6, DB8-DB11 intervals were highest.

In the distribution of sediments with respect to each other, the elements Y and U were found as the highest and lowest, respectively (Y>Th>U). So; these values show a parallelism in sediments between the intervals of DB1-DB5 (Figure 11). The values of these elements tend to increase in the interval of DB5-DB11, but tend to decrease in the interval of DB13-DB15. Based on shale values of Krauskopf (1982), the elements of Y and Th are low, but the element U is high in the interval of DB7-DB11 in all samples.

In the trace element distribution of sediment samples (V, Ga, Rb, Sr, Zr, Nb, Ba, La and Ce) relatively to each other, the elements V and Sr were observed as the highest in DB6 and DB8, respectively (Figure 12). Also; the elements of V, Ga, Rb, Zr, Nb, Ba, La and Ce in sediment samples between the intervals of DB7-DB12 show a parallel tendency to increase and decrease. When the shale values of Krauskopf (1982) were compared with sediment samples, it was observed that Sr element was high between the interval of DB8-DB11, and La element was on the threshold value, but V, Ga, Rb, Zr, Nb, Ba and Ce elements were low.

Table 5- Elementary analysis results of sediment samples.

ID / ppm	DB-1	DB-2	DB-3	DB-4	DB-5	DB-6	DB-7	DB-8	DB-9	DB-10	DB-11	DB-12	DB-13	DB-14	DB-15	Şeyl (Krauskopf, 1982)
CaO	22256	5888	10984	3150	36082	7427	98550	236911	177998	144989	156165	20298	183715	70255	42259	
Sc	3.64	3.59	6.97	5.01	8.72	10.93	0	0	4.24	4.51	4.55	5.59	8.4	12.65	3.82	
TiO_2	6407	6331	7205	8915	4332	3346	6567	9045	11438	11697	11572	7234	9226	6115	1110	
V	59.59	65.92	71.59	78.71	67.02	438.18	97.78	97.38	88.64	94.57	100.77	52.24	68.85	109.05	34.88	130
Cr	758	635	1038	1020	1283	991	704	307	253	242	231	676	504	658	1046	100
Mn	462	235	353	310	705	262	486	324	371	310	328	472	1056	702	609	850
Fe_2O_3	38833	32770	46598	43298	88274	255432	58844	49101	52765	53080	56681	32687	94478	93410	57355	0.00047 (Fe)
Co	38.05	44.43	43.8	43.36	57.74	34.93	33.82	27.78	46.46	23.09	21.14	37.1	27.03	41.64	50.55	20
Ni	392	382	524	469	1009	640	418	184	144	153	154	309	378	514	805	80
Cu	3.25	2.49	2.97	1.97	15.24	5.58	11.21	16.92	16.54	20.98	22.24	2.22	16.68	16.02	11.38	50
Zn	25.28	18.15	29.5	26.25	30.91	38.81	45.17	56.02	54.75	61.43	64.59	19.38	16.02	32.72	18.04	90
Ga	3.63	4.06	4.45	4.19	3.14	3.99	5.37	6.39	7.99	8.59	8.82	3.21	1.46	3.76	1.35	25
Rb	20.62	22.19	23.34	22.2	9.63	14.82	34.43	53.46	62.88	69.88	71.96	20.3	12.06	13.85	5.82	140
Sr	84.76	55.26	59.69	53.61	73.39	82.18	343.37	889.88	706.17	493.19	611.84	79	181.29	108.66	73.77	400
Y	5.52	5.15	5.08	5.43	3.1	11.01	10.68	17.35	19.89	19.39	19.34	6.2	9.89	6.5	2.13	35
Zr	26.51	27.89	24.06	26.36	7.3	31.33	59.41	90.26	123.18	142.46	134.09	30.8	25.76	19.51	5.16	180
Nb	4.54	4.2	2.96	3.72	0.06	2.17	5.44	7.54	10.1	11.45	11.07	5.06	0.61	0.49	0.33	15
Ba	45.26	43.9	30.84	41.7	0	40.88	80.69	121.47	154.92	160.9	162.59	48.04	0	0	21.65	600
La	10.61	4.99	8.85	2.17	0.17	8.83	10.71	26.13	39.79	32.01	33.94	8.95	4.01	4.14	0.43	40
Ce	1.39	3.52	0	0	0	19.64	16.71	45.35	56.66	49.85	51.44	-0.03	0.64	0	0	70
Pb	14.54	16.75	13.93	12.61	4.48	26.06	16.48	25.56	22.71	25.01	24.48	17.96	6.6	5.98	4.51	20
Th	1.64	2.11	1.59	1.94	0.27	1.66	5.01	7.02	9.48	8.66	10.02	1.63	1.34	1.1	1.44	12
U	0.25	-0.14	0.24	0.68	0.54	0.13	3.78	6.67	5.81	4.91	6.88	0.47	1.74	0.61	1.35	3.5

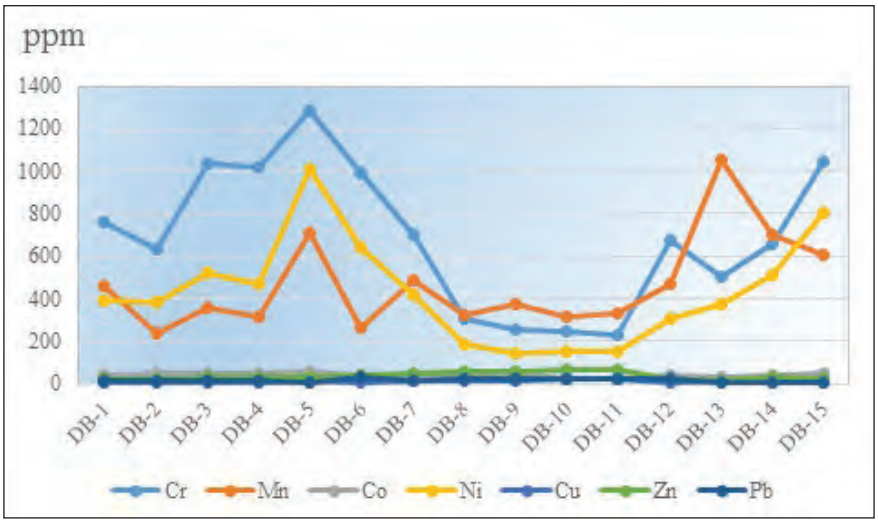

Figure 10- Distribution of heavy metals in sediment samples.

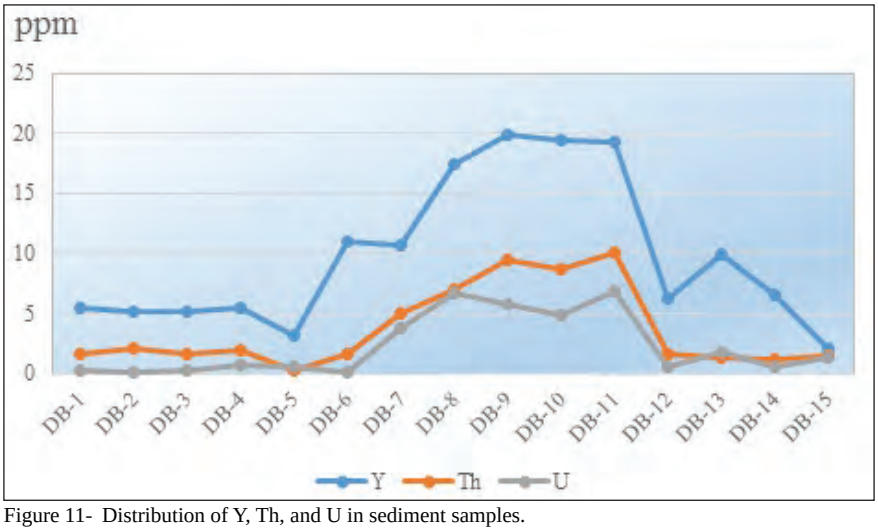

Figure 11- Distribution of Y, Th, and U in sediment samples.

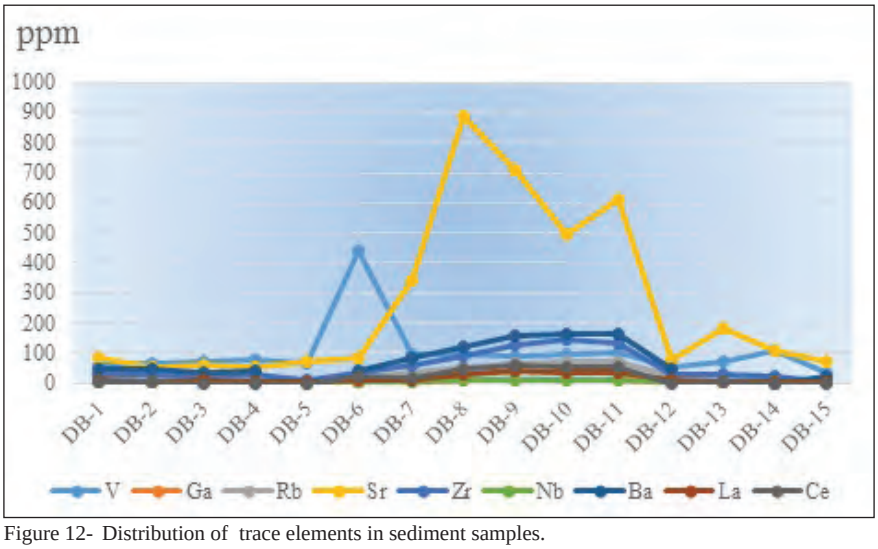

Figure 12- Distribution of trace elements in sediment samples.

4.3. The Evaluation of Total Alfa and Total Beta Characteristics of the Sea Water Samples

In sea water samples, the T-Spring values are high in total alfa and beta counting (Table 6). In samples of D100 and G100, the total alfa values are the same; however, the total beta counting in G100 is high and has a value close to the T-source value. The total beta values of K-150 and D-100 samples are close to each other. However, it is low in T-source in the measurement of total dissolved material, it provides the same value in other samples.

4.4. The Evaluation of Microprobe Analyses of Colored Tests

It was detected that Na, Mg, Al, Si, and K elements in tests did not occur in the sediment content. Whereas Fe and Ca elements are present in tests in addition to the sediments, their contents in tests were determined on a very low value. The distribution of elements in tests of *Peneroplis planatus* as Ca>Si>Al>Mg (Figure 13). When colored (tests ID 16, 17, 18 and 19) and normal individual (test ID 20) were compared according to the tests of *Peneroplis planatus*, which were collected from the sample DB7, it was observed that Fe element was determined as the lowest in normal individual. However, the other elements (Na, Mg, Al, Si, K and Ca) were determined at intermediate values for general distribution.

In colored tests of *Lachlanella variolata* (test ID 20) (Figure 14) collected from the sample DB8 and *Elphidium crispum* (test ID 22), the elements have the characteristics of Ca>Si>Al>Mg (Figure 15). Also; Ca element is high in the colored tests of *Ammonia*

Table 6- Coordinates, total alpha, total beta and TDS values at sampling of sea water.

Sample ID	Coordinates (WGS 84)		Date	Total Alpha		Total Beta		TDS
	North	East		Bq/L	±	Bq/L	±	g/l
K-150	38° 1'54.30"	26°52'4.28"	12.04.2016	0.08	0.014	17.78	3.7	44
T-Spring	38° 1'52.30"	26°52'1.30"	12.04.2016	1.14	0.121	19.87	2.27	38
D-100	38° 1'48.98"	26°52'4.49"	12.04.2016	0.1	0.017	17.93	3.73	44
G-100	38° 1'46.74"	26°52'1.95"	12.04.2016	0.1	0.016	19.76	4.11	44

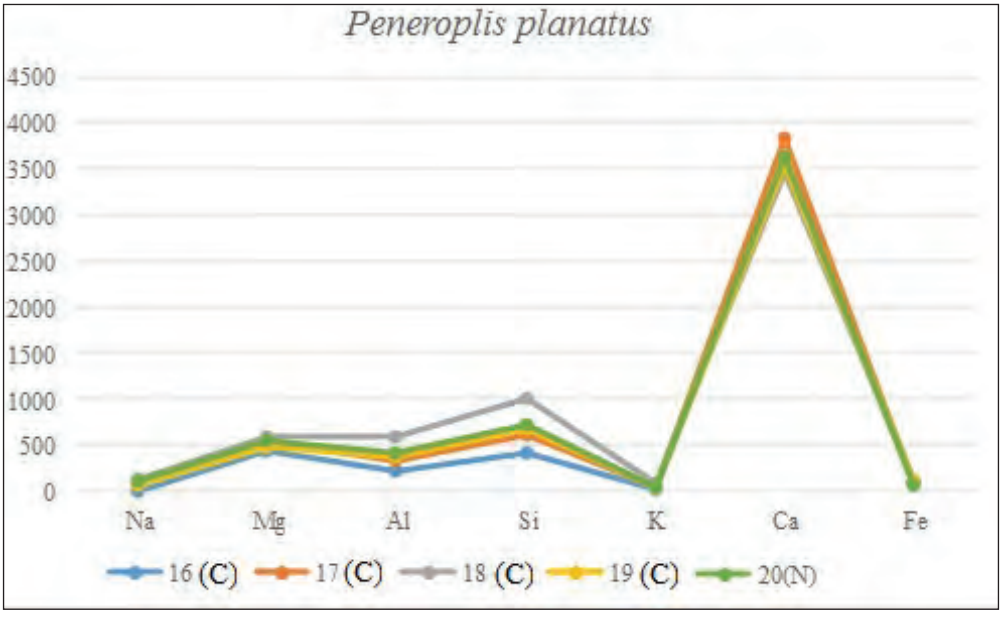

Figure 13- Distribution of elements in tests of *Peneroplis planatus*.

parkinsoniana (test ID 23), which were collected from the same sample (Figure 16). However, the characteristics of Ca>Si>Mg>Al is observed in *Quenqueloculina lamarckiana* (test ID 24) (Figure 17). In colored tests of *Elphidium crispum* (tests ID 26 and 27) collected from the sample DB10 and in the colored test of *Elphidium crispum* (test ID 22) in sample DB8, Ca>Si>Al>Mg was detected (Figure 15). Nonetheless, Al element is the lowest and Fe element is the highest in the colored test 25 in sample DB10. When the tests are compared with the shale values of Krauskopf (1982) it was observed that all elements were low, but only Al, Si, Ca and Fe elements were high with respect to the sea water values.

5. Discussion and Results

The most important finding in the study area is the abundance of *Amphistegina lobifera* Larsen individuals in samples taken at certain points. The presence of

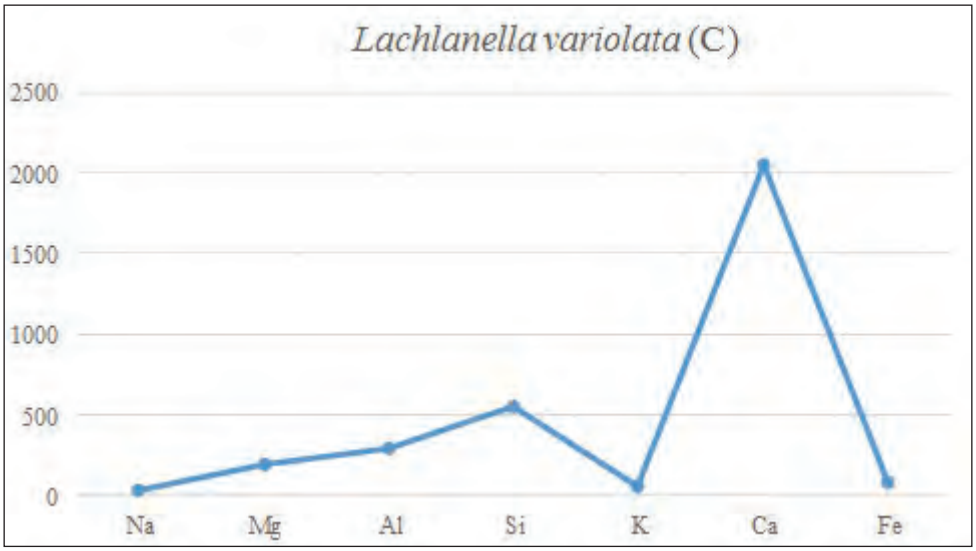

Figure 14- Distribution of elements in coloured test of *Lachlanella variolata*.

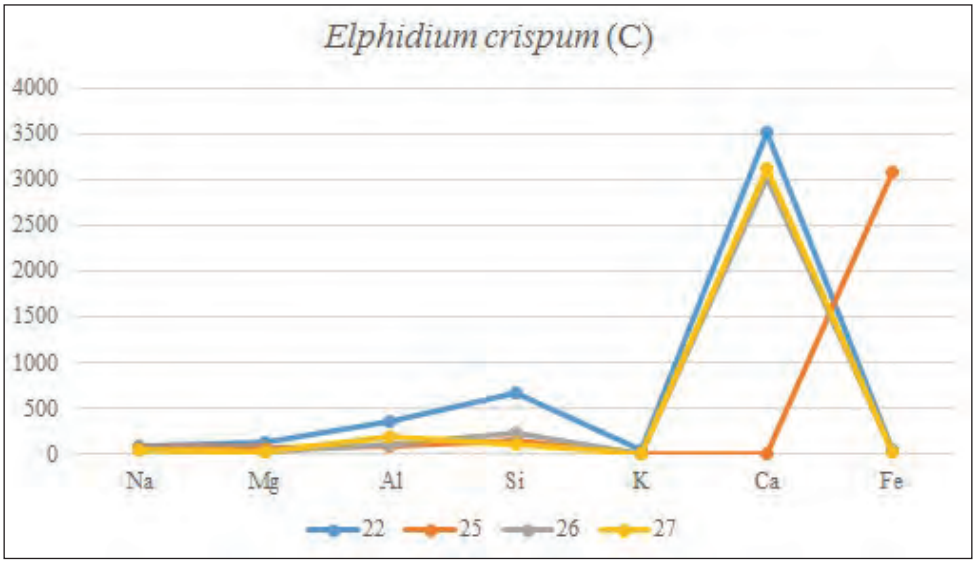

Figure 15- Distribution of elements in coloured tests of *Elphidium crispum*.

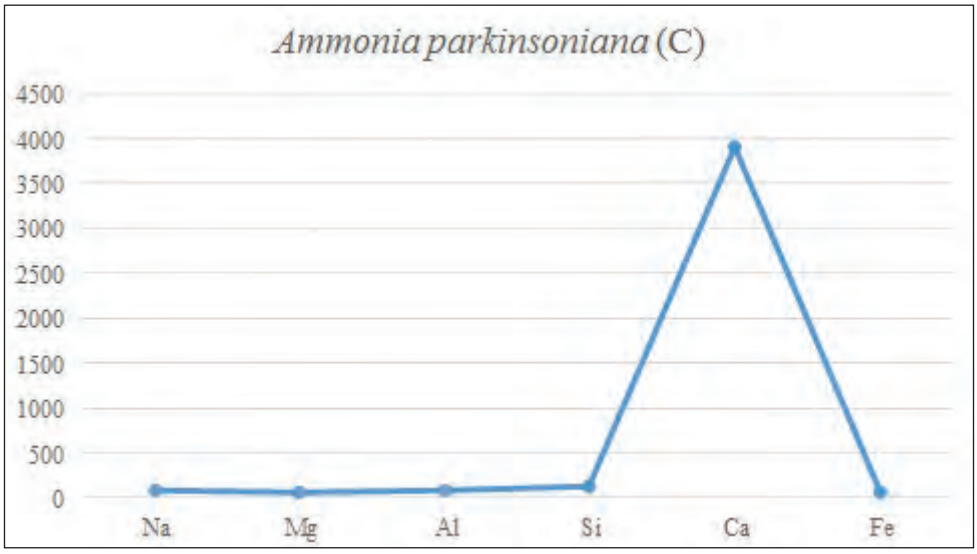

Figure 16- Distribution of elements in coloured test of *Ammonia parkinsoniana*.

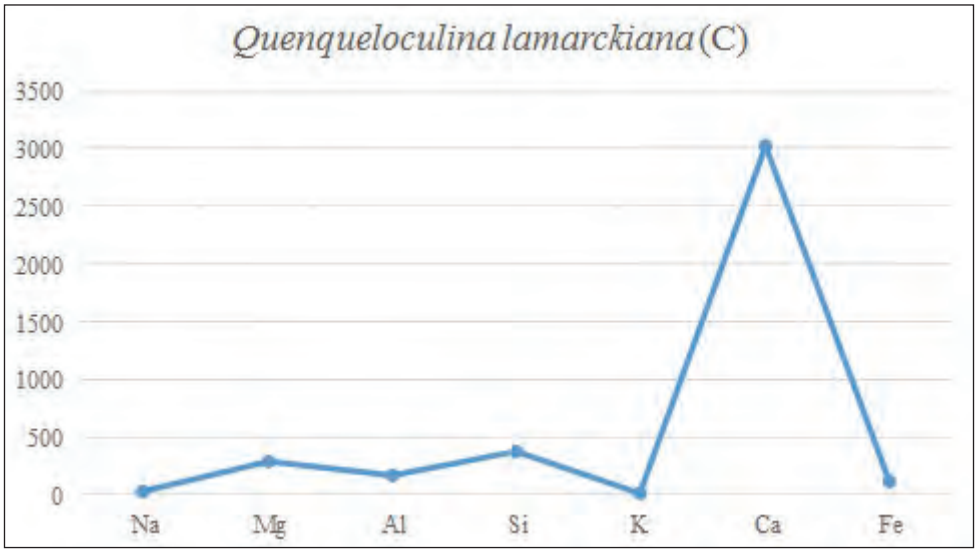

Figure 17- Distribution of elements in coloured test of *Quenqueloculina lamarckiana*.

hot springs, which occur due to the fault line/lines both on the shore areas and in the sea according to the Tuzla Fault, can be considered as the main reason of this abundance (Figure 18). Big similarities are observed between structural geological features of the region and foraminifer assemblage observed in this manner and the benthic foraminifer assemblage of the submarine water spring area located in the Kuşadası Bay (Meriç et al., 2014). It is also interesting in regional scale to encounter *Amphistegina lobifera* Larsen individuals abundantly in the NW section of the Karaburun Peninsula (Meriç et al., 2012*b*). The presence of any hot spring hasn't been detected in this area. Despite that; any *Amphistegina lobifera* Larsen individual/individuals hasn't/haven't been detected in the investigation which has been carried out on 39 samples, although there is also a thermal spring in the Çeşme Ilıca Bay (Meriç et al., 2012*a*). The temperature of the spring here was measured as 28.4°C. This value is 19.6°C in spring in the Kuşadası Bay and is 17.5°C in the surrounding area. However; the bottom water temperature is 23.3°C at sampling points taken from the Doğanbey Bay, and is 19°C in the surrounding area. Although the zoogeographic distribution and bio-ecological conditions formed by thermal activities, in which Indo-Pacific originated

Amphistegina lobifera Larsen individuals were observed, have been interpreted as regional and even point features. The case that they were observed in Marmaris, Datça, Gökova and Kuşadası Bays and in Gökçeada, and that they were heavily populated especially in the Kuşadası Bay and also to have been represented by only one individual only in one of the samples in another study carried out (Meriç et al., 2009*d*). Also, this genus in the southern part of the Dilek Peninsula and to have been quite abundant in the NW shoreline of the Karaburun Peninsula, put forward that these foraminifers mentioned in different localities of the Aegean Sea have been populated in those areas by finding suitable conditions for themselves and maintained their lives (Avşar et al., 2009; Meriç et al., 2010; Yokeş et al., 2014).

When total alfa and beta countings of the springs in the study area are correlated with other hot springs located in Çeşme-Ilıca in northwest and the Kuşadası Bay in south, sea water samples of the Çeşme-Ilıca show resemblance with other hot springs in this area (Yenal et al., 1975; Meriç et al., 2012*a*). However, the total alfa and beta countings of hot springs in the Kuşadası Bay (Güzelçamlı, Kemerli, Kuşadası Kaynağı, Doğanbey, Karakoç, Cumali) are in different values (Yokeş et al., 2014).

Special to the Doğanbey Cape samples, *Amphistegina lobifera* Larsen individuals were not observed between the depths of 3.70-7.00 m at the temperature of 23°C (22.6-22.9°C). Few individuals (3-4 individuals) were observed between the depths of 0-16 m at temperatures of 20-23°C (20-23.3°C). Between depths of 18-32 m at temperatures of 19-20°C (19-20.3°C) they are found abundantly (more than 25 individuals). According to this situation; the ideal live interval of *Amphistegina lobifera* Larsen for the region was determined between the depths of 18-32 m and nearly at the temperatures of 19-20°C. As

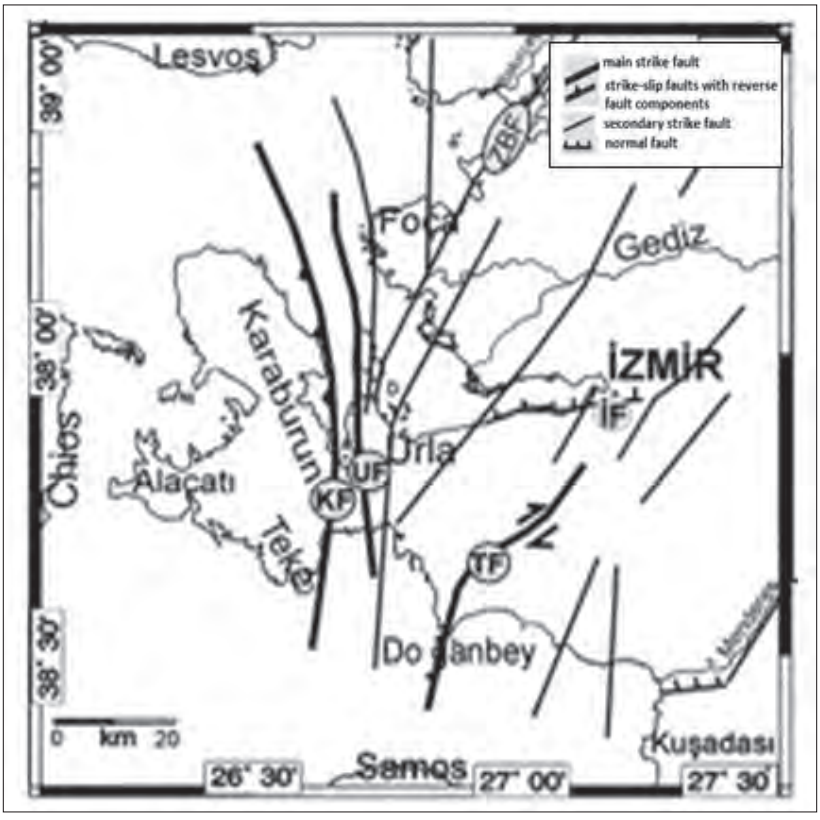

Figure 18- Identifiable and interpretable faults in Izmir and arrounding (Ocakoğlu and Demirbağ 2005).(KF: Karaburun Fault, ZBF: Zeytindağ-Bergama Fault, UF: Urla Fault, TF: Tuzla Fault, İF: İzmir Fault).

another feature, it was detected that the conductivity values have been increasing as being approached to the hot spring; however, the number of individuals have been decreasing in measurements taken by the CTD instrument (Table 7).

When these temperature values were taken into consideration, it was noticed that *Amphistegina lobifera Larsen* did not prefer warm environments. Some researchers (Zmiri et al., 1974; Langer and Hottinger, 2000; Langer et al., 2012) suggest that the change in sea water temperatures is the main cause in the distribution of amphisteginid foraminifers in Eastern Mediterranean. The reason why *Amphistegina lobifera* individuals are not encountered around the Ilıca Bay hot spring is the higher radioactivity in this area in addition to higher water temperature (Meriç et al., 2012*a*). Also, rich foraminifer, ostracod and mollusc assemblages in sediment samples 7, 8, 9, 10 and 11 puts forward the presence of a common feature for the study area (Tables 2, 3 and 4).

Table 7- Coordinate, depth, bottom temperature, salinity and conductivity values of the sampling points and the abundance distribution of *Amphistegina lobifera* Larsen.

Sample ID	Depth (m)	Temperature* (°C)	Salinity* (‰)	EC* (mS/cm)	Individual number of *Amphistegina lobifera*
1	3.7	22.9	39.2	56.4	0
2	5.5	22.9	39.2	56.3	0
3	7.0	22.6	39.2	56	0
4	5.5	22.7	39.2	56	0
12	1.0	---	---	---	0
13	0.3	---	---	---	0
15	0.2	---	---	---	0
5	7.5	22.8	39.2	56.2	1-4
6	15.9	20	39.2	53	1-4
14	0.3	23	39	56.5	1-4
7	18.0	20.3	39.2	53.3	>25
8	19.0	19.9	39.2	52.9	>25
9	31.8	19	39.2	51.9	>25
10	27.7	19.8	39.2	52.8	>25
11	21.2	20.2	39.2	53.3	>25

Another significant feature for the region is to have been encountered quite a few *Peneroplis planatus* (Fichtel and Moll) with colored tests. It was also determined that Na, Mg, Al, Si and K elements had the highest value in the colored test of *Peneroplis planatus* (test ID 18) due to the microprobe analyses carried out on tests of *Peneroplis planatus*, *Lachlanella variolata*, *Ammonia parkinsoniana*, *Quenqueloculina lamarckiana* and *Elphidium crispum* in sediment samples DB7, DB8 and DB10 (Plates 1 and 2). The values of Ca and Fe are the highest in *Ammonia parkinsoniana* (test ID 23) and *Elphidium crispum* (test ID 25), respectively. As a result, when tests and geochemical contents of the sediments were compared with each other, any parallelism or resemblance couldn't have been found. As it is in the above-mentioned regions, the activity of heavy metals and trace elements, which are contained by hot waters, can be considered for the acquisition of this property. Also, some foraminifers in which morphological defects are observed can be stated as another evidence of this opinion (figure 4 and 6 at Plate 3). However, any morphological anomaly effect of bio-ecological diversity and of environmental conditions on the distribution of ostracod and mollusc assemblages and on the individuals as pointwise wasn't observed in this study.

Acknowledgement

The authors would like to thank to İnci Süleymangil (Moda, İstanbul) who gave first preliminary information about the study area, Bülent Erişen who helped and spent his valuable time during the preparation of samples (Budin Chemicals Industry and Trade Limited, Çiğli, İzmir), Assoc. Prof. Salim Öncel who helped for the photography of samples under the electron microscope (Gebze Technical University, Gebze, Kocaeli), physicist Ahmet Nazım who photographed samples in great detail and performed their microprobe analyses (Gebze Technical University, Dept. of Material Science and Engineering, Gebze, Kocaeli).

References

Athersuch, J., Horne, D.J., Whittaker, J.E. 1989. Marine and brackish water ostracods. Synopses of the British Fauna (New Series), E.J.Brill., 43, 1-343.

Avşar, N., Meriç, E. 2001. Çeşme-Ilıca Koyu (İzmir) bölgesi güncel bentik foraminiferlerinin sistematik dağılımı. H.Ü. Yerbilimleri, 24, 13-22.

Avşar, N., Meriç, E., Çevik, M.G., Dinçer, F. 2009. Büyük Menderes Nehri önü (B Türkiye) kıta sahanlığı bölgesi güncel bentik foraminifer toplulukları. H.Ü. Yerbilimleri, 30 (2), 127-144.

Babin, C. 1980. Elements of Palaeontology. John Wiley and Sons. Chichester. 446s.

Bignot, G. 1985. Elements of micropaleontology**.** Graham and Trotman Ltd., London, 217s.

Bonaduce, G., Ciampo, G., Masoli, M. 1975. Distribution of ostracoda in the Adriatic Sea. Pubblicazioni della Stazione Zoologica di Napoli 40 (Suppl.), 1–304.

Breman, E. 1975. The Distribution of Ostracodes in the Bottom Sediments Of The Adriatic Sea. Vrije Universiteit te Amsterdam, Krips Repro, Meppel, 165p.

Erol, O. 1991. Türkiye Jeomorfoloji Haritası. 1/1.000.000. Maden Tetkik ve Arama Genel Müdürlüğü, Ankara.

Erol, O. 1997. Büyük Menderes Deltası'nın foto-jeomorfolojik incelemesi. Ege Coğrafya Derg., 9, 1-42.

Eryılmaz, M. 1996. Ege Denizi'nde Anadolu'nun Doğal Uzantısının Saptanmasında Kullanılan Yerbilimleri Kriterleri, Doktora Tezi, İstanbul Üniversitesi, İstanbul (unpublished).

Eryılmaz M. 2003. Ege Denizi'nin paleocoğrafik gelişimi. Mersin Ü. Müh. Fak. Jeoloji Müh. Böl. 10.yıl Sempozyumu, 15-18 Ekim 2003, Mersin, 96.

Eryılmaz, M., Aydın, Ş. 2001. Türkiye, Ege Denizi, yüzey sediment dağılım haritası Ölçek 1:1.102.000. Dz.K.K. Sey.Hid. ve Oşi. Dairesi, İstanbul.

Eryılmaz, M., Yücesoy-Eryılmaz F. 2001. Ege Denizi'nin sualtı morfolojisi ve Anadolu'nun Doğu Ege Denizi'ndeki doğal uzantısı. Ç.Ü. Yerbilimleri (Geosound), 39, 117-132,

Eryılmaz, M., Yücesoy-Eryılmaz, F. 2014. Underwater Morphology, Oceanography and Recent Sediment Distribution Of Kuşadaşı Bay (West Of Turkey). Fifth International Symposium "Monitoring of Mediterranean coastal areas: problems and measurement techniques, 17-19 June 2014, Livorno (Italy), 655-664.

Eryılmaz, M.,Yücesoy-Eryılmaz F., Doğan E., Yüce H., Bayraktar T. 1998. Ege Denizi'nin sualtı morfolojisi ve Anadolu'nun Doğu Ege Denizi'ndeki doğal uzantısı. 51.Türkiye Jeoloji Kurultayı, 16-20 Şubat 1998, Ankara, 60-61.

Eryılmaz M., Yücesoy-Eryılmaz F., Meriç, E. 2014. Oceanography Of Kuşadasi Gulf West Of Turkey. Quick Lake H 2014 – An International Workshop on Lakes and Human Interactions, 15-19 September, 2014, Ankara and Konya, 37.

Folk, L.R.1974. Petrology of sedimentary rock. Hemphill Publ.Co., Texas, 182 p.

Guillaume, M.C., Peypouquet, J.P, Tetart, J. 1985. Quaternaire et actuel. H.J. Oertli (Ed.). Atlas des Ostracodes de France. Bulletin Centres Rechearche Exploration Proceeding Elf-Aquitaine. Mémoire 9, 337-377.

Hartmann, G., Puri, S.H. 1974. Summary of neontological and paleontotogical classification of ostracoda. Mitteilungen aus dem Zoologischen Staatsinstitut und Zoologischem Museum in Hamburg, 70, 7-73.

http://erkmensenan.blogspot.com/2010/07/lebedos-urkmez.html

Joachim, C., Langer, M.R. 2008. The 80 most common Ostracods from the Bay of Fetovaia Elba Island (Mediterranean Sea). Universität Bonn, 29p.

Krauskopf, K.B. 1982. Introduction to Geochemistry. 2nd edition. MacGraw- Hill, New York. 617p.

Langer, R. M., Hottinger, I. 2000. Biogeogrphy of selected "larger" fodraminifera. Micropaleontology, 46, supplement 1, 105-126.

Langer, R. M., Weinmann, A. E., Lötters, S., Rödder, D. 2012."Strangers" in paradise modeling the biogeographic range expansion of the foraminifera Amphistegina in the Mediterranean Sea. Journal of Foraminiferal Research, 42 (3), 234-244.

Meriç, E., Avşar, N. 2001. Benthic foraminiferal fauna of Gökçeada Island (Northern Aegean Sea) and its local variations. Acta Adriatica, 42 (1), 125-150.

Meriç, E., Avşar, N., Nazik, A. 2002*a*. Bozcaada (Kuzey Ege Denizi) bentik foraminifer ve ostrakod faunası ile bu toplulukta gözlenen yerel değişimler. Ç.Ü. Yerbilimleri (Geosound), 40-41, 97-119.

Meriç, E., Avşar, N., Bergin, F. 2002*b*. Midilli Adası (Yunanistan-Kuzeydoğu Ege Denizi) bentik foraminifer faunası ve bu toplulukta gözlenen yerel değişimler. Ç.Ü. Yerbilimleri (Geosound), 40-41, 177-193.

Meriç, E., Avşar, N., Bergin, F., Barut, İ.F. 2003*a*. Edremit Körfezi (Kuzey Ege Denizi, Türkiye) bentik foraminifer topluluğu ile ekolojik koşulların incelenmesi. Ç.Ü. Yerbilimleri (Geosound), 43, 169-182.

Meriç, E., Avşar, N., Bergin, F., Barut, İ.F. 2003*b*. A note on three abnormal samples of benthic foraminifers from the Dikili Bay (Turkey) in northeastern Aegean Sea: Peneroplis planatus (Fichtel ve Moll), Rosalina sp. and Elphidium crispum (Linné). Bulletin of the Mineral Research and Exploration, 127, 1-14.

Meriç, E., Avşar, N., Bergin, F. 2004. Benthic foraminifera of Eastern Aegean Sea (Turkey) Systematics and Autoecology. Turkish Marine Research Foundation and Chamber Of Geological Engineers of Turkey, Publication 18, 306 p.

Meriç, E., Avşar, N., Mekik, F., Yokeş, B., Barut, İ.F., Dora, Ö., Suner, F., Yücesoy-Eryılmaz, F., Eryılmaz, M., Dinçer, F., Kam, E. 2009*a*. Alibey ve Maden Adaları (Ayvalık-Balıkesir) Çevresi Genç Çökellerinde Gözlenen Bentik Foraminifer Kavkılarındaki Anormal Oluşumlar ve Nedenleri. Türkiye Jeoloji Bülteni, 52(1), 31-84.

Meriç, E., Avşar, N., Barut, İ.F., Yokeş, M.B., Taş, S., Eryılmaz, M., Dinçer, F., Bircan, C. 2009*b*. Kuşadası (Aydın) Deniz Dibi Mineralli Su Kaynağı Çevresi Bentik F oraminifer Topluluğu Hakkında Görüs ve Yorumlar. 13. Sualtı Bilim ve Teknolojisi Toplantısı (SBT 2009) 7-8 Kasım 2009, Lefkoşa/KKTC, 80-92.

Meriç, E., Avsar, N., Barut, İ. F., Yokeş, M.B., Taş S., Eryilmaz, M., Dincer, F., Bircan. 2009*c*. Opinion and comments on the benthic foraminiferal assemblages observed around the mineral submarine springs in Kuşadası (Aydın). Earth System Evolution and the Mediterrenean Area From 23 MA To The Present, 2009, Italy Vol 45 n. 1/4, 222-223.

Meriç, E., Avşar, N., Barut, İ.F., Yokeş, B., Dinçer, F. 2009*d*. Doğu Ege Denizi Kıyı Alanlarında Termal Mineralli Su Kaynaklarının Bentik Foraminifer Topluluklarına Etkisi. İstanbul Yerbilimleri Dergisi, 22 (2), 163-174.

Meriç, E., Yokeş, M.B., Avşar, N., Bircan, C. 2010. An oasis for alien benthic foraminifera in the Aegean Sea. Aquatic Invasions, 5 (2), 191-195.

Meriç, E., Yokeş, B., Avşar, N. 2011. A new guest in Ilıca Bay (Çeşme-İzmir-Turkey);Coscinospira acicularis. Journal of Marine Biological Association of the United Kingdom, 4, e94, 1-5.

Meriç, E., Avşar, N., Nazik, A., Yokeş, M., Barut, İ. F., Eryılmaz, M., Kam, E., Taşkın, H., Başsarı, A., Dinçer, F., Bircan, C., Kaygun, A. 2012*a*. Ilıca Koyu (Çeşme-İzmir) bentik foraminifer-ostrakod toplulukları ile Pasifik Okyanusu ve Kızıldeniz kökenli göçmen foraminiferler ve anormal bireyler. Maden Tetkik ve Arama Dergisi, 145, 62-78.

Meriç, E., Avşar, N., Nazik, A., Yokeş, Dora, Ö., Barut, İ. F., Eryılmaz, M., Dinçer, F., Kam, E., Aksu, A., Taşkın, H., Başsarı, A., Bircan, C., Kaygun, A. 2012*b*. Karaburun Yarımadası kuzey kıyılarının oşinografik özelliklerinin bentik foraminifer ve ostrakod toplulukları üzerindeki etkileri. Maden Tetkik ve Arama Dergisi, 145, 22-47.

Meriç, E., Avşar, N., Yokeş, M. B., Dinçer, F. 2014. Atlas of recent benthic foraminifera from Turkey. Micropaleontology, 60 (3-4), 211-398.

Meteoroloji Bülteni, 1984. Ortalama ve eksterm sıcaklık, yağış değerleri bülteni. T.C. Devlet Meteoroloji İşleri Genel Müdürlüğü, 678 s., Ankara.

Mostafawi, N., Matzke-Karasz, R. 2006. Pliocene Ostracoda of Cephalonia, Greece. The Unrevised species of Uliczny (1969). Revista Española de Micropaleontología 38, 11-48.

Ocakoğlu, N., Demirbağ, E. 2005. Investigation of the active tectonism of İzmir Gulf and surrounding offshore area by means of multi-channel seismic reflection data. Journal of İstanbul Technical University Engineering (serie d), 4 (6).

Öztürk B., Doğan A., Bitlis-Bakır B., Salman A. 2014. Marine molluscs of the Turkish coasts: an updated checklist. Turkish Journal of Zoology. 38, 832-879.

Van Morkhoven, F.P.C.M. 1963. Post-palaeozoic Ostracoda. Their Morphology, Taxonomy, and Economic Use. Vol. II, Generic Descriptions, Amsterdam – London – New York, Elsevier Publishing Company, 1-478.

Yassini, I. 1979. The littoral system ostracodes from the bay of Bou-İsmail, Algiers, Algeria, National Iranian Oil Company. Revista Espanola de Micropaleontologia XI, 353-416.

Yenal, O., Usman, N., Bilecen, L., Kanan, E., Öz, G., Öz, Ü., Göksel, S.A, Alkan, H., Yassa, K. 1975. Türkiye Maden Suları (3), Ege Bölgesi, İ.Ü. Tıp Fakültesi Hidroklimatoloji Kürsüsü, Sermet Matbaası, 351s.

Yokeş, M. B., Meriç, E., Avşar, N., Barut, I., Taş, S., Eryılmaz, M., Dinçer, F., Bircan, C. 2014. Opinions and comments on the benthic foraminiferal assemblage observed around the mineral submarine spring in Kuşadası (Aydın, Turkey). Marine Biodiversity Record, 7, e103, 1-17.

Zangger, E., Malz, H. 1989. Late Pleistocene, Holocene, and Recent ostracods from the Gulf of Argos, Greece. Courier Forschungsinstitut Senckenberg 113, 159-175.

Zmiri, A., Kahan, D., Hochstein, S., Reis, Z. 1974. Phototaxis and thermotaxis in some species of Amphistegina (Foraminifera). Journal of Protozoology, 21, 133-138.

PLATES

Plate 1

1. *Adelosina mediterranensis* (Le Calvez J. ve Y.). External view, sample no. 8.
2. *Adelosina mediterranensis* (Le Calvez J. ve Y.). External view, sample no. 8.
3. *Adelosina mediterranensis* (Le Calvez J. ve Y.). External view, sample no 8.
4. *Adelosina pulchella* d'Orbigny. External view, sample no. 8.
5. *Spiroloculina antillarum* d'Orbigny. External view, sample no. 8.
6. *Spiroloculina excavata* d'Orbigny. External view, sample no. 8.
7. *Cycloforina contorta* (d'Orbigny). External view, sample no. 8.
8. *Quinqueloculina lamarckiana* d'Orbigny. External view, sample no. 8.
9. *Quinqueloculina lamarckiana* d'Orbigny. External view, sample no. 8.
10. *Triloculina marioni* Schlumberger. External view, sample no. 8.
11. *Peneroplis pertusus* (Forskal). External view, sample no. 8.
12. *Peneroplis planatus* (Fichtel ve Moll). External view, sample no. 7.
13. *Peneroplis planatus* (Fichtel ve Moll). External view, sample no. 7.
14. *Peneroplis planatus* (Fichtel ve Moll). External view, sample no. 7.
15. *Rosalina bradyi* Cushman. External views, a. spiral side and b. umbilical sides, sample no. 8.
16. *Rosalina bradyi* Cushman. External views, a. spiral side and b. umbilical sides, sample no. 10.
17. *Cyclocibicides vermiculatus* (d'Orbigny). External view, sample no. 8.


1
2
3
4
5
6
7
8
9
10
11a
11b
12
13
14
15a
15b
16a
16b
17

Plate 2

1. *Ammonia parkinsoniana* (‘Orbigny). External views, a. spiral side and b. umbilical sides, sample no. 8.
2. *Ammonia parkinsoniana* (‘Orbigny). External views, a. spiral side and b. umbilical sides, sample no. 10.
3. *Elphidium advenum* (Cushman). External view, sample no. 11.
4. *Elphidium crispum* (Linné). External view, sample no. 7.
5. *Elphidium crispum* (Linné). External view, sample no. 8.
6. *Elphidium crispum* (Linné). External view, sample no. 10.
7. *Elphidium crispum* (Linné). External view, sample no. 10.


1a
1b
2a
2b
3
4
5
6
7

Plate 3

1. *Peneroplis planatus* (Fichtel ve Moll). External view, sample no. 7.
2. *Peneroplis planatus* (Fichtel ve Moll). External view, sample no. 8.
3. *Peneroplis planatus* (Fichtel ve Moll). External view, sample no. 8.
4. *Lobatula lobatula* (Walker ve Jacob). External view, spiral side, sample no. 11.
5. *Lobatula lobatula* (Walker ve Jacob). External view, spiral side, sample no. 11.
6. *Cibicidella variabilis* (d'Orbigny). External view, spiral side, sample no. 11.
7. *Elphidium crispum* (Linné). External view, sample no. 7.
8. *Elphidium crispum* (Linné). External view, sample no. 8.
9. *Elphidium crispum* (Linné). External view, sample no. 8.
10. *Elphidium crispum* (Linné). External view, sample no. 9.
11. *Elphidium crispum* (Linné). External view, sample no. 9.
12. *Elphidium crispum* (Linné). External view, sample no. 10.
13. *Elphidium crispum* (Linné). External view, sample no. 10.
14. *Elphidium crispum* (Linné). External view, sample no. 9.

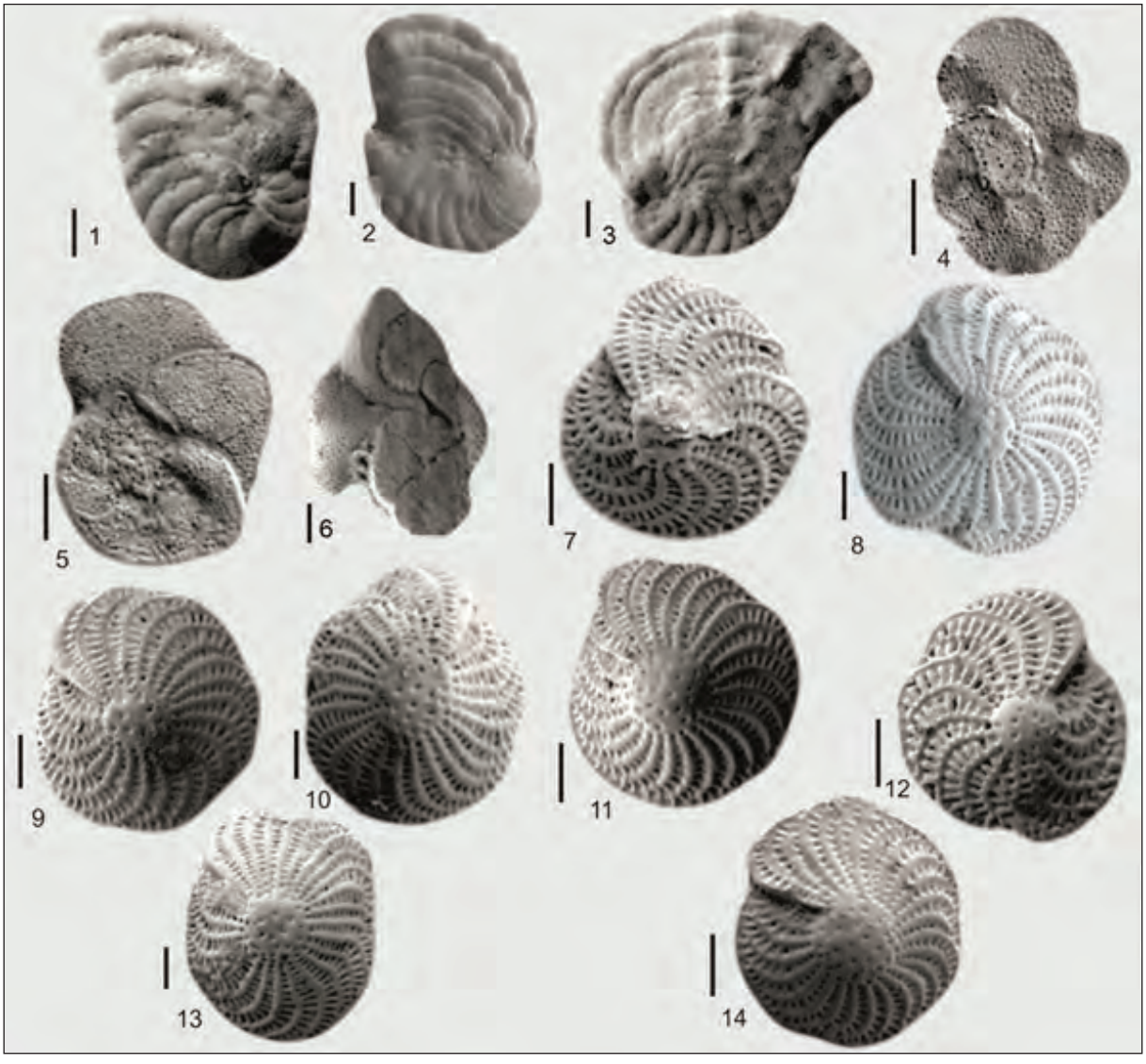
1
2
3
4
5
6
7
8
9
10
11
12
13
14

Bull. Min. Res. Exp. (2018) 156: 117-136

Bulletin of the Mineral Research and Exploration

http://bulletin.mta.gov.tr

Palynology of the Kılçak formation (Early Miocene) from Central Anatolia: Implications for palaeoclimate and palaeoenvironment

Nurdan YAVUZ*[a] and Şükrü Sinan DEMİRER[b]

[a]*Maden Tetkik ve Arama Genel Müdürlüğü, Paleontoloji ve Petrografi Araştırmaları Koordinatörlüğü, Ankara. orcid.org/0000-0002-1141-401X.*
[b]*Maden Tetkik ve Arama Genel Müdürlüğü, Paleontoloji ve Petrografi Araştırmaları Koordinatörlüğü, Ankara. orcid.org/0000-0001-9100-678X.*

Research Article

Keywords:
Palynology, palaeoclimate, early Miocene, Kılçak formation, Central Anatolia.

ABSTRACT

The palynological analysis of the early Miocene successions of the Kılçak formation (Central Anatoia, Turkey) was carried out in order to reconstruct the palaeovegetation. The pollen spectra indicate a flora dominated by Pinus, co-dominance of Cupressaceae in one of the investigated successions, and lower percentages of trees such as Taxodioideae within Cupressaceae, *Quercus* deciduous type, *Carya*, *Carpinus*, *Ulmus*, Engelhardioideae, *Salix*, *Alnus* and *Juglans*. Herbs are represented by minor amounts of Poaceae, Amaranthaceae/Chenopodiaceae and Asteraceae. This flora indicates the presence of a Taxodium topogenous mire with a nearby riparian vegetation and broadleaved deciduous mixed forests developed in the surrounding distant mountainous areas. $\delta^{13}C$ analysis shows that the vegetation was dominated by C3 plants. The Kılçak palynoflora reflects a humid, warm-temperate climate being compatible with the global warm conditions maintained during the early Miocene.

Received Date: 01.06.2017
Accepted Date: 30.11.2017

1. Introduction

The Kılçak formation is the oldest Neogene unit in the Çankırı Basin (Central Anatolia) and exposed in a small area only around Kılçak village (Figures 1 and 2). The Kılçak locality is one of the well-known rodent-type sections in the Eastern Mediterranean and the age of the unit is tightly constrained by the rodent fauna (Bruijn and Saraç, 1992; Bruijn et al., 1993; Bruijn and Koenigswald, 1994; Ünay, 1994; Hoek Ostende, 1992, 1995*a* and *b*). However, the section from which fossils were collected, is at present completely covered by landslides (Kaymakçı, 2000).

The lens-shaped and thin (up to 30-cm- thick) coal lenses nearby Kılçak village were exploited by villagers but due to the low calorific value of the coal and due to landslides the mining actvities were stopped. The Kılçak fauna was originally described by a German team in the late 1960s from an open-pit lignite mine (Sickenberg et al., 1975). The deposits which yielded the Kılçak faunas have been included in different formations by different researchers. Şen et al. (1998), were the first to propose that the fossiliferous deposits at Kılçak must be distinguished as a different stratigraphic unit. Subsequently, Kaymakçı (2000) made the first formal definition of the Kıçak formation and outlined its lithological characteristics along a reference section located 1 km east of the Kılçak village (Figure 3). Rodent samples collected from this section, were studied by Hans de Bruijn and fitted to the MN-1 and the lower part of the MN-2 zones corresponding to the lower part of the early Miocene (Aquitanian) (Kaymakçı, 2000). Later, Özcan (2003) demonstrated that the Kılçak formation also crops out at a different site than the one originally described at the Kılçak village (Figure 2). From this outcrop Karadenizli et al. (2004) studied a stratigraphic section (Sülüklü Göl) and assigned an age of MN 1-3 (early Miocene) based on the following mammal fossils: *Galerix* sp., *Soricidae*

* *Corresponding author: Nurdan YAVUZ, nurdanyavuz@hotmail.com*
http://dx.doi.org/10.19111/bulletinofmre.395784

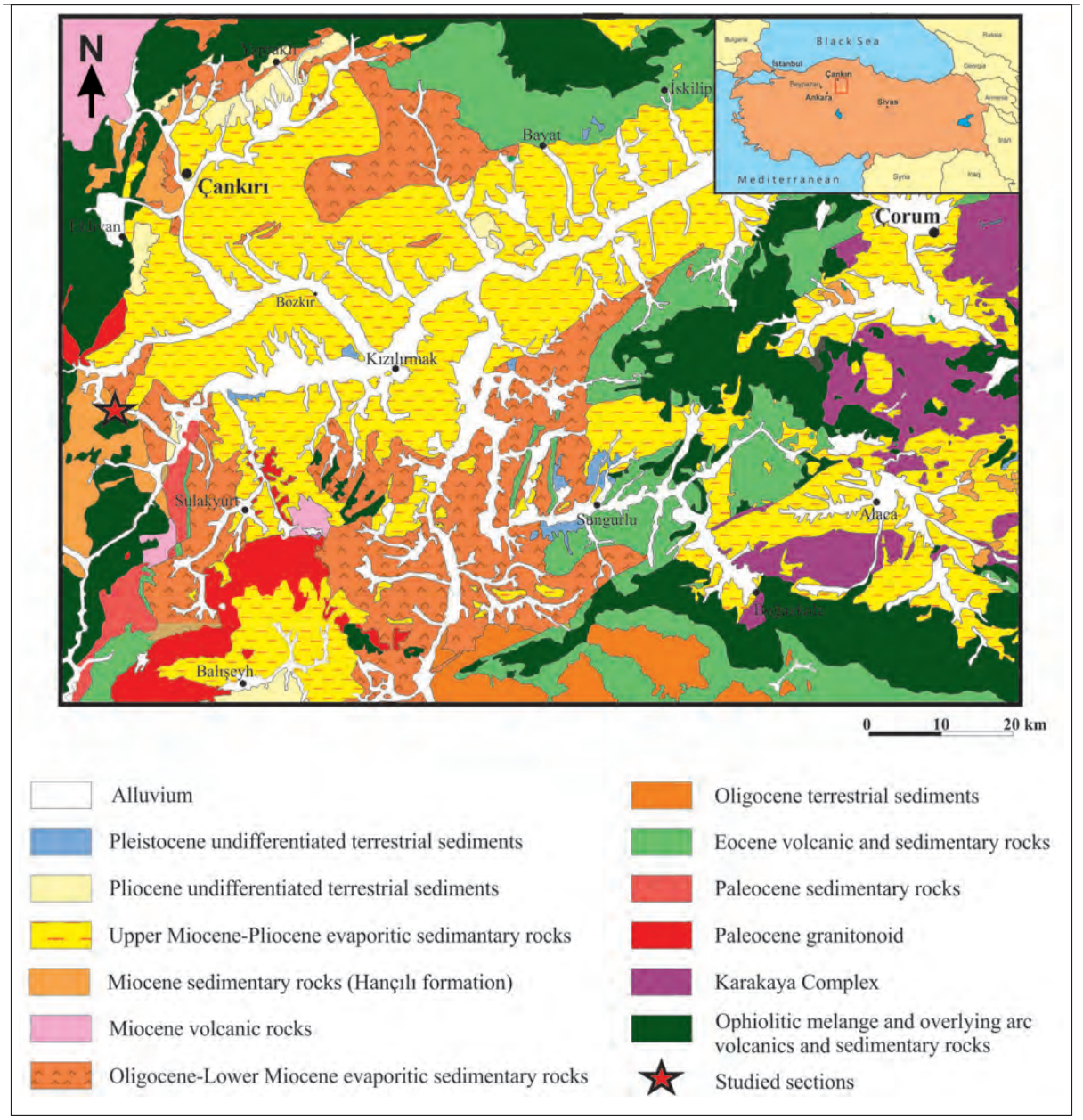

Figure 1- Geological map of the Çankırı-Çorum Basin (modified from MTA 2002).

indet., *Albertona* nov. sp., *Ctenodactylidae* indet., *Debruijnia* sp., *Spanocricetodon* sp., *Democricetodon* sp., *Megacricetodon* sp., and *Cricetodon versteegri* (identification by Gerçek Saraç).

The current study presents the first palynological and stable isotope ($\delta^{13}C$) analyses carried out on samples collected from organic-rich layers along the measured sections, from which rodent samples had earlier been collected and identified. A main aim of this study is to discuss environmental and climatic conditions during the early Miocene deposition of the Kılçak formation.

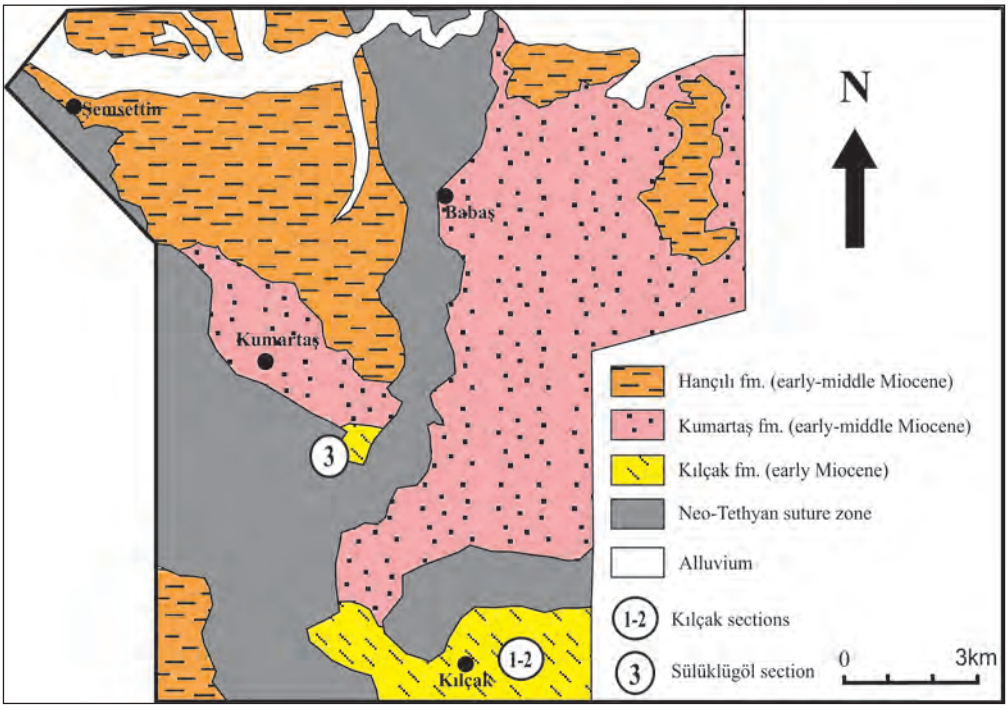

Figure 2- The distribution of the Kılçak Formation (Karadenizli et al., 2004).

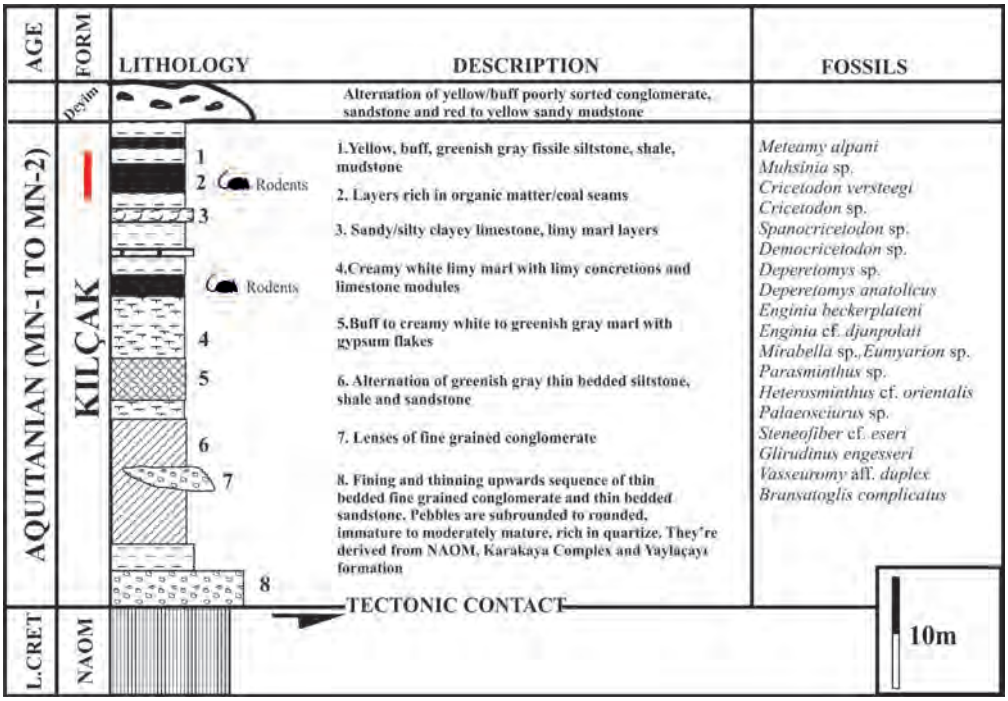

Figure 3- Generalized section of the Kılçak Formation (Kaymakcı, 2000). Red line indicates tentative corelation of Kılçak sections.

2. Geological Setting

The Çankırı Basin lies within the İzmir-Ankara-Erzincan suture which demarcates the former position of the northern branch of the Neo-Tethyan Ocean (Kaymakçı, 2000). The Çankırı fore-arc basin was formed by northward subduction of the Neo-Tethyan Ocean floor beneath the Sakarya continent (Figure 4). During the Late Palaeocene-Early Eocene it was covered by a transgressive sea. Beginning in

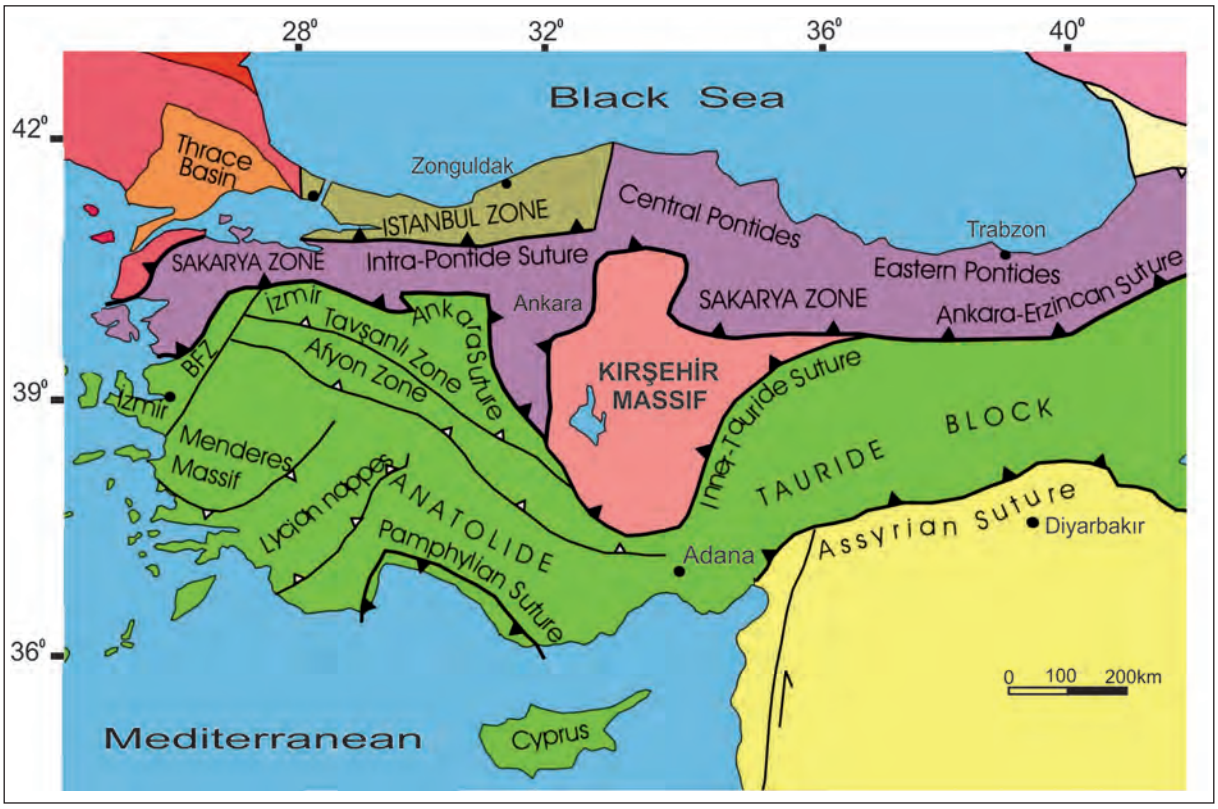

Figure 4- Tectonic map of Turkey and the surrounding areas (Okay and Tüysüz, 1999). The omega shape of the Ankara-Erzican Suture, confining the upper boundry of the Kırşehir Massif, defines the approximate boundary of the Çankırı Basin.

the Middle Eocene, mainly south-vergent thrusts developed around the Çankırı Basin. Due to the compressional regime older units surrounding the basin thrusted over younger in-fills, the basin rose, shallowed up and became a continental intermontane basin. During the Late Eocene-Oligocene terrestrial deposits and evaporites were deposited. It was characterized by alluvial fans during Oligocene while evaporitic lake deposits were formed during the Late Miocene-Pliocene (Tüysüz and Dellaloğlu, 1994) (Figure 4).

The Early Tertiary lithologies of the Çankırı Basin include units formed and deposited in various tectonic/depositional settings, ranging from accretionary wedge, fore-arc, to inter-arc to collisional settings. The collision and indentation of the Kırşehir Block with Sakarya Continent in the Late Paleocene to Oligocene gave rise to an anticlockwise rotation of the western rim and a clockwise rotation of the eastern rim, which subsequently resulted in the Ω-shape of the Çankırı Basin (Kaymakçı, 2000) (Figure 4).

The oldest Neogene unit in the Çankırı Basin is the Kılçak formation of Aquitanian age. It is followed in order of younging, by the Altıntaş formation of Burdigalian age, the Hançılı formation of Burdigalian to Langhian age, the Çandır formation of Burdigalian (?) to Serravalian age, the Bayındır formation of Tortonian age, the Kızılırmak formation of Messinian to Pliocene age, the Bozkır formation of early Pliocene age and the Değim formation of early Quaternary age (Kaymakçı, 2000).

The Kılçak formation, the focus of this study, was deposited during a phase of compressive deformation which terminated synchronous with the end of Kılçak deposition. The Kılçak formation unconformably overlies the pre-Neogene units and is tectonically overlain by the North Anatolian Ophiolitic Melange (Kaymakçı, 2000).

3. Materials and Methods

Since landslides are very common in the Kılçak area, great caution is needed to collect *in situ* samples. A total of thirty three samples from two undisturbed sections very close to the faunal level of Kaymakcı (2000) and sixteen samples close to the mammal locality of Karadenizli et al. (2004) were collected (Figure 5, 6A, B). The number of palynologically

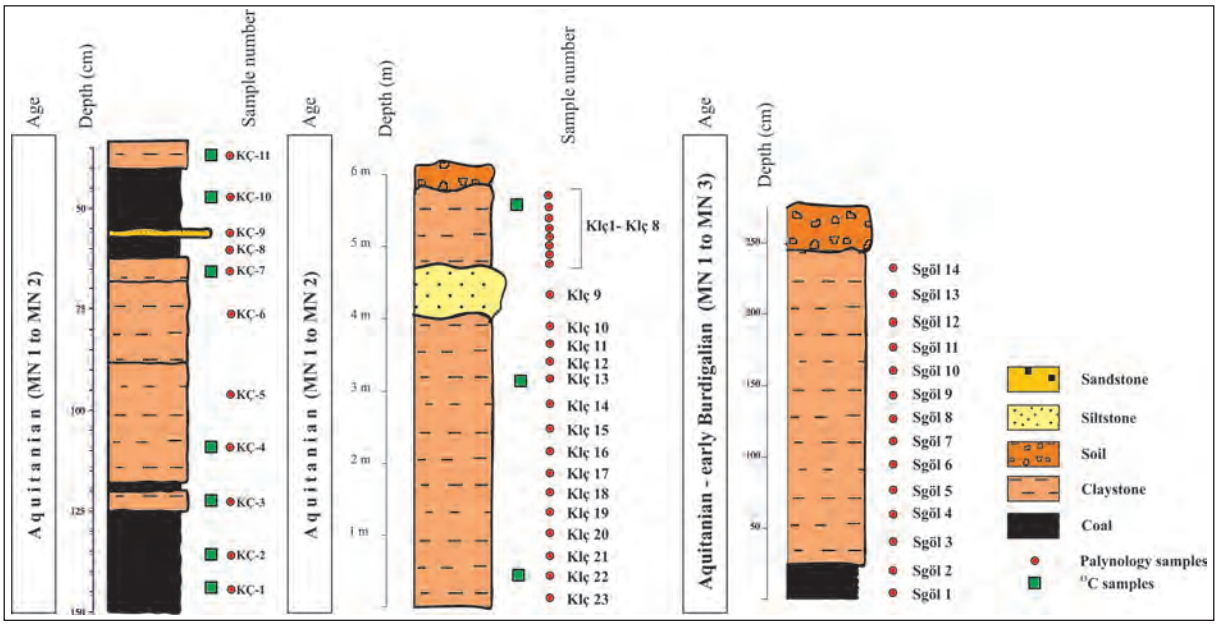

Figure 5- Kılçak-1, Kılçak-2 and Sülüklügöl stratigraphic sections.

Figure 6- A) Close up view of Kılçak-1 section. B) Close up view of Kılçak-2.

productive samples are nine out of eleven from the Kılçak-1 section (X:534282, Y:4451640), four out of twenty three from the Kılçak-2 section (X:533438, Y:4451831), and nine out of fourteen from the Sülüklügöl section (X:533800, Y:4456649).

Samples for pollen analysis were prepared using standard palynological techniques, in the Palynology Laboratory of the General Directorate of Mineral Research and Exploration. This included successive treatment with HCl, HF and KOH. After each acid treatment, the samples were washed with distilled water. Separation between organic and inorganic fractions was achieved using a $ZnCl_2$ solution of a density of 2.10 g/cm^3. The residue was sieved at 10 µm using a nylon mesh, mixed with glycerine, and mounted on microscope slides. Counting was performed at 400× magnification to a minimum pollen sum of 200 pollen grains with a Nikon Eclipse-Ni transmitted light microscope. The identification of pollen grains was accomplished to the lowest taxonomic level possible by comparing the fossils with their present-day relatives using pollen atlases and the keys of Faegri and Iversen (1989) and Moore et al. (1991). Detailed pollen diagrams (Figures 7, 8 and 9) using the programmes TILIA and TILIA GRAPH (Grimm, 2005) and a synthetic pollen diagram (Suc, 1984) taking into account ecological and climatic requirements of plants were constructed (Figure 10). In the synthetic pollen diagram taxa were grouped according to their ecological properties following Fauquette et al. (2006) and Jimenez-Moreno (2006).

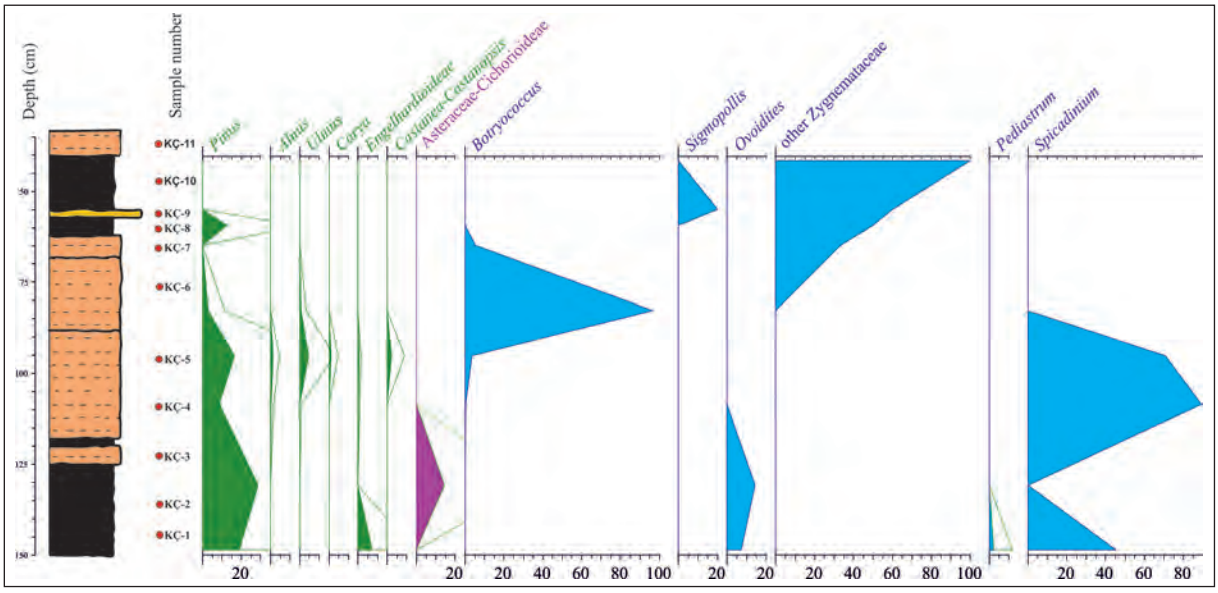

Figure 7- Palynological diagram of Kılçak-1 stratigraphic section.

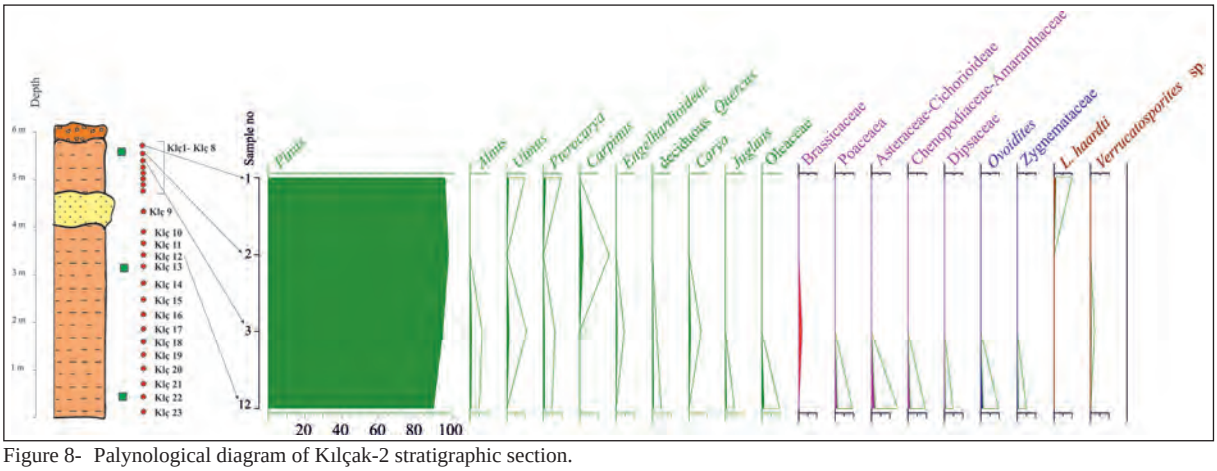

Figure 8- Palynological diagram of Kılçak-2 stratigraphic section.

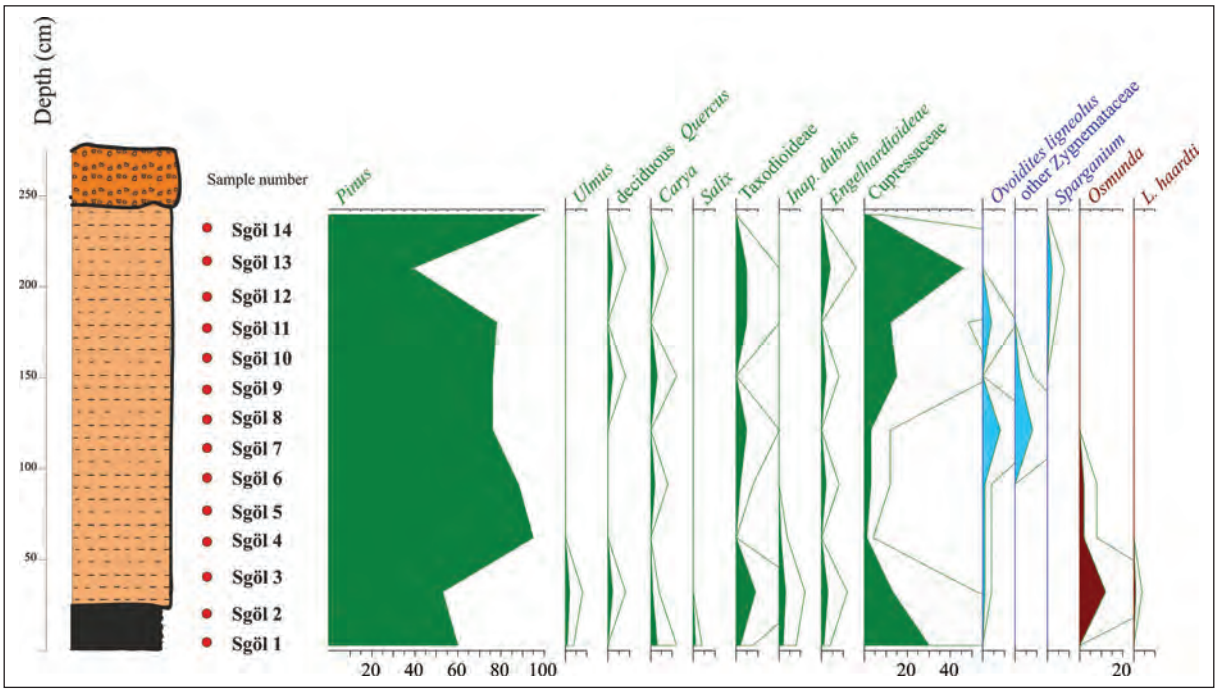

Figure 9- Palynological diagram of Sülüklügöl stratigraphic section.

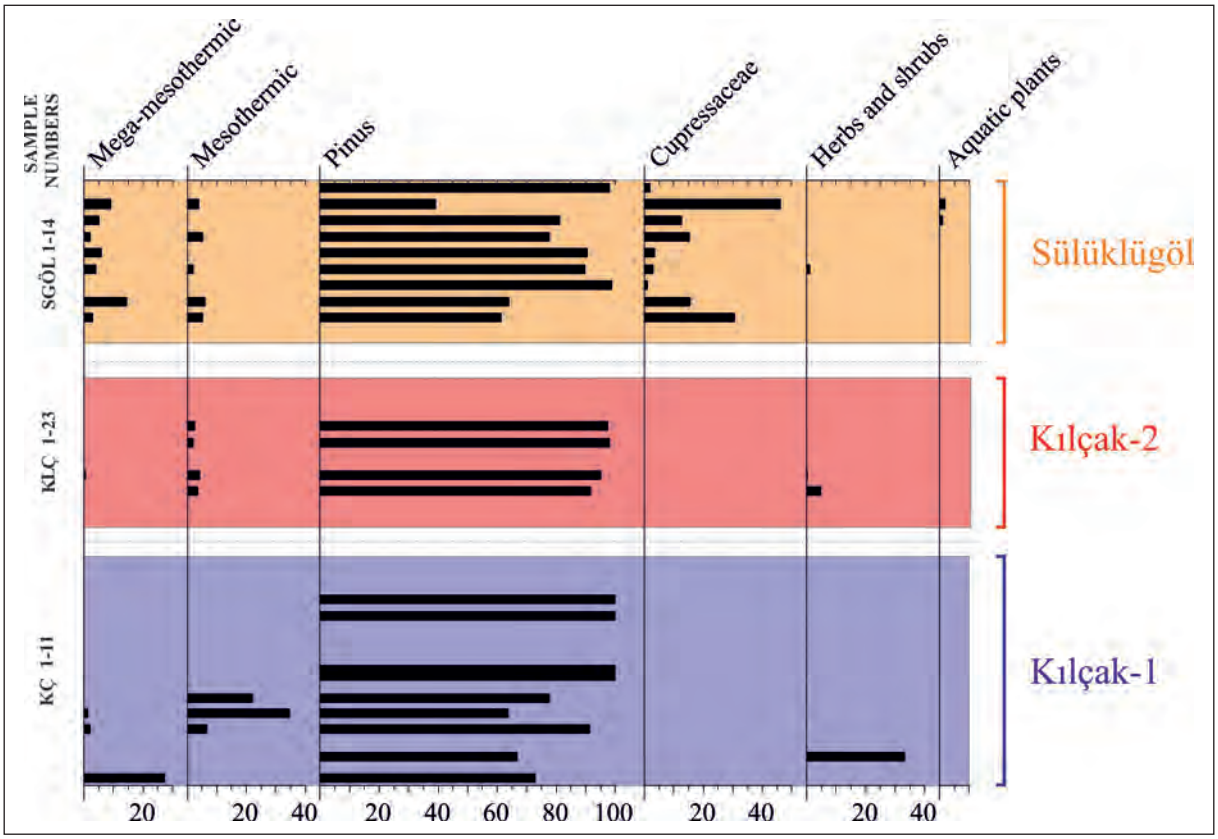

Figure 10- Synthetic pollen diagram of Kılçak-1, Kılçak-2 and Sülüklügöl stratigrahic sections.1. Mega-mesothermic (=subtropical) elements (Taxodioideae, Engelhardioideae, *Carya*); 2. Mesothermic (=warm-temperate) elements (deciduous *Quercus, Pterocarya, Carpinus, Juglans, Ulmus, Alnus, Salix,* Oleaceae, *Castanea–Castanopsis* type); 3. *Pinus* and poorly preserved Pinaceae; 4. Cupressaceae; 5. Herbs and shrubs (Poaceae, Asteraceae/Cichorioideae, Brassicaceae, Chenopodiaceae/Amaranthaceae, Dipsacaceae); 6. Aquatic plants (*Sparganium*).

Microphotographs of selected palynomorphs are given in plate 1.

Seven samples from the Kılçak-1 section and three samples from the Kılçak-2 section were selected for stable isotope analysis (Figure 5). $\delta^{13}C$ determinations were carried out on a continuous-flow gas-ratio mass spectrometer (Finnigan Delta PlusXL) coupled to an elemental analyzer at the Enviromental Isotope Laboratory in University of Arizona. Analytical precision was better than ±0.08‰. Calibration to the VPDB standard was performed by repeated measurements of international reference standards NBS-19 and NBS-18.

Mosbrugger and Utescher (1997) proposed a method, the Coexistence Approach (CA), for quantitative reconstructions of Tertiary terrestrial palaeoclimate data using plant fossils. This method widely accepted in the scientific community and numerous palaeoclimate reconstructions are done especially in European countries since the day of its publication. The method is based on the assumption that Tertiary plant taxa have similar climatic requirements to their nearest living relatives. The aim of the coexistence approach is to find for a given fossil flora and a given climate parameter the climatic interval in which all nearest living relatives of the fossil flora can coexist. According to the method, at least 10 taxa contributing climate data are required to obtain significant results. With respect to the low diversity of the palynomorphs, the CA was applicable on a summary record of Kılçak-2 (e.g. on a flora list combined from all Kılçak-2 samples). Data were calculated for mean annual temperature (MAT), cold and warm month means (CMT, WMT), mean annual precipitation (MAP), as well as monthly precipitation data for the wettest, driest and warmest months (MPwet, MPdry, MPwarm). All climate data calculated are given in table 1. With 19 taxa contributing with climate data and 100 % overlapping for each variable the analysis deliveres reliable results.

4. Results and Discussion

4.1.Palynoflora

Pinus fluctuates between 3 and 28% in the Kılçak-1 pollen diagram (Figure 7). Pollen of *Alnus, Ulmus, Carya,* Engelhardioideae and *Castanea-Castanopsis* participate with frequencies below 7% while that of Asteraceae-Cichorioideae by 14%. *Spicadinium* exist in the lower parts of the the Kılçak-1 section with a maximum of 89%. Zygnemataceae is present in the upper part reaching 100% at the very top of the section. *Ovoidites* and *Sigmopollis* are represented by lower percentages (7–20%). *Botryococcus* has its maximum (96%) in the middle part of the section. *Pediastrum* is present only at the bottom of the section (2%).

The Kılçak-2 pollen diagram is characterized by predominance of *Pinus* ranging from 90 to 98% (Figure 8). *Alnus, Ulmus, Pterocarya, Carpinus,* Engelhardioideae, deciduous *Quercus, Carya, Juglans,* Oleaceae are represented by low percentages (<2%). Brassicacaeae, Poaceaea, Asteraceae-Cichorioideae, Chenopodiaceae - Amaranthaceae and Dipsacaceae are present in the lower part of the section with low percentages (0-2%). Zygnemataceae and *Ovoidites* occur in trace amounts. Spores are represented by low percentages of *Laevigatosporites haardti* (Polypodiaceae) (<2%) and *Verrucatosporites* sp. (Polypodiaceae) (<1%).

The Sülüklügöl pollen diagram is dominated by *Pinus* that fluctuates between 39 to 98% with an average of 74% (Figure 9). Cupressaceae ranging from 1 to 46% are well represented and increase towards the top of the section. Taxodioideae fluctuates between 0 and 9%. *Ulmus* and *Salix* are present in the lower part of the section at low percentages (<2%). *Carya,* deciduous *Quercus* and Engelhardioideae have more uniform distributions ranging from 0 to 4%. Zygnemataceae and *Ovoidites ligneolus* reach their maximum (8%) in the middle part of the section. *Sparganium* is present only in the upper part (1 to 2%). *Osmunda* is well represented at the base of the section with a maximum of 12% while *Laevigatosporites haardti* (Polypodiaceae) occurs at very low amounts (1%).

4.2. $\delta^{13}C$ Analysis

The stable carbon isotope ratio difference for a sample relative to the PDB (Pee Dee Belemnite) standard is given as :

$$\delta^{13}C(‰)=[(R_{sample}-R_{PDB})/R_{PDB}]x1000$$

where R is the isotope ratio $^{13}C/^{12}C$. The Pee Dee Belemnite (PDB) being established as a standart for ^{13}C analysis, is based on a Cretaceous marine fossil (*Belemnitella americana*) found within the Pee Dee Formation in South Carolina. This material displays an anomalously high $^{13}C/^{12}C$ ratio (0.0112372); higher than nearly all other natural carbon-based substances.

Table 1- Coexistence Approach results of Kılçak-2 samples (Summary).

Fossil taxon	**Reference taxon**	MATmin	MATmax	CMTmin	CMTmax	WMTmin	WMTmax	MAPmin	MAPmax	MPWETmin	MPWETmax	MPDRYmin	MPDRYmax	MPWARMmin	MPWARMmax
dimension		°C	°C	°C	°C	°C	°C	mm	mm	mm	mm	mm	mm	mm	mm
Alnus sp.	*Alnus* sp.	-13,3	27,4	-40,9	25,6	4,9	38,6	160	2730	25	353	0	135	0	533
Asteraceae-Cichorioideae															
Brassiacaceae															
Carpinus cf. *betulus*	*Carpinus betulus*	5,3	17,6	-7,5	9,7	17,4	26,4	471	1958	56	236	1	85	6	219
Carpinus cf. *orientalis*	*Carpinus orientalis*	7,7	18,3	-5,3	10,9	18,6	27,6	402	1548	71	191	3	82	3	122
Carya sp.	*Carya* sp.	4,4	26,6	-11,5	22,2	19,3	30,6	373	1724	68	434	8	93	45	258
Castanea, *Castanopsis*	*Castanea*, *Castanopsis*	6,9	27,7	-8,2	27	14,5	28,9	473	10798	70	2446	2	165	1	1100
Chenopodiaceae, Amaranthaceae															
Cupressaceae	Cupressaceae	-15,6	26,5	-48,9	26,1	11,2	32,9	184	4486	22	409	0	326	0	378
Dipsacaceae	Dipsacaceae	-1,7	24,6	-25,4	23,6	16,2	29,4	24	1828	8	343	0	85	0	239
Engelhardioideae	Engelhardioideae	13,8	27	3,1	25	20,6	33,6	740	10798	150	2446	5	152	79	1100
Juglans sp.	*Juglans* sp.	0	27,5	-22,7	25	9,5	31,2	210	2617	28	582	1	114	2	189
Laevigatosporites haardtii															
Myriophyllum sp.	*Myriophyllum verticillatum*	-0,4	17	-21,7	10,3	13,9	26,3	422	2648	68	369	9	108	26	344
Oleaceae	Oleaceae	-1,1	27,7	-25,8	27	19,6	33,1	37	3293	8	985	0	165	0	320
Osmunda sp.	*Osmunda* sp.	0,2	27,4	-16,6	25,6	13,9	30,6	206	4150	34	914	0	89	2	228
Pinus sp.	*Pinus* sp.	-9,2	25,5	-36,8	21,4	7,1	32,9	180	10798	28	2446	0	94	0	1100
Poaceae															
Pterocarya sp.	*Pterocarya* sp.	3,9	24,2	-12,8	17	15,3	31,6	246	2648	46	424	1	64	2	424
Quercus sp. (deciduous)	*Quercus* sp. (deciduous)	-1,4	27	-25,1	25,9	8,4	28,3	201	10798	33	2446	0	180	5	1100
Quercus sp. (evergreen)	*Quercus* (evergreen)	11,7	19,5	0,4	13,3	18,8	26,1	224	1800	48	159	0	72	0	116
Salix sp.	*Salix* sp.	-17	27,7	-50,1	26,5	7,6	32,9	122	2399	22	448	0	108	0	252
Taxodioideae	Taxodioideae	3,8	25	-9,4	19,8	13,7	31,2	290	2615	60	448	0	114	3	431
Ulmus sp.	*Ulmus* sp.	-4,9	26,6	-25,8	26,1	16	29,4	201	3285	33	569	0	100	0	239
Verrucatosporites sp.															
CA results															
no. of taxa with climate data	19														
CA intervals															
min		13,8		3,1		20,6		740		150		9		79	
max		17		9,7		26,1		1548		159		64		116	
taxa coexisting (%)		100		100		100		100		100		100		100	

Therefore, for convenience, it is assigned a $\delta^{13}C$ value of zero, giving almost all other naturally-occurring samples negative delta values (http://siel.uga.edu/stable-isotope-overview).

The $\delta^{13}C$ values of the fine-grained and organic rich sediments of Kılçak formation are presented in table 2. The $\delta^{13}C$ values of the Kılçak-1 samples range between -24.6‰ and -25.8‰ with a mean of -25.1‰ while that of the Kılçak-2 samples range between -26.4‰ and -27.0‰ with a mean of -26.7‰. The $\delta^{13}C$ values of both Kılçak-1 and Kılçak-2 samples show minor fluctuations with very close mean values pointing to the persistence of C3 vegetation during the studied time-span.

Table 2- $\delta^{13}C$ values of bulk organic sediment samples from Kılçak, Central Anatolia. [a]Sample number assigned at Enviromental Isotope Laboratory, University of Arizona.

Lab. number[a]	$\delta^{13}C$ (‰)
KC-11	-25.0
KC-10	-24.6
KC-07	-25.7
KC-04	-24.9
KC-03	-25.0
KC-02	-25.0
KC-01	-25.8
KLC-22	-26.7
KLC-13	-26.4
KLC-02	-27.0

The $^{13}C/^{12}C$ ratio in organic lake sediments depends on various factors (such as temperature, CO_2 supply, latitude effect, change in terrestrial vegetation, change in organic productivity etc.) affecting the ^{13}C content of the samples. The differences in $^{13}C/^{12}C$ ratio in terrestrial plants is the result of differences in the metabolic pathways during the synthesis of the plant material. The C3 metabolic pathway (the Calvin cycle) generally results in lower $^{13}C/^{12}C$ ratio than the C4 metabolic pathway (Håkansson, 1985). The range in $\delta^{13}C$ for C3 plants is from -33 to -22‰ and for C4 plants from -20 to -10‰ (Bender, 1971). The $\delta^{13}C$ values of the Kılçak samples indicate that vegetation was dominated by C3 plants during deposition.

One of the main reasons of lower $\delta^{13}C$ values of samples is the abundant presence of halophyts which are salt-resistant or salt-tolerant plants that thrive and complete their life cycles in soils containing high salt concentrations. Valero-Garces et al. (2000) indicated that low $\delta^{13}C$ values (mean -23‰) of samples of Salada Medina playa lake (Spain) are due to the presence of high amounts of Chenopodiaceae which have a very high salt-tolerance. The sporadic presence of halophytic Chenopodiaceae in the Kılçak samples shows that the reason of low $\delta^{13}C$ values are not halophytes but the dominance of C3 plants within the vegetation (Figure 11).

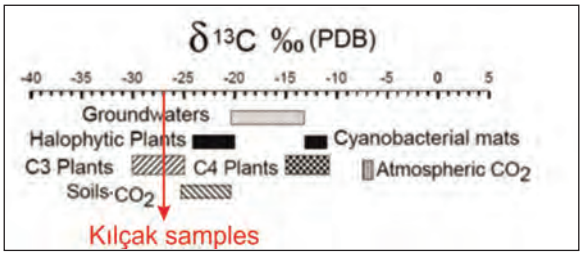

Figure 11- Sources of carbon in the Salada Mediana: C3 and C4 plants, halophytic plants, cyanobacterial mats, atmospheric CO_2 and soil CO_2 (Valero-Garces et al., 2000).

4.3.Paleoflora and Vegetation

The Kılçak-1 pollen diagram is dominated by freshwater algae. The identified algae are characteristic for stagnant (*Botryococcus* - Worobiec, 2010; *Ovoidites* - Rich et al., 1982; *Spicadinium* - Yi, 1997) or slowly flowing (*Sigmopollis* - Van Geel et al. 1983) shallow water. Zygnemataceae are among the most common algae in fresh waters. Most representatives of this cosmopolitan algal group occur in shallow, stagnant, clean, oxygen-rich waters (Worobiec, 2010). The Kılçak-1 pollen assemblage also has an arboreal component (*Pinus*, *Alnus*, *Ulmus*, *Carya*, Engelhardioideae, *Castanea-Castanopsis*) which must have constituted the surrounding vegetation of the freshwater lake/pond.

The Kılçak-2 pollen diagram records the presence of a tree association with the predominance of *Pinus* and a minor proportion of broadleaved trees (*Alnus*, *Ulmus*, *Pterocarya*, *Carpinus*, Engelhardioideae, deciduous *Quercus*, *Carya*, *Juglans*). Although *Pinus* is usually over represented in pollen diagrams because of its prolific pollen production and long distance transport (Denton and Karlen, 1973; Suc and Drivaliari, 1991; Traverse 2008), a mean value of 95 indicates the presence of an *in situ* pine forest. Minor amounts of Poaceae, Asteraceae-Cichorioideae and

Dipsacaceae probably reflect the understory within this forest. This mixed forest constituted the upland extention of the arboreal vegetation identified through the Kılçak-1 palynoflora.

The Sülüklügöl pollen flora is dominated by trees. *Pinus* dominates this flora with continuous presence of Cupressaceae and almost continuous presence of Taxodiaceae and Engelhardioideae. Cupressaceae pollen grains can not be identified to lower taxonomic levels. However, as frequency trends of Cupressaceae and Taxodioideae are similar, it is assumed that Cupressaceae were represented by taxa requiring warm and humid conditions, such as those (e.g., *Chamaecyparis*) living today in wetlands along the Gulf Coast of the United States (Mylecraine et al., 2004). The Sülüklügöl palynoflora indicates a topogenous mire vegetation.

The data obtained from this study indicates that during the early Miocene a *Taxodium* topogenous mire was developed in the Kılçak area near the lake shore. *Sparganium* represents a floral assemblage bordering the freshwater lake. Near the lake a riparian forest consisting of *Carya*, *Alnus*, *Salix* and *Pterocarya* was developed. This forest hosted some ferns characterized by the dominance of *Osmunda* and less *Laevigatosporites haardti* (Polypodiaceaea). The poor record of non-bisaccates of altogether (< 5 %) and the low diversity of arboreal taxa in general usually indicate the absence of local forest vegetation. However, there were tree associations composed dominantly of *Pinus* and broadleaved angiosperms (Engelhardioideae, *Carpinus*, *Castanea-Castanopsis*, deciduous *Quercus*, *Juglans* and *Ulmus*), and a herbaceous ground cover (Gramineae and Chenopodiaceae/Amaranthaceae).

Neogene swamp forest with Taxodioideae, alike Sülüklügöl, as main components and associated mainly with Cupressaceae, *Nyssa* and *Glyptostrobus* are identified from many European basins by palynological studies (Stach et. al., 1982; Nagy, 1992*a*,*b*; Kohlman-Adamska, 1993; Popescu, 2001; Yavuz-Işık, 2007; Yavuz-Işık and Demirci, 2009; Larsson et al., 2011; Ivanov and Worobiec, 2017; Biltekin, 2017). Kohlman-Adamska (1993) stated that pollen analysis of the Neogene deposits from the Wyrzysk region (north-western Polland) revealed the presence of a Taxodiaceae-Cupressaceae forest with *Taxodium, Nyssa, Glyptostrobus, Alnus, Salix, Betula, Palmae*, Polypodiaceae, Osmundaceae, Cyperaceae, Gramineae and *Typha* associated with a mixed deciduous-coniferous forest, a riparian forest, a mire and wetlands.

4.4. Palaeoclimate Implications

Wick (2000) showed that terrestrial plant ecosystems respond fairly well to environmental changes and minor climatic fluctuations are significantly more distinct in the pollen record than in other proxy data. Thus the consistent and continuous occurrence of mega-mesothermic and mesothermic plants within the Kılçak area (Figure 10) points to a subtropical to warm temperate climate.

Mega-mesothermic elements are rich in early Miocene coal-forming basins of Europe (Takahashi and Jux, 1991; Kohlman-Adamska, 1993; Kvacek, 1998; Kolcon and Sachsenhofer, 1999; Yavuz-Işık, 2007; Kayseri-Özer 2013; Bouchal et. al., 2016, 2017). *Taxodium* and *Glyptostrobus* are main components of these mire forests. Today *Taxodium distichum* is present in the coastal mires of northeastern America (Thompson et al., 1999) and *Glyptostrobus* grows in swampy lowlands within the evergreen broad-leaved forest in China (Chen and Chen, 1998).

Comprehensive palaeobotanical and palynological studies conducted on Miocene assemblages of Europe (Thomson and Pflug, 1953; Sadowska, 1997; Figueiral et al., 1999; Kolcon and Sachsenhofer, 1999; Magyar et al., 1999; Nagy, 1992*a*; Ivanov et al., 2002, 2011; Erdei et al., 2007; Bouchal et. al., 2016, 2017), show that generally a warm temperate vegetation prevailed, with a humid/semihumid character, influencing the changing floras during the Miocene. In wet areas, mire-forest associations thrived (Utescher et al., 2007) like that of the Kılçak area.

CA results reveal warm temperate, humid climate conditions, with MAT ranging from 13.8–17 °C, CMT from 3.1 to 9.7 °C and WMT from 20.6 to 26.1 °C, with Engelhardioideae in each case determining the lower CA interval limits (Table 1). The high MAP (740–1548 mm), MPwet (150–159 mm), and MPwarm (79–116 mm) values also relate to the presence of Engelhardioideae (Table 1). In the early Miocene, the Kılçak area experienced warm temperate (MAT ~14–20 °C), overall humid (MAP ~750–1500 mm) conditions of a C Koeppen climate type (Kottek et al., 2006).

Ivanov et al. (2011) examined Miocene vegetation and climate dynamics in the Eastern and Central

Paratethys and stated that early Miocene climate was warm and humid with MAT values mainly above 16 °C and annual rainfalls over 1000 mm. Akkiraz et al. (2011) calculated palaeoprecipitation values, based on palynoflora, specifically for Turkey, and stated that MAP exceeded 1200 mm during the Aquitanian and early-middle Serravallian. The authors also calculated the precipitation of the driest month (LMP) and suggested values between 36 and 48 mm which indicates humid conditions in the Aquitanian. Akgün et al. (2007) stated that warm subtropical climatic conditions prevailed in western Anatolia during the Chattian and Aquitanian periods with MAT values between 16.5–21.3 °C. Additionally, Yavuz-Işık et al. (2011) stated that the MAP was between 1000 and 1100 mm and the MAT was between 14.6 and 16.6 °C in the early-middle Miocene by examining sedimentary sequences of Eskihisar lignite mine (Muğla, SW Anatolia). Kayseri-Özer (2013) calculated MAT values between 13.3–20.8 °C and MAP between 1122–1595 mm based on early Miocene palynoflora identified from Muş area (eastern Anatolia). The climatic conditions reflected by the early Miocene Kılçak palynoflora is in accordance with the aforementioned studies.

5. Conclusions

The palynological data of Kılçak and Sülüklügöl sections enabled the reconstruction of the vegetation and climate in the Kılçak area during the early Miocene.

The Kılçak-1 section was dominated by fresh water alga. The vegetation of this section has moderate amount of *Pinus* (max. 28%) and lesser amounts of deciduous trees and Asteraceae. The vegetation in the Kılçak-2 section was dominated by *Pinus* with minor occurrences of broadleaved trees (*Alnus, Ulmus, Pterocarya*, *Carpinus orientelis, C. betulus,* deciduous *Quercus*, evergreen *Quercus, Carya, Castanea, Juglans, Salix*, Oleaceae) and herbs (Brassicacaeae, Poaceaea, Asteraceae-Cichorioideae, Chenopodiaceae-Amaranthaceae, Dipsacaceae). The vegetation in the Sülüklügöl section was dominated by *Pinus* with moderate amount of Cupressaceae and lesser amounts of Taxodioideae, Engelhardioideae, *Ulmus, Salix, Carya* and deciduous *Quercus*.

All in all, the late Miocene Kılçak flora reflects presence of a freshwater body (with *Spicadinium*, Zygnemataceae, and *Botryococcus*) surrounded sparsely by Gramineae and Chenopodiaceae and associated with a riparian vegetation (*Carya, Alnus*, *Salix* and *Pterocarya*) and tree associations composed of *Pinus* and warmth-loving Angiosperms. Such vegetation suggests a humid, warm temperate climate for the Kılçak area as supported by the CA analysis (MAT ~14–20 °C and MAP ~750–1500 mm). The $\delta^{13}C$ values (between −24.6‰ and −27.0‰) indicate a predominance of C3 plants.

Acknowledgements

This research was funded by the project 2013-30-14-17 (General Directorate of Mineral Research and Exploration, Ankara). We like to thank Torsten Utescher for his constructive comments and appreciate his help for CA Analysis. The suggestions of Thomas Denk, Mine Sezgül Kayseri-Özer and an anonymous reviewer also contributed to manuscript.

References

Akkiraz, M. S., Akgün, F., Utescher, T., Bruch, A. A., Mosbrugger, V. 2011. Precipitation gradients during the Miocene in Western and Central Turkey as quantified from pollen data. Palaeogeography, Palaeoclimatology, Palaeoecology, 304 (3–4), 276-290.

Akgün, F., Kayseri, M. S., Akkiraz, M. S. 2007. Paleoclimatic evolution and vegetational changes during the Late Oligocene– Miocene period in Western and Central Anatolia (Turkey). Palaeogeography Palaeoclimatology Palaeoecology 253, 56–90.

Bender, M. M. 1971. Variations in the $^{13}C/^{12}C$ ratios of plants in relation to the pathway of photosynthetic carbon dioxide fixation. Phytochemistry, 10, 1239-1243.

Biltekin, D., 2017. Palaeovegetational and Palaeoclimatic Changes During the Early Miocene in Central Taurus, Turkey. Yerbilimleri, 38 (1), 101-114.

Bouchal, J. M., Zetter, R., Grímsson, F., Denk, T. 2016. The middle Miocene palynoflora and palaeoenvironments of Eskihisar (Yatağan basin, south-western Anatolia): a combined LM and SEM investigation. Botanical Journal of the Linnean Society, 182, 14–79.

Bouchal, J. M., Mayda, S., Akgün, F., Grímsson, F., Zetter, R., Denk, T. 2017. Miocene palynoflora of the Tınaz lignite mine, Muğla, southwest Anatolia: taxonomy, palaeoecology and local vegetation change. Review of Palaeobotany and Palynology, 243: 1–36.

Bruijn, H. De, Saraç, G. 1992. Early Miocene rodent faunas from eastern Mediterranean area. Part II. Mirabella (Paracricetodontinae, Muroidea). Proc. Kon. Nederl. Akad. Wetensch., Amsterdam, B 95, 25-40.

Bruijn, H. De, Fahlbusch, V., Saraç, G., Ünay, E. 1993. Early Miocene rodent faunas from eastern Mediterranean area. Part III. The genera Deperetomys and Cricetodon, with a discussion on the evolutionary history of the Cricetodontini. Proc. Kon. Nederl. Akad. Wetensch., Amsterdam, B 96, 151-216.

Bruijn, H. De, Koenigswald, W. Von. 1994. Early Miocene rodent faunas from eastern Mediterranean area. Part V. The genus Enginia (Muroidea) with a discussion of the structure of the incisor enamel. Proc. Kon. Nederl. Akad. Wetensch., Amsterdam, B 97, 381-405.

Chen, L., Chen, Q. 1998. The forest diversity in China. In: Boufford, D.E., Ohba, H. (Eds.), Sino-Japanese flora, its characteristics and diversification. The University of Tokyo Bulletin, 37, Tokyo.

Denton, G. H., Karlen, W. 1973. Holocene climatic variations—their pattern and possible cause. Quaternary Research, 3, 155–205.

Erdei, B., Hably, L., Kázmér, M., Utescher, T., Bruch, A.A. 2007. Neogene flora and vegetation development of the Pannonian domain in relation to palaeoclimate and palaeogeography. Palaeogeography, Palaeoclimatology, Palaeoecology, 253 (1–2), 115-140.

Faegri, K., Iversen, J. 1989. Textbook of Pollen Analysis. Wiley, Chichester, 327p.

Fauquette, S., Suc, J.-P., Bertini, A., Popescu, S.-M.,Warny, S., Bachiri Taoufic, N., Perez Villa, M.-F., Chikhi, H., Feddi, N., Subally, D., Clauzon, G., Ferrier, J. 2006. How much did climate force the Messinian salinity crisis? Quantified climatic conditions from pollen records in the Mediterranean region. Palaeogeography, Palaeoclimatology, Palaeoecology, 238, 281–301.

Figueiral, I., Mosbrugger, V., Rowe, N. P., Ashraf, A. R., Utescher, T., Jones, T. P. 1999. TheMiocene peat-forming vegetation of northwestern Germany: an analysis of wood remains and comparisons with previous palynological interpretations. Review of Paleobotany and Palynology, 104, 239–266.

Grimm, E. C. 2005. TILIA and TILIA GRAPH. PC spreadsheet and graphics software for pollen data, llinois State Museum, Springfield.

Håkansson, S. 1985. A review of various factors influencing the stable carbon isotope ratio of organic lake sediments by the change from glacial to postglacial environmental conditions. Quaternary Science Reviews, 4, 135 -146.

Hoek Ostende, L. W. Van den. 1992. Insectivore faunas from the Lower Miocene of Anatolia. Part 1. Erinaceidae. Proc. Kon. Nederl. Akad. Wetensch., Amsterdam, B 95, 437-467.

Hoek Ostende, L. W. Van den. 1995*a*. Insectivore faunas from the Lower Miocene of Anatolia. Part 2. Dinosorex (Heterosoricidae). Proc. Kon. Nederl. Akad. Wetensch., Amsterdam, B 98, 1-18.

Hoek Ostende, L. W. Van den. 1995*b*. Insectivore faunas from the Lower Miocene of Anatolia. Part 3. Dimylidae. Proc. Kon. Nederl. Akad. Wetensch., Amsterdam, B 98, 19-38.

Ivanov, D., Ashraf, A. R., Mosbrugger, V., Palamarev, E. 2002. Palynological evidence for Miocene climate change in the Forecarpathian Basin (Central Paratethys, NW Bulgaria). Palaeogeography, Palaeoclimatology, Palaeoecology, 178, 19–37.

Ivanov, D., Utescher, T., Mosbrugger, V., Syabryaj, S., Djordjević-Milutinovic, D., Molchanoff, S. 2011. Miocene vegetation and climate dynamics in Eastern and Central Paratethys (Southeastern Europe). Palaeogeography, Palaeoclimatology, Palaeoecology, 304, 262–275.

Ivanov, D., Worobiec, E. 2017. Middle Miocene (Badenian) vegetation and climate dynamics in Bulgaria and Poland based on pollen data. Palaeogeography, Palaeoclimatology, Palaeoecology, 467, 83–94.

Jimenez-Moreno, G. 2006. Progressive substitution of a subtropical forest for a temperate one during the middle Miocene climate cooling in Central Europe according to palynological data from cores Tengelic-2 and Hidas-53 (Pannonian Basin, Hungary). Review of Palaeobotany and Palynology, 142, 1–14.

Karadenizli, L. Saraç, G., Şen, Ş., Seyitoğlu, G., Antoine, P. O., Kazancı, N., Varol, B., Alçiçek, M. C., Gül, A., Erten, H., Esat, K., Özcan, F., Savaşçı, D., Antoine, A., Filoreau, X., Hervet, S., Bouvrain, G., De Bonis, L., Hakyemez, H. Y. 2004. Çankırı – Çorum havzasının batı ve güney kesiminin memeli fosillere dayalı Oligo-Miyosen biyostratigrafisi ve dolgulama evrimi. Directorate of Mineral Research and Exploration Report No: 10706, 199 s. Ankara (unpublished).

Kaymakçı, N. 2000. Tectono-stratigraphical evolution of the Çankırı Basin (Central Anatolia, Turkey). Doktora Tezi, Geologica Ultraiectina No. 190., 247 p.

Kayseri-Özer, M. S. 2013. Spatial distribution of climatic conditions from the Middle Eocene to Late Miocene based on palynoflora in Central, Eastern and Western Anatolia. Geodinamica Acta, 26 (1-2) 122-157.

Kohlman-Adamska, A. 1993. Pollen analysis of the Neogene deposits from the Wyrzysk region, north-western Poland. Acta Paleobotanica, 31 (3), 91–297.

Kolcon, I., Sachsenhofer, R. F. 1999. Petrography, palynology, and depositional environments of the early Miocene Oberdorf lignite seam (Styrian Basin,Austria). International Journal of Coal Geology, 41, 275–308.

Kottek, M., Grieser, J., Beck, C., Rudolf, B., Rubel, F. 2006. World Map of the Köppen–Geiger climate classification updated. Meteorologische Zeitschrift, 15, 259–263.

Kvacek, Z. 1998. Bilinia: a window on Early Miocene marshland environments. Review of Palaeobotany and Palynology, 101, 111–123.

Larsson, L. M., Dybkjær, K., Rasmussen, E. S., Piasecki, S., Utescher, T., Vajda, V. 2011. Miocene climate evolution of northern Europe: A palynological investigation from Denmark. Palaeogeography, Palaeoclimatology, Palaeoecology, 309, Issues 3–4, 161-175.

Maden Tetkik ve Arama Genel Müdürlüğü. 2002. 1/500.000 ölçekli Türkiye Jeoloji Haritası, Sinop Paftası. Maden Tetkik ve Arama Genel Müdürlüğü, Ankara.

Magyar, I., Geary, D. H., Müller, P. 1999. Paleogeographic evolution of the Late Miocene Lake Pannon in Central Europé. Palaeogeography, Palaeoclimatology, Palaeoecology, 147, 151–167.

Moore, P., Webb, J., Collinson, M. 1991. Pollen Analysis. Blackwell, Oxford, 205p.

Mosbrugger, V., Utescher, T. 1997. The Coexistence Approach — a method for quantitative reconstructions of Tertiary terrestrial paleoclimate data using the plant fossils. Palaeogeography, Palaeoclimatology, Palaeoecology, 134, 61–86.

Mylecraine, K. A., Kuser, J. E., Smouse, P. E., Zimmerman, G. L. 2004. Geographic allozyme variation in Atlantic white-cedar, Chamaecyparis thyoides (Cupressaceae). Canadian Journal of Forest Research, 34, 2443–2454.

Nagy, E. 1992*a*. A comprehensive study of Neogene sporomorphs in Hungary. Geologica Hungarica, Series Palaeontologica, Fasiculus 53, 379p.

Nagy, E. 1992*b*. Climatic conditions in the Hungarian Neogene on the basis of palynology. Paleontologica I Evolucio, No. 24-25, 455-459.

Okay, A., Tüysüz, O. 1999. Tethyan sutures of northern Turkey. In «The Mediterranean Basins: Tertiary extension within the Alpine orogen» (eds. B. Durand, L. Jolivet, F. Horváth and M. Séranne). Geological Society, London, Special Publication, 156, 475-515.

Özcan, F. 2003. Kılçak Formasyonunun Çankırı havzası stratigrafisindeki yeri ve tektonik konumu. Yüksek Lisans Tezi, Ankara Üniversitesi Fen Bilimleri Enstitüsü, 43s. Ankara (unpublished).

Popescu, S.-M. 2001. Repetitive changes in Early Pliocene vegetation revealed by high-resolution pollen analysis: revised cyclostratigraphy of southwestern Romania. Review of Palaeobotany and Palynology 120, 181–202.

Rich, F. J., Kuehn, D., Davies, T. D. 1982. The paleoecological significance of Ovoidites. Palynology, 6, 19–28.

Sadowska, A. 1997. Miocene palynology in the Gliwice Region (Upper Silesia), Poland. Bulletin of the Polish Academy of Sciences, Earth Sciences 45, 203–210.

Sickenberg, O., Becker-Platen, J. D., Benda, L., Berg, D., Engesser, B., Gaziry, W., Heissig, K., Hünermann, K. A., Sandaar, P. Y., Schmidt-Kittler, N., Staesche, K., Steffens, P., Tobien, H. 1975. Die Gliederung des höheren Jungtertiärs und Altquartärs in der Türkei nach Vertebraten und ihre Bedeutung für die internationale Neogen-Stratigraphie. Geologisches Jahrbuch B, 15, 1-167.

Stable Isotope Ecology Laboratory-University of Georgia. http://siel.uga.edu/stable - isotope - overview. 26.04.2017

Stach, E., Mackowsky, M. T., Teichmüller, M., Taylor, G. H., Chandra, D., Teichmüller, R. 1982. Stach's Textbook of Coal Petrology. Gebrüder Borntraeger, Berlin, 535p.

Suc, J.-P. 1984. Origin and evolution of the Mediterraneae vegetation and climate in Europe. Nature, 307, 429–432.

Suc J-P., Drivaliari, A. 1991. Transport of bisaccate coniferous fossil pollen grains to coastal sediments: an example from the earliest Pliocene Orb Ria (Languedoc, Southern France). Review of Palaeobotany and Palynology, 70, 247–253.

Şen, Ş., Seyitoğlu, G., Karadenizli, L., Kazancı, N., Varol, B., Araz, H. 1998. Mammalian biochronolgy of Neogene deposits and its correlation with the lithostratigraphy in the Çankırı-Çorum basin, central Anatolia, Turkey. Eclogae Geologicae Helvetiae, 91, 307-320.

Takahashi, K., Jux, U. 1991. Miocene palynomorphs from lignites of the Soma Basin (West Anatolia, Turkey). Bulletin of Faculty of Liberal Arts, Nagasaki University (Natural Science), vol. 32 (81), pp. 7–165.

Thomson, P. W., Pflug, H. 1953. Pollen und Sporen des mitteleuropäischen Tertiärs. Palaeontographica B, 94, 1–138.

Thompson, R. S., Anderson, K. H., Bartlein, P.J . 1999. Atlas of relations between climatic parameters and distributions of important trees and shrubs in North America. United States Geological Survey Special Paper 1650/A, 1-269.

Traverse, A. 2008. Paleopalynology. Springer, Dordrecht, 813p.

Tüysüz, O., Dellaloğlu, A.A. 1994. Orta Anadolu'da Çankırı havzası ve çevresinin Erken Tersiyer'deki paleocoğrafik evrimi. Türkiye 10. Petrol Kongresi Bildiriler Kitabı, 56-75.

Utescher, T., Erdei, B., François, L., Mosbrugger, V. 2007. Tree diversity in the Miocene forests of Western Eurasia. Palaeogeography, Palaeoclimatology, Palaeoecology, 253, 226–250.

Ünay, E. 1994. Early Miocene faunas from eastern Mediterranean area. Part IV. The Gliridae. Proc. Kon. Nederl. Akad. Wetensch., Amsterdam, B 97, 445-490.

Valero-Garces, B. L., Delgado-Huertas, A., Navas, A., Machin, J., Gonzalez-Samperiz, P., Kelts, K. 2000. Quaternary palaeohydrological evolution of a playa lake: Salada Mediana, central Ebro Basin, Spain. Sedimentology, 47, 1135-1156.

Van Geel, B., Hallewas, D. P., Pals, J. P. 1983. A Late Holocene deposits under the Westfriese Zeedijk near Enkhuizen (Prov.Noord-Holland, The Netherlands): palaeoecological and archaeological aspects. Review of Palaeobotany and Palynology, 38, 269–335.

Wick, L. 2000. Vegetational response to climatic changes recorded in Swiss Late Glacial lake sediments. Palaeogeography, Palaeoclimatology, Palaeoecology, 159, 231–250.

Worobiec, E.2010. Late Miocene freshwater phytoplankton from Józefina (Poland). Micropaleontology, 56 (6), 517-537.

Yavuz-Işık, N. 2007. Pollen analysis of coal-bearing Miocene sedimentary rocks from the Seyitömer Basin (Kütahya), Western Anatolia. Geobios 40, 701–708.

Yavuz-Işık, N., Demirci, C. 2009. Miocene spores and pollen from Pelitçik Basin, Turkey–environmental and climatic implications. Comptes Rendus Palevol, 8, 437–446.

Yavuz-Işık, N., Tokmakkaya, P., Utescher, T. 2011. Palaeoclimatic and Palaeovegetational data from the early-Middle Miocene of Western Anatolia (Muğla-Eskihisar). 64. Türkiye Jeoloji Kurultayı, Ankara.

Yi, S. 1997. Zygnematacean zygospores and other freshwater algae from the Upper Cretaceous of the Yellow Sea Basin, southwest coast of Korea. Cretaceous Research, 18, 515 – 544.

PLATE

Plate

1. *Laevigatosporites haardti* (Sülüklügöl)

2. Trilete spore (Sülüklügöl)

3. *Osmunda* (Sülüklügöl)

4. *Pinus* (Sülüklügöl)

5. *Pinus* (Kılçak)

6. Taxodioideae (Sülüklügöl)

7. Cupressaceae (Sülüklügöl)

8. *Carya* (Sülüklügöl)

9. Engelhardioideae (Sülüklügöl)

10. *Ulmus* (Kılçak)

11. *Fagus* (Kılçak)

12. *Sparganium* (Sülüklügöl)

13. a,b) Dipsacaceae (Kılçak)

14. *Botryococcus* (Kılçak)

15. *Spicadinium* (Kılçak)

16. Zygnemataceae (Sülüklügöl)

17. *Spirogyra* (Sülüklügöl)

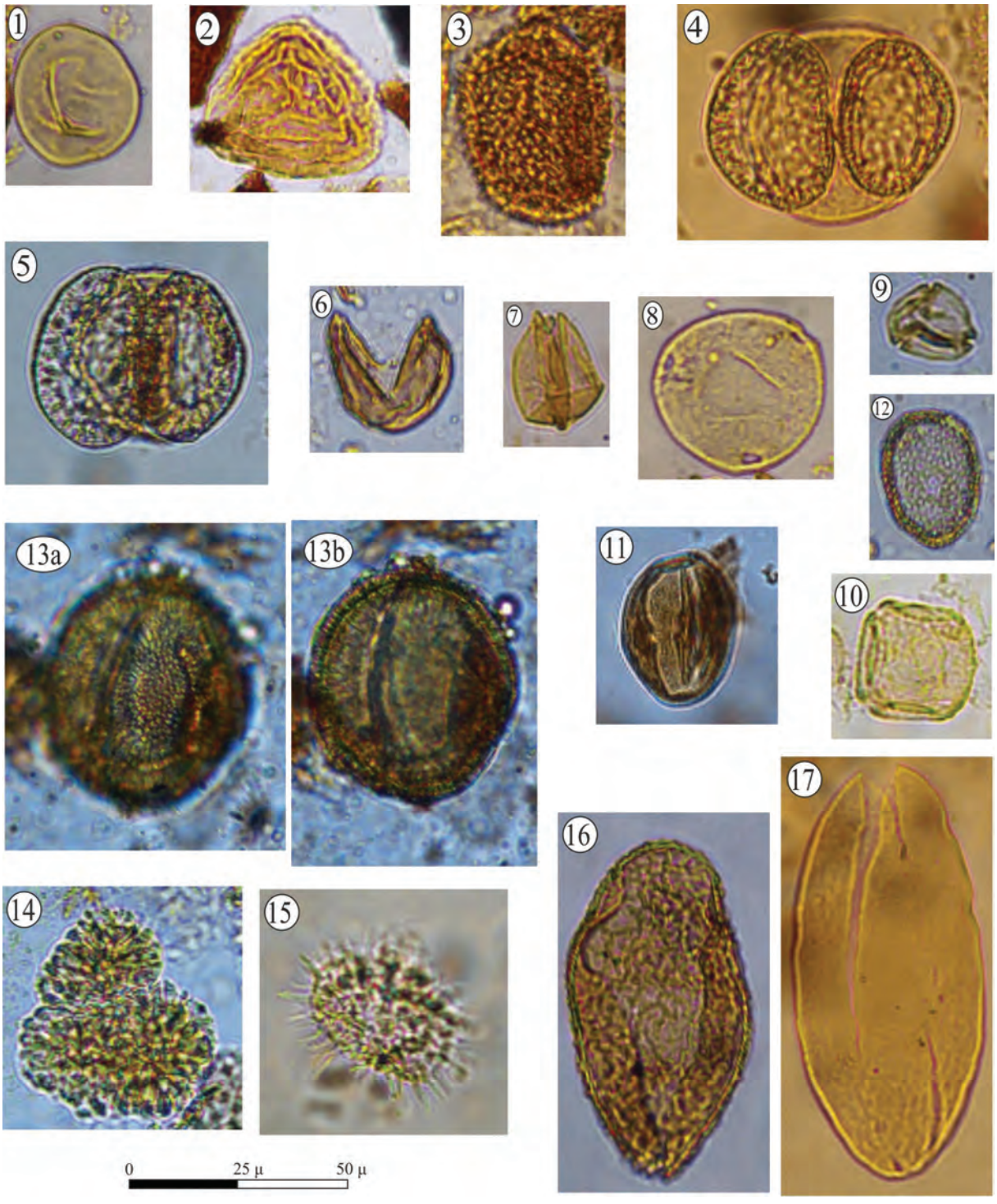
1
2
3
4
5
6
7
8
9
12
13a
13b
11
10
17
16
14
15
0
25 µ
50 µ

Bull. Min. Res. Exp. (2018) 156: 137-150

Bulletin of the Mineral Research and Exploration

http://bulletin.mta.gov.tr

Mineralogical findings from manganese deposits in the Artova Ophiolite Complex, Derbent-Eymir area, Yozgat, Turkey

Nursel ÖKSÜZ[a*]

[a]*Bozok University, Engineering and Architecture Faculty, Department of Geological Engineering, Yozgat, Turkey. orcid.org/0000-0001-7371-3202*

Research Article

Keywords:
Artova ophiolite, manganese oxide, mineralogy, geochemistry, Yozgat-Turkey.

ABSTRACT

The Artova Ophiolitic Complex (AOC), which formed in association with Alpine Ophiolites, is exposed in the NE part of central Anatolia, in the interior of the central Black Sea region and within the borders of Çorum and Yozgat. The Derbent-Eymir manganese- oxide deposit under investigation occurs within this ophiolitic complex. The mineral association in Derbent ore is composed chiefly of pyrolusite, manganite and lesser amounts of ramsdellite, magnetite and goethite. Calcite is the main gangue mineral. The mineral association in Eymir ore is represented by pyrolusite, braunite, neltnerite, jacobsite, psilomelane and trace amount of limonite accompanied by some gangue minerals such as quartz and calcite. Electron microprobe analysis was carried out on pyrolusite, braunite and psilomelane minerals. While pyrolusite from Eymir has higher Si, Al, Mn and Ca, pyrolusite from the Derbent ore has lower Fe, K and Ba contents. Pyrolusite in the Eymir ore has higher Si, Al, Mn and Ca (10.28-7.06; 3.19-1.28; 87.98-81.88; 2.38-1.97 respectively) and lower Fe, K and Ba (0.31-0.16; 0.02-0.00; 0.07-0.00 respectively) contents in comparison to pyrolusite in the Derbent ore. Element variations in core-rim zones of spherical pyrolusites and manganite crystals elongated towards the gangue are quite noticeable. Both Eymir and Derbent ore deposits are low-temperature hydrothermal deposits. Geochemical variations recorded in various manganese minerals are found to be strongly dependent on the changes in pH and temperature of the ore-forming solution and distance to the spreading center.

Received Date: 21.02.2017
Accepted Date: 16.10.2017

1. Introduction

Turkey comprises an E-W trending component of the Alpine-Himalayan orogenic belt which occurs at the border between Laurasia to the north and Gondwana to the south. The Alpine-Himalayan orogenic system was formed by the closure of different branches of the Tethys Ocean. During the closure of the Tethys Ocean, various continental fragments of Laurasia and Gondwana collided. The land of Anatolia has been shaped as an orogenic collage which is composed of these continental fragments and the relict oceanic materials (radiolarian chert, basalt, pelagic shale, pelagic limestone, sandstone and serpentinite) between them (Okay and Tüysüz, 1999). The Artova Ophiolitic Complex (AOC) is one of the ophiolites tectonically sandwiched between the continental fragments and is a part of the Alpine-Himalayan orogenic system (Okay and Tüysüz, 1999). The manganese deposits in Derbent and Eymir (Yozgat) regions formed syngenetically associated with radiolarites in the Alpine ophiolite.

The present work focuses on the mineral paragenesis and geochemistry of manganese deposits in the Derbent and Eymir (Yozgat) areas. The manganese deposits are located 30 km NW and 80 km NE of Yozgat city, respectively. According to geological, mineralogical and geochemical data (major, trace and REE), the Derbent manganese deposit was formed by both hydrothermal and hydrogenous-diagenetic processes (Öksüz 2011*a*). The Eymir deposit was stated to be a volcanosedimentary type deposit where hydrothermal and hydrogenous processes exerted

* *Corresponding author: Nursel ÖKSÜZ, nursel.oksuz@bozok.edu.tr*
http://dx.doi.org/10.19111/bulletinofmre.334245

primary control (Öksüz, 2011*b*). Although Derbent and Eymir deposits are of the same type, their mineral associations are quite different. Thus, this work focuses on the examination of the geochemical and mineralogical variations in the Derbent and Eymir manganese deposits in order to infer which processes or factors were responsible for the observed differences. For this, the mineralogy of the ores was thoroughly examined (ore microscopy, X-ray diffraction, Raman spectroscopy and electron microprobe analysis) and ore paragenesis and structural-textural relations were determined.

2. Geological Setting

The lithologic units in the study area are composed of Paleozoic-Mesozoic metamorphics, radiolarite-bearing ophiolitic series, lower Eocene flysch, Lutetian transgressive series, Lutetian volcanic rocks and Neogene terrestrial sediments. The basement rocks are composed of metamorphic rocks of the Central Anatolian Massif consisting of quartzites, marbles, calcschists and amphibolite schists and crystalline rocks are represented by gabbro, diorite, granite and granodiorite. The basement rocks are overlain by the upper Cretaceous ophiolitic series rocks which are known as the Artova Ophiolitic Complex (AOC) (Özcan et al., 1980). The ophiolitic mélange is composed chiefly of limestone and marl, radiolarite, amygdaloidal basalt, pillow lava and serpentinites. Based on fossil assemblages recorded in the sedimentary units, the emplacement age of the ophiolite was dated to the Upper Cretaceous-Paleocene (Özcan et al., 1980). The lower Eocene sedimentary sequences in this region comprise turbidites which conform to the upper Cretaceous rocks. The basal conglomerate of the Lutetian unconformably overlies the lower Eocene units and partly the ophiolitic series. The lower Eocene units are characterized mostly by thick flysch layers, and lava and tuffs deposited in a shallow marine environment. The Lutetian volcanic series consists of lava including agglomerate, tuffs and tuffites of basaltic and andesitic composition. The upper Cretaceous and Lutetian units in the study area are the products of submarine volcanism (Özcan et al., 1980). The Neogene units consisting of sand, clay and lacustrine sediments are the youngest deposits in the region (Ketin, 1966; Akçay and Beyazpirinç, 2017; Figure 1). The ophiolitic series and lower Eocene rocks underwent several deformation events and therefore, metamorphics and crystalline basement rocks, serpentines and radiolarite-bearing ophiolitic series and lower Eocene layers were intensely fractured and folded.

The Derbent and Eymir manganese oxide deposits, located in the Çorum-Yozgat region in the NE part of central Anatolia and interior central Black Sea region, occur in the Artova Ophiolitic Complex (AOC) (Özcan et al., 1980), which formed in association

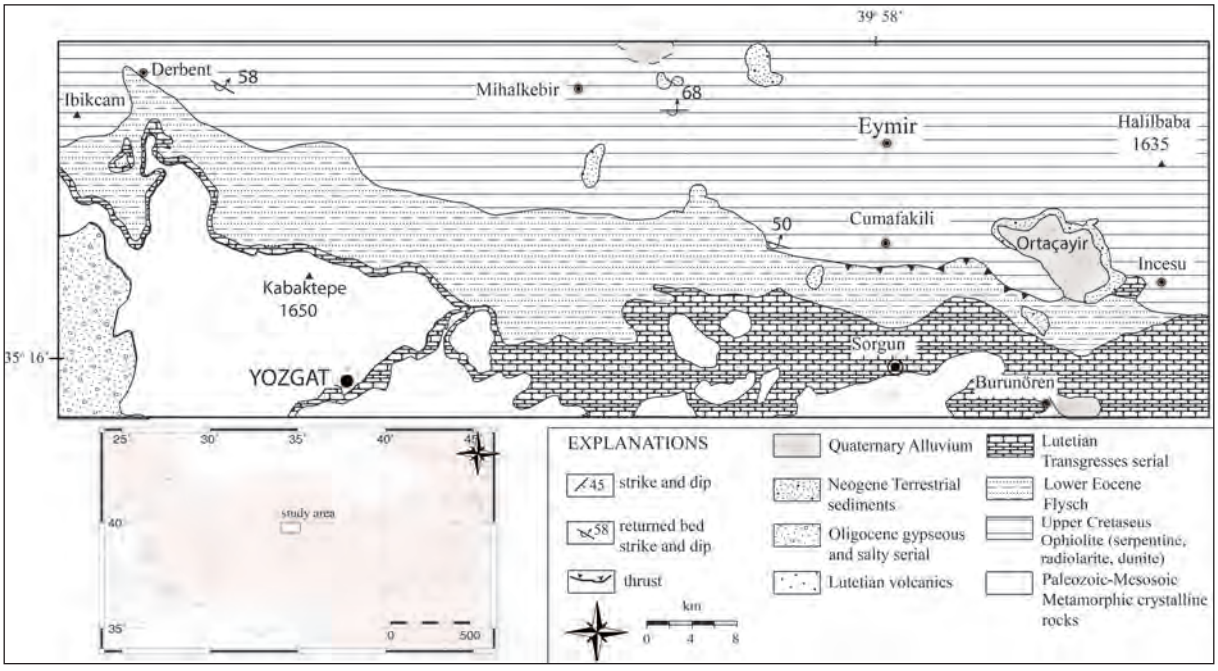

Figure 1- Location and geological map of the Derbent area (modified from Ketin 1966).

with Alpine ophiolites emplaced during the Turonian-Paleocene (Özcan et al., 1980). The manganese deposits in the study area are generally fractured and folded, developed in banded and lenticular shape, and are syngenetic with radiolarite cherts.

3. Materials and Methods

A total of 29 and 20 manganese ore samples (about 500 g) were collected from the Derbent and Eymir manganese oxide deposits, respectively. Forty-nine polished sections were studied with ore microscopy at the Bozok University Laboratory. Petrographic study was supported by X-ray diffraction analyses which were conducted on 10 samples at the of Turkish Petroleum Corporation (TPAO) Laboratories. X-Ray diffraction (XRD) analyses were carried out by a Philips PW 1800 diffractometer with a Cu anode operating at a generator voltage of 40 kV. Major oxide and trace element contents were determined using X-ray fluorescence (XRF) and inductively coupled plasma-optical emission spectrometry (ICP-OES), respectively, and REEs were analyzed via inductively coupled plasma-mass spectrometry (ICP-MS). Ore minerals were also studied with a Thermo Scientific DXR Raman Microscope at the Geological Department of Ankara University. The Raman spectra were evaluated with Crystal Sleuth program. Electron Probe Microanalyser (EPMA) analyses (backscattered electron (BSE) image) were performed by Cameca SX 100 at the laboratories of Austria Leoban University on a total of 51 points for selected pyrolusite, manganite, braunite and psilomelane. Microprobe analysis was conducted on spherical pyrolusite from core to rim of this mineral, while this analysis was done along a traverse from the ore mineral to the gangue (calcite) on elongated manganite.

4. Ore Geology

The deposit in the Derbent area is laminated (Figure 2A), but ore deposits in the Eymir area occur with laminated and lenticular shapes (Figure 2B). Both ore deposits are syngenetically hosted by the radiolarite cherts. The manganese ores associated with the radiolarites are intensively fractured and folded.

4.1. Ore Microscopy

The ore minerals in the Derbent area are mainly pyrolusite and manganite associated with trace amounts of ramsdellite, magnetite and goethite. In the Eymir area, the ore is composed of dominant pyrolusite, braunite, neltnerite, psilomelane and has trace amounts of limonite.

4.1.1. Manganese Minerals

Pyrolusite in Derbent has a typical spherical structure formed by the radiolarites. Radiolarian intervals are very common within the ore samples (Figure 3A). Pyrolusite veinlets occur due to the replacement of radiolarians. These are also present within the calcite veins (Figure 3B). Spherical pyrolusite crystals and radial pyrolusites with a core are observed (Figure 3B). Pyrolusites are mostly anhedral and subhedral. Spherical and radial pyrolusites surrounding a core and overlapping spherical crusts are also observed (Figure 3C, D).

Pyrolusite in this area is accompanied by magnetite and goethite (Figure 4A). The Raman spectra of pyrolusite are shown in figure 5A.

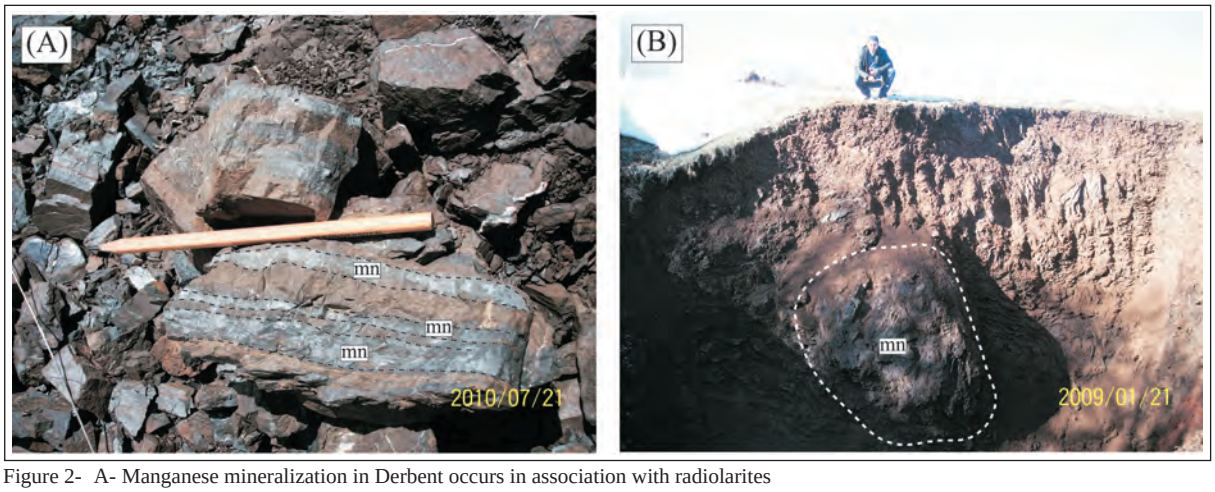

Figure 2- A- Manganese mineralization in Derbent occurs in association with radiolarites
B- Lens shaped mineralization in the Eymir deposit (rd: radiolarite, mn: manganese).

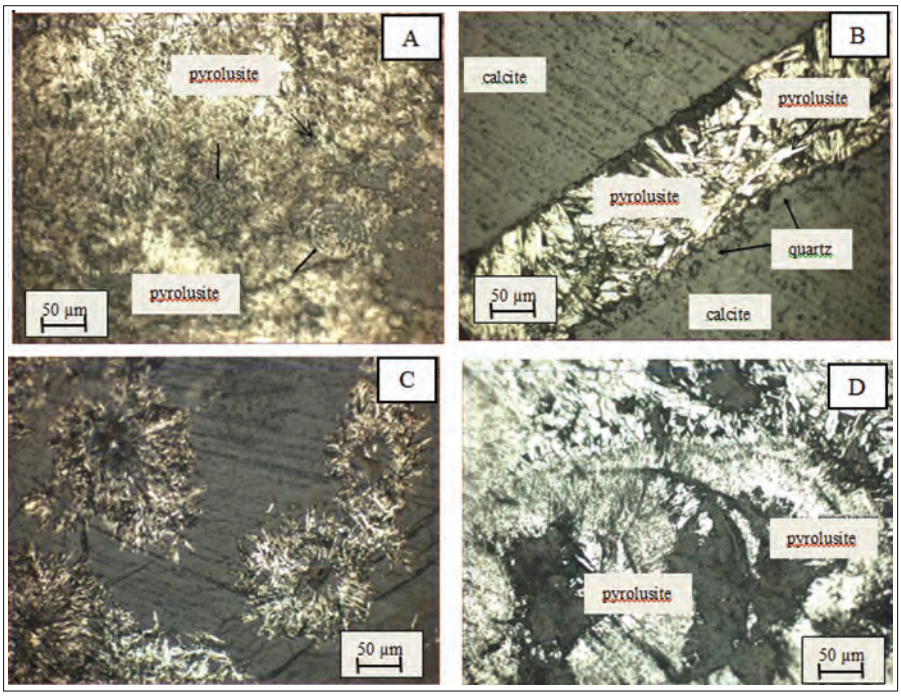

Figure 3- A- Different radiolarite remnants in Eymir: white and yellowish white parts ara pyrolusite, gray parts are gangue. Typical radiolarite remnants in Eymir (it show by arrow). 20x. B- Pyrolusite and quartz vein are settled in the cracks of calcite in Eymir. 20x. C- Radial pyrolusite occurring spherically around the core in Derbent. White and strong blue parts are gangue. 20x. D- The spherical pyrolusite substituted by the gangue in Eymir. Fibrous and barky pyrolusite in Derbent. 20x

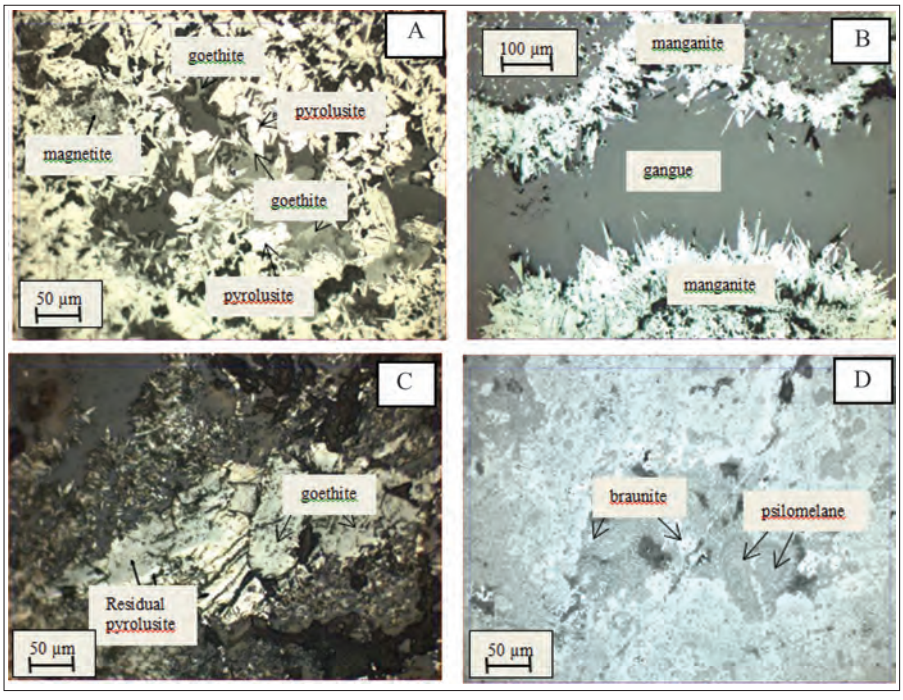

Figure 4- A- Magnetite, pyrolusite and pseudomorps of limonite and pyrolusite in Derbent. Dark gray and black are gangue (d: the pyrolusite is substituted the goethite from the edges of them) 20x. B- Manganite is shown as space filler in Derbent. Manganite crystals elongated towards the gangue (gangue is quartz) 10x. C- Goethiting of pyrolusite in Derbent mineralization. Whites are pyrolusite, grays are goethite. Pyrolusite remnants, thin vein and white parts are seen in goethite. 20x. D- Colloidal manganese mineralization consist of braunite and psilomelane in Eymir (white coloured minerals are braunite, gray coloured minerals are psilomelane). 20x.

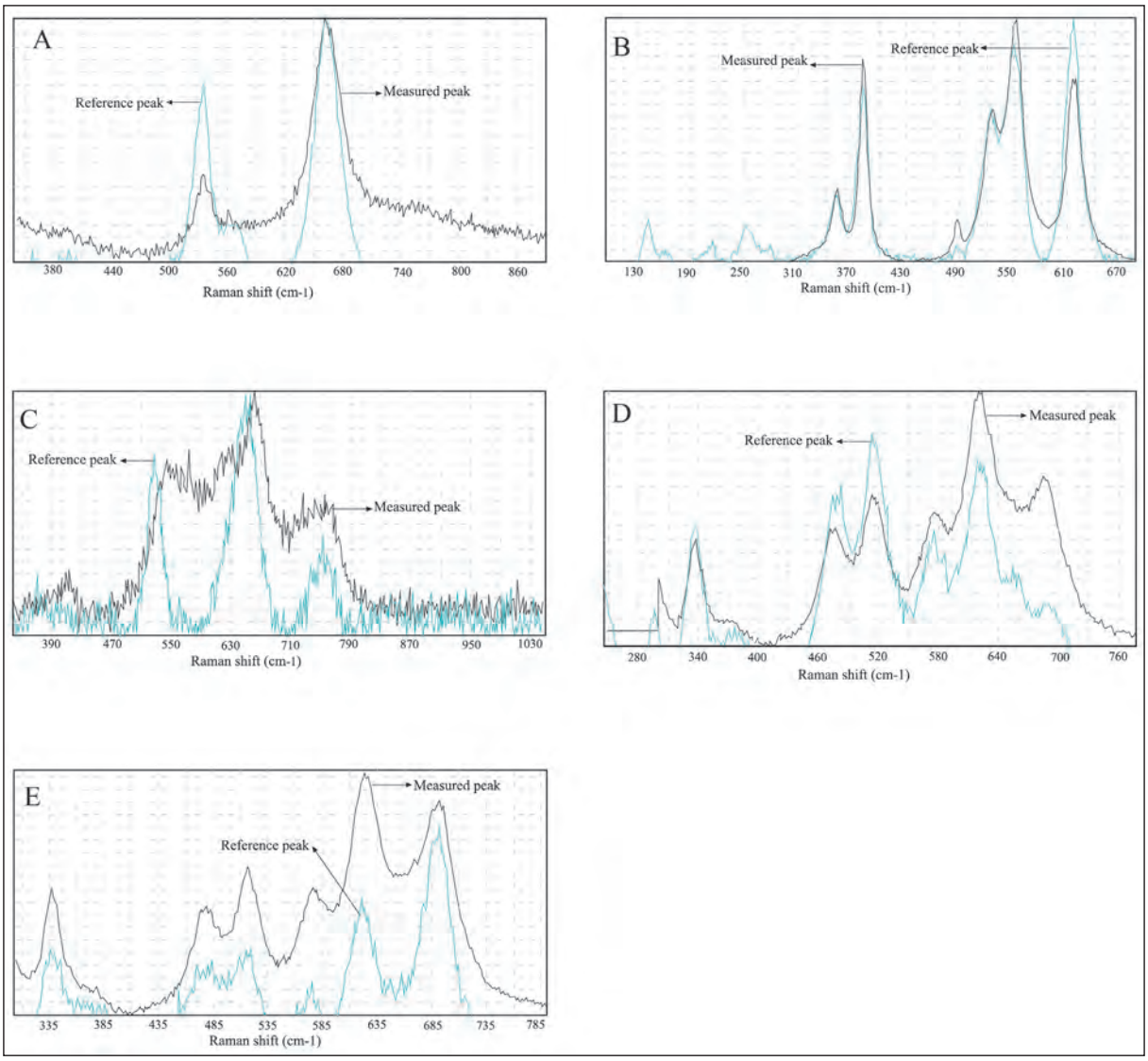

Figure 5- (A) Raman spectra of pyrolusite, (B) Raman spectra of manganite, (C) Raman spectra of ramsdellite, (D) Raman spectra of braunite, (E) Raman spectra of neltnerite.

Manganite is the main mineral in the Derbent deposit. The manganite is composed of radial crystals extending into the gangue (Figure 4B). It is also observed as interstitial fill and is noted for gray-brown color and strong anisotropy. Dissolution is also present in the form of capillaries in manganites. In addition, manganites are replaced by quartz. The Raman spectra of manganite are shown in figure 5B.

Ramsdellite was determined by the Raman spectra method (Figure 5C). A secondary mineral in manganese deposits, it formed by inversion of pyrolusite or oxidative dehydrogenation of groutite (Ramdohr, 1980).

Braunite and psilomelane are the most dominant minerals in the Eymir ore. Braunite is characteristic with slight brownish color and weak anisotropy. Psilomelane is gray color and displays strong anisotropy. In polished sections braunite and psilomelane are found together. Braunite associated with psilomelane in the deposit is characterized by colloidal textures and the psilomelane occurs as euhedral grains (Figure 4D). The Raman spectra of braunite are shown in figure 5D.

Neltnerite is the Ca-analogue of braunite observed in hydrothermal manganese oxide deposits (Baudracco-Grittie, 1985). Neltnerite is isostructural

with braunite. The Raman spectra of neltnerite are shown in figure 5E.

4.1.2. Iron Minerals

Magnetite and goethite in the Derbent ore are uncommon minerals and goethite mostly occurs due to alteration of pyrolusite (Figure 4C).

Jacobsite is observed to be associated with limonite as inclusions in pyrolusite. These pyrolusites are thought to be the product of inversion of jacobsite. The cracks within jacobsite are filled with gangue minerals. During this transformation, jacobsite becomes limonite with a greenish blue tone, replacing gray from the edges.

4.2. Mineral Chemistry

Microprobe analyses were conducted on pyrolusite, manganite, braunite and psilomelane from both Derbent and Eymir deposits. The analyses are shown in tables 1-3. Jacobsite and magnetite are too fine-grained to be analyzed.

Based on the results of microprobe analysis of pyrolusite samples, the average chemical formula of pyrolusite from the Derbent area was computed as $(Mn_{1.91\text{-}1.80}Fe_{0.03\text{-}0.01}Si_{0.03\text{-}0.01}Al_{0.07\text{-}0.01}K_{0.03\text{-}0.01}Ba_{0.03\text{-}0.00})O_2$ and from the Eymir area was computed as $(Mn_{1.59\text{-}1.36}Fe_{0.03\text{-}0.00}Si_{0.24\text{-}0.15}Al_{0.08\text{-}0.03}Ca_{0.05\text{-}0.04})O_2$.

Based on the results of microprobe analysis, pyrolusite from the Eymir ore (with average concentrations of Si: 9.81%; Al: 2.40%; Mn: 84.87%; Ca: 2.14%) has higher Si, Al and Ca content in comparison to pyrolusite from the Derbent ore (with average concentrations of Si: Si: 0.73%; Al: 1.64%; Mn: 94.16%; Ca: 0.28%). In addition, Fe, K and Ba concentrations in pyrolusite from the Eymir area (with average concentrations of Fe: 0.44%; K: 0.01%; Ba: 0.03%) are lower than those from the Derbent area (with average concentrations of Fe 0.85%; K 0.52%; Ba 1.20%) (Tables 1 to 3).

Mn, Fe, K and Ti concentrations from spherical pyrolusite crystals in the Derbent ore are found to increase from core to rim, while K content shows an inverse trend (Figure 6).

Based on the results of microprobe analysis of samples from the Derbent ore, the chemical formula of manganite was computed as $Mn_{1.97\text{-}1.91}Si_{0.04\text{-}0.01}O(OH)$ and the average composition is: Si = 0.91%; Fe = 0.11%; Al = 0.09%; Mn = 97.45%; Ca = 0.02%.

Mn, Si and Fe concentrations of elongated manganite crystals in the Derbent ore were examined and it was found that Mn and Si contents increase towards the gangue while Fe content first increases and then partly decreases (Figure 7).

Based on the results of microprobe analysis of samples from the Eymir ore, the chemical formulas of braunite and psilomelane were computed as, $(Mn_{10.29\text{-}9.18}Al_{0.27\text{-}0.05}Fe_{0.03\text{-}0.01}Ca_{0.51\text{-}0.31})O_8[Si_{1.09\text{-}0.60}O_4]$ and $(Si_{0.53\text{-}0.00}Al_{0.11\text{-}0.01}Ti_{0.08\text{-}0.00}Fe_{11.38\text{-}0.01}Mg_{0.49\text{-}0.00}Ca_{0.57\text{-}0.01})Mn_{13.61\text{-}0.00}O_{16}(OH)_4$ with average compositions of braunite and psilomelane of Si: 6.27%; Fe: 0.15%; Al: 0.94%; Mn: 89.21%; Ca: 2.66%, Si: 26.21%; Fe: 0.19%; Al: 0.33%; Mn: 69.97%; Ca: 2.29% respectively.

Table 1- Electron microprobe analyses of manganite (mn) and pyrolusite (pr) samples of Derbent manganese deposit

Samples elements	mn1	mn2	mn3	mn4	mn5	mn6	mn7	mn8	**pr38**	**pr46**	**pr7**	**pr9**	**pr10**	**pr11**	**pr13**	**pr21**	**pr22**	**pr1**
SiO_2	0.89	1.21	0.42	1.26	0.47	1.61	0.85	0.55	0.22	0.34	1.35	0.27	1.34	0.43	1.31	0.46	1.12	0.50
TiO_2	0.07	0.00	0.00	0.15	0.03	0.00	0.00	0.00	0.17	0.35	0.03	0.07	0.07	0.05	0.00	0.13	0.07	0.15
Al_2O_3	0.09	0.17	0.06	0.08	0.11	0.06	0.02	0.13	0.43	1.02	2.80	1.78	1.13	1.76	1.28	2.31	1.15	2.70
Fe_2O_3	0.16	0.14	0.17	0.16	0.09	0.06	0.09	0.04	1.00	1.70	0.37	0.93	0.76	0.81	0.69	0.44	0.77	1.04
MnO	97.30	96.53	98.21	96.94	98.20	96.96	97.24	98.21	94.03	94.06	94.02	95.33	95.99	95.68	92.41	92.49	93.25	94.35
MgO	0.18	0.13	0.17	0.22	0.15	0.27	0.18	0.27	0.07	0.10	0.08	0.05	0.12	0.08	0.00	0.03	0.05	0.15
CaO	0.03	0.03	0.01	0.00	0.04	0.00	0.01	0.01	0.35	0.41	0.22	0.27	0.22	0.20	0.31	0.22	0.34	0.22
Na_2O	0.00	0.00	0.00	0.00	0.11	0.00	0.00	0.00	0.22	0.05	0.00	0.00	0.00	0.00	0.08	0.08	0.11	0.00
K_2O	0.01	0.01	0.00	0.00	0.00	0.01	0.02	0.04	1.14	0.81	0.43	0.39	0.18	0.29	0.43	0.72	0.60	0.25
BaO	0.00	0.00	0.01	0.00	0.00	0.00	0.00	0.08	2.18	0.91	0.58	0.84	0.45	0.58	2.89	1.34	1.59	0.59
Total	98.73	98.22	99.05	98.81	99.20	98.97	98.41	99.33	99.81	99.75	99.88	99.93	100.26	99.88	99.40	98.22	99.05	99.95
Formulae on the basis of 2 Oxygenes																		
	mn1	mn2	mn3	mn4	mn5	mn6	mn7	mn8	**pr38**	**pr46**	**pr7**	**pr9**	**pr10**	**pr11**	**pr13**	**pr21**	**pr22**	**pr1**
Si	0.02	0.03	0.01	0.03	0.01	0.04	0.02	0.01	0.01	0.01	0.03	0.01	0.03	0.01	0.03	0.01	0.03	0.01
Ti	0.00	0.00	0.00	0.00	0.00	0.00	0.00	0.00	0.00	0.01	0.00	0.00	0.00	0.00	0.00	0.00	0.00	0.00
Al	0.00	0.00	0.00	0.00	0.00	0.00	0.00	0.00	0.01	0.03	0.07	0.05	0.03	0.05	0.04	0.06	0.03	0.07
Fe	0.00	0.00	0.00	0.00	0.00	0.00	0.00	0.00	0.02	0.03	0.01	0.02	0.01	0.02	0.01	0.01	0.02	0.02
Mn	1.94	1.93	1.97	1.92	1.96	1.91	1.95	1.96	1.91	1.87	1.80	1.88	1.86	1.88	1.85	1.85	1.86	1.83
Mg	0.01	0.00	0.01	0.01	0.01	0.01	0.01	0.01	0.00	0.00	0.00	0.00	0.00	0.00	0.00	0.00	0.00	0.01
Ca	0.00	0.00	0.00	0.00	0.00	0.00	0.00	0.00	0.01	0.01	0.01	0.01	0.01	0.00	0.01	0.01	0.01	0.01
Na	0.00	0.00	0.00	0.00	0.01	0.00	0.00	0.00	0.01	0.00	0.00	0.00	0.00	0.00	0.00	0.00	0.01	0.00
K	0.00	0.00	0.00	0.00	0.00	0.00	0.00	0.00	0.03	0.02	0.01	0.01	0.01	0.01	0.01	0.02	0.02	0.01
Ba	0.00	0.00	0.00	0.00	0.00	0.00	0.00	0.00	0.02	0.01	0.01	0.01	0.00	0.01	0.03	0.01	0.01	0.01
Total	1.98	1.97	1.99	1.97	1.99	1.96	1.98	1.99	2.03	1.99	1.94	1.98	1.96	1.97	1.99	1.98	1.98	1.96

Table 2- Electron microprobe analyses of braunite (br) samples of Eymir manganese deposit.

Samples element	br6	br8	br9	br12	br15	br16	br17	br19	br20	br21	br25
SiO_2	5.47	7.21	4.81	8.58	6.68	5.74	8.48	5.70	4.53	5.63	6.13
TiO_2	0.07	0.02	0.13	0.00	0.00	0.00	0.01	0.00	0.15	0.20	0.00
Al_2O_3	1.66	1.81	0.98	0.36	0.98	1.00	1.38	0.59	0.36	0.30	0.89
Fe_2O_3	0.29	0.16	0.06	0.16	0.07	0.10	0.23	0.07	0.19	0.16	0.16
MnO	88.01	87.33	91.04	87.23	89.32	90.06	86.03	90.58	91.72	90.33	89.71
MgO	0.22	0.15	0.12	0.08	0.02	0.13	0.15	0.05	0.00	0.00	0.12
CaO	3.71	2.24	2.31	2.70	2.55	2.49	2.38	2.87	2.62	2.64	2.70
Na_2O	0.00	0.00	0.11	0.00	0.00	0.05	0.00	0.00	0.00	0.00	0.00
K_2O	0.00	0.01	0.00	0.00	0.00	0.00	0.00	0.00	0.00	0.00	0.00
BaO	0.00	0.03	0.00	0.00	0.00	0.03	0.00	0.00	0.00	0.00	0.06
Total	99.43	98.96	99.56	99.11	99.62	99.60	98.66	99.86	99.57	99.26	99.77
Formulae on the basis of 12 Oxygenes											
	br6	**br8**	**br9**	**br12**	**br15**	**br16**	**br17**	**br19**	**br20**	**br21**	**br25**
Si	0.71	0.92	0.63	1.09	0.86	0.74	1.07	0.74	0.60	0.79	0.74
Ti	0.01	0.00	0.01	0.00	0.00	0.00	0.00	0.00	0.01	0.00	0.02
Al	0.25	0.27	0.15	0.05	0.15	0.15	0.20	0.09	0.06	0.14	0.05
Fe	0.03	0.02	0.01	0.02	0.01	0.01	0.02	0.01	0.02	0.02	0.02
Mn	9.61	9.40	10.12	9.35	9.70	9.89	9.18	9.97	10.29	9.80	10.03
Mg	0.04	0.03	0.02	0.02	0.00	0.03	0.03	0.01	0.00	0.02	0.00
Ca	0.51	0.31	0.32	0.37	0.35	0.35	0.32	0.40	0.37	0.37	0.37
Na	0.00	0.00	0.03	0.00	0.00	0.01	0.00	0.00	0.00	0.00	0.00
K	**0.00**	0.00	0.00	0.00	0.00	0.00	0.00	0.00	0.00	0.00	0.00
Ba	0.00	0.00	0.00	0.00	0.00	0.00	0.00	0.00	0.00	0.00	0.00
Total	11.16	10.95	11.29	10.89	11.07	11.19	10.83	11.21	11.36	11.14	11.22

Table 3- Electron microprobe analyses of psilomelane (ps) and pyrolusite (pr) samples of Eymir manganese deposit.

Samples element	ps10	ps11	ps12	ps14	ps15	ps16	ps17	ps19	ps21	ps22	ps35	**pr1**	**pr2**	**pr3**	**pr4**	**pr6**	**pr7**	**pr8**
SiO_2	25.78	28.88	33.89	21.53	14.38	22.83	32.35	30.02	26.04	22.13	30.53	7.06	8.79	9.17	12.32	9.36	11.72	10.28
TiO_2	0.08	0.03	0.05	0.00	0.00	0.03	0.00	0.00	0.20	0.00	0.05	0.00	0.03	0.03	0.00	0.00	0.03	0.03
Al_2O_3	0.51	0.17	0.25	0.38	0.21	0.19	0.57	0.25	0.36	0.26	0.43	1.28	3.14	2.12	3.06	2.59	1.44	3.19
Fe_2O_3	0.13	0.23	0.16	0.19	0.30	0.36	0.11	0.26	0.13	0.10	0.09	0.16	0.30	0.21	0.30	0.31	0.21	1.62
MnO	70.31	67.03	61.03	75.39	82.31	72.80	64.44	65.29	70.32	74.44	66.35	87.98	85.21	86.23	81.88	85.33	84.33	83.12
MgO	0.15	0.12	0.03	0.00	0.27	0.38	0.31	0.28	0.08	0.03	0.02	0.15	0.25	0.28	0.23	0.15	0.03	0.13
CaO	2.17	2.50	2.24	2.01	2.73	2.83	1.64	2.24	2.50	2.55	1.74	2.38	1.99	2.18	1.97	2.00	2.32	2.13
Na_2O	0.00	0.01	0.00	0.00	0.04	0.04	0.05	0.00	0.01	0.05	0.03	0.00	0.04	0.00	0.08	0.00	0.00	0.00
K_2O	0.02	0.00	0.02	0.00	0.00	0.05	0.04	0.00	0.01	0.01	0.01	0.02	0.00	0.00	0.00	0.00	0.00	0.02
BaO	0.03	0.07	0.07	0.00	0.17	0.17	0.30	0.11	0.04	0.09	0.07	0.03	0.04	0.04	0.00	0.00	0.00	0.07
Total	99.18	99.04	97.74	99.50	100.41	99.68	99.81	98.45	99.69	99.66	99.32	99.06	99.79	100.26	99.84	99.74	100.08	100.59
Formulae on the basis of 20 Oxygenes												**2 Oxygenes**						
	ps10	ps11	ps12	ps14	ps15	ps16	ps17	ps19	ps21	ps22	ps35	**pr1**	**pr2**	**pr3**	**pr4**	**pr6**	**pr7**	**pr8**
Si	4.49	4.90	5.53	3.92	2.81	4.09	5.27	5.05	4.51	0.00	0.01	0.15	0.18	0.19	0.24	0.19	0.23	0.20
Ti	0.01	0.00	0.01	0.00	0.00	0.00	0.00	0.00	0.03	0.06	0.08	0.00	0.00	0.00	0.00	0.00	0.00	0.00
Al	0.10	0.03	0.05	0.08	0.05	0.04	0.11	0.05	0.07	0.02	0.01	0.03	0.08	0.05	0.07	0.06	0.03	0.07
Fe	0.02	0.03	0.02	0.03	0.05	0.05	0.01	0.04	0.02	11.38	9.35	0.00	0.01	0.00	0.00	0.01	0.00	0.03
Mn	10.37	9.63	8.43	11.62	13.61	11.04	8.90	9.31	10.31	0.01	0.00	1.59	1.47	1.49	1.36	1.47	1.43	1.40
Mg	0.04	0.03	0.01	0.00	0.08	0.10	0.08	0.07	0.02	0.49	0.31	0.00	0.01	0.01	0.01	0.00	0.00	0.00
Ca	0.41	0.45	0.39	0.39	0.57	0.54	0.29	0.40	0.46	0.02	0.01	0.05	0.04	0.05	0.04	0.04	0.05	0.05
Na	0.00	0.00	0.00	0.00	0.02	0.01	0.02	0.00	0.00	0.00	0.00	0.00	0.00	0.00	0.00	0.00	0.00	0.00
K	0.00	0.00	0.00	0.00	0.00	0.01	0.01	0.00	0.00	0.01	0.01	0.00	0.00	0.00	0.00	0.00	0.00	0.00
Ba	0.00	0.00	0.00	0.00	0.01	0.01	0.02	0.01	0.00	0.00	0.00	0.00	0.00	0.00	0.00	0.00	0.00	0.00
Total	15.45	15.09	14.45	16.04	17.19	15.91	14.70	14.93	15.43	14.88	14.88	1.83	1.78	1.79	1.73	1.78	1.75	1.76

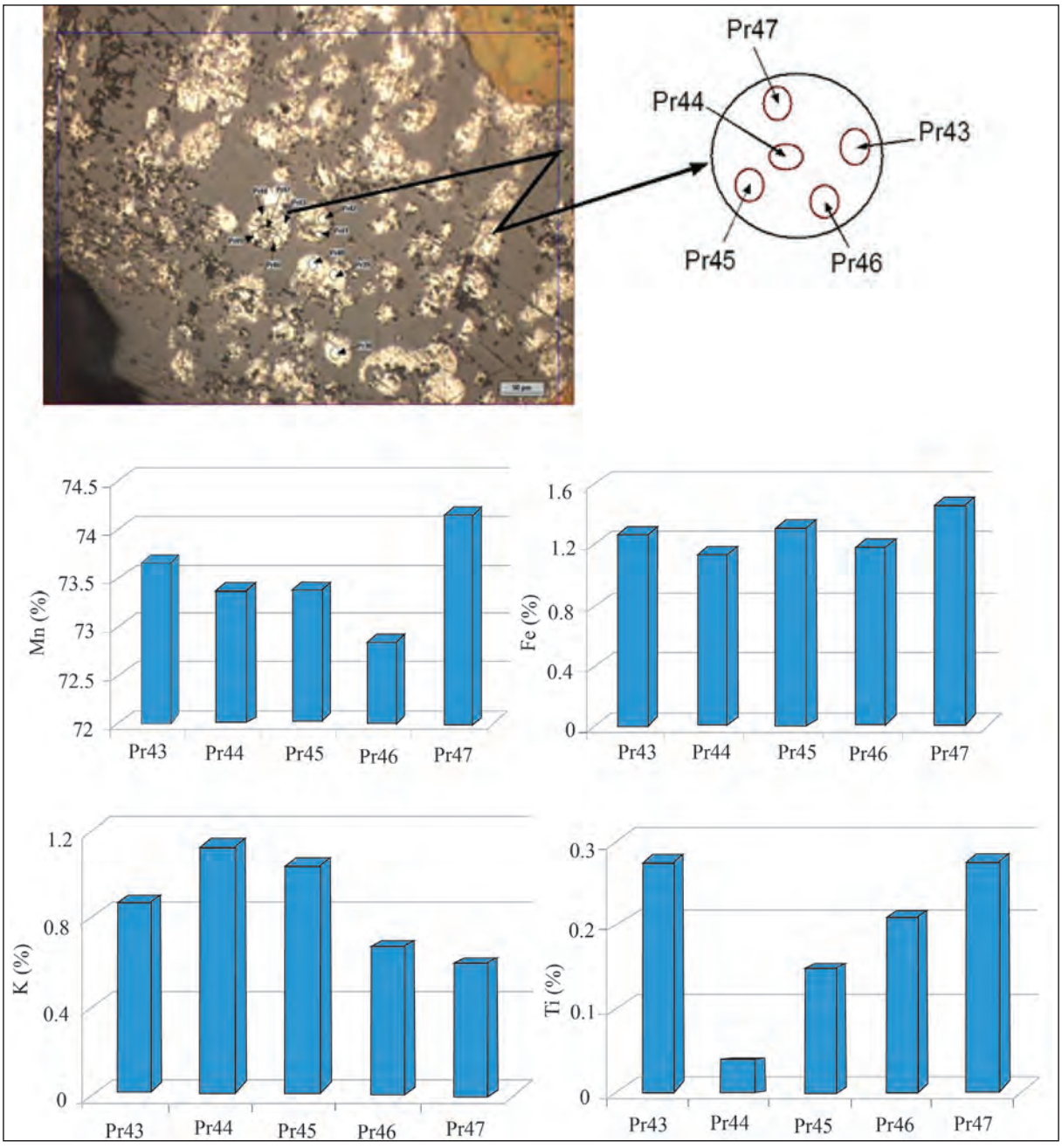

Figure 6- Signed microprobe points in spherical pyrolusite and variation diagram for Mn, Fe, Ti and K concentrations in Eymir region.

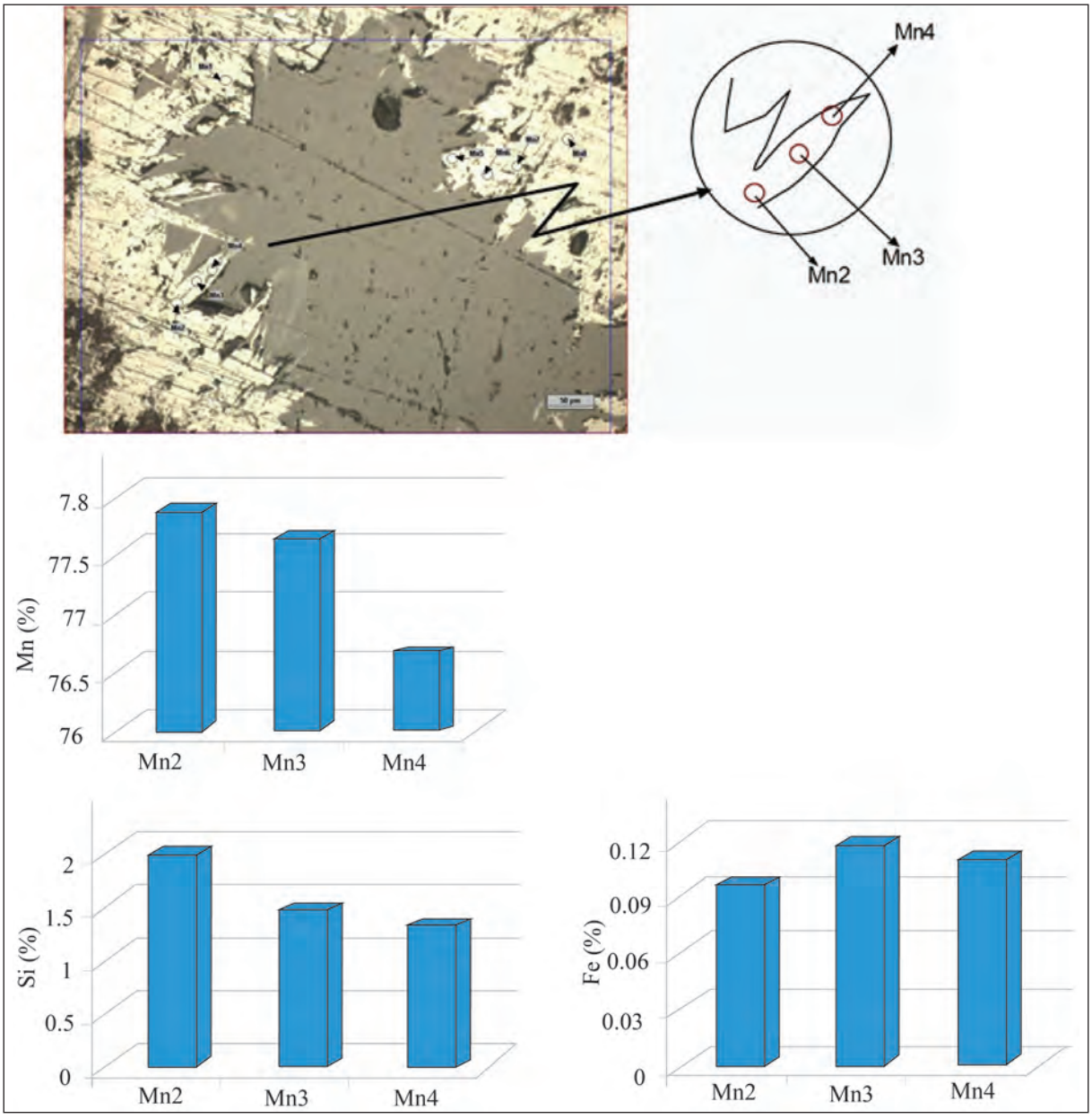

Figure 7- Microprobe measured points in manganite crystals and variation diagram for Mn, Si and Fe concentrations in Derbent region

5. Results and Discussion

The manganese deposits syngenetically occurred with radiolarites within the Artova Ophiolitic Complex (AOC) (Özcan et al., 1980) which developed within Turonian-Paleocene-aged Alpine ophiolitic series. The deposits were also affected by orogenic deformation in the region, thus they are intensely folded and fractured.

In the present work, manganese deposits in these areas were found to have similar geologic characteristics but ore paragenesis and ore mineral chemistry yielded different trends. According to some workers, certain manganese minerals reflect the properties of depositional environment and the origin of mineralization (Stanton, 1972; Roy, 1968; Nicholson, 1992*a*,*b*). For example, rhodochrosite, pyrolusite, cryptomelane, psilomelane and manganite are common manganese minerals within sedimentary deposits. Braunite generally occurs in volcanogenic deposits (Stanton, 1972). Jacobsite, spessartite and rhodonite are formed in metamorphic conditions

and are indicative of increasing temperature. Rhodochrosite occurs in sedimentary, hydrothermal and metamorphosed deposits and is deposited in moderately-reducing environments (Roy, 1968). Manganite, pyrolusite, psilomelane and cryptomelane are minerals characteristic of supergene conditions and are formed by the oxidation of primary manganese minerals (Ramdohr, 1980). Pyrolusite occurs in both supergene and hydrothermal environments and therefore is not an indicator of provenance (Nicholson, 1992*a, b*). It also forms in environments with high oxidation potential regardless of pH value (Krauskopf, 1989). Ramsdellite in the Derbent area is thought to be formed by transformation of pyrolusite. Pyrolusite and manganite are low-temperature minerals but braunite occurs at relatively higher temperatures (Roy, 1997).

Pyrolusite, which is mostly observed in low-temperature hydrothermal deposits, occurs due to the replacement of manganese oxide minerals like manganite and ramsdellite (Ramdohr, 1980). Pyrolusite is observed in both Derbent and Eymir ores. Pyrolusite in the Eymir area is thought to have a supergene origin (Öksüz, 2011*b*) as anhedral pyrolusite pseudomorphs are observed and Si, Al, Mn and Ca contents of pyrolusite in the Eymir ore are higher than those in the Derbent ore. Fe, K and Ba concentrations of pyrolusite in the Eymir area are lower than those in the Derbent area (Tables 1 and 3). Iron is the first soluble element and manganese stays in solution for a longer time (Nicholson, 1992*b*). Precipitation of iron and manganese from the solution requires gradual and regular change in the pH value (Hem, 1972; Krauskopf, 1989). Thus, Fe-rich minerals are found in areas close to the center of active submarine hydrothermal regions since their mobility is low, while manganese oxides are deposited in distal parts of the volcanic area (Choi and Hariya, 1992). Consequently, manganese oxide deposits (the presence of pyrolusite) are indicative of distal areas from spreading center. It is known that both deposits in the study area were rapidly deposited from hydrothermal solutions and are consistent with hydrothermal exhalative manganese deposits in modern spreading centers and formed in distal parts of spreading centers (Öksüz, 2011*b*). Moreover, data from this study indicates that pyrolusites in the Eymir area have higher Mn content and lower Fe content which might indicate that the deposit at Derbent is closer to the spreading center (Öksüz, 2011*a, b*; Öksüz and Okuyucu 2014).

Colloform texture is indicated by concentric rhythmic bands with concave-convex surface, in which the curvature is always convex towards the younger surface. Sometimes, it is observed as spheroid, mammillary, or botryoidal forms (Pettijohn, 1975; Salem, et al., 2012). Spherical and colloidal textures are created by precipitation from colloidal hot aqueous solutions or gels emerging from below (Salem et al., 2012). Space-fill texture is described as the deposition of younger minerals along vugs, fractures and cracks between the older ones. It is observed as the presence of quartz and calcite within manganese and iron minerals (Salem, et al., 2012).

Mn, Fe and Ti concentrations of spherical pyrolusite crystals in the Derbent ore are found to increase from core to rim while K content decreases from core to rim. Mn and Si concentrations of elongated manganite crystals at Derbent increase towards the gangue, while Fe content first increases and then partly decreases. This may be show the change in physicochemical conditions observed in the mineralization (Eh and / or Eh, T, P).

Results of paragenetic and geochemical evaluation indicate that deposits in the Eymir and Derbent areas are low-temperature hydrothermal deposits. Geochemical variations observed in the studied manganese minerals strongly depend on changes in pH-Eh and temperature of the ore-forming solution and distance to the spreading center.

Acknowledgements

This study is supported by The Scientific and Technological Research Council of Turkey (TUBITAK) (project no. 109Y167) and Bozok University Research Fund (project no. B.F.F.M/2009-06). The appreciation is extended to Dr. İbrahim Uysal for his help in EMP analysis.

References

Akçay, A.E., Beyazpirinç, M. 2017. The geologıcal evolution of Sorgun (Yozgat)-Yıldızeli (Sivas) foreland basin, petrographic, geochemical aspects and geochronology of the volcanism active in the basin Bull.Min.Res.Exp., 155, pp.71-80

Baudracco-Gritti, C. 1985. Subslilution du manganese bivalent par du calcium dans les mineraux du groupe: Braunite, neltnerite, braunite II. Bulletin de Mineralogie 108, 437-445.

Choi, J.H., Hariya, Y. 1992. Geochemistry and Depositional Environment of Mn Oxide deposits in the Tokoro Belt. Northeastern Hokkaido, Japan. Economic Geology, 87, 1265-1274.

Hem, J.D. 1972. Chemical Factors that Influence the Availability of Iron and Manganesein Agueous Systems. Geol. Soc. America Bull., 83, 443-450.

Ketin, İ. 1966. Tectonic Units of Anatolia. General Directorate of Mineral Research and Exploration Report no: 66, 20-34, Ankara (unpublished).

Krauskopf, K.B. 1989. Introduction to Geochemistry. McGraw-Hill International Editions, Earth and Planetary Science Series, Km Keong Printing Co. Pte. Ltd. Republic of Singapore 617.

Nicholson, K. 1992*a*. Genetic Types of Manganese Oxide Deposits in Scotland: Indicators of Paleo-Ocean-Spreading Rate and a Devonian Geochemical Mobility Boundary. Economic Geology 87, 1301-1309.

Nicholson, K. 1992*b*. Contrasting Mineralogical-Geochemical Signatures of Manganese Oxides: Guides to Metallogenesis. Economic Geology 87, 1253-1264.

Okay, A., Tüysüz, O. 1999. Tethyan Sutures of Northern Turkey. In: The Mediterranean Basins: Tertiary Extension Within the Alpine Orogen (eds. B. Durand, L. Jolivet, F. Horvath and M. Serrane), Geological Society of London, Special Publication, 156, 475-515.

Öksüz, N. 2011*a*. Geochemistry and the Origin of Manganese Mineralizations in Derbent (Turkey-Yozgat) Region. Bulletin of the Earth Sciences Application and Research Centre of Hacettepe University 32, 213-234

Öksüz, N. 2011*b*. Geochemical Characteristics of the Eymir (Sorgun-Yozgat) Manganese Deposit, Turkey. Journal of Rare Earths, 29 (3), 287-296.

Öksüz N., Okuyucu N. 2014. Mineralogy, Geochemistry, and Origin of Buyukmahal Manganese Mineralization in the Artova Ophiolitic Complex, Yozgat, Turkey. Journal of Chemistry Volume 2014, Article ID 837972, 11 pages http://dx.doi.org/10.1155/2014/837972

Özcan, A., Erkan, A., Keskin, E. 1980. General Geology of the North Anatolian Fault and Kirsehir Massif. General Directorate of Mineral Research and Exploration, Report no: 6722, Ankara (unpublished).

Pettijohn, F.G. 1975. Sedimentary rocks, 3rd edn. Harper and Row, New York, pp. 628.

Ramdohr, P. 1980. The Ore Minerals and Their Intergrowth. Pergamon Press, Oxford, London, New York.

Roy, S. 1968. Mineralogy of the Different Genetic Types of Manganese Deposits. Economic Geology, v. 63, pp. 760-786.

Roy, S. 1997. Genetic Diversity of Manganese Deposition in the Terrestrial Geological Record. In: Nicholson, K., Hein, J. R., Bühn, B. and Dasgupta, S. (eds). 1997. Manganese Mineralization: Geochemistry and Mineralogy of Terrestrial and Marine Deposits. Geological Society Special Publication, London, v. 119, pp. 5-27.

Salem, I.A., İbrahim, M. E., Monsef, M.A.E. 2012. Mineralogy, geochemistry, and origin of hydrothermal manganese veins at Wadi Malik, Southern Eastern Desert, Egypt Arabian Journal of Geosciences, v. 5, pp. 385-406.

Stanton, R.L. 1972. Ore Petrology. McGraw-Hill, New York.

Bull. Min. Res. Exp. (2018) 156: 151-166

Bulletin of the Mineral Research and Exploration

http://bulletin.mta.gov.tr

Petrographic and palynological investigations of Sinanpaşa (Afyon) Miocene coals

Elif AKISKA[a*]

[a]*Ankara University, Faculty of Engineering, Department of Geological Engineering, 06830, Gölbaşı, Ankara. orcid.org/0000-0002-6180-4710*

Research Article

Keywords:
Coal petrography, maceral, palynology, paleoclimate, Afyon.

ABSTRACT

In this study, petrographical and palynological analyses of coal samples from two regions (the Kırka region in the south, and the Karacaören region in the north) of the Sinanpaşa (Afyon) Neogene basin were performed. The coal-bearing Neogene sediments indicate the occurrence of five facies: paleosol, matrix-supported conglomerate, coal-bearing mudstone, sandstone-claystone and laminated mudstones. Coal layers are mainly within coal-bearing mudstone facies. In addition, there are various types of coalified materials in matrix-supported conglomerate and sandstone-claystone facies. Based on coal petrography, an interpretation of the coal-forming environment was made. The investigated coals mainly contain a huminite maceral group. From the reflection values (R_{max}), these coals can be classified as sub-bituminous in rank, and as being deposited in swamp zones associated with limnic environments. The palynological data indicates that all studied coal-bearing units are of Mid-Miocene age. On the other hand, based on MAT, CMT, WMT and MAP parameters, it can be stated that at that time climatic conditions changed seasonally in the study area. Humid climatic conditions prevailed during the period when the peat was formed, then later transformed into the coal layers examined in this manuscript.

Received Date: 22.03.2017
Accepted Date: 25.05.2017

1. Introduction

Many basins, which are bounded by normal faults, were formed in western Anatolia during the Cenozoic (Şengör and Yılmaz, 1981; Robertson and Dixon, 1984; Koçyiğit, 1984; Şengör et al., 1985; Zanchi et al., 1993; Ersoy et al., 2011) and the basins with NW-SE extensions were affected by pre-Neogene fault growth; however, the basins with E-W extensions were formed during the N-S-trending extensional tectonic movement (Kaya, 1979, 1981; Gürsoy et al., 2003; Koçyiğit and Özacar, 2003; Koçyiğit and Deveci, 2007). These basins are filled with thick sedimentary and volcanic deposits. In the case of the sedimentary deposits, they form mainly the alluvial fan, fluvial and lacustrine rock units (Helvacı and Yağmurlu, 1995; Öcal and Göktaş, 2011).

The Sinanpaşa (Afyon) Neogene basin is one of several volcano-sedimentary basins in western Anatolia. The basin has suffered two different periods of volcanic activity, which spread over vast areas during the Cenozoic time interval, and so exhibits differences in terms of volcanism dynamic and age (Aydar, 1998; Francalanci et al., 2000). They are represented by the Seydiler ignimbrites and the Afyon volcanism, respectively (Aydar, 1998). In the case of the Seydiler ignimbrites, they were deposited in the Early Miocene (Yalçın, 1988; Anderson, 1997); while the Afyon volcanism, which developed synchronously with the lacustrine deposition, took place in the Mid-Late Miocene (Besang et al., 1977).

The alluvial fan, the fluvial and lacustrine deposits in the study area were formed in the Mid-Miocene. The coal fields outcropping to the south and north of the research area, the Kırka and Karacaören coal fields, were investigated in this study. Geological investigations in the region were carried out in detail by Karamenderesi (1972), Metin et al. (1987), Kartalkanat et al. (1990) and Koçyiğit and Deveci (2007). In addition; the detailed field surveys of coal

* *Corresponding author: Elif AKISKA, egunen@eng.ankara.edu.tr*
http://dx.doi.org/10.19111/bulletinofmre.363345

seams that form the stages when the lake had first opened, were conducted by Becker-Platen (1967) and Konyalı (1968). There is no data for any petrographical or palynological studies on the coal units until today.

The purpose of this study is to gain information on the climatic conditions of the period, and age of the coal units in the Sinanpaşa Basin with the help of petrographical and palynological investigations. In part of the Western Anatolian Neogene basins similar studies have already been carried out (Akgün and Akyol, 1999; Akgün et al., 2007), and this study will make up for the shortcomings in research in the Sinanpaşa Basin.

2. Regional Geology

The Sinanpaşa Neogene basin is surrounded by Mesozoic dolomite, dolomitic limestone and limestones in the north, Paleozoic Afyon metamorphics formed by metaclastic metavolcanic and recrystallized limestone in the east (Metin et al., 1987) and Mesozoic (Özgül et al., 1991) dolomite, dolomitic limestone and crystallized limestone in the south (Figure 1). The outcropping rocks in the Sinanpaşa basin are formed from Paleozoic and Mesozoic basement rocks, the Neogene basin fill deposits are mostly represented by Miocene and Quaternary units (Karamenderesi, 1972; Çevikbaş et al., 1988) (Figure 2).

Mid-Miocene deposition begins with alluvial fan deposits formed by dark yellow to orange conglomerate, pebbly sandstone and sandstone located in the Kırka region. The thickness of this alluvial fan deposit varies between 50-300 m. This deposit, which forms the basement of Mid-Miocene deposits, overlies the basement with an angular unconformity at the bottom, and is overlain by the Mid-Miocene lacustrine deposits in lateral and vertical transitions (Metin et al., 1987). The lacustrine deposits of the Mid-Miocene time are represented by the carbonate facies to the north and south of the basin. In stages, when the lake was first opened, the coal-bearing sediments were deposited.

Coal-bearing deposits are wide spread in around the Kırka region in S-SW, and in the Karacaören region in N-NW parts of the basin. The thickness of the coal-bearing layers, which have many lateral continuities, is a few meters, and located within a 150-200 m thick deposit. This deposit was studied from bottom to top in 5 facies; a) paleosol, b) matrix supported conglomerate, c) coal-bearing mudstone, d) sandstone-claystone and e) dirty white laminated mudstone (Figure 3).

a) Paleosol: The red paleosol layers, which forms the lowest section, can be observed in the form of 40-70 cm thick interlayers among yellow-red mudstone, siltstone and sandstone and, occasionally conglomerates can be observed. In them, pebble grains with limestone-marble components are located, mostly of metamorphic origin. The cross bedded sandstones with very fine to fine sand can also be observed at the bottom of the paleosol zones.

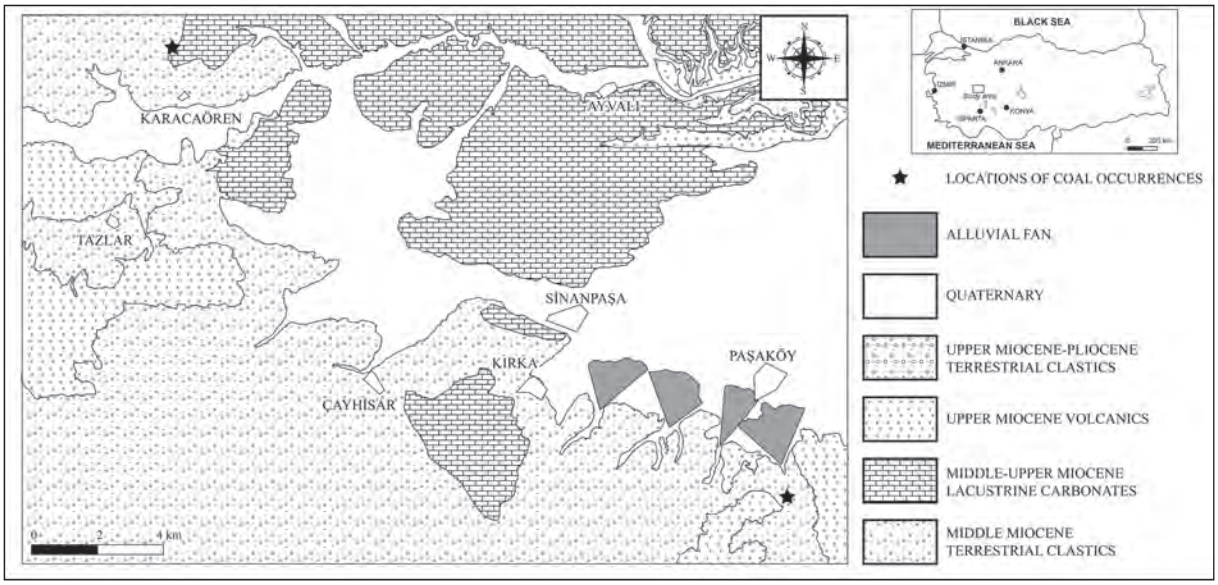

Figure 1- Geological map of Sinanpaşa (Afyon) basin (modified from Metin et al., 1987).

b) Matrix supported conglomerate: It overlies the paleosol layer and has a thickness of 15-20 m. The bottom of this unit, which can be observed as having white-gray tones, is erosional. When its macroscopic features are examined, it can be seen that the pebbles are bonded by the matrix, which is formed from the carbonate sand and carbonate mud. The layers become markedly thinner in a lateral direction within a few 100 meters. In the upper parts of these conglomerate layers the mudstone dramatically increases, as well as the low graded coal layers.

c) Coal-bearing mudstone: This facies is made-up of 5-15 cm thick coal-bearing layers which alternate with gray mudstone. There are 5 coal seams in it. The total thickness of the coal with clayey interlayers is around 5 m. Coal-bearing layers thin-out and disappear into the mixture of micro breccia and mudstone lithology, at the endpoints of a few hundred meter lateral dispersion in a NE-SW direction (Figure 3). These are dark brown-black in color, with intercalations of laminated mud, and contain many plant roots. Thinning out coal-bearing layers reflect the feature of a typical peat with characteristics of

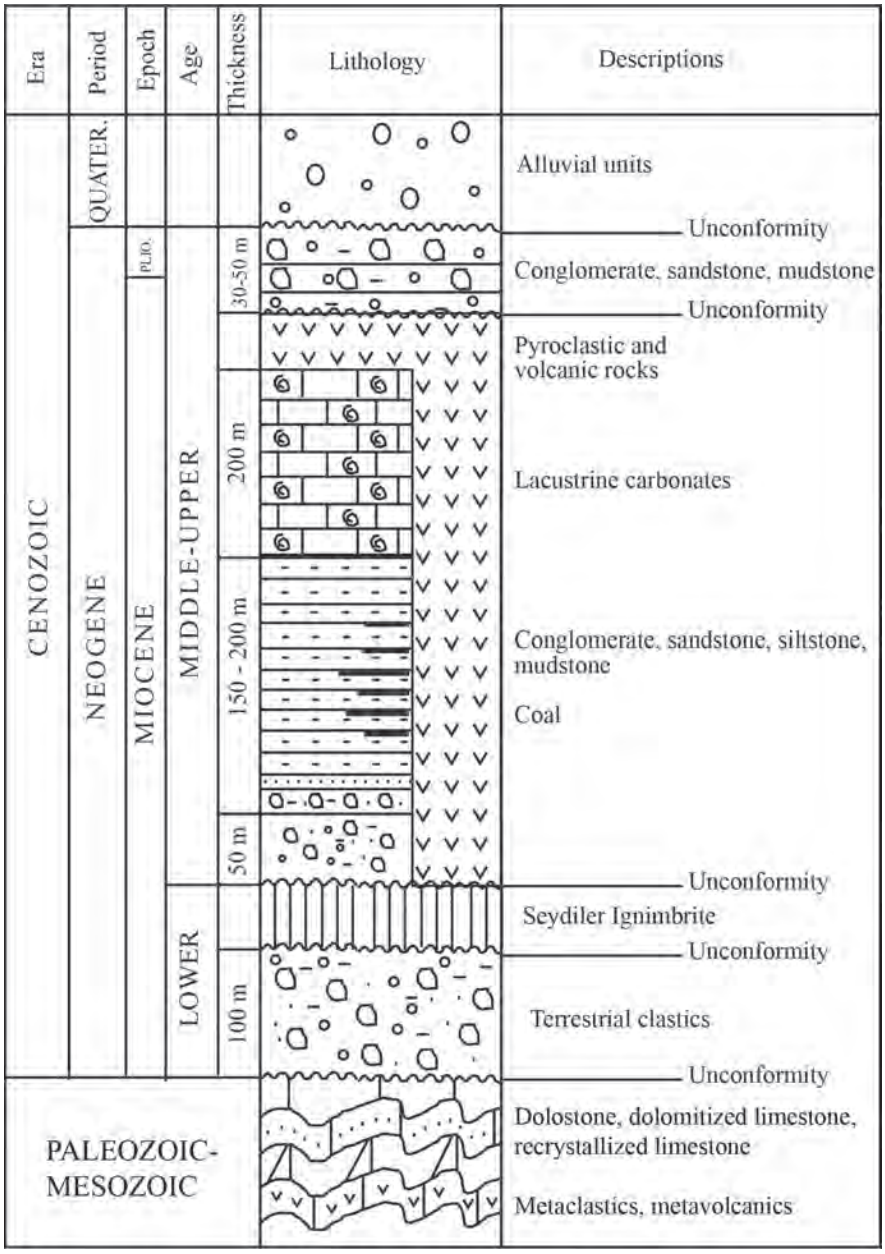

Figure 2- Columnar section of Sinanpaşa (Afyon) basin (modified from Metin et al., 1987).

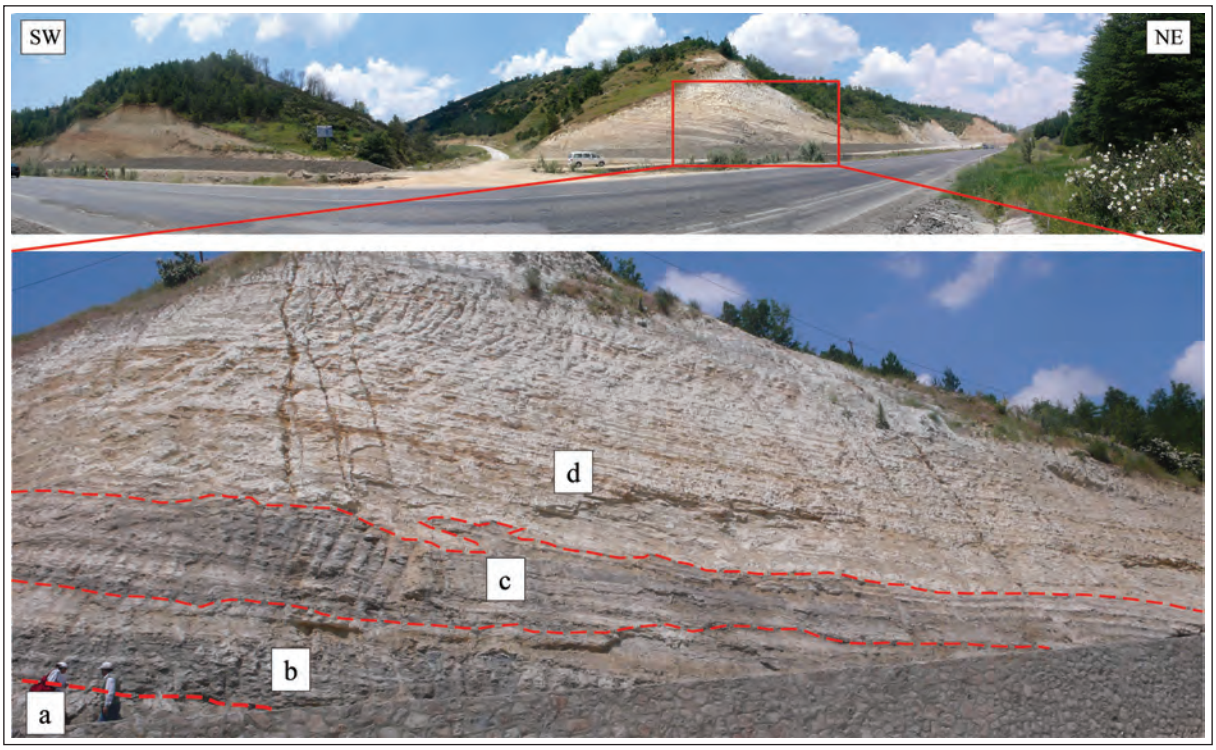

Figure 3- General and detail view of coal levels in the area (a: paleosol, b: matrix supported conglomerate, c: coal bearing mudstone, d: sandstone-claystone facies).

limited dispersion, silt size material and rhythmic alternation (Günen, 2011).

d) Sandstone-claystone facies: This facies alternates with coal-bearing sandstones and is formed by approximately 10 m thick gray sandstones and claystone. In them, the coal seams have completely disappeared, but they consist of coalified, blocky coal-bearing fragments in different size (between 30-50 cm).

e) Laminated mudstone: It alternates with sandstone-claystone facies and is overlain by the lacustrine carbonates. It has a thickness varying between 20-50 m. These are yellow to gray in color, parallel laminated, weak to medium compacted, and consist of fossilized plant root and mold, which are considered descriptive features.

3. Material and Method

The systematical sampling from coal-bearing layers from bottom to top was made within narrow intervals (mostly 10-50 cm), perpendicular to veins, depending on the change of macroscopic features (brightness and dullness) of the coal veins. However, a number of coal samples were taken from the underground mining quarry, as well as the lower and upper layers (The Karacaören Coal Enterprise). Besides; the units of the same layers on the ground were sampled by means of point sampling in different areas.

Petrographical investigations of the coal-bearing units were carried out in the Division of Mineralogy and Petrography Laboratories of the Mineral Analyses and Technology Department in the General Directorate of Mineral and Exploration (MTA). The following materials were utilized for analyses; the Leitz MPV-SP brand photomultiplier microscope, oil immersion lens with a magnification of 32x, polishing oil with an incidence angle of 1,518%, sapphire standard with a reflection value (R) of 0.548% for reflection measurements, and the software GEOR. In the determination of microscopic components in the samples, nearly 400 points for each sample were studied and detected by the point counting method. After the microscopic components of samples had been determined in detail they were subjected to sensitive polishing and prepared for the reflection measurements. The maximum reflection values (R_{max}) were detected during the reflection measurements. Coal petrography studies and descriptions were done

according to Stach et al. (1982), Ward (1984), ICCP (1994) and ICCP (2001).

The samples selected for palynological studies were crushed and then washed with different acids, such as; HCl, HF, HNO_3 and KOH, in order to remove them from calcium, silica and organic materials based on palynologic sample preparation techniques. For each sample 1-4 slides were prepared then sample count and selections were made. For paleoclimatic interpretations the method of "Coexistence Approach" was used (Mosbrugger and Utescher, 1997). The purpose of this method is to determine the interval of different paleoclimatic parameters of a given fossil. At the end of this method, the "coexistence" interval was obtained. This is considered the best descriptor for explaining which plant types live at what temperature for each climatic parameter. The application of the "Coexistence Approach" method was done using around 2000 Paleoflora Databases (for more information: www.paleoflora.de) for plants which lived in Tertiary conditions, by means of ClimStat software. The palinoflora obtained in this study was interpreted using 4 climatic parameters. These are the values of "Mean annual temperature" (MAT), "Mean temperature of the coldest month" (CMT), "Mean temperature of the warmest Month" (WMT) and "Mean annual precipitation" (MAP).

4. Coal Petrography

Coal-bearing layers in the Sinanpaşa basin exhibit wide spreads to the east of the Kırka region located in the S-SE of the basin, and around the Karacaören region located in the N-NW of the basin. The petrographical investigations of the coal samples taken in both regions were completed and the results of the coal petrography analysis were used for environmental interpretations.

4.1. Kırka Region

When looking at microscopic components of the eight coal samples collected from this region, the macerals ranging from most to least in abundance are ordered as; the huminite, liptinite and inertinite macerals. The relatively high inertinite ratio is due to oxidation (Hacquebard et al., 1967; Toprak, 1984).

In several studies it was observed that corpohuminite tissues (Figure 4a), with their homogenous rounded sights, began to disappear among huminite macerals. Also; ulminite macerals (ICCP, 1994), with their typical views in which lineaments that had formed by the accretion of tissues on each other are dominant, can be widely observed. Besides; gelinite macerals were also observed (Figure 4b) with their homogenous and nonwoven views with wide surfaces.

Among liptinite macerals; the sporinites, which formed due to the flattened spore and pollens parallel to the bedding, and cutinites (Figure 4c) which had formed because of the leaf cuticles, were determined as the most dominant macerals. In addition; the resinite macerals, which had been formed by resins released from the plants, were also observed. Resinites are generally observed in the form of amorphous void infillings or in rounded, oval shapes (Stopes, 1935; Toprak, 1996).

Funginites are the most common inertinite maceral in these coals. They are rounded to oval in shape (ICCP, 2001). However, the macrinite maceral is typical with non-textured views covering wide surfaces. It has been emphasized that the macrinites with these views and formations are the most important component of the lignite and sub bituminous coals of Turkey (Toprak, 2009).

The percentage of maceral groups and inorganic materials in these coal samples and R_{max} reflection values are given in table 1. According to this Table, the percentage of clay and other silicate minerals were observed, varying from 5-11%. Pyrite varies from 7-10%, wherein framboidal pyrite is 4%, granular (idiomorph) pyrite is 2% and fracture filling is 1-2%. The framboidal pyrite (Figure 4d) indicates a stagnant swamp environment and the growth is due to in-situ bacteria (Stach et al., 1982).

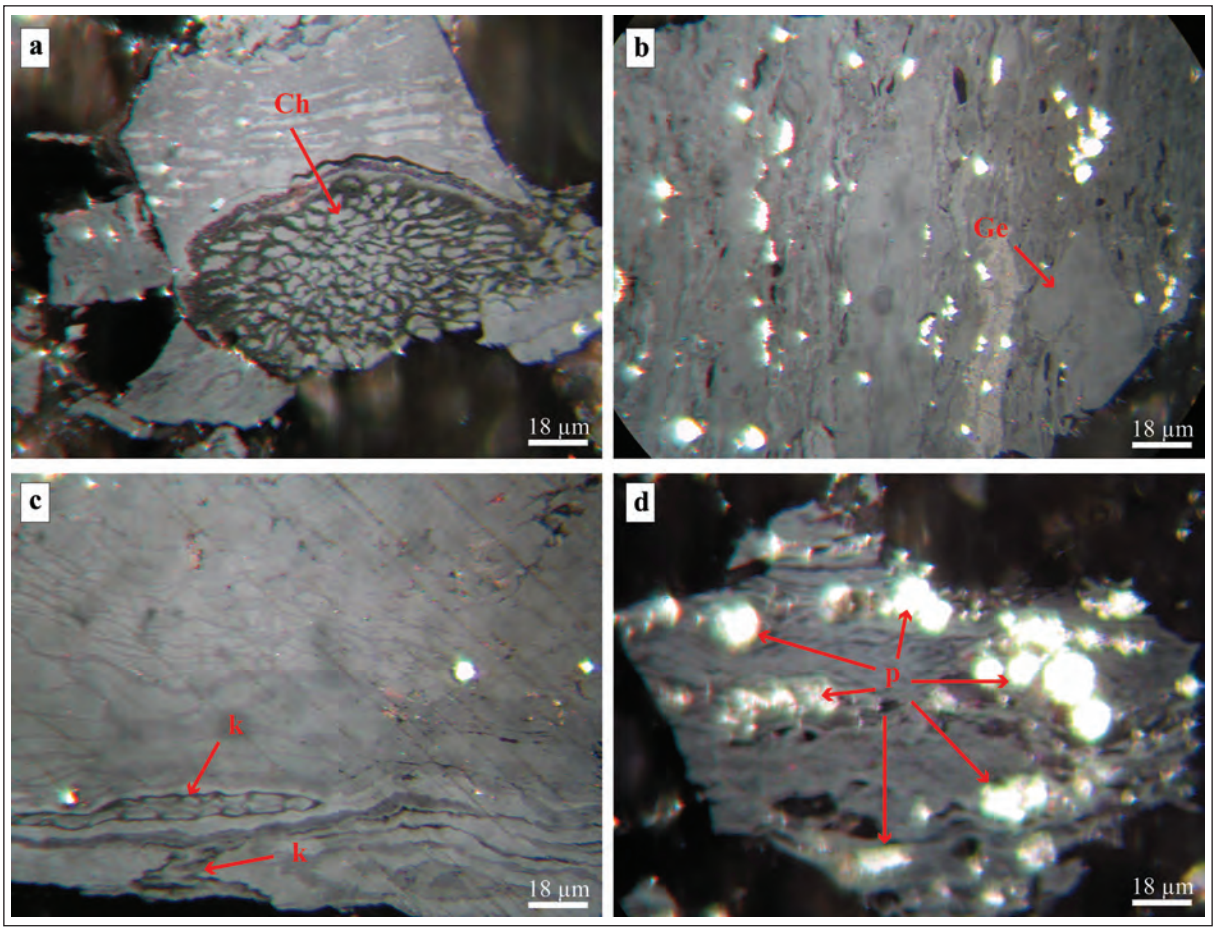

Figure 4- a) Corpohuminite maceral (Ch) with rounded appearance, b) Non-textured gelinite maceral (Ge) with homogenous and wide surfaces, c) Cutinite macerals (k) occurring from leaf fossils, d) fromboidal pyrites (p) formed in coal.

4.2. Karacaören Region

When looking at the microscopic components of 5 coal samples collected from this region, macerals ranging from most to least in abundance are ordered as; the huminite, liptinite and inertinite macerals. High organic material content of the coals most likely indicates the sulfate inputs, and that the organic material sedimentation is in excess.

In previous studies, the most dominant type among the huminite macerals were the gelinites, and there were also humotelinites and humodetrinites (clastic huminites) in significant amounts. Gelinites are typical with their homogenous and nonwoven views and their wide surfaces (Sỳkorová et al., 2005) (Figure 5a). In addition, ulminite macerals (Figure 5b) with views in which tissues begin to disappear, and atrinite and densinite macerals with views that consist of thin huminite clastics were found.

Among liptinite macerals; the sporinites, which had been formed by flattened spore and pollens parallel to the bedding, and thin cutinites (Figure 5c), which had been formed by the leaf cuticles, were found to be the most dominant macerals. In addition; the macrinites, known as most dominant inertinite maceral in coals of the basin, were typically observed in their nonwoven state (Figure 5d).

The percentage of maceral groups and inorganic materials obtained from coal samples and R_{max} reflection values are given in table 2. According to the figures, pyrite presence was detected at 7% in total volume, with 5% for framboidal pyrites and 2% for granular (idiomorph) pyrites. Besides; the percentage of clay and other organic materials was determined as 24%. High clay ratio shows that average clastic material input into the environment has increased. Micro-lamination structures of which coal-clay alternation formed can be typically observed in the study area.

Table 1- Maceral and mineral components of coal occurrences in Kırka area.

Sample No	Rmax (%)	HUMINITE				Tot. Hum.	LIPTINITE			Tot. Lipt.	INERTINITE				Tot. Inet.	PYRITE			Tot. Pyrite	CLAY etc.
		Humotelinite		Humodetrinite (Densinite)	Gelohuminite															
		Text	Ulm		Gelinite		Spor	Resinite	Cutinite		Fus.	Macr.	Fu	I.det.		Pseu	Grn.	Cf		
EG-5	0,436	1	8	7	62	78	3	1	1	5	-	3	1	1	5	4	2	1	7	5
EG-16	0,440	2	9	6	49	66	4	2	1	7	-	2	1	-	3	4	4	2	10	11
EG-17	0,473	1	8	5	61	75	3	1	1	5	-	3	1	1	5	4	2	1	7	5
EG-18	0,440	2	8	8	63	81	4	1	1	6	-	3	1	1	5	3	1	1	5	3
EG-19	0,435	1	8	7	62	78	3	1	1	5	-	3	1	1	5	4	2	1	7	5
EG-20	0,442	2	7	7	60	76	4	3	1	8	-	2	1	-	3	3	2	2	7	6
EG-24	0,412	1	8	6	60	75	3	1	1	5	-	2	1	1	4	4	3	2	9	7
EG-26	0,436	1	7	5	62	75	3	1	1	5	-	3	1	-	4	4	4	2	10	6
EG-27	0,465	2	7	7	62	78	4	2	1	7	-	3	1	1	5	2	2	1	5	5

(Tot: Total, Hum: Huminite, Lipt: Liptinite, Inet: Inertinite, I.det: Inertodetrinite, Text: Textinite, Ulm: Ulminite, Spor: Sporinite, Fus: Fusinite, Macr: Macrinite, Fu: Funginite, Pseu: Framboidal, Grn: idiomorph crystalline, Cf: Crack fill, Clay etc: Clay and carbonate minerals).

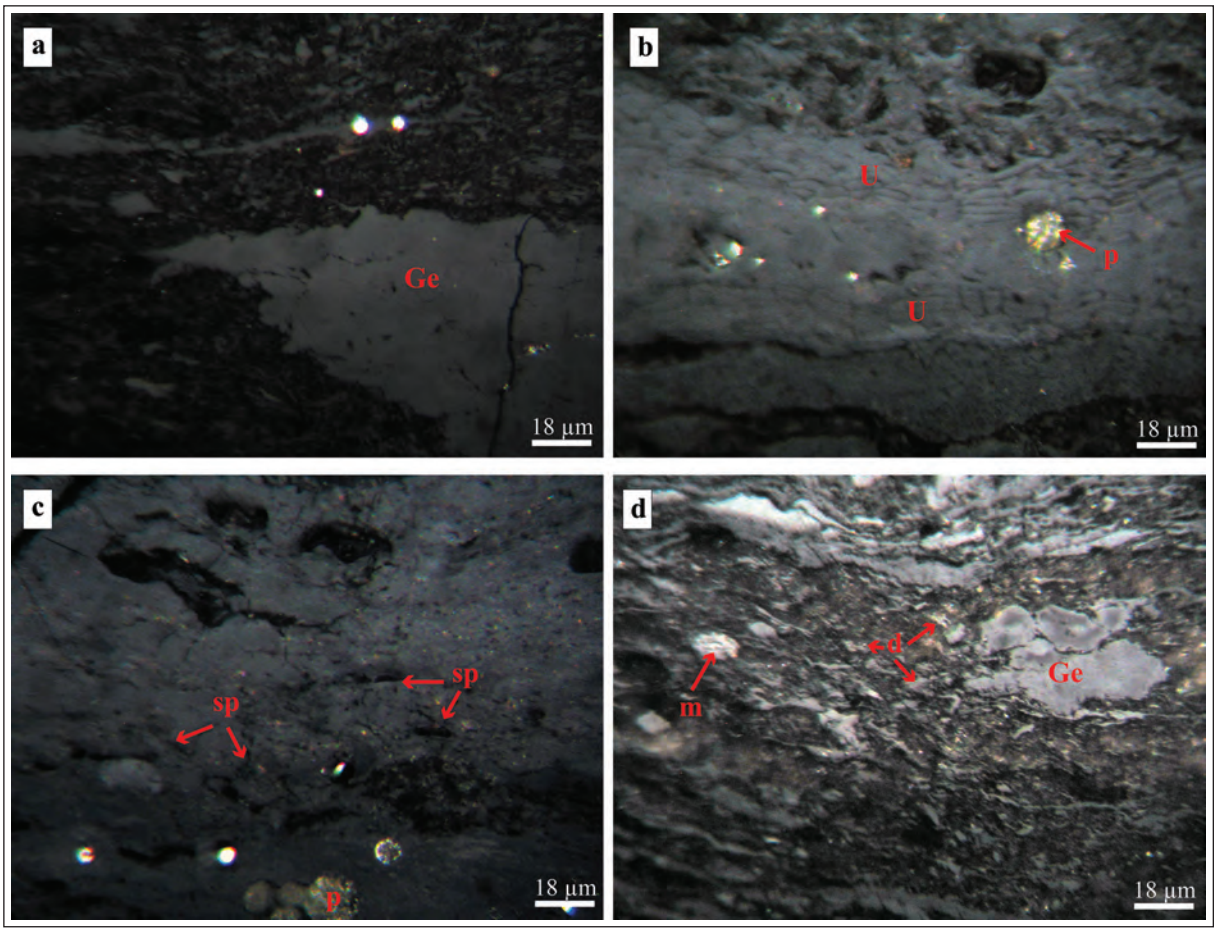

Figure 5- a) Non-textured gelinite maceral (Ge)with wide surfaces, b) Ulminite macerals (U) with disappearing textures and framboidal pyrites (p), c) Non-textured macrinite (m), homogenous gelinite (Ge) and densinite maceral (d) including fine huminite fragments, d) Sporinite macerals (sp) formed by spors and polens with framboidal pyrites (p).

5. Discussion

5.1. Palynology

A total of 13 samples, of which 8 samples were from road cuts along the Afyon-Sandıklı autoroad and 5 samples from Çalışlar-Karacaören, were passed through palynological sample preparation stages and made ready for microscopic studies. However, it was noticed that samples were poor in terms of sporomorph content and their forms were not well preserved. In sporomorph communities obtained as a result of studies carried out on samples, the spore diversity was very low and only *Laevigatosporites* genus was abundant (Table 3). Among the gymnosperm pollens; the pollens of *Picea* and *Pinus* genus conifers, swamp plants and pollens of Taxodioideae and Cupressaceae appear. Among angiosperms, the species of Chenopodiaceae and Graminae families, which show wide flat areas, were observed in small amounts. Chenopodiaceae, Graminae and Umbelliferae in the Miocene of Turkey have been recorded only in the deposits from Mid-Miocene in small amounts, though it has been detected that the percentages of these forms had increased in the Late Miocene or younger deposits (Benda, 1971; Benda and Meunlenkamp, 1990; Akgün and Akyol, 1999; Akgün et al., 2000; Akgün et al., 2007). Therefore; the samples obtained from the study area should be even older than Upper Miocene. The spore forms inherited from Oligocene (Leiotriletes maxoides ssp. maxoides and maximus, Verrucatosporites, Lycopodiumsporites, Polypodiaceoisporites) were not encountered in samples, even at low ratios, during the early Miocene. Besides; the angiosperm forms, of which their vertical distributions concern the whole Cenozoic, accompany other forms, though in low diversity. So, looking at all the aforementioned reasons the age of samples is said to be in Mid-Miocene.

Table 2- Maceral and mineral components of coal occurerences in Karacaören area.

Sample No	Rmax (%)	HUMINITE						Tot. Hum.	LIPTINITE			Tot. Lipt.	INERTINITE		Tot. Inet.	PYRITE			Tot. Pyrite	CLAY etc.
		Humotelinite		Detrohuminite		Gelohuminite														
		Text	Ulm	Attr.	Dens.	Gelinite	Co.hum.		Spor	Alginite	Cutinite		Fus.	Macr.		Pseu	Grn	Cf		
K-1	0,524	3	12	4	11	28	1	59	3	2	1	6	1	3	4	5	2	-	7	24
K-2	0,520	2	10	4	10	22	1	49	4	2	1	7	-	2	2	4	4	-	8	21
K-3	0,530	3	11	5	11	25	1	52	3	2	1	6	-	3	3	5	2	-	7	21
K-4	0,526	3	11	4	11	26	1	56	4	1	1	6	1	3	4	5	2	-	7	25
K-5	0,524	3	12	4	12	26	1	58	3	2	1	6	-	4	4	4	3	-	7	24

(Tot: Total, Hum: Huminite, Lipt: Liptinite, Inet: İnertinite, Text: Textinite, Ulm: Ulminite, Dens: Densinite, Spor: Sporinite, Fus: Fusinite, Co.hum: Corpohuminite, Macr: Macrinite, Pseu: Framboidal, Grn: idiomorph crystalline, Cf: Crack fill, Clay etc: Clay and carbonate minerals).

Table 3- Sporomorphs and botanical affinities of the samples.

SPOROMORPH	BOTANICAL AFFINITIES
Laevigatosporites haardti (Potonié and Venitz) Thomson and Pflug ssp. *haardti* Krutzsch	Polypodiaceae
Graminidites sp.	*Graminae*
Inaperturopollenites dubius (Potonié and Venkatachala) Thomson and Pflug	Taxodioideae
Cupressacidites cuspidateaformis (Zaklinskaja) Krutzsch	Cupressaceae
Pityosporites microalatus (Potonié) Thomson and Pflug	Pinaceae; *Pinus* haploxyon tip
Piceapollis planoides Krutzsch	*Picea*
Pityosporites pristinipollinius (Traverse) Krutzsch	*Pinus*
Pinuspollenites macroinsignis (Krutzsch) Planderova	*Pinus*
Piceaepollenites alatus R.Potonie	Pinaceae
Piceapollis praemarianus Krutzsch	*Picea*
Pityosporites sp.	Pinaceae
Caryapollenites simplex (Potonié) Thomson and Pflug	*Carya cordiformis*
Alnipollenites verus R.Potonié	Betulaceae; *Alnus*
Tricolpopollenites microhenrici (Potonié) Thomson and Pflug	Fagaceae; ? *Quercus*
Tricolpopollenites henrici (Potonié) Thomson and Pflug	Fagaceae; ? *Quercus*
Tricolpopollenites densus Pflug *in* Thomson and Pflug	*Quercus*
Oleoidearumpollenites microreticulatus (Flug *in* Thomson and Pflug) Zimbinska-Tworzydlo	Oleaceae
Tricolporopollenites cingulum (Potonié) Thomson and Pflug ssp. o*viformis* (Potonié) Thomson and Pflug	Castanea-Castanopsis
Tricolporopollenites krucshi (Potonié) Thomson and Pflug	*Nyssa*
Araliaceoipollenites euphorii	Araliaceae
Rhoipites cf. pseudocingulum	Anacardiaceae, *Rhus*
Periporopollenites multiporatus Pflug and Thomson *in* Thomson and Pflug	Chenopodiaceae
Tetracolporopollenites sp.	Sapotaceae

The forms of the Nyssacea family, which are observed all the time and known as the swamp forms in the Mid-Miocene of Turkey, and Alnus, Quercus, Castanea-Castanopsis, Anacardiaceae and Araliaceae, which are observed during the Mid-Miocene representing the mixed forest community, take place in the obtained community. Consequently; the age of the samples obtained from the measured section supports the Mid-Miocene.

5.2. Environmental Interpretation

When the maceral distributions of coals located in Kırka and Karacaören regions in the Sinanpaşa basin were plotted on the ternary diagram, it was clear that these coals were formed by the huminite (mostly galenite) rich macerals and consisted of liptinite (mostly sporinite) and inertinite (mostly macrinite) groups of macerals, though in small amounts (Figure 6).

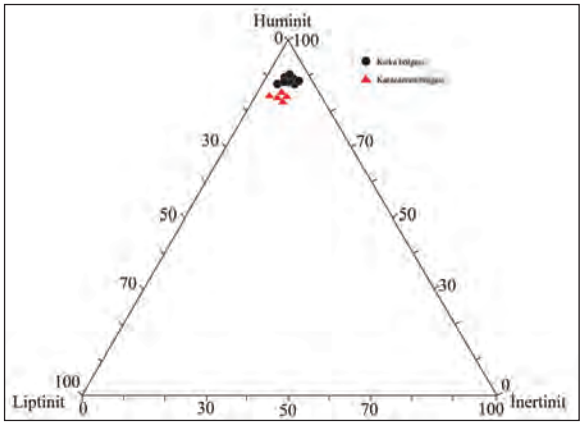

Figure 6- Ternary diagram of maceral groups in Kırka and Karacaören coal occurrences.

The analyses performed on the coals are important in terms of detecting the old depositional environments and their conditions. Many researchers have carried out investigations into this subject and aimed at finding parameters that could solve the old depositional environments of samples (Spackman, 1958; Diessel, 1986; Kalkreuth and Leckie, 1989; Lamberson et al., 1991). In this study, the values of GI (gelification index) and TPI (tissue preservation index) were determined using a graphic which had been developed by Diessel (1986), and improved by Kalkreuth and Leckie (1989) and Lamberson et al. (1991) for the environmental interpretation of the coals. The results are shown in figure 7. Accordingly;

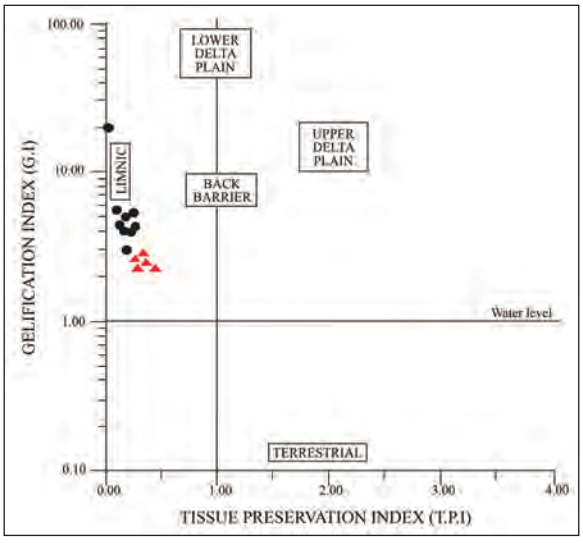

Figure 7- Coal facies diagram with depositional environments (Diessel, 1986; Kalkreuth and Leckie, 1989; Lamberson et al. 1991) (see figure 6 for the explanations of the symbols).

the maceral contents, tissues and gelifications of both regions show similarities. It was observed that coal samples collected from both regions had occurred in the lacustrine environment 1.00 line above the Y axis (above water level) in figure 7. When this data was taken into consideration as sedimantological and palynological data, it was noticed that the coals in the basin had been deposited in swamp zones associated with lakes. Besides; the high gelinite maceral component indicates that coals were developed in swamp environments which increased the gelification (Diessel, 1986; Toprak, 1996).

The R_{max} (%) values of the coals in the Kırka region being lower than 0.47 shows that the maximum paleotemperature value of the environment is below 100°C and corresponds to sub bituminous as coal rank (Stach et al., 1982; Ward, 1984). In addition; the R_{max} values of the coals in the Karacaören region are higher than 0.47. R_{max} values of these coals, the increased levels are partly attributed to the increase in the oxidation in similar geological environments (Toprak, 2009).

5.3. Paleoclimate

The plants to which polens and spores belong in the palynological community are assessed in order to understand the climatic conditions. Numerical climatic assessments were made using the "Coexistence Approach" method, developed by Mosbrugger and Utescher (1997).

When the Sinanpaşa Mid-Miocene palynoflora was studied it was seen that pollens, which belonged to plants that could develop in cool climates, had been more dominant (eg. Pinaceae, Carya, Quercus and Alnus). The numerical climatic calculations of this flora were made by the ClimStat software using 21 species. These numerical values support that the deposition of coal-bearing deposits occurred under cool climatic conditions. These paleoclimate conditions are represented by the numerical values MAT: 13,3–18,1°C, CMT: 0,9–8,3°C, WMT: 23,6–27,0°C and MAP: 622-1322 mm (Figure 8).

Akgün et al. (2007) stated that the West Anatolian Mid-Miocene low numerical temperature values of MAT (~12-17°C) and CMT (~2-9°C) were lower than the Early Miocene. It was also seen that numerical findings obtained from this study were compatible with other Mid-Miocene numerical values. The lower boundary of MAP being low and the upper boundary being high makes us consider the presence of seasonal change. Besides; the high MAP value explains the presence of *Alnus* and *Nyssa* plants which can evolve on a stream bank or in a swamp environment with high water levels defined as sporomorph flora in the study area.

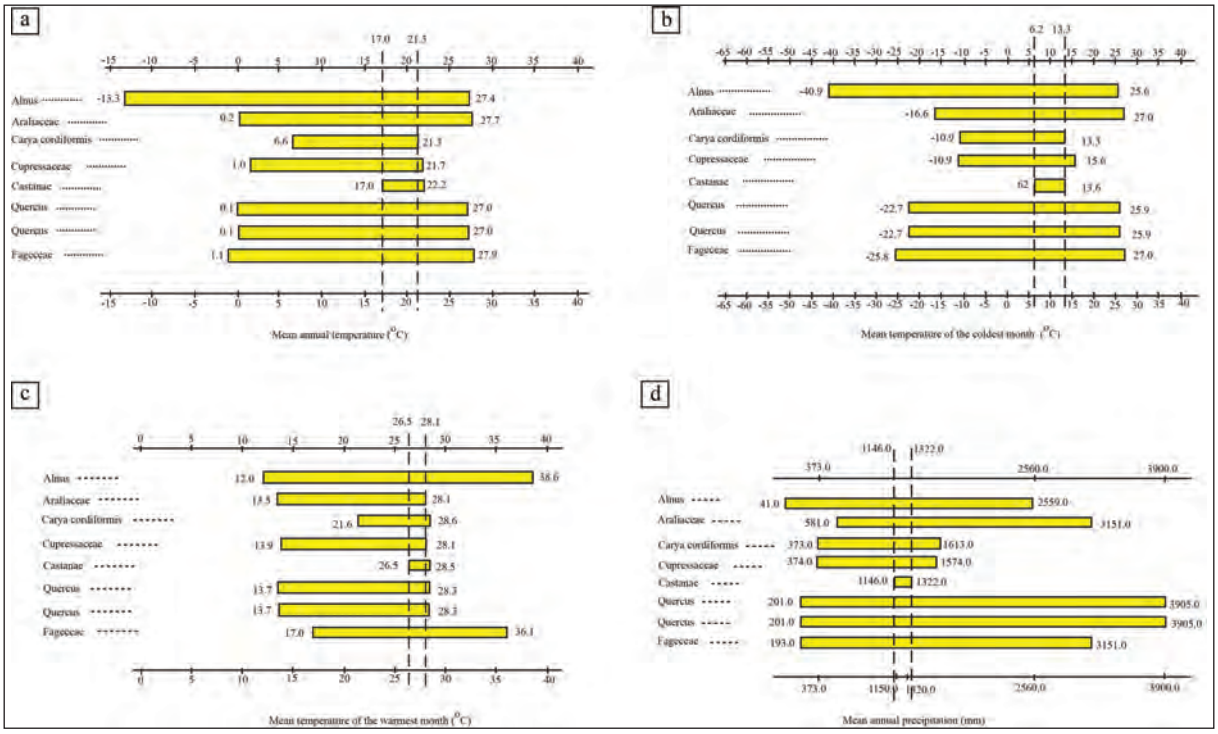

Figure 8- Numerical climatic calculations ; a) Mean annual temperature, b) Mean temperature of the coldest month, c) Mean temperature of the warmest month, d) Mean annual precipitation.

5. Conclusions

The Miocene deposition in the study area begins with the alluvial fan deposits at the bottom and grades into lacustrine deposits in the upper layers. Coal-bearing layers were detected in stages when the lake was first opened. These layers crop out in the Kırka region in the South and in the Karacaören region in the North of the investigated area.

As a result of petrographical investigation of the coal-bearing units taken from both regions, it was observed that these regions presented similar petrographical features. So, it was determined that both regions had huminite rich coals and consisted of liptinite and inertinite in small amounts.

It was found that the R_{max} (%) values of the coals in the Kırka region ranged between 0.44-0.47. According to the studies carried out on the coals these values correspond to sub bituminous coals (Stach et al., 1982; Ward, 1984). In addition, the R_{max} (%) values of the coals from the Karacaören region were found to be high (>0.47%), which makes us consider the presence of increasing oxidation in the environment. Besides; the presence of the Afyon volcanism and tectonic activities in and around the study area might have also been a factor in the increase of the R_{max} values as it had been in similar coal fields in Turkey (Toprak, 2009).

In the study area, mainly the swamp forms of the Nyssaceae family and the forms of the mixed forest community (*Alnus*, *Quercus*, *Castanea-Castanopsis*, Anacardiaceae and Araliaceae) were detected. The age of coal-bearing units in the study area indicates the Mid-Miocene because of the presence of the forms observed in the Mid-Miocene of Turkey.

As a result of paleoclimate studies carried out, it was found that MAT and CMT temperature values were low, however, MAP values were variable. This situation makes us consider whether climatic conditions have changed due to seasonality in the study area. As a result; the presence of cool climate conditions during the time of the coal production based on palynological data in this study should be mentioned. This data is compatible with climate conditions that prevail in Western Anatolia during the Mid-Miocene time.

Acknowledgements

This manuscript constitutes a part of the PhD thesis of the author. The author would like to give thanks to Baki Varol who offered help and support during the field work, and in writing this article. The author also gives thanks to Selami Toprak for his contributions in the coal petrography section, to Funda Akgün for her support during the assessments and interpretations of palynological data, and to reviewers for their constructive criticism during the preparation of this article. This study has been supported by project 06B4343006 of the Scientific Research Project Office of the Ankara University.

References

Akgün, F., Akyol, E. 1999. Palynostratigraphy of the coal-bearing Neogene deposits graben in Büyük Menderes Western Anatolia. Geobios 32(3), 367-383.

Akgün, F., Kaya, T., Forsten, A., Atalay, Z. 2000. Biostratigraphic data (Mammalia and Palynology) from the Upper Miocene İncesu Formation at Düzyayla (Hafik Sivas, Central Anataloia). Turkish Journal of Earth Sciences 9, 57-67.

Akgün, F., Kayseri, M.S., Akkiraz, M.S. 2007. Palaeoclimatic evolution and vegetational changes during the Late Oligocene-Miocene Period in the Western and Central Anatolia (Turkey). Palaeogeography, Palaeoclimatology, Palaeoecology 253, 1-2, 56–90.

Anderson, D. 1997. The Relationship Between Magmatism and Borate Mineralisation in Western Turkey. PhD Thesis, University of Leicester, 138 p. Leicester (unpublished).

Aydar, E. 1998. Early Miocene to Quaternary evolution of volcanism and the basin formation in western Anatolia: a review. Journal of volcanology and Geothermal Research 85, 69-82.

Becker-Platen, J.D. 1967. Afyon-Sincanlı-Güney havzasının Linyit Etütü. Maden Tetkik ve Arama Genel Müdürlüğü Rapor No: 6108, Ankara (unpublished).

Benda, L. 1971. Grundzüge einer pollenanalytischen Gliederung des türkischen Jungtertiärs (Känozoikum und Braunkohle der türkei). 4. Beihefte zum Geologischen Jahrbuch 113, 1-46.

Benda, L., Meunlenkamp, J.E. 1990. Biostratigraphic correlations in the Eastern Mediterranean Neogene 9. Sporomorph associations and event stratigraphy of the Eastern Mediterranean Neogene. Newsletter on Stratigraphy 23, 1-10.

Besang, C., Echart, F.J., Harre, W., Keruzer, H., Muller, P. 1977. Radiometrische altersbestimmungen an Neogenen erup-tigesteinen der Turkei. Geologisches Jahrbuch 25, 3-36.

Çevikbaş, A., Ercan, T., Metin, S. 1988. Geology and regional distribution of Neogene volcanics between Afyon Şuhut. Journal of Pure and Applied Sciences, 21(1-3), 479-499.

Diessel, C.F.K. 1986. The correlation between coal facies and depositional environments, Advances in the Study of the Sydney Basin. Proceedings of the 20th Newcastle Symposium, 1986, University of New Castle, 19-22.

Ersoy, Y. E., Helvacı, C., Palmer, M. R. 2011. Stratigraphic, structural and geochemical features of the NE–SW trending Neogene volcano-sedimentary basins in western Anatolia: Implications for associations of supra-detachment and transtensional strike-slip basin formation in extensional tectonic setting. Journal of Asian Earth Sciences 41, 2, 159-183.

Francalanci, L., Innocenti, F., Manetti, P., Savascin, M.Y. 2000. Neogene alkaline volcanism of the Afyon-Isparta area, Turkey: petrogenesis and geodynamic implications. Mineralogy and Petrology 70, 285-312.

Günen, E. 2011. Sincanlı Afyon Neojen havzası birimlerinin sedimantolojisi. Doktora Tezi, Ankara Üniversitesi, 200 s. Ankara (unpublished).

Gürsoy, H., Piper, J.D.A., Tatar, O. 2003. Neotectonic deformation in the western sector of tectonic escape in Anatolia: palaeomagnetic study of the Afyon region, central Turkey. Tectonophysics 374, 57-79.

Hacquebard, P. A., Birmingham, T. F., Diessel, J.R. 1967. Petrography of Canadian colas in relation to environment of deposition. Symposium. on the Science and Technology of Coal, 1967, Ottawa, 29-31.

Helvacı, C., Yağmurlu, F. 1995. Geological setting and economic potential of the lignite and evaporite-bearing Neogene basins of Western Anatolia, Turkey. Israel Journal of Earth Sciences 44, 91-105.

International Committee for Coal and Organic Petrology (ICCP). 1994. International Handbook of Coal Petrology.

International Committee for Coal and Organic Petrology (ICCP). 2001. The new inertinite classification. Fuel 80, 459-471.

Kalkreuth, W., Leckie, D. 1989. Sedimentalogical and petrographical characteristics of Cretaceous Strandplain coals: A model for coal accumulation from the North American Western Interior Seaway. International Journal of Coal Geology 12, 381-424.

Karamenderesi, İ.H. 1972. Afyon K 24b paftası detay jeolojik etüdü ve jeotermal alan olanakları. Maden Tetkik ve Arama Genel Müdürlüğü Rapor No: 5733, Ankara (unpublished).

Kartalkanat, A., Mutlu, H., Küçükayman, A. 1990. Afyon-Bayat-İhsaniye-Sincanlı I (ÖİR: 653), II (ÖİR: 653) ve III (ÖİR: 2149) nolu bortuzu sahalarının maden jeolojisi raporu. Maden Tetkik ve Arama Genel Müdürlüğü Rapor No: 3092, Ankara (unpublished).

Kaya, O. 1979. Ortadoğu Ege çöküntüsünün (Neojen) stratigrafisi ve tekniği. Türkiye Jeoloji Kurumu Bülteni 22, 35-58.

Kaya, O. 1981. Miocene reference section for the coastal parts of West Anatolia. Newsletters on Stratigraphy 10, 3, 164-191.

Koçyiğit, A. 1984. Güneybatı Türkiye ve yakın dolaylarında levha içi yeni tektonik gelişim. Türkiye Jeoloji Kurumu Bülteni 27, 1-16.

Koçyiğit, A., Özacar, A.A. 2003. Extensional Neotectonic regime through the NE edge of the outer Isparta Angle, SW Turkey: New field and seismic data. Turkish journal of Earth Sciences 12, 67-90.

Koçyiğit, A., Deveci Ş. 2007. Çukurören-Çobanlar (Afyon) arasındaki deprem kaynaklarının (aktif fayların) belirlenmesi. Türkiye Bilimsel ve Teknik Araştırma Kurumu Proje No: 106Y209, 71 s, Ankara (unpublished).

Konyalı, Y. 1968. Sincanlı Dumlupınar Bölgesinin Jeolojisi ve linyit Etüdleri. Maden Tetkik ve Arama Genel Müdürlüğü Rapor No: 4404, Ankara (unpublished).

Lamberson, M. N., Bustin, R.M., Kalkreuth, W. 1991. Lithotype (maceral) composition and variation as correlated with paleo-wetland environments, Gates Formation, Northeastern British Colombia, Canada. International Journal of Coal Geology 18, 87-125.

Metin, S., Genç, İ., Bulut, V. 1987. Afyon ve dolayının jeolojisi. Maden Tetkik ve Arama Genel Müdürlüğü Rapor No: 2113, Ankara (unpublished).

Mosbrugger, V., Utescher, T. 1997. The Coextistence approach-a method for quantitative reconstructions of Tertiary terrestrial paleoclimate data using plant fossils. Palaeogeography, Palaeoclimatology, Palaeoecology 134, 1-4, 61-86.

Öcal, H., Göktaş, F. 2011. 1:100000 ölçekli Türkiye Jeoloji Haritaları Afyon-K24 paftası. Maden Tetkik ve Arama Genel Müdürlüğü Jeoloji Etütleri Dairesi, No: 158, 31 s, Ankara.

Özgül, N., Bölükbaşı, S., Alkan, H., Öztaş, Y. 1991. Sultandağları Sandıklı Homa-Akdağı yöresinin jeolojisi. Türkiye Petrolleri Anonim Ortaklığı Arama Grubu Rapor No: 3028, Ankara (unpublished).

Robertson, A.H.F., Dixon, J.E. 1984. Introduction: Aspects of the geological evolution of the eastern Mediterranean. Dixon, J.E., Robertson, A.H.F. (Ed.). The Evolution of the Eastern Mediterranean. Geological Society of London. Special Publication 17, 1-74.

Spackman, W. 1958. Maceral concept and the study of modern environments as a means of understanding the nature of coal. The New York Academy of Science Series II, 20, 411-423.

Stach, E., Mackowsky, M.T., Teichmüller, M., Taylor, G.H., Chandra, D., Teichmüller, R. 1982. Stach's textbook of coal petrology. Gebrüder Bornträger, 535 p.

Stopes, M.C. 1935. On the petrology of banded bituminous coals. Fuel 14, 4-13.

Sỳkorovå, I., Pickel, W., Christanis, K., Wolf, M., Taylor, G. H., Flores, D. 2005. Classification of huminite-ICCP System 1994. International Journal of Coal Geology 62, 85-106.

Şengör, A.M.C., Yılmaz, Y. 1981. Tethyan evolution of Turkey: a plate tectonic approach. Tectonophysics 75, 181-241.

Şengör, A.M.C., Görür, N., Şaroğlu, F. 1985. Strike-slip faulting and related basin formation in zones of tectonic escape: as a case study. Biddle, K.T., Christie-Blick, N. (Ed.). Strike-slip Faulting and Basin Formation. SEPM Special Publication Series 37, 227-264.

Toprak, S. 1984. Petrographic characterization of coals in Kozlu-Kılıç Formation (Wesphalian A) Zonguldak-Turkey. Thesis of Msc., University of Pittsburgh, USA (unpublished).

Toprak, S. 1996. Alpagut-Dodurga (Osmancık-Çorum) bölgesi çevresindeki kömürlerin oluşum ortamları ve özelliklerinin belirlenmesi., Doktora Tezi, H.Ü. Mühendislik Fakültesi, 164 s. Ankara (unpublished).

Toprak, S. 2009. Petrographic properties of major coal seams in Turkey and their formation. International Journal of Coal Geology 78, 263-275.

Ward, C.R. 1984. Coal geology and coal technology. Blackwell Scientific Publications, 345 p.

Yalçın, H. 1988. Kırka (Eskişehir) yöresi volkanosedimanter oluşumlarının mineralojik-petrografik ve jeokimyasal incelenmesi. Doktora Tezi H.Ü. Mühendislik Fakültesi, 209 s, Ankara (unpublished).

Zanchi, A., Kissel, C., Tapırdamaz, C. 1993. Late Cenozoic and Quaternary brittle continental deformation in western Turkey. Bulletin de la Societe Geologique de France 164, 507-517.

Bull. Min. Res. Exp. (2018) 156: 167-178

Bulletin of the Mineral Research and Exploration

http://bulletin.mta.gov.tr

Separation of geochemical anomalies using inverse distant weighting (IDW) and concentration-area (C-A) fractal modeling based on stream sediments data in Janja Region, SE Iran

Marzieh HOSSEİNİNASAB[a] and Ali Akbar DAYA[b*]

[a]*Department of Mining Engineering, University of Sistan and Baluchestan Iran. https://orcid.org/0000-0002-0964-5863.*
[b]*Department of Mining Engineering, University of Sistan and Baluchestan Iran. https://orcid.org/0000-0002-9628-978.*

Research Article

Keywords:
Geochemical anomalies; Stream sediments; Concentration-area fractal model; Janja; Sistan and Baluchestan.

ABSTRACT

In this study, the Inverse Distant Weighting (IDW) and the Concentration –area (C-A) fractal methods were used for identifications of geochemical anomalies in Janja region, SE Iran. Eight elements (Au, Cu, Mn, Zn, Fe, As, Mo, and Pb) from 300 stream sediment samples were used. The studied area was gridded by 250 m×250 m cells. Estimation of unsampled locations were carried out by inverse distant squared weighting (IDWS) method. Geochemical maps were generated. Log- log plots of cumulative frequency of elemental concentrations versus related areas were constructed. Threshold values were obtained by finding break points in the log-log plots. There were four geochemical populations for As, Fe, Mo, Pb and Zn and five geochemical populations for Au, Cu, and Mn. The resulted geochemical anomaly maps obtained from fractal modelling showed that Anomalies of Zn, Mo, Mn, Fe, Cu and As located in southeastern part of study area. There was a good correlation between faults and elementals anomalies. It can be concluded that mineralization occurred along the faults. There was a correlation between anomalies and sedimentary rocks (alluvium and recent alluvium sediments) in SE part of study area. Gold anomalies were located in the NW parts of the studied area. There was a strong relationship between the location of Au anomalies and fault systems in the NW parts of the studied area. Iron concentrations were sporadic and correspond to the sedimentary volcanic rock and turbidites.

Received Date: 08.10.2016
Accepted Date: 23.10.2017

1. Introduction

The regional geochemical exploration is important in order to reduce the wide area to small areas, reduce the costs and risks of investment. Identification of geochemical anomalies from the background is one of the most important tasks in exploration geochemical studies. For anomaly separation, statistical methods were used frequently. In spite of successfulness, these methods have some disadvantageous. These include, removing some of data as the outliers, not considering to the spatial distribution of data, not considering to the geometric shape of anomaly and having condition of following normal distribution for data.

There are many interpolation methods. One of the most widely used is the inverse distance weighted (IDW) method. Inverse distance weighting (IDW) interpolation method often are used prior to contouring data. The reason is that most contouring procedures need values on a regularly-spaced grid. IDW assumes that each input point has a local influence that diminishes with distance. It weights the points nearer to the processing cell greater than those further away. A specified number of points within a specified radius can be used to determine the output value of each location.

In recent years, fractal analysis method was considered as a useful tool for separating geochemical anomalies. Today, especially in Iran, geochemical exploration studies focused on the stream sediments. These studies in detailed exploration phase, have an important role for finding optimistic area in regional scale. The most important results from any exploration geochemical statistical analysis is the separating

* *Corresponding author: Ali Akbar DAYA, aliakbardaya@eng.usb.ac.ir*
http://dx.doi.org/10.19111/bulletinofmre.351449

different anomalies from each other and determines the background value for every element in the study area.

Based on Euclidean geometry, the around physical objects can be defined as shapes without dimension, one, two, and three-dimension. In Euclidean geometry, the dimension can be an integer such as one, two, three, and so on; but there are some phenomena in the world that cannot be justified in the framework of Euclidean geometry. For example, there is no possibility to determine some phenomena or events, such as the roughness of the surface of the mountains, shape of the coastline and many other natural objects and events by integer; also, the coordinate axes which are defined for describing these phenomena and events may not be perpendicular (Dimri, 2000). According to a non-Euclidean viewpoint, some phenomena and events can be considered as a Rational number in some cases. In these cases, the dimension can be changed from zero to one, from one to two or more. This viewpoint was the basis of the Fractal Geometry which was established by Mandelbrot (1983).

Fractal methods were proposed by Mandelbrot for the first time in 1983. Since 1990, different methods for anomaly separation were proposed based on the fractal methods (Cheng et al., 1994; Cheng et al., 1999; Davis, 2002; Afzal et al., 2011; Daya, 2015*a*; Daya, 2015*b*; Daya and Afzal, 2015; Daya et al., 2017). Fractal concentration- area (C-A) method was first used by Cheng et al (1994). It is based on fractal behavior of geochemical distribution in nature. In every contour map, the enclosed area decreases when the value of the contour increases. This is also true for elemental concentration contour map. From these contours, an optimum threshold for anomaly separation can be found by using a log-log plot for the element concentration-area relation. This threshold corresponds to the sudden change in the log-log plot. Log–log plots in concentration- area fractal method is a proper tool for separating and decomposing geological phenomena such as rock types, alteration units and more importantly mineralization. Theoretical Fractal studies and recent studies in earth science show that some geological processes such as mineralization, sedimentation, deposition, volcanic eruptions, morphology, and others have the characteristics of self-resemblance. Therefore, it can be found some evidences for fractal dimension from these cases (Cheng, 1999).

In this study, the geochemical exploration data related to stream sediments of Janja region were processed. The Concentration –area fractal model was used for determining the geochemical anomalies in Janja region, SE Iran. Eight elements (Au, Cu, Mn, Zn, Fe, As, Mo, and Pb) from 300 stream sediment samples were used to identify geochemical anomalies.

2. Methodology

2.1. Inverse Distance Weighting (IDW) Method

Many interpolation methods have been developed. One of the simplest and most widely used is the inverse distance weighted (IDW) method. IDW is based on the spatial dependence, it can be assumed that estimated values are more similar to nearby values than to distant values. The inverse distance weighted method estimates the value z of a point P as a function of the z-values of the nearest n points. The more distant a point, the less it influences the estimate. The advantage of the IDW method is that it is intuitive and its implementation is straightforward. Its main disadvantage is related to the determination of the weights based only on the location and ignoring the variance of the values.

The assigned values to unknown points are calculated with a weighted average of the values available at the known points. The name given to this type of methods was motivated by the weighted average applied, since it resorts to the inverse of the distance to each known point when assigning weights.

In the current paper, the study area was gridded by 250 m×250 m cells. Estimation of unsampled locations were carried out by inverse distant weighting (IDW) method. Then primary geochemical maps were generated.

2.2. Concentration-Area Fractal Model

Cheng et al. (1994) proposed the concentration–area fractal model, which may be used for anomaly separation, as the following form:

$$K(\rho \leq t) \propto \rho^{-a1}; \quad \mathrm{K(p} \geq) \ \mathrm{p}^{-a2}$$

Where $K(\rho)$ denotes the area with concentration values greater than the contour value ρ; t represents the threshold; and $a1$ and $a2$ are characteristic exponents. In the current study the following approach was used to calculate $K(\rho)$: $K(\rho)$ are the values obtained by

box counting of elemental concentration values. By box counting, one superimposes grid with cells in the region. The area $K(\rho)$ for a given ρ is equal to the number of cells multiplied by cell area with concentration values greater than ρ. The breaks between straight-line segments on this plot and the corresponding values of ρ have been used as thresholds to separate geochemical values into different components, at the same time representing different causal factors, such as lithological differences and geochemical processes (Daya, 2015a; Daya, 2015b). Factors such as mineralizing events and surficial geochemical element concentrations are important to be considered (Goncalves et al., 1998; Lima et al., 2003; Daya, 2015*a*; Daya, 2015*b*; Daya and Afzal., 2015; Afzal et al., 2010).

3. Geological Setting of Janja Area

The studied area is near the Sefidabeh, a district of Poshtab of Zabol city. The oldest rocks of the region are sedimentary rocks with flyschfacies largely dispersed in the region. Igneous rocks of the study area are mainly in the form of dykes from the trend of East - West and North East - South West which penetrated in sedimentary rocks and they have changed the general trend of the rocks (Figure 1; Camp and Griffis, 1982).

The region has general east-west and NE-SW trends structures. These trends followed by the inclined collision of Lut plate with Neh complex at the end of Eocene, continue the compressing movements; and at the end of Oligocene, the pressure, as sliding-stretching movements, has appeared in line with some old breaks and a much younger coupled system. Upper Miocene right turning tectonics affecting of old systems of the area which are related to the closure of east Flysch basin of Iran (Eocene-Oligocene) creates suitable stretching spaces for discharging lava. Dikes in the studied area are visible in form of altered and non-altered porphyritic in texture (Griffis et al., 1977; 1978).

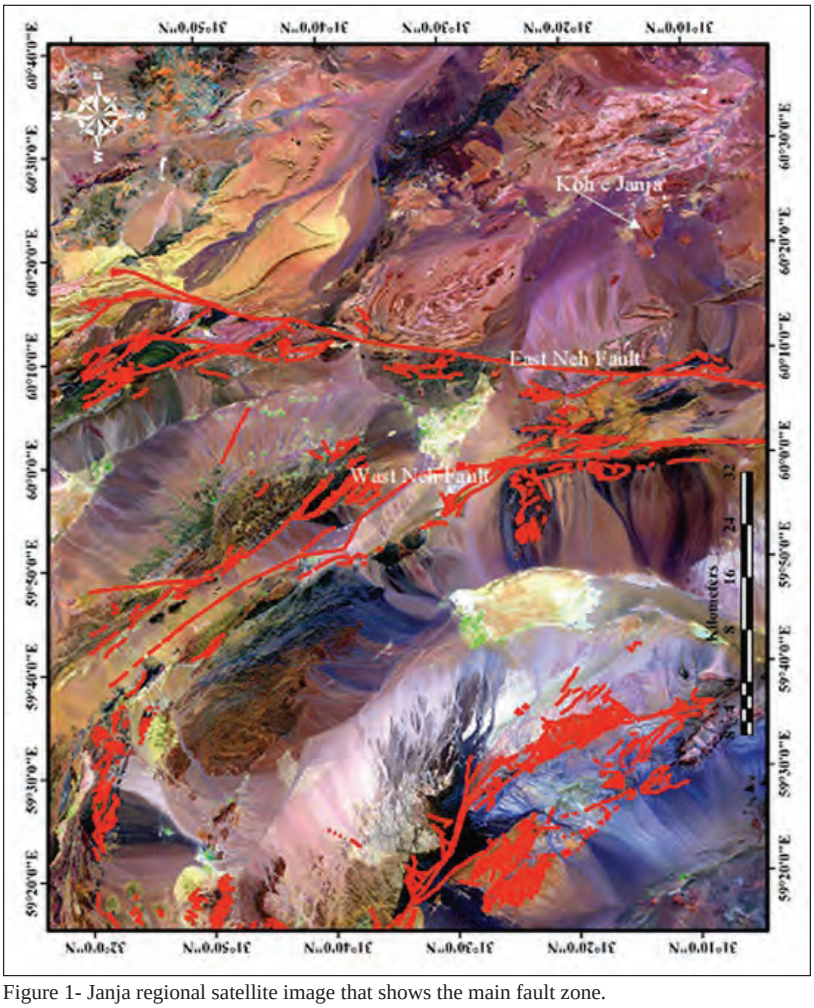

Figure 1- Janja regional satellite image that shows the main fault zone.

The main minerals of rocks in the region in hand specimen are amphibole (hornblende) and plagioclase (Figure 2). In addition to the main mineral in microscopic levels, there are secondary minerals of epidote, chlorite, calcite and opaque minerals. The results of the modal mineralogy studies and chemical analysis showed that these rocks are much more granodiorite to diorite in terms of lithological composition and they are in calc-alkaline range in terms of magmatic series.

Field investigations and laboratory studies that were done on igneous and metamorphic rocks showed that the studied region didn't have a lithological diversity. Igneous rocks are diorite dikes and sedimentary rocks include shale, sandstone and carbonate rocks (limestone and mudstone) which have undergone a weak transformation and heterology due to penetration dikes. These rocks along with dikes are form the highlands of this region. The metamorphic rocks in Janja region include slate and hornfels. It seems that protoliths of these rocks were carbonate shale and limestone which were undergone a weak transformation. It seems that in the last stages of the magmatic dikes cooling, hydrothermal fluids get out and at the time of penetrating the rock walls, it leads to the formation of minerals in them.

Potential mineralization in the area is done in two ways. The main form of mineralization in the area is associated with the transformation and alteration. The effect of this process include transforming the rocks, creating Calc-silicate rocks containing garnet, propillite alteration, making rocks siliceous, and the presence of sulfur minerals such as pyrite and chalcopyrite. The mineralization occurred as micro-riche fillings and the formation of iron oxides with copper carbonates (malachite and azurite) which were local and especially on the periphery of the main mineralization veinlets in form of low zones, show this kind of surface mineralization (Thomson and Howarth, 1978).

4. Sampling, Modeling and Data Analysis

In order to determine the anomaly area, the concentration of 8 elements of Au, Cu, Mn, Zn, Fe, As, Mo, and Pb in 300 points of region's stream sediments were measured and recorded. Figure 3 shows the location of sampling points in the studied region.

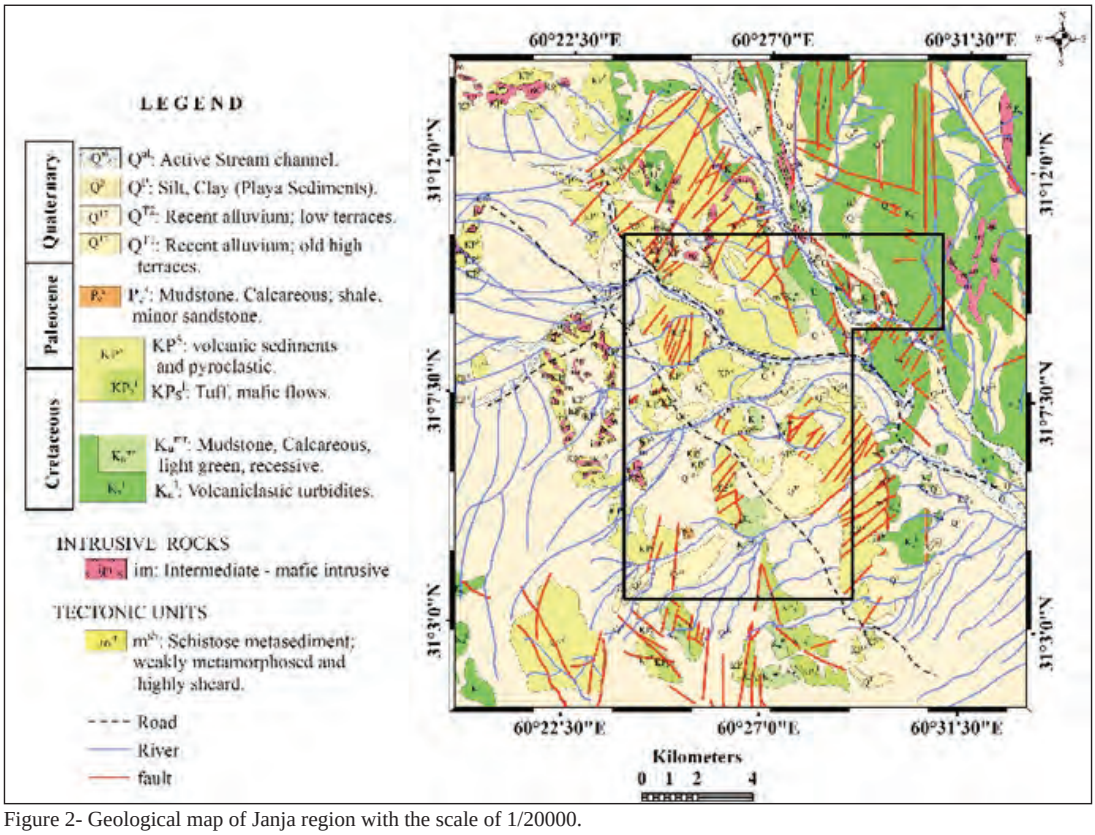

Figure 2- Geological map of Janja region with the scale of 1/20000.

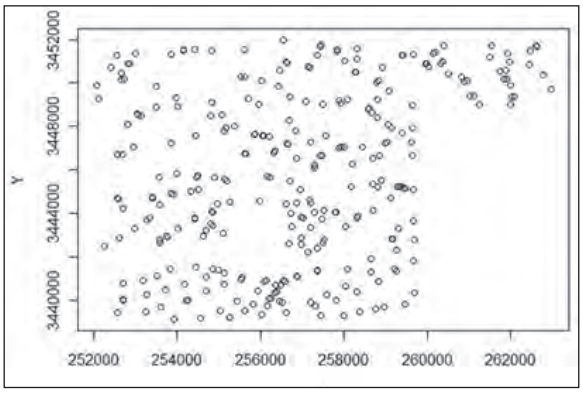

Figure 3- The location of stream sediments samples in Janja region.

The statistical investigation of collected data of stream sediment in the region in estimating and identifying the statistical features of the raw data, particularly the nature of their distribution function, help in better analysis of data resulting from estimation. Therefore, identifying the statistical variables of society including mean, variance, coefficient of variation, and in particular the skewness which implies on being normal or abnormal function of data distribution will be helpful (Jimenez-Espinosa et al., 1993). Statistical analysis was carried out by SPSS Statistical Software. In table 1, a summary of descriptive statistical observations is stated. Among all these factors, the shape of distribution function and its deviation from the normal distribution and the possibility of converting data to the normal distribution in the estimation process is very important (Jimenez-Espinosa et al., 1993). Therefore, it is necessary to draw a diagram and frequency distribution of data for these variables (Figure 4). In figure 4, to describe the data, histogram of variables is shown.

Statistical results revealed that mean values of As, Au, Cu, Fe, Mn, Mo, Pb and Zn were 15.34, 0.77,

Table 1- As, Au, Cu, Fe, Mn, Mo, Pb and Zn statistical parameters of 300 stream sediment samples from Janja region.

Element (ppm)	N	Min	Max	Mean	Std. Deviation
As	300	0.26	88.30	15.34	10.86
Au	300	0.01	3.00	0.77	0.49
Cu	300	0.12	133.12	22.43	14.16
Fe	300	174.0	88117.0	30127.61	16222.7
Mn	300	6.70	4063.05	822.10	520.90
Mo	300	0.01	5.93	0.89	0.61
Pb	300	0.20	378.20	67.60	53.05
Zn	300	0.92	435.71	64.27	43.45

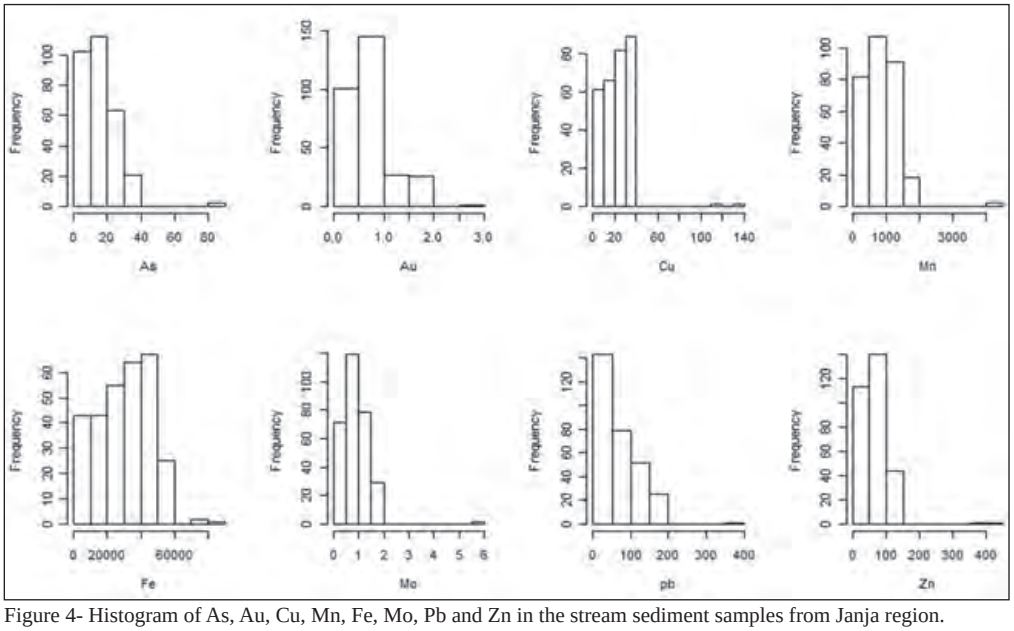

Figure 4- Histogram of As, Au, Cu, Mn, Fe, Mo, Pb and Zn in the stream sediment samples from Janja region.

22.43, 30127.61, 822.10, 0.89, 67.60, and 64.27 ppm, respectively. Their distributions are as shown in figure 4. Table 1 lists the statistical parameters of As, Au, Cu, Fe, Mn, Mo, Pb and Zn. Histograms of Mo, Mn and Fe appeared to be approximately symmetric. However, the histograms for other elements in the region do not show normal distributions.

To check the process, the diagram of data balance was plotted. The contour line is a curve that connects all the points with the same concentration. The reason of drawing the contour line of data is to see whether the mean of random field is constant or not. Figure 5 shows the contour lines curve for 8 studied elements. Since there isn't any special pattern in these figures, the mean of random field is considered as fixed.

5. Discussion

Geochemical maps were generated with Inverse Distance Weighing (IDW) method. IDW method was used for estimation. The maps were drawn by Rockworks software package. IDW method clarifies the concentration of region boundaries. It is more applicable and suitable to use Inverse Distance Weighing method rather than kriging. Kriging has high amounts of truncation errors for the upper and lower boundaries of region elemental concentrations (Afzal et al., 2010).

The studied area was gridded by 250 m×250 m cells. The proposed gridding pattern was applied because the principals of concentration- area fractal model was relied on the existence of partition function, and the sampled data could not be utilized efficiently; also, because one cannot sample the whole region, and for prediction of any parameter, i.e., elemental concentrations, gridding of the studied area was necessary and one cannot do otherwise (Afzal et al., 2010). The needed partition function to be applied in C-A fractal model is based on the assumption of having a cell characterization in the region in order to predict the area which has a special concentration. By this method the problem of over sampling will be solved because the concentration- fractal model automatically will remove any grid-related problem in division of the area into smaller elements and consequently; the original fractal character is preserved (Afzal et al., 2010).

5.1. Application of Concentration-Area (C-A) Fractal Model

Estimation of unsampled locations have been carried out by inverse distant squared weighting (IDWS) method. Then the elemental concentrations were sorted from low to high. Then the frequency of every element was calculated. Log- log plots of cumulative frequency of elemental concentrations versus related areas were drawn. Straight lines were fitted to the resulted log-log plots. There are a few break points in these plots. These are threshold values that separating populations of geochemical concentration. Figure 6 shows log-log plots for studied elements (Au, Cu, Zn, Fe, Mn, Mo, As and Pb) in the Janja region.

There are four geochemical populations for As, Fe, Mo, Pb and Zn and five geochemical populations for Au, Cu, and Mn as illustrated in figure 6. Based on the C-A log–log plot, there are four enrichment phases for As within threshold values equal to 14.15, 31.50 and 73.70 ppm where higher than the last threshold value the extreme As enrichment phase in the study area (Table 2). The population below 28282 ppm and between 32859 and 73130 ppm are the low and moderate phase of Fe enrichment, respectively. In addition, the population of upper than 73130 ppm has a high enrichment phase of Fe in the study area. Moreover, Cu C–A log–log plot shows five geochemical populations for this element with threshold values equal to 20, 28.5, 36.6, and 109 ppm (Table 2). Low and moderate Mn phases are below 812 ppm and between 1408 and 3294 ppm, but high phase has high value of Mn higher than 3827 ppm. Molybdenum has four enrichment phases in the study area based on Mo C–A log–log plot, as depicted in figure 6. Their threshold values equaled to 0.77, 1.50 and 4.95 ppm. Lower than 0.77 ppm is a low Mo enrichment phase in this area and moderate occurred between 1.50 and 4.95 ppm and population of upper than 4.95 ppm has a high enrichment phase of Mo (Table 2). Based on the results of the C–A model, the anomaly maps of every element were drawn (Figure 7, 8).

In figures 7 and 8, as shown in the right sidebar of maps, there is an increase in concentration as we go from yellow to red. In the other words, yellow means the backgrounds and the red shows the anomalies in that area.

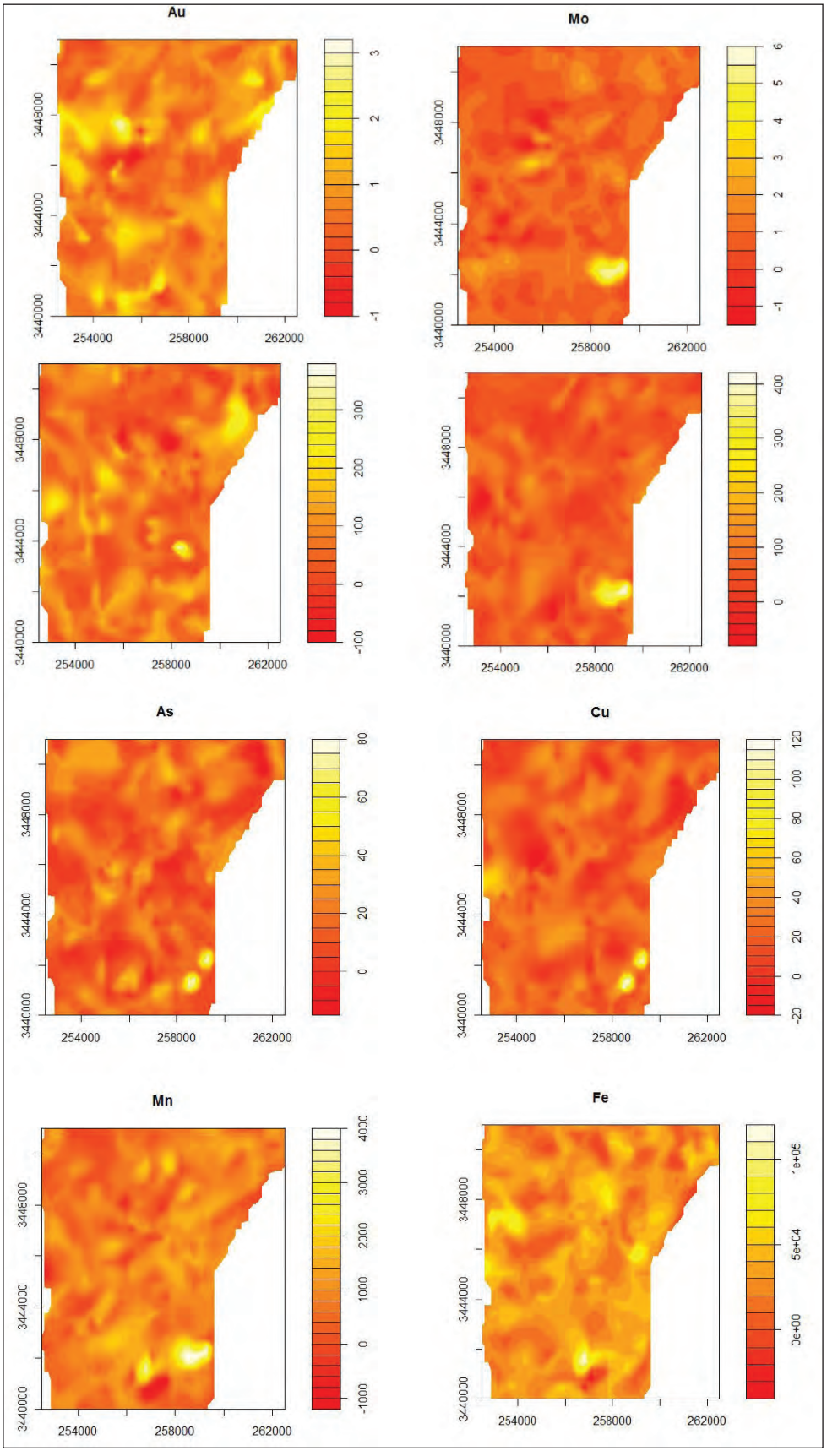

Figure 5- Contour line diagrams for 8 studied elements.

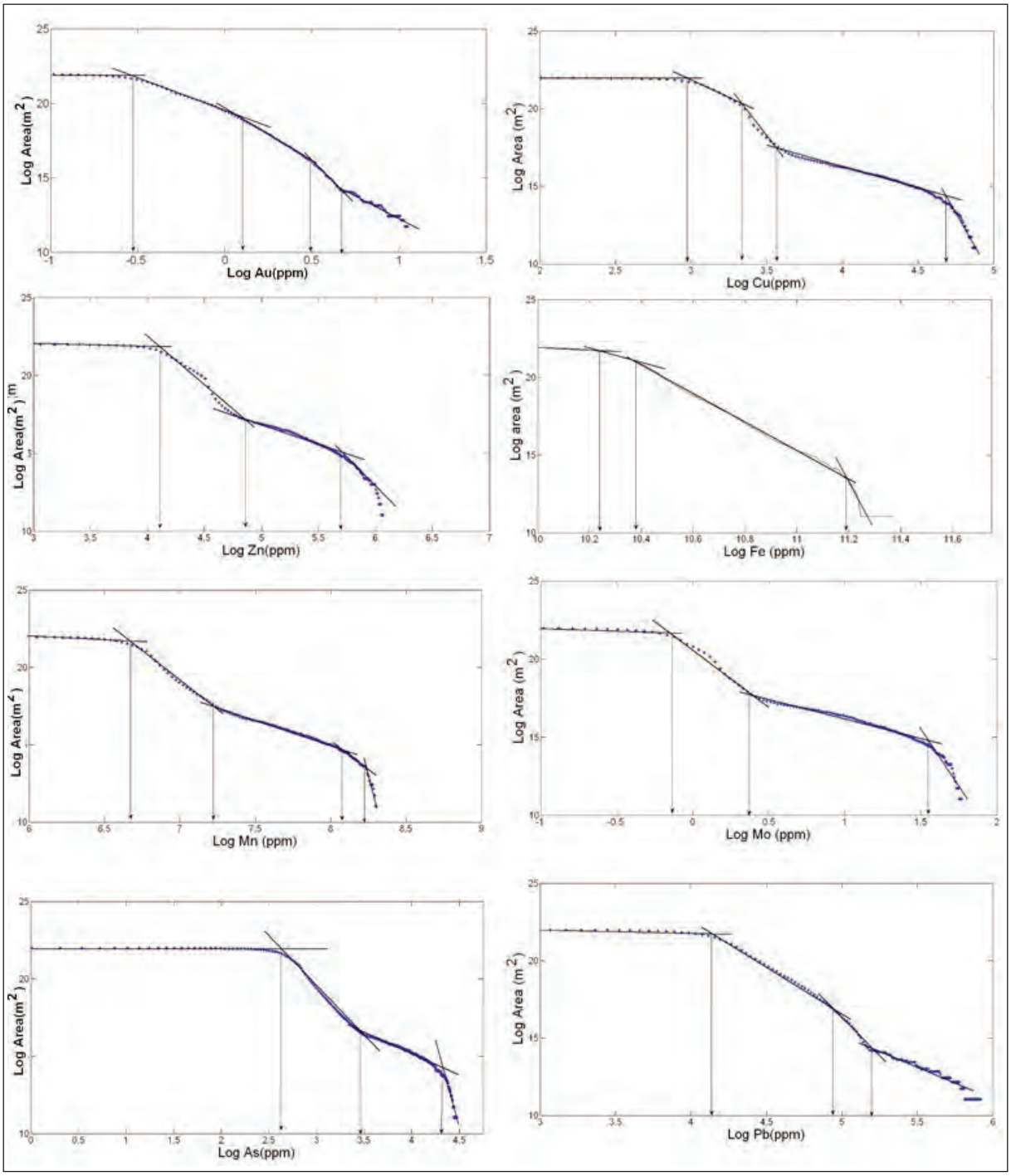

Figure 6- Log–log plots (C–A model) for Au, Cu, Zn, Fe, Mn, Mo, As and Pb.

5.2. Relationship Between Elemental Anomalies Resulted by C-A Fractal Model

By comparing the figure 7 and 8, it is concluded that concentration of elements has an inverse relationship with Au concentration, in a way that in the area in which the concentration of elements is high, the concentration of gold is low. It is observed that there is a direct correlation between the Fe anomalies and the Au anomalies (Figure 7). Therefore, using the magnetometry method can be a useful tool in determining the areas containing gold. By comparing figures 7 and 8, it is observed that there isn't any good correlation between manganese, lead, and zinc with

Table 2- Thresholds of C-A model for different geochemical anomalies of Au, Cu, Zn, Fe, Mn, Mo, As and Pb.

Element (ppm)	C-A fractal model		
	Low	Moderate	High
Au	0.60	1.16	1.65
Cu	20.10	28.50	36.6
Zn	61.56	121.50	284.30
Fe	28282.54	32859.63	73130.45
Mn	812.40	1408.10	3294.47
Mo	0.78	1.50	4.95
As	14.15	31.50	73.70
Pb	63.43	134.30	190.57

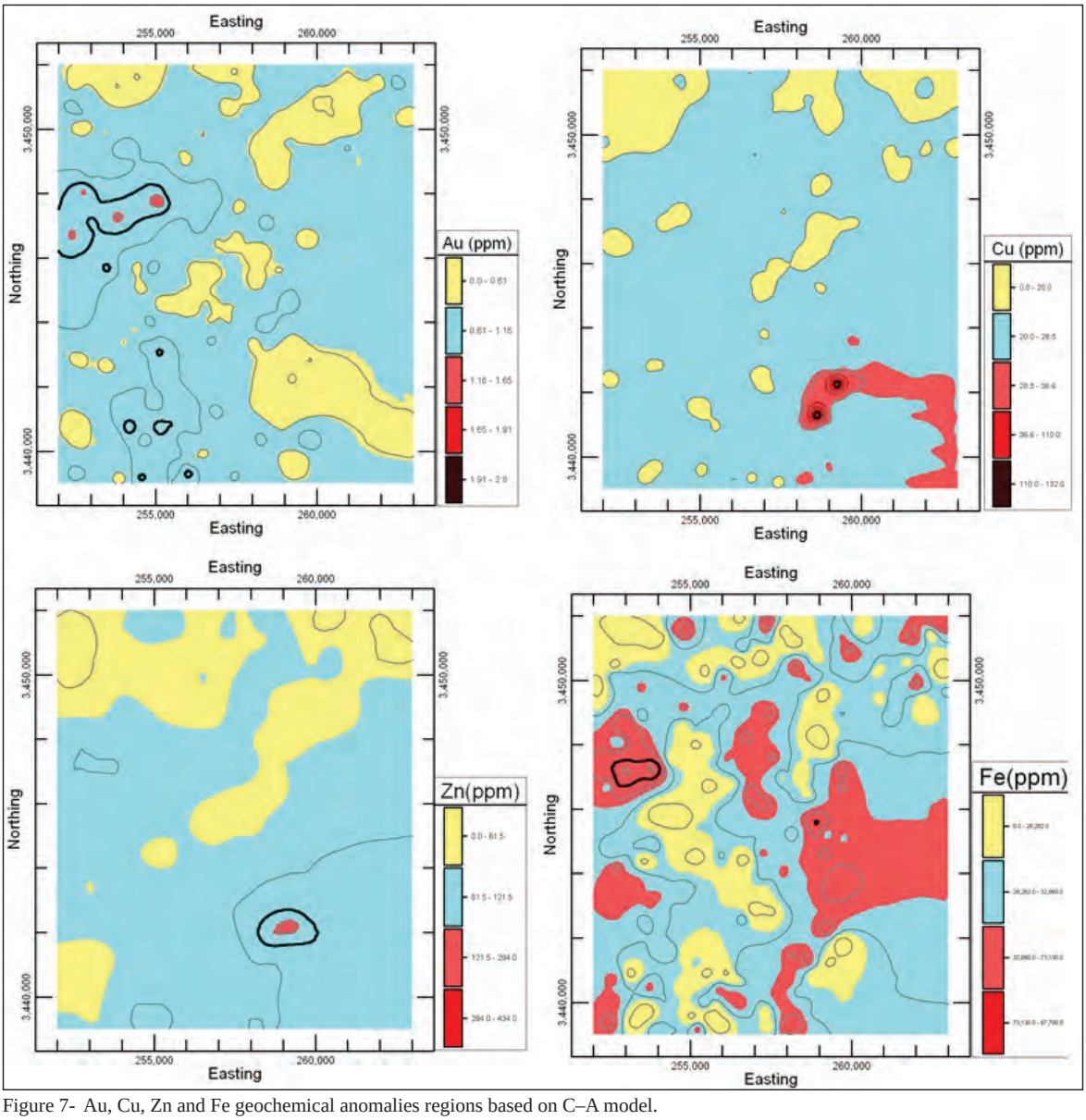

Figure 7- Au, Cu, Zn and Fe geochemical anomalies regions based on C–A model.

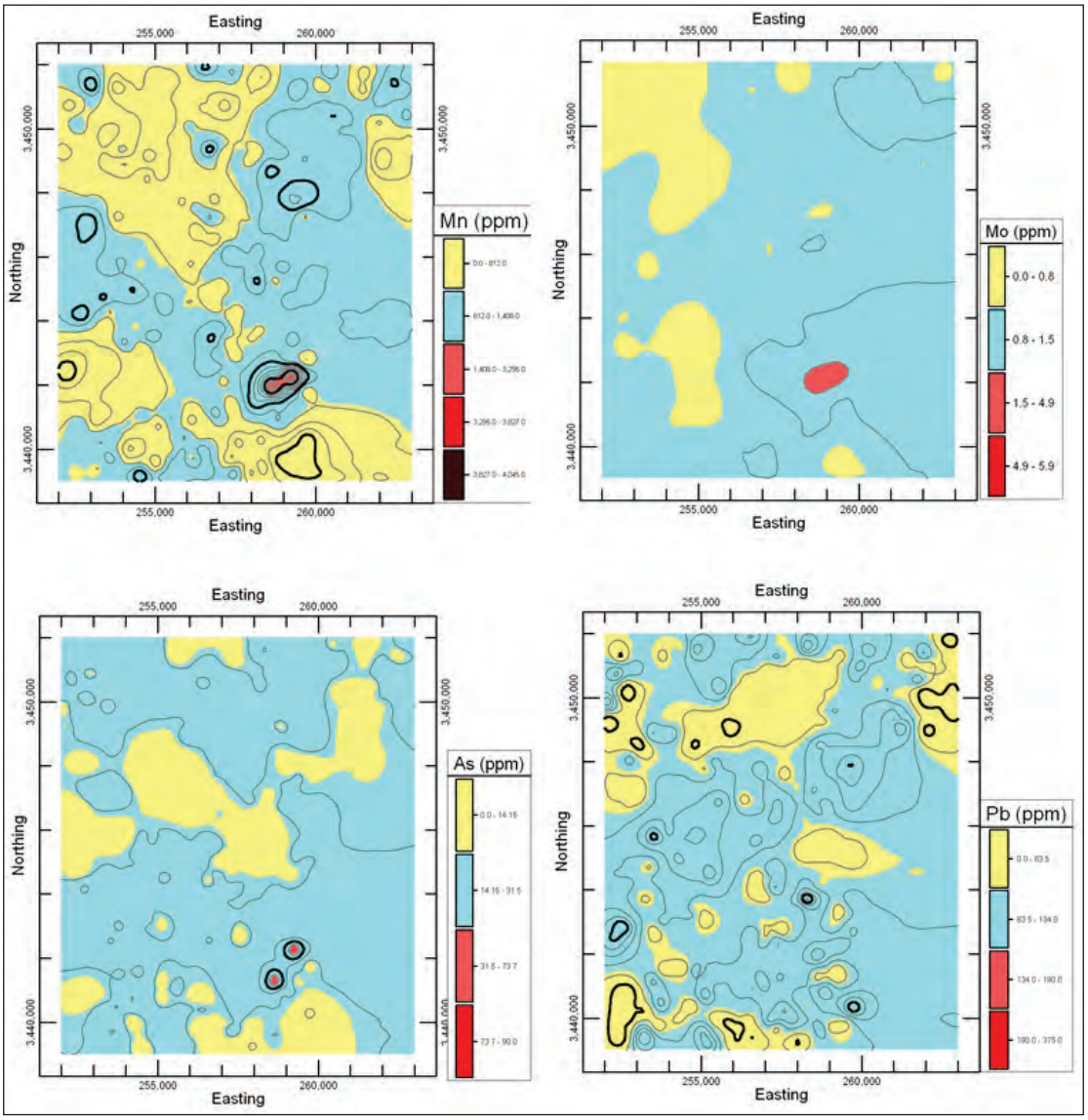

Figure 8- Mn, Mo, As and Pb geochemical anomalies regions based on C–A model.

gold. These elements cannot be a good guidance for determining the anomaly of gold in the region. Finally, the maps show that the correlation between the concentrations of molybdenum with copper is, to some extent, good. Given that the studied region is located within the mineral zone of Khash-Nehbandan, this area is the host of hydrothermal mineralization. The correlation between Cu, Zn, Mn, As, and molybdenum confirms this hydrothermal mineralization. Near this area, there is an antimony deposit of Sefidabeh. Totally, there is a correlation between the copper anomalies in the studied area with iron and molybdenum anomalies, which can be the proof of the porphyry origin of copper in this region; As it can be seen in figures7 and 8, the surface geochemical maps show the geochemical anomalies in southeastern part of area for Cu, Mo, Mn and As. It also can be seen in figure 2, the origin of this mineralization is likely a series of porphyry dykes with diorite composition, which have stopped the flyschfacies sedimentary units.

5.3. Correlation of Anomalies with Geological Process

Anomalies of Zn, Mo, Mn, Fe, Cu and As located in southeastern part of study area. Arsenic anomalies are accompanied with Cu and Mo anomalies. It can be said that As is a trace for mineralization. There is a good correlation between faults and elementals anomalies. It can be concluded that mineralization occurred along the faults. It can also be said that the type of

mineralization is porphyry or vein type deposits. In most of the cases Cu and Mo mineralization are in porphyritic type and occurred in stockworks, veinlets and veins. The general trend of faults in this part of the studied are is northwest-south east (Figure2). There is an important point here that the strike of anomalies is the same as the strike of faults (Figs 7, 8, 2). It means that mineralization or enrichment are along the faults. Regarding lithology, there is a correlation between anomalies and sedimentary rocks (alluvium and recent alluvium sediments) in SE part of study area. These alluviums can be generated by weathering of volcanic and intrusive rocks. In addition, these anomalies correspond to the tuffs and turbidities in the SE part of the studied area. Gold anomalies are located in the NW parts of the studied area. There is a strong relationship between the location of Au anomalies and fault systems in the NW parts of the studied area. It can be interpreted that the gold mineralization occurred along the fault systems. The Gold anomalies are correlated to volcanic sedimentary rocks.

Iron concentrations are sporadic and correspond to the volcano-sedimentary rock and turbidites. There is a good correlation between the Fe anomalies and Faults in the study area. There is a direct relationship between Fe anomalies and Au anomalies in the NW part of the study area. Existence of Au and Fe anomalies in this part can be interpreted as the presence of hematization or limonitization alterations. As a result of these alterations Au enrichment occurred.

6. Conclusion

The concentration-area (C-A) fractal model is as a filter in geochemical prospecting when attempting to differentiate between anomalous samples and those belonging to geochemical background. In this study, this model was used for determining the anomaly map of eight elements in the studied area. The surface geochemical maps showed the existence of geochemical anomalies in southeastern part of the studied area for Zn, Mo, Mn, Cu and As. There are four geochemical populations for As, Fe, Mo, Pb and Zn and five geochemical populations for Au, Cu, and Mn. Except of the Iron anomaly, the anomalies of elements has an inverse relationship with Au concentration, in a way that in the area in which the concentrations of elements are high, the concentration of gold is low. The maps shows that the correlation between the anomalies of molybdenum with copper is, to some extent, good. Given that the studied region is located within the mineral zone of Khash-Nehbandan, this area is the host of hydrothermal mineralization, especially epithermal as well as the porphyry deposits. The surface geochemical maps show the geochemical anomalies in southeastern part of area for Cu, Mo, Mn and Arsenic. The origin of this mineralization is likely a series of porphyry dykes with diorite composition, which have stopped the flyschfacies sedimentary units. There is a good correlation between faults and elementals anomalies. It can be concluded that mineralization occurred along the faults. It can be said that the type of mineralization is porphyry or vein type deposits. There is a correlation between anomalies and sedimentary rocks (alluvium and recent alluvium sediments) in SE part of study area. Gold anomalies are located in the NW parts of the studied area. There is a strong relationship between the location of Au anomalies and fault systems in the NW parts of the studied area. It can be interpreted that the gold mineralization occurred along the fault systems. The gold anomalies are correlated to volcano-sedimentary rocks.

References

Afzal, P., Khakzad, A., Moarefvand, P., Rashidnejad Omran, N., Esfandiari, B., Fadakar Alghalandis, Y. 2010. Geochemical anomaly separation by multifractal modeling in Kahang (Gor Gor) porphyry system, Central Iran, Journal of Geochemical Exploration 104, 34–46.

Afzal P., Fadakar Alghalandis Y., Khakzad A., Moarefvand P., Rashidnejad Omran N. 2011. Delineation of mineralization zones in porphyry Cu 304 deposits by fractal concentration–volume modeling. Journal Geochemical Exploration 108, 220–232.

Camp, V.E., Griffis, R.J. 1982. Character, genesis and tectonic setting of igneous rocks in Sistan suture zone. Lithos, Vol.15, pp.21-239.

Cheng, Q. 1999. Spatial and scaling modeling for geochemical anomaly separation: Journal of Geochemical Exploration, 65,175–194.

Cheng, Q., Agterberg, F.P., Ballantyne, S.B. 1994. The separation of geochemical anomalies from background by fractal methods. Journal Geochemical Exploration 51,109–130.

Daya, A.A. 2015*a*. Comparative study of C–A, C–P, and N–S fractal methods for separating geochemical anomalies from background: A case study of Kamoshgaran region, northwest of Iran. Journal of Geochemical Exploration. 150: 52–63.

Daya, A.A. 2015*b*. Application of concentration–area method for separating geochemical anomalies from background: a case study of Shorabhaji region, northwest of Iran. Arabian Journal of Geosciences. 8:3905–3913.

Daya, A.A, Afzal, P. 2015. Comparative study of concentration-area (C-A) and spectrum-area (S-A) fractal models for separating geochemical anomalies in Shorabhaji region, NW Iran. Arabian Journal of Geosciences 8:8263–8275.

Daya, A.A., Boomeri, M., Mazraee. 2017. Identification of Geochemical Anomalies by Using of Concentration-Area (C-A) Fractal Model in Nakhilab Region, SE Iran. Journal of Mining and Mineral Engineering. 8,70-81.

Davis, John C. 2002. Statistics and Data Analysis in Geology, 3th ed. John Wiley & Sons Inc, New York.

Dimri, V. 2000. Application fractals in earth sciences: Springer- Verlag, New York.

Goncalves, M.A., Vairinho, M., Oliveira, V. 1998. Study of geochemical anomalies in Mombeja area using a multifractal methodology and geostatistics. In: Buccianti A, Nardi G, Potenza R (eds) IVIAMG'98. De Frede, Ischia Island, pp 590–595.

Griffis, R.J., Meixner, H.M., Griffis,A.T., Bondar, W.F, Leitch, C.H.B. 1977-1978. Report on preliminary mineral reconnaissance aest block, East Iran, *Geology and Mineral Survey of Iran.*

Lima, A., De Vivo, B., Cicchella, D., Cortini, M., Albanese, S. 2003. Multifractal IDW interpolation and fractal filtering method in environmental studies: an application on regional stream sediments of Campania region (Italy). Applied Geochemistry 18, 1853–1865.

Mandelbrot, B.B. 1983. The Fractal Geometry of Nature (Update and augmented edition), Freeman, New York, 468 pp.

Jimenez-Espinosa, R., Sousa, A.J., Chica-Olmo, M. 1993. Identification of geochemical anomalies using principal component analysis and factorial kriging analysis, Journal of Geochemical Exploration, 46, 245-256.

Thomson, M., Howarth, R.J. 1978. A new approach to the Estimation of Analytical precision, Journal of Geochemical Exploration, Vol.9.

Bull. Min. Res. Exp. (2018) 156: 179-192

Bulletin of the Mineral Research and Exploration

http://bulletin.mta.gov.tr

Use of Moran's I and robust statistics to separate geochemical anomalies in Jiurui area (Southeast China)

Tien Thanh NGUYEN[a*]

[a]*Ha Noi University of Natural Resources and Environment, Ha Noi, Viet Nam. orcid.org/0000-0002-7600-5858.*

Research Article

Keywords:
Anomaly distribution, Terrestrial Moran Statistic, Robust Statistics, Jiurui Copper Field.

ABSTRACT

Separation of geochemical anomalies from background plays an important role in the study of exploration geochemistry. The limitations of commonly used methods are not taken into account spatial correlation, variability and the unsatisfactory of the statistical assumption of the normality of geochemical data. For solving these limitations, an indirect method for the separation of geochemical anomalies is proposed based on anomaly separation of local Moran's I_i values using robust statistics in this study. The experiment was carried out using 1481 samples collected from Jiurui copper prospect (southeast China). The steps for the anomaly separation are (i) spatial association and variability were first analyzied by means of Moran scatterplots at six spatial scales (2, 4, 6, 8, 10 and 12 km) using both raw data and Box-Cox transformed data; (ii) local Moran's I_i was used to measure spatial autocorrelationat these six local scales; (iii) anomalous separation was finally performed using the MEDIAN ± 1.5*IQR (IQR: interquartile range) rule on local Moran's I_i values. The results show that geochemical anomalies are mostly concentrated around known ore-deposits, according the objective reality and a strong correlation with known ore-deposits in Jiurui copper prospect.

Received Date: 15.03.2017
Accepted Date: 04.11.2017

1. Introduction

Geochemical anomaly separation is a fundamental issue in the operation of geochemical exploration, which is defined as a region where the concentration of an element is greater than a certain threshold value by statistical parameters, such as mean, median, mode, and standard deviation (Bolviken, 1992; Cheng, 1996; Davis, 2002; Li, 2003; Liu et al., 2013). In the 1960s, several procedures were recommended to select a threshold from background such as top 2½% selecting, the MEAN ± 2SDEV (SDEV: standard deviation) rule (Hawkes and Webb, 1962), frequency analysis including histogram, probability, Q-Q plots, and box-plot (Sinclair, 1974, 1976, 1991; Stanley and Sinclair, 1989; Garrett, 1989). The data distribution is important because these classical methods assume normality or lognormality. They do not, however, consider the shape, extent and magnitude of anomalous areas and disregard its spatial variability (Afzal et al., 2010; 2013; Hashemi et al., 2010; Momeni et al., 2016; Nazarpour et at., 2015, 2016; Rajabzadeh et al., 2015) and that must be known when applying these classical statistical methods. But this basic requirement has been still widely neglected in many studies (Philip and Watson, 1987; Rock, 1988). These statistical methods usually assumed that the concentration of ore elements in the crust follow a normal or log-normal distribution (Ahrens, 1953, 1954*a*, *b*, 1957) due to the existence of extreme values and outliers (Reiman et al., 2005), even for Box-Cox or log-transformed data (Liu et al., 2017; McGrath and Loveland, 1992; Nguyen et al., 2014). The widely-used, classical statistical methods are likely to fail for strongly skewed data (Reimann and Filzmoser, 2000) for not being warranted for assumptions of normality, independence, and identical distribution. Therefore, many methods for outlier detection have been proposed based on robust

**Corresponding author: Tien Thanh NGUYEN, tdgis_ntthanh@163.com*
http://dx.doi.org/ 10.19111/bulletinofmre.351376

statistics (Barnett and Lewis, 1994; Dutter et al., 2003; Huber, 1981; Hampel et al., 1986; Rousseeuw and Leroy, 1987). Recently, Reimann (2005) used robust statistics (Huber, 1981) and exploratory data analysis (EDA) techniques (Tukey, 1977) including the boxplot and the MEDIAN ± 2*MAD (MAD: median absolute deviation) rule for the estimation of threshold values and the range of background data, in which the MEDIAN ±2*MAD does not adequately build on statistical assumptions. Another approach for the identification of extreme values is the MEDIAN ± 1.5*IQR (IQR: interquartile range; Tukey, 1977). The estimators of MEDIAN, MAD and IQR are widely available statistical software packages (Reiman, 2005).

Geochemistry properties and processes are defined in different scales. In many cases, spatial variation is not random, but tends to follow a pattern in which variability decreases as distance decreases between points in space as Tobler (1979). Therefore, it is important to take into account spatial correlation and variability of geochemical data when separating geochemcal anomaly. These non-spatial statistical methods (classical and robust statistics) ignore the spatial information or autocorrelation structure of the geochemical data.In geography, spatial information or autocorrelation structure can be identified by association statistics such as Getis's G index (Getis and Ord, 1992), Geary's C (Geary, 1954), spatial scan statistics (Ishioka et al., 2007), Tango's C index (Tango, 1995; Zhang and Lin, 2006), and local Moran's I. These statistics have been widely used for many fields of study such as biological sciences (Legendre and Gauthier, 2014) environmental planning (Brody et al., 2006), environmental sciences (Zhang and McGrath, 2004; Ruiz-Rivera and Paul, 2016), criminal study (Wang et al., 2016), andmortality rates (Martins-Melo, 2016, 2017), especially in geochemical exploration (Nguyen et al., 2014, 2016). The local Moran's I_i has been used to identify Cu anomalies in Jiurui copper mining area, but spatial scales were chosen randomly without scientific basis (Nguyen et al., 2014). Recently, Nguyen et al. (2016) proposed a method for the identification of spatial clusters and outlier of an association of Cu, Au, Mo, Ag, Pb, Zn, As, and Sb elements based on a combination of robust Mahalanobis distance and local Moran's I_i. In this study, we focus on the performance of a robust statistic (the MEDIAN ± 1.5*IQR) and Moran's I to separate Cu anomalies from 1341 stream sediment samples.

2. Geological Setting and Dataset

Jiurui district is an important copper miningarea in China's Jiangxi province and rich in copper reserves. It is locatedin the middle and lower Yangtze River metallogenic belt with copper-iron mineralization and North West Gate - Fengshan mountain cave. Around 154,968 million tons of copper, gold and silver reserves were discovered in Jiurui area. A total of 16 copper mineralized zones, three molybdenite orebodies and 120 small orebodies were found in the mining area with an average copper grade of 0.69%. According to the Jiangxi provincial government, the region produced 651,000 million tons of refined copper in the first half of 2014, up 11% from the previous year.Iron and copper deposits are one of the main ore deposits in the downstream in the area. The formation of rocks and ores control the distribution of large ore deposit. The main tectonic belt and its vicinity are located in shallow ore prospecting target area, Wushan Chengmenshan mining area, the edge and deep prospecting potential. Iron copper deposits are divided into two metallogenic series: (i) submarine exhalative related activities found that metallogenic series are any hydrothermal deposits from the injection to the bottom of the sea environment, (ii) intermediate acid hypabyssal intrusive activities-related ore deposits; refers to the formation of intrusive rocks of carboniferous sand Triassic strata in contact zone and rock deposits. Skarn, iron-copper, porphyry copper, key, vein copper, gold are the main types of deposits in the study area.

A total of 1482 multi-element sediment geochemical samples (1 composite sample per 4 km^2) representing 5364 km^2 were collected from regional stream sediment surveys (Figure 3). Twenty-three indexes were found in a composite sample, including Ag, As, Au, Be, Cd, Cu, Hg, Li, Mn, Mo, Nb, Pb, Sb, Sn, Th, V, W, Y, Zn, Al_2O_3, CaO, K_2O, Na_2O in which silver, gold, copper are three ore-forming elements. Three geochemical associations of elements causing anomalous area in the study area include Cu, Au, Mo, Ag, Pb, Zn, As, Sb;Mo, Sb, Zn, Ag, V and Sn, W, Sb, Mo, Zn, Ag, As. Two metallogenic with a total of 13 ore deposits were found at the time of data collection.

Raw data was first checked including two aspects: data checking and processing of missing semi-quantitative and unreliable data. The initial phase for raw data checking consists of simple and obvious procedures carried out in the first stage of acceptance

the results from the laboratory. The integrity and validity of dataset were checked. During the initial data checking phase missing, non-numeric, coded an unreliable results were dealt with. Obvious misfit such as results that are way out of expected ranges and control samples that clearly do not conform to expected values were identified by looking at the data. Unreliable data and coordinates were also corrected. A total of 51 duplicate samples in 1482 collected sediment samples were removed.

3. Methodology

The process of separation of Cu anomalies using Moran's and robust statistics can be expressed in figure 1.

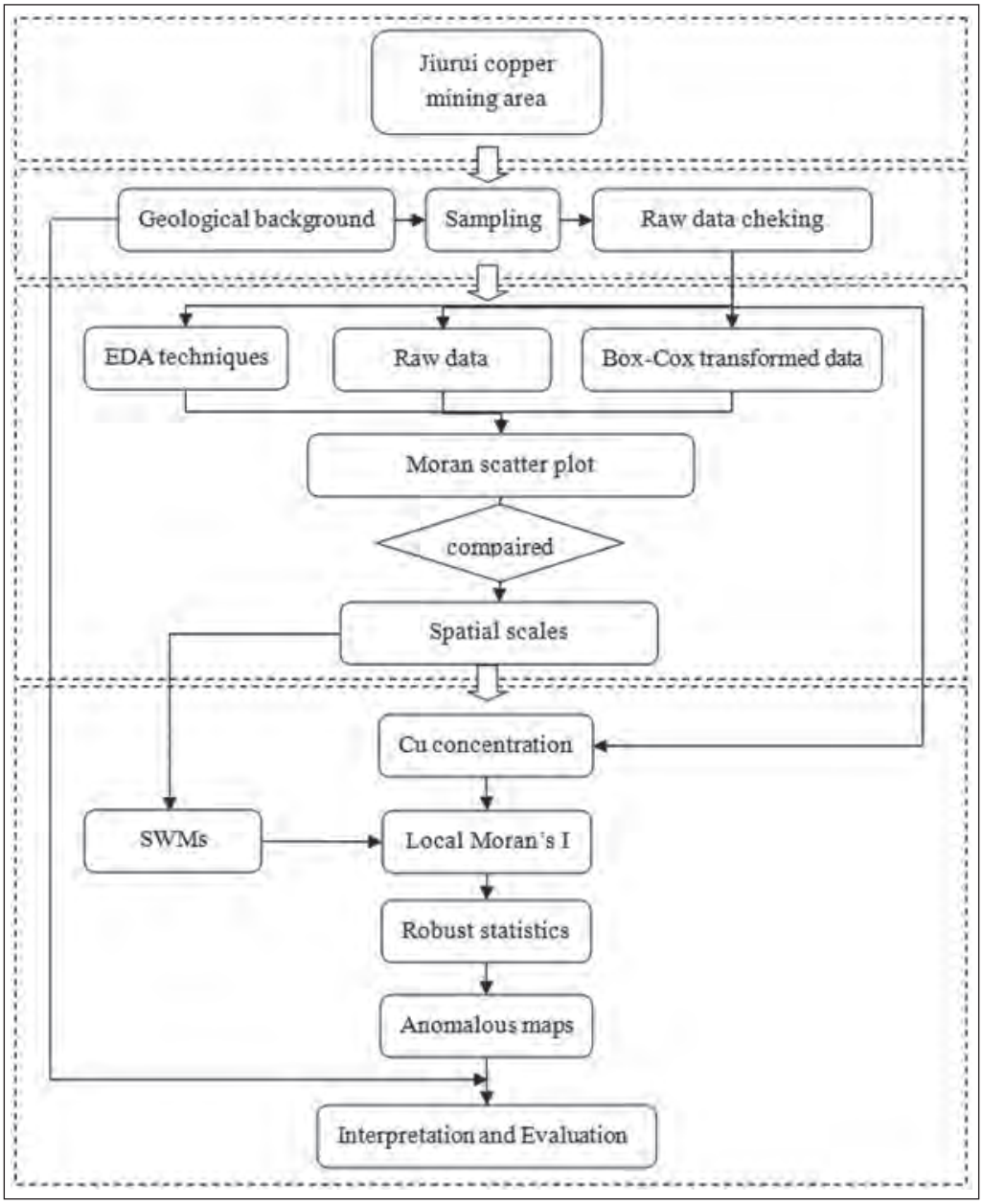

Figure 1- Flow chat for the separation of geochemical anomalies using Moran's I and robust statistics.

3.1. Moran Scatterplot

Global Moran's *I* statistic is given by the expression (Cliff and Ord, 1981):

$$I = \frac{N}{S_0}\frac{\sum_{i=1}^{N}\sum_{j=1}^{N} W_{ij}(x_i-\bar{x})(x_j-\bar{x})}{\sum_{i=1}^{N}(x_i-\bar{x})^2} \quad (1)$$

where: x_i and x_j are the values of observed variable at sites *i* and *j*; *d* is the distance class considered in the calculation; S_0 is the sum of the weights W_{ij}, given by: $S_0 = \sum_{i=1}^{N}\sum_{j=1}^{N} W_{ij}$; $\bar{x}$ is the sample mean of the observed variable, given by: $\bar{x} = \sum_{i=1}^{N} \frac{x_i}{N}$; *N* stands for the number of observations with

$$W_{ij} = \begin{cases} 1 & \text{if } d_{ij} < d \\ 0 & \text{otherwise} \end{cases}$$

W_{ij} is spatial weight matrix for a given distance *d* and d_{ij} is the distance between the observations *i* and *j*. The spatial weight matrix computed from a given distance is row-standardized so that the sums of the weights for a trap are equal to one (Cocu et al., 2005):

$$W_{ij}^{s} = W_{ij} * \left(\sum_{j}^{n} W_{ij}\right)^{-1} \text{ such that } \sum_{j}^{n} W_{ij}^{s} = 1$$

where each row sums to 1 leading to the normalizing factor S_0 equals to *N*. In this case, this is the preferred way to implement this test (Anselin, 1992). This allows a comparison of the spatial autocorrelation statistics between the various neighboring distances because, for each of them, identical importance is attached to all the neighbors independently of their number. The numerator of Equ. (1) corresponds to the covariance between contiguous samples. This covariance is zero in the absence of spatial autocorrelation, positive in the presence of positive spatial autocorrelation, and negative in the presence of negative spatial autocorrelation. The covariance is standardized by the denominator, which is a measure of the variance of the samples. In the calculation of the statistic, the mean of the samples is a reference (Cocu, 2005): (i) when *I* = 0: the covariance between contiguous samples is zero, the neighborhood does not play any part; there is no spatial autocorrelation.The observed spatial pattern of values is equally as likely as any other spatial pattern; (ii) when *I* > 0: the places are more similar. If they are contiguous, the spatial autocorrelation is positive. Similar values, either high or low values are more spatially clustered than could be caused purely by chance; and (iii) when *I* < 0: the places are more alike if they are far apart; the spatial autocorrelation is negative, the spatial pattern is regular.

Values for global Moran's *I* statistics need not be constrained to the interval [-1, 1]. Usually, $|I| < 1$, unless regions with extreme values of $x_i - \bar{x}$ are heavily weighted. The theoretical upper bound is (Cliff and Ord, 1981; Haining, 1990; Bailey and Gatrell, 1995):

$$|I| \le \frac{N}{\sum_{i\neq j}\sum_{j=1}^{n} W_{ij}} \left\{ \frac{\sum_{i\neq j}\left[\sum_{j=1}^{N} W_{ij}(x_i-\bar{x})\right]^2}{\sum_{i=1}^{N}(x_i-\bar{x})^2} \right\}^{1/2} \quad (2)$$

The significance of any observed value of Moran *I* can be judged by comparing it to its expected value , but it must also be account for the expected variability in the *I* statistic under the appropriate null hypothesis. This is where the distributional assumptions about the data become very important. With the randomization assumptions, the data values are reassigned among the *N* fixed locations, providing a randomization distribution against which we can judge our observed value. If our observed value of *I* lies in the tails of this distribution, we reject the assumption of independence among the observations and conclude that there is significant spatial autocorrelation in the data (Waller and Gotway, 2004). If relying on the normality assumptions, the z-score $z = [I - \mathrm{E}(I)]/\sqrt{\mathrm{Var}(I)}$ is compared to a standard normal distribution where E(*I*) and Var(*I*) are a given in Equ. (3) and (4) (Cliff and Ord, 1981):

$$\mathrm{E}(I) = \frac{-1}{N-1} \quad (3)$$

$$\mathrm{Var}(I) = \mathrm{E}(I^2) - [\mathrm{E}(I)]^2 \quad (4)$$

3.2.The Local Moran Statistic

Anselin (1992, 1995) developed measures of spatial autocorrelation at a local scale. A local Moran statistic for statistic for an observation *i* may be defined as (Anselin, 1995):

$$I_i = \frac{(x_i-\bar{x})}{m_2}\sum_{j\in J_i}^{N} W_{ij}(x_j-\bar{x}) \quad (5)$$

where the summation over *j* is such that only neighboring values $j \in J_i$ are included. For ease of interpretation, the weights may be in row-standardized form, though this is not necessary, and by convention, $W_{ij} = 0$;

$$m_2 = \frac{1}{N}\sum_{j=1}^{N}(x_i-\bar{x})^2$$

m_2 as the second moment. For a row-standardized spatial weight matrix $S_0 = N$, and for standardized variables (i.e., with the mean subtracted and divided by the standard deviation), $m_{2=1}$. When: (i) $I_i = 0$: there

is no spatial autocorrelation; (ii) $I_i > 0$: the spatial autocorrelation is positive. It conveys the presence of an association of values similar to the place *i* where the statistic is measured (hot spots); and (iii) $I_i < 0$: the spatial autocorrelation is negative, corresponding to an association of values that are opposed to the place *i* where the statistic is measured (cold spots).

The moments for I_i under the null hypothesis of no spatial association can be derived using the principles outlined in Cliff and Ord (1981). An advantage of this technique is that the significance of the null hypothesis can be tested. It is possible to quantify the probability that a spatial pattern as extreme as that observed could have appeared by chance. For a randomization hypothesis, the expected value E(I_i) turns out to be (Anselin, 1995):

$$E(I_i) = \frac{-W_i}{N-1}, \quad (6)$$

with as the sum of the row elements, $\sum_{j=1}^{N} W_{ij}$, and the variance Var(I_i) is found as:

$$\mathrm{Var(I_i)} = \frac{\mathrm{W_{i(2)}(N-b_2)}}{\mathrm{N-1}} + \frac{\mathrm{2W_{i(kh)}(2b_2-N)}}{\mathrm{(N-1)(N-2)}} - \frac{\mathrm{W_i^2}}{\mathrm{(N-1)^2}}, \quad (7)$$

where:

$$b_2 = \frac{m_4}{m_2^2};\ m_k = \frac{1}{N}\sum_{i=1}^{N}(x_i - \bar{x})^k;\ W_{i(2)} = \sum_{j\neq i}^{N} W_{ij}^2;\ \text{and}\ 2W_{i(kh)} = \sum_{k\neq i}^{N}\sum_{h\neq i}^{N} W_{ik}W_{ih}$$

A test for significant local Moran I_i may be based on these moments, although the exact distribution of local Moran I_i is still unknown (Anselin, 1995). Moran's I_i can also be standardized so that its significance leve can be tested based on an assumption of a normal distribution (Anselin, 1995; Levine, 2004). However, since the probability distribution of Moran's I_i may not necessarily be normal, especially when the raw data are heavily skewed, a method called "conditional permutation" (Anselin, 1995) is preferred as it makes no assumption about the data. Under a conditional permutation, when the value on a location is being assessed, its value is fixed and all the other values are randomly shuffled on all the other locations. Each time when the other values are shuffled, the local Moran's I_i statistic is calculated to form a reference distribution. The significance level can be estimated by comparing the observed index with these simulated values, and it is called "pseudo significance" (Anselin, 2005). The pseudo significance is computed as (M+1)/(R+1) where R is the number of permutations and M is the number of instances where a statistic computed from the permutations is equal to or greater than the observed value (for positive local Moran' I_i) or less or equal to the observed value (for negative local Moran's I_i) (Spatial Analysis Laboratory, 2007).

3.3. Robust Statistics

The local Moran's I_i statisticis well suited to identifying the existence of pockets of spatial association, to assess assumptions of stationarity and to identify distances beyond which no discernible association remains (Getis and Ord, 1996). If the underlying process is stable throughout the data, then one would expect the local indications to show little variation around their average. In other words, local values that are very different from the mean (or median) would indicate locations that contribute more than their expected share to the global statistic. These may be outliers or high leverage points (Anselin, 1995), local Moran's I_i values are not normally distributed. Therefore, robust statistics were used to identify outliers in a set of local Moran's I_i values by means of the MEDIAN ± 1.5*IQR rule expressed in Equ. (8):

$$\mathrm{IQR} = \mathrm{Q_3} - \mathrm{Q_1} \quad (8)$$

where: quartile 1 (Q_1) and 3 (Q_3) are the 25th and 75th percentile of ordered local Moran's I_i values or median of lower half and upper half of local Moran's I_i values.

3.4. Data Processing

The global, local Moran's I_i statistic and Moran's scatter plots were created in spatial statistics sofware - *GeoDA* (version 095i) in which both the global and local Moran's I_i statistics were tested using 999 permutations, and the significance level (p-value) was set to 0.05 (5%). The descriptive statistical parameters (mean, median, IQR), EDA techniques (histograms, density trace, 1-D scatter plots, boxplots, QQ plots and empirical cumulative distribution function plots) and Box-Cox transformation of geochemical data were performed by using the *StatDA* and *MASS* packages of Statistical Modeling and Computing - *R* Language (version i386 2.15.0). All of maps were visualized using *ArcGIS 9.3* software.

4. Results and Discussions

4.1. Cu Concentration in the Study Area

The spatial distribution of Cu in the study area shows the influence of mineral deposits. There is a high

value pattern of Cu in the north and the east. There are also some relatively high values scattered in the north-west where no deposits have so far been detected showing the complexity or spatial heterogeneity of Cu concentration (Figure 2). It is likely the high values (or extreme values) of Cu concentration were caused by mineralization.

The minimum, median, mean, and maximum values of Cu concentration are 9.2, 27.1, 37.3 and 1926 µg/g, respectively. It can be realized that the mean value of Cu concentration is 10.2 µg/g larger than the median value of 27.1 µg/g, therefore the distribution of Cu concentration has a positive skew. The skewness for Cu is 15.8 (much larger than zero), indicating that the size of the right-handed tail is larger than the left-handed tail. Cu has an asymmetrical distribution with a long tail to the right and a positive skew. The kurtosis of 288.5 (much larger than zero) indicates the distribution has heavier tails and a sharper peak than the normal distribution. Essentially it can be concluded that the distribution of Cu concentration is far from symmetrical. Many high values occur mostly in the north and in the east, where Cu and multi-metal deposits were found in the east-northern part (Figure 2). They may be influenced by extraneous and exotic

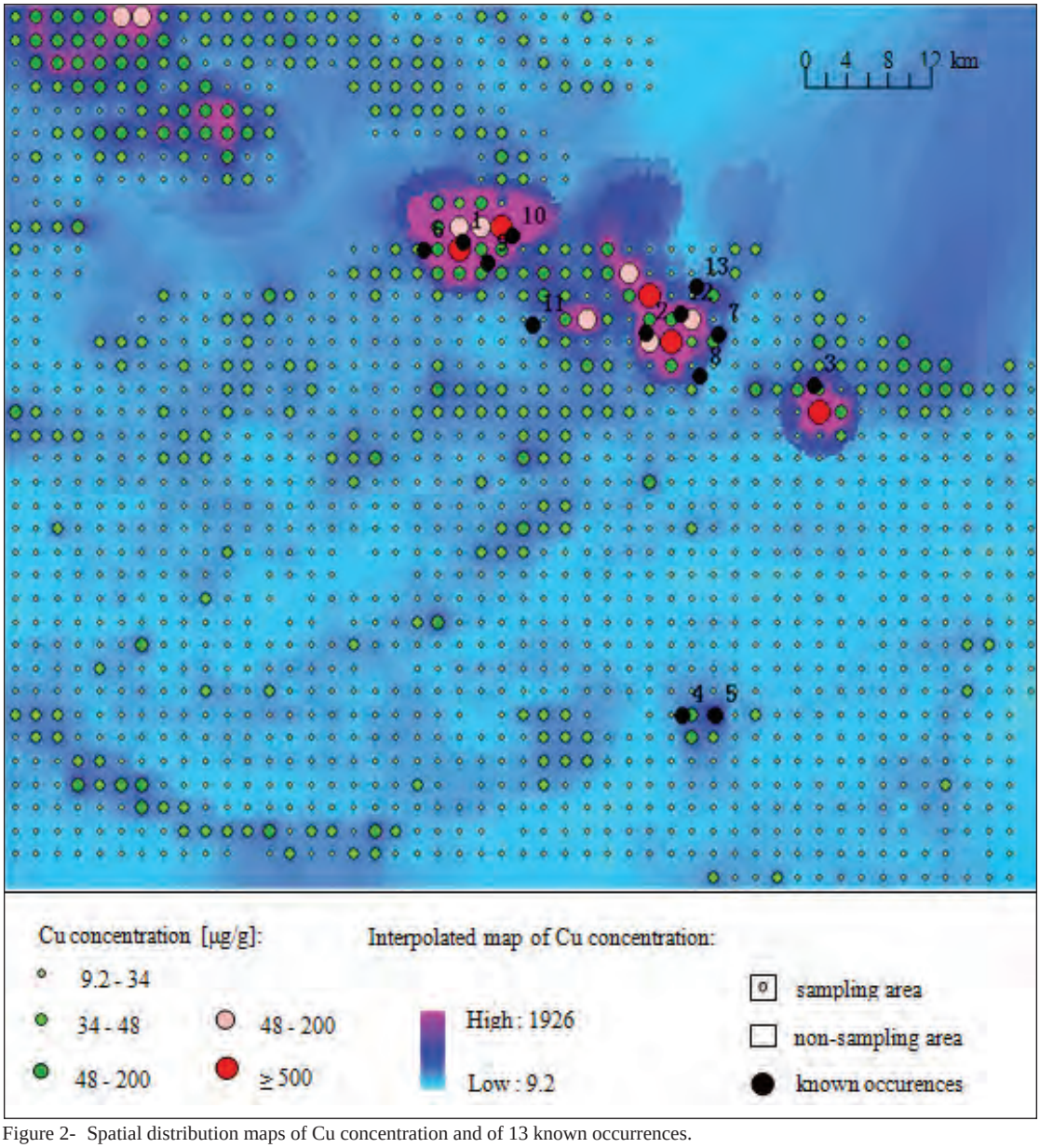

Figure 2- Spatial distribution maps of Cu concentration and of 13 known occurrences.

processes such as those related to rare rock types and mineral deposit formation processes, thus, care must be taken in interpreting the high values

Figure 3 shows the distribution of the variable Cu. It can be seen from the histogram, the distribution of raw data is skewed strongly to the right caused by many very high values (Figure 3 left). The distances of these high values are far from the main body of the data. The distribution is obviously not normal but extremely skewed to the right. Due to typical asymmetrical, a sigmoidal S-shape is not present in the empirical cumulative distribution function plot (Figure 3 right).

A curved pattern is found in the Q-Q plot (quantile-by-quantile plot) and it is in the shape of a bow (Figure 4 left). This indicates skewing because datais consistently below the line representing the quantiles of the standard normal distribution. Most of the points lie quite close to the line, and the ends are below it, the skewing is thus to the right. Data points do not follow a straight line. The plot show the upper tail of the distribution strongly deviates from normality. Cu concentrations are strongly skewed right and the rightmost data points are outliers.

The distribution of Cu concentration is right skewed, in order to reduce the influences of extreme

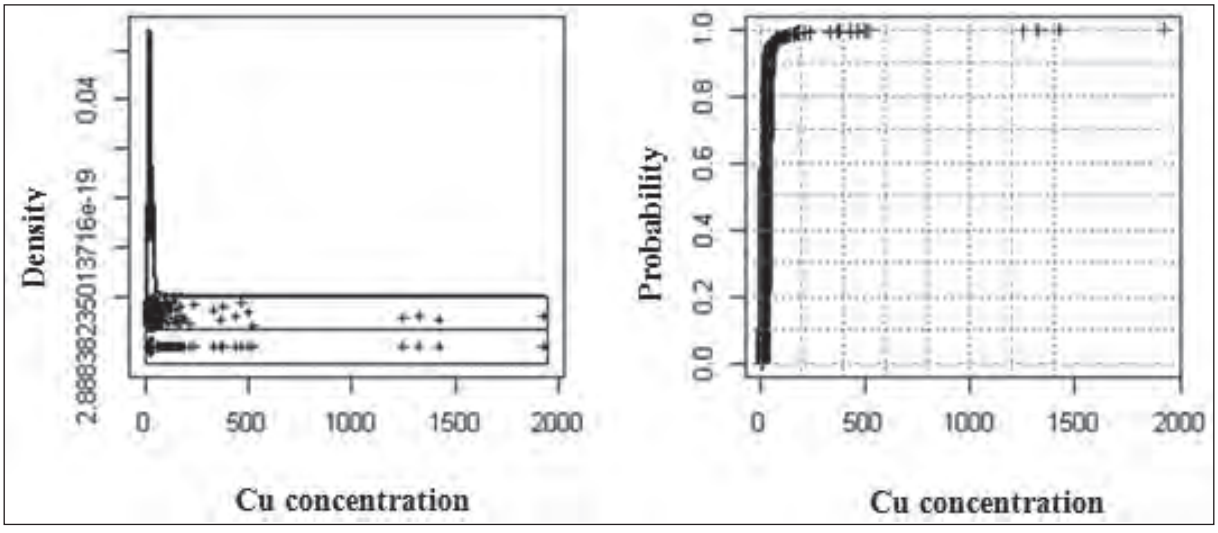

Figure 3- Histogram, density trace, 1-D scatter plot, boxplot (left) and empirical cumulative distribution functionplot (right) for raw data..

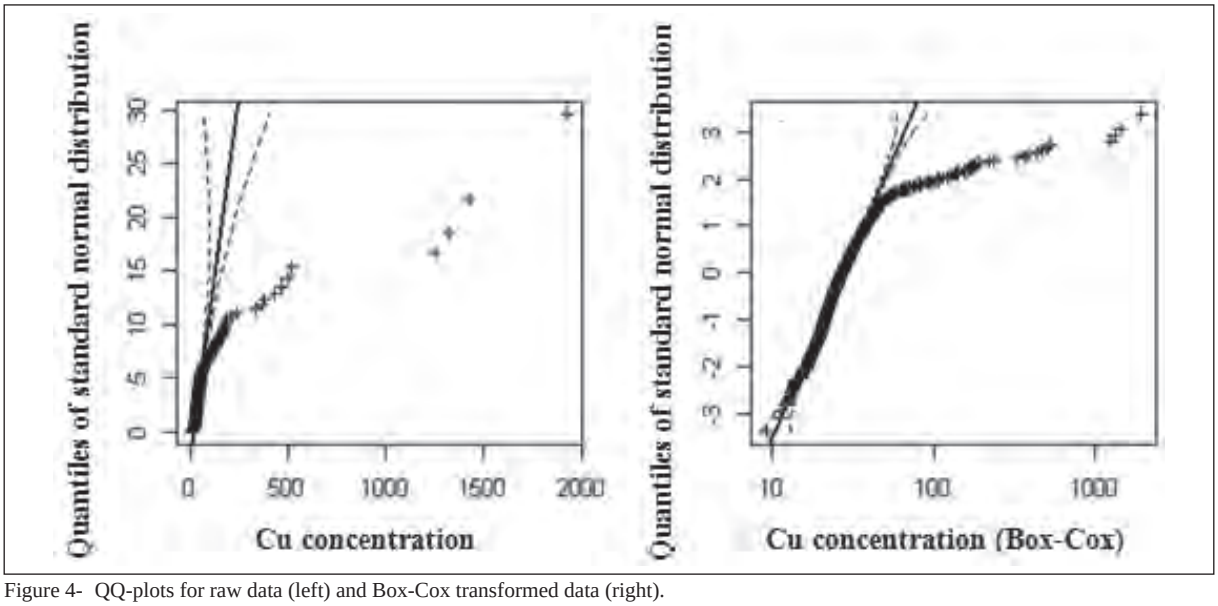

Figure 4- QQ-plots for raw data (left) and Box-Cox transformed data (right).

values, outliers and to obtain vital information of values about the shape of the distribution.Data is rescaled by using Box-Cox transformation to make the data normal. For Box-Cox transformed data, the minimum, median, mean and maximum values are 0.91, 0.99, 0.99 and 1.03 μg/g, respectively. The mean is equivalent to the median, which shows that transformed data is evenly divided around the mean. The kurtosis of -0.156 is close to zero (greater than -1.0 and less than 1.0), indicating that the distribution of the transformed data is close to symmetrical. The kurtosis of 2.034 is much smaller for the Box-Cox data, indicating the peak and tails of the distribution almost does not differ from the normal distribution.

The Box-Cox transformation results in an almost symmetrical distribution of the strongly right skewed data. The histogram and density trace still show a slight right skew (Figure 5 left). The empirical cumulative distribution function plot begins to display an S-shape (Figure 5 right), however the right skew is still clearly reflected. The QQ-plot from Box-Cox transformed data show the upper tail of the distribution less deviates from normality (Figure 4 right). More data points follow the straight line. Less extreme values dominate the Q-Q plot.

4.2. Spatial Scales

It has been proven in Hoang et al. (2017) that the variance of the Cu variable levels off when at distance of 12.4km, beyond this distance, the sampling units are not spatially correlated. Therefore, in order to investigate the effects of different spatial scales on the results, six spatial scales were considered in this study where d = 2, 4, 6, 8, 10 and 12 km in this study. In this case, the weights for neighboring locations were assigned as 1 if the distances were within the band, otherwise the weights were 0.It can be seen from Moran scatter plots (Figure 6) that the values of all of global Moran's I statistic at thesespatial scales(below 12 km) are positive, indicating neighboring samples tend to have similar values. The spatial pattern of Cu concentration is clustered. The values of the global Moran's *I* statistic decreased when bands increased.

For the raw data, the Moran scatter plots are dominated by high-high clusters (above the mean) in the upper right quadrants (Figure 6-1a, b, c, d, e, and f) representing positive spatial association. A few data points occurred in the upper left quadrantsrepresenting low values surrounded by high values and at the lower right quadrants representing high values surrounded by low values. Almost no data points were found in the lower right quadrant, which indicates no spatial association between low values. The global Moran's *I* value of 0.1591 indicates the strongest spatial association at spatial scale 2km. Moran's *I* values reduce to 0.1186 and 0.0993 at spatial scales of 4 and 6km respectively, indicating weaker spatial association. The values of Moran's *I* are of 0.0712, 0.0526 and 0.0437 and close to zero when spatial scales reach 8,10 and 12 km. Number of neighboring samples N increased at thesebands, E(*I*) approaches zero, resulting in no spatial correlation between neighboring samples.

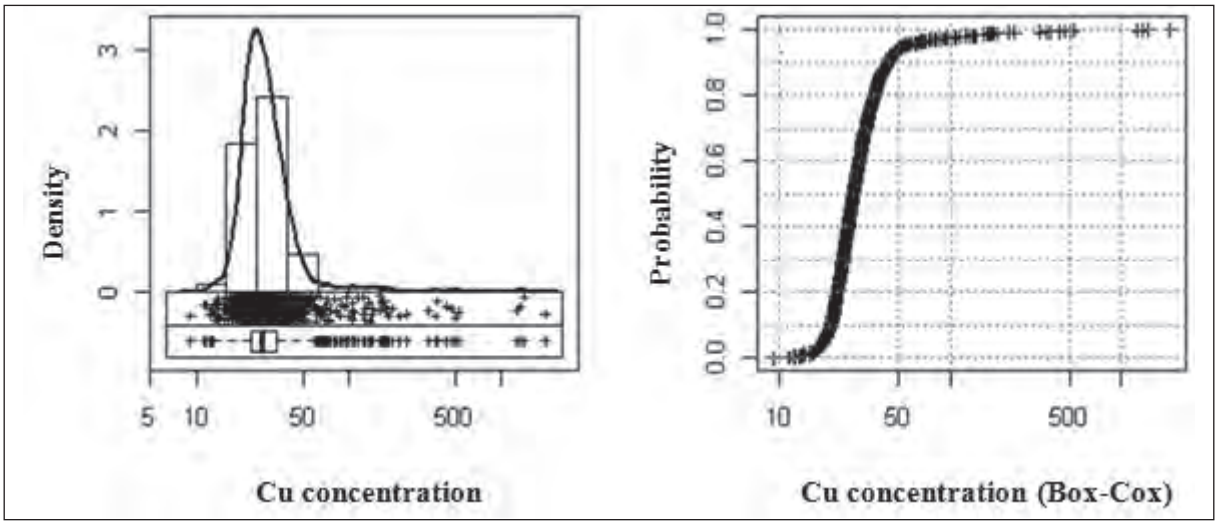

Figure 5- Histogram, density trace, 1-D scatter plot, boxplot (left) and empirical cumulative distribution functionplot (right) for Box-Cox transformed data.

For Box-Cox transformed data,global Moran's *I* values are much higher at all six spatial scales when compared with the results for raw data, therefore,we can see spatial patterns more clearly (Figure 6-2a, b, c, d, e, and f). The values of Moran's *I* for the first three bands are 0.5642, 0.4755 and 0.3947, indicating a stronger positive spatial association in Box-Cox transformed data. Data points are dominated in the upper right and lower left quadrants in these plots. More points were found in the upper right quadrants where high values are surrounded by high values. Moran's values reduce to 0.3460, 0.3075 and 0.2874 and gradually approach to zero at bands of 8, 10 and 12km. However, spatial pattern of high-high clusters are still dominated by these plots.

4.3. Anomaly Separation and Evaluation

The data distribution of local Moran's I_i is strongly skewed-right due to high values and outliers as mentioned above. The MEDIAN ± 1.5*IQR formula was applied to separate anomalies from Box-Cox transformed local Moran's I_i values. The results of

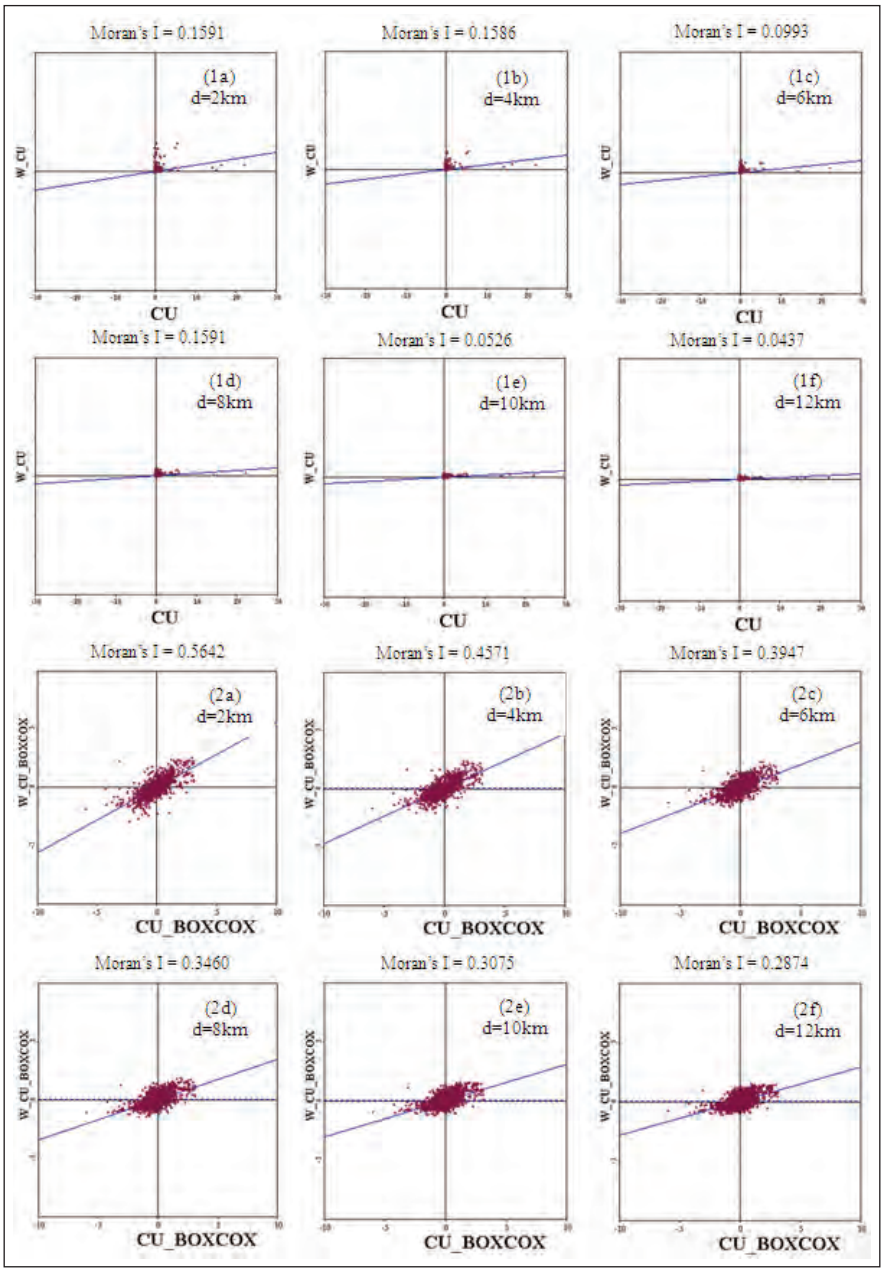

Figure 6- Moran scatterplots for Cu: raw data (1a,b,c,d,e,f), Box-Cox transformed data (2a,b,c,d,e,f).

Table 1- Summary table of statistical parameters of local Moran's I_i

Spatial scales (km)	1st Qu.	Median	2rd Qu.	IQR	(Med+ 1.5*IQR)	Anomalous area (km^2)	Backgrdound area (km^2)
d=2	0.0039	0.0146	0.0278	0.0240	0.05061	372	5.552
d=4	0.0031	0.0141	0.0261	0.0240	0.04858	392	5.332
d=6	0.0033	0.0135	0.0248	0.0216	0.04587	388	5.336
d=8	0.0026	0.0134	0.0243	0.0216	0.04586	364	5.360
d=10	0.0015	0.0133	0.0234	0.0219	0.04612	352	5.372
d=12	0.0009	0.0127	0.0234	0.0225	0.04655	332	5.392

(1st Qu. = 1st quartile; Median = median value; 3rd Qu. = 3rd quartile; IQR = interquartile range)

anomaly separation are summarized in table 1 and visualized in figure 7.

It can be seen from figure 7, generally, anomalous areas are found in the north and in the east of the study area at all of six spatial scales, where a metallogenic belt was found including Cu and multi-metal deposits marked by 6, 1, 9, 10, 2, 13, 7 and 8 in the east-northern part. Total anomalous area is 372 km^2 at the first spatial scale and increased slightly to 392 km^2 and 388 km^2 at spatial scales of 4 to 6 km, while background areas are 5552, 5332 and 5336 km^2 respectively (Figure 7-a, b, c). However, the anomalous areas are significantly reduced to 364, 352 and 332 km^2 as the spatial scales increase to 8, 10 and 12 km, while background areas are increased by 5,360, 5,372 and 5.392 km^2 (Figure 7-d, e, f). Anomalies are mostly concentrated around known ore-deposits marked by 6, 1, 9, 10, 2, 13, 7 and 8 in the east-northern part (except ore-deposits No. 4 and 5) due to the influences of extraneous and exotic process such as mineral mineralization. A part of anomalies occurred in the northwest of the study area at all six spatial scales, where no known ore deposits were found in this area. No anomalies were found in the southern part where ore deposit 4 and 5 were located (Figure 6) due to weak anomalies in this area.

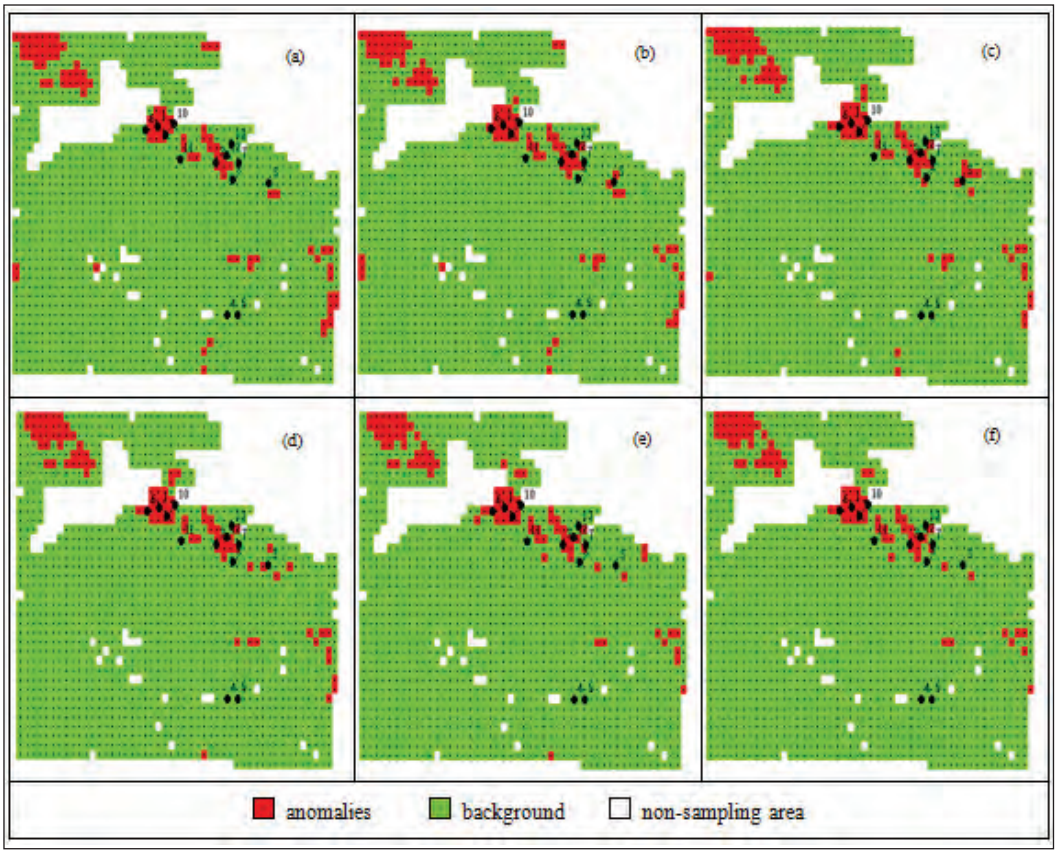

Figure 7- Spatial distribution map of Cu anomalies using local Moran's *Ii* at six different spatial scales.

5. Conclusions

In this study, a new method was used to separate geochemical anomalies based on local Moran's I_i and robust statistics. The method takes into account spatial correlation and variability, which demonstrates a strong case for geochemical data where the assumption of of normality is usually violated. Cu anomalies was separated from 1481 composite samples in Jiurui copper mining area. The process of the anomalous separation includes (1) the analysis of spatial association and variability using Moran scatterplot at different spatial scalesfor both raw data and Box-Cox transformed data, (2) the measure of spatial autocorrelation using local Moran's I_i and (3) the application of the MEDIAN ± 1.5*IQR formula on local Moran's I_i values to separate anomalies. Two important conclusions can be drawn when applying this method: (i) the anomalous separationis strongly affected by the existence of extreme and high values (outliers), therefore, data transformation is a necessary step to reduce their influences; (ii) spatial weight matrices (spatial scales) do affect the results, therefore, it is important to measure spatial autocorrelationof geochemical data at several scales. It was shown that, anomalies were mostly concentrated around known ore-deposits, according to the objective reality and have strong conformity with known ore-deposits in Jiurui copper mining area.Weak anomalies were still not found in areas around ore-deposits No 4 and 5, therefore, the method need further improvement to separate weak anomalies.

Acknowledgments

I would like to thank to reviewers for insightful comments on this manuscript and Dr. Peng Gong from China University of Geosciences for the data collection.

References

Afzal, P., Khakzad, A., Moarefvand, P., Rashidnejad Omran, N., Esfandiari, B., Fadakar Alghalandis, Y. 2010. Geochemical anomaly separation by multifractal modeling in Kahang (Gor Gor) porphyry system, Central Iran, Journal of Geochemical Exploration, 104, 34-46.

Afzal, P., Harati, H., Fadakar Alghalandis, Y., Yasrebi, A.B. 2013. Application of spectrum–area fractal model to identify of geochemical anomalies based on soil data in Kahang porphyry-type Cu deposit, Iran. Chemie der Erde/Geochemistry, 73, 533-543.

Ahrens, L. 1953. A fundamental law of geochemistry. Nature, 172,1148.

Ahrens, L. 1954*a*. The lognormal distribution of the elements (a fundamental law of geochemistry and its subsidiary). Geochim Cosmochi Acta, 5,49-74.

Ahrens, L. 1954*b*. The lognormal distribution of the elements II. Geochim Cosmochi Acta, 6,121-132.

Ahrens, L. 1957. Lognormal-type distribution III. Geochim Cosmochi Acta, 11,205-213.

Anselin L. 1992. Spacestat Tutorial: A workbook for using SpaceStat in the analysis of spatial data.Urbana: University of Illinois.

Anselin, L. 1995. Local indicators of spatial association-LISA. Geographical Analysis, 27, 2, 93-115.

Anselin, L. 2005. Exploring spatial data with GeoDa™: A workbook. Urbana: Spatial Analysis Laboratory and Center for Spatially Integrated Social Science, Department of Agriculture and Consumer Economics, University of Illinois, Urbana-Champaign.

Bailey T. C., Gatrell A. C. 1995. Interactive Spatial Data Analysis. Harlow: Addison Wesley Longman, 413p.

Barnett, V., Lewis T. 1994. Outliers in statistical data. New York: Wiley and Sons, 582p.

Bolviken, B., Stokke, P.R., Feder, J., Jossang, T. 1992. Journal of Geochemical Exploration, 43, 91-109.

Brody, S.D., Highfield, W.E., Thornton, S. 2006. Planning at the urban fringe: an examination of the factors influencing nonconforming development patterns in southern Florida. Environment and Planning B Planning and Desig, 2006, 33,1, 75-96.

Cheng, Q., Agterberg, F.P. 1996. Mathematical Geology, 28, 1-16.

Cocu N., Harrington R., Hulle M., Rounsevell, M.D.A. 2005. Spatial autocorrelation as a tool for identifying the geographical patterns of aphid annual abundance. Agricultural and Forest Entomology, 2005, 7, 1, 31-43.

Cliff, A.D., Ord, J.K. 1981. Spatial Processes, Models and Applications. London – Pion, 266p.

Davis, J.C. 2002. Statistics and data analysis in Geology (3th ed.). John Wiley and Sons Inc., New York, 656p.

Dutter, R., Filzmoser, P., Gather, U., Rousseeuw, P. 2003. Developments in Robust Statistics. International

Conference on Robust Statistics, Vorai, Austria, 23-27 July, 2001. Physica Verlag, Heidelberg.

Garrett, R. 1989. A cry from the heart. Explore, 66, 18-20

Geary, R.C. 1954. The Contiguity Ratio and Statistical Mapping. The Incorporated Statistician, 5, 3,115-145.

Getis, A., Ord, J.K. 1992. The analysis of spatial association by use of distance statistics. Geographical Analysis, 24, 3, 189-206.

Getis, A., Ord, J.K. 1996. Local spatial statistics: an overview. In Longley P, Batty M (eds) Spatial analysis: modelling in a GIS environment. Cambridge (UK), GeoInformation International, 269–285.

Haining R. 1990. Spatial Data Analysis in the Social and Environmental Sciences. Cambridge: Cambridge University Press, 432p.

Hampel, F.R., Ronchetti, E.M., Rousseeuw, P.J. 1986. Robust Statistics: The Approach Based on Influence Functions. New York: Wiley.

Hashemi, M., Afzal, P., Ras, I. Abedini, M.V. 2010. Geochemical anomaly separation by Concentration-Area fractal model in Bardaskan area, NE Iran. Journal of Mining and Metallurgy, 46A, 1-10.

Hawkes, H.E., Webb, J.S. 1962. Geochemistry in mineral exploration. New York: Harper.

Hoang, A.H., Vu, D.T., Nguyen, T.T. 2017. Spatial Variability Analysis of Cu Content: A Case Study in Jiurui Copper Mining Area. International Journal of Applied Geospatial Research, 8,1, 81- 93.

Huber, P.J. 1981. Robust statistics. New York: Wiley and Sons, 1981.

Ishioka, F., Kurihara, K., Suito, H., Horikawa, Y., Ono, Y. 2007. Detection of hotspots for three-dimensional spatial data and its application to environmental pollution data. Journal of Environmental Science for Sustainable Society, 1, 15-24.

Legendre, P., Gauthier, O. 2014. Statistical methods for temporal and space –time analysis of community composition data. Proc. R. Soc. B, 281, 20132728. http://dx.doi.org/10.1098/rspb.2013.2728.

Levine, N. 2004. CrimeStat III: A spatial statistics program for the analysis of crime incident locations. Ned Levine and Assocaitions, Houston, TX, and the National Institute of Justice, Washington, DC.

Li, Ch., Ma, T., Shi, J.. 2003. Journal of Geochemical Exploration, 77, 167-175.

Liu, Y., Cheng, Q., Xia, Q., Wang, X. 2013. Application of singularity analysis for mineral potential identification using geochemical data - A case study: Nanling W–Sn–Mo polymetallic metallogenic belt, South China. Journal of Geochemical Exploration, 134, 61-72.

Liu, Y., Zhou, K., Cheng, Q. 2017. A new method for geochemical anomaly separation based on the distribution patterns of singularity indices. Computers and Geosciences, 105, 139-147.

Martins-Melo, F.R., Ramos, A.N., Alencar, C.H., Heukelbach, J. 2016. Trends and spatial patterns of mortality related to neglected tropical diseases in Brazil. Parasite Epidemiology and Control, 1, 2, 56-65.

Martins-Melo, F.R. Ramos, A.N., Alencar, C.H, Lima, M.S. 2017. Epidemiology of soil-transmitted helminthiases-related mortality in Brazil. Parasitology, 144, 5, 669-679.

McGrath, S.P., Loveland, P.J. 1992. The Soil Geochemical Atlas of England and Wales. Blackie Academic and Professional, Glasgow, 101p.

Momeni, S., Shahrokhi, S.V., Afzal, P., Sadeghi, B., Farhadinejad, T., Nikzad, M.R. 2016. Delineation of the Cr mineralization based on the stream sediment data utilizing fractal modeling and factor analysis in the Khoy 1:100,000 sheet, NW Iran. Bulletin of the Mineral Research and Exploration, 152, 1-17.

Nazarpour, A., Omran, N.R., Paydar, G.R., Sadeghi, B., Matroud, F., Nejad, A.M. 2015. Application ofclassical statistics, logratio transformation and multifractal approaches to delineate geochemical anomalies in the Zarshuran gold district, NW Iran. Chemie der Erde-Geochemistry, 75,1, 117-132.

Nazarpour, A., Paydar, G.R., Carranza, E.J.M. 2016. Stepwise regression for recognition of geochemical anomalies: Case study in Takab area, NW Iran. Journal of Geochemical Exploration, 168, 150-162.

Nguyen, T. T., Liu, X. G., Ren, Z. 2014. A Study Of Geochemical Exploration Spatial Cluster Identificaton Based On Local Spatial Autocorrelation. Geophysical and Geochemical Exploration, 38, 2, 370-376.

Nguyen, T.T, Vu, D.T., Trinh, L.H., Nguyen, T.L.H. 2016. Spatial Cluster and Outlier Identification

of Geochemical Association of Elements: A Case Study in Juirui Copper Mining Area. Bull. Min. Res. Exp., 153, 159-167.

Philip, G.M., Watson, D.F. 1987. Probabilism in geological data analysis. Geological Magazine, 124, 6, 577-583.

Rajabzadeh, M.A., Yazadni, S., Nazarpour, A., Ahmadi, A. 2015. Application Of Fractal Concentration-Area Method In Identification Of Geochemical Anomalies In Stream Sediments From Mazayejan Area, Suorian 1: 100.000 Sheet, Fars Province. Geochemistry, 4, 1, 15-20.

Reimann, C., Filzmoser, P. 2000. Normal and lognormal data distribution in geochemistry: death of a myth. Consequences for the statistical treatment of geochemical and environmental data. Environmental geology, 39, 9, 1001-1014.

Reimann, C., Filzmoser P., Garrett, R.G.2005. Background and threshold: critical comparison of methods of determination. Science of the Total Environment, 346, 1-3,1-16.

Rock, N., 1988. Numerical geology. New York Berlin Heidelberg: Springger Verlag, 427p.

Rousseeuw, P. J., Leroy, A. M. 1987. Robust regression and outlier detection. John Wiley and Sons - New York, 329p.

Ruiz-Rivera, N., Paul, V.L. 2016. Urban segregation in Latin America. Habitat International, 54, 1-2.

Sinclair, A.J. 1974. Selection of threshold in geochemical data using probability graphs. Journal of Geochemical Exploration, 3,129-149.

Sinclair, A.J. 1976. Application of probability graphs in mineral exploration. Association of Applied Geochemists, 4, 95.

Sinclair, A.J. 1991. A fundamental approach to threshold estimation in exploration geochemistry. Probability plots revisited. Journal of Geochemical Exploration, 41,1-22.

Spatial Analysis Laboratory. 2007. GeoDa: an introduction to spatial data analyses. Spatial Analysis Laboratory Department of Geography. Urbana: University of Illinois.

Stanley, C.R., Sinclair, A.J. 1989. Comparison of probability plots and gap statistics in the selection of threshold for exploration geochemistry data. Journal of Geochemical Exploration, 32, 355-357.

Tango, T. 1995. A class of test for detecting 'general' and 'focused' clustering of rare diseases. Statistics in Medicine, 14, 21-22, 2323-2334.

Tobler, W.R. 1979. Smooth Pychnophylactic Interpolation for Geographical Regions. Journal of the American Statistical Association, 74, 367, 519-530.

Tukey, J.W. 1977. Exploratory Data Analysis. Reading: Addison-Wesley, 1977.

Waller, L., Gotway, C.A. 2004. Applied Spatial Statistics for Public Health Data. John Wiley and Sons - New Jersey, 520p.

Wang, F., Hu, Y., Wang, S., Li, X. 2016. Local indicator of colocation quotient with a statistical significance test: examining spatial association of crime and facilities. The Professional Geographer, 69, 22-31.

Zhang, C.S., McGrath, D. 2004. Geostatistical and GIS analyses on soil organic carbon concentrations in grassland of southeastern Ireland from two different periods. Geoderma, 119, 3-4, 261-275.

Zhang, T.L., Lin G. 2006. A supplemental indicator of high-value or low-value spatial clustering. Geographical Analysis, 38, 2, 209-225.

Bull. Min. Res. Exp. (2018) 156: 193-204

Bulletin of the Mineral Research and Exploration

http://bulletin.mta.gov.tr

Assessment of souil liquefaction using the energy approach

Kamil KAYABALI[a]*, Pınar YILMAZ[b], Mustafa FENER[c], Özgür AKTÜRK[d] and Farhad HABIBZADEH[e]

[a]*Ankara University Geological Engineering Department, Gölbaşı, Ankara , Türkiye orcid.org/0000-0002-0228-0777*
[b]*General Directorate of Mineral Research and Exploration, Department of Feasibilty Study, Ankara, Türkiye orcid.org/0000-0002-2749-8924*
[c]*Ankara University Geological Engineering Department, Ankara 06100, Türkiye orcid.org/0000-0003-0491-3205*
[d]*Akdeniz University Geological Engineering Department, Antalya, 07038, Türkiye orcid.org/0000-0001-7703-5779*
[e]*Ankara University Geological Engineering Department, Ankara 06100, Türkiye orcid.org/0000-0001-5672-5834.*

Research Article

Keywords:
Liquefaction, stress method, strain method, energy method, earthquake energy.

ABSTRACT

Damage to structures during earthquakes may be fully or partly caused by soil liquefaction, which has been the subject of extensive research for several decades. Liquefaction susceptibility of a sandy deposit is performed by comparing the resistance of a soil to liquefaction (i.e., capacity) to the load imparted by an earthquake (i.e., demand). In this regard, the stress-based method of liquefaction assessment is by far the most popular. It involves uncertainties mostly related to the computation of the maximum horizontal ground acceleration (a_{max}) at bedrock. A site response analysis or a simplified assumption is necessary to determine the a_{max} on the ground level as well. Developing from the stress-based approach, the strain-based approach has also similar constraints. There exist laboratory techniques such as torsional shear to determine the capacity of a sandy soil in terms of liquefaction energy per unit volume. Likewise, the energy of a strong motion record can be set by employing simple physics principles. For this, a velocity time history and the unit mass of the soil are employed to compute the demand of any strong motion record. The scope of this investigation is to illustrate the usability of the energy-based method for the evaluation of soil liquefaction. The deficiencies of the stress- and strain-based approaches are outlined and the advantages of the energy-based approach are discussed.

Received Date: 01.08.2017
Accepted Date: 28.09.2017

1. Introduction

Loose sand undergoes densification, which entails an increase in pore water pressure, when subjected to ground shaking or other type of cyclic loading. When the excess pore pressure equals the effective stress, the phenomenon known as liquefaction takes place. The liquefaction of saturated loose sands during strong ground motion is a major cause of damage and catastrophic failure in buildings, embankments, and other civil engineering structures. The most spectacular manifestations of ground failure due to soil liquefaction were observed during the 1964 Niigata, 1989 Loma Prieta, and 1999 Chi-Chi earthquakes.

Because many factors influence the mechanism of liquefaction, the assessment of the liquefaction potential of cohesionless soils is a complex engineering problem. Such factors include the magnitude and intensity of an earthquake, the seismic attenuation characteristics, the distance from the hypocenter, propagation path effects, soil type and properties, confining pressure, the geometry of soil layers, and other site-specific conditions (Law et al., 1990).

Extensive liquefaction research has been performed over the last few decades. Numerous researchers have investigated the liquefaction potential of sands using laboratory methods (DeAlba et al., 1976; Ladd et al., 1989), field methods (Davis and Berrill, 2001; Çetin et al., 2004), and numerical techniques (Chen et al., 2005; Baziar and Jafarian, 2007; Zhang et al., 2015; Kokusho et al., 2015; Kokusho and Mimori, 2015).

* *Corresponding author: Kamil KAYABALI, kayabali@ankara.edu.tr*
http://dx.doi.org/10.19111/bulletinofmre.351257

Several procedures have been developed to evaluate the liquefaction potential of cohesionless soils in the field. The evaluation tools can be categorized into three main groups: 1) Stress-based procedures, 2) strain-based procedures, and 3) energy-based procedures (Green, 2001; Zhang et al., 2015). By far, the stress-based approach (Seed and Idriss, 1971) is the most commonly employed technique for liquefaction evaluation in the field.

The scope of this investigation is to outline the basic principles of the three approaches on soil liquefaction, to bring forward the deficiencies of the stress-based and strain-based procedures, and to propose the energy-based approach as a new and practical tool for the assessment of soil liquefaction in the field in accordance with further improvements.

2. Background on Soil Liquefaction Evaluation Methods

Soil liquefaction evaluation techniques unambiguously attempt to determine two factors: The first is the strength of the soil against the occurrence of liquefaction, or its "capacity." The second is the load imparted to the soil by the earthquake, or the "demand" (Green, 2001; Alavi and Gandomi, 2012). The factor of safety against liquefaction is defined as the ratio of capacity to demand.

2.1 The Stress-Based Method

By far the most commonly employed method for liquefaction evaluation is the stress-based method (Seed and Idriss, 1971; Whitman, 1971). It is often based on empirical data from field observations and laboratory investigations, and has been continually updated (Youd et al., 2001; Çetin et al., 2004) as new contributions have come in from ongoing research.

Demand in the stress-based approach based on the Seed simplified method is the amplitude of the load imparted by the earthquake, defined as the cyclic stress ratio (CSR):

$$CSR = \frac{\tau_{ort}}{\sigma'_o} = 0.65 \frac{a_{max}}{g} \frac{\sigma_o}{\sigma'_o} r_d \quad (1)$$

where CSR = cyclic stress ratio, τ_{ave} = average shear stress imposed by the strong ground motion, a_{max} = maximum horizontal acceleration on the ground surface, g = gravitational acceleration, σ_o' = initial effective vertical stress at depth z, σ_o = total vertical stress at depth z, and r_d = dimensionless stress reduction factor. The quantity of r_d varies with depth and an average value is computed by the following relationship (NCEER, 1997):

$$r_d = \frac{(1.0 - 0.4113z^{0.5} + 0.04052z + 0.001753z^{1.5})}{(1.0 - 0.4117z^{0.5} + 0.05729z - 0.006205z^{1.5} + 0.00121z^2)} \quad (2)$$

Equation (1) is valid only for M = 7.5 earthquakes. Seismic events other than M = 7.5 are taken into account by introducing a "magnitude scaling factor" (MSF), for which a number of empirical forms have been proposed by different researchers. The most recent version of MSF relationships is given by Idriss and Boulanger (2006) as follows:

$$MSF = 6.9 \exp(-0.25M) - 0.058 \quad (\text{valid when } MSF \leq 1.8) \quad (3)$$

The CSR for earthquakes other than M = 7.5 is obtained by dividing the result of Equation (1) by the MSF obtained from Equation (3).

The resistance of cohesionless soils to liquefaction, or capacity, is usually expressed by the standard penetration resistance of $(N_1)_{60}$, which stands for a standard penetration test (SPT) blow count based on a hammer impact efficiency of 60% and an overburden pressure of 1 atm. It should be noted that $(N_1)_{60}$ is for clean sands; it should be modified to take into account fines content (FC) to obtain an equivalent clean sand value, $(N_1)_{60cs}$, as follows (Youd et al., 2001):

$$(N_1)_{60cs} = (N_1)_{60} + \exp\left[1.63 + \frac{9.7}{FC+0.1} - \left(\frac{15.7}{FC+0.1}\right)^2\right] \quad (4)$$

For the stress-based approach, Seed and Idriss (1971) proposed 65% of maximum shear stress for 15 cycles of applied cyclic load. Ishihara and Yasuda (1972, 1975), using a pattern of time histories of shear stress scaled from the recorded strong ground motions of the Niigata earthquake, found that equivalent shear stress was 57% of maximum shear stress, rather than the 65% proposed by Seed and Idriss (1971). Accordingly, the Seed simplified approach overpredicts the average shear stress imparted by the earthquake by some 12%.

One other important issue to be addressed is the maximum horizontal ground acceleration, a_{max}, on the ground surface. Once the epicentral distance from the causative fault or the earthquake source to the project site and the magnitude of the earthquake are known, the maximum horizontal ground acceleration for bedrock can be computed by using an appropriate strong motion attenuation relationship. The use of

proper values for both the magnitude and the distance is of utmost importance; yet, the magnitude, the type of distance to be used (e.g., epicentral distance, hypocentral distance, or distance to the causative fault), and even the attenuation relationship itself inherits some degrees of uncertainties. Computation of the maximum horizontal ground acceleration on the ground surface involves a site response analysis, which requires a detailed set of information such as small-strain shear wave velocity profile, thickness, strain compatible modulus/damping curves and total density of soil layers with regard to the soil profile at a project site. It is a costly procedure and commonly carried out for significant engineering structures (i.e., power plants, high-rise buildings, etc.). The alternative to the determination of a_{max} on the ground surface through a site response analysis is the use of a simplified approach employing charts such as those given by Seed and Idriss (1982), which provides only an approximation for a_{max} on the ground surface of overly simplified soil profiles, such as shallow sand soils, deep cohesive soils, and alike. A site response analysis might end up with a significantly "amplified" strong motion, which, in turn, results in a higher CSR. The amplification factor in Seed and Idriss (1982) is only for a non-liquefied ground and does not account for soil nonlinearity in the liquefied soil. That's among the reasons for over estimation of the a_{max} at the surface.

Acceleration is a vector, and ground acceleration has three components. The stress-based approach considers only the higher of two horizontal a_{max} values; some researchers argue that the vertical component should also be taken into account (Atkinson, 1986; Law et al., 1990).

2.2. The Strain-Based Method

This procedure is based on the hypothesis that pore pressure begins to develop when shear strain reaches the threshold value. It was first proposed by Dobry et al. (1982). It was derived from the mechanics of two interacting idealized sand grains and then generalized for natural soil deposits (Green, 2001; Baziar and Jafarian, 2007; Alavi and Gandomi, 2012). The amplitude of the earthquake-induced cyclic shear strain, or demand, is determined by following relationship:

$$\gamma = \frac{0.65\frac{a_{max}}{g}\sigma_o r_d}{G_{max}\left(\frac{G}{G_{max}}\right)_\gamma} \quad (5)$$

where G_{max} = shear modulus corresponding to $\gamma = 10^{-4}\%$, G/G_{max} = ratio of shear moduli corresponding to γ and $\gamma = 10^{-4}\%$ (Green, 2001). The other variables are the same as those for Equation (1). Upon a series of strain-controlled cyclic tests on saturated undrained clean sand specimens, Dobry et al. (1982) showed that the capacity, or the threshold shear strain (γ_{th}), for liquefaction to initiate is approximately 0.11%.

Practical difficulties pertinent to determining the variables of Equation (5) mainly include ascertaining G_{max} and ratio of shear moduli. For the former, either in situ tests (e.g., a downhole test, a crosshole test, etc.) or complex empirical forms are required. For the latter, each soil has its own characteristic of shear modulus degradation. Laboratory determination of the ratio of shear moduli as a function of shear strain is cumbersome. Although a number of shear modulus degradation curves have been published, they provide only an approximation for the targeted threshold shear strain for a specific type of soil.

The alternative use of the strain-based procedure involves the concept of the total strain energy required for the onset of liquefaction as obtained either from laboratory experiments or records of strong ground motion. A typical cyclic load test provides stress, strain, and pore pressure data. Hysteresis loops of shear stress-strain as a function of time such as the one shown in figure 1 is obtained. The strain energy

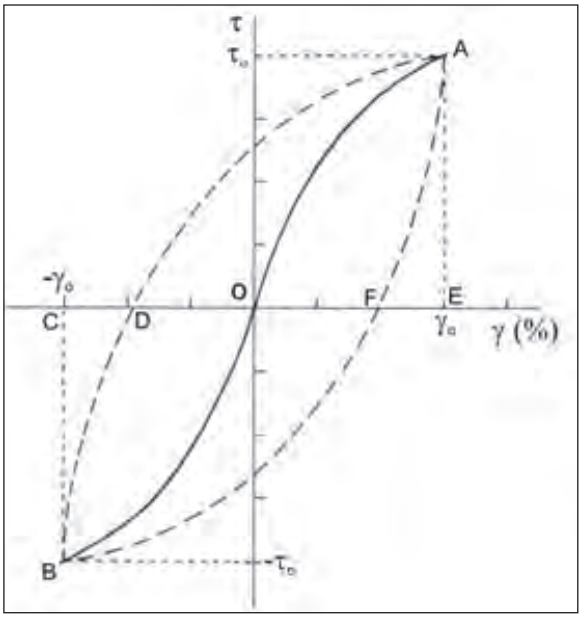

Figure 1- A typical shear stress–strain hysteresis loop (modified from Hardin and Drenevich, 1972).

for each cycle of loading is equivalent to the area inside the hysteresis loop of BDAFB in figure 1 (Ostadan, 1996; Green, 2001; Zhang et al., 2015). The instantaneous energy and its summation over time intervals are computed until the onset of liquefaction. The summation of the energy at this time is used as the measure of the capacity of the soil specimen against liquefaction (Alavi and Gandomi, 2012). This observation has prompted the formulation of the energy-based approach, details of which are presented in the following sub-section.

Although the strain-based approach is theoretically reasonable, it is less popular than the stress-based procedure due to the fact that the strain approach only estimates the initiation of pore pressure buildup, which is essential for liquefaction to occur, but does not necessarily imply that liquefaction will occur. The main deficiency of this method is the greater difficulty of estimating cyclic shear strain compared with cyclic shear stress (Seed, 1980; Zhang et al., 2015).

2.3. The Energy-Based Method

The concept of energy in the analysis of densification and liquefaction of sands was first introduced by Nemat-Nasser and Shokooh (1979). The energy, which is associated with the permanent rearrangement of sand particles, under a certain set of conditions leading to liquefaction, is a constant quantity. The accumulated energy per unit volume (J/m^3) associated with the permanent rearrangement of particles is given by the area inside the hysteresis loop developed during a cycle (Figure 1). The accumulated energy per unit volume (δW) absorbed by the specimen until it liquefies is given as follows (Figueroa et al., 1994; Liang et al., 1995):

$$\delta W = \sum_{i=1}^{n-1} \frac{1}{2}(\tau_i + \tau_{i+1})(\gamma_{i+1} - \gamma_i) \quad (6)$$

where τ = shear stress, γ = shear strain and n = number of cycles recorded to liquefaction.

To predict liquefaction, the strain energy to initiate liquefaction is compared with the strain energy imparted by earthquake to the sand layer during the seismic design event. The experiments revealed that the build-up of the excess pore pressure is proportional to the total strain energy in all loading cycles up to the initial liquefaction (Alavi and Gandomi, 2012). David and Berrill (2001) conducted a study for field verification of pore pressure and dissipated energy during earthquakes and concluded that the dissipated energy density may be remarkably well correlated with pore pressure increases in field conditions.

Figueroa et al. (1994) conducted a series of tests on Reid Bedford sand using a hollow-cylinder torsional shear device. They established a relationship between the dissipated energy per unit volume imparted to the soil to reach liquefaction and parameters such as effective confining pressure, relative density, and amplitude of shear strain:

$$\log(W) = 2.002 + 0.00477\sigma'_{mean} + 0.0116D_r \quad (7)$$

where W = measured strain energy density required for triggering liquefaction (J/m^3), σ'_{mean} = initial effective mean confining pressure (kPa), and D_r = initial relative density (%).

A few of similar relationships compiled by Alavi and Gandomi (2012) are as follows:

$$\log(W) = 2.062 + 0.0039\sigma'_{mean} + 0.0124D_r \quad \text{(Liang, 1995)} \quad (8)$$

$$\log(W) = 1.164 + 0.0124\sigma'_{mean} + 0.0209D_r \quad \text{(Dief and Figueroa, 2001)} \quad (9)$$

$$\log(W) = 2.1028 + 0.004566\sigma'_{mean} + 0.005685D_r + 0.001821FC - 0.02868C_u + 2.0214D_{50} \quad \text{(Baziar and Jafarian, 2007)} \quad (10)$$

where FC = percentage of fines content, C_u = coefficient of uniformity, and D_{50} = mean grain size (mm). The most recent empirical expression relating the measured strain energy (W; in kJ/m^3) for liquefaction to the initial mean stress (in kPa), and relative density (D_r; in decimals), was provided by Jafarian et al. (2012):

$$W = 0.1363P'_o(D_r^{4,925}) + 5.375\,(10^{-3}P'_o) \quad (11)$$

The main advantages of the energy-based method over the stress-based and strain-based approaches are that: 1) the energy is a scalar quantity expressed by a single number; 2) it is not necessary to decompose the time history of shear stress to find an equivalent cycle number for selected average stress or strain level; and 3) its use encompasses both stress and strain, as well as material properties (Law et al., 1990; Liang et al., 1995). For the field case, soils amplify the ground motion in certain frequency ranges. They do attenuate it in other frequency ranges. This implies that, whether part of the motion is amplified or attenuated, the total

energy traveling through and dissipated in a soil remains unchanged (Law et al., 1990).

3. The Proposed Method

It is possible to compute the quantity of energy, E (in Joules), released during an earthquake. The total energy released from an earthquake is given by (Gutenberg and Richter, 1956):

$$E = 10^{4.8 + 1.5M} \quad (12)$$

where M is the magnitude on the Richter scale (Law et al., 1990). Some of this energy is dissipated by inelastic attenuation along ray paths, and further attenuation occurs due to geometric spreading (Davis and Berrill, 1982). Only a very small fraction of this energy arrives at any site. The following procedure explains how the energy imparted by an earthquake on a unit of mass is computed.

The work imparted on a system (W) is explained as follows (anonymous physics rule):

$$W = 0.5mV^2 \quad (13)$$

where m is mass and V is velocity. For practical purposes, the system is defined as 1 m^3 of soil. To determine the work imparted by an earthquake on a unit volume of soil, a strong motion record such as an acceleration-time history is needed. This acceleration time history is simply integrated with respect to time to transform it into a velocity-time history. Once the mass of unit soil (it is actually absolute value of the saturated density since the volume is 1 unit) is known, it is used directly in a spreadsheet program to obtain either the work-time history or cumulative work versus the time. Figures 2 and 3 show the acceleration and velocity time histories for the September 20, 1999, Chi-Chi, Taiwan, earthquake (M_w = 7.6) recorded at Taichung, Taiwan (station No.: TCU045). The work time history of the event is computed for a saturated soil with a density of 2000 kg/m^3 (Figure 4). Figure 5 includes the cumulative energy for the same event. As figure 5 implies, the total work imparted on 1 cubic meter of soil, for which the mass is 2000 kg, during an event lasting 40 seconds is 7.9 kJ. For

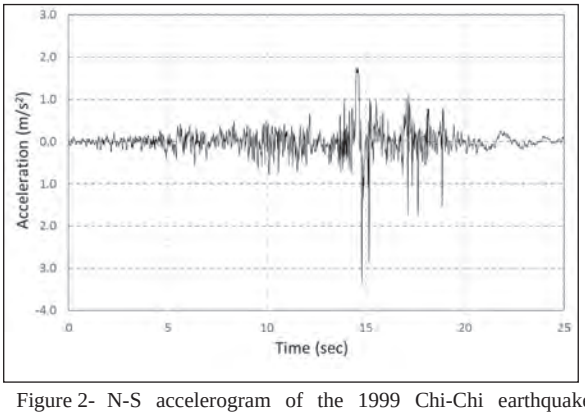

Figure 2- N-S accelerogram of the 1999 Chi-Chi earthquake recorded at Taichung (Miaoli-Shitan School), Taiwan.

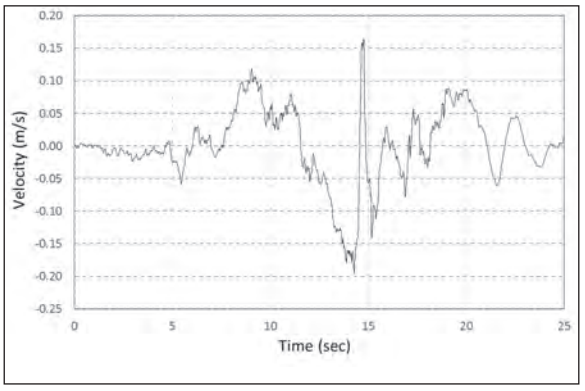

Figure 3- The velocity time history for the Taichung (Miaoli-Shitan School), Taiwan acceleration record.

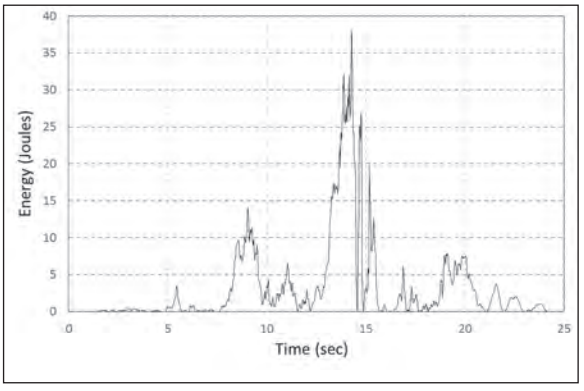

Figure 4- The work time history for the Taichung (Miaoli-Shitan School), Taiwan acceleration record.

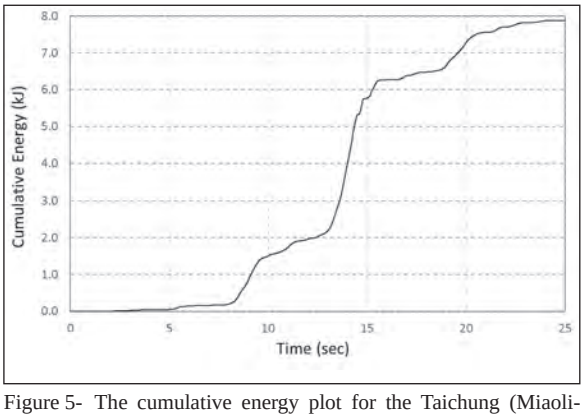

Figure 5- The cumulative energy plot for the Taichung (Miaoli-Shitan School), Taiwan acceleration record.

practical considerations, only the significant portion of the 90-second record is taken. In other words, the beginning and the ending parts of the acceleration record that do not contribute significantly to the cumulative energy are simply omitted. Removal of such portions of the record can be done by a simple spread-sheet operation.

The next step after the procedure for computing the energy of a specific record of strong ground motion involves determining the soil parameters.

The strain energy equations formulated through Equations 7–11 all involve the use of the initial effective mean confining pressure, σ'_{mean}. The difficulty of determining σ'_{mean} in situ should be appreciated. In field conditions, the initial effective overburden stress (σ'_v) is commonly used as the representative of effective shear strength rather than the initial mean effective stress, σ'_{mean} or P'_o, which could be interchangeably related as (Seed et al., 1986):

$$\sigma'_{ort} = \left(\frac{1+2K_o}{3}\right)\sigma'_v \quad (14)$$

where K_o = coefficient of lateral earth pressure at rest. It is defined by the following generic form as:

$$K_o = 1 - \sin(\phi') \quad (15)$$

The effective angle of internal friction, ϕ', in Equation (15) can be determined as (Hatanaka and Uchida, 1996):

$$\phi' = (20N_{1,60})^{0.5} + 20 \quad (16)$$

Finally, the relative density is defined as follows (Skempton, 1986):

$$D_r = 15(N_{1,60})^{0.5} \quad (17)$$

The characterization of soil parameters to be used in determining "capacity" is carried out by the following order:

i) The corrected blow count ($N_{1,60}$) is determined from the standard penetration test (considering the uncertainties with the standard penetration test, an alternative and more reliable way of obtaining relative density directly can be done by employing the cone penetration test)

ii) The effective initial vertical stress (σ'_{vo}) is computed using the field data

iii) ϕ' is determined from Equation (16)

iv) K_o is computed from Equation (15)

v) K_o and σ'_{vo} are plugged into Equation (14) to get σ'_{mean}

vi) Equation (17) is employed to compute the relative density for clean sands; Equation (4) is employed to find the "equivalent" relative density for fine-grained soils

vii) The capacity of a soil against liquefaction is computed using any of the Equations 7–11.

Once the mean effective stress and the relative density are at hand, the energy required to liquefy the soil concerned can easily be computed. The total unit mass, M_t, is then employed to obtain the energy imparted by the earthquake on 1 m^3 of saturated soil. The final step is only a comparison between the capacity and demand.

To provide an idea of the typical energy applied on a cubic meter of soil at any point in the vertical soil profile, table 1 was constructed. The saturated density was assumed as 2000 kg/m^3 for all calculations. Table 1 includes some significant events in the world along with some characteristics of near-source records of strong ground motion.

To show how the energy imparted by an earthquake onto a cubic meter volume of soil changes with distance and site conditions, table 2 was prepared using strong motion records obtained during the October 18, 1989, Loma Prieta event. The saturated density was assumed the same as before. All strong motion data used for the construction of tables 1 and 2 came from the Pacific Earthquake Engineering Research Center.

To demonstrate how the proposed method works table 3 was constructed which covers 4 field cases; the two of them experienced liquefaction and the two did not during the Loma Prieta event. The partial data in table 3, namely a_{max}, depths to layer of interest and water table, the total and effective vertical stresses on the layer, $(N_1)_{60}$, fines content and $(N_1)_{60cs}$ were taken from Idriss and Boulanger (2010). γ_{sat} and M_t were deduced from the imported data using the depth to water table, the total stress and the effective stress in the same data source. σ'_{mean}, K_o, ϕ' and D_r were computed using the equations of 14-17. The capacities (W_{liq}) were calculated for 4 different empirical

Table 1- Some characteristics of significant events in the world along with their energy imparted onto one cubic meter of soil (M_w: moment magnitude; a_{max}: maximum horizontal ground acceleration; R: distance to causative fault; W: total work done; *: M_L).

Event	M_w	Station No.	a_{max} (g)	R (km)	W (kJ/m^3)
Chi-Chi Taiwan Sep. 20, 1999	7.6	TCU045	0.34	25	7.9
Hollister (USA) April 9, 1961	5.6*	USGS1028	0.18	21	3.0
Imperial Valley (USA) Oct. 15, 1979	6.5	USGS5115	0.37	16	3.0
Kobe (Japan) Jan. 16, 1995	6.9	CUE90	0.34	22	17
Kocaeli (Turkey) August 17, 1999	7.4	KOERI330	0.32	23	103
Landers (USA) June 28, 1992	7.3	SCE24	0.73	2.0	12.4
Loma Prieta (USA) Oct. 18, 1989	7.0	CDMG47381	0.37	6.3	18.4
Northridge (USA) Jan. 17, 1994	6.7	CDMG24278	0.58	24	21.1

Table 2- Computed cumulative works for the strong motion records of the 1989 Loma Prieta earthquake obtained from different parts of California, USA.

Location	Station No.	R (km)	a_{max} (g)	Site geology	W (kJ/m^3)
Capitola	CMG47125	16	0.47	Alluvium/Building	14.4
Hollister	CMG47189	25	0.07	Rock/Free field	3.73
Fremont	CMG57064	35	0.10	Alluvium/Building	2.41
Hayward	CMG58219	45	0.08	Rock/Building	1.76
San Francisco	CMG58539	53	0.10	Rock/Free field	0.74
Piedmont	CMG58338	64	0.08	Rock/Free field	1.37
Point Bonita	CMG58042	73	0.07	Rock/Building	2.21
Larkspur	USGS1590	85	0.14	Marsh/Building	7.71
Olema	CMG68003	107	0.16	Alluvium/Building	4.04

relationships (Equations 7, 8, 9 and 11) by employing the appropriate mean effective stresses and the relative densities.

For the computation of demands the strong ground motion records nearest to the site of interest were selected. Figure 6 shows the time histories of acceleration, velocity and the cumulative work for the 2 cases. The first site of liquefaction (Case #1) is the Treasure Island (site geology: alluvium). There exists a seismic recording station in Treasure Island. For this field the unit mass for the soil was taken as 1800 kg which resulted in a demand of 5200 J/m^3 (Figure 6) when the equation 13 was used along with the velocity time history of the Treasure Island. Since the demand for the Treasure Island record is greater than the soil capacities calculated using the 4 predictive equations the liquefaction at this site is verified from the viewpoint of the proposed method. The Case #2 is for a site which did not liquefy during the Loma Prieta event. This site is located at Moss Landing, San Francisco and the nearest recording site is located in Salinas, San Francisco (site geology: fill). The demand for this site is calculated as 2200 J/m^3 (Figure 6) using the unit mass of 1900 kg which is smaller than the capacities computed using the predictive equations of Dief and Figueroa (2001) and Jafarian et al. (2012). This finding is also in agreement with the framework of the proposed method; however, Figueroa et al. (1994) and Liang (1995) predictive equations resulted in

Table 3- Computed liquefaction energies and earthquake energies for 4 different cases (γ_{sat} = unit weight, M_t = mass of the soil for the volume of 1 m^3, W_{liq} = energy required for liquefaction, W_{quake} = energy imposed by the earthquake over soil. Data from Idriss and Boulanger, 2010).

		Case #1	**Case #2**	**Case #3**	**Case #4**
Earthquake and site		**Loma Prieta Treasure Island**	**Loma Prieta Sandboldt UC-B10**	**Loma Prieta Sandboldt UC-B10**	**Loma Prieta Alameda Bay Farm Dike**
M_w		6.9	6.9	6.9	6.9
a_{max} (g)		0.16	0.28	0.28	0.24
Liquefaction ?		Yes	No	Yes	No
Depth to layer (m)		6.5	6.1	3.0	6.5
Depth to water table (m)		1.5	1.8	1.8	3.0
σ_V (kPa) (kPa)		116	115	55	125
σ'_V (kPa) (kPa)		67	73	43	91
$(N_1)_{60}$		6.4	34.4	15.3	43.3
Fines content (%)		20	5	2	7
$(N_1)_{60cs}$		10.8	34.4	15.3	43.4
γ_{sat} (kN/m^3)		18.0	19.0	18.0	19.5
M_t (kg)		1800	1900	1900	1950
ϕ' (°)		31.3	46.2	37.5	49.4
K_o		0.48	0.28	0.39	0.24
σ'_{mean} (kPa)		44	38	26	45
D_r (%)		49	88	59	99
W_{liq} (J/m^3)	Figueroa et al. (1994)	606	1596	638	2297
	Liang (1995)	698	1998	775	2891
	Dief and Figueroa (2001)	546	2966	509	6080
	Jafarian et. al., (2012)	236	2949	389	5983
W_{quake} (J/m^3)		5200	2200	2200	5600

smaller capacities than the demand. The third location (Case #3) is a site of liquefaction in Moss Landing as well. The unit mass of soil at this site is also 1900 kg and thus the cumulative work or the demand is the same as that for Case #2, namely 2200 J/m^3, which is greater than all the capacities calculated using the 4 predictive equations which supports the hypothesis presented in this investigation. The last location (Case #4) is Alameda Bay Farm Dike in San Francisco. No liquefaction was observed at this site during the event of Loma Prieta. The nearest recording site is at the Treasure Island. The unit mass of 1950 kg for this site along with the equation 13 and the velocity time history of Treasure Island (Figure 6) resulted in a cumulative work or demand of 5600 J/m^3, for which the two of the equations predicted no-liquefaction and the two of them predicted liquefaction as for the Case #2.

The comparison between the capacities and demands using the limited number of case studies suggests that the proposed method has a premise to be used in soil liquefaction analysis. While the demands computed using the unit mass and a velocity time history is somewhat unambiguous, the computation of capacities is likely to cover some degrees of uncertainties. The failure of the proposed method to predict soil liquefaction using the two of the predictive equations may be attributed to such uncertainties.

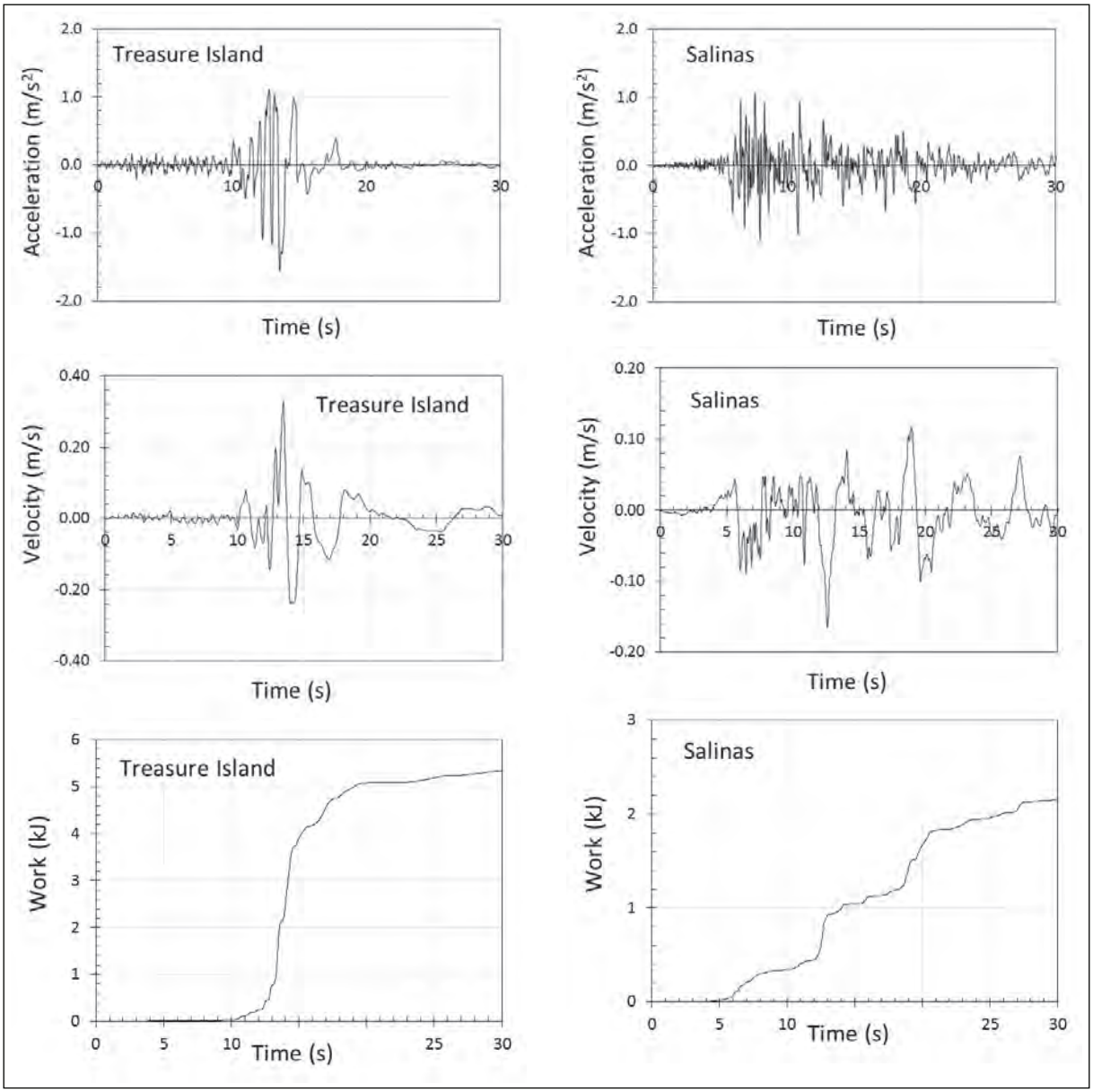

Figure 6- Example time histories of acceleration, velocity and cumulative work for the cases examined.

4. Discussion and Conclusions

The present study resulted in the following conclusions:

The resistance of a sandy deposit against liquefaction can be determined in terms of energy per unit volume. Based upon a series of laboratory tests, some researchers have established empirical relationships allowing the computation of liquefaction energy by employing simple soil parameters such as the relative density and the effective mean confining stress at the layer of interest.

The energy level of a seismic event at any site can be simply determined by the kinetic energy formula. The unit mass of a saturated soil is employed in the formula along with the velocity time history to obtain the total energy of the strong motion record.

The susceptibility of a sandy deposit for liquefaction can be easily checked by a number of strong motion records encompassing a large range of magnitudes and varying distances, using the concept of “earthquake energy.”

The stress- and strain-based procedures to determine demand require a_{max} on the ground level as the major input. Due to uncertainties of attenuation relationships the computation of a_{max} could be significantly speculative. Moreover, a site response analysis or an oversimplified assumption is to be made to convert a_{max} at bedrock level to a_{max} on the ground level. Because the total energy traveling through and being dissipated in a soil remains unchanged, neither a_{max} at bedrock level nor a site response analysis for a_{max} on the ground level is needed for the energy-based procedure. This is probably the most distinctive superiority of the energy-based approach over the other two methods of liquefaction assessment.

Both the stress-based and the strain-based procedures to compute demand involve the use of an average shear stress value of 65%. Some researchers argue that this value is conservative. The computation of the energy of a strong motion record does not involve such a correction procedure.

Both the stress- and strain-based approaches also involve a depth correction factor, r_d, and the proposed method does not need this approximation either.

The results presented herein are based solely on the limited number of case studies. A great number of case analyses is needed in order for the energy-based method to be used in soil liquefaction analyses reliably. There is an ongoing research on the subject matter by the authors covering worldwide data.

References

Alavi, A.H., Gandomi, A.H. 2012. Energy-based numerical models for assessment of soil liquefaction. Geoscience Frontiers 3(4), 541-555.

Atkinson, G. M. 1986. Ground motion for eastern North America. Ontario Hydro, Toronto, Ont., Report, 86353.

Baziar, M.H., Jafarian, Y. 2007. Assessment of liquefaction triggering using strain energy concept and ANN model, capacity energy. Soil Dynamics and Earthquake Engineering, 27, 1056–1072.

Chen Y. R., Hsieh, S. C., Chen, J. W., Shih, C. C. 2005. Energy-based probabilistic evaluation of soil liquefaction, Soil Dynamics and Earthquake Engineering 25(1):55-68. Davis, R.O., Berrill, J.B. 1982. Energy dissipation and seismic liquefaction in sands. Earthquake Engineering and Structural Dynamics, 10, 59-68.

Çetin, K.O., Seed, R.B., Der-Kiureghian, A., Tokimatsu, K., Harder, Jr. L.F., Kayen, R.E., Moss, R.E.S. 2004. Standard penetration test-based probabilistic and deterministic assessment of seismic soil liquefaction potential. Journal of Geotechnical and Geoenvironmental Engineering, ASCE 130(12),1314–1340.

Davis, R.O., Berrill, J.B. 2001. Pore pressure and dissipated energy in earthquakes-Field verification. Journal of Geotechnical and Geoenvironmental Engineering, ASCE, 127(3), 269-274.

DeAlba, P.S., Seed, H.B. Chan, C.K. 1976. Sand liquefaction in large-scale simple shear tests. Journal of Geotechnical Engineering Division ASCE, 102(GT9): 909–927.

Dief, H.M., Figueroa, J.L. 2001. Liquefaction assessment by the energy method through centrifuge modeling. In: Zeng, X.W. (Ed.), Proceedings of the NSF International Workshop on Earthquake Simulation in Geotechnical Engineering. CWRU, Cleveland, OH.

Dobry, R., Ladd, R., Yokel, F., Chung, R., Powell. D. 1982. Prediction of pore water pressure buildup and liquefaction of sands during earthquakes by the cyclic strain method. National Bureau of Standards Building Science Series, US Dept of Commerce, 138 p.

Figueroa, J.L., Saada, A.S., Liang, L., Dahisaria, M.N. 1994. Evaluation of soil liquefaction by energy principles. Journal of Geotechnical Engineering, ASCE, 120(9): 1554–1569.

Green, R.A. 2001. Energy-based evaluation and remediation of liquefiable soils. PhD dissertation, Virginia Polytechnic Institute and State University, Blacksburg, VA.

Gutenberg, B. Richter, C.F. 1956. Earthquake magnitude, intensity and acceleration. Bulletin of the Seismological Society of America, 46, 104-105.

Hardin, B.O., Drenevich, V.P. 1972. Shear modulus and damping in soils – design and curves. ASCE Journal of the Soil Mechanics and Foundations Division, 94 (SM3), 689-708.

Hatanaka M., Uchida A. 1996. Empirical Correlation between Penetration Resistance and Internal Friction Angle of Sandy Soils. Soils and Foundations, 36(4): 1-9.

Idriss, I.M., Boulanger, R.W. 2006. Semi-empirical procedures for evaluating liquefaction potential during earthquakes. Soil Dynamics and Earthquake Engineering, 26, 115-130.

Idriss, I.M., Boulanger, R.W. 2010. SPT-based liquefaction triggering procedures. Report No. UCD/CGM-10-02, Center for Geotechnical Modeling Department, University of California Davis, California, USA, 136 pp.

Ishihara, K., Yasuda, S. 1972. Sand liquefaction due to irregular excitation. Soils and Foundations, 12(4), 65-77.

Ishihara, K., Yasuda, S. 1975. Soil liquefaction in hollow cylinder torsion under irregular excitation. Soils and Foundations, 15(1), 45-59.

Jafarian, Y., Towhata, I., Baziar, M.H., Noorzad, A., Bahmanpour, A. 2012. Strain energy based evaluation of liquefaction and residual pore water pressure in sands using cyclic torsional shear experiments. Soil Dynamics and Earthquake Engineering, 35, 13-28.

Kokusho T., Mimori, Y. 2015. Liquefaction potential evaluations by energy-based method and stress-based method for various ground motions, Soil Dynamics and Earthquake Engineering, 75, 130-146. Kokusho T., Mimori, Y., Kaneko, Y., 2015. Energy-based liquefaction potential evaluation and its application to a case history, 8th Int. Conf. on Earthquake Geotechnical Engineering, New Zealand.

Kokusho, T., Mimori, Y., Kaneko, Y., 2015, Energy-Based Liquefaction Potential Evaluation and its Application to a Case History: 6th Int'l. Conf. Earthquake Geotechnical Engineering, 1-4 November 2015, Christchuech, New Zealand.

Ladd, R.S., Dobry, R., Yokel, F.Y., Chung, R.M. 1989. Pore water pressure buildup in clean sands because of cyclic straining. ASTM Geotechnical Testing Journal, 12(1), 2208-2228.

Law, K.T., Cao, Y.L., He, G.N. 1990. An energy approach for assessing seismic liquefaction potential. Canadian Geotechnical Journal, 27, 320–329.

Liang, L. 1995. Development of an energy method for evaluating the liquefaction potential of a soil deposit. PhD dissertation, Department of Civil Engineering, Case Western Reserve University, Cleveland, OH.

Liang, L., Figueroa, J.L., Saada, A.S. 1995. Liquefaction under random loading: a unit energy approach. Journal of Geotechnical Engineering, ASCE 121(11). 776-781.

NCEER, 1997. Proceeding of the NCEER Workshop on Evaluation of Liquefaction Resistance of Soils. T. L. Youd and I. M. Idriss, eds., Technical Report NCEER-97-0022, National Center for Earthquake Engineering Research, State University of New York, Buffalo, 276 pp.

Nemat-Nasser S., Shokooh, A.A. 1979. Unified approach to densification and liquefaction of cohesionless sand in cyclic shearing. Can Geotech J 1979; 16(4), 659-678.

Ostadan, F., Deng, N., Arango, I. 1996. Energy-based method for liquefaction potential evaluation - Phase I, feasibility study. U.S. Department of Commerce, Technology Administration, National Institute of Standards and Technology, Building and Fire Research Laboratory.

Seed, H.B. 1980. Closure to soil liquefaction and cyclic mobility evaluation for level ground during earthquakes. J. Geotech. Eng. ASCE 106 (GT6), 724.

Seed, H.B., Idriss, I.M. 1971. Simplified procedure for evaluating soil liquefaction potential. J Soil Mech Found Div., ASCE, 97 (SM8): 1249–1274.

Seed, H.B., Idriss, I.M. 1982. Ground motions and soil liquefaction during earthquakes. Monograph Series, Earthquake Engineering Research Institute, Oakland, CA, 134 p.

Seed, H.B., Wong, R.T., Idriss, I.M., Tokimatsu, K. 1986. Moduli and damping factors for dynamic analyses of cohesionless soils. Journal of Geotechnical Engineering, 112(GT11), 1016-1032.

Skempton, A.W. 1986. Standard penetration test procedures and the effects in sand of overburden pressure, relative density, particle size, aging, and overconsolidation. Geotechnique, 21, 305-321.

Whitman, R.V. 1971. Resistance of soil to liquefaction and settlement. Soils and Foundations, 11(4), 59-68.

Youd, T.L., Idriss, I.M., Andrus, R.D., Arango, I., Castro, G., Christian, J.T., Dobry, R., Finn, W.D.L., Harder, L.F., Hynes, M.E., Ishihara, K., Koester, J.P., Liao, S.S.C., Marcuson, W.F., Martin, G.R., Mitchell, J.K., Moriwaki, Y., Power, M.S., Robertson, P.K., Seed, R.B., Stokoe, K.H. 2001. Liquefaction resistance of soils - Summary report from the 1996 NCEER and 1998 NCEER/NSF workshops on evaluation of liquefaction resistance of soils. Journal of Geotechnical and Geoenvironmental Engineering 127(4), 817-833.

Zhang W, Goh A.T.C., Zhang, Y., Chen, Y., Xiao, Y. 2015. Assessment of soil liquefaction based on capacity energy concept and multivariate adaptive regression splines: Engineering Geology, 188, 29-37.

Bull. Min. Res. Exp. (2018) 156: 205-220

Bulletin of the Mineral Research and Exploration

http://bulletin.mta.gov.tr

Determination of predominant site period of loose terestrial units (Caliche) by microtremor measurements

Kıvanç ZORLU[a]*

[a]*Mersin University, Faculty of Engineering, Department of Geological Engineering, Çiftlikköy Campus, Mersin orcid.org/0000-0002-2086-7379.*

Research Article

Keywords:
Adana, microtremor, earthquake, caliche, Nakamura method.

ABSTRACT

The caliche profiles that have been observed in arid-semi arid climate regions can be described as terrestrial formations which are vertical succession and composed predominantly of calcium carbonate. At the top of the caliche profile, there is hard pan leyer as a weak rock and soft pan layer characterized by loose soil is existed. Caliche is formed by the displacement and/or cementation of soil, rock, and weathered material, and is usually found in unsaturated zones. In the study area, consist of caliche units located in Adana. It is noteworthy that the caliches of Quaternary is widely crop out throughout the region, exhibited a flat topography in the region locate at this unit. The paleosolic deposits in the Adana Basin, which is characterized by climate oscillations in the Pleistocene and surface waters rich in carbonate, following draining, capillarity and weathering, initially formed as a result of sedimentological and followed by pedological processes. Adana is located in the I. and II. degree seismic zone, where many earthquakes have been observed in historical and instrumental periods. It was found that the greatest structural damage sustained by the earthquakes that occurred in Adana especially in 1998, was seen in the buildings located on caliche ; it is believed that the damage caused to the buildings located on chalice can be attributed to the of morphologically distinct layers or horizons. This study determines the sediment amplification characteristics and horizontal to vertical spectral ratio (H/V) within the borders. Accordingly, to demonstrate H/V between the hard pan and the soft pan horizon of the caliche, 24 microtremor measurements were performed on locations with soft pan, on locations with no hard pan, and on locations where the profile directly begins with the soft pan.

Received Date: 27.02.2017
Accepted Date: 14.09.2017

1. Introduction

The increase in damage rates during earthquakes is directly related to the lithological characteristics of the ground built on, in addition to the structural characteristics of the building. Rock or soil sites display different behaviours during earthquakes, with the effects of earthquakes observed more in soil. According to Terzaghi and Peck (1967), hard soils are those with a single axis compression resistance of over 400 kPa. Clayton and Serratrice (1977) stated that materials called hard soil and weak rock were located at the boundary between soil and rock. According to these researchers, in spite of determining the resistance of hard soil and weak rock with a variety of laboratory experiments, there was still uncertainty in defining these types of material. While the engineering characteristics of these types of materials were ignored in previous years, currently more detailed investigation of the characteristics of these materials have begun due to the rapidly increasing construction and resulting engineering problems experienced (Clayton and Serratrice, 1977). One of the most important studies on classification of hard soils and weak rocks belongs to Johsonston and Novello (1993). These types of material are found in the centre of a broad span ranging from soft clay and loose sand to hard rock. Accordingly, weak rocks have single axis compression resistance values between 0.5 MPa and 25 MPa. Researchers have defined material with single axis compression resistance values smaller than 0.5 MPa as being “soil” and material with values above 25 MPa as “hard rock”. Caliche types display a profile with transition from weak rock to loosely-structured sandy, silty, clayey soil. The levels in the

* *Corresponding author: Kıvanç ZORLU, kivancgeo@mersin.edu.tr*
http://dx.doi.org/10.19111/bulletinofmre.348301

caliche profile in the study area are accepted as C (soft rock) and E (soft ground) in the site classification of the National Earthquake Hazard Reduction Program (NEHRP). According to NEHRP, these classes have S-wave velocity values (V_{s30} m/s) of >1500 m/s and >180 m/s, respectively. According to Eurocode 8 site class criteria, the caliche profile levels may be assessed as A (rock and rock or geologic formation containing at least 5 m weak material at surface) and D (loose to moderate-low cohesion layers or dominantly soft to hard cohesive). According to this classification system, the S-wave velocities are <800 m/s and >180 m/s, respectively (Halaç, 2016).

Goudie and Pye (1983) defined caliches as continental formations dominated by calcium carbonate with zoning in the vertical direction and horizontal or nearly horizontal placement, with transition from loose state to very compressed states. Caliche, mainly in unsaturated zones, indicates substitution and/or cementation of soil, rock and weathered material. When mechanical and structural characteristics are noted, caliche type units may be called collapsible soils (soils with potential for collapse) (Popescu, 1986; Rollins et al., 1993, Zorlu and Kasapoğlu, 2009). In the literature soils with potential for collapse are generally stated to be residual granitic material, tuffs, alluvial fans, loess and carbonate rocks (Rogers, 1995). These types of soils generally contain very small amounts of clay, with silt and fine sand grain size material. Clay content between 10 to 20% is ideal in terms of collapse. If the clay amount exceeds these proportions, the material typically displays plastic clay behaviour and collapse mechanisms do not occur. Very low amounts of clay content and insufficient bonds between particles provides the unstable structure necessary for collapse (Steven, 1998). Collapsible soils are characterised by large volume changes (reduction in volume) under fixed stress when they become saturated. These types of material display higher stability in dry situations, have very low density porous structure and are material that loses stability when wet.

This study aims to assess some dynamic properties of caliche outcropping in the I and II degree earthquake region of Adana and surroundings with buildings damaged in the 27 June 1998 Adana-Ceyhan earthquake (Aydan et al., 1998) and with this aim microtremor studies were performed. Microtremor measurements were used to assess the predominant site period and the relative ground amplification effect.

2. Geology of the Study Area

The study area is located in the Eastern Mediterranean region between Adana province and Ceyhan county (Figure 1). One of the most rapidly urbanizing areas in Turkey, Adana is the most important city in the Mediterranean region in terms of trade and industry. Generally the study area contains Late Cretaceous, Oligo-Miocene, Miocene, Pliocene and Quaternary rocks and again caliches of the same age (Figure 2).

Upper Cretaceous: As seen on the simplified geology map given in figure 2, Upper Cretaceous-aged rocks are observed as large blocks along Haramidağ, Mount Cebel-i Nur and Kürt Dağı (Kürt Mountain) near the study area. These units with volcanosedimentary character are represented by tuff containing manganese limestone, volcanic sandstone, clayey limestone and agglomerates. In terms of topography, Upper Cretaceous rocks are observed in areas with high slope and generally have tectonic contacts. In units observed as blocks, limestones have many fractures and fragile structure (Kozlu, 1987).

Oligo-Miocene: Oligo-Miocene-aged units have olistostromal character and form by the combination of different blocks. The matrix of the unit is turbiditic with abundant plankton fossils and clastic structure. Generally large olistostrome blocks are surrounded by conglomerates found scattered through different levels of the sequence. The unit is observed in topographic areas with moderate slopes and was formed by rapid deposition of erosion products from different sedimentary and ophiolitic rocks in the area in a narrow and long basin transported by rivers (Kozlu, 1987).

Miocene: Of Miocene-aged units, the Güvenç formation is observed in northwest sections of the study area near Alihoca village. The Güvenç formation has moderate-thick layers and occasional cross-bedding and was deposited in the Burdigalian-Serravallian according to results in Yetiş (1987). Comprising gray conglomerate and sandstone, the unit is observed in areas with high-slope topography. Miocene-aged units that occur in the stratigraphic sequence of the region but do not outcrop in the study area include the Karaisalı, Köpekli, Cingöz and Kuzgun formations (Kozlu, 1987).

Pliocene: Pliocene-aged units in the study area are called the Handere formation. The Handere formation

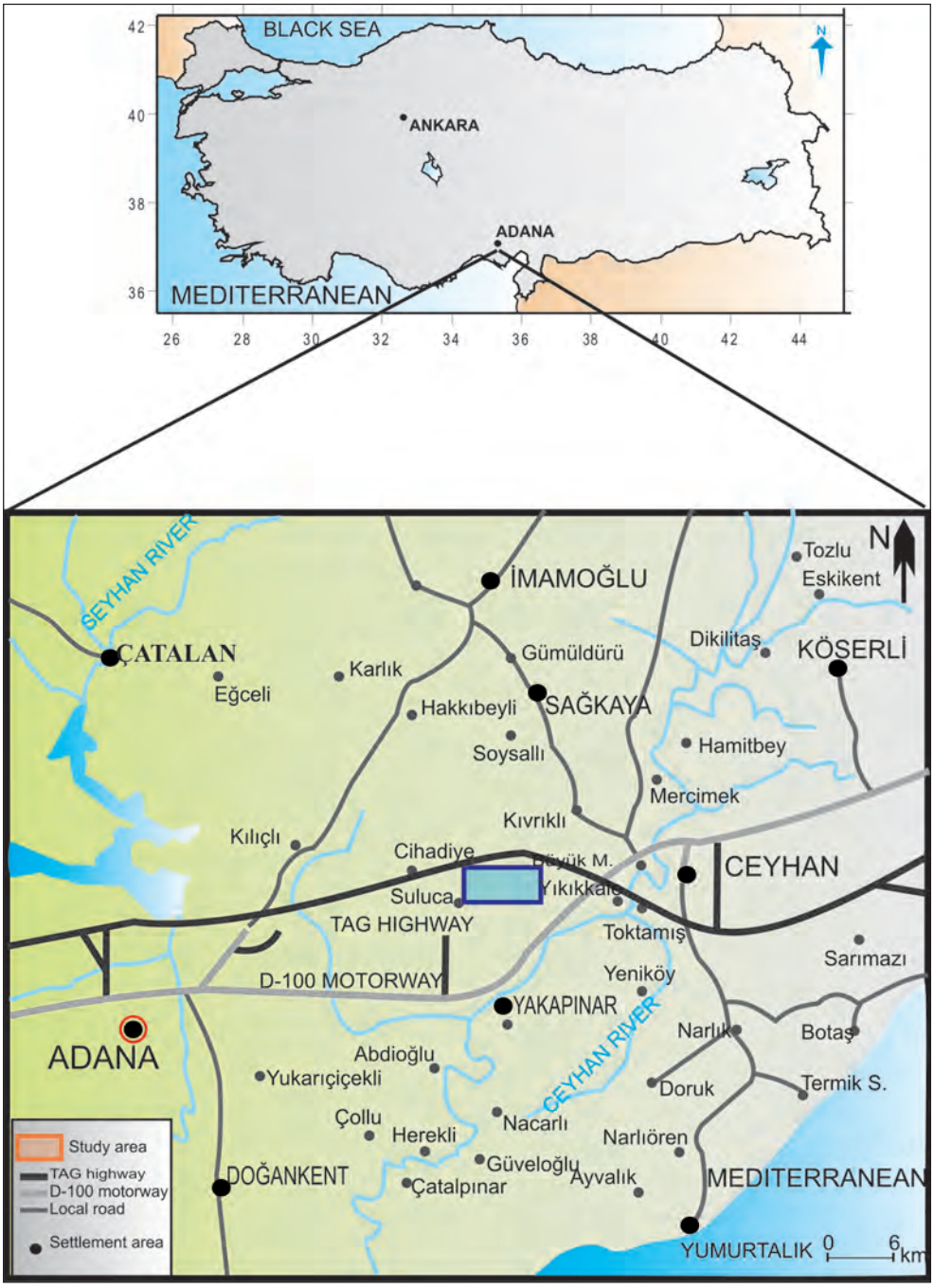

Figure 1- Location map of the study area.

outcrops north of Adana and Misis, generally in areas with moderate slope topography. The sandstone, siltstone, marl, mudstone and pebble sandstone comprising this formation generally have light brown to light gray colour with total thickness of nearly 700 m (Yetiş, 1978). The formation has moderately thick layers, with occasional cross-bedding observed in the units. These units were formed by erosion of high elevation areas after orogenesis of the Tauride Mountains, followed by transportation and deposition at lower elevations. Conglomerates are very common in this sedimentary sequence. The upper contact of the Handere formation is covered by caliche commonly observed in the Adana Basin and occasionally by young alluvium.

Quaternary: Caliche and alluvium sequences comprise Quaternary-aged sediments. Quaternary-

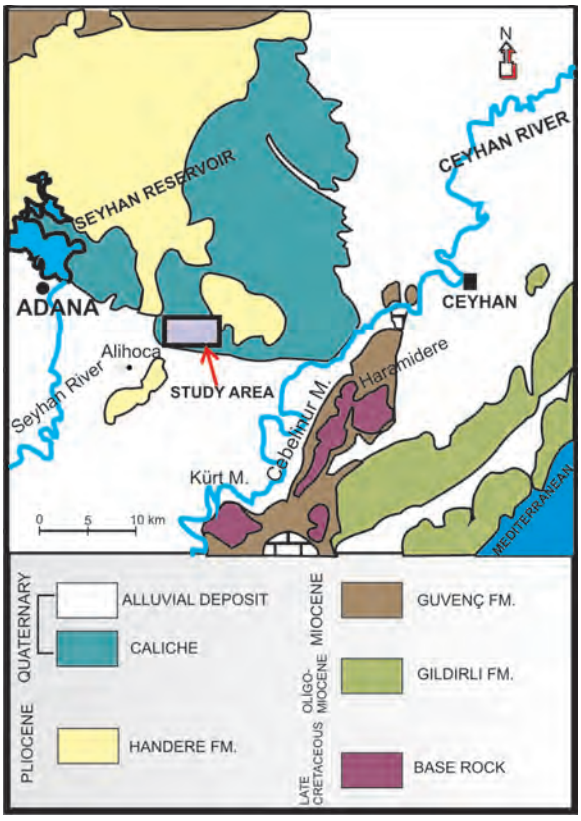

Figure 2- Geology map of the study area.

aged caliche has very large distribution in the region between Adana-Ceyhan and is noted in settlement areas, especially with low slope. When assessed in these terms, it appears that caliches have a significant spatial distribution in the region. Within the 400 km^2 area covered by caliche, 81% of the area has topographic slope of less than 10^o with 16% having slope of 10^o-20^o, and only 3% with slope above 20^o. The area where Adana Organised Industrial Zone is located generally has topography with slope less than 10^o and is completely covered with caliche.

Palaeosolic caliches in the Adana Basin formed as a result of firstly sedimentalogic and then pedological mechanisms after climate oscillations in the Pleistocene and with filtration, capillarity and decomposition events together with carbonate-rich surface waters. The age of these caliches is accepted as Quaternary (Şenol, 1989).

One of the most important elements in caliche formation is basement rock, which is the Pliocene-aged Handere formation in this region. Differences in the lithological properties of the basement rock may cause changes in the caliche prolife formed at local scale (Şenol, 1989).

Caliches in the study area have a profile formed of hard caliche with soft rock quality and soft caliche (formed of pebble-sandy and silty-clayey levels) with soil quality. These levels generally display variations over short distances in the region, with some levels not observed in some areas or thicknesses varying significantly.

Alluvium: In the study area, there is ancient alluvium forming the Adana and Misis-Andırın basins and young alluvium observed along rivers. The ancient alluvium generally are covered by plant soil. Young alluvium developed along rivers, and generally is poorly sorted, cemented pebble, sand and silt and clay size material.

3. Determination of Predominant Site Period and Investigation of Effect of Sediment Amplification

In line with the aim of the study, 24 microtremor (micro vibration) records were obtained to determine the predominant site period and ground amplification for caliche observed in Adana province, Ceyhan county (Figure 3). The Nakamura (1989) method was used to interpret microtremor records. In addition to microtremor measurements for the study area in general, measurements were completed around structures damaged during the 1998 Adana-Ceyhan earthquake. To determine the amplification difference between hard pan and soft caliche, records obtained in areas with hard caliche and in areas where the profile began directly with soft caliche had the traditional spectral ratio and Nakamura (1989) techniques applied to research the effect on relative ground amplification of hard caliche.

3.1. Microtremor Measurement Methods

Microtremors are low amplitude (1-10 micron) vibrations that may occur anywhere and anytime caused by oceanic, atmospheric or artificial sources (traffic, industrial machinery). Microtremors may be known seismic wave types (S, P, surface wave, etc.) or a combination of several (Udwadia and Trifunac 1973).

The vibration of the ground under a structure during an earthquake, in other words shaking, exposes the engineering structure to vibrations. When the period of the engineering structure and the ground it sits on are close to each other, resonance occurs and linked to this the damage may be greater than

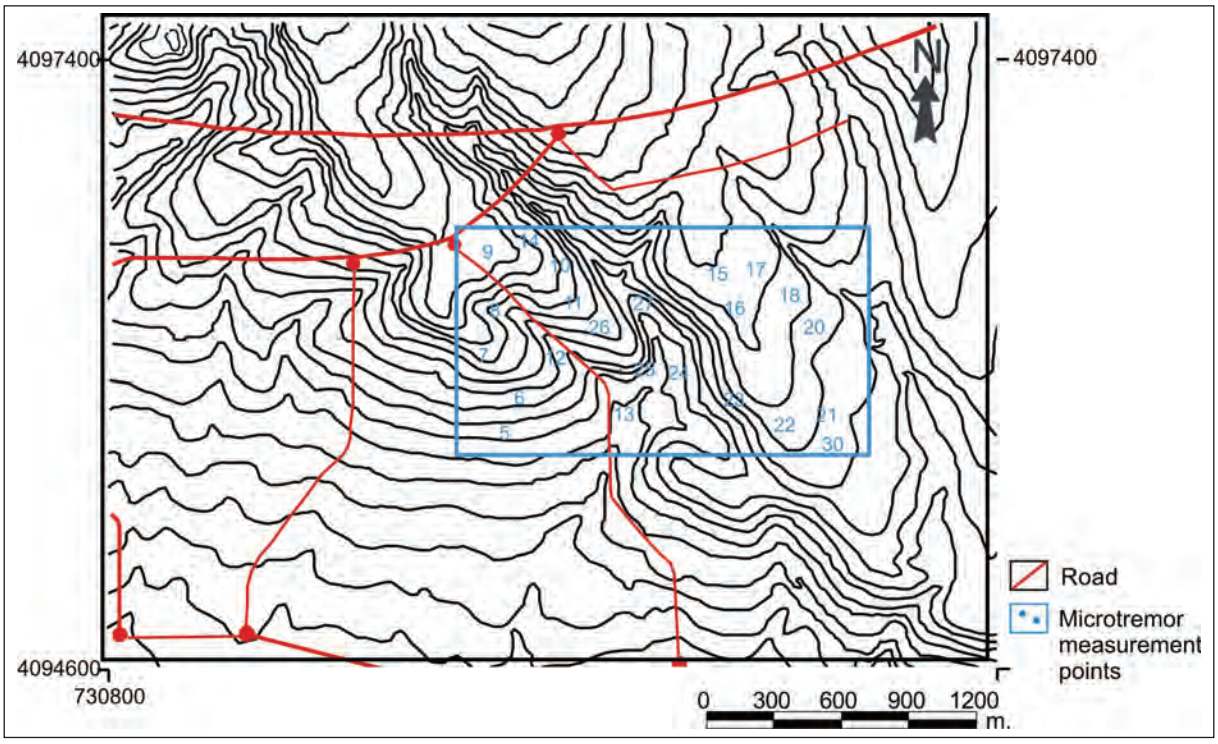

Figure 3- Location of microtremor measurements with the aim of determining predominant site period and relative ground amplification.

expected. Currently investigations after earthquakes have observed the structure-site resonance effect as an effect that increases damage (Wenk et al., 1998). Wenk et al. (1998) stated that after the 1998 Adana-Ceyhan earthquake, studies of 65 damaged buildings found that the most damaged buildings mainly had five and seven floors and the building frequencies varied from 1.5-2 Hz. Additionally, Çelebi (1998) used the Nakamura method based on acceleration records from Ceyhan station and stated that the transfer function obtained peaked at 1-1.5 Hz.

3.2. Methods Used and Data Processing

Microtremor measurements performed during the study used an Akashi brand JEP-6A3 model, and 3 component flat receptors with frequency band from 0.2-20 Hz. The acceleration data recorded by these receptors were stored in a Datamark LS-8000WD data recorder. Locations where microtremor records were taken were determined based on the size of the study area by applying a grid system with measurements taken nearby for points coinciding with buildings or roads. Measurements were taken as 3 minute records. The microtremor records were drawn with zero axis off-set correction and 1-10 Hz band transition Butterworth-type filter applied (Figure 4).

In the next stage, the Fourier amplitude spectra were obtained for each component in the frequency environment (Figure 5), with 0.4 band interval Parzen window applied while obtaining these spectra. After microtremor records were processed as above and made ready for evaluation, the Nakamura spectrum and traditional spectral ratio methods were applied.

3.3. Traditional Spectral Ratio Technique

In this method, the ratio of spectra from the location where data obtained from microtremor records are assessed is obtained with the spectrum obtained from a certain reference point. To apply this technique, the record has zero axis off-set correction and 1-10 Hz ban transition Butterworth type filter applied. Later the spectra for each component in the frequency environment are obtained. The ratio of spectra obtained from hard pan and soft caliche were obtained in the amplitude environment depending on components and recalculated with source and road effects removed. Additionally, spectrum smoothing was completed with the 0.5 Hz band width Parzen window (Figures 6 and 7).

3.4. Nakamura Method

The Nakamura method (Nakamura, 1989) is based on microtremor measurements and finding the ratio of

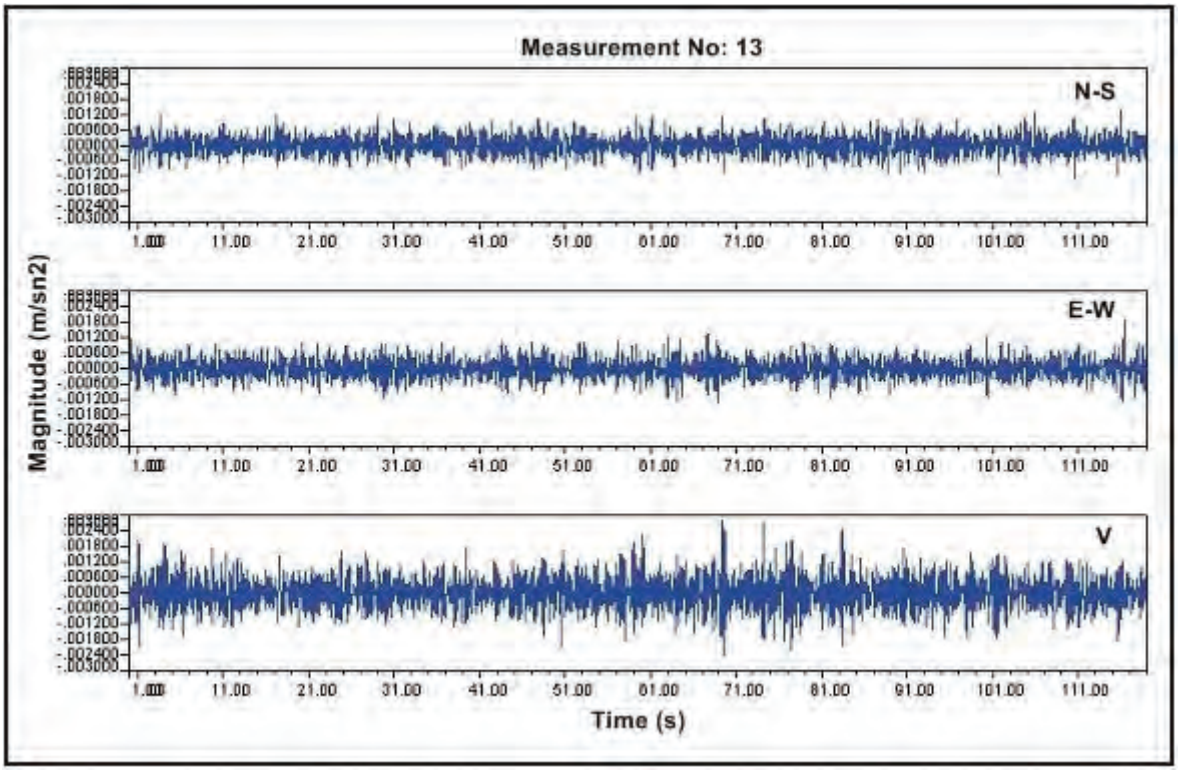

Figure 4- Three components from measurement point 11 in the study area, 3 minute microtremor record showing N-S (north-south), E-W (east-west) and UD (vertical) components.

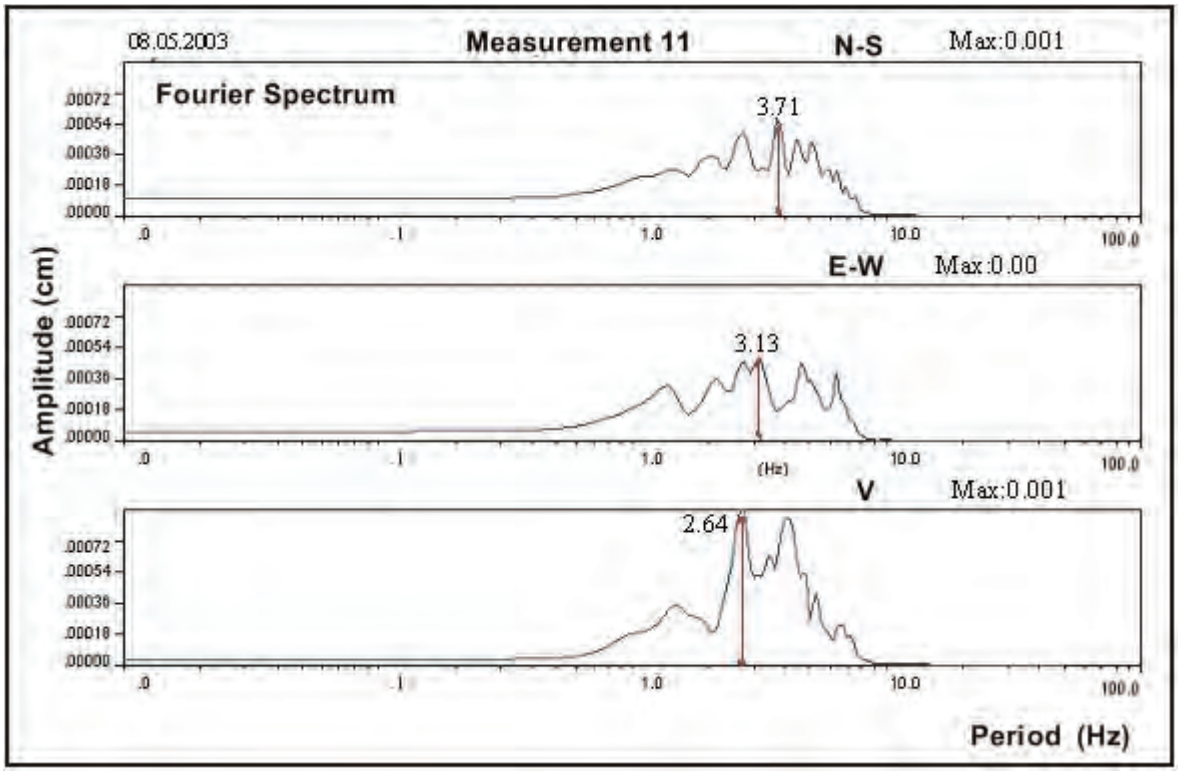

Figure 5- Three components from measurement point 11 in the study area, Fourier amplitude spectra of microtremor record showing N-S (north-south), E-W (east-west) and UD (vertical) components.

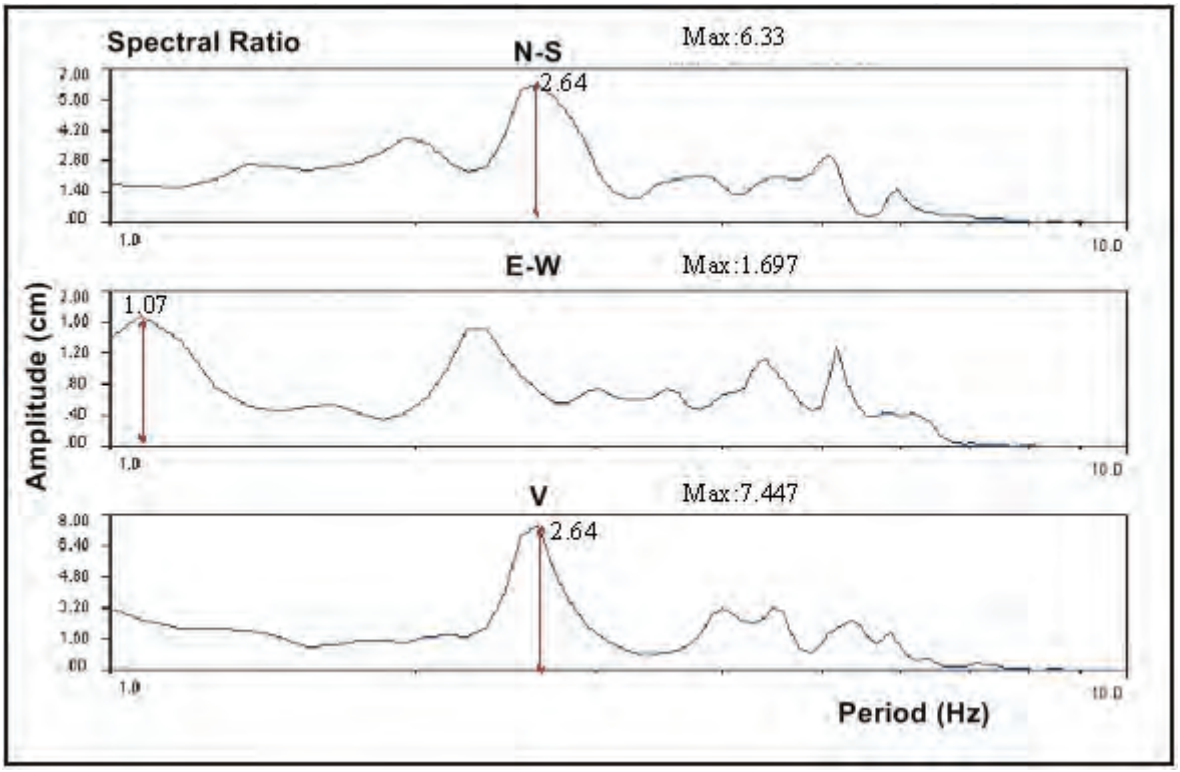

Figure 6- Spectra calculated from records obtained from pebble-block layer and hard pan layer using "traditional spectral ratio technique" and amplitude and amplification difference between hard pan caliche and soft pan levels (coarse grained level).

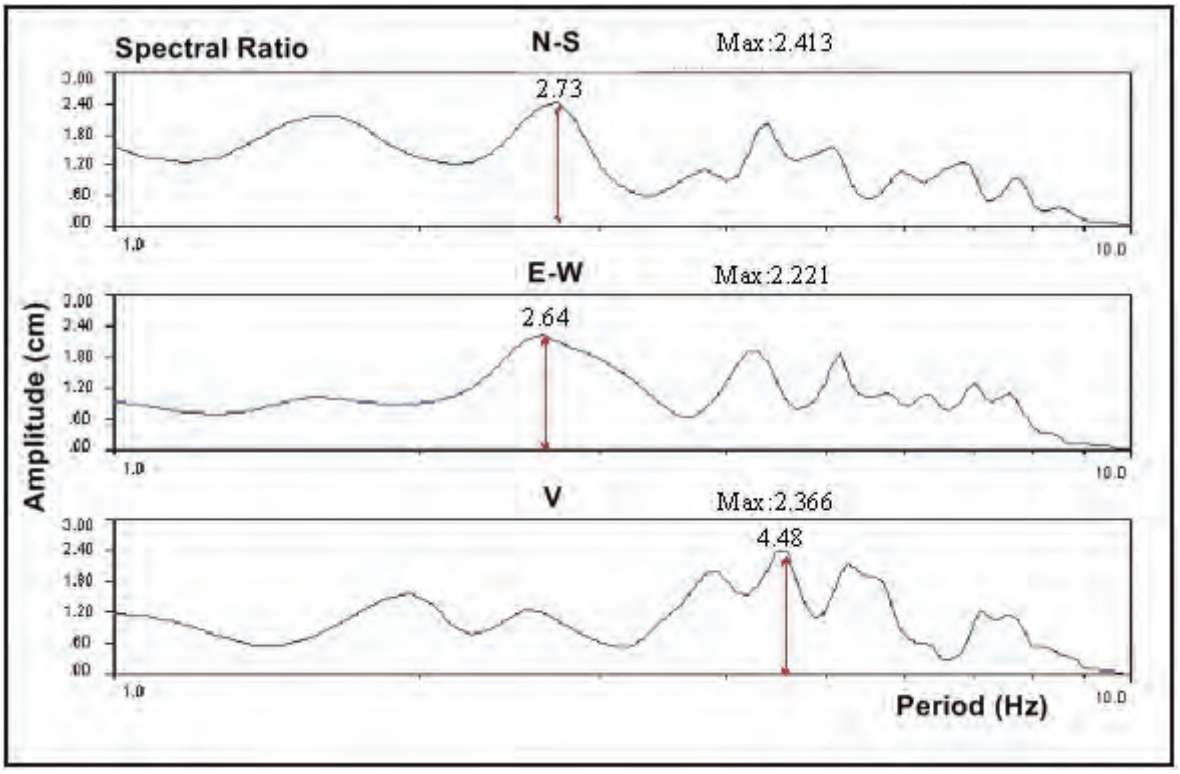

Figure 7- Spectra calculated from records obtained from hard pan and silty-sandy levels using "traditional spectral ratio technique" and amplitude and amplification difference between hard pan caliche and soft pan levels (coarse grained level).

horizontal and vertical spectra (H/V). Vertical motion is mainly dominant in artificial vibration sources and causes Rayleigh waves. The Rayleigh wave effect is clearly observed in the vertical component. As a result, Rayleigh waves are assumed to be the noise of microtremors and an attempt is made to remove the effect.

In this method, the effect of Rayleigh waves accepted as noise is reduced to a minimum. As a result, studies are performed in the early hours of the morning from 02:00-04:00 to prevent measurements being affected by traffic noise or other artificial external noises.

Additionally, continuous measurements of the basement rock and the caliche profile above it may display differences in H/V ratios. By taking the Fourier amplitude spectra of time data obtained from microtremor measurements, studies can separately obtain spectra for each component in the frequency environment. In the next stage, the ratio of horizontal spectra with vertical spectra in each frequency interval is obtained with Eq. 1 used during this process. H/V calculations were completed with GEODAS Data Acquisition System 1.14. Additionally, the ratio of the geometric mean of the amplitude of the horizontal component is taken with the vertical component, with spectrum smoothing performed with a 0.5 Hz band width Parzen window (Figure 8).

$$H/V = \sqrt{S_{NS}^{\ 2} + S_{EW}^{\ 2}} / S_{UD} \qquad (1)$$

H/V : Horizontal and vertical spectral ratio

S_{NS} : North-south component

S_{EW} : East-west component

S_{UD} : Vertical component

3.5. Assessment of Data and Results

In this study research into the effect of relative ground amplification on hard pan and soft caliche levels found the following results.

a) When the Fourier spectra of data obtained from microtremor measurements are examined, it is not possible to state a single predominant mode. When the spectra are generally examined, this situation is clearly observed.

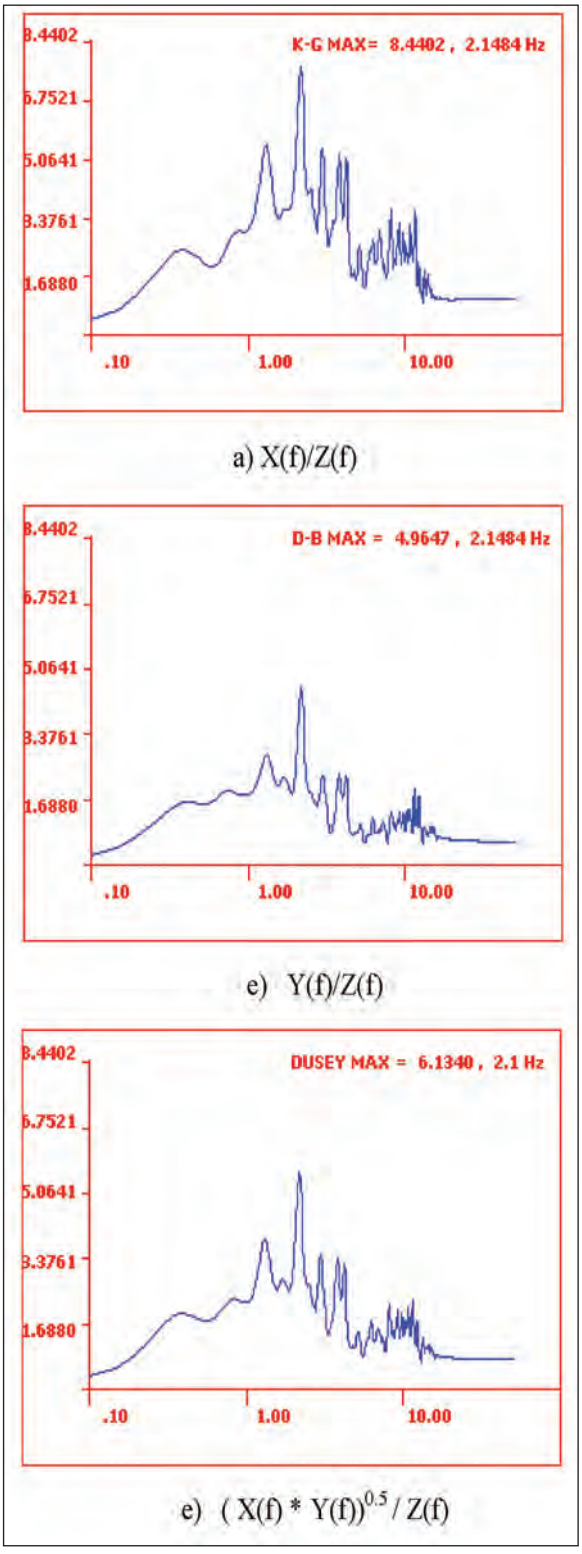

Figure 8- Typical H/V spectra obtained using the Nakamura (1989) technique on the microtremor record (horizontal axis : period, vertical axis : amplitude).

b) There are three modes that appear predominant; in other words it is possible to mention three frequency intervals. The first mode on the spectra is 5.7 Hz interval (0.2-0.1 s period) hard pan effect, the second mode is for soft caliche levels with 2-3 Hz interval (0.5-0.3 s period) for pebble-block level and silty-sandy level and finally there is a 1-2 Hz interval (0.9-0.5 s period) where the effect of the underlying clay unit that is generally not observed in the field is noted.

c) Measurements of hard pan determined the predominant site period from Fourier spectrum as 7 Hz (0.14 s) (Figure 9b). When the Nakamura spectrum is obtained, the predominant amplitude is 5.5 Hz (0.18 s) and it appears to provide 1.5 times relative ground amplification (Figure 9c).

d) When measurements are investigated from pebble-block levels at the surface in areas without a hard pan level, or where it has been removed, the Nakamura spectrum has 2.8 Hz (0.37 s) predominant site period (Figure 10b) providing 1.25 times relative ground amplification (Figure 10c).

e) Measurements taken in the silty-sandy level where there is no hard pan or pebble-blocky layer of soft caliche had 1.75 Hz (0.57 s) predominant site period and provided 1.8 times amplification (Figure 11c).

f) When the traditional spectral ratio method is applied to hard pan and soft caliche levels, the pebble-block layer of soft caliche was observed to have 1.79 Hz (0.56 s) with 6-7 times relative ground amplification compared to hard pan. For the silty-sandy level, at 2.5 Hz (0.4 s) period there was 2.4 times maximum amplification compared to hard pan.

These data were taken from a trench where hard pan, and the pebble-blocky layer and silty-sandy layer of soft caliche are found together, which makes it possible to state that all three records are affected by the same source. As a result, the variations in amplification and periods is due to the variation within the geologic units.

Though the site period values determined with the traditional spectral ratio method are in the same interval compared to the Nakamura spectrum, the difference in amplification values is due to the hard pan acting like a high-pass filter and thus it is natural that it exaggerates amplitudes in its own natural period (10-4 Hz) and suppresses the others. Similarly the pebble-blocky and silty-sandy layers of soft caliche tend to exaggerate signals in their own predominant period intervals (3.3-1.6 Hz). In conclusion, when the ratio of the hard pan spectrum to the others is obtained, as the ratio increases for the same frequency values, the amplification will be different. Additionally, the pebble-block level period and amplification value is larger than the silty-sandy level and this is a topic that needs to be emphasised for structures with many floors or high period built on the pebble-block level.

Two microtremor measurements were made in the front and back garden of the Organised Industrial Zone Administration building that was severely damaged by the Adana-Ceyhan earthquake. When the Nakamura spectrum of the first record in the front garden is examined (Figure 12), there is 0.23 s (4.3 Hz) site period with 3.1 times relative ground amplification, while the second record had 0.27 s (0.37 Hz) site period with 2.7 times relative ground amplification (Figure 13). When the traditional spectral ratio technique, accepted as a measurement reference, is obtained from the soft caliche and hard pan in the area where the administration building is located, there is 0.23 s (4.3 Hz) site period in N-S direction with 11 times ground amplification, 0.2 s (5.2 Hz) in E-W direction with 8 times amplification and 0.17 s (5.9 Hz) vertical period with 6.7 times amplification, as observed on figure 14. These results show the site of the administration building had 0.23-0.3 s (4.3-3.3 Hz) predominant period interval with mean 3 times amplification. According to the approach in Eq. 2 recommended for structures in Turkey by Bayülke (1978), assuming the administration building is a 3-floor reinforced concrete building with 0.2-0.3 s (5-3.3 Hz) period, it is in the same period interval as the site. The damage was most probably the result of the structure resonating with the ground.

$$T_a = 0.1 \times N \quad (2)$$

Here; T_a, building period (s) and N is the number of floors in the building.

Coordinates of the measurement points, predominant site period and relative ground amplification values are presented in Table 1. The spatial distribution of the predominant site period obtained from Nakamura spectra and the ground

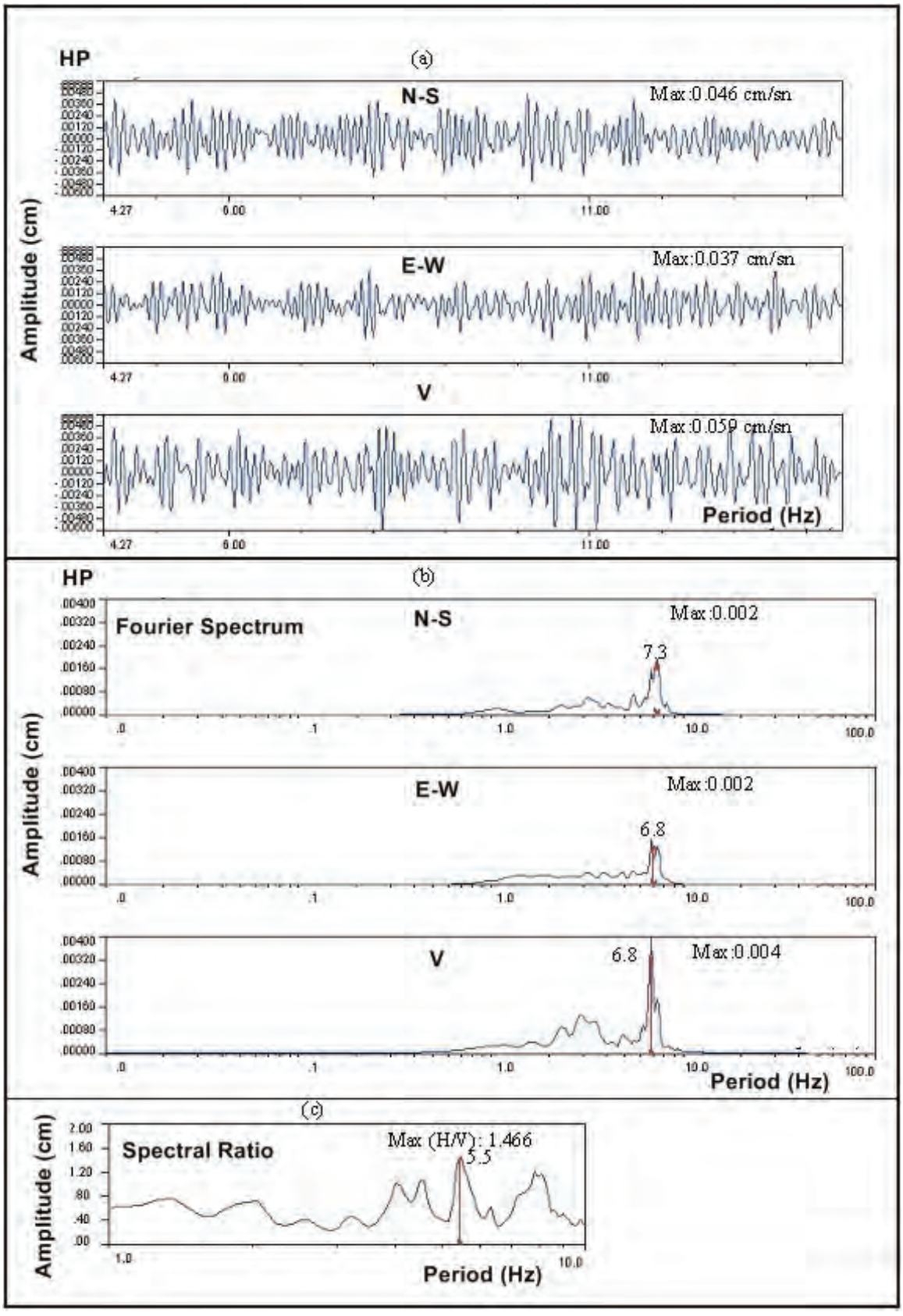

Figure 9- Fourier spectra and H/V spectra obtained with Nakamura (1989) method for hard pan records.

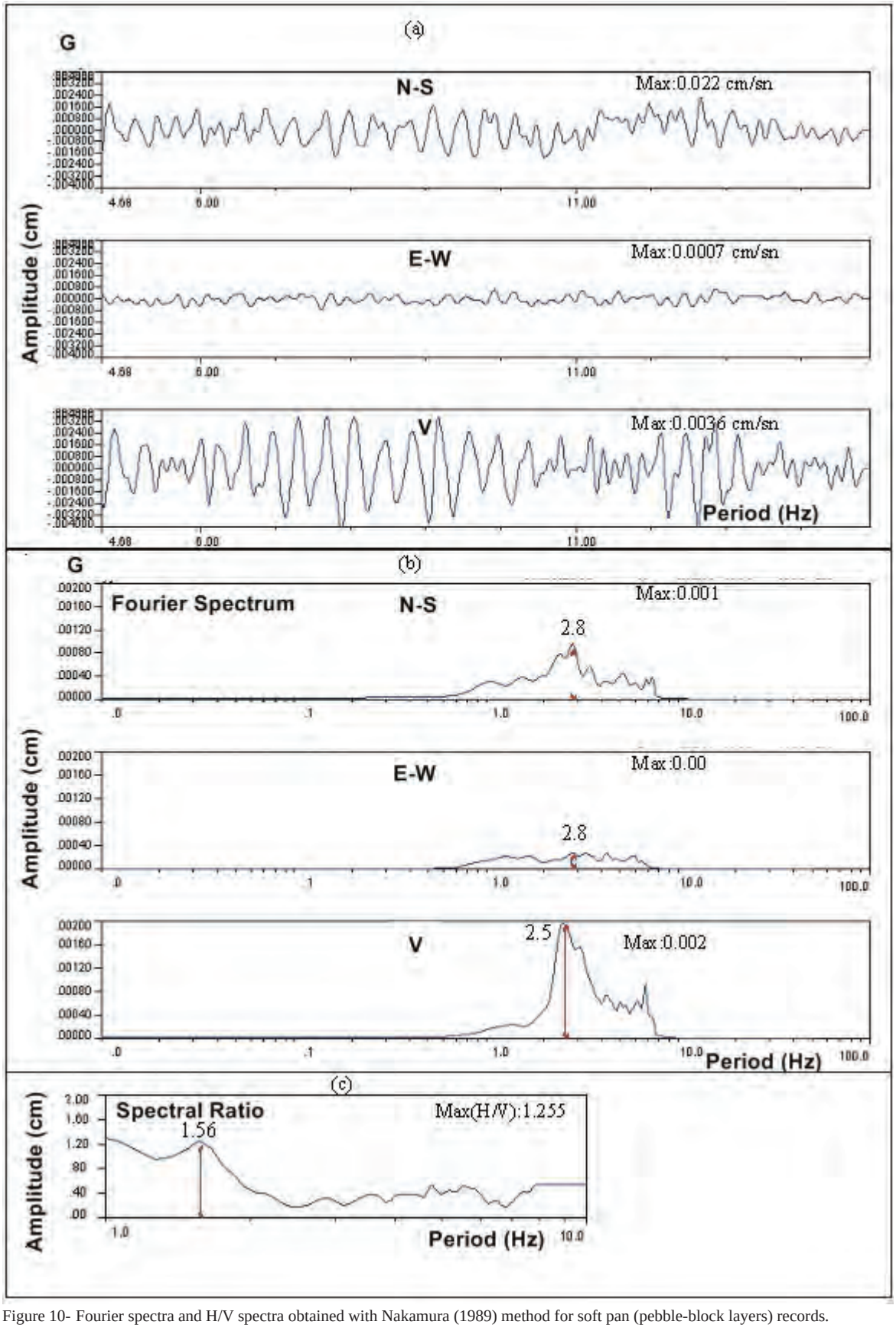

Figure 10- Fourier spectra and H/V spectra obtained with Nakamura (1989) method for soft pan (pebble-block layers) records.

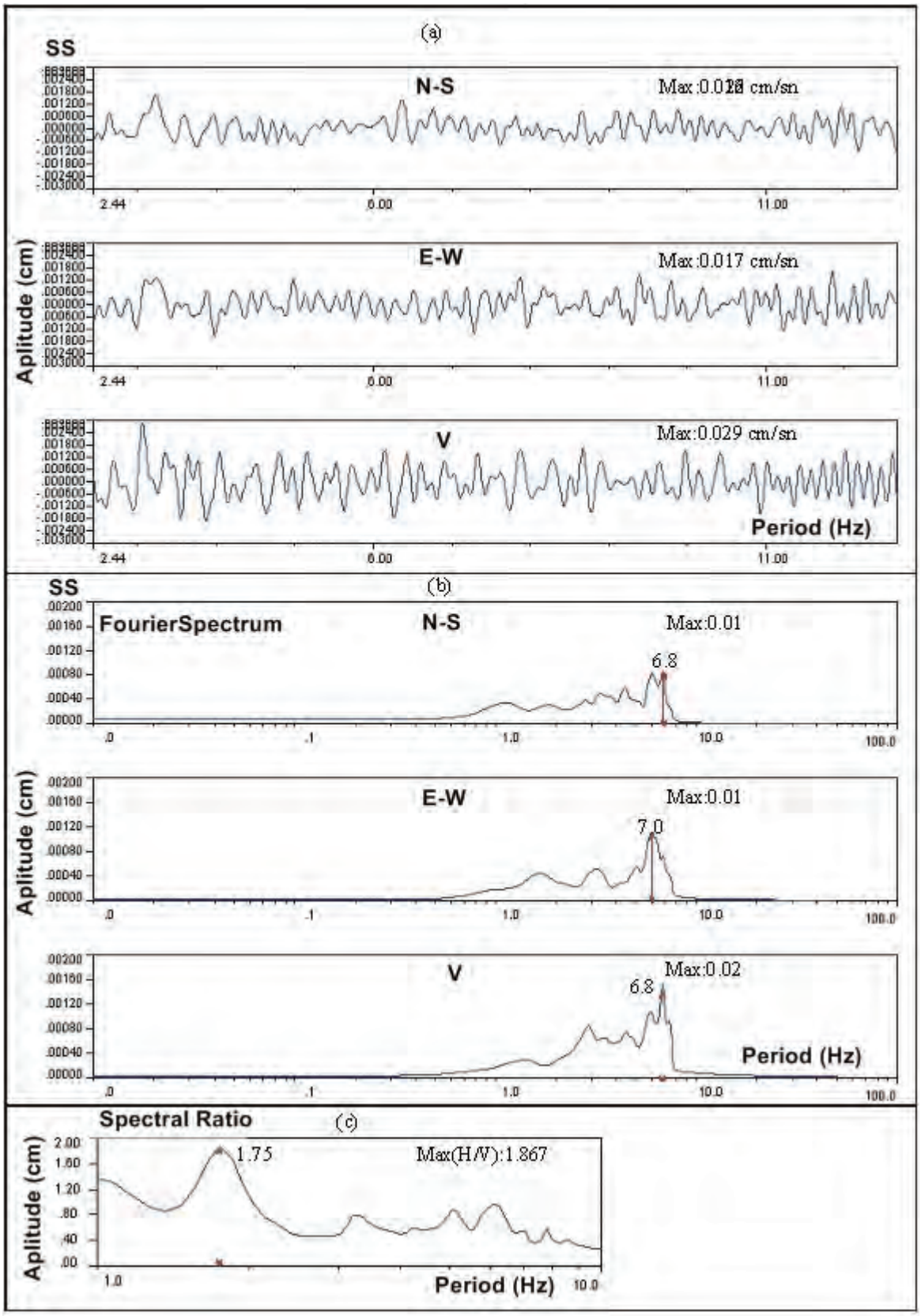

Figure 11- Fourier spectra and H/V spectra obtained with Nakamura (1989) method for soft pan (silty-sandy layer)

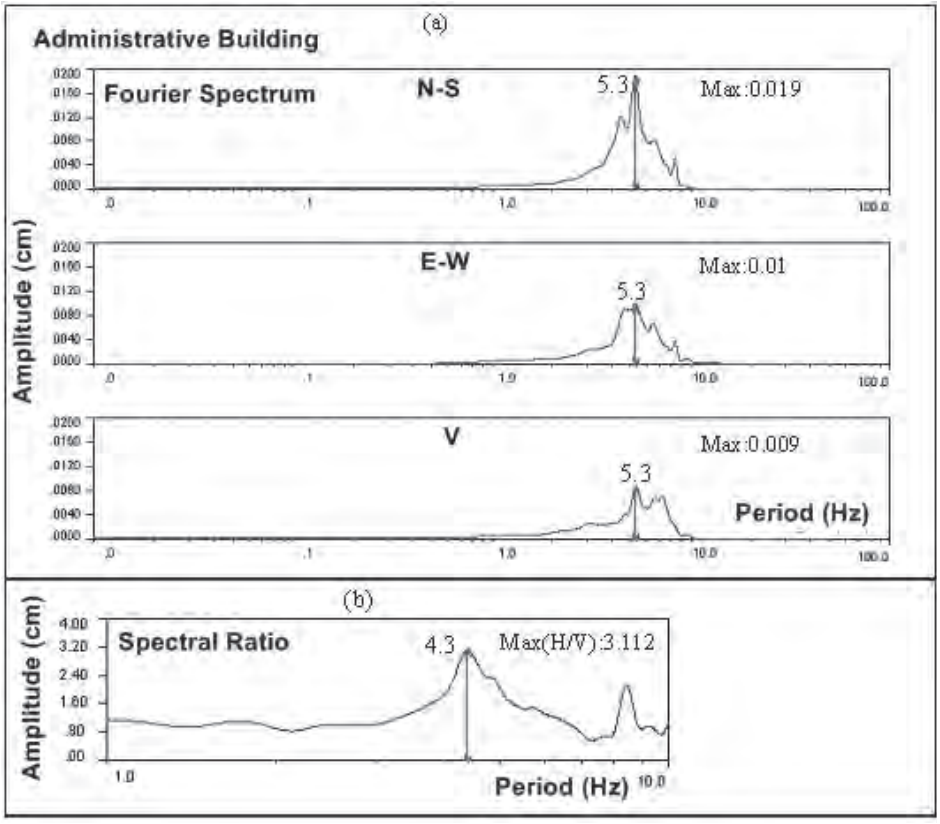

Figure 12- First record from garden of the Adana Organised Industrial Zone Administration building (N-S direction parallel to long axis of building).

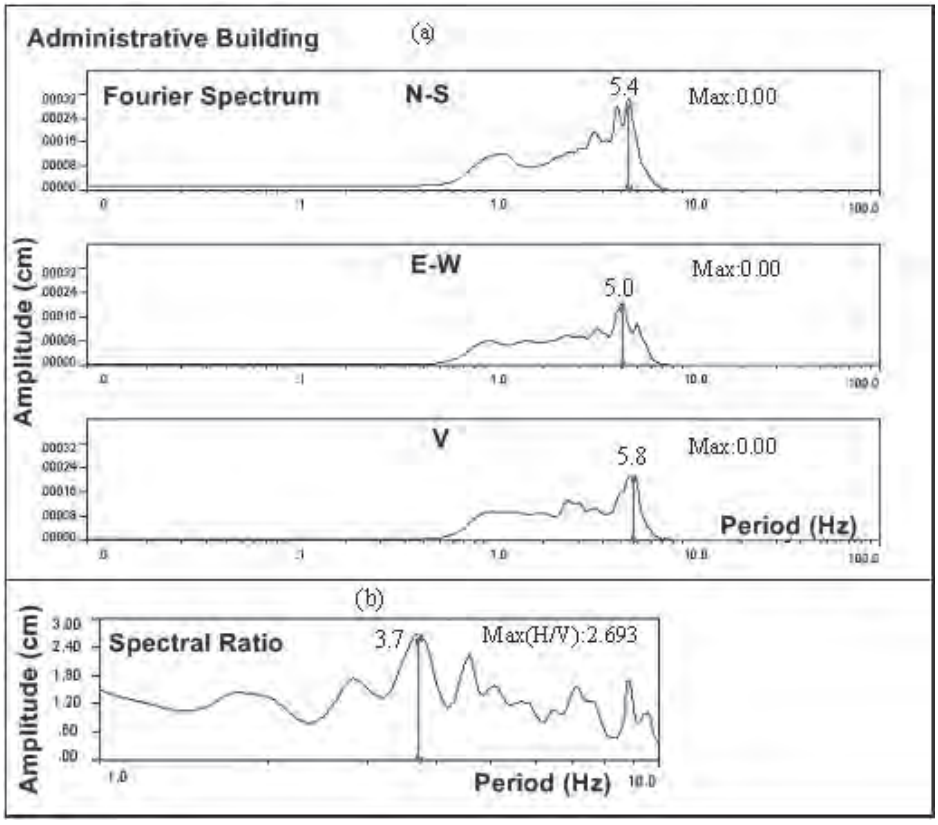

Figure 13- Second record from garden of Adana Organised Industrial Zone Administration building (N-S direction parallel to long axis of building).

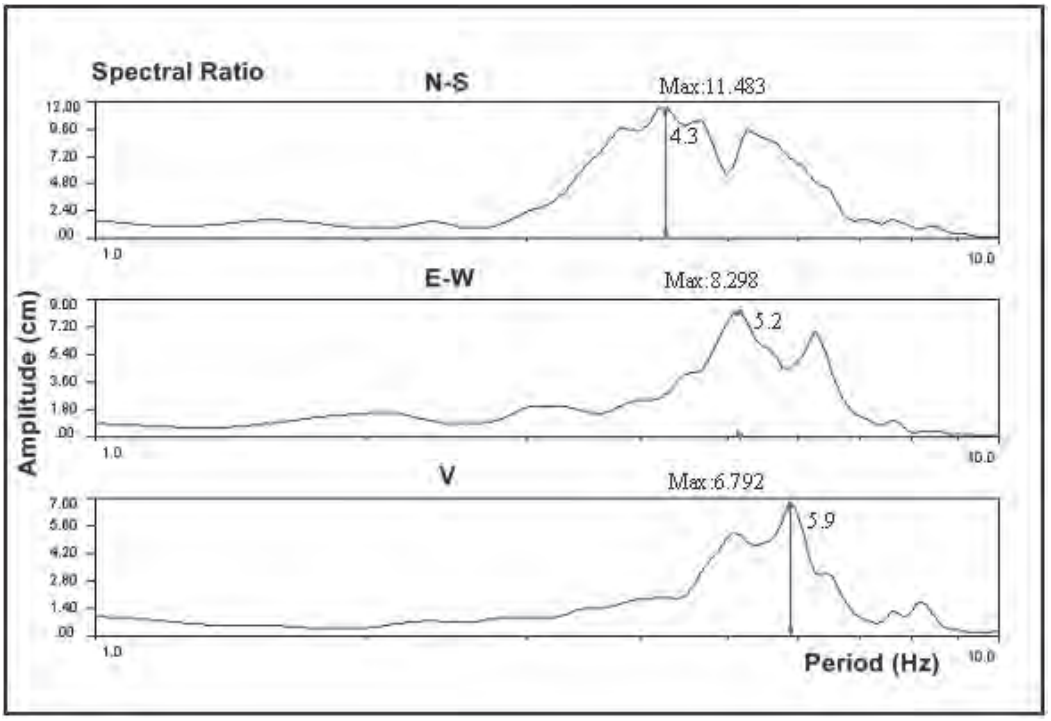

Figure 14- Amplification formed when traditional spectral ratio technique is applied to soft pan level compared to hard pan level for ground at the damaged administration building.

amplification at these periods are shown on maps in figure 15 and 16. For estimation of values from points that could not be measured, a zone map was not created considering errors due to the lack of sufficient measurement points and it was considered more appropriate to give values as points.

In addition to microtremor measurements completed in the study area, measurements were obtained beside damaged buildings, including the administration building severely damaged in the 1998 Adana-Ceyhan earthquake. In these areas the predominant site period and the ground amplification values for these periods

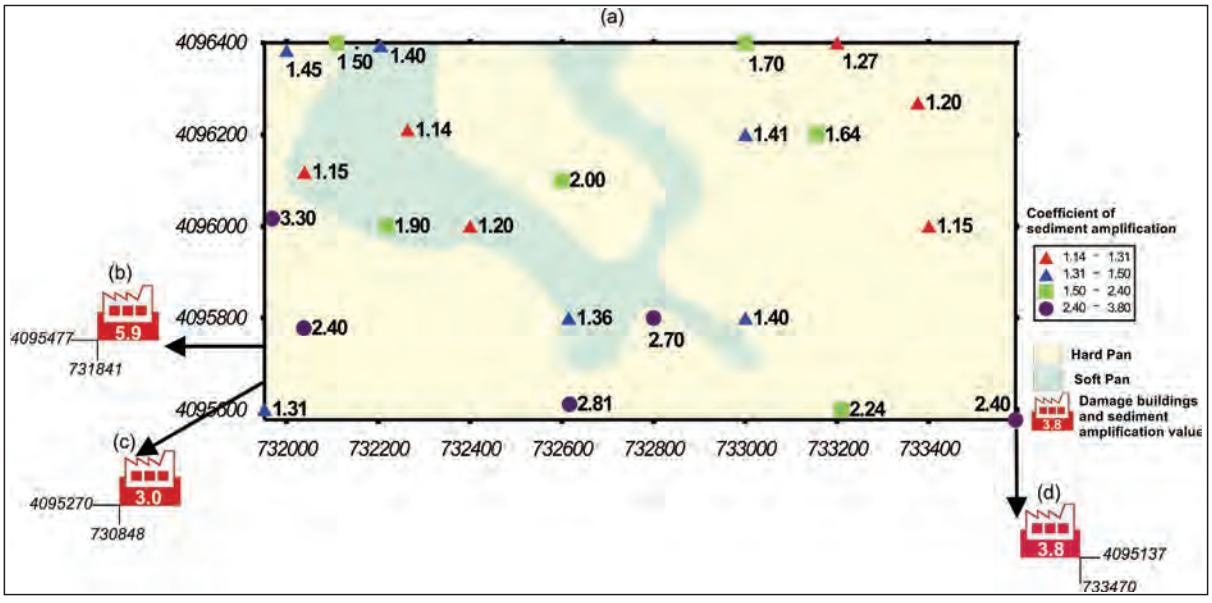

Figure 15- Relative amplification values obtained from Nakamura spectra (a) spatial distribution in the study area and (b, c, d) amplification values found from some damaged buildings outside the measurement area.

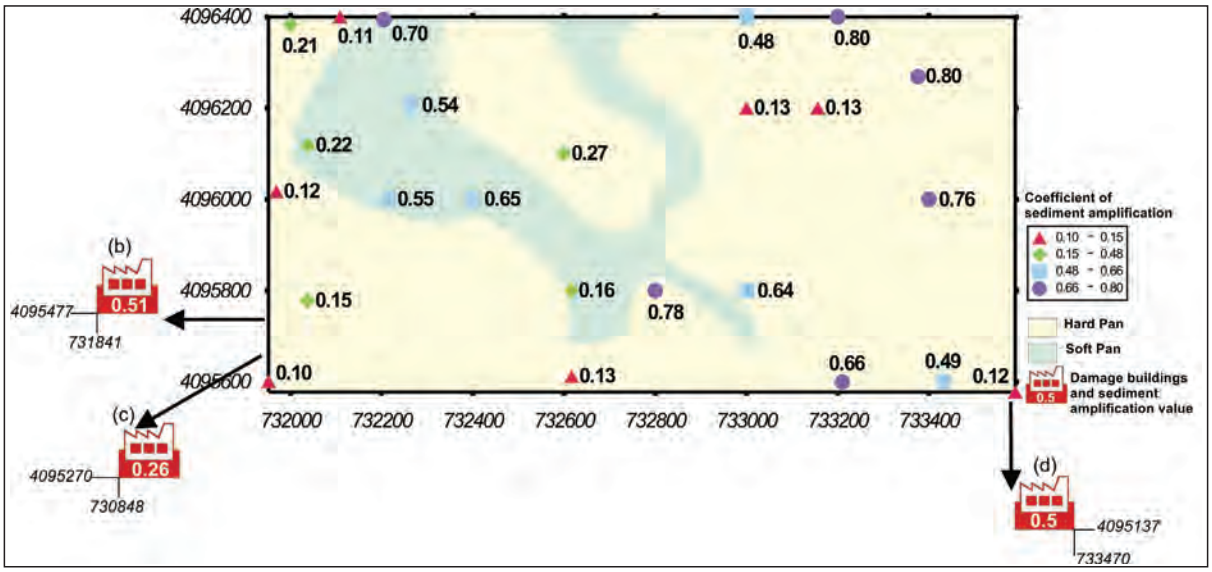

Figure 16- Predominant site periods obtained from Nakamura spectra (a) spatial distribution in the study area and (b, c, d) predominant site periods from some damaged buildings outside the measurement area.

Table 1- Predominant site period and data and coordinates used to create maps for amplification at these periods.

Measurement point	Ground Type	Longitude	Latitude	Amplification	Dominant Period (s)
1	HPC	731952	4095601	1.3	0.1
2	HPC	732038	4095778	2.4	0.2
3	HPC	731969	4096017	3.3	0.1
4	HPC	732039	4096118	1.2	0.2
5	HPC	732000	4096383	1.5	0.2
6	SPC	732205	4096394	1.4	0.7
7	P	732264	4096210	1.1	0.5
8	P	732218	4096000	1.9	0.6
9	HPC	732617	4095612	2.8	0.1
10	HPC	732109	4096400	1.5	0.1
11	SC (HPC)	733000	4096400	1.7	0.5
12	SC (HPC)	733000	4096200	1.4	0.1
13	SC (HPC)	733200	4096400	1.3	0.8
14	SC (HPC)	733376	4096269	1.2	0.8
15	HPC	733156	4096200	1.6	0.1
16	SC (HPC)	733400	4096000	1.2	0.8
17	HPC	733432	4095600	3.8	0.5
18	HPC	733210	4095600	2.2	0.7
19	HPC	733000	4095800	1.4	0.6
20	HPC	732800	4095800	2.7	0.8
21	SPC	732615	4095800	1.4	0.2
22	P	732400	4096000	1.2	0.7
23	HPC	732600	4096100	2.0	0.3
24	HPC	733589	4095578	2.4	0.1

HPC: Hard pan caliche, SPC: Soft pan caliche, SC: Soil cover, P: Pebble-block level

were determined. The severely-damaged buildings are 3- and 4-floor reinforced concrete buildings, with the building period and site period in the same interval and damage occurred due to the buildings resonating with the ground. The predominant site periods and ground amplification values for these periods for the locations of damaged buildings outside the area chosen for microtremor measurements are shown on figures 15 and 16 along with the building coordinates.

In conclusion, it was determined from these maps that the predominant site periods vary from 0.1-0.8 s with ground amplification varying from 1.14-3.8 times. The relative amplification values from measurements taken on hard pan have higher values compared to those obtained from soft caliche with the hard pan having an increasing effect on relative ground amplification. The cause of the amplification on hard pan may be shown as the interaction of wave amplitudes due to repeated reflections and wave scatter between the hard pan and the underlying discontinuities (transitions between different levels within the caliche profile). Wave phases overlap increasing the amplitudes and reaching the surface which is considered to be the true cause of amplification.

References

Aydan, Ö., Ulusay, R., Kumsar, H., Sönmez, H., Tuncay, E. 1998. A site investigation of Adana-Ceyhan Earthquake of June 27, 1998. Turkish Earthquake Foundation. TDV/DR006-30 131p.

Bayülke, N. 1978. Tuğla yığla yapıların depremdeki davranışı. Deprem Araştırma Enstitüsü Bülteni, 6 (22), 26-41.

Clayton, C. R. I., Serratrice, J. F. 1977. The mechanical properties and behaviour of hard soils ad soft rocks. Proceedings of Geotechnical Engineering of Hard Soils - Soft Rocks Symposium, Athens, Greece,

Çelebi, M. 1998. The Adana-Ceyhan Earthquake of June 27, 1998, Learning From Earthquakes. EERI Special Earthquake Report, Earthquake Engineering Research Institute Newsletter, 32, (9) 1-5

Goudie, P. A., Pye, K. 1983. Chemical sediments and geomorphology, Academic Press, London, 93-131.

Halaç, B. 2016. Deprem yönetmeliklerindeki zemin sınıflandırma kriterlerinin zemin büyütme açısından incelenmesi. İstanbul Teknik Üniversitesi, Fen Bilimleri Enstitüsü Yüksek Lisans Tezi, 100s.

Johsonston, I. W., Novello, E. A. 1993. Soft rock in the geotechnical spectrum, Proceedings of Geotechnical Engineering of Hard Soils - Soft Rocks Symposium Under the Auspices of the ISSMFE, Athens, Greece, 1, 177-183.

Kozlu, H. 1987. Misis-Andırın dolaylarının stratigrafisi ve yapısal evrimi, Türkiye 7. Petrol Kongresi Bildiriler Kitabı, 104-117.

Nakamura, Y. 1989. A method for dynamic characteristics estimation of subsurface using microtremor on the ground surface, Quaterly Report of RTRI, Railway Technical Research Institue (RTRI) , 30, 1, 25-33.

Popescu, M. E. 1986. A comparision between the behaviour of swelling and collapsing soils. Eng. Geo. , 23, 145-163.

Rogers, C. D. F. 1995. Types and distribution of collapsible soils, in: Derbyshire, E., Dijkstra, T. and Smalley, I. (eds), "Genesis and properties of collapsible soils", 1-17., NATO Ası Series, Kluwer Academic Publisher, Netherlands.

Rollins, K. M., Rollins, R. L., Smith, T. D., Beckwith, G. H. 1993. Identification and characterization of collapsible gravels, Journal of Geotechnical Engineering, 120, 3, 528-542.

Steven, L. 1998. Evaluation design and mitigation of project sites in collapsible soils areas in Western Colorado. Project Report 45 p. (yayımlanmamış).

Şenol, M. 1989. Adana-Balcalı/Çatalan Bölgesinin Genç Tersiyer-Kuvaterner İstifinin Lito-Pedolojik ve Sedimantolojik İncelemesi. Doktora Tezi, Ç.Ü Fen Bilimleri Ens., 128s. (yayımlanmamış).

Terzaghi, K., Peck, B.R. 1967. Soil Mechanics in Engineering Practice. John Willey and Sons Inc., 729 p.

Udwadia, F., E. Trifunac, M.D. 1973. Comparison of earthquake and mircrotremor ground motions in El Centro, California. Bull. Seism. Soc. Am., 63, 1227-1253.

Wenk, T., Lacave, C., Peter, K. 1998. The Adana-Ceyhan earthquake of June 27, 1998. Swiss Society for Earthquake Engineering and Structural Dynamics (report), 1-47.

Yetiş, C. 1987. Adana kuzeyinin jeolojisi ve şehir merkezinin bazı temel sorunlarıa ilişik gözlemler. Çukurova Üniversitesi, Müh-Mim. Fak. Dergisi, 115-123.

Zorlu K., Kasapoğlu, K.E. 2009. "Determination of geomechanical properties and collapse potential of a caliche by in-situ and laboratory tests, Environmental Geology, 56 (7), 1449-1459.

Bulletin of the Mineral Research and Exploration

http://bulletin.mta.gov.tr

The Hydrogeological investigation of Plajköy spring (Elazığ)

Özlem ÖZTEKİN OKAN[a]* Atahan GÜVEN[b] and Bahattin ÇETİNDAĞ[c]

[a]*Fırat University, Faculty of Engineering, Department of Geological Engineering, 23119, Elazığ. orcid.org/0000-0003-2934-2170*
[b]*Erciyes University, Tomarza Vocational High School, Department of Construction, Kayseri. orcid.org/0000-0003-1590-5374*
[c]*Fırat University, Faculty of Engineering, Department of Geological Engineering, 23119, Elazığ. orcid.org/0000-0003- 1590-5374*

Research Article

Keywords:
Plajköy spring, Elazığ, protection zone, storage capacity, discharge coefficient, catchment area.

ABSTRACT

Plajköy spring discharges at the close locations to the SE shore of Lake Hazar. Lake Hazar is a tectonic Lake in Elazığ city. Plajköy spring is a fault spring that is mainly recharging from the volcanites, dikes and blocky volcanosedimentary units of Middle Eocene Maden Complex. These units have gained secondary permeability and porosity related with the active tectonics that is effective in the studied area. The present catchment system of the spring could not collect the springs and leaks discharging from different points around the system. The discharge of the catchment is measured by specific volume method while the other springs' and leaks' is measured by using triangular weir. Before the discharge measurement of the leaks and the springs, they have been directed to a channel. The discharge of the present catchment system and the leaks have measured twice in a month during one year period beginning from October of 2012 to November of 2013. The discharge coefficient of the spring is calculated $1.33*10^{-3}$ day^{-1}. Discharge coefficient of the spring depends on the geometry and intensity of the active fracture systems in the region. Calculated discharge coefficient indicates that the spring discharge is related with the narrow fissures, fractures and pores. The total volume of discharged groundwater in the real regime of the Plajköy spring is calculated as $52* 10^3$ m^3 during the period from 31st of March, 2013 to the 13rd of October, 2013 by Maillet formula. The spring water is Ca- Mg- HCO_3 type water related with the chemical analyses. The chemical and microbiological analyses of the spring water are correlated with the drinking water standarts of Turkey TS 266 (TSE, 2005) and World Health Organization (2004), and it is seen that the spring water is suitable for drinking. The Plajköy spring will be used more efficiently without exposed to pollution by the new catchment plan and protection zone map that are consequently proposed in the present study.

Received Date: 15.02.2016
Accepted Date: 09.01.2018

1. Introduction

Turkey is not a water-rich country. The increasing population and water requirements in the country have made it mandatory to search for and operate new water resources. To ensure the sustainability of current groundwater resources, rational use is necessary. As in general in Turkey, the study area of the province of Elazığ has an increasing population due to migration from surrounding provinces and as the available water resources are insufficient, there is a need for drinking water.

In recession period when the aquifer is not fed by external effects, the reserves above the aquifer discharge level of the springs are drained. In this period when the watershed of the resources does not have precipitation or if precipitation is too low to affect the aquifer, variations in discharges of springs may be shown on discharge variation graphs and discharge curves which have attracted the attention of many researchers. The basic formula for the discharge graph of the recession period of springs was given by Maillet (1905). After this basic study, studies were completed on more complicated systems involving two or more aquifers and the changes occurring on discharge graphs

* *Corresponding author: Özlem ÖZTEKİN OKAN, ooztekin@firat.edu.tr*
http://dx.doi.org/10.19111/bulletinofmre.376767

and the factors causing these changes were investigated by many researchers (Coutagne, 1968; Mangin, 1975; Padilla et al., 1994). In recent times, environments with different hydrogeologic characteristics have been modelled in laboratory conditions to draw and interpret discharge curves. According to these researches, the recession curve of a spring is related to geologic and hydrologic factors like precipitation in the region, and the geology of the recharge area, along with hydrogeologic characteristics of the aquifer (e.g., porosity, permeability, transmissivity) and situations like pumping from groundwater (Kovacs and Perrochet, 2008; Liu and Li, 2012; Farlin and Maloszewski, 2013; Azeez et al., 2015).

The study area is located south of Elazığ and southeast of Lake Hazar, which experiences intense summer tourism (Figure 1). Geologic studies with different aims have been performed in the study area and surroundings. Kaya (1992), in a study about the geology of the studied spring area and surroundings, stated the oldest unit in the region was the Upper Jurassic-Lower Cretaceous ophiolites, overlain above an angular unconformity by the Maastrichtian-Lower Eocene Hazar Group comprising red mudstone followed by flysch units to finally end in limestones, from bottom to top. A study by Gürocak (1993) on Sivrice county west of the study area mentions that the flysch of the Hazar Group is overlain above an unconformity by the Maden Complex comprising limestone, andesite, basalt, volcanic breccia and crosscutting diabase dikes. Güven (2013) studied the hydrogeology of the Lake Hazar region and stated that

Figure 1- Location maps of the study area.

the primary porosity of the volcanics within the Maden Group was very low. Due to tectonic activity affecting these rocks in the region they gained a fractured-fissured structure to provide secondary porosity and permeability. The study stated that the groundwater flow direction within these units was controlled by the distribution of fractures-fissures and by fault lines. Aksoy et al. (2007) investigated the Lake Hazar basin as part of the East Anatolian Fault System within the study area and described it as a negative flower structure on a strike-slip fault geometry. Çelik (2008) stated that there was nearly 30 km of offset between outcrops of an olistostromal unit from the Middle Eocene Maden Complex on the north and south blocks of the fault in the section of the East Anatolian Fault System between Palu- Lake Hazar (Elazığ).

The population living in the study area is low in the winter months and high in the summer months. The increasing population in the summer months is linked to camping tourism and summer housing sites around Lake Hazar. The drinking and useable water requirements of Plajköy are provided by two different drill wells with flows of 17 l/s and 22 l/s. In the summer months while the drinking and useable water requirements for the settled and temporary population are provided by both drill wells, in the winter the water requirements of the settled population are provided by a single drill well. However, in the summer months apart from the available water network, the local people and temporary population also obtain their drinking water from Plajköy spring, the topic of this study. The sedimentary units belonging to the Hazar Group (especially limestones) and the volcanics, sub-volcanic and volcanosedimentary units belonging to the Maden Complex outcropping in the area have gained discontinuities linked to active tectonism in the region and as a result are permeable. Coastal aquifers forming within these units have been polluted by soda water from Lake Hazar with the majority of wells drilled in these formations affected by this intrusion. Thus, due to the requirements for drinking and useable water, the formation of this spring, is very important for the area and especially for the increasing human population during the summer months and the settled population, even though the discharge is not high (mean 3.01 l/s). The spring has a current catchment; however it is not sufficient for the spring area. In fact on the east and west edges of the catchment there is flowing water outside the catchment. The current catchment does not collect the the water in the spring area into a single point. In this study the reserve above discharge level and hydrochemical properties of the Plajköy spring were investigated, the appropriateness of the spring water for drinking and using purposes were determined and a new catchment plan and protection areas of the spring were created.

1.1. Material and Method

The spring discharges from 4 fountains due to a 2x2 m cement manhole previously constructed in part of the spring. The discharges from these fountains and the other springs without catchments were measured twice a month for 1 year. The discharges from the fountains were measured with the specific volume method. The springs and leaks from other points outside the catchment were directed into a single channel and discharges were measured with a triangular weir. For chemical analysis of water, water samples were obtained in 100 mL polyethylene bottles twice during the year in the wet (May 2014) and dry (October 2014) periods. When sampling in the field, the temperature, pH and electrical conductivity of the water was measured with YSI 63 brand multiparameter measurement device. Water sampling in the field was completed according to TS EN ISO 5667 standards. For cation and anion analyses, water samples were taken in two separate bottles. After water sampling, the cation analysis bottle had HNO_3 added to bring pH<2. Chemical analyses of the water were completed in Hacettepe University Water Chemistry Laboratory. Cation analyses of water used a Dionex LC (liquid chromatography) 25 brand chromatography system, while anion analyses were completed with a Dionex ICS (ion chromatography system)-1000. Bicarbonate (HCO_3^-) was measured with the titration method using an automatic burette system. For microbiological analyses water samples were placed in sterile sample containers with 250 mL volume and sodium thiosulphate according to EN ISO 19458 standards. Microbiological analyses of water were completed with the membrane filtration method in Elazığ Municipality Water Quality Control Laboratory. Disturbed samples had porosity determined with the compression method (Canik, 1998), while permeability was determined with the box with holes in the base method (Schoeller, 1962) and with constant-head method. Orientation measurements of fractures were assessed with the stereographic projection technique using the DIPS (Diedrisch and Hoek, 1989) computer program. Mineral saturation indices of groundwater were calculated with Phreeqci 3.3.8 program (Parkhurst and Appelo, 1999).

2. Geology and Hydrogeology

The basement of the study area comprises the Maastrichtian-Lower Eocene Hazar Group, overlain by the Middle Eocene Maden Complex and Quaternary-aged alluvium covers the top of the sequence (Figure 2).

The Maastrichtian-Lower Eocene Hazar group was first called the "Hazar Complex" by Perinçek (1979) and Tuna and Dülger (1979), before being named the "Hazar Group" by Aktaş and Robertson (1984) (Kaya, 2004). The unit outcrops widely in the northeast of the study area, while the marl, clayey sandstone and claystone intercalations of the unit are observed in a narrow area of a roadcut east of Gezinistasyonu Neighbourhood (Figure 3). The Hazar Group units are overlain above an angular unconformity by the Middle Eocene Maden Complex near Kızıltepe village.

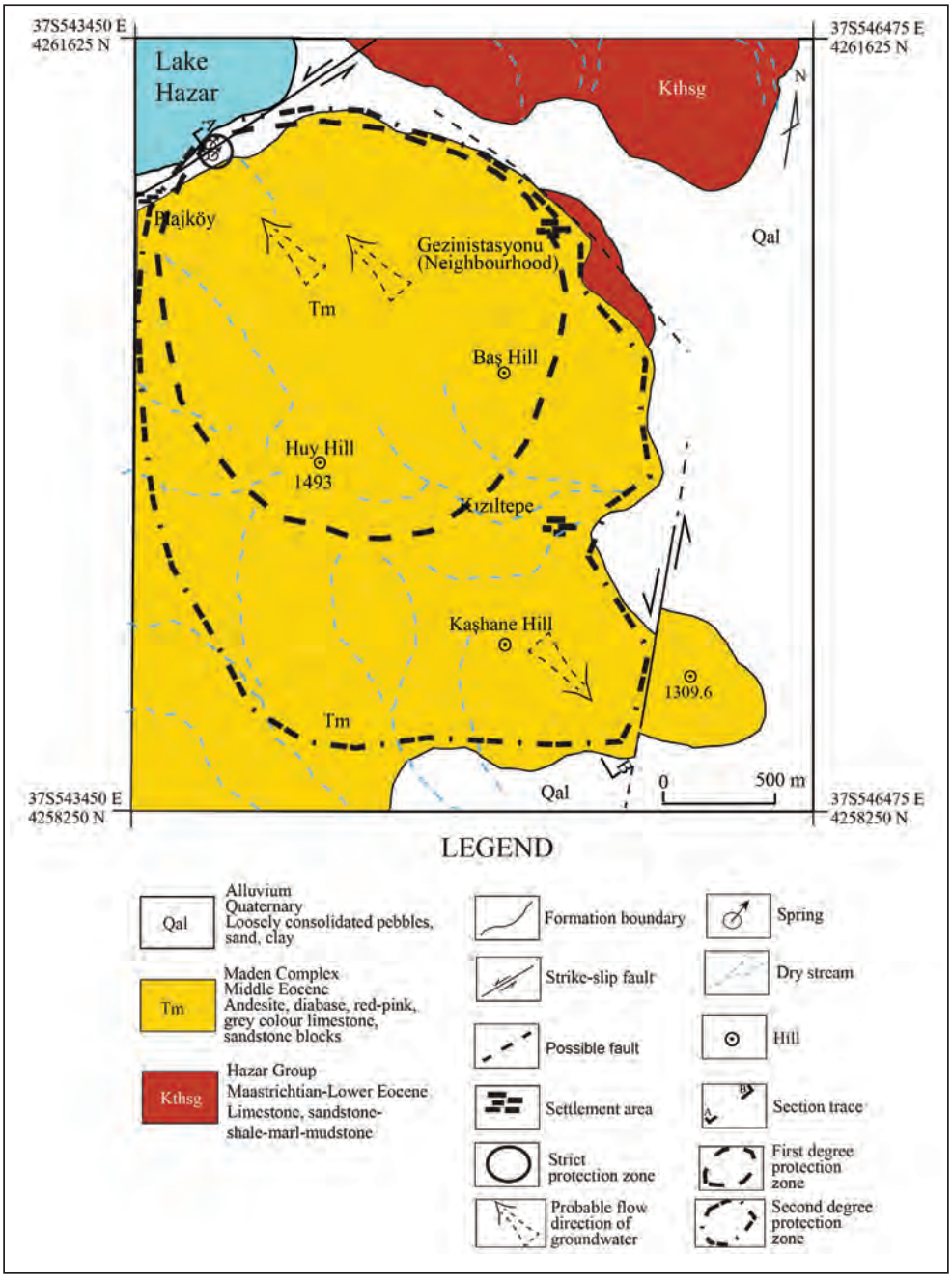

Figure 2- Geologic map of Plajköy spring and close vicinity and protection zones of the spring.

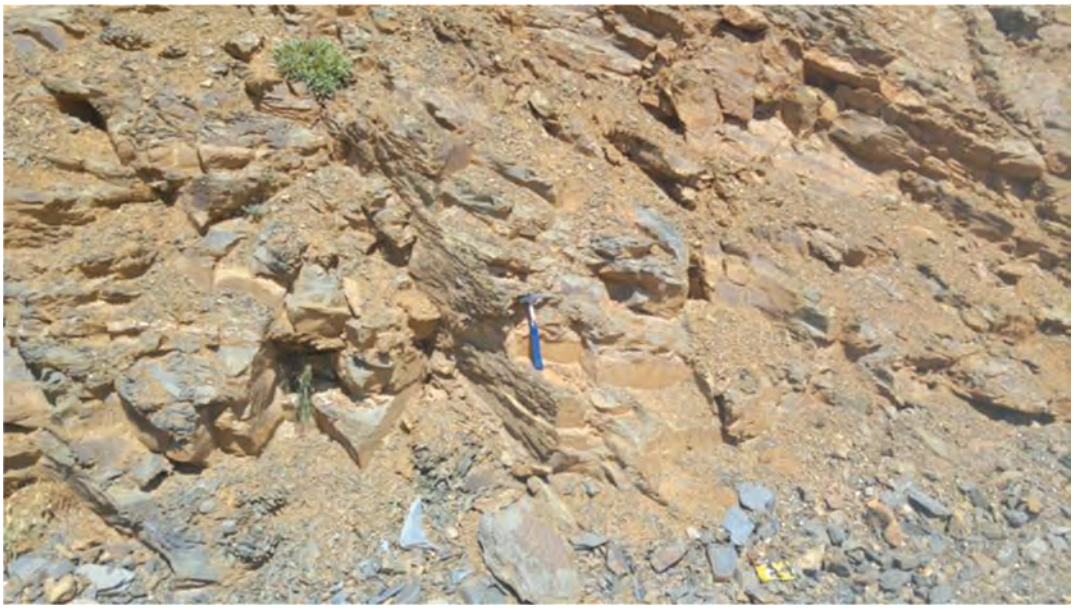

Figure 3- Flysch levels of the Hazar Group outcropping at the roadcut SE of Gezinistasyonu Neighbourhood (View direction NW, coordinates 37S545734E, 4260110N)

Units belonging to the Middle Eocene Maden Complex near Lake Hazar generally begin with conglomerate at the base, passing upward through sandstone layers, occasionally silicified reddish brown-grey coloured sandstone-mudstone-marl intercalations before grading up into grey neritic and micritic limestones. The very top of the unit comprises red-pink pelagic limestones. All these units display lateral and vertical transitions, accompanied by andesitic and basaltic volcanics in the form of interlayers (Kaya, 2004). With broad outcrops at Kızıltepe village, Baş Tepe, Huy Tepe, and Kaşhane Tepe in the study area, the Maden Complex is mainly represented by volcanics with occasional altered diabase dikes observed. The majority of the volcanics in the study area have andesitic composition. The volcanics and diabase rocks have intense fracturing and fissuring linked to the tectonism active in the region, and have a very weathered and altered appearance within valleys. The fractures and fissures developed within the volcanics and diabase are filled with secondary calcite (Figure 4 a,b,c). Due to the active tectonic activity in the region, there are blocks of very fractured sandstones and limestones found within the volcanics in the study area in narrow areas too small to map. The dominant lithologies in the recharge area of the spring are volcanics, diabase and volcanosedimentary units of the Maden Complex that have been intensely affected by the active tectonism in the region.

Quaternary-aged alluvium unconformably overlies the Hazar Group and Maden Complex in the region. The Quaternary alluvium has a very broad distribution in the study area within the East Anatolian Fault Zone where tectonism is intense from northeast of Kızıltepe village to the area to the south. The unit is represented by badly sorted pebbles, sand, clay and silt with loose consolidation. With less clear layering, the alluvium has horizontal placement (Kaya, 1992).

With intense tectonism, the left-lateral strike-slip East Anatolian Fault Zone passes through the study area. The East Anatolian Fault forms a zone 5-6 km wide in the region. It is not observed as a single fault in the study area, but comprises several parallel, large faults with NE-SW strike (N60°E) (Kaya, 2004). The formation of Plajköy spring within the study area is related to this fault zone.

To determine the protection zones for the spring, disturbed samples of the altered volcanics and diabase rocks forming the recharge area were obtained and hydrogeological characteristics determined in the laboratory. The porosity and permeability experiments on samples taken from vertical trenches outcropping in the recharge area of the spring were performed in the laboratory. The porosity values for recharge lithology were from 45.95-46.88%, while the permeability values were between 3.61×10^{-3} m/s and 1.7×10^{-3} m/s. The porosity and permeability values of the unit are very high.

Figure 4 (a, b, c)- Fractures and fracture fill within volcanics of the Maden Complex. Northern slopes of Kaşhane Hill (View direction toward SE, coordinates 37S545407E, 4259214 N).

2.1. Formation of Plajköy Spring

Plajköy spring is recharged from the very fractured and fissured volcanic and sub-volcanic rocks (diabase) and blocky volcanosedimentary units of the Maden Complex. The fracture system developing linked to active tectonism in the region has provided the unit with secondary porosity and permeability. Orientation measurements from 103 fractures within the aquifer formation for the spring of the Maden Complex comprising volcanics, sub-volcanic and volcanosedimentary rocks were assessed with a computer program and it was determined that these rocks contained 3 joint sets (Figure 5). When the rose diagram is investigated, fractures in the unit mainly strike NW-SE and NE-SW and the joint sets were determined as 302/32, 208/10 and 54/13 according to density. These fractures and fissures are very intense in the upper levels and as they are linked they reduce and are lost as the depth increases. This situation allows the volcanics, sub-volcanic rocks and blocky volcanosedimentary units of the Maden Complex to form both the aquifer for the spring and the impermeable base of the aquifer. The flysch from the Hazar Group, outcropping in a very small area of the study area, is not considered to have any effect on the formation of the spring.

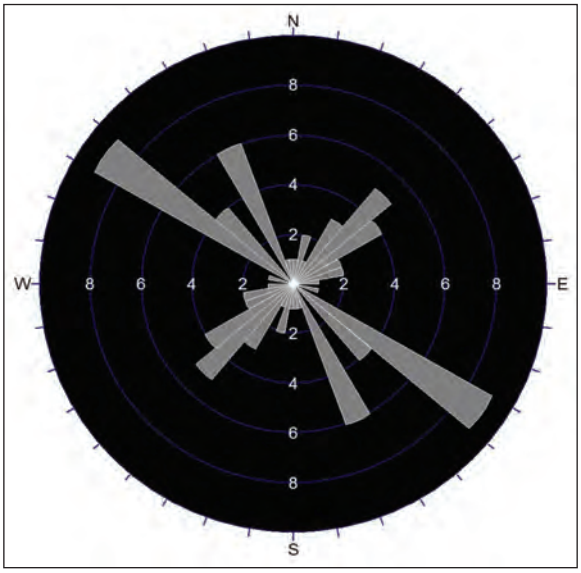

Figure 5- Rose diagram of fracture orientations measured in volcanic, sub-volcanic and volcanosedimentary rocks of the Maden Complex.

Precipitation moving within the very fractured volcanics, sub-volcanics and blocky volcanosedimentary rocks passes along a left-lateral strike-slip fault within the study area and forms a spring area rising to the surface through alluvium at different points (Figures 6 and 7).

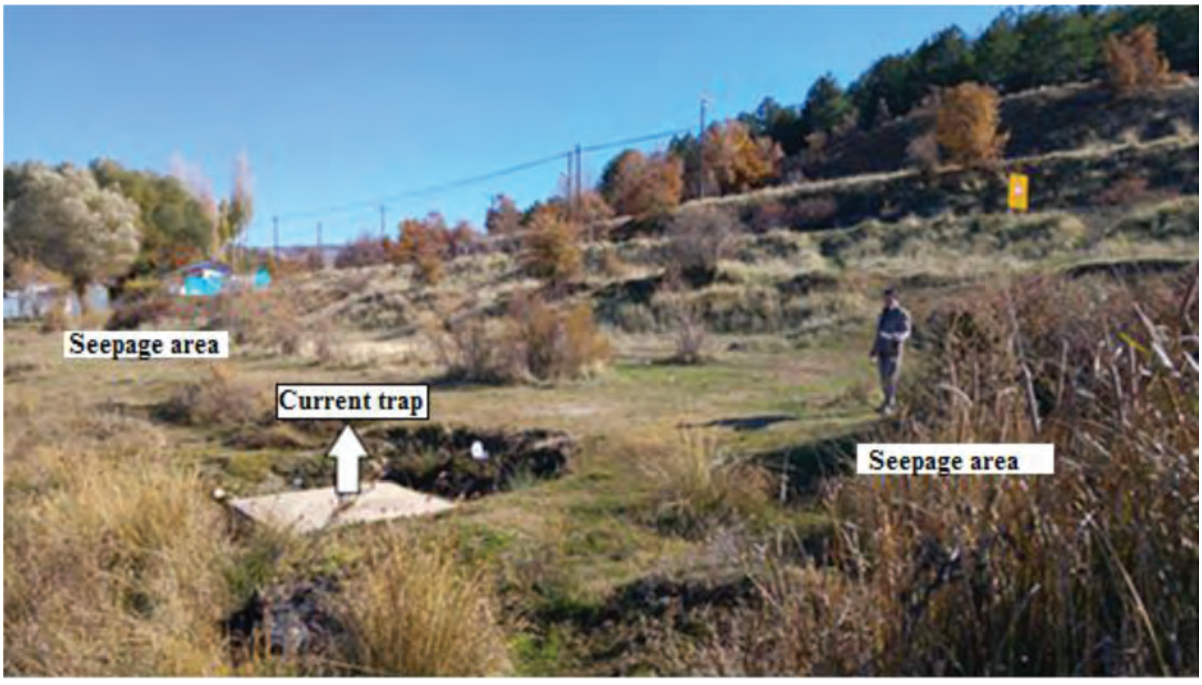

Figure 6- Plajköy ppring, southeast coast of Lake Hazar (View direction toward NE, coordinates 37S544105E, 4261455N).

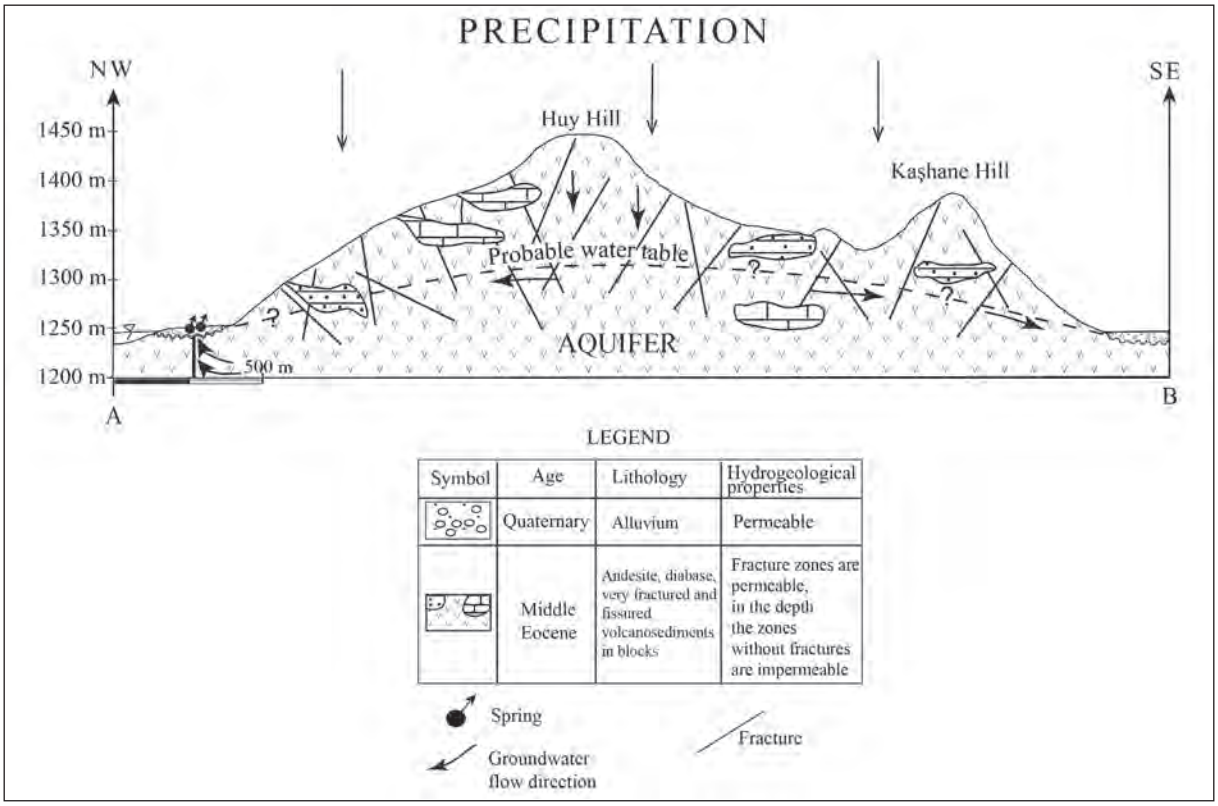

Figure 7- Hydrogeological section showing formation of Plajköy spring (thickness of lithologic units shown schematically).

2.2. Discharge-Precipitation Relationship of Plajköy Spring

The discharge variation of the spring was measured two times per month from 28/10/2012 to 30/10/2013. The recession period is observed on the discharge variation graph of the spring for the studied period (Figure 8). The highest discharge from the spring was 3.48 l/s, lowest discharge was 2.60 l/s with mean discharge of 3.01 l/s. The low values for the spring discharge is due to the recharge area not being very large. The lowest discharge was measured on the 28 October 2012, with highest discharge measured on 31 March 2013 representing the period when the spring is recharged by precipitation. Argillitization linked to the alteration of the volcanics and sub-volcanic rocks found in the recharge area of the spring delays the precipitation from reaching the aquifer. As seen on Figure 8, the effect of increased rain in the months of September-October appears to be delayed by 28-30 days before the discharge of the spring increases.

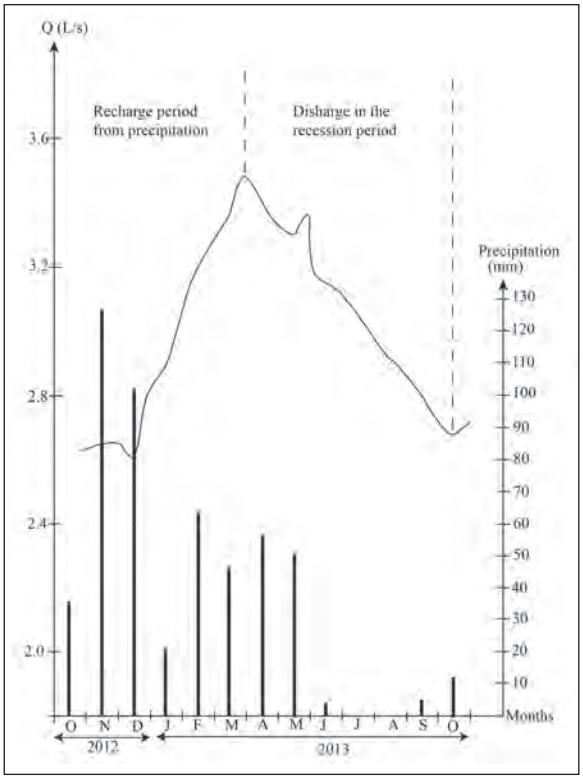

Figure 8- Discharge-precipitation graph of Plajköy ppring.

2.2.1. Calculation and Interpretation of Recession Coefficient and Storage Capacity

The recession period of the spring encompasses 31 March 2013 to 13 October 2013. The log Q = f(t) graph of the spring for this period was drawn with a straight line decreasing from time t_0 (Figure 9). The general equation for this curve is given by the exponential function recommended by Maillet.

$Q= q_0 * e^{-\alpha(t-to)}$

In the above equation;

q= discharge at time t (m^3/s)

q_0= discharge at the beginning of the recession (time t_o) (m^3/s)

a= recession coefficient (day^{-1})

$t-t_0$= duration since the start of recession (day)

The discharge at the start of recession was 3.48 l/s, while at the end of the dry period it was 2.68 l/s (Figure 9). The recession coefficient (α) is calculated from the recession curve with the following equation:

$\alpha = \log q_0 - \log q / (t-t_o) * \log e$

Taking the initial discharge of recession q_0= 3.48 l/s and q= 2.68 L/s, a was calculated as $1.33*10^{-3}$ day^1.

There are many scientific studies on interpreting the recession coefficients of springs. According to Schoeller (1962; 1967), in general recession coefficients with values around $n*10^{-3}$ represent springs with water discharged by laminar flow in very narrow fissures and fractures or in pores around grains, while values from $n*10^{-2}$ to $n*10^{-1}$ represent springs discharged by turbulently flowing water through broad fissures and dissolution channels. Smart and Hobbs (1986) and Liu and Li (2012) stated that discharge from karstic rocks was related to three variables. These are recharge (diffusive or concentrated), storage (significant or small volumes) and flow type. A study by Ebrahimi et al. (2007) stated that the recession coefficient of karstic limestone dominated by diffusive flow is proportionally lower compared to karstic systems dominated by turbulent flow. Fiorillo (2011) stated that different recession coefficients during the discharge duration of aquifers were related to differences in aquifer geometry or hydraulic character. There is a very close correlation between the recession coefficient and especially the effective porosity of the aquifer and the location of the water table. As a result, during the discharge period, variations in these two parameters will cause changes

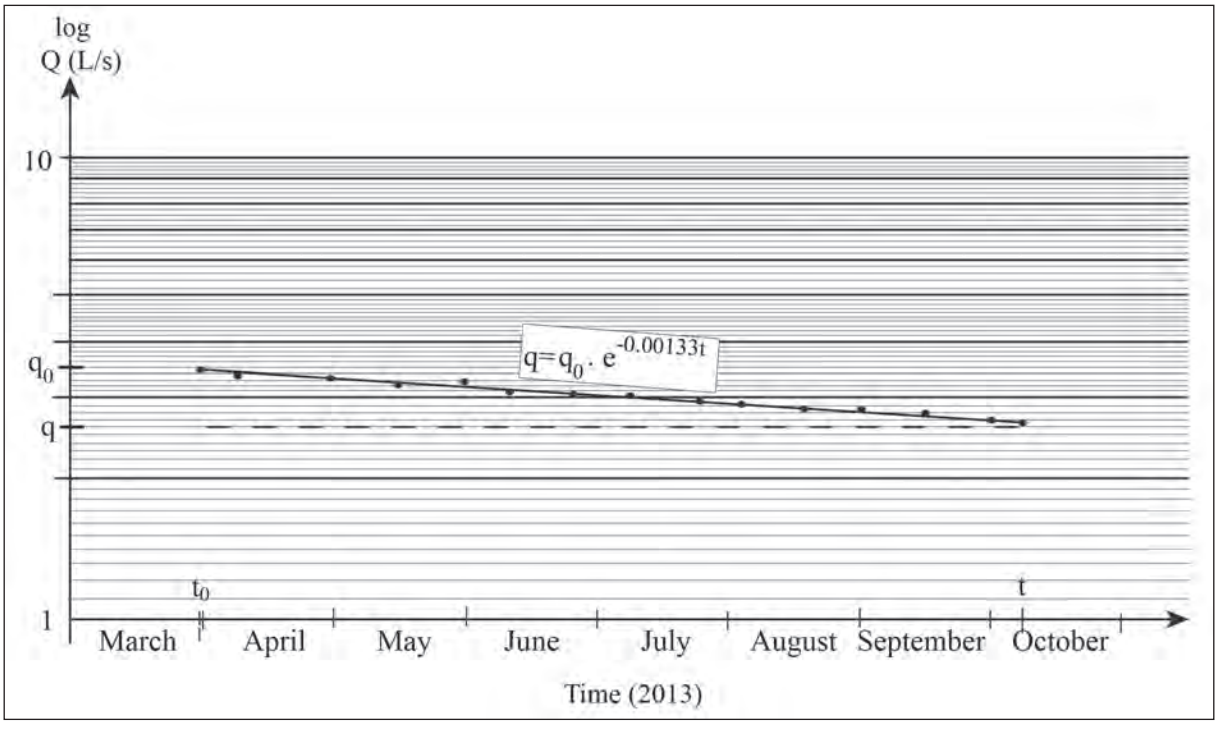

Figure 9- Discharge curve for recession period of the spring (2013).

in the recession curve (Fiorillo, 2011; Fiorillo et al., 2012). The recession coefficient of the studied spring is related to the geometry and density of the fracture system affecting the region with the calculated recession coefficient representing recharge of the spring through narrow fissures, fractures and pores (Çetindağ and Öztekin, 2001; Çetindağ, 2002; Kovack et al., 2005; Ebrahimi et al., 2007) .

The water storage capacity above the discharge level in the recession period of Plajköy spring for 2012 to 2013 was calculated using the following formula from Maillet (1905);

$V_0 = (q_0/\alpha) * 86400$

On the 31 March 2013 in the recession period, the water storage capacity of the spring (V_0) was calculated as $2.26*10^5$ m^3 above the discharge level. Between 31 March 2013 and 13 October 2013, the amount of water discharged from Plajköy spring in the recession period was calculated as $52*10^3$ m^3.

According to data from the Turkish Statistical Institute (2014), the amount of water for drinking and domestic using purposes per person is 203 L per day. In the study area, the spring is used for drinking and domestic usage by the local people and the temporary camping population especially in the summer months. The population of Plajköy is mean 5000 people in the summer months. If this spring alone was used for drinking and domestic usage by a population of 5000, the period of use in the dry period was calculated as 51 days.

2.3. Hydrochemical Characteristics of Plajköy Spring

The chemical and microbiological analysis results for water samples taken from fountain of the present catchment for the studied spring are given in table 1. For the wet and dry periods, the pH of the water is 7.03 and 8.30, while electrical conductivity is 421 and 438 µS/cm. The pH value of the spring varies in wet and dry periods (Table 1).

The pH of Plajköy spring is neutral in the wet period and alkaline in the dry period. The lower pH values in the wet period are considered to be related to the low pH of precipitation recharging the aquifer or to increasing CO_2 in the circulation region of the groundwater (Güler et al., 2017). The enrichment of water by CO_2 is very effective in areas close to the surface and at soil level. In regions close to the surface, CO_2 is created during the oxidation process added by organic material and microorganisms and by respiration of plant roots (Milanovic, 1981). The pine forest area found in the recharge area of the spring is thought to play an important role in enriching the groundwater in CO_2 during the rainy period. In the dry period, the increase in pH is related to the hydrolysis of silicates in reducing conditions affecting groundwater moving through fractures and fissures at depth (Garrels and Christ, 1965; Boughton and McCoy, 2006; Kebede et al., 2005). Additionally, in the period with low recharge, the increasing water-rock interaction linked to the low hydraulic gradient may cause an increase in pH.

The hydrolysis of silicates is represented by the following equation:

$$Rock + H_2CO_3 \rightarrow Cations + H_4SiO_4 + HCO_3^- + \text{Secondary minerals}$$ (Ako et al., 2011)

The saturation indices calculated for the spring water are given in table 2. In May when the dissolution mechanism is effective the spring water is not saturated with calcite, aragonite and dolomite minerals, but becomes saturated in October. The dissolution of carbonates and silicates is completed related to the decrease in CO_2 as water percolates to greater depths along fissures and fractures.

The electrical conductivity of the spring water is lower in May, while it is slightly higher in October (Table 1). The effect of precipitation on the recharge of the aquifer in May is shown in figure 8. The low electrical conductivity of water in the month of May

Table 1- Chemical and microbiological analysis results of Plajköy Spring (Analysis results in mg/l; no E. coli or coliform bacteria were encountered during microbiological analysis of water samples).

Sample name	T (°C)	pH	EC (µS/cm)	Na^+	K^+	Ca^{+2}	Mg^{+2}	HCO_3^-	Cl-	SO_4^{-2}	NO_2^-	NO_3^-	PO_4^{-3}	NH_4^+	Hardness (d°h Fr)
Plajköy Spring (May, 2014)	16.40	7.03	421	10.96	1.07	62.78	16.24	260.10	2.13	15.46	<0.01	1.92	<0.01	0.17	22.45
Plajköy Spring (October, 2014)	15.50	8.30	438	10.64	1.11	63.93	19.33	274.50	2.20	14.27	<0.01	1.91	<0.01	0.47	24.00

Table 2- Saturation indices of Plajköy Spring.

Mineral	Saturation index	
	May, 2014	October, 2014
Anhydrite	-2.81	-2.87
Aragonite	-0.40	0.85
Calcite	-0.25	1.00
Dolomite	-0.87	1.70
Gypsum	-2.41	-2.46
Halite	-9.18	-9.18
Sylvite	-9.72	-9.68

representing the rainy period is related to the high hydraulic gradient and rapid flow linked to recharge by rain. During rapid movement of rain water, the water-rock interaction is lower. In the month of October, representing the dry period with low spring discharge, the water has higher electrical conductivity. In this period when the effect of rain on recharge is reduced, the hydraulic gradient decreases slowing the rate of groundwater flow causing an increase in the duration of water-rock interaction. The increase in water-rock interaction increases the electrical conductivity of water.

On the Schoeller diagram, the dominant cation found in the water is Ca^{+2}, with the dominant anion HCO_3^- and the water appears to be Ca-Mg-HCO_3 type. On the Piper diagram, the water is grouped in the 5th region. This region indicates groundwater with carbonate hardness above 50% containing $CaCO_3$ and $MgCO_3$. The chemical composition of the spring water does not show clear differences between wet and dry periods except in the ion concentrations of Ca^{+2}, Mg^{+2} and HCO_3^- (Figure 10a,b). In the dry period, the Ca^{+2}, Mg^{+2} and HCO_3^- ion concentrations are relatively high compared to the rainy period. In the dry period in addition to the increase in dissolution of carbonates linked to increasing water-rock interaction, the hydrolysis of silicates (like olivine, pyroxene, plagioclase, alkali feldspar) affects the increase in these ions' concentrations (Kimball, 1981; Kebede et al. 2005).

The sources of the Ca^{+2} ions in the spring water comprise dissolution of limestones outcropping in the region and dissolution of Ca^{+2} ions found in silicate minerals like anorthite, pyroxenite and amphibole within volcanic rocks. Additionally, the secondary calcite formations along fissures and fractures related to active tectonism in outcropping rocks in the region forms a source for Ca^{+2} ions in groundwater. The Mg^{+2} ion concentration in the spring water was 16.24 mg/l in May (2014), while it increased to 19.33 mg/l in October (2014) (Table 1). The source of the Mg^{+2} ions in the water is the dissolution of magnesium-composition minerals like olivine, biotite and hornblende within volcanic rocks of the Maden Complex. It is estimated that K^+ passes into groundwater due to dissolution of mica and feldspar minerals within volcanic rocks outcropping in the study area. The source of Na^+ in the studied spring water is related to dissolution of Na feldspars within volcanic rocks in the area. The increasing HCO_3^- ions in October, representing the dry period, is a result of dissolution of limestone

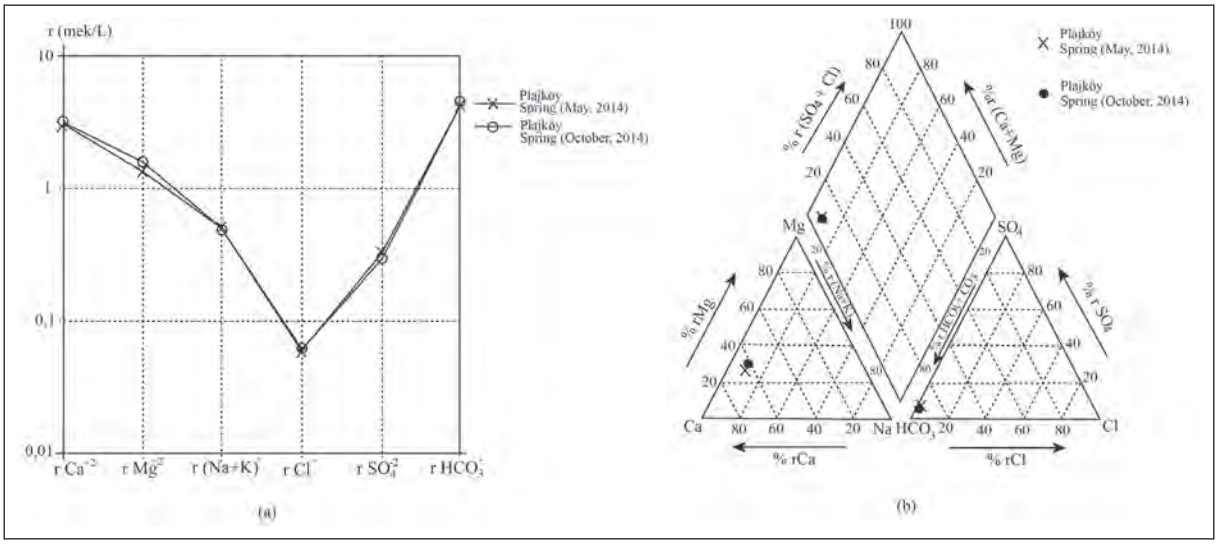

Figure 10- Schoeller (a) and Piper (b) diagrams of Plajköy spring.

outcropping in the region by CO_2-rich groundwater and the hydrolysis of silicate minerals. The source of SO_4^{-2} ions in the spring water is estimated to be $FeSO_4$ formed by oxidation of pyrite (FeS_2). Previous studies have identified pyrite within the Maden Complex (Altunbey and Sağıroğlu, 1995; Yıldırım and Eroğlu, 2015). The source of Cl^- ions in investigated spring water may be related to rainwater. When the water is assessed in terms of pH, electrical conductivity and analyzed ions according to the TS 266 (TSE, 2005) and WHO (2004) drinking water standards, it was determined to be appropriate for drinking (Table 3).

Microbiological analysis of water found no E. coli and coliform bacteria indicating the water is appropriate for drinking. However, the NH_4^+ concentration of the water is very close to the limit value (0.5 mg/L) stated in the TS 266 (2005) drinking water standards showing the water is polluted. The concentration of ammonium (NH_4^+) is considered to be related to the use of animal fertilisers used in garden agriculture by the local people in the settlement areas of Plajköy, Gezinistasyonu Neighbourhood and Kızıltepe within the recharge area of the spring.

2.4. Determination of Plajköy Spring Catchment Plan and Protection Zones

The Plajköy spring area comprises several water outlets in the form of a line. Part of the spring has had a catchment constructed; however this catchment does not have the capacity or features to drain all the water in the spring area. The current catchment only encompasses one point in the spring area, captures a small percentage of the water and was not designed to protect against surface pollutants. There are many frequent leaks over nearly 100 m in the field. A catchment was planned that can collect all springs and leaks within the fault zone.

Beginning from the current catchment in the spring area, two trenches should be opened with an east-west orientation, with width of 80 cm and depth of 1 m in a "V" shape from the spring area and the downstream side toward the manhole. These trenches should be extended to encompass all points of discharge. If the base of these trenches follows the groundwater, a fine pebble layer of rounded pebbles with diameter 0.5-1 cm (nearly 15 cm thick) should be placed in the base, while the downstream side of the trenches should be covered with cement. Porous pipes with appropriate diameter for the total flow of the springs should be placed within the trenches to ensure collection of groundwater within the pipes. The porous pipes should be covered with pebbles and as there is a possibility of surface pollutants that may contaminate the groundwater, a clay or weak cement layer should be laid above the pebble layer to prevent seepage of pollutants (Yüzer et al., 1992; Canik, 1998) (Figure 11 a,b).

Table 3- Limit values for drinking water determined by the Turkish Standards Institute (TS 266, 2005) and the World Health Organisation (WHO, 2004) and Plajköy Spring chemical analysis results (na = no analysis).

Parameters	**Turkish Standards Institude TS 266-200**	**World Health Organization (WHO, 2004)**	**Plajköy Spring (October, 2014)**
pH	6.5 – 9.5	6.5 – 8.5	8.30
Electrical conductivity (µS/cm)	2.500	–	438
Ammonium (mg/l)	0.500	1.500	0.47
Sulphate (mg/l)	250.0	250.0	14.27
Magnesium (mg/l)	50	–	19.33
Sodium (mg/l)	200	200	10.64
Potassium (mg/l)	12	–	1.11
Calcium (mg/l)	200	–	63.93
Chloride (mg/l)	250.0	250.0	2.20
Hardness (Fs°)	–	50.0	24.00
Nitrit e(mg/l)	0.500	–	<0.01
Nitrate (mg/l)	50.0	50.0	1.91
MICROBIOLOGICAL PROPERTIES			
E. Coli	0/100 ml	–	0
Coliform	0/100 ml	–	0

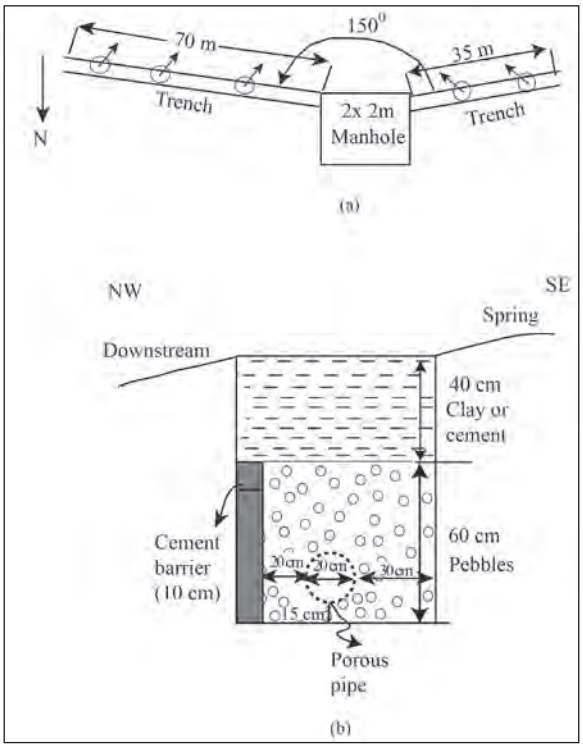

Figure 11- Plan view (a) and section along the trench (b) of the catchment system.

The collection manhole (2x2 m dimensions) should be used to provide water for use through perforations mounted on the downstream wall. To ensure hygienic conditions the inner wall of the catchment should be covered by glass or porcelain material. Excess drainage perforations should definitely be mounted in the upper levels of the perforations to prevent damage to the catchment due to excessive discharges. If the groundwater is to be transported to higher elevations, it is possible to place a pump appropriate to the discharge within the manhole. The discharge level of the spring will be reduced to 0.8 m with this recommended catchment plan, which is estimated to increase yield. Considering the swamp area (leaks) around the old catchment, it is estimated that the discharge from the new catchment will result in a nearly 50% increase.

The declaration published by the General Directorate of State Hydraulic Works about determining the protection zones for aquifers and springs providing drinking water determines the strict protection zone in fields with fractured and fissured aquifers as between 50 and 100 meters around the area of the discharge point of the spring or water drill well in the direction of groundwater flow depending on the properties of the fractured aquifer (Resmi Gazete, 2012). The strict protection zone for Plajköy spring is shown on figure 2 to cover an area with a radius of 100 m. Within the strict protection zone, permission should not be given for any structure, solid or liquid waste discharge or transmission. This area should be expropriated and protected by the authority or authorities using the drinking water with title deeds for the protection area processed and reported to the ministry. The area should be surrounded by barbed wire by the authority using the water.

The first degree protection zone is the region between the limit equal to the distance that the rain water travels from the recharge area at the surface to the discharge point for groundwater percolating through the aquifer in 50 (fifty) days and the strict protection zone (Resmi Gazete, 2012). The first degree protection zone for the fractured aquifer feeding the studied springs is determined by considering the orientations of the fracture systems developed within the recharge area, the flow direction of groundwater and the porosity and permeability values. The second degree protection zone is determined by considering the region from the outer limits of the first degree protection zone to the edge of the recharge area for the spring (Figure 2). Within the recharge area of the Plajköy spring, the domestic waste emptied by local people into the valleys is a potential pollutant for the spring water. It is necessary that this waste is stored in a region to be determined outside the first degree protection zone. Within the first degree protection zone, permission should not be granted for urban development (apart from recreational facilities); air strips and roads; railroads; urban and domestic waste (including solid and fluid waste) storage, production and destruction; cemeteries; mining activities, industrial factories and organised industrial zones; nuclear activities; use and storage of fertilisers and pesticides; fuel storage and transmission facilities e.g., LPG stations; and storage facilities (tailings dams) for solid waste and hazardous waste. Within second degree protection zones, permission should not be given for storage and extraction of material causing water pollution; nuclear activities; metallurgy and petrochemical facilities; and storage facilities (tailings dams) for solid waste and hazardous waste (Resmi Gazete, 2012).

3. Conclusion

Plajköy spring is a low-discharge fault spring in fractured and fissured volcanic, sub-volcanic and blocky volcanosedimentary units belonging to the Maden Complex. In the period when the spring was studied, the recession coefficient was calculated as $1.33*10^{-3}$ day^{-1} with this value indicating laminar flow through narrow fissures, factures and pores. On 31 March 2013 the amount of water storage above the discharge level for the recession period of Plajköy spring was calculated as (V_0) $2.26*10^5$ m^3. The amount of groundwater discharged from the spring during the recession period from 31 March 2013 to the 13 October was calculated as $52*10^3$ m^3. The dominant cation in spring water is Ca^{+2}, with dominant anion HCO_3^- and the water is Ca- Mg- HCO_3 type. The chemical and microbiological analyses of the spring water were determined as being appropriate for drinking when assessed according to drinking water standards.

Gaining great importance due to the increasing population especially in the summer months, the proposed catchment system for Plajköy spring is estimated to increase the yield by nearly 50%. Additionally, the spring protection zones determined for this catchment area within this study will ensure the sustainability of groundwater quality at high risk of being affected by surface pollutants.

Acknowledgements

This study was completed as part of projects MF.12.28 and MF.11.43 supported by Fırat University. Additionally the authors wish to thank the reviewers for their contributions to the manuscript.

References

Ako, A.A., Shimada, j., Hosono, T., Ichiyanga, K., Nkeng, G,E., Fantong, W.Y., Eyong, G.E.T., Roger, N.N. 2011. Evaluation of groundwater quality and its suitability for drinking, domestic, and agricultural uses in the Banana Plain (Mbanga, Njombe, Penja) of the Cameroon volcanic line. Environ Geochem Health, DOI: 10.007/s 10653-010-9371-1.

Aksoy, E., İnceöz, M., Koçyiğit, A. 2007. Lake Hazar Basin: A negative flower structure on the East Anatolian Fault System (EAFS), SE Turkey. Turkish J Earth Sci, 16: 319- 338.

Aktaş, G., Robertson, A.H.Y. 1984. The Maden Complex, SE Turkey: Evolution of a Neotethyan active margin, In: J. E. Dixon ve A.H.F. Robertson (Eds.), Geo. Soc. Spec. Publ. No: 17, 375- 403.

Altunbey, M., Sağıroğlu, A. 1995. Koçkale- Elazığ manganez cevherleşmelerinin özellikleri ve kökeni. Maden Tetkik ve Arama Dergisi, 117, 139-148.

Azeez, N.H., West, L.J., Bottrell, S.H. 2015. Numerical simulation of spring hydrograph recession curves for evaluating behavior of the East Yorkshire Chalk Aquifer. Proceedings of the 14th sinkhole conference, National Cave and Karst Research Institute.

Boughton, C.J., McCoy, K.J. 2006. Hydrogeology, aquifer chemistry and groundwater quality in Morgan county, West Virginia. Scientific investigations report 2006-5198, U.S. Geological survey, Reston, Virginia.

Canik, B. 1998. Hidrojeoloji, yeraltı sularının aranması, işletilmesi, kimyası. Ankara Üniversitesi Fen Fakültesi, 286 s. Ankara.

Çelik, H. 2008. Doğu Anadolu Fay Sistemi'nde Sivrice Fay Zonu'nun Palu-Hazar Gölü (Elazığ) arasındaki bölümünde atımla ilgili yeni arazi bulgusu. Fırat Üniv. Fen ve Müh. Bil. Dergisi, 20 (2), 305-314.

Çetindağ, B. 2002. Dipsiz Göl (Elazığ) Kaynağı'nın hidrojeoloji incelemesi, Fırat Üniversitesi Fen ve Mühendislik Bilimleri Dergisi, 14 (1), 169- 180.

Çetindağ, B., Öztekin, Ö. 2001. Haroğlu (Elazığ) Kaynağı'nın hidrojeoloji incelemesi, Geosound/ Yerbilimleri, 38, 153-162.

Coutagne, A. 1968. Les variations de debit en periode non influencee par les precipitations. La Houille Blanche, 416- 436.

Diedrisch, M. S., Hoek, E. 1989. DIPS: A computer program for stereographic net (ver. 2.2, Advanced vertion). rock engineering group, Department of Civil Engineering, University of Toronto, Kanada.

Ebrahimi, B., Pasandi, M., Ahmadipour, M.R. 2007. Hydrodynamic behaviour of karstic aquifers in Boroujerd, Western Iran. Hydrological Sciences Journal, 52 (1).

Farlin, J., Maloszewski, P. 2013. On the use of spring baseflow recession for a more accurate parameterization of aquifer transit time distribution functions. Hydrol. Earth Syst. Sci., 17, 1825- 1831.

Fiorillo, F. 2011, Tank-reservoir drainage as a simulation of recession limb of karst spring hydrographs. Hydrogeology Journal, v. 19, p. 1009–1019.

Fiorillo, F., Revellino, P., Ventafridda, G. 2012. Karst aquifer draining during dry periods. Journal of Cave and Karst Studies, v. 74, no. 2.

Garrels, R.M., Christ, C.L. 1965. Solutions, minerals and equilibria: San Francisco, Calif., Freeman, Cooper & company, p.379-402.

Güler, C., Thyne, G.D., Tağa, H., Yıldırım, Ü. 2017. Processes governing alkaline groundwater chemistry within a fractured rock (ophiolitic melange) aquifer underlying a seasonally inhabited headwater area in the Aladağlar range (Adana, Turkey). Geofluids (in print).

Gürocak, Z. 1993. Sivrice (Elazığ) çevresinin jeolojisi. Fırat Üniversitesi Fen Bilimleri Enstitüsü, Yüksek Lisans Tezi, 65 s, Elazığ.

Güven, A. 2013. Hazar Gölü (Elazığ) çevresindeki alüvyon akiferlerinin hidrojeoloji incelemesi. Fırat Üniversitesi Fen Bilimleri Enstitüsü, Yüksek Lisans Tezi, 76 s, Elazığ.

Kaya, A. 1992. Gezin – Maden (Elazığ) çevresinde jeolojik araştırmalar. Fırat Üniversitesi Fen Bilimleri Enstitüsü, Yüksek Lisans Tezi, 72 s, Elazığ.

Kaya, A. 2004. Gezin (Maden- Elazığ) çevresinin jeolojisi. Pamukkale Üniversitesi Mühendislik Bilimleri Dergisi, 10 (1), 41-50.

Kebede, S., Travi, Y., Alemayehu, T., Ayenew, T. 2005. Groundwater recharge, circulation and geochemical evolution in the source region of the Blue Nile river, Ethiopia. Applied Geochemistry, 20, 1658-1676.

Kimball, B.A. 1981. Geochemistry of spring water, Southeastern Uinta Basin, Utah and Colorado (Geological survey water-supply paper 2074). U.S. Government printing office, Washington.

Kovacs, A., Perrochet, P. 2008. A quantitative approach to spring hydrograph decomposition. Journal of Hydrology, 352, 1-2, 16-29.

Kovacs, A., Perrochet, P., Kiraly, L., Jeannin, P.Y. 2005. A quantitative method for the characterization of karst aquifers based on spring hydrograph analysis. Journal of Hydrology, 303, 152–164.

Liu, L., Li, X. 2012. A Laboratory study of spring hydrograph in karst triple void media, southwestern China. Civil Engineering and Urban Planning 2012, 6-11.

Maillet, E. 1905. Essais d'hydrolique souterraine et fluviale. Libreirie scientifique, A. Hermann, 218, Paris.

Mangin, A. 1975. Contribution a` l'e´tude hydrodynamique des aquife´res karstiques: Troisieme partie: constitution et fonctionnement des aquife`res karstiques: Annales de Spe´le´ologie, v. 30, no. 1, p. 21–124.

Milanovic, P.T. 1981. Karst Hydrogeology. Water resources publications, P.O. Box 2841, Littleton, Colorado, Amerika Birleşik Devletleri.

Padilla, A., Pulido-Bosch, A., Mangin, A. 1994. Relative importance of baseflow and quickflow from hydrographs of karst spring, Ground Water, 32, 267–277.

Parkhurst D. L., Appelo C.A.J. 1999. Phreeqc (Version 2), A computer program for speciation, batch-reaction, one-dimensional transport, and inverse geochemical calculations. U.S. Geological Survey Water Resources Investigation.

Perinçek, D. 1979. The geology of Hazro- Korudağ- Çüngüş- Maden- Ergani- Hazar- Elazığ- Malatya region. Guide book, Geol. Soc. of Turkey, Spec. Publ., 33.

Resmi Gazete, Tarih 10 Ekim 2012, Sayı 28437.

Schoeller, H. 1962**.** Les Eaux sutterraines, Masson et cie, 67, Paris.

Schoeller, H. 1967. Hydrodynamique dans le karst (E'coulement et emmagasinement). Chronique d'hydrogeologie No:10, 5-20, Paris.

Smart, P. L., Hobbs, S.L. 1986. Characterization of carbonate aquifers: A conceptual base. In Environmental Problems in Karst Terrain and Their Solutions, 1-14, Dublin, Ohio: National Water Well Association.

TSE, 2005. TS266, Türk İçme Suyu Standartları, Türk Standartları Enstitüsü, Ankara.

Tuna, E., Dülger, S. 1979. Elazığ- Palu- Pertek bölgesinin jeolojisi. TPAO Arşivi, Rapor No: 1363 (unpublished).

Turkish Statistical Institute, 2014. Türkiye İstatistik Kurumu Haber Bülteni, Sayı: 18779.

WHO, 2004. World Health Organization, 2004. Guidelines for drinking-water quality. Vol. 1.

Yıldırım, N., Eroğlu, M. 2015. Maden Karmaşığına ait dasitik kayaçlarla ilişkili hidrotermal tip bakır cevherleşmelerine Güneydoğu Anadolu'dan bir örnek (Yukarı Şeyhler, Diyarbakır). MTA Doğal Kaynaklar ve Ekonomi Bülteni, 19, 31-42.

Yüzer, E., Öztaş, T., Mutlu, O. 1992**.** İstanbul-Taşdelen ve Karakulak kaynak sularının hidrojeolojisi ve kaptaj sorunlarına çözüm önerileri. Jeoloji Mühendisliği Dergisi, 41, 51-62.

Bull. Min. Res. Exp. (2018) 156: 237-246

Bulletin of the Mineral Research and Exploration

http://bulletin.mta.gov.tr

Characterization and dewatering of borax clayey tailings by mono- and dual-flocculants systems

Nuray KARAPINAR[a]*

[a]*General Directorate of Mineral Research and Exploration Department of Environmental Research Ankara. orcid.org/0000-0001-8098-721X*

Research Article

Keywords:
Borax, beneficiation, tailings, dewatering, flocculation.

ABSTRACT

This study includes dewatering of Kırka Borax Concentrator tailings by flocculation with mono- and dual-flocculants systems. Four polyacrylamide (PAM)-typed anionic and a poly diallyl-dimethyl-ammonium chloride (PolyDADMAC)-typed cationic polymers were used as flocculants in mono- and dual-flocculants systems to flocculate tailings. Tailings slurry sample used in the experiments were taken from the discharge point of Kırka Borax Concentrator. Prior to the flocculation tests, physical, chemical and mineralogical analysis were carried out to characterize the tailings slurry. Results reveal that while tailings solid consists mainly of dolomite and montmorillonite with some unrecoverable boron mineral fines and very minor amount of calcite and quartz, tailings water is typical with the content of quite high dissolved carbonate and borax with a pH of 9.4. Flocculation tests were performed in one liter graduated cylinder at inherent pH of the tailings slurry sample. Settling rate and turbidity of overflow was measured as important factors for evaluating the flocculation performance of different flocculants. The tailings slurry as received showed a very low settling behavior due to the clay content and high percentage of fine particles. Flocculation of tailings with anionic flocculants accelerated the settling rate of particles without providing a clear supernatant. But, dual-flocculants system, in which anionic and cationic type polymeric flocculants were used, was able to provide a clear supernatant at relatively higher settling rates.

Received Date: 08.02.2017
Accepted Date: 14.09.2017

1. Introduction

Tailings, a kind of mining waste, are the fine grained residue of the mineral processing plant in which the desired raw materials are separated from the gang minerals and appear as slurries due to mixing with water during processing. The disposal of these tailings has been a major issue in many mines and generally a public relations challenge for the mining industry. The traditional method of disposing of the tailings is to use a tailings pond and a dam. However, from the environmental point of view, thickening tailings disposal system has been accepted as a more effective method (Newman et al., 2001); the removal of water not only can create a better storage system but can also assist in water recovery which is major issue as many mines where the water is scarce.

Borate deposit in Kırka is known as the largest Na-Borate deposit in the World. The deposit contains primarily borax, with only secondary colemanite and ulexite and minor amounts of hydroboracite, inderite, inyoite, kurnakovite, meyerhofferite, tincalconite, and tunellite (Garrett, 1998). Borate layers in the deposit, containing minor amounts of celestite, calcite, and dolomite, are interlayered with clay horizons containing some volcanic tuff (frequently altered to zeolites), quartz, biotite, and feldspar. The clay rock is mainly consists of smectite type swelling clay and dolomite minerals in varying proportions, having a range of colors from very pale green to white (Helvacı, 2015).

The run-of-mine ore, having an average grade of 25% B_2O_3 and containing high amounts of insoluble impurities, is processed in the Kırka Concentrator to

* *Corresponding author: Nuray KARAPINAR, nuray.karapinar@mta.gov.tr*
http://dx.doi.org/10.19111/bulletinofmre.336392

produce a borax concentrate of 32–34% B_2O_3. The beneficiation process is comprised of washing the crushed and scrubbed ore at ambient temperature to remove gangue minerals which generate borax saturated tailings slurry containing 8-10 % clay-sized particles. The tailings solid is mixture of clay minerals, dolomite and of fewer amounts of other finely divided gang minerals as well as considerable amount of borax (Garrett, 1998). This tailings slurry is directly sent to the tailing ponds by gravity for natural settling without any treatment. Although, process water is further collected and re-used in the beneficiation process, a large amount of water and large areas of land are tied up by impounding these clayey tailings for a long period of time. This situation causes serious technical and environmental problems in terms of the need for additional ponds and the challenges for the closure and rehabilitation of the tailings ponds. Therefore, an effective tailings disposal method is necessary for the borax clayey tailings regarding to both environmental and technical point of view. In this regard, surface disposition of tailings in paste form has been accepted as a new disposal method for minimizing the engineering and environmental challenges associated with the tailings disposal (Karapınar, 2009). Paste is simply dewatered/thickened tailings with little or no water bleed that has non-segregating nature (Robinsky, 1999; Newman et al., 2001; Verbung, 2001). Thickened tailings disposal involves taking the process tailings, thickening it (and simultaneously dewatering) with a high-rate or paste thickener, then pumping it to the disposal site. Unlike conventional thickener, those thickeners produce a thickened underflow in the form of paste rather than slurry and could be disposed of by surface stacking instead of impounding. Regardless of the type of the thickener employed, flocculation process is a compulsory pretreatment step in dewatering of the fine and colloidal suspensions and it involves destabilization of fine/colloidal particle dispersions by addition of a flocculants either natural or synthetic having a wide range of molecular weights and ionic characters. Depending on the flocculant types and suspension characteristics, the flocculation process may occur by one or a combination of mechanism, namely: polymer bridging, charge compensation or neutralization, polymer-particle surface complex formation and depletion flocculation (Gregory 1985, 1987).

There are few studies on understanding the flocculation behavior of borax clay tailings, carried out both on the actual plant tailings (Sabah and Yeşilkaya, 2000) and on the synthetic dispersions prepared in laboratory by using clayey materials obtained from the deposit (Gür et al., 1994,1996; Hoşten and Çırak 2013; Çırak and Hoşten, 2012, 2015). These include comparative studies between Polyacrylamide (PAM) and Polyethylene Oxide (PEO) typed flocculants, i.e. conventional and non-conventional (3-D branched structure) PAM-typed anionic flocculants, PAM- and PEO-typed non- ionic flocculants. It was reported that the nonionic PEO performed better than the PAM-typed flocculants in reducing the supernatant turbidity (Gür et al., 1994;1996; Hoşten and Çırak 2013; Çırak and Hoşten, 2012; 2015). Sabah and Yeşilkaya (2000) reported that the PAM-typed anionic flocculants performed much better than PAM typed non-ionic flocculant in terms of the settling rate, but still at quite a high flocculant consumption of 1176 g/ton solids and the use of coagulants together with an anionic flocculant did not improve the flocculation efficiency.

Apart from above studies, Taşpınar and Çalışan (nd) studied the flocculation and filtration behavior of four different colored clay minerals supplied from Kırka borax deposit by using four different types of surfactants (non-ionic, anionic, cationic, amphoteric) and a non-ionic PAM-typed flocculant. They reported that surfactants used together with flocculant result in a decrease in flocculation efficiency in terms of turbidity and its effect is varied with the composition of the clay material in terms of its montmorillonite and dolomite content. Çebi et al. (1994) studied the dewatering of the concentrator and Borax Rafinery Plant tailings by centrifuge decanter. They reported that flocculant addition is needed for the mechanical dewatering even when the centrifuge decanter is used to enhance solid-liquid separation.

In this study, laboratory flocculation experiments were carried out with the aim of the defining the effective flocculant(s) for the dewatering of Kırka Borax Concentrator tailings either in mono- flocculant system with PAM-typed anionic flocculant and dual-flocculants system with PAM- typed anionic and poly diallyl-dimethyl-ammonium chloride (polyDADMAC)-typed cationic flocculants.

2. Materials and Methods

Tailings slurry sample (60 L) used in the experiments were taken from the discharge point of Etibor Kırka Borax Concentrator. Tailings characterization studies were carried out both in terms of tailings solids and water. For analysis, 1 L

representative sample was filtered and both solid and liquid phases were analyzed. The mineral composition of the tailings was determined by X-Ray diffraction analysis. The chemical composition of the tailing solid was analyzed by X-ray fluorescence (XRF) spectrometer. The boron content of the tailings solids was only determined by volumetric analysis. Tailings water was analyzed for cations by ICP-MS. Titration method was used for the determination of carbonate content of the tailings water. Particle size analysis was carried out by wet sieving technique. Solid content of tailings slurry was determined.

The flocculation tests were performed in one liter graduated cylinder with 900 ml slurry in mono-flocculant and 800 ml slurry in dual-flocculants system. The tests were done at inherent pH of the sample which was about 9.4. Stock solutions of anionic and cationic focculants were prepared in the concentration of 0.2 (w/v) and 2 % (v/v), respectively. The stock solutions were used within 7 days of preparation. A fresh daily working diluted anionic and cationic flocculant solutions were used and added by pouring into slurry as 100 ml solution of each. In mono-flocculant tests, immediately after the addition of the flocculant, the cylinder was shaken and stirred by five upside down for good mixing. The flocculated slurry was then left for settling for 24 hours. In dual-flocculants tests, a desired amount of anionic floculant solution was first added to the slurry. After the shaking, cationic flocculant was added and the slurry was shaken by additional five upside down, and finally left for settling. At appropriate time intervals, mud height was measured. Four PAM-typed commercial anionic flocculants (Hengfloc 64014, Hydrofloc 9180 LV, Magnofloc 336, Magnofloc 1011) and one PolyDADMAC-typed cationic flocculant (Hydrofloc CPX 400) were used in flocculation experiments (Table 1).

Settling rate and turbidity of overflow were measured as important factors for evaluating the flocculation performance of different flocculants. Following a 5 min of settling period, a 20 ml sample of the supernatant was withdrawn from the suspension depth of 3 cm with the help of glass pipette and its turbidity as percent of transmittance was measured using a UV spectrophotometer at the wavelength of 675 nm. The initial settling rate of the flocculated slurry in the 1000 cm^3 cylinder was determined by recording the time taken for the "mud line" (solid-liquid interface) to pass between the 900 and 735 cm^3 marks (5 cm of distance in free settling zone). All tests were done under ambient conditions at 22.0 ±0.1 °C.

3. Results and Discussion

3.1. Characterization of Tailings

Mineralogical analysis showed that tailings solid mainly consists of dolomite, montmorillonite and boron minerals and minor amount of calcite and quartz (Figure 1). Chemical composition of tailings solid as well as the tailings water was given in table 2 and table 3.

Tailings water contains high amount of dissolved Na and boron (Table 2) due to the solubility of borax in water even at ambient temperature. Measured pH of

Table 2- Chemical composition of the tailings solid.

Component	%
SiO_2	19,4
Al_2O_3	1,4
Fe_2O_3	0,4
CaO	17,2
MgO	14,7
Na_2O	5,9
K_2O	0,9
TiO_2	0,1
B_2O_3	12,6
LoI	28,97

Table 1- Characteristics of flocculants used*

Commercial name	Type	Charge density	Molecular weight
Hengfloc 64014	Anionic (PAM)	medium/high	medium
Hydrofloc 9180 LV	Anionic (PAM)	medium/high	high
Magnofloc 1011	Anionic (PAM)	low	high/very high
Magnofloc 336	Anionic (PAM)	medium	high/very high
Hydrofloc CPX 400	Cationic (PDADMAC)	**	low

*obtained from the supplier **no information provided

Table 3- Chemical composition of tailings water.

Component	Tailings water, ppm
B_T	2234
Na	5760
Ca	2,5
Mg	5,78
K	176
Fe_T	<0.3
CO_3^{-2}	4650
HCO_3^-	4453

T: total

the tailings is about 9.4. It is known that the dissolved borax buffers the suspensions at about pH 9.3 at which borax has minimum solubility (Hançer et al., 1993). Therefore, the tailings slurry discharged from the borax concentrator contains both dissolved and solid boron, as saturated with the borax. In addition to borax dissolution, high amount of dissolved carbonate and bicarbonate of tailings water revealed that the carbonate minerals such as dolomite and calcite are dissolved in buffered borax solution. Therefore, carbonate and bicarbonate ions in tailings water will contribute to the buffering capacity of the tailings water (Stumm and Morgan, 1996). However, when compared with carbonate content of the tailings water, concentration of dissolved Ca and Mg ions is rather low. This is probably the result of largely due to the precipitation of Ca and Mg boron and /or carbonate compounds rather than due to the removal of cations by clay particles via adsorption/ion exchange. Indeed, XRD pattern of the tailings solid indicates the sign of the existence of amorphous compound confirming the precipitation of Ca and Mg compounds in the slurry. Similarly, Sarı (2008) showed that cations released from the dissolution of dolomite and calcite in boric acid solutions may cause the loss of boron by post precipitation borates compounds. In fact, the ratio of boron to sodium of tailings water (0.4) is smaller than its theoretical ratio of borax solid (0.95), indicating the dissolved boron loss from the tailings water.

Chemical analysis result showed that the tailings water contains a variety of dissolved ions due to the dissolution of carbonate and boron minerals and the release from clay mineral particles in solution, leads to alkaline water as well as with high ion content.

The percent solid by weight of the tailings slurry sample was determined as 10.5 % (w/v). Particle

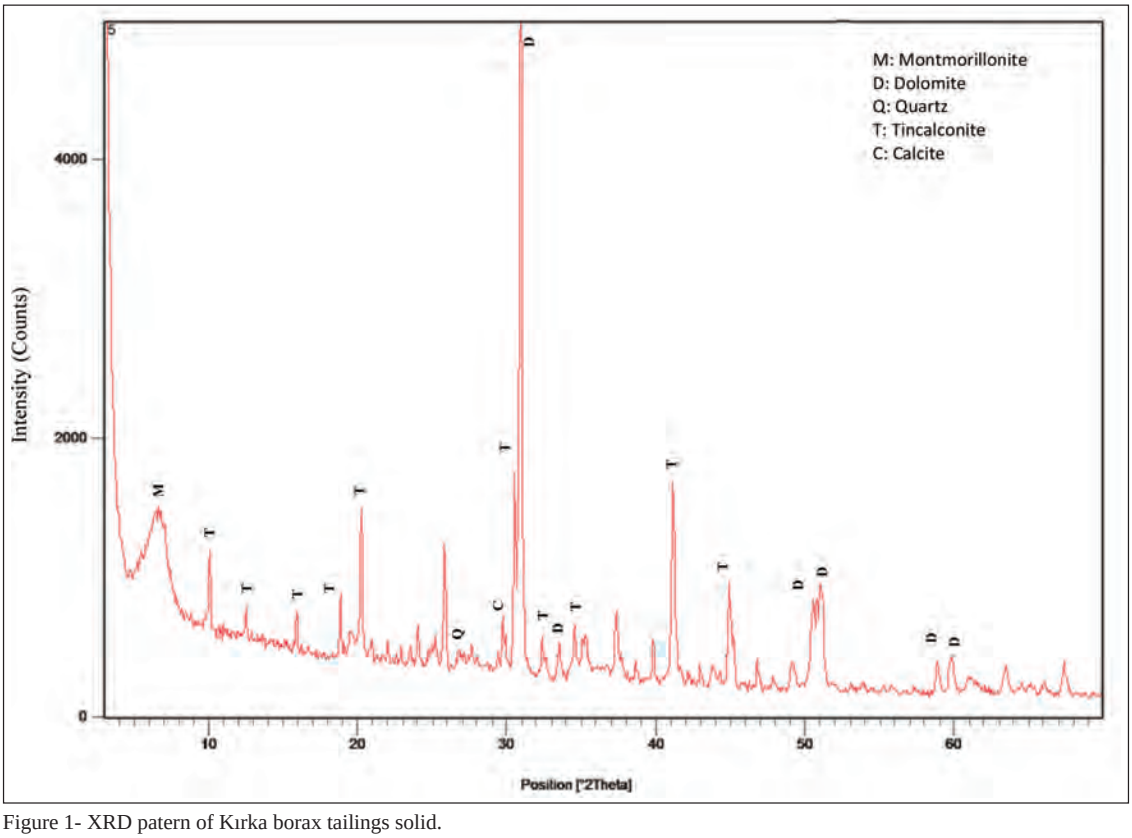

Figure 1- XRD patern of Kırka borax tailings solid.

size analysis of tailings solid showed that 76% of the solid is below 38 μm and about 13.51 % of it is above 100 μm. The percentage of slime size (< 20 μm) determined from the Gaudin-Schuhman type of plot constitutes about 71.22 % of the overall material which has trouble in solid liquid separation.

3.2. Flocculation Tests

Measured pH of the tailings slurry is around 9.4 at which dissolved borax buffered the suspension. Due to the obstacles such as addition of large amount of chemicals to modify the buffered pH of the tailings slurry, flocculation test were performed at the inherent pH of the tailings slurry. Any flocculants having good performance at this pH value could be the best flocculant(s) for the flocculation of borax concentrator tailings.

Since the tailings slurry without flocculant addition settles very slowly, having a settling rate of 0.0013 cm/min (Karapınar, 2016), the effects of different anionic flocculants on tailings settling rate were investigated in the range of 25-40 ppm and the results were given in figure 2-6.

These results reveal that Hengfloc 64014 and Hydrofloc 9180 LV exhibited better flocculation

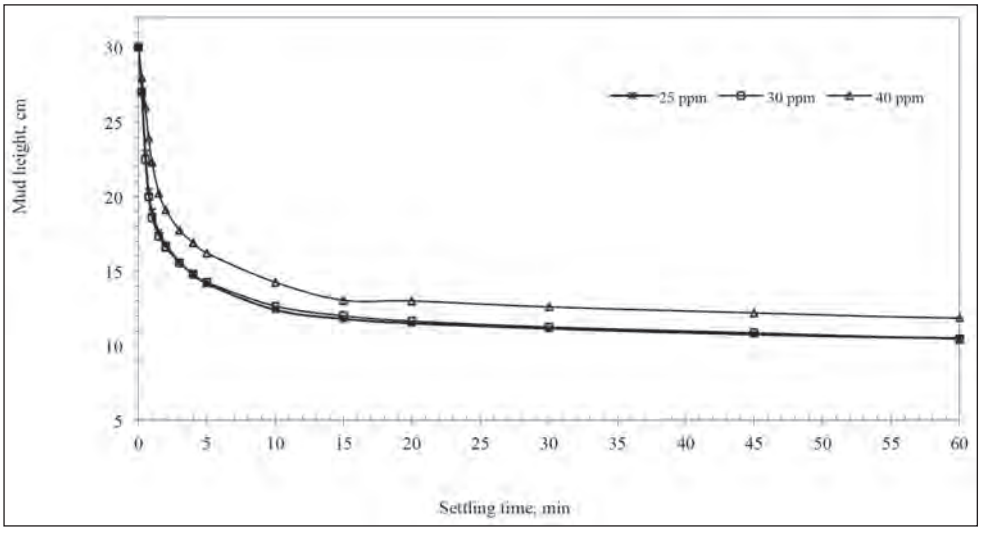

Figure 2- Settling behavior of tailings slurry flocculated by anionic flocculant Hengfloc 64014.

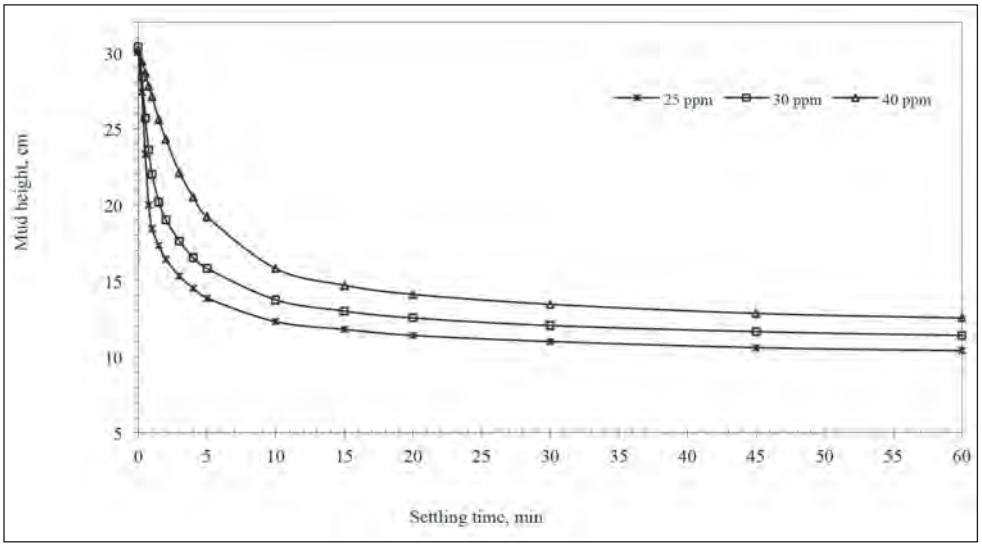

Figure 3- Settling behavior of tailings slurry flocculated by anionic flocculant Hydrofloc 9180 LV.

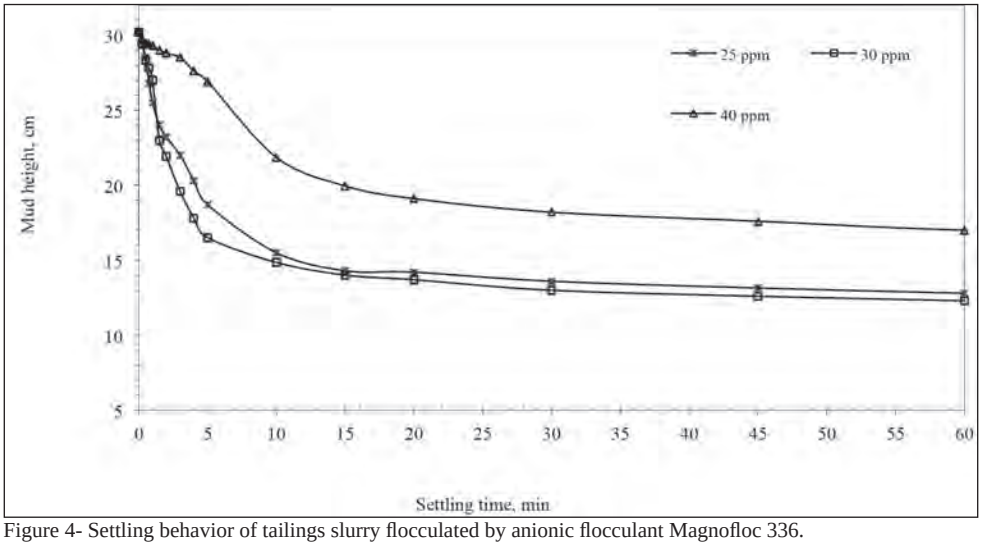

Figure 4- Settling behavior of tailings slurry flocculated by anionic flocculant Magnofloc 336.

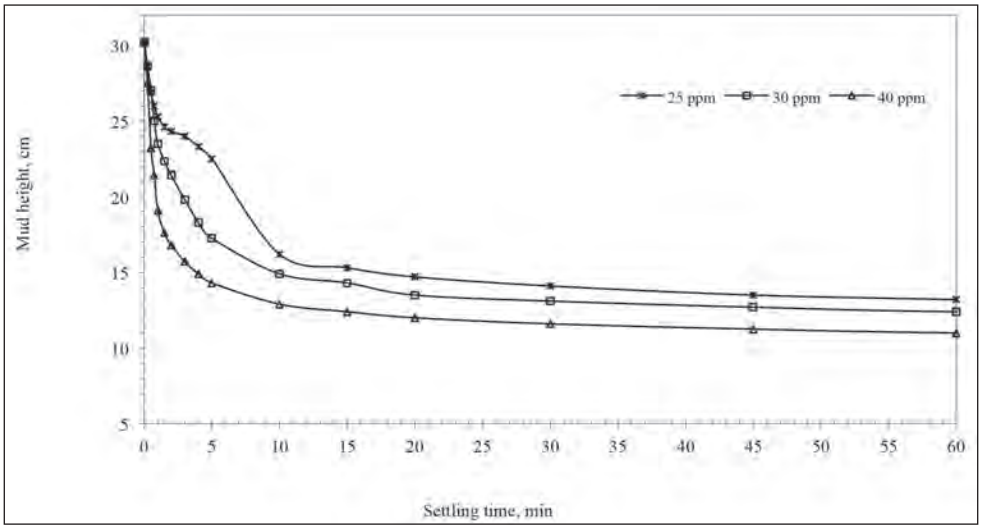

Figure 5- Settling behavior of tailings slurry flocculated by anionic flocculant Magnofloc 1011.

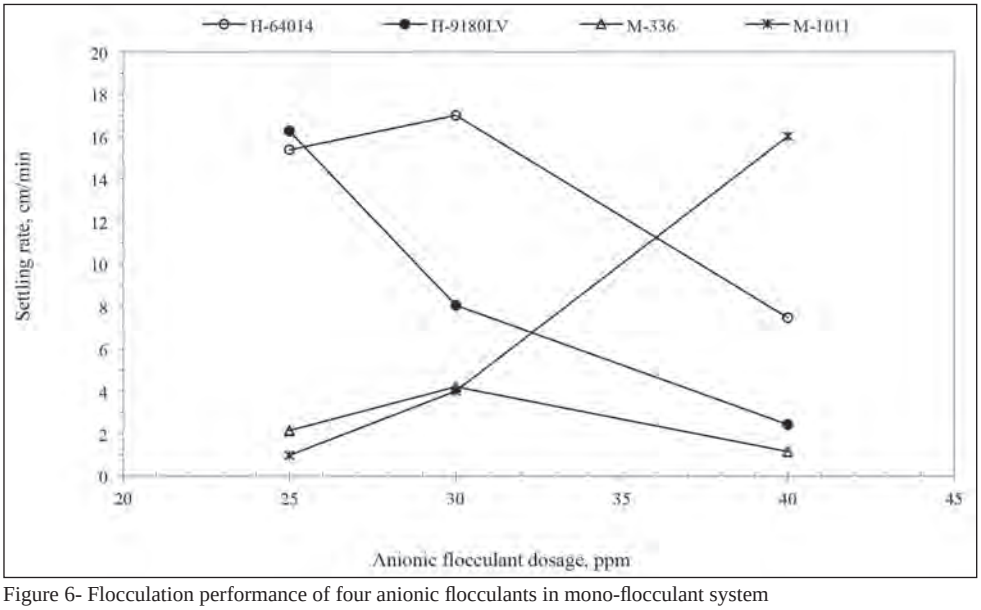

Figure 6- Flocculation performance of four anionic flocculants in mono-flocculant system

performance than other two anionic flocculants in terms of settling rate. Regarding the settling rate, optimum flocculant dosages was 30 ppm for Hengfloc 64014 and Magnofloc 336. However, an increase in dosage of Hydrofloc 9180 LV leads to a descending path in settling rate. On the contrary, Magnofloc 1011 exhibit an ascending trend of settling rate with the increasing of dosage. Therefore, Hydrofloc 9180 LV and Magnofloc 1011 showed their best performance at 25 ppm and 40 ppm of flocculant dosages, respectively.

At 25 ppm flocculant dosage, flocculation performance of both Hengfloc 64014 and Hydrofloc 9180 LV and both Magnofloc 336 and Magnofloc 1011 were very close to each other, respectively. At 30 ppm flocculant dosage, flocculation performance of different flocculants decreases in following order: Hengfloc 64014>Hydrofloc 9180 LV>Magnofloc 336=Magnofloc 1011.

A summary of results presented in figure 3-6 illustrates the fact that an increase in molecular weight of the polymer with a certain anionicity causes the flocculation performance to be reduced dramatically in terms of settling rate. However, decreasing of polymer anionicty from medium to low with high/very high molecular weight leads to an increase in dosage to be obtained same degree of settling rate with polymers having medium anionicity and medium/high molecular weight.

Although, high settling rates were obtained, the effectiveness of anionic flocculants studied in providing a clear supernatant was very poor. The turbidity of supernatant was too high to be measured, suggesting that a significant amount of the fine fraction of the slurry lags behind the settling mass and remains suspended. Furthermore, the supernatant was so turbid that a second solid/liquid interface was occurred in the supernatant after a period of time.

Lower flocculation efficiency of borax clayey tailings has been attributed to both the week flocculation behavior of dolomite (Moudgil and Behl, 1993; Gür et al, 1994; Moudgil et al., 1995; Akdeniz et al., 2003; Hoşten and Çırak, 2013) and clay being Mg-rich trioctahedral clay (Çırak and Hoşten, 2015). Both mineral are Mg- rich minerals and develop Mg-enriched surfaces. Çırak and Hoşten (2015) have claimed that due to its strong hydration property of Mg-surfaces, flocculant adsorption may be hindered as well as the particle-particle interaction. Another reason for the weak flocculation behavior of borax clayey tailings has been explained by the possible lack of isolated hydroxyl group on dolomite surfaces which are vital for the particle-polymer interaction (Çırak and Hoşten, 2015).

Infact, for Kırka borax clayey tailings slurry in which mainly dolomite, montmorillonite and borax exist, dissolution, adsorption and cation exchange would be dominant mechanisms governing the flocculation of the suspension. Whilst the dissolution of borax even at ambient temperatures releases boron and sodium ions into the solution, dissolution of carbonate minerals in borax solution releases Ca and Mg ions into solution as well. There is also exchange cations released into solution from clay minerals. Previous studies shows that boron and magnesium adsorption onto clay surfaces deteriorate flocculation (Sabah and Yeşilkaya, 2000; Hoşten and Çırak, 2013) whereas sodium and calcium adsorption enhance the flocculation (Gür et al., 1994; Çırak and Hoşten, 2015). In addition to cations and boron anions, dissolved carbonate may govern the flocculation by affecting dissolution of carbonates, surface charge of the particles, configuration of the polymer in water and hence flocculant adsorption.

Results showed that the desired supernatant clarity was not able to be obtained by using anionic flocculant only. Therefore, oppositely charged dual-flocculants combinations were tested to enhance the performance of mono- flocculant system. The aim was to obtain more effective solid-liquid separation in terms of settling rate and overflow clarity. Hengfloc 64014 and Hydrofloc 9180 LV was chosen as an anionic flocculant in combination with PolyDADMAC- typed cationic flocculant (Hydrofloc CPX 400) for further studies in dual-flocculants tests. The amount of anionic flocculant used in dual-flocculants system was kept as 30 ppm.

The settling behavior of tailings slurry flocculated by anionic and cationic flocculants combinations are given in figure 7-8. Any amount of cationic flocculant addition resulted in an improvement of the supernatant clarity at the expense of settling rate. Flocculation performance was greatly diminished at the excess amount of cationic flocculant dosages particularly in terms of settling rate. Taking into consideration of the measured transmittance value of process water (81.7 % T), the required amount of cationic flocculant to obtain the desired turbidity level is as minimum as 60 ppm in dual-flocculants system.

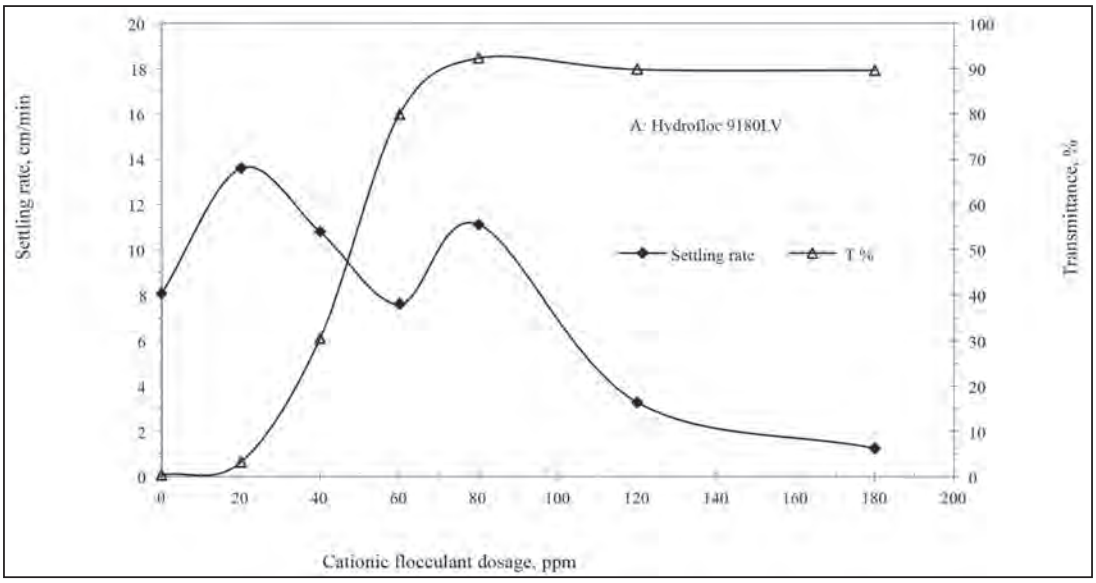

Figure 7- Effects of cationic flocculant (hydrofloc CPX 400) on borax tailings settling rate and supernatant quality in dual-flocculants system (Hydrofloc 9180 LV=30 ppm).

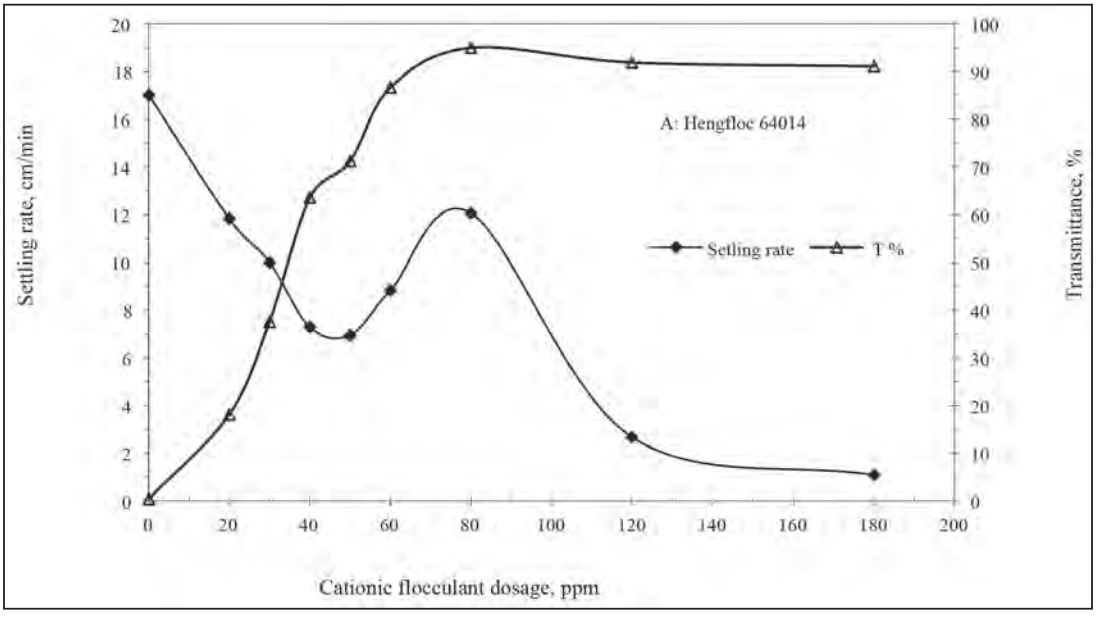

Figure 8- Effects of cationic flocculant (Hydrofloc CPX 400) on borax tailings settling rate and supernatant quality in dual-flocculants system (Hengfloc 64014=30 ppm)

4. Conclusions

Characterization of borax concentrator tailings indicates that tailings solid mainly consists of dolomite, montmorillonite and some unrecoverable boron minerals. Over 75% of tailings solid are finer than 38 μm and tailings water has a high ionic strength due to the dissolution of dolomite and borax in solution and buffered with the borax as well as carbonate. Therefore, flocculation behavior of colloidal dolomite and clay mineral particles in alkaline water at natural pH of the slurry (about pH=9.4) define the flocculation characteristics of borax tailings slurry.

In mono-flocculant tests, amongst flocculants studied, Hengfloc 64014 and Hydrofloc 9180 LV showed better similar flocculation ability than the other two flocculants. At 30 ppm flocculant dosage,

flocculation performance of different flocculants decreases to following order: Hengfloc 64014 > Hydrofloc 9180 LV > Magnofloc 336=Magnofloc 1011. In the studied range of flocculant dosages, it was not possible to obtained clear supernatant only with the use of anionic flocculants. However, any improvement in supernatant clarity was only obtained by using dual-flocculants system in which combination of anionic (PAM-typed) and cationic (polyDADMAC-typed) flocculants are used.

When compared the mono-flocculant system, a reduction in settling rate was observed but a major improvement in supernatant clarity was obtained. In dual-flocculants tests, optimum results were obtained by anionic and cationic flocculant combination at around 25-30 ppm and 60-80 ppm, respectively, indicating about 10.0 cm/min of settling rate and over 80.0 % of transmittance value.

It can be concluded that dual-flocculants combination in which PAM-typed anionic and PolyDADMAC-typed cationic polymers used is playing a favorable role in the flocculation of borax clayey tailings. But, in addition to flocculation tests for selecting correct polymer(s), a follow-up study is needed to test the obtaining of underflow paste product both at laboratory and on-site testing in order to decide thickener type and size.

References

Akdeniz, Y., Özmıhçı, F., Duvarcı, Ç.Ö., Balköse, D., Ülkü, S. 2003. Characterization of colloidal phase in hot aqueous solutions of Kırka tincalconite mineral. XI. National Clay, 3-6 September 2003. İzmir, 603-613.

Çebi, H., Yersel E., Poslu K., Behar A., Nesner R., Laangenbrick R.N. 1994. Solid-liquid separation of Etibank kırka Borax Plant effluents by centrifugal decanter, in: H. Demirel, S. Sayin (Eds.), Progress in Mineral Processing Technology, A.A. Balkema, Rotterdam, 513-516.

Çırak, M., Hoşten, Ç. 2012. Preliminary flocculation study of two different clay suspensions in borax solution, proceedings of the 15th national clay Symposium of Turkey 2012. 261-271.

Çırak, M., Hoşten, Ç. 2015. Characterization of clay rock samples of a borax ore in relation to their problematical flocculation behavior. Powder Technology, 284, 452-458.

Garrett, D.E. 1998. Borates: Handbook of Deposits, Processing, Properties and Use, *Academic Press*, San Diego, 1998.

Gregory, J. 1985. The use of polymeric flocculants. In: Proceedings of the Engineering Foundation Conference on Flocculation, Sedimentation and Consolidation, The Clister Sea Island, Georgia, USA, 125–137.

Gregory, J. 1987. Flocculation by polymers and polyelectrolytes. In: Tadros, Th.F. (Ed.), Solid/liquid Dispersions. Academic Press, London, 163–181.

Gür, G., Türkay, S., Bulutçu, A.N. 1994. The effects of the process conditions on the flocculation of tincal slimes, in: H. Demirel, S. Sayin (Eds.), Progress in Mineral Processing Technology, A.A. Balkema, Rotterdam, 501–503.

Gür, G., Türkay, S., Bulutçu, A.N. 1996. Comparison of polyethylene oxide and polyacrylamides as flocculating agent for the flocculation of tincal slimes, in: M. Kemal, et al., (Eds.), Changing Scopes in Mineral Processing, A.A. Balkema, Rotterdam, 649–653.

Hançer, M., Kaytaz Y., Çelik, M.S. 1993. Flotation of borax with anionic and cationic collectors in saturated solutions, proceeding of 13rd Mining Congress, 10-14 May, Istanbul, 519-527.

Helvacı, C. 2015. Geological features of Neogene basins hosting borate deposits: an overview of the deposits and future forecast, Turkey. Bulletin of Mineral Research and Exploration, 151:173-219.

Hoşten, C., Çırak, M. 2013. Flocculation behavior of clayey dolomites in borax solutions, Powder Technology, 235, 263–270.

Karapınar, N. 2009. Maden atık yönetimi: Macun teknolojisi kullanımı. Madencilik, 48(1),31-42.

Karapınar, N. 2016. Investigation of dewatering possibilities of Kırka Boraks Konsantratör atıklarının susuzlandırma imkanlarının araştırılması. Directorate of Mineral Research and Exploration Report No: 11864, Ankara. (unpublished).

Moudgil, B.M., Behl, S. 1993. Flocculation behavior of dolomite, in: Proceedings of the XVIII International Mineral Processing Congress, Australasian Institute of Mining and Metallurgy, Sydney, 1993, 1309–1313.

Moudgil, B. M., Matur, S., Behl, S. 1995. Flocculation behavior of dolomite with polyethylene oxide. Minerals and Metallurgical Processing, 12(4), 219-224.

Newman, P., White R., Cadden, A. 2001. Paste- the future of tailings disposal. Proceedings of the International Conference on Mining and the Environment, 594-603.

Robinsky, E.I. 1999. Tailings dam failures need not be disasters- Thickened tailings disposal (TTD) system. CIM Bulletin. 92(1028), 140-142.

Sabah, E., Yeşilkaya, L. 2000. Evaluation of the settling behavior of Kirka borax concentrator tailings using different type of polymers, Ore Dressing, 2,1–12.

Sarı, M. 2008. Dissolution kinetics of various minerals in boric acid soluition. Thesis (M.Sc.) -- İstanbul Technical University, Institute of Science and Technology (url: http://hdl.handle.net/11527/2692)

Stumm, W., Morgan, J.J. 1996. Aquatic chemistry, chemical equilibria and rates in natural water, 3rd edition, a Wiley-Interface Science.

Taşpınar, O., Çalışan, E. (n.d.). Flocculation and filtration behavior of tincal clays and different minerals in the presence of surfactants and flocculants. The bulletin of the Istanbul Technical Univeristy. 56(1): 1-7.

Verbung, R.B.M. 2001. Use of paste technology for tailings disposal: potential environmental benefits and requirements for geochemical characterization, International Mine Water Association Symposium, Belo Horizonte, Brazil 2001, 1-13.

Bull. Min. Res. Exp. (2018) 156: 247-258

Bulletin of the Mineral Research and Exploration

http://bulletin.mta.gov.tr

The Naşa intrusion (Western Anatolia) and its tectonic implication: A joint analyses of gravity and earthquake catalog data

C. Ertan TOKER[a]*, Emin U. ULUGERGERLİ[b] and Ali R. KILIÇ[c]

[a]*Department of Geophysical Researches, General Directorate of Mineral Research and Exploration, Ankara, Turkey. orcid org/0000-0002-4923-9835*
[b]*Çanakkale Onsekiz Mart University, Geophysic Department Çanakkale. orcid.org/0000-0001-5639-1109*
[c]*Department of Geophysical Researches, General Directorate of Mineral Research and Exploration, Ankara, Turkey. orcid 0000-0002-2127-249X*

Research Article

Keywords:
Gravity, Earthquake, Simav, Graben, edge detection, Euler deconvolution.

Received Date: 21.10.2016
Accepted Date: 28.09.2017

ABSTRACT

The gravity data gathered in and around the Simav Graben in Western Anatolia were reprocessed and reinterpreted by using the standard deviation filter and the Euler deconvolution. The joint evaluation of results from the interpretation of gravity data and seismological studies indicates the presence of new intrusive structures in the vicinity of Simav. The intrusion is located in the eastern margin of the graben and has a thickness of 12-15 km at 2.5-3 km depth below the surface. Numerous earthquakes recorded in the eastern part of the graben are associated with this intrusion. Besides, the multi-dimensional modelling study of the gravity data allowed us to display the Simav Graben, the fold of the Simav Fault, the intrusion named as Naşa, and the epicenters of earthquake within the same tectonic frame. All tectonic structures were marked on the three dimensional relief model.

1. Introduction

It is important to understand the boundaries of geological structures and tectonic discontinuities while exploring the subsurface. In this context, when processing the geophysical data, especially those gathered from the gravity method, it is aimed to clarify the geological setting by increasing the resolution of structural elements and tectonic components and to be contributed to tectonic and geodynamic interpretations. The number of the data processing software and filter applications suggested to obtain much clear and meaningful boundaries are increasing steadily. These filters, also known as the edge detector, produce successful results when they are applied to synthetic data either as single or sequentially. However, the applications on real data show that there is still a need for new techniques (Arısoy and Dikmen, 2013; Cooper, 2013; Zhou et al., 2013).

The Simav Graben, which is one of the West Anatolian grabens, has become subject to many investigations in order to demarcate the intra-graben structure and margins of the basin. Some of the previous studies used seismological data to explain the mechanism of the Simav Fault, which forms the graben boundary, and the causation of earthquakes (Bekler et al., 2011; Toker, 2014; Gündoğdu et al., 2016; Kartal and Kadiroğlu, 2014). In addition, the components of tectonic structures and their formation mechanisms were investigated by evaluating the focal distribution geometry of earthquakes in the graben.

The gravity data of the Simav Graben were evaluated by both the conventional approach (Demirbaş and Uslu, 1984) and imaging techniques (Toker, 2014). The moving standard deviation (MSD) filter can be an example to imaging techniques. In previous studies, the usage of an MSD filter with a fixed window size of 2x2 of which its sensitivity cannot be adjusted because of the window dimension, was suggested as an image processing filter (Jassim, 2013). However in this study, the "moving standard deviation with variable dimension" (MSDVD) filter

* *Corresponding author: C. Ertan TOKER, toker.ertan@gmail.com*
http://dx.doi.org/10.19076/mta.346159

was applied to the potential field data. The processed data were interpreted in order to infer new geological and tectonic information.

The purpose of boundary detection methods is to enhance the variations in data. To do that; first the derivatives in different degrees are calculated, then new images are obtained either from the combination or ratios (phase) of these derivatives. The analytical signal and vertical derivative (Miller and Singh, 1994) methods can be given as examples to such image enhancement processes. The second vertical derivative of the analytical signal (Hsu et al, 1996), the total horizontal derivative of tilt angle (Verdusco et al., 2004), the hyperbolic tilt angle, the second vertical derivative of the hyperbolic tilt angle (Cooper and Cowan, 2004) and the analytical signal obtained from the tilt angle (Ansari and Alamdar, 2011) were utilized in previous studies. The MSD filter was previously compared with Sobel and Kany filters as the edge detector in image processing (Jassim, 2013). In this study, it was demonstrated that the MSDVD filter could also be used in detecting the boundaries of geological structures.

2. Method

The results that are obtained from the application of MSDVD on to data will be examined. The sensitivity of the filter depends on the window size and can be changed optionally. The most important characteristic of this process, which is a kind of image enhancement technique, is that it does not require any sort of derivative or phase calculation. In this respect, it differs from derivative and phase filters. This laterally sensitive filter uses data statistic and produces structurally enhanced information in the output. In the following sections, first we will present the results obtained by application of filter both on the synthetic and Simav data. Later on; we will produce images, which show boundaries of the geological units, and relief map of the study area by using three dimensional standard Euler deconvolution, then assess the elements of emerging geological structures.

2.1. Conceptual Model Application

İn generally the standard deviation is given in the following formula as;

$$\sigma = ((\sum(x)^2 - n*x^2)/(n-1))^{1/2} \quad (1)$$

The equation calculates the variations of "x" variables from n sequential observations around the mean value. The input "x" is an array and contains the measurements along a line. If "x" contains two dimensional variables then standard deviations are calculated by moving the weighted filter windows in k x k window size. The weight values are obtained from deviations off the mean value over data windows. By selecting the "k" index the window size and sensitivity can be adjusted.

In order to obtain a symmetric filter, the k should be set as positive and integer number.

In generally "windowed moving standard deviation" given as;

$$M = \text{movstd}(Amxn,k) \quad (2)$$

returns an array of local k-point standard deviation values. Each standard deviation is calculated over a sliding window of length k across neighboring elements of A (https://www.mathworks.com/help/matlab/ref/std.html).

$$\text{Filter windows} = (2*k+1, 2*k+1) \quad (3)$$

In equation (3), the filter dimensions will be 3,3 for k=1. Similarly; the filter will be 5,5 for k=2. This filter is centered by moving for each elements of the data and standard deviations are calculated over the data grid. By means of weighted and filtered value assigned to the filter center the numerical array representing the structural elements are obtained. Along the edges of data array, the filter is applied by reducing its size (Cooper and Cowan, 2008).

Synthetic data are produced for the model given in figure 1a. The results of 3x3 MSDVD and 5x5 MSDVD are seen in figures 1 b) and 1 c), respectively. In the case of increased "k", it is seen that the anomaly of the horizontal, long prism located at the central part becomes stronger and the structure gains weight (Figure 1 c). Anomalies of the prisms get widens towards the inner edges of the structures. In the map of 2^{nd} vertical derivatives given in figure 1 d), the structure boundaries are enhanced depending on the derivation direction. The values of the 2^{nd} vertical derivative vary between +20 and -15 mgal/km. Despite that, the range in figure 1 b) varies between 0 and +45 mgal and presents much stable variations. Figure 1e shows the horizontal gradient which is similar to figure 1 b). However, it is obtained by derivatives.

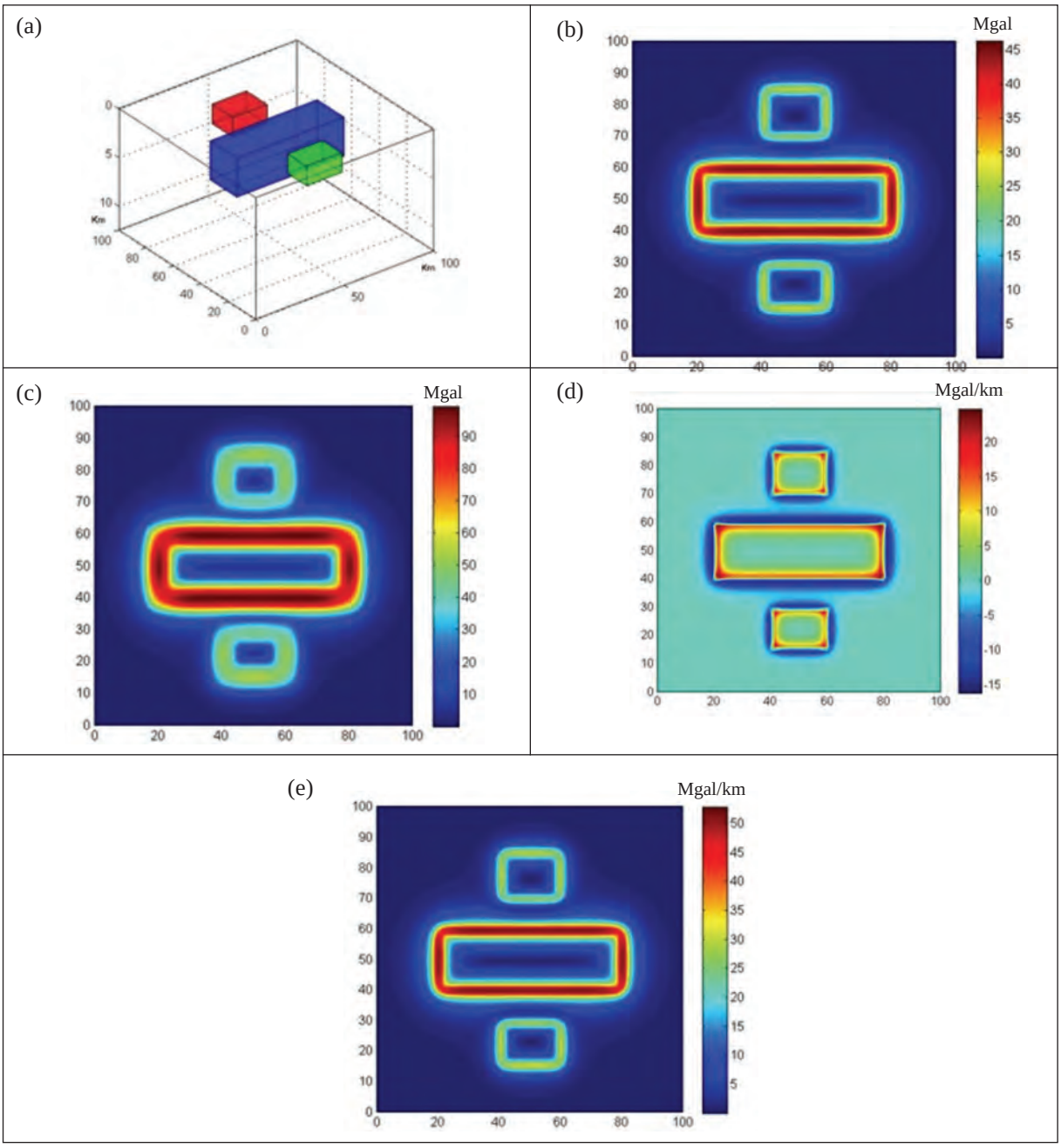

Figure 1- In order to compare the results of MSDVD, the responds of the multiple structures with different density and depth were used. The blue structure has a density of 2.7 gr/cm^3 at depth of 5 km, the red structure has a density of 2.5 gr/cm^3 at depth of 1 km and the green structure has a density of 2.9 gr/cm^3 at depth of 1 km (a). The responds are given for (3x3) dimensional filter in (b), (5x5) dimensional filter in (c), vertical derivative in (d) and horizontal derivative in (e).

In figure 2, the prisms with known depth and density of the Simav Graben are used. The thickening and condensing borders show an enhanced image of the prisms (Figure 2a). The amplitudes vary inversely proportional with the depth and the amplitude ratios are preserved (Figure 2b).

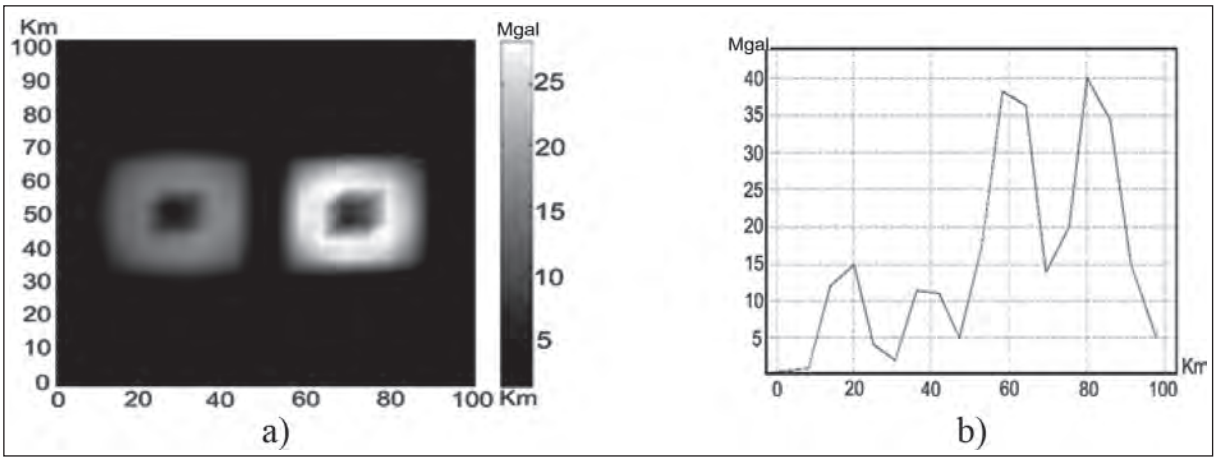

Figure 2- Selected dimensions and depths of prisms to see the effects on the graben scale: shallow prism (right) 20x20x1.2 km d=2.2 gr/cm^3 and deep prism (left) 20x20x13 km d=2.9 gr/cm^3. a) MSDVD result for the prisms, b) values along the center line crossing both prisms, the shallow prism gives a higher standard deviation value.

3. Geological Setting of the Study Area

The Aegean grabens, including the Simav Graben, have attracted investigators since 60's (Arpat and Bingöl, 1969). The E-W directional Pliocene?-Quaternary depression area restricted by the Simav Fault, which delimits the NE-SW directional Demirci, Selendi, Gördes basins in the north, is called as the Simav Graben (Şaroğlu, 2002). Seyitoğlu et al. (1997), from the resolutions of fault mechanism, stated that the Simav Fault was an active and listric fault. This structure is one of the latest products of N-S extensional tectonic, which affects the Aegean region in Late Oligocene-Early Miocene period (Seyitoğlu et al., 1997).

Geomorphological evidences point out that the plain in which the Simav Lake is located has been depressed by the earthquakes within last ten thousand years (Doğan and Emre, 2006). Another suggestion is that the Simav fault is 205 km long slip fault which is bounded to the Gelenbe fault zone in west and to the Sultandağı fault in east (Doğan and Emre, 2006). The northern border of the fault is limited by the Naşa Fault zone, which is formed by a set of normal faults, and the Emet (Kütahya) Fault Zone located in far north (Emre et al., 2012). According to Emre et al. (2012), the Simav plain, which is the largest structural depression that developed within the Simav Fault, is a basin that formed in right-stepping segment between the Simav and Şaphane faults. The regional map (Figure 3), shows the geology of the Simav and its vicinity, and the study area.

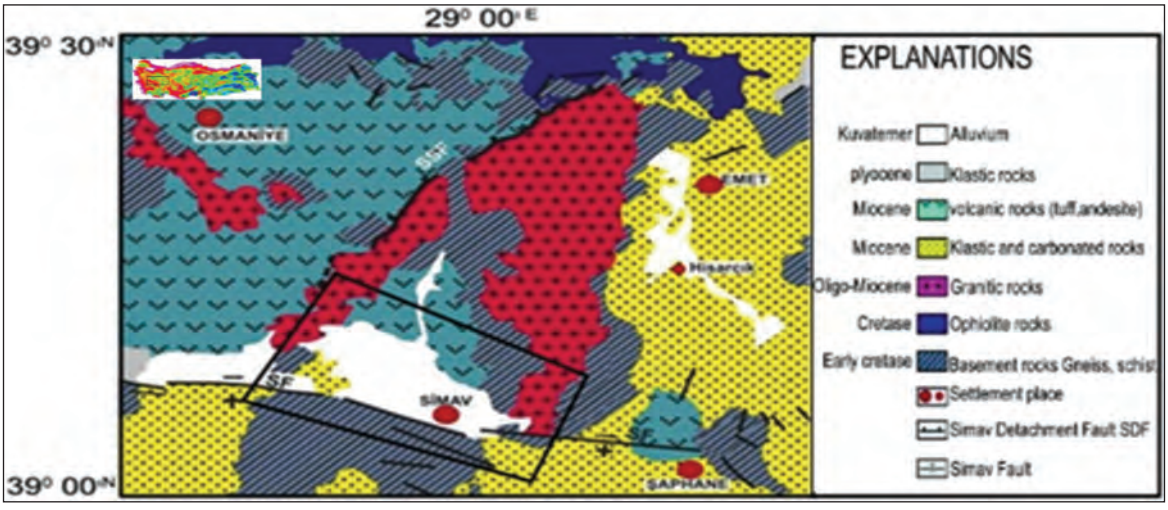

Figure 3- The geology of Simav and its vicinity (modified from MTA, 2002). Black square indicates the study area.

Emre et al. (2006) stated that the recent tectonic deformation, in which the earthquakes had occurred, was caused by the normal and strike slip faults. The investigators emphasize that the most significant earthquake epicenters are the NW-SE directional, right lateral Simav fault and the NW-SE directional Naşa Fault Zone consisting of a set of parallel faults (dipping towards southwest between 55°-65°). The debates on whether the Simav fault is a normal fault as stated by Seyitoğlu et al. (1997) or a right lateral strike slip fault as suggested by Emre et al. (2012) still continue today.

Gündoğdu et al. (2016), presented the offsets on river beds in the stream drainage network by conducting lineament analysis, and suggested that the Simav Fault had continued its strike slip movement even in recent times (Figure 3).

The Simav Graben, is a tectonic junction of which its upper surface has a triangular geometry in the region between the Simav Fault and the Naşa Fault zones (Emre et al., 2006). Its lower edge and tip extend in NW and SE directions, respectively.

The Simav fault in south of the Simav Graben is a NE dipping, steeply inclined with a decreasing slope as going deeper the form of semi-graben. This is also an asymmetrical semi-graben in which the antithetic normal faults developed with their roots extending to the Simav fault.

In the east of the Simav basin, the corner structure created by the intersection of the Simav fault and the Naşa Fault zone, (Figure 4, inside the white circle) is clearly observed in the data (Toker, 2014).

The presence of a third discontinuity (SW-NE directional) that cuts this intersection can be seen from the lineaments in the surface data. This discontinuity can also be traced on the three dimensional gravity depth interface (13-15 km) obtained by the iterative inverse solution method.

It is known that earthquakes occurred in the graben are associated with the characteristics of tectonic junction. The Simav fault bends and changes its direction within the Simav graben.

4. The Application of Methods to the Gravity Data

Data used in this study was measured by MTA in 1984. The gravity data, including base stations, were collected at 964 points. The station interval is approximately 250 m. The Bouguer density value was set as 2.67 gr/cm^3 and the Bouguer anomaly map was produced after routine processing steps (Demirbaş and Uslu, 1984). The shape and location of the graben can be traced on the gravity map (Figure 4). The data vary between -55 and -75 mGal (Figure 5b). In the gravity map, the value ranges between -60 and -64 mGal represent granitoids, and the values ranging between -72 and -74 mGal represent gneisses which extend along the lower edge of the graben (Toker, 2014). Blue areas in figure 5b present the gravity effect of the Quaternary alluvial fill. The area shown with white line in figures 5b, c, d and e is the subject of this study.

The results of 3x3-dimensional MSDVD application by setting k=1 and 9x9-dimensional MSDVD application by setting k=4 are shown in figures 5c and d, respectively.

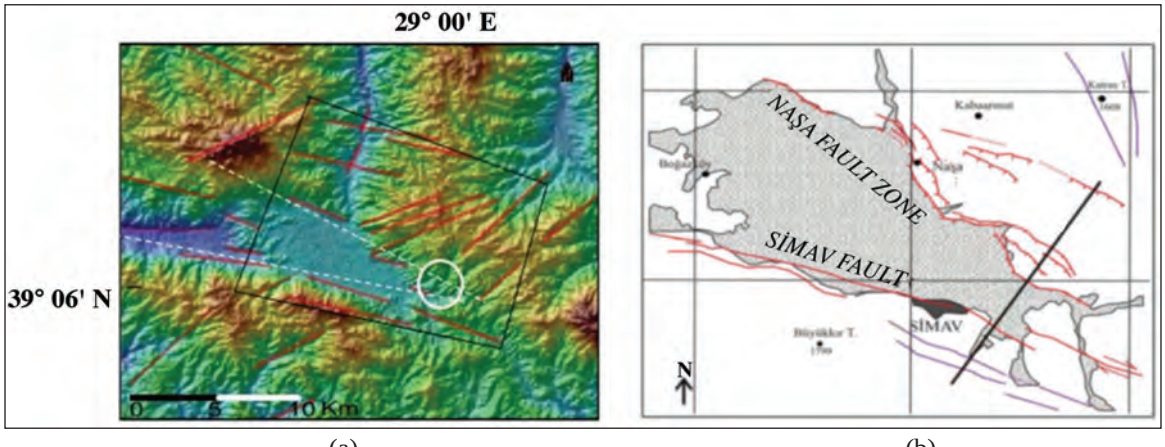

Figure 4- a) Lineament analysis of Simav and its vicinity (white circle: corner structure, see text for explanation), b) active faults in the region (Emre et al., 2012).

The map shown in figure 5 c) appears to be simplified in figure 5 d) due to the reduced sensitivity. The map in figure 5 d) is composed of both graben itself and a circular intrusive structure that is forced into SW part of the graben.

The sun shading (Cooper and Cowan, 2003) technique was applied to the Bouguer data at a height of 500 m from SW (Figure 5e).

The relief map obtained from the standard 3D Euler Deconvolution is shown in figure 5f (Thompson, 1982; Reid et al., 1990).The target structure is marked with red dashed circle.

The gravity map has a high resolution and the conceptual model of the graben is supported by the data (Toker, 2014). The depth of the infill of the graben reaches 1200-1300 m in the model by means of two dimensional gravity inverse solution. This thickness

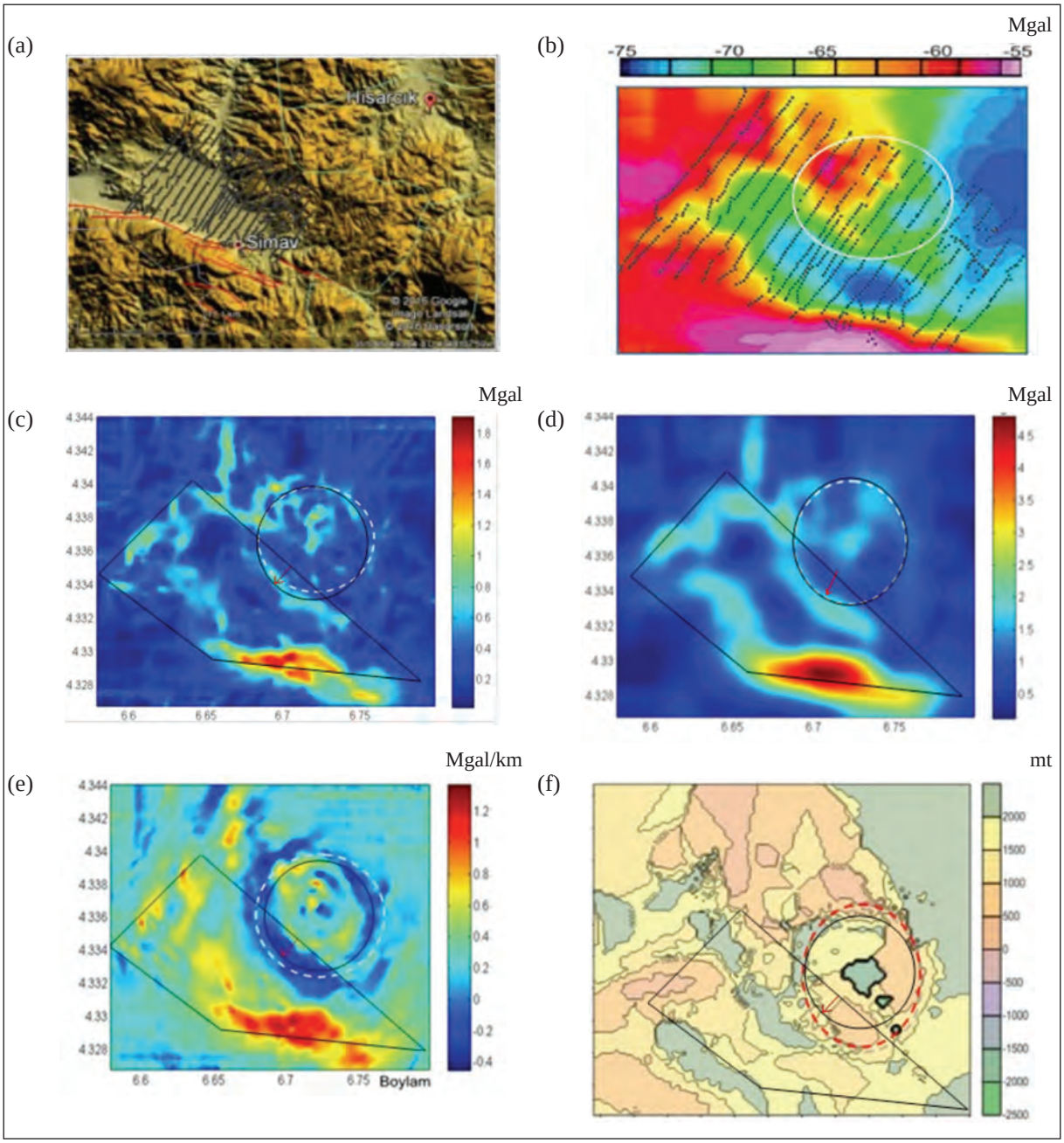

Figure 5- a) Study area, b) Bouguer map, c) MSDVD for k=1 (3x3), d) MSDVD for k=4 (9x9), e) 500 m. sun shading, f) Euler relief map (see text for details).

decreases towards northward and westward starting from the Simav settlement area (Toker, 2014).

The result of the three-dimensional modelling showed that the depth of the interface between the Simav fault and the Nasa Fault zones lies within a range of 13-15 km's, and the traces of a discontinuity in the GB - NE direction (Toker, 2014). With the reprocessing of the data, the information was obtained not only in terms of linearity and boundary relationships but also in terms of geological mass.

In edge detection analyses, the structural boundaries can be traced by using derivative and phase components.

Using a MSDVD filter with a 9x9 window size, the existence of a circular structure which emplaced in to 2/5 of the graben by forcing was revealed. The MSDVD filter exhibits positive features such as not having negative effects on the phase filter due to lacking of the oscillation caused by the vertical derivative (Toker et al., 2014) as well as strengthening the effect of geological structure.

The boundaries and the relief of this structure were investigated by the three-dimensional standard Euler deconvolution (Table 1). The structural index is 1 and the window size is 2219 x 2219 m. There is no altitude information. The depth is defined up to 20 times of the station interval.

To the north of the graben, it is observed that there is a root in the middle of this circular structure and this root extends downward deeper than 2 km (Figure 5f).

Within the frame of this study, a circular structure, which some researchers identified as the Roof Subsidence, is envisaged as intrusions with a diameter of about 9 km by locating its existence and geometry from geophysical data.

Table 1- 3d Euler Deconvolution parameters.

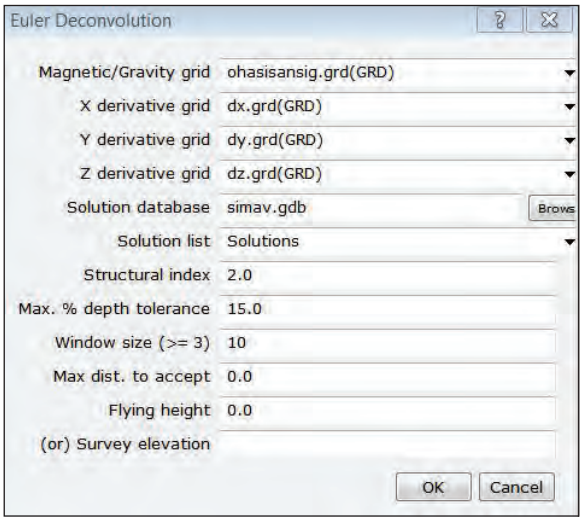

The study showed that the appropriate MSDVD size for this region is 9x9 in terms of lean imaging of the tectonic elements.

However; it should be kept in mind that these values are data and target dependent. When working in other areas, different size of filters should be tested and site specific filter dimensions should always be sought.

5. Seismological Activity

Approximately 1086 earthquake records were taken from Bogazici University Kandilli Observatory data base (www.koeri.boun.edu.tr / scripts / sondepremler.asp, 2016), and their distributions are shown in figure 6. The epicenters of earthquakes become dense around 5-10 km and their depths show a distribution down to 25 km (Figure 7).

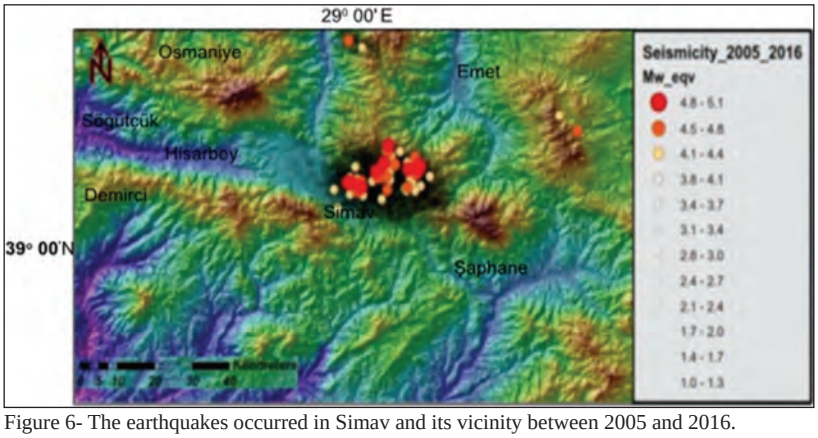

Figure 6- The earthquakes occurred in Simav and its vicinity between 2005 and 2016.

Kartal and Kadiroğlu (2014) examined 39 earthquakes magnitudes of which are greater than 4.0. The earthquakes are divided into two groups, SW and NE groups, at the area in the east of the proposed structure. Table 2 shows those related to the circular structure. The occurrence intervals of earthquakes on the chart are very short. Five of them occurred with one day interval and on the same circular structure.

The distribution geometry of the in hypocenter and epicenters of the earthquake is given in figure 7 as 3D. Figure 7 inset shows that there are two intrusions connected to each other in the region where the distribution of the hypocenters are concentrated. The image shows that the locations of the hypocenters related to the boundaries of the intrusion and that when these intrusion rise or change direction, these movements create small earthquakes.

Table 2- Earthquakes that occurred over the circular intrusion (Kartal and Kadiroğlu, 2014).

No	Date	Time (GMT)	Lat.	Lon.	Depth	MI	Direct1	Slope1	Angle1	Direc2	Slope2	Angle2
1	19.05.2011	20:15:22:79	39.1328	29.0820	24.46	5.7	149	35	-45	278	66	-117
4	19.05.2011	21:21:29:45	39.1128	29.0317	06.99	4.3	127	44	-68	278	50	-110
7	20.05.2011	00:58:33:05	39.1147	29.0837	17.38	4.3	84	26	-80	252	64	-95
9	20.05.2011	05:00:36.19	39.1202	29.0872	07.09	4.2	79	46	-79	243	45	-101
10	21.05.2011	21:43:08.56	39.1037	29.0513	07.00	4.0	302	43	-92	124	47	-89
11	24.05.2011	02:55:28.91	39.1013	29.0217	16.80	4.2	44	58	-87	219	32	-94
15	29.05.2011	01:31:39.16	39.1425	29.0853	05.04	4.5	129	37	-50	263	63	-116
19	27.06.2011	21:13:58.53	39.1108	29.0260	18.27	5.0	156	33	-65	307	60	-105
22	03.07.2011	14:16:28.51	39.1037	29.0147	10.78	4.1	159	47	-36	275	64	-131
34	03.05.2012	16:16:04.27	39.1018	29.0390	25.41	4.6	153	48	-60	292	50	-119

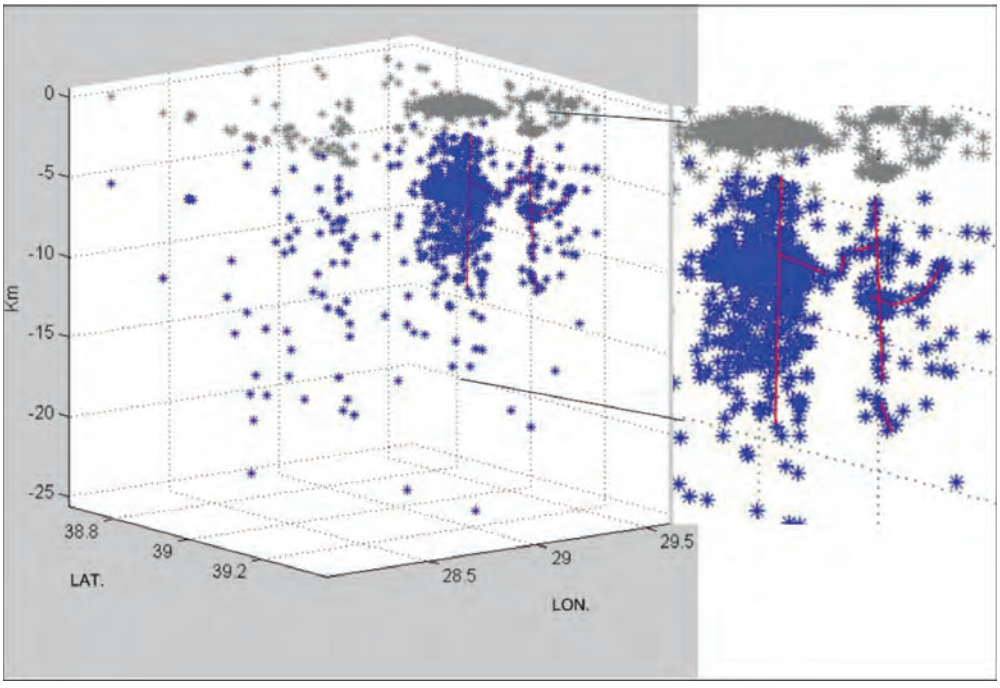

Figure 7- Distribution geometry (dark blue: hypocenter, gray: epicenter). Red lines indicate the probable structural relationship and nearly parallel the vertical axes (B.Ü. Kandilli Obsevatory catalog).

6. 3D Modelling of the Circular Structure

In order to make the depression area distinguishable in 2D depth map, cross sections were taken (Figure 8a). In these sections; there are seen circular structures in which sectional images of deep blue traps are located and the depth information belonging to those images. There are also observed columnar structures, which have traces of contours starting from the center of the circular structure to the right. Their depths rest on the boundary of the block diagram and are most probably continuous. It is considered that these are the structures, which are revealed by the monitoring of earthquake epicenters, and possess images that resemble to combined structures.

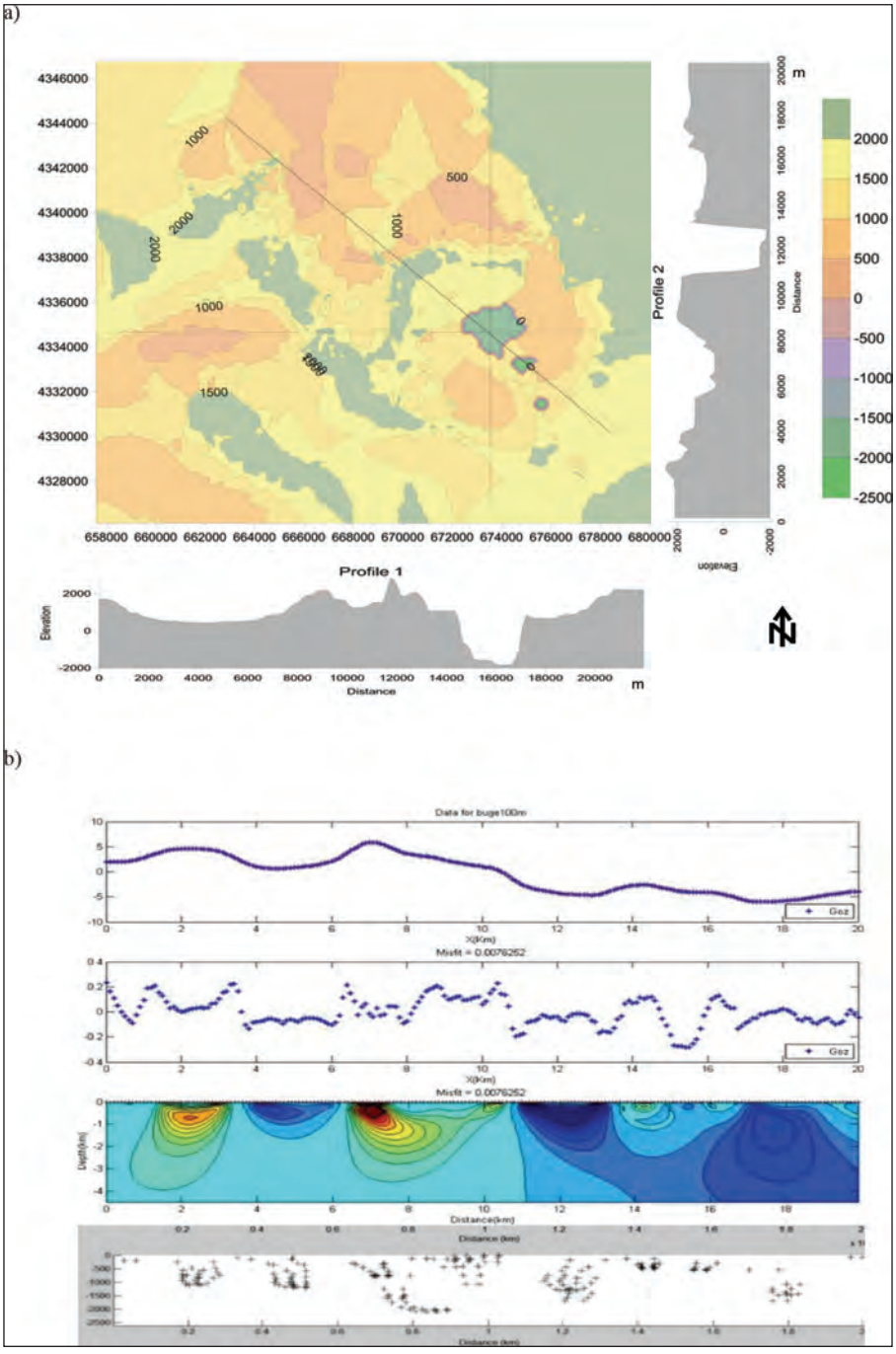

Figure 8- **a)** The bottom topography of the circular structure along the profiles, **b)** comparison of the results from 2D inverse solution and tilt depth method with horizontal cylinder approach**.**

In order to see the gravity distribution of the model in figure 8b, a model was generated by 2D inverse solution from the data taken along the brown colored line. The depth interval for 2D model was selected as 0-4.5 km by trials.

The presented density value makes differences with respect to 2670 kg/m^3. The incompatibility was detected as 0.0076624. In figure 8b, the result obtained by the tilt method is seen and the target structure between the distances of 4-6 km's was imaged as certain (Cooper, 2011). The depth comparison was not made.

Figure 9 shows a three-dimensional gravitational relief map obtained by the standard Euler Deconvolution method. The relief map clearly shows the Simav fault and the Naşa fault which surround the Simav half graben. Besides, the figure 9 also shows the presence and the depth of the circular structure in the northern part.

7. Discussion

The existence of a buried circular structure, which has not previously been revealed in the gravitational data, was investigated. When we were changed structural indice for dyke model (ı=2), relief has not been changing. Model was stable for both indices.

Here, with the weighing ability of the MSDVD filter to the structural information an image similar to

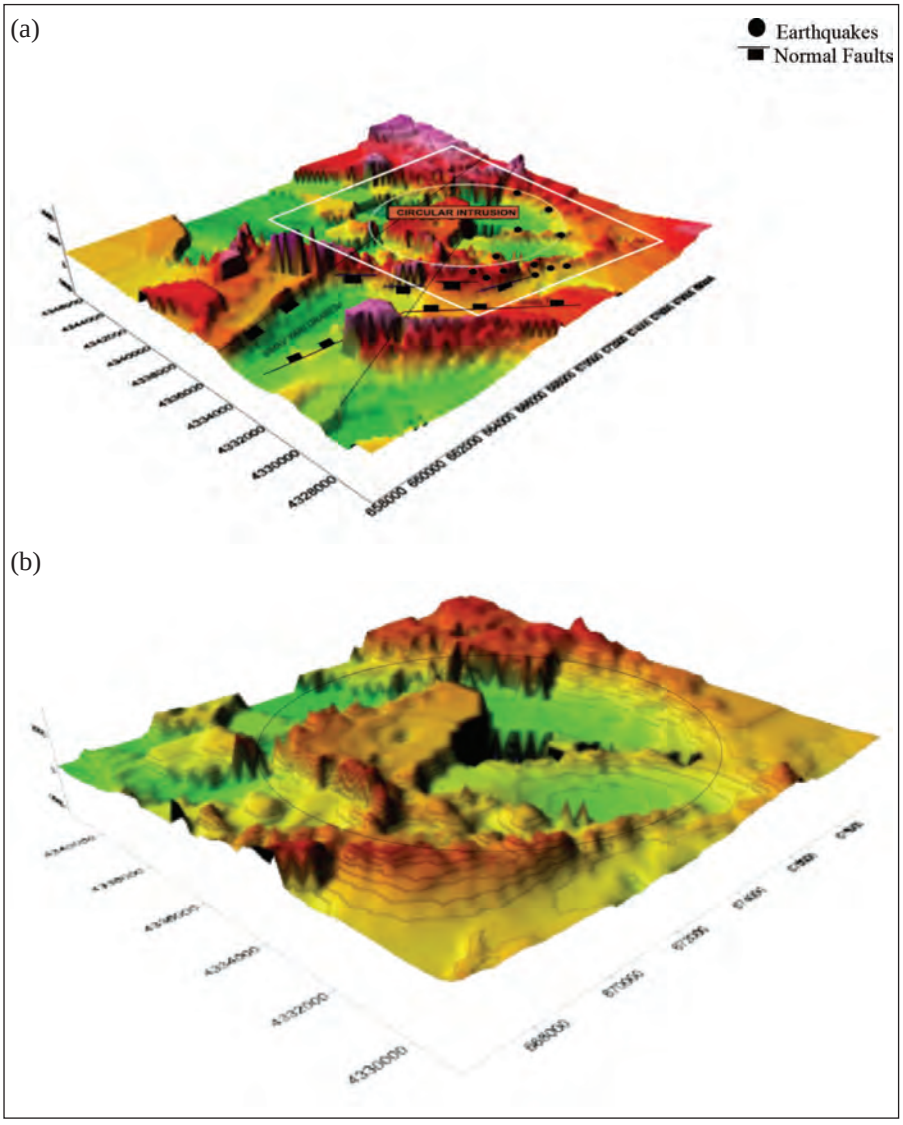

Figure 9- **a)** 3D relief image of the gravity data obtained from the 3D standard Euler deconvolution, **b)** The close-up view of the circular structure.

the horizontal derivative was obtained without using derivative and phase filter.

The MSDVD was used to illuminate structure-boundary relationships. The experiments performed in this work showed that an operator with a size of 9x9 was appropriate for this field. It should not be forgotten that these values will change when working in different regions.

Before applying the real data, testing on synthetic data and supporting with modeling exercises is the most appropriate way to select the operator size.

The circular structure suggested in this study is connected to earthquakes down to 25 km in depth and triggered these earthquakes.

In the previous study, the intersecting discontinuities in the graben were revealed (Toker, 2014).

In this study, it is thought that the junction of discontinuities creates a weak zone where magmatic melt easily and rapidly ascends, and mobilizes the circular structure.

As a result, it is thought that magmatic melt migrates through weak geological zones (contact, faults, etc.) and creates new pathways for itself.

It is also thought that earthquakes that occurred in the region is due to the location of the circular structure (29.00E longitude 39.10N latitude).

The surface traces of these earthquakes need to be investigated with respect to the location of the circular structure. In addition, an additional geophysical work is needed in this area. The investigation of acoustic, resistivity and magnetic susceptibility parameters will help resolve the problem.

8. Result and Suggestions

Basically, three cases can be count on the earthquakes that occur in the region. Earthquakes created by,

- The intersection zone where the Simav Fault, the Naşa Fault and the deep seated SW-NE directional discontinuity cross each other,

- The presence of a structure of intrusions rising at the junction of these discontinuities,

- The corporate work of both conditions given above.

In this work, the gravity data were reprocessed and modelled to reveal the existence of a tectonic junction and intrusive structure with circular geometry. This intrusion is the result of horizontal and vertical tectonic activities of the region.

It is concluded that earthquakes, which occurred in the region, are caused by these intrusions and the tectonic junction formed by the active faults.

If the area among three settlements is to be used as a living area, the necessary measures for the building safety must be taken into consideration. It is believed that this area has a priority in terms of preventing future inconveniences.

Acknowledgements

Data utilized in this study belong to the General Directorate of Mineral Research and Exploration (MTA) and was published with the written permission of the organization. We are thankful to MTA for their supports. The software was implemented from D'errico (2016). F. Alkan Tetik and Recep Çakır contributed to this article with their valuable opinions and suggestions. We also would like to thank to referees for their critics and constructive suggestions.

References

Ansari, A. H., Alamdar, K. 2011. A new edge detection method based on the analytic signal of tilt angle (ASTA) for magnetic and gravity anomalies, IJST A2: 81-88, Iranian Journal of Science and Technology.

Arısoy, M.Ö., Dikmen, Ü. 2011. Potensoft: MATLAB based software for potential field data processing, modeling and mapping, Computer And Geoscience, 37, 7, s. 935 – 942.

Arpat, E., Bingöl, E. 1969. Ege bölgesi graben sisteminin gelişimi üzerine düşünceler, Maden Tetkik ve Arama Dergisi, 73, 1-9, Ankara.

Bekler, T., Demirci, A., Özden, S., Kalafat, D. 2011. Simav, Emet fay zonlarındaki optimum kaynak parametrelerinin analizi, 1. Türkiye Deprem Mühendisliği ve Sismoloji Konferansı, ODTÜ, Ankara.

Boğaziçi Üniversitesi Kandilli Rasathanesi Deprem Kataloğu. 2016. www.koeri.boun.edu.tr/scripts/sondepremler.asp

Cooper, G.R.J., 2011. The Semi-Automatic Interpretation of Gravity Profile Data March 2011, Computers and Geosciences 37(8) DOI: 10.1016/j.cageo.2011.02.016.

Cooper, G. R. J. 2013. Reply to "A Discussion about the Hyperbolic Tilt Angle Method by Zhou et al.", Computers and Geosciences, 52, 496-497.

Cooper, G.R.J., Cowan, D.R. 2003. Sunshading geophysical data using fractional order horizontal gradients. The Leading Edge. 22:204

Cooper, G.R.J., Cowan, D.R. 2004. Filtering using variable order vertical derivatives. Computer and Geoscience, 30, 455-459.

Demirbaş, Ş., Uslu A. 1984. Kütahya Simav Gravite Etüdü, Maden Tetkik ve Arama Genel Müdürlüğü Rapor No: 8136, Ankara (unpublished).

D'errico, J. 2016. Personel Web Page https://www.mathworks.com/matlabcentral/.../869215-john-

Doğan, A., Emre, Ö. 2006. Ege graben sisteminin kuzey sınırı: Sındırgı Sincanlı Fay Zonu, 59. Türkiye Jeoloji Kurultayı, Bildiriler Kitabı.

Emre, Ö., Duman, T.Y., Olgun, Ş., Özalp, S. 2012. Türkiye diri fay haritası (renwed), Maden Tetkik ve Arama Yayınları, Ankara.

Doğan, A., Emre, Ö. 2006. Ege graben sisteminin kuzey sınırı: Sındırgı Sincanlı Fay Zonu, 59. Türkiye Jeoloji Kurultayı, Bildiriler Kitabı.

Gündoğdu, E., Özden, S., Karaca, Ö. 2016. Comparative structural analysis of field data from Simav fault and surrounding area with alos-palsar and landsat images, Journal of the graduate school of natural and applied sciences of Erciyes University Vol :32 No:1

Hsu, S.K., Sibuet, J.C., Shyu, C.T. 1996. Depth to magnetic source using generalized analytic signal,Geophysics, 61, 373-386.

Jassim, F.A. 2013. Semi – optimal edge detector based on simple standard deviation with adjusted thresholding, International Journal of Computer Applications (0975 – 8887) Volume 68– No.2, April 2013.

Kartal, R.F., Kadiroğlu, F.T. 2014. 2011-2012 Simav Earthquakes (Ml=5.7, Ml=5.0, Ml=5.4) and Relationship with the Tectonic Structure of the Region Yerbilimleri, Bulletin of the Earth Sciences Application and Research Centre of Hacettepe University 35 (3), 185-198.

MTA 2002. General Directorate of Mineral Research and Exploration. http://www.mta.gov.tr/v30/hizmetler/500cd.

Miller, H. G., Sing, V. 1994. Potential field tilt - A new concept for location of potential field sources Journal of Applied Geophysics, 32, 213-217

Oasis montaj Sofware, 2009 www.geosoft.com/resources/goto/oasis-montaj-7.1 Queens Quay Terminal 207 Queens Quay West Suite 810, PO Box 131 Toronto, ON Canada M5J 1A7

Reid, A. B., Allsop, J. M., Granser, H., Millett, A. J., Somerton, I. W. 1990. Magnetic interpretation in three dimensions using Euler deconvolution, Geophysics, 55, 80–91, http://dx.doi.org/10.1190/1.1442774

Seyitoğlu, G. 1997. The Simav Graben: An example of young E-W trending structures in the late cenosoic extensional system of western Turkey. Turkish Journal of Earth Science, 6, 135-141, TÜBİTAK, Turkey.

Toker, C. E. 2014. Geophysical analysis and modelling of the Simav basin, Western Anatolia. Bulletin of the Mineral Research and Exploration. 148, 119-135, Ankara.

Toker, C. E., Çiftçi, Y., Ayva, A., Kürçer, A. 2014. Two examples for imaging buried geological boundaries: Sinkhole structure and Seyit Hacı fault, Karapınar, Konya. Bulletin of the Mineral Research and Exploration. 149, 189-199, Ankara.

Thompson, D. T. 1982. EULDPH: A new technique for making computer-assisted depth estimates from magnetic data, Geophysics, 47, 31–37, http://dx.doi.org/10.1190/1.1441278

Verdusco, B., Fairhead, J.D., Green, C.M. 2004. New insigth in to magnetic derivatives for structural mapping, Leading Edge, 23 (2), 116-119.

Zhou, W., Do, X., Li, J. 2013. A Discussion about hyperbolic tilt angle method, Computer and Geoscience, V. 52, p. 493-495.

Editorial...

The Bull.Min.Res.Exp., which periodically maintains its publication life in Turkey since 1936 in the area of earth sciences, has been proceeding to the target of being among the international magazines and has been accepted to the Emerging Source Citation Index (ESCI) by April 2018 (the articles published in the Bull.Min.Res. Exp. in 2017 will also be included in the scanning). The requirement to be scanned by ESCI, which is required to be included in the most prestigious scanning system, Science Citation Index (SCI), has been completed in this context.

The Bull.Min.Res.Exp. has the characteristics of being a journal of earth science in which the articles consisting of data and assessments related to scientific and technical researches. It is systematically published twice a year both in Turkish and English. The articles for each issue are also available on the MTA website (www.mta.gov.tr) as ".pdf" format in full text.

Although there are many well-known magazines published by various Turkish universities and other organizations in the field of earth sciences, the number of scientific journals scanned in international indexes is relatively small compared to other countries. The Bull.Min.Res.Exp., which has begun to be published since June 2012 with its new concept, accepts articles via internet and all procedures are made through internet during review of articles. In databases, there are critical items such as; the diversity of referees, the number of citations, the importance of ethical publishing and the provision of all fields in the area of earth sciences. The Bull.Min.Res. Exp. has met all these criteria.

With changes made in the academic development criteria in our country especially in the last period, the number of articles sent to the Bull.Min.Res.Exp, which is also scanned by the ULAKBİM, has accelerated.

The articles sent to the Bull.Min.Res.Exp are not only from inside our country but also from countries that cooperate with the MTA and from the Middle East countries. With the admission of our bulletin at ESCI, we have the belief that new articles will come as well as from other countries in the near future.

It is important for our journal to be scanned by various international indexes and this cause many advantages in reaching numerous readers, introducing international studies in our country and promoting our organization. The Turkish version of the Bull.Res.Min.Exp. is scanned in the database of ULAKBİM, and the English version is scanned by ESCI as well as in databases of Thompson Reuters Heat Master List, Georef, Geological Abstracts, Mineralogic Abstracts, DOAJ and Scopus.

We emphasize that the target of the Bull.Res.Min.Exp. will be the SCI Expanded and the Editorial Board and the Executive Publication Editorial will work with a great effort to achieve this goal. We would like to thank you for your contributions and wait for your supports that will continue.

With regards.

PUBLICATION RULES FOR THE BULLETIN OF THE GENERAL DIRECTORATE OF MINERAL RESEARCH AND EXPLORATION

1. Aims of Publication

- To contribute to the providing of scientific communication on geosciences in Turkey and international community.
- To announce and share researches in all fields of geoscientific studies in Turkey with geoscientists worldwide.
- To announce scientific researches and practices on geoscientific surveys carried out by the General Directorate of Mineral Research and Exploration (MTA) to the public.
- To use the journal as an effective media for international publication exchange by keeping the journal in high quality, scope and format.
- To contribute to the development of Turkish language as a scientific language.

2. Scope

At least one of the following qualifications is required for publishing the papers in the *Bulletin of Mineral Research and Exploration*.

2.1. Research Articles and Review Articles

2.1.1. Original Scientific Researches

- These articles cover and contribute to the main subjects of the earth sciences, the original scientific researches and its results related to all aspects of disciplines in geoscience like exploration and evaluation of the underground sources and environmental problems, and
- The studies, which apply new aspects and methods for the solution of problems about the earth sciences and researches, which apply new aspects and methods for the solution of the problems, in the engineering sciences carried out in MTA.

2.1.2. Review articles

- These papers include comphrehensive scholarly review articles that summarize and critically assess previous geoscientific researches with a new perspective and reveal a new approach.

2.2. Discussion/Reply

- This type of article is intended for the discussion of papers that have already been published in the latest issue of the *Bulletin*. The discussion/reply type articles, which criticize all or a part of a recently published article, are published in the following first issue if it is submitted within six months after the publication of the *Bulletin*.
- The discussions are sent to the corresponding author of the original paper to get their reply before publication. The discussions abut the paper with two or more authors are sent only to the corresponding author.
- If the review article is not published within the prescribed preiod then it is published alone. Later sent replies are not published. Re-criticising of the replies is not allowed.
- The authors should obey the rules of scientific ethics and discussions in their discussion/reply papers. The papers in this category should not exceed four printed pages of the journal including figures and tables etc. The format of the papers should be compatible with the “Spelling Rules” of the *Bulletin.*

2.3. Short Notes

- The short notes part of the *Bulletin* covers short, brief and concisely written research reports for papers including the data obtained from ongoing and/or completed scientific researches and practices related to geoscience and new and/or preliminary factual findings from Turkey and worldwide.
- The short notes will follow a streamlined schedule and will normally be published in the following first or second issue shortly after submission of the paper to the *Bulletin*.
- This type of articles should not exceed four printed pages of the journal including figures, tables and an abstract.

3. Submission and Reviewing of Manuscripts

Manuscript to be submitted for publishing in the Journal must be written clearly and concisely in Turkish and/or English and prepared in the *Bulletin of Mineral Research and Exploration* style guidelines. All submissions should be made online at the **http://.dergi.mta.gov.tr** website.

- The manuscript submitted for reviews must not have been published partially or completely previously in another journal.

- The rejected manuscripts are not returned back to author(s) whereas a letter of statement indicating the reason of rejection is sent to the corresponding author.

- Submitted manuscripts must follow the *Bulletin* style and format guidelines. Otherwise, the manuscript which does not follow the journals' style and format guidelines, is given back to corresponding author without any reviewing.

- Every manuscript which passes initial Editorial treatise is reviewed by at least two independent reviewers selected by the Editors. Reviewers' reports are carefully considered by the Editors and associated editors.

- The manuscript that need to be corrected with the advices of reviewer(s) is sent back to corresponding author(s) to assess and make the required corrections suggested by reviewer(s) and editors. The authors should prepare a letter of well-reasoned statement explaining which corrections are considered or not.

- If there are any suggestions given by editors and referees that are not accepted and corrected by the author, then it should be sent to the Editor's Office with corrected copies of the report explaining the reason for not accepting these suggestions and corrections.

- Figures and tabless should be 1/3 of the main text.

- To be published in the *Bulletin of Mineral Research and Exploration*, the printed lenght of the manuscript should not exceed 30 printed pages of the journal including an abstract, figures and tables. The publication of longer manuscripts will be evaluated by Editorial Board if it can be published or not.

- The authors must do the reviewer's corrections and proposals in 60 days and must upload to the system.

- At the printing stage after the last control, the first print of the manuscript are sent to the author/ authors in pdf version and asked from the author/ authors to make the press control.

4. Publication Language and Periods

- *The Bulletin of Mineral Research and Exploration* is published at least twice a year and each issue is published both in Turkish and English. Thus, the manuscripts are accepted in Turkish or English. The spelling and punctuation guidelines of Turkish Language Institution are preferred for the Turkish issue. However, the technical terms related to geology are used in accordance with the decision of the Editorial Board.

5. Spelling Draft

- Manuscripts should be written in word format in A4 (29.7 x 21 cm) size and double-spaced with font size Times New Roman 10-point, margins of 25 mm at the sides, top and bottom of each page.

- The formulas requiring the use of special characters and symbols must be submitted by the symbols part of the Microsoft Office Word Program on computer.

- Initial letters of the words in sub-titles must be capital. The first degree titles in the manuscript must be numbered and left-aligned, 10 point bold Times New Roman must be used. The second degree titles must be numbered and left-aligned, they must be written with 10 point normal Times New Roman. The third degree titles must be numbered and left-aligned, they must be written with 10 point italic Times New Roman. The fourth degree titles must be left-aligned without having any number; 10 point italic Times New Roman must be used. The text must continue placing a colon after the title without paragraph returns (See: Sample article: http://bulletin.mta.gov.tr).

- One line spacing must be left after paragraphs within text.

- Paragraphs must begin with 0.5 mm indent.

- The manuscript must include the below sections respectively;

  - Title Page
  - The Name and Surname of the author and * sign (Adress, e-mail adres must be given at the bottom of the page)
  - Abstract
  - Key Words

- o Introduction
- o Body
- o Discussion
- o Conclusion
- o Acknowledgements
- o References

5.1. Title of the Article

- The title must be short, specific and informative and written with small letters font size Times New Roman 10-point bold. The title mustn't contain the subjects insufficiently processed in the article.

5.2. The Name of the Author, Address and E-Mail Adress

- The name and surname of the author/authors must be written without affiliations. Name must be written in small letters, the surname must be written in capital letters.
- At the affiliation (work adres) written after the name and the surname of the author/authors only the name of the company must be written, the author's job mustn't be written.
- Information about the adresses must be given at the next line as 10-point and italic.
- At the articles with two or more than two authors, the numbers must be written above the surnames of the authors, the informations about their adresses must be given at the next line by leaving one space line. Also, at this part the corresponding author must be indicated by the (*) symbol and the telephone, FAX and e-mail address of the corresponding author must be given.
- Abbreviations must not be made while writing the name of the uthor and the affiliation adres. Adresses must be given in Turkish in the Turkish version, in English in the English version.
- At the end of the article the name of the corresponding author and contact informations must be added.

5.3. Abstract

- The abstract must be understandable before having a look at the text.
- The abstract should state briefly the overall purpose of the research, the aim of the article, its contributions to the known theories, new data, principle results and major conclusions.
- Tha abstract must contain short and brief sentences.
- Addressing other sections and illustrations of the text or other writings must be avoided.
- The information, which have not been mentioned in the text, must not be in the abstract.
- The article must be written as one paragraph, preferably. Please provide an abstract which doesn't exceed 200 words.
- The abstract must be written with 10-point, normal Times New Roman in single-spaced lines.
- "Abstract" must not be given for the writings that will be located in "Short Notes" section.
- The English abstract must be under the title of "Abstract".

5.4. Key Words

Immediately after the abstract, please provide up to 5 key words and with each words seperated by comma. These key words will be used for indexing purposes.

5.5. Introduction

- The introduction section should state the objectives of the work, research methods, location of the study area and provide an adequate and brief background by avoiding a detailed literature survey.
- Non-standard or uncommon classifications or abbreviations should be avoided. But if essential, then they must be defined at their first mention and used consistently thereafter. Seperate paragraphs could be organized for each of the subjects at the introduction part. If it is necessary, the subtitle can be given for each of them (for example method, material, terminology etc.).
- When pre-information is needed for facilitating the understanding of the text, this section can also be used (for example, statistical data, bringing out the formulas, experiment or application methods, and others).

5.6. Body

- In this chapter, there must be data, findings and opinions that are intended to convey to the reader about the subject. The body section forms the main part of the article.
- The data used in other sections such as "Abstract", "Discussions", and "Results" are caused by this section.
- While processing the subject, the care must be taken not to go beyond the objective highlighted in the "Introduction" section. The knowledge, which do not contribute to the realization of the purpose of the article or are useless for conclusion, must not be included.
- All data used and the opinions put forward in this section must prove the findings obtained from the studies or they must be based on a reference by citation.
- The guidance and methods to be followed in processing subjects vary according to the characteristics of the subjects mentioned. Various topic titles can be used in this section as many as necessary.

5.7. Discussions

- Discussion of the data and findings that are objectively transferred in the Main Text section of the article should be done in this section. This must be written as a seperate section from the results section.

5.8. Conclusions

- The main conclusion of the study provided by data and findings of the research should be stated concisely and concretely in this section.
- **T**he subjects that are not mentioned sufficiently and/or unprocessed in the body section must not be included in this section.
- The conclusions can be given in the form of substances in order to emphasize the results of the research and to make the expression understandable.

5.9. Acknowledgements

In this section, the significant contributions made in the realization of investigation that form the topic of the paper is specified. While specifying contributions, the attitude diverted the original purpose of this section away is not recommended. Acknowledgements must be made according to the following examples.

- This study was carried out within scope of .....project.
- I/we would like to thank to …… for contributing to the development of this article with his/her critiques.
- Academic and/or authoritorial affiliations are written for the contributions made because of requirement of ordinary task.

For example:

- o "Prof. Dr. İ. Enver Altınlı has led the studies".
- o "The opinions and warnings of Dr. Tandoğan Engin are considered in determining the chemistry of chrome minerals."

- The contributions made out of the requirement of ordinary task:

For example:

o "I would like to thank to Professor Dr. Melih Tokay who gives the opportunity to benefit from unpublished field notes"; "I would like to thank to the preliminary-Plan Chief Engineer Ethem Göğer, State Hydraulic Work, 5th Zone". Academic and / or task-occupational titles are indicated for such contributions.

- The contributions, which are made because of requirement of ordinary task but do not necessitate responsibility of the contributor mustn't be specified.

For example:

o Sentences such as "I would like to thank to our General Manager, Head of Department or Mr. / Mrs. President ……who has provided me the opportunity to research" must not be used.

5.10. References

- All references cited in the text should be given in the reference list.
- The authors must be careful about the accuracy of the references. Publication names must be written in full.

- Reference list must be written in Times New Roman, 9-point type face.
- The reference list must be alphabetized by the last names of the first author of each work.
- If an author's more than one work is mentioned, then ranking must be made with respect to the publication year from old to new.
- In the case that an author's more than one work in the same year is cited, the lower-case alphabet letters must be used right after publication year (for example; Saklar, 2011a, b).
- If the same author has a publication with more than one co-author, firstly the ones having single author are ranked in chronological order, then the ones having multiple authors are ranked in chronological order.
- In the following examples, the information related to works cited is regulated in accordance with different document/work types, considering punctuation marks as well.
- If the document is located in a periodical publication (if it is an article), then the information about the document must be given in the following order: surnames of the author/authors, initial letters of author's/authors' first names. Year of publication. Name of the document. Name of the publication where the document is published, volume and/ or the issue number, numbers of the first and last pages of the document.

For example:

  - o Pamir, H.N. 1953. Türkiye'de kurulacak bir hidrojeoloji enstitüsü hakkında rapor. Türkiye Jeoloji Bülteni 4, 1, 63-68.
  - o Barnes, F., Kaya, O. 1963. İstanbul bölgesinde bulunan Karbonifer'in genel stratigrafisi. Maden Tetkik ve Arama Dergisi 61, 1-9.
  - o Robertson, A.H.F. 2002. Overview of the genesis and emplacement of Mesozoic ophiolites in the Eastern Mediterranean Tethyan region. Lithos 65, 1-67.

- If more than one document by the same authors is cited, first the documents having single name must be placed in chronological order, second the documents having two names must be listed in accordance with the chronological order and second author's surname, and finally the docments having multiple names must be listed in accordance with chronological order and third author's surname.
- If the document is a book, then; the surname of the author/authors, initial letters of the author's/ authors' first names. Year of publication. Name of the book (initial letters are capital). Name of the organization, which has published the book, name of the publication where the document is published, volume and/ or the issue number, total pages of the book.

For example

  - o Meric, E. 1983. Foraminiferler. Maden Tetkik ve Arama Genel Müdürlüğü Eğitim Serisi 23, 280 s.
  - o Einsele, G. 1992. Sedimentary Basins. Springer-Verlag, 628 p.

- If the document is published in a book containing the writings of various authors, the usual sequence is followed for the documents in a periodic publication. Then the editor's surname and initial letters of their name/names are written. "Ed.", which is an abbreviation of the editor word, is written in parentheses. Name of the book containing the document (initial letters are capital). Name of the organization which has published the book. Place of publication, volume number (issue number, if any) of the publication where the document is published, numbers of the first and last page of the document.

For example:

  - o Göncüoğlu, M.C., Turhan, N., Şentürk, K., Özcan, A., Uysal, Ş., Yalınız, K. 2000. A geotraverse across northwestern Turkey. Bozkurt, E., Winchester, J.A., Piper, J.D.A. (Ed.). Tectonics and Magmatism in Turkey and the Surrounding Area. Geological Society of London Special Publication 173, 139-162.
  - o Anderson, L. 1967. Latest information from seismic observations. Gaskell, T.F. (Ed.). The Earth's Mantle. Academic Press. London, 335-420.

- If the name of a book, where various authors' writings have been collected, is specified, those must be indicated respectively: book's editor/

editors' surname/surnames and initial letters of their name/names. "Ed.", which is an abbreviation of the editor word, must be written in parentheses. Year of Publication. Name of the book (initial letters are capital). Name of the organization which has published the book, total pages of the book.

For example:

- o Gaskel, T.F. (Ed.) 1967. The Earth's Mantle. Academic Press, 520 p.

- If the document is an abstract published in a Proceedings Book of a scientific activity such as conference/symposium/workshop …etc., the information about the document must be given in the following order: surnames of the author/authors, initial letters of author's/authors' first names. Year of publication. Title of the abstract. Name, date and place of the meeting where the Proceedings Book is published, numbers of the first and last pages of the abstract in the Proceedings Book.

For example:

- o Yılmaz, Y. 2001. Some striking features of the Anatolian geology. 4. International Turkish Geology Symposiums 24-28 September 2001, London, 13-14.

- o Öztunalı, Ö., Yeniyol, M. 1980. Yunak (Konya) yöresi kayaçlarının petrojenezi. Türkiye Jeoloji Kurumu 34. Bilim Teknik Kurultayı, 1980, Ankara, 36

- If the document is one of the unpublished documents as a report, lecture notes, and so on, the information about the document must be given by writing the word "unpublished" in parentheses at the end of information about the document after it is specified in accordance with usual order which is implemented for a document included in a periodic publication.

For example:

- o Özdemir, C. Biçen, C. 1971. Erzincan İli, İliç ilçesi ve civarı demir etütleri raporu. *General Directorate of Mineral Research and Exploration Report No: 4461*, 21 p. Ankara (unpublished).

- o Akyol, E. 1978. Palinoloji ders notları. EÜ Fen Fakültesi Yerbilimleri Bölümü, 45 p., İzmir (unpublished).

- The followings must be specified for the notes of unpublished courses, seminars, and so on: name of the document and course organizer. Place of the meeting, name of the book, corresponding page numbers must be given.

For example:

- o Walker, G. R. Mutti, E. 1973.Turbidite facies and facies associations. Pacific Section Society for Sedimentary Geology Short Course. Annaheim. Turbitides and Deep Water Sedimantation, 119-157.

- If the document is a thesis, the followings are written: surname of the author, initial letter of the author's first name. Year of Publication. Name of the thesis. Thesis type, the university where it is given, the total number of pages, the city and "unpublished" word in parentheses.

For example:

- o Seymen, İ. 1982. Kaman dolayında Kırşehir Masifi'nin jeolojisi. Doçentlik Tezi, İTÜ Maden Fakültesi, 145 s. İstanbul (unpublished).

- Anonymous works must be regulated according to the publishing organization.

For example:

- o MTA. 1964. 1/500.000 ölçekli Türkiye Jeoloji Haritası, İstanbul Paftası. Maden Tetkik ve Arama Genel Müdürlüğü, Ankara.

- The date after the name of the author is not given for on-printing documents; "in press" and / or "on review" words in parenthesis must be written. The name of the article and the source of publication must be specified, volume and page number must not be given.

For example:

- o Ishihara, S. The granitoid and mineralization. Economic Geology 75th Anniversary (in press).

- Organization name, web address, date of access on web address must be indicated for the information downloaded from the internet. Turkish sources must be given directly in Turkish and they must be written in Turkish characters.

For example:

- o ERD (Earthquake Research Department of

Turkey). **http://www.afad.gov.tr**. March 3, 2013.

- While specifying work cited, the original language must be used; translation of the title of the article must not be done.

6. Illustrations

- All drawings, photographs, plates and tables of the article are called as "illustration".
- The illustrations must be used when the use of them is inevitable or when they facilitate the understanding of the subject.
- While selecting and arranging the illustrations' form and dimensions, the page size and layout of the *Bulletin* must be considered. The unnecessary loss of space must be prevented as much as possible.
- The pictures must have high quality, high resolution suitable for printing.
- The number of illustrations must be proportional to the size of the text.
- All illustrations must be sent as in separate files independent from the text.
- While describing illustrations in the text, the abbreviations must be avoided and descriptions must be numbered in the order they are mentioned in the text.
- Photographs and plates must be given as computer files containing EPS, TIFF, or JPEG files in 600 dpi and higher resolutions (1200 dpi is preferable) so that all details can be seen in the stage of examination of writing.

6.1. Figures

- Drawings and photos (except for the plates in the text) will be evaluated together as "Figure" and they must be numbered in the order they are mentioned in the text.
- The figures published in the *Bulletin of Mineral Research and Exploration* must be prepared in computer considering the dimensions of single-column width 7.4 m or double-column width 15.8 cm. Figure area together with the writing at the bottom should not exceed 15.8x21in maximum.
- Unnecessasry details must not be given in figures or care must be taken not to use much space for information transfer.
- Figures must be arranged in such a way to be printed in black/white or colored.
- The figure explanations being justified in two margins must be as follows:

  Figure 1. Sandıklı İlçesinin (Afyon); a) güneybatısının jeolojik haritası, b) İnceleme alanının genel dikme kesiti (Seymen 1981), c) Türkiye'nin önemli neotektonik yapıları (Koçyiğit 1994'den değiştirilerek).

  Figure 1.a) Sandıklı ilçesinin güneybatısının jeolojik haritası, b) İnceleme alanının genel dikme kesiti (Seymen 1981), c) Türkiye'nin önemli neotektonik yapıları (Koçyiğit 1994'den değiştirilerek).
- Drawings must be made by well-known computer programs painstakingly, neatly and cleanly.
- Using fine lines, which can disappear when figures shrinks, must be avoided. Symbols or letters used in all drawings must be in Times New Roman and not less than 2 mm in size when shrink.
- All standardized icons used in the drawings must be explained preferably in the drawing or with figure caption if they are too long.
- Linear scale must be used for all drawings. Author's name, figure description, figure number must not be included into the drawing.
- Photos must be in quality and quantity that will reflect the objectives of the subject.

6.2. Plates

- Plates must be used when needed a combination of more than one photo and the publication on a special quality paper.
- Plate sizes must be equal to the size of available magazine page space.
- Figure numbers and linear scale must be written under each of the shapes located on the Plate.
- The original plates must be added to the final copy, which will be submitted, if the article is accepted.
- Figures and plates must be independently numbered. Figures must be numbered in Latin numerals and plates with Roman numerals (e.g., Figure1, Plate I).

- There must be no description text on Figures.

6.3. Tables

- All tables must be prepared preferably in word format in Times New Roman fonts.
- Tables together with table top writing must not exceed 15x8 cm in size.
- The table explanations being justified in two margins must be as follows:

Table 1- Hydrogeochemical analysis results of geothermal waters in the study area.

7. Nomenclature and Abbreviations

- Non-standard and uncommon nomenclature abbreviations should be avoided in the text. But if essential, then they must be described as below. In cases where unusual nomenclatures and unstandardized abbreviations are considered to be compulsory, the way followed and method must be described.
- Full stop must not be placed between the initials of words for standardized abbreviations (MER, SHW, etc.).
- Geographical directions must be abbreviated in English language as follows: N, S, E, W, NE …etc.
- The first time used abbreviations in the text are presented in parenthesis, the parenthesis is not used for subsequent uses.
- The metric system must be used as units of measurement.
- Figure, plate and table names in the article must not be abbreviated. For example, "as shown in the generalized stratigraphic cross-section of the region (Figure 1……..."

7.1. Stratigraphic Terminology

Stratigraphic classifications and nomenclatures must be appropriate with the rules of International Commision on Stratigraphy and/or Turkish Stratigraphic Committee. The formation names, which have been accepted by International Commision on Stratigraphy and/or Turkey Stratigraphy Committee, should be used in the manuscript.

7.2. Paleontologic Terminology

Fossil names in phrases must be stated according to the following examples:

o For the use of authentic fossil names;

e.g. Limestone with *Nummulites*

o When the authentic fossil name is not used;

o e.g. nummulitic Limestone

o Other examples of use;

e.g. The type and species of Alveolina/ Alveolina type and species

- Taxonomic ranks must be made according to the following examples:

Super family: Alveolinacea Ehrenberg, 1939	*Not reference, Not stated in the Reference section*
Family: Borelidae Schmarda, 1871	
Type genus: *Borelis* de Montfort, 1808	
Type species: *Borelis melenoides de Montfort, 1808*; *Nautilus melo* Fitchel and Moll, 1789	
Borelis vonderschmitti (Schweighauser, 1951) (Plate, Figure, Figure in Body Text)	*Schweighauser, 1951 not reference*
1951 *Neoalveolina vonderschmitti* Schweighauser, page 468, figure 1-4	*Cited Scweighauser (1951), stated in the Reference section.*
1974 *Borelis vonderschmitti* (Schweighauser), Hottinger, page, 67, plate 98, figure 1.7	*Cited Hottinger (1974), stated in the Reference section.*

- The names of the fossils should be stated according to the rules given below:

  - o For the first use of the fossil names, the type, spieces and the author names must be fully indicated;

    Alveolina aragoensis Hottinger

    Alveolina cf. *aragoensis* Hottinger

    Alveolina aff. *aragoensis Hottinger*

  - o When a species is mentioned for the second time in the text;

    A.aragoensis

    *A.*cf.*aragoensis*

    *A.*aff.*aragoensis*

  - o It is accepted as citiation if stated as *Alveolina aragoensis* Hottinger (1966).

- The statement of plates and figures (especially for the articles of paleontology):

  - o for the statement of species mentioned in the body text;

  Borelis vonderschmitti (Schweighauser, 1951).

  (plate, figure, figure in the body text).

  - o When cited for other articles;

  1951 *Neoalveolina vonderschmitti* Schweighauser, page 468, figure 1-4, figure in body text

  1974 *Borelis vonderschmitti* (Schweighauser), Hottinger, page 67, plate 98, figure 1-7

- For the citation in the text

  (Schweighauser, 1951, page, plate, figure, figure in the body text)

  (Hottinger, 1974, page, plate, figure 67, plate 98, figure 1-7, figure in the body text.)

8. Citations

All citations in the body text must be indicated by the last name of the author(s) and the year of publication, respectively. The citations in the text must be given in following formats:

- For publications written by single author;

  - It is known that fold axes of Devonian and Carboniferious aged units around Istanbul is in NS direction (Ketin, 1953, 1956; Altınlı, 1999).

  - Altınlı (1972, 1976) defined the general characteristics of Bilecik sandstone in detail.

- For publications written by two authors;

  - The upper parts of the unit contain Ilerdian fossils (Sirel and Gündüz, 1976; Keskin and Turhan, 1987, 1989).

- For publications written by three or more authors;

  According to Caner et al. (1975) the Alıcı formation reflects the fluvial conditions.

  The unit disappears by wedging out in the East direction (Tokay et al., 1984).

- If reference is not directly obtained but can be found in another reference, the cross-reference should be given as follows:

  - It is known that Lebling has mentioned the existence of Lias around Çakraz (Lebling, 1932: from Charles, 1933).

9. Reprints

The author(s) will receive (2) two hard copies of the related issues.

10. Copyright and Conditions of Publication

- It is necessary that the work submitted for the publication must be original and has not been previously unpublished in whole or partially.

- It is necessarry that the authors who send their publications to the *Bulletin of Mineral Research and Exploration* hereby accept the conditions of publication of the Bulletin in advance.

- All copyrights of the accepted manuscripts belong to MTA. The author or corresponding author on behalf of all authors (for papers with multiple authors) must sign and give the agreement under the terms indicated by the Regulations of Executive Publication Committee. Upon acceptance of an article, MTA can pay royalty to the authors upon their request according to the terms under the "Regulations of Executive Publication Committe" and the "Regulations of Royalty Payment of Public Office and Institutions"

All the information and forms about the *Bulletin of Mineral Research and Explorations* can be obtained from **http://dergi.mta.gov.tr**